July 2017

Characterization of Electronic and Ionic Transport in Soft and Hard Functional Materials

Lawrence A. Renna
University of Massachusetts Amherst

CHARACTERIZATION OF ELECTRONIC AND IONIC TRANSPORT IN SOFT AND HARD FUNCTIONAL MATERIALS

A Dissertation Presented

by

LAWRENCE A. RENNA

Submitted to the Graduate School of the
University of Massachusetts Amherst in partial fulfillment
of the requirements for the degree of

DOCTOR OF PHILOSOPHY

May 2017

Department of Chemistry

CHARACTERIZATION OF ELECTRONIC AND IONIC TRANSPORT IN SOFT AND HARD FUNCTIONAL MATERIALS

A Dissertation Presented

by

LAWRENCE A. RENNA

Approved as to style and content by:

_____
D. Venkataraman, Chair

_____
Michael D. Barnes, Member

_____
Anthony D. Dinsmore, Member

_____
Dimitrios Maroudas, Member

_____
Richard W. Vachet, Head
Department of Chemistry

DEDICATION

To my family:

To my parents Larry D. and Judy who have always supported me and told me how proud they were even from the other side of the world.

To my sister Sarah, who is a truly great and caring person.

To my grandparents Clifford and Carol, who supported me with this computer, which all of my PhD work was written on.

To Hilary and Larry W.B., who have taught me the true joys of love and family.

ACKNOWLEDGMENTS

My time at University of Massachusetts Amherst has been highly collaborative and fulfilling. I would like to start by thanking my committee: Prof. Michael Barnes for his advice on scanning probe techniques, Prof. Anthony Dinsmore for all the useful discussions on nanoparticle assemblies, and making physics more accessible, Prof. Dimitrios Maroudas for his continued encouragement that I can do computation, and Prof. Paul Lahti for thinking enough of me to support me through EFRC. I am very grateful for all their input over my time here.

I would like to thank all the DV group members that have made my time a pleasurable and successful one: Dr. Sravan Surampudi, Dr. Dana Algaier, Dr. Timothy Gehan, Connor Boyle, Seung Pyo Jeong, Christie Cutting, Sashi Debnath, Gautam Satishchandran, and Julia Lenef. I would also like to thank Prof. Alex Ribbe, Prof. Thomas Russell, Prof. Ramesh Adhikari, Prof. Mark Tuominen, and Dr. Sekar Thirunavukkarasu for their help and contributions. I would also like to thank my former advisors Prof. Rein Kirss and Prof. Yongwoo Lee for getting me excited about science as an undergrad.

I would like to extend a special acknowledgment to Dr. Yao Liu from Prof. Russell's group for a truly great collaboration. Yao is an expert at device fabrication and testing, and I have enjoyed working with and learning from him. Together we have done some really nice work.

I would especially like to acknowledge Prof. Monojit Bag who has had an enormous impact on me as a scientist. Mono and I spent many hours talking science and developing ideas. Even from India, Mono has still provided invaluable help in my research. Mono was also an excellent teacher, I remember a time he picked a simple laser pointer, and just started explaining the physics involved in its operation. This is just an example of how good Mono was to me when he was at UMass.

Last, and most importantly, I must thank my advisor DV. DV has been the best best advisor, mentor, colleague, and friend I could hope for. DV has provided countless advice to me, no matter how many times I changed my mind or seemed confused. I always felt comfortable to run into his office, tell him my problems; and he always helped me.

His excitement and enthusiasm for science, and the research we are doing in the lab is highly infectious; this is the reason I enjoy spending my days in the lab. He is almost always available to his and other students, and loves to discuss science. DV lacks the ego that sometimes develops in research faculty that prevents them from openly discussing science with others. He is not worried about sharing his ideas, and therefore has open discussions across campus, which has led to great collaborations and opportunities for our lab.

DV helps me and the other students become better professional scientists by sharing with us and involving us in all aspects of academic research. DV is very good at supporting his students based on their individual needs, he can tailor his mentor style to cater to what will be most beneficial to each student; I believe this is a valuable skill that is not persistent throughout graduate school mentors. DV does not just think that professors should focus on grant writing and graduate students should just be in the lab; this helps make his students more well-rounded and better prepared for what lies beyond graduate school.

Simply put, DV breaks down the hierarchical barrier that can exist between students and professors. He wants to involve students in all aspects of the Ph.D. experience and discuss exciting science with them.

Thank you so much DV.

ABSTRACT

CHARACTERIZATION OF ELECTRONIC AND IONIC TRANSPORT IN SOFT AND HARD FUNCTIONAL MATERIALS

MAY 2017

LAWRENCE A. RENNA

B.S., NORTHEASTERN UNIVERSITY

Ph.D., UNIVERSITY OF MASSACHUSETTS AMHERST

Directed by: Professor D. Venkataraman

Control over concurrent transport of multiple carrier types is desired in both soft and hard materials. For both types of materials, I demonstrate ways to characterize and execute governance over *both electronic and ionic transport*, and apply these concepts in the fabrication of devices with applications in conducting composites, photovoltaics, electrochemical energy storage, and memristors.

In soft materials, such as polymers, the topology of the binary polymer mesoscale morphology has major implications on the charge/ion transport. Traditional approaches to co-continuous structures involve either using blends of polymers or diblock copolymers. In polymer blends, the structures are kinetically trapped and thus have poor long term stability. In diblock polymers, such morphologies are not universally accessible to non-random coil polymers. I discuss an approach to binary polymer mesoscale morphologies via the assembly of polymer nanoparticles. In this strategy, polymers are assembled into spherical nanoparticles, which are then assembled into hierarchical mesoscale structures. First, I demonstrate, experimentally and computationally, that the electrical transport in semiconducting/insulating polymer nanoparticle assemblies can be predictably tuned according to power law percolation scaling. Then I show that nanoparticle

assemblies can be utilized for tunable concurrent transport of electrons and holes for photovoltaics, and for electronic and ionic charges aimed at applications in electrochemical energy storage.

For hard materials, I detail the characterization of mixed electronic and ionic transport in hybrid organic/inorganic lead triiodide perovskites. I used the understanding of mixed electronic and ionic transport in these materials to explain poorly understood phenomena such as photo-instability and current-voltage hysteresis. Then, I show several examples of interfacial materials, and the characterization and implications of their respective work functions, as charge transport materials to control selective charge extraction from perovskites. And finally, I show how interfacial charge transport materials with ionic functionality can be used to change the interfacial chemistry at perovskite/charge transport material interfaces to control both electronic and ionic transport. In this regard, I demonstrate how an adsorbing interface for mobile ions can be used to control current-voltage hysteresis and state-dependent resistance, introducing a novel paradigm of interfacial ion adsorption to fabricate novel perovskite-based memristor devices.

TABLE OF CONTENTS

LIST OF TABLES

LIST OF FIGURES

CHAPTER 1

INTRODUCTION

1.1 Concurrent Transport in Soft and Hard Materials

The ability to control and tune transport, whether it be charge, ion, heat, or mass, is ubiquitously sought after in both hard and soft materials. In materials chemistry, there are a few general approaches to control transport: 1) the synthesis of materials with atomic to molecular (<1 nm) level properties, 2) the assembly and subsequent structure of molecules and molecular aggregates with properties on the nanoscale (1-100 nm) to mesoscale (>100 nm-100 μm), and 3) the use of interfacial materials to tune the the interfacial and bulk properties of the material. The natural progression of the problem is how does one execute systematic control of concurrent transport of multiple carriers, *e.g.* electronic and ionic, or holes and electrons, in a composite material. This document has two major thrusts: 1) for soft materials, the fabrication of binary polymer morphologies for concurrent transport of two types of carriers, and 2) for hard materials, the use of interfaces to control electronic and ionic conduction in hybrid organic/inorganic lead triiodide perovskites. This work shows the potential impact of these materials on conducting composites, photovoltaics, lithium ion batteries, and memristors.

1.1.1 Soft Materials: Polymers

In soft, carbon-based materials, transport properties are dictated by the molecular structure, the assembly of molecules into nanoscale aggregates, and the assembly of those nanoscale aggregates into mesoscale structures. A useful example of this concept of hierarchical structure property correlations is poly(alkylthiophene), a semiconducting polymer composed of conjugated thiophene rings with solubilizing alkyl substituents. The electronic transport through materials composed of poly(alkylthiophene) is impacted by its structure on multiple length

scales. The conduction of electronic charges through a polymer chain occurs through the overlap of π-molecular orbitals, which is determined by the connectivity of thiophene monomers in the polymer chain. Polymer chains can assemble into nanoscale aggregates, *e.g.* nanowires, and the electronic properties of nanoscale aggregates are highly sensitive to the "order" of polymer chain packing, this has a measurable impact on the transport of charges between polymer chains. Lastly, the assembly of nanoscale aggregates, and their connected topologies, affects transport of charges over larger, device relevant length scales. Thus the structure of poly(alkylthiophene) on multiple length scales has a profound impact on the charge transport properties. Now if one wanted to achieve bicontinuous conduction of two different types of charge carriers in binary polymeric systems, this hierarchical control must be exercised over both polymer types simultaneously; this has proven difficult to achieve. I will focus on the polymer morphologies on the nano- and mesoscale.

Particularly for polymers, there is a general problem to assemble two or more polymers into nanoscale and mesoscale structures with desired structural control, over a broad range of materials, to execute governance over transport properties. [1-8] The phase behavior of two polymers[*] is dictated by the equilibrium thermodynamics, phase separation dynamics, and crystallization kinetics, in short a myriad complicated and intertwined processes. Polymer blends can exist in a single phase mixed state, or a phase separated state. In an equilibrium phase separated state, interfacial energy is reduced by minimizing surface area resulting in large domains. As the mixing of polymers is rather complex, I'll discuss the simplest case, the mixing of two linear homopolymers, polymer architecture, *e.g.* graft block copolymers, star block

[*] This introduction on polymer-polymer phase behavior is a summary of the article: Bates, F. "Polymer-polymer phase behavior." *Science* 251.4996 (1991): 898-905.

copolymers, has a major influence on the mixing thermodynamics. The interaction energy between polymer segments determines the sign and extent of mixing. Polymer segment-segment interaction is approximated by the Flory-Huggins parameter (χ): $\chi = \frac{1}{k_B T}\left[\epsilon_{AB} - \frac{1}{2}(\epsilon_{AA} - \epsilon_{BB})\right]$, where ϵ_{ij} is the contact energy between *i* and *j* polymer segments and k_B is Boltzmann's constant or by: $\chi = aT^{-1} + \beta$, where *a* and β are the experimentally measured enthalpy and excess entropy coefficients respectively. If χ is positive, then the energy of mixing is higher than the energy of a phase separated state. ϵ_{ij} can be estimated by the van der Waals forces between polymer segments: $\epsilon_{ij} = -\sum_{i,j} \frac{3}{4} \frac{I_i I_j}{I_i + I_j} \frac{\alpha_i \alpha_j}{r_{ij}^6}$, where *I* is the ionization potential, α is polarizability, and *r* is the interaction distance. Flory and Huggins determined the change in Gibbs free energy for polymer mixtures: $\frac{\Delta G_m}{k_B T} = \frac{\phi_A}{N_A} \ln \phi_A + \frac{(1-\phi_A)}{N_B} \ln(1 - \phi_A) + \phi_A(1 - \phi_A)\chi$, where N_x is the number of segments per polymer chain, and ϕ_A is the volume fraction of polymer *A*. By evaluating this equation for equilibrium, stability and criticality, the phase diagram (see Figure 1) can be calculated. There exists a critical point between one and two phases for polymer blends, and the critical volume fraction (ϕ_c) and critical Flory-Huggins parameter (χ_c) are calculated by $\phi_c = \frac{N_A^{1/2}}{N_A^{1/2} + N_B^{1/2}}$ and $\chi_c = \frac{\left(N_A^{1/2} + N_B^{1/2}\right)^2}{2 N_A N_B}$ respectively. Thus, the phase behavior can be tuned by changing N_A/N_B, or by changing changing structural or chemical aspects of the polymer. The power of this illustrated in mixtures of protonated and deuterated homopolymers, which can phase separate at high molecular weights.[9]

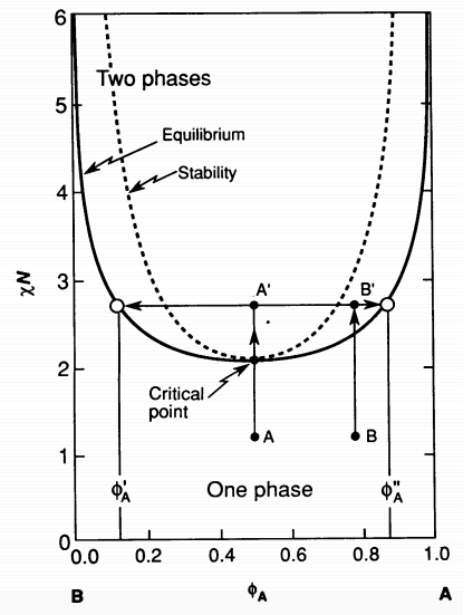

Figure 1: Phase diagram for polymer blends. Adapted with permission form Ref. [9].

The dynamics of phase separation are categorized as nucleation and growth, or spinodal decomposition, shown in Figure 2. The former occurs by diffusion of polymer chains into growing beads of the lesser phase, until an equilibrium state is reached, and then growth proceeds, albeit slowly, via Ostwald ripening and coalescence. If a polymer mixture exists in a thermodynamically unstable state, it can spontaneously phase separate into metastable random bicontinuous morphologies, in what is known as spinodal decomposition. The phases grow in order to reduce interfacial area into larger domains. These metastable bicontinuous morphologies will coarsen over time,[9] and thus must be kinetically trapped by thermal quenching[10] and jamming of particles at the interface.[11,12]

Further, when functional semi-crystalline polymers, crystallization kinetics cloud the understanding of polymer-polymer phase behavior. There exists many local minimum in the free energy landscape.[13] In many cases desired morphologies, *e.g.* bicontinuous morphologies, are unobtainable in desired systems.

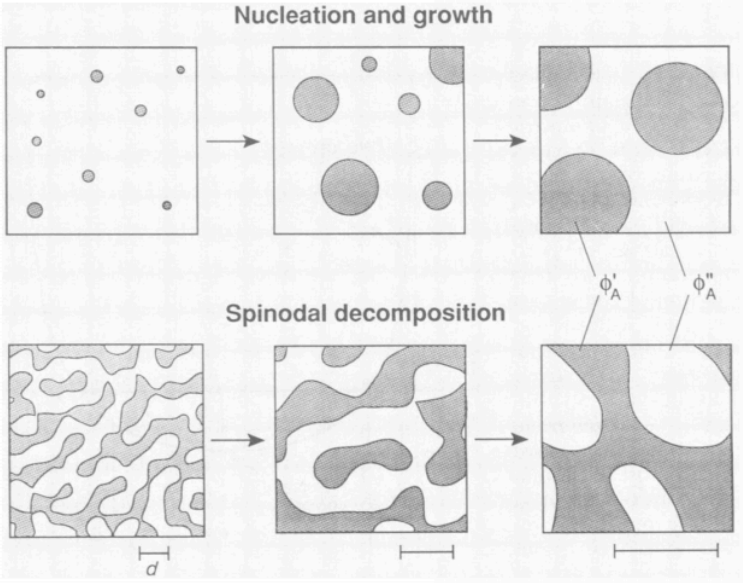

Figure 2: The dynamics of polymer-polymer phase separation (top) nucleation and growth and (bottom) spinodal decomposition. Adapted with permission from Ref. [9].

It is important to mention diblock copolymers as an approach to achieve desired morphologies, particularly bicontinuous morphologies. In the diblock copolymer approach, the two polymer are covalently bound, thus no matter how much (energetically) the system wants to phase separate, it can only do so as a far a polymer chains can stretch resulting in microphase not macroscopic phase separation of polymer constituents.[9] Therefore, the enthalpy of microphase separation $H \sim \chi$, confining the connections between blocks to interfaces. The polymer stretches in order to form uniform phase density; stretching reduces the configurational entropy of the polymer, entropy $S \sim N^{-1}$, (where N is the degree of polymerization). Thus the state of microphase separation in diblock copolymers is defined by the product: χN. The crossover between entropically and enthalpically dominated states occurs at $\chi N \approx 10$, the so-called order-disorder transition. In this first order transition, entropically favored disordered microphase separation goes to a periodic, ordered microphase separated state. The volume fraction of one block to

another, f, affects the shape and symmetry of the separated microphases (see Figure 3), and has little dependence χN, at sufficiently high χ, co-called the strong segregation limit. The phase diagram, shown in Figure 4 for the well-studied polystyrene-*b*-polyisoprene, contains body-centered cubic lattice ($f < 0.17$), hexagonally packed cylindrical lattice ($0.17 < f < 0.28$), a bicontinuous double diamond structure ($0.28 < f < 0.34$) of the minority phase in a matrix of the major phase, and lamellar structure ($0.34 < f < 0.62$). The phase diagram is symmetric for 1-f, that is, the phase diagram is the same, but the major and minor phase switch.[9]

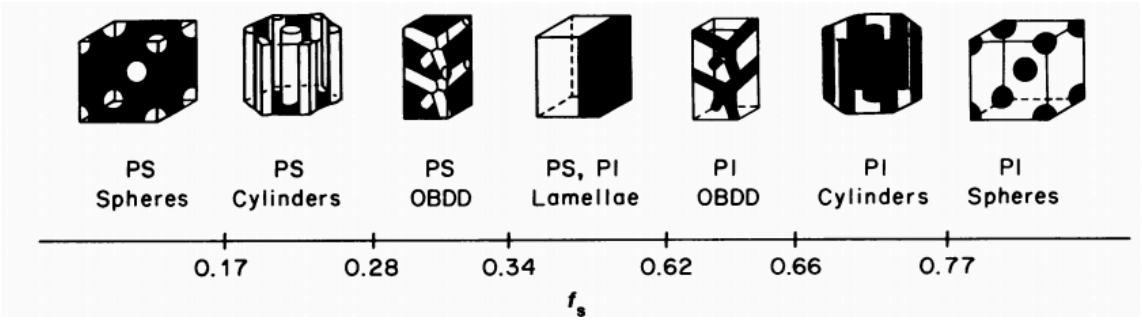

Figure 3: Ordered phase symmetry of diblock copolymer by varying the volume fraction (f) of the two blocks. Adapted with permission from Ref. [9].

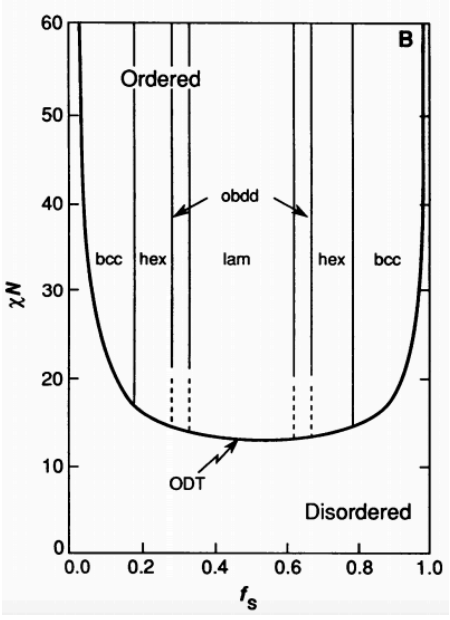

Figure 4: Diblock copolymer phase diagram. Adapted with permission from Ref. [9].

Though[†] an amazing array of useful structures have been created using diblock copolymers, there are several issues that have prevented diblock copolymers from being ubiquitously used for the fabrication of desired polymer morphologies. The first is obvious, the synthesis of diblock or multiblock copolymers adds additional layer of complexity to fabrication process. Secondly, as noted by F. S. Bates,[9] there is inherent non-universality to the diblock copolymer phase diagram. At moderate χ, *i.e.* weak segregation limit, "a unique phase diagram can be associated with each value of N". Further, some diblock copolymers have a thermally accessible order-order transition, while some polymers clearly do not. Lastly, although the bicontinuous structure is established for coil-coil diblock copolymer,[14] this morphology is atypical in rod-rod and rod-coil block copolymers,[15-20] thus making it difficult to form with rigid conjugated polymers which are desired for electronic and optoelectronic applications. Additionally, the bicontinuous morphology will not form if the blocks of the diblock copolymer are miscible. This example illustrates the need for new strategies to create nanoscale morphologies through self-assembly, which provides access to structures that are not obtainable using current methods. In Chapter 2.1 NANOPARTICLE ASSEMBLIES AS A MEANS TO REALIZE BINARY POLYMER MESOSTRUCTURE I discuss a new approach to polymer morphologies via the self-assembly of polymer nanoparticles, and demonstrate tunable concurrent conduction. In this method, polymers can be assembled in to nanoparticles with control over the nanoscale packing, and the nanoparticles can be assembled into mesoscale morphologies with predictable structures and properties. First, I answer the question: what are the rules for charge percolation in

---

[†] Section is adapted, in parts, with permission from a book chapter: Renna, Lawrence A., Timothy S. Gehan, and D. Venkataraman. "Polymer Nanostructures through Packing of Spheres." *Optical Properties of Functional Polymers and Nano Engineering Applications* 1 (2014): 227.

semiconductor/insulator polymer nanoparticle assemblies? I then apply those concepts to concurrent conduction of holes and electrons for photovoltaics, and for ionic and electronic charges with applications in electrochemical energy storage. I also address the question regarding what structures can be obtained in binary nanoparticle assemblies using a combination of experiment and computation.

1.1.2 Hard Materials: Perovskites

Hard, mixed electronic-ionic conductors (MEICs)[‡] are different from binary polymer blends because they only contain one phase. According to Reiss,[21] transport in MEICs occurs through defects. In MEICs, there are five types of charged defects that can exist, they are: 1) mobile ionic defects with static charge, 2) mobile ionic defects with variable charge, 3) immobile ionic defects with static charge, 4) immobile ionic defects with variable charge, and 5) electrons in the conduction band and holes in the valence band. Immobile defects are still important to consider because they are intimately linked to mobile ones, discussed later on. Generally, electron conduction occurs in solid-state semiconductors when electrons are promoted to the conduction band, and hole conduction occurs when electrons are removed from the valence band. In semiconductors, electrons can be promoted across the band gap to the conduction band thermally or optically; also electrons can be injected into conduction bands from electrodes. Alternatively, electronic conduction may also occur through a hopping mechanism through dopant/vacancy defect bands. The electronic charge carrier transport mechanism can be determined experimentally by the dependence on the ratio of dopant ions. For example, in yttria-stabilized

---

[‡] I would like to acknowledge the use of Riess, Ilan. "Solid State Electrochemistry." *Israel Journal of Chemistry* 48.3- 4 (2008): 143-158 as an important source for understanding solid MEICs.

zirconia with Mn dopant atoms, electronic conduction is proportional to [Mn(II)]/[Mn(III)], while hoping conductivity is proportional to [Mn(II)][Mn(III)].[21]

According to Riess ionic conduction occurs in solid MEICs when the bonding is predominantly ionic. Riess also states that there are two criteria to have ionic conduction: 1) there must be a vacancy "not far" from an ion, to hop to, and 2) sufficient thermal energy must be applied in order to overcome the activation energy barrier between the two states. The motion of ion hopping in a sublattice of ions M, goes like $M^{zq} + V_M \rightarrow V_M + M^{zq}$, where z is the valency, q is the elementary charge, and V_M is a vacancy for ion M. In general, vacancies for ion hoping are the next nearest neighbor to the hopping ion, see Figure 5. Thus, the energy barrier to hopping is due to the repulsion of the oppositely charged nearest neighbor which the hopping ion must pass to occupy a vacancy. It is also important to consider the sublattice that contains hopping ions and vacancies, because the energy of the left and right state in the above equation for the motion of ions must be equal or at least similar. If ions occupy two different types of sites, division into two sublattices is required for hoping.[21]

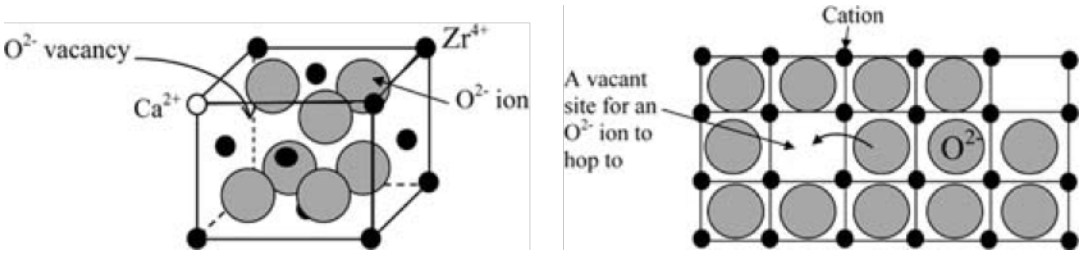

Figure 5: Oxygen vacancy hopping in ZrO2 doped with CaO. Adapted wither permission from Ref. [21]

Another ionic transport mechanism in MEICs is through interstitial sites, the natively unoccupied site between nearest neighbors in a given lattice. In this transport mechanism, ions can be promoted to an interstitial defect state, and then hop from interstitial site to a nearby

interstitial site. When many ions occupy interstitial defect sites the sublattice that it occupied "quasi-melts", and ions flow like a fluid around the rigid sublattice of the oppositely charged ions.[21]

Furthermore, mobile ions in a lattice polarize nearby ions, repelling ions with the same polarity sign and attracting those with different polarity. This polarization results in a lower energy trap state for the ion. There is a characteristic relaxation time (τ) for this polarization, thus the frequency of an applied AC voltage must by large enough, such that the period is shorter than the trap polarization time τ, where the τ depends on the temperature.[21]

As the ionic transport mechanism in MEICs is hopping from point defects, *e.g.* vacancies or interstitial sites, both thermally activated processes, ionic conductivity decreases as the temperature decreases, however there are still examples of high ion conductivity at low temperatures, *e.g.* Ag_4RbI_5. Point defects for ionic transport can be created, according to Riess, by thermal excitation, extrinsic doping, or chemical changes such as changes in stoichiometry or partial pressure.[21]

It was mentioned previously, that immobile and mobile defect sites can be intimately connected, and in fact, in some MEICs, the ionic and electronic transport can be connected. To illustrate this, consider the example of $Gd_{0.18}Ce_{0.92}O_{1.95}$, which contains ~5% oxygen ion vacancies (immobile ionic defects with fixed charge). Oxygen vacancies act like donors (see Figure 6), because they leave loosely bound electrons in the inorganic lattice, at energy levels between the valence and conduction bands. These electrons can be thermally promoted to the conduction band, *i.e.* electronic transport. Under certain conditions, O^{2-} can hop though vacancies, and actually leave the system, effectively doping the solid further by increasing the

number of oxygen ion vacancies. Thus, in $Gd_{0.18}Ce_{0.92}O_{1.95}$, the ionic transport affects the electronic transport.[21]

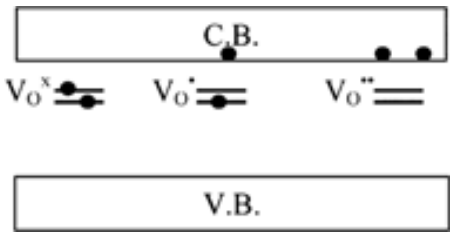

Figure 6: Oxygen vacancy energy levels in $Gd_{0.18}Ce_{0.92}O_{1.95}$, and how it behaves as a donor. The vacancy states from left to fight are, neutral defect with two electrons, defect with 1- charge, where an electron has been promoted to the conduction band (C.B.), and an oxygen vacancy with a 2- charge, where both electrons have been promoted to the C.B. Adapted with permission form Ref. [21].

Interfacial materials also play an important role in the transport of electronic and ionic species. Intuitively, if an interface is blocking to a particular mobile species, it will tend to accumulate at the interface (space charge). Therefore, to prevent the buildup of electronic charges at an interface, the interfacial materials should have appropriate energy levels with respect to the bulk conductor, and sufficient charge carrier mobility to transport charges.[22] The work function of interfacial charge transport materials also creates a built in potential across a material, which affect the charge transport through the bulk.[23,24] In general, interfaces with ionic conductors can be various degrees of blocking, conducting, adsorbing, or reactive.[25] For ionic conducting interfaces, interfaces can provide new kinetic pathways to transport, or alter the point defect concentration at the interface. Ionic conductivity has been shown to dramatically increase in space charge regions.[26] Furthermore, the lattice structure match or mismatch affects the transport of ions at an interface. For example, there is a significant energy barrier for Ag^+ to transport across an AgI|Ag interface.[21] As mentioned previously in many MEICs, the electronic and ionic transport are intimately connected, therefore, the use of an interfacial

materials that affects the transport of one species could impact the transport of the other. For example, the accumulation of ions at an interface can create a polarization across the bulk of a material, which in turn affects the transport of electronic charges,[27,28] even resulting in ON/OFF current switching.[29]

Though there are many different materials that are MEICs, I will focus on the perovskite family of structures, with stoichiometry AMX_3. Many metal oxide perovskites have been shown to have concurrent electronic and oxygen ion conduction.[30] Recently, a class of organo-Pb/Sn trihalide perovskites have garnered attention due to their use as active materials in highly efficient photovoltaics,[31-34] and other varying applications,[35-40] see Chapter 3.1 . Though these materials exhibit highly desirable optoelectronic properties, they also display some undesirable and not fully understood properties, such as: poor stability under ambient conditions,[31,41] current-voltage hysteresis,[42] switchable photocurrent direction,[29] and maybe most importantly, they degrade upon prolonged exposure to sunlight.[43] I answer some of these questions by combinding concepts from mixed conductors to these materials. Though ionic transport in metal oxide perovskites has been known for decades,[30] but it has largely been unexplored in organo-Pb/Sn trihalide perovskites. There have been some reports which have explored ionic drift/transport in the these perovskite materials,[28,29,44-48] though the cause, impact, and the ability to control ionic transport has not yet been fully understood. Interestingly, these perovskites are ambipolar (they transport holes and electrons) and ionic conductors, thus they conduct more than two types of mobile species, depending on how many types of ions, *i.e.* organic cation, halide, are also transported.

A main question addressed herein, is how can we control electronic and ionic transport in perovskite materials. The approach addressed in this document is the use of interfaces to control

electronic and ionic transport in organo-Pb/Sn trihalide perovskites. For electronic transport, we study the use of charge transport materials on charge extraction from perovskite layers, particularly how work function modification at interfaces affects electronic transport. For ionic transport, we elucidate the contributing factors to ionic transport in perovskite layers, and then use charge transport materials with different ionic properties, at interfaces with perovskites, in order to control ionic transport.

CHAPTER 2

ELECTRONIC AND IONIC TRANSPORT IN BINARY POLYMER NANOPARTICLES ASSEMBLIES

2.1 Nanoparticle Assemblies as a Means to Realize Binary Polymer Mesostructures

The purpose of this chapter[§] is to introduce the need for controlled assembly of materials on multiple length scales, and how nanoparticles can be used as building blocks to construct functional materials. Fabricating macromolecular mesoscale assemblies containing disparate components with targeted molecular order for each of the components on the nanoscale and targeted assembly of the components in the mesoscale is a challenge. In this chapter, we explore the self-assembly of polymer nanoparticles as a viable route to obtain tunable mesostructured materials. We describe the state-of-the-art methods available for and the challenges to obtain spherical and nonspherical polymer nanoparticles. We discuss the predicted ordered assemblies and disordered assemblies of nanoparticles and the challenges to obtain these assemblies in polymer nanoparticles. We also comment on the rich and future opportunities in the burgeoning field of polymer nanoparticle assemblies.

Macromolecular mesoscale science—the fabrication and study of macroscopic macromolecular assemblies with molecular packing features in multiple length scales—is an emerging area of research, rich with exciting scientific and technological challenges and opportunities.[49-51] The archetypical and often quoted example of a macromolecular mesoscale assembly is the tobacco

---

[§] This chapter was adapted with permission from the Perspective: Renna, Lawrence A., Connor J. Boyle, Timothy S. Gehan, and D. Venkataraman. "Polymer Nanoparticle Assemblies: A Versatile Route to Functional Mesostructures." *Macromolecules* 48, no. 18 (2015): 6353-6368, Thus, I would like to acknowledge Connor J. Boyle, Timothy S. Gehan, and D. Venkataraman for their valuable collaboration on this Perspective.

mosaic virus, wherein the constituent protein assembles into discrete nanoscale assemblies, which self-assemble into a helical rod around a single-stranded RNA core.[52] Inspired by such examples from nature, the self-assembly of nanoscale building blocks is emerging as a powerful approach towards creating mesoscale structures with control of the assembly at multiple length scales. Representative examples of such building blocks include but are not limited to inorganic nanoparticles,[53,54] tethered particles,[55-59] macromolecules,[60-63] polymer micelles and nanoparticles,[64-69] foams and soft colloids,[70-74] and liquid crystals[75] (Figure 7). These building blocks have provided a fantastic array of structures, morphologies, and materials.[76] The stage is now set to address the next major challenge in this area—fabrication of macromolecular mesoscale assemblies containing *disparate* components with targeted molecular order for *each* of the components on the nanoscale, and targeted assembly of the components in the mesoscale.[49]

There are many existing examples of polymer-based materials and composites that require integration of two or more disparate components and their assembly into specific hierarchical structures.[77-89] Many of these materials have competing, but precise requirements of molecular assembly at the nanoscale and overall macroscopic morphology. Therefore, fabricating such materials is a challenge. The method of choice for fabricating such materials is by blending disparate components. But, an inherent limitation of blending is that the morphology is often dictated by the interplay and delicate balance of multiple kinetic processes.[90] Thus, achieving targeted molecular order for *each* of the components at *multiple* length scales is difficult and perhaps impossible. The outcome is typically a compromise that sacrifices performance. Thus, we desperately need a method that allows disparate components to be individually optimized for molecular order on the nanoscale, and the assembly of these

components into mesoscale structures. Such a method can serve as a mix-and-match platform technology enabling systematic and efficient incorporation of a spectrum of functionalities in materials, thus vastly expanding the scope of polymer-based materials.

In recent years, there is a burgeoning interest in using nanoparticles as building blocks to create mesoscale assemblies.[53,91-95] Assemblies of nanoparticles are dictated by the principles of packing of geometric shapes and interparticle interactions. For example, spherical, nanoparticles can self-assemble into ordered or disordered mesoscale structures, which can be predicted from the principles of sphere packing.[96-99] Thus, in principle, there are no constraints on the nature of the nanoparticles and one can mix multiple and disparate components! The promise and prognosis of nanoparticle assemblies is captured aptly by the following quote in a recent review article: "The simplicity of supraparticle assemblies, their multifunctionality, structural versatility, and similarity with viral particles represent interesting directions for future research in nanostructures".[100] Most recent studies on nanoparticle assemblies have been dominated by inorganic nanoparticles, and we direct the reader to key comprehensive reviews that have appeared on this subject.[53,54,101,102] In this Chapter, we focus on the promise and prognosis of polymer nanoparticle assemblies.

What can we learn about nanoparticle assemblies if polymer nanoparticles are used instead of inorganic nanoparticles? The consensus in the field is that we understand 'ideal' nanoparticle assemblies, i.e. nanoparticles that interact with simple interaction potentials.[103,104] Our understanding of assemblies of anisotropic nanoparticles and of nanoparticles with long-range and short-range interactions is not fully developed. As we will discuss in this Chapter, because of the fantastic diversity of polymers and polymer architectures, polymer nanoparticles provide a versatile platform to tune the interparticle interactions by the choice of the polymers and surface

functionalization. The polymer architectures and their self-assembling propensities can be exploited to create an array of anisotropic nanoparticles with chemically distinct patches and specific interparticle interactions. These opportunities are unique to polymers and cannot be easily accessed in inorganic nanoparticles.

We turn to another important question: how can polymer nanoparticle assemblies lead to advances in macromolecular science, the focus of this journal? First, nanoparticle assemblies can provide easy access to morphologies that are difficult to obtain using existing tools for self-assembly or with desired materials. An illustrative example is the bulk heterojunction structure in photovoltaics, a bicontinuous percolating structure derived from two semiconductor components that are miscible.[105-108] There is a strong process dependence of the morphology on fabrication solvents and additives, their vapor pressures, the ordering and aggregation kinetics of the polymers, phase separation, and post-processing conditions.[109,110] Balancing these processes has been more of an art than a science, whether in the laboratory or on the production line.[111-113] Although bottom-up approaches have been explored,[114,115] controlling the molecular assembly over multiple length scales to achieve morphology suitable for photovoltaic applications has so far remains elusive. As we will illustrate in this Chapter, bicontinuous percolating structures can be obtained in a straightforward manner through binary nanoparticle assemblies.[116] Second, in polymer nanoparticle assemblies, component polymer nanoparticles can be separately optimized with the desired internal packing and size at the nanoscale and then assembled for desired properties. Thus, we can control the molecular assembly in multiple length scales for *each* component of a multicomponent assembly. Third, one can fabricate virtually any polymer into a nanoparticle. Therefore, if one maintains geometry and symmetry of interaction potential one can assemble *any* polymer nanoscale building block to obtain desired polymer

mesoscale morphologies (Figure 8). And one can combine polymer nanoscale building blocks with any other desired nanoscale building blocks to create composite mesoscale assemblies! The possibilities are endless.

The use of polymer-based nanoscale building blocks to create mesoscale structures opens up new and exciting opportunities in the areas of macromolecular self-assembly, supramolecular chemistry, and mesoscale science—from development of new tools for polymer self-assembly to expanding the array of hierarchical structures and morphologies to new polymer-based applications (Figure 7).[49,117]

This Chapter is organized into three sections. The first section focuses on the fabrication of the building blocks—polymer nanoparticles. These nanoparticles are entirely composed of polymers and may have surface functionalities for assembly. In this section, we discuss common methods for the fabrication of nanoparticles, polymer morphologies and assemblies *within* the nanoparticles, and fabrication of nanoparticle clusters. The second section focuses on nanoparticle assemblies. In this section, we discuss the roles of shape of the nanoparticles and interparticle interactions on the structures of nanoparticle assemblies. The third section focuses on functional nanoparticle assemblies. In this section, we discuss the use of nanoparticle assemblies to fabricate active layers of existing and perspective functional materials. In each section, we provide our perspective of the existing challenges and emerging opportunities. We use three length scale in this Chapter: molecular (<1 nm), nanoscale (1-100 nm), and mesoscale (>100 nm-100 μm).[118] The boundaries of these categories are diffuse.

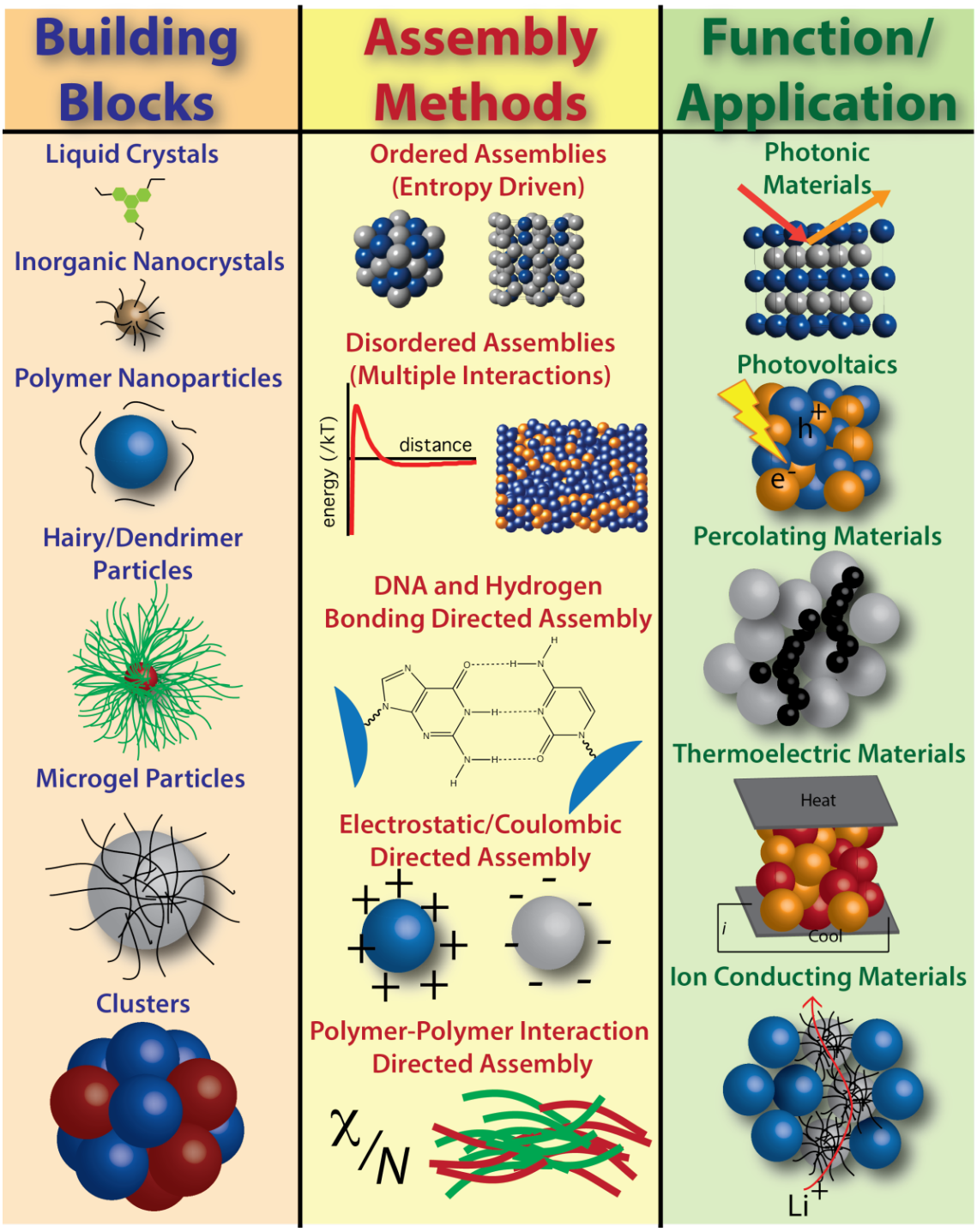

Figure 7: Building blocks, assembly methods, and potential applications in mesoscale polymer and macromolecular science.

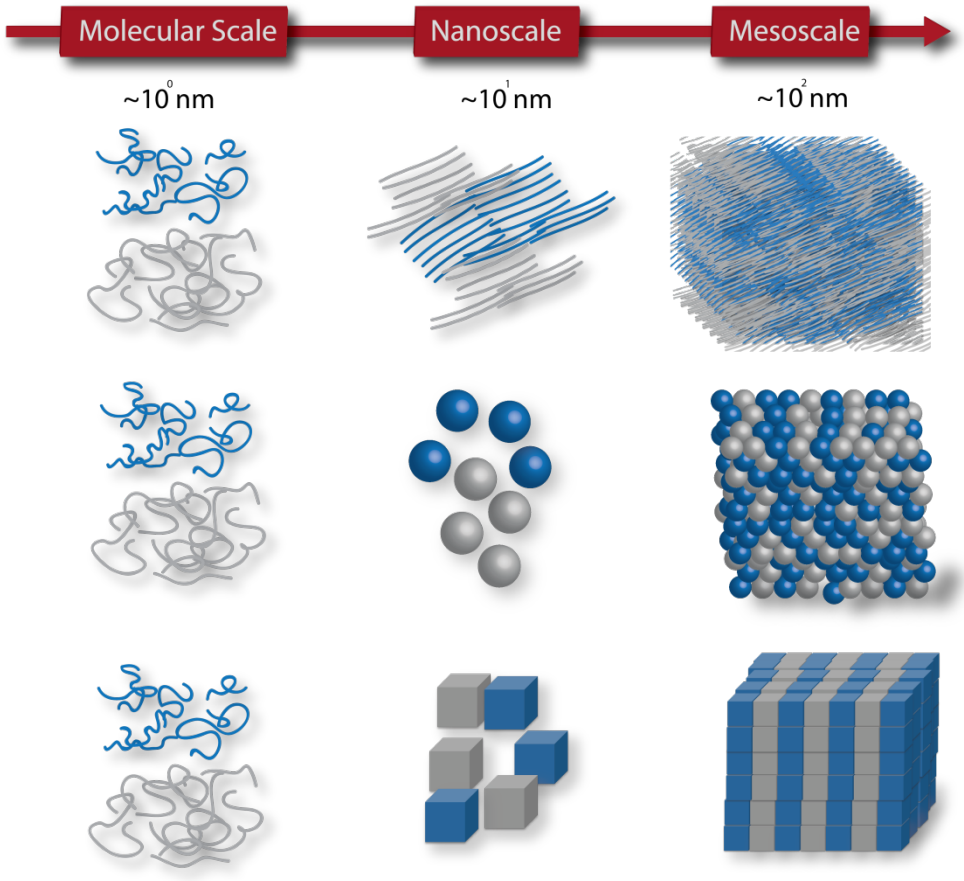

Figure 8: Schematic representation of the organization of polymers from the molecular scale, to the nanoscale, to the mesoscale using conventional polymer assembly techniques, and the new geometrically dictated assembly of nanoscale building blocks (e.g. spheres and cubes) to achieve polymer mesostructures.

2.1.1 Fabricating Polymer Nanoparticles

The first step to geometric assembly is the fabrication of polymer nanoparticles of specific geometric shapes. Two common methods of preparing polymer nanoparticles are: *direct polymerization nanoparticle fabrication*, where the nanoparticles are fabricated directly from the polymerization of the monomers, and by *post-polymerization nanoparticle fabrication*, where polymer nanoparticles are prepared from a pre-formed polymer. We direct the reader to an

excellent review[119] by Rao and Geckeler for the description of various methods for polymer nanoparticle fabrication.

2.1.1.1 Direct Polymerization Nanoparticle Fabrication

Direct polymerization is typically the polymerization of monomer droplets through emulsion, micro-emulsion, or mini-emulsion techniques. Direct polymerization typically provides spherical nanoparticles with low size dispersity (< 10%)[120] and the size of the nanoparticles is easily controlled by varying the monomer, surfactant, or co-stabilizer concentrations.[121] Direct polymerization can also be surfactant-free, but the sizes of the nanoparticles obtained by this method are typically >150 nm.[119] The polymers within the nanoparticles can be cross-linked with appropriate co-monomers to retain the shape of the nanoparticle and disperse them in various solvents.[120,122,123] Direct polymerization is well established for obtaining polymer nanoparticles from styrene-based and acrylate-based monomers.[120,121,124,125] More recently, this method has been used to fabricate nanoparticles using palladium-mediated cross-coupling reactions,[126-130] and other controlled polymerization techniques,[120,131-134] thus expanding the scope of the monomers that can be used.

2.1.1.2 Post-Polymerization Nanoparticle Fabrication

Post-polymerization nanoparticle fabrication, as the name indicates, is the fabrication of nanoparticles using synthesized polymers. Two of the most common post-polymerization methods are the solvent evaporation method and the reprecipitation method.[119] In the solvent evaporation method (see Figure 9), the polymer is dissolved in an ‘oil’ phase, typically a ‘good’ solvent for the polymer that is immiscible with water, and the solution is added to an aqueous surfactant solution.[64,135] Removal of the solvent (‘oil’ phase) at elevated temperature provides aqueous dispersions of polymer nanoparticles. The miniemulsion method is a type of

solvent evaporation method wherein an oil-in-water emulsion is subjected to ultrasonication to create droplets of the 'oil' phase stabilized by surfactants.[119,124,136] In principle, this method can be used with any two or more *immiscible* solvents. In practice, water is typically the dispersing solvent, thus the dispersing phase choice is limited. In the reprecipitation method, the polymer is dissolved in a 'good' solvent for the polymer and is quickly added to a 'poor' solvent for the polymer that is *miscible* with the 'good' solvent.[119,137,138] Water and various alcohols are common 'poor' solvents or dispersing solvents for reprecipitated polymer nanoparticles. Post-polymerization methods typically yield spherical nanoparticles, but the size dispersity obtained in these methods are larger compared to nanoparticles prepared by direct polymerization; the underlying reason for this large size dispersity is not well understood.[139,140] Post-polymerization methods are broader in scope in terms of the polymers and molecules that can be used. Moreover, the polymer aggregation within the nanoparticle can be tuned by varying the fabrication conditions. Control of the polymer aggregation during the reprecipitation method is possible, for example, by varying the temperature of the 'good' solvent[141] or by varying the amount of 'poor' solvent added and the duration of aggregation.[142] This is in sharp contrast to the lack of control offered by rapid addition of polymer solution to a large excess of 'poor' solvent. For nanoparticles prepared by the solvent evaporation method, polymer aggregation can be controlled by the choice of 'oil' phase or solvent mixture.[135] Polymer aggregation may also be adjusted post-fabrication by hydrothermal annealing of the aqueous nanoparticle dispersion.[138,143]

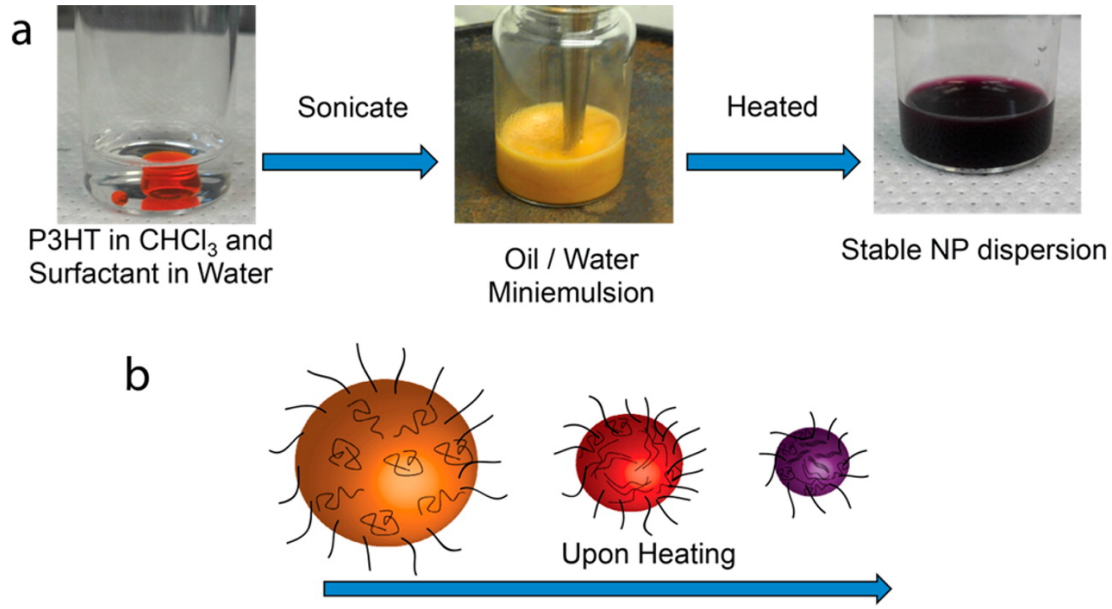

Figure 9: Typical post-polymerization miniemulsion fabrication of polymer nanoparticles. (a) Photograph images of miniemulsion process. (b) Pictorial representation of the packing of polymers in emulsion droplet as 'good' solvent is evaporated to form polymer nanoparticle.

A key disadvantage of the post-polymerization method is that the polymers within the nanoparticle are typically not cross-linked thus restricting the choice of dispersing phase for the nanoparticles to poor solvents for the polymer. Thus, there is an opportunity for synthetic chemists to develop methods efficiently cross-link polymers within the nanoparticles without substantially affecting the polymer packing.

When to use direct polymerization or post-polymerization methods for nanoparticle fabrication? The answer depends on the polymer, nature of the desired assembly, and desired functionality. Both methods can be used to prepare a wide range of nanoparticle sizes. Typically, nanoparticles obtained using the direct polymerization method have low nanoparticle size dispersity.[126,139,144] Since most polymerization techniques allow for cross-linking, nanoparticles obtained by direct polymerization fabrication can easily be cross-linked with the appropriate co-monomer[120,122,123] providing stable nanoparticles that can be dispersed in a

wide variety of solvents. However, controlling the intraparticle polymer morphology during direct polymerization is difficult, since the conditions that influence the morphology must also facilitate the polymerization. Moreover, since polymer synthesis and nanoparticle fabrication occurs concurrently, the polymer(s) cannot be purified prior to nanoparticle formation. In post-polymerization methods, since the polymer synthesis and nanoparticle fabrication are decoupled, if a polymer can be synthesized, one can make nanoparticles. Thus, one can use a large array of polymers and polymer architectures. Post-polymerization methods also offer greater control over the *intraparticle* polymer morphology since the conditions that influence morphology may be tuned during nanoparticle fabrication. A major difficulty of this technique is the cross-linking of polymers within the nanoparticle; the functionality has to be built into the polymer in order to fabricate cross-linked polymer nanoparticles.[145-147] Also, post-polymerization methods may be impractical used if the desired polymer is insoluble in common solvents. Nonetheless, post-polymerization nanoparticle fabrication is a more versatile method for preparing polymer nanoparticles with a wide range of polymers. For nanoparticles of polymers with complex architecture (e.g. block copolymers), post-polymerization methods offer significant advantages compared to direct polymerization, such as the ability to control the synthesis, purification, and self-assembly of the complex polymer in a stepwise fashion.

2.1.1.3 Polymer Nanoparticles with Multicompartmentalized Structure.

The polymer architecture serves as an important tool to obtain interesting nanostructures within polymer nanoparticles, leading to nanoparticles such as Janus particles,[148-150] patchy particles,[151-154] or particles with soft corona.[65-67,155-157] Such morphologies *within* the nanoparticles can be used to direct the interactions *between* the nanoparticles. A straightforward way to obtain nanoparticles with complex internal structures is by blending multiple polymers.

Polymer blend nanoparticles can be prepared by (1) seeded miniemulsion polymerization,[158] in which the monomer for the desired second polymer is added to a pre-existing dispersion of the seed polymer and then polymerized, (2) by a miniemulsion method[159] in which multiple polymers are both dissolved in the 'oil' phase of the miniemulsion, or (3) by a reprecipitation method[152] in which multiple polymers are dissolved in the 'good' solvent prior to the addition of 'poor' solvent. The intraparticle morphologies of polymer blend nanoparticles has been predicted based on the principle of surface energy minimization.[160] The expected thermodynamic morphology is the one that minimizes the sum of interfacial tension between the two polymers and between each of the polymers and dispersing phase. For example, one can expect Janus-type nanoparticles if the interfacial tension between each polymer with the dispersing phase is comparable. Core-shell nanoparticles can be expected if one polymer has a greater interfacial tension with the dispersing phase than the other polymer. The type and amount of surfactant, additives, and choice of dispersing phase can modify these interfacial tensions.

The use of diblock copolymers instead of polymer blends expands the scope of nanostructures within the particle (Figure 10),[151,152] many of which cannot be obtained from polymer blend nanoparticles. These morphologies can be predicted by models of diblock copolymers within confined spaces[161] (Figure 10) based on the ratio of particle diameter (D) to polymer chain length (L_0), and the surface affinity of one of the polymer blocks, α. These predictions have been validated in polystyrene-*b*-polyisoprene (PS-*b*-PI) nanoparticles[151] prepared by a modified reprecipitation method.

The intraparticle morphologies of polymer nanoparticles can be further complexified by simply mixing a block copolymer with a homopolymer or another block copolymer. For example, Janus-type polymer nanoparticles in which each hemisphere contains a different morphology

have been obtained using AB/C diblock copolymer/homopolymer blends[150] or AB/AC diblock copolymer blend nanoparticles.[162] The intraparticle morphologies obtainable by combining various polymers and/or block copolymers are clearly an opportunity to add complexity and diversity to the polymer mesostructures from polymer nanoparticle assemblies. This strategy offers a rational way to impart the desired polymer nanostructure within each nanoparticle prior to assembly. Moreover, the non-uniform surface of these particles presents the ability to design anisotropic interactions. For example, Müller and coworkers have demonstrated the power of this approach[67,163] using linear ABC triblock terpolymer nanoparticles to create patchy particles assembled in 2D networks; however there still exists a breadth of opportunity in these systems such as 3D networks of multiblock copolymer nanoparticles.

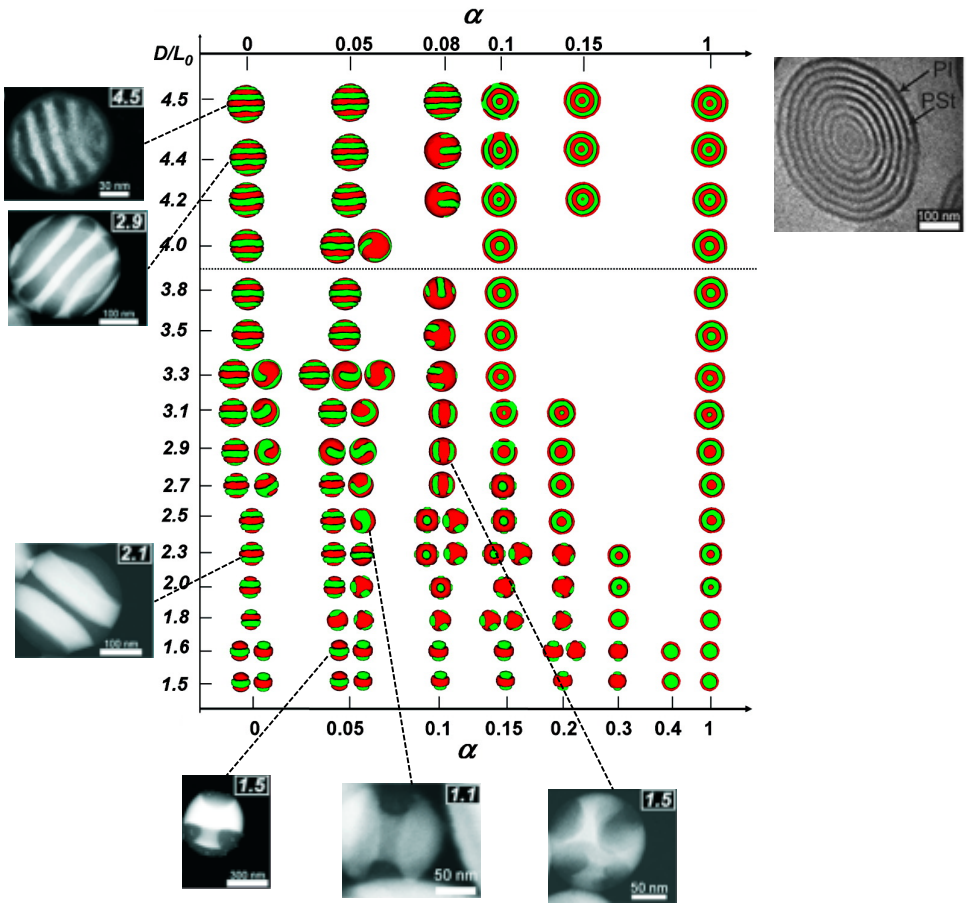

Figure 10: Simulated intraparticle morphologies predicted based on pore surface affinity (α) and ratio of particle diameter to polymer length (D/L_0). Dashed lines indicate experimentally observed morphologies in PS-*b*-PI nanoparticles, by STEM of OsO_4 stained nanoparticles, with D/L_0 inset. The number of lamellae found experimentally sometimes deviates slightly from the predicted number for a given D/L_0. Adapted with permission from references by Yu et al.[161] and Higuchi et al.[152], [151]

2.1.1.4 Making Non-spherical Polymer Nanoparticles.

Methods for the formation of spherical polymer nanoparticles are abundant, but methods for the formation of non-spherical polymer nanoparticles are rare. Non-spherical polymer nanoparticles are desired to expand the breadth of possible self-assembled morphologies, as different geometries have different assembly motifs. Non-spherical inorganic nanocrystals are prepared via different crystalline polymorphs or by selective growth of a particular crystalline

face.[164-166] Compared to inorganic nanoparticles, bottom-up fabrication of non-spherical polymer nanoparticles has not been well explored for the simple reason that polymers are typically semicrystalline[167] and therefore it is difficult to crystallize polymers within nanoparticles with defined crystal faces for shape control. Thus far, the most useful techniques are top-down, and have been used to control the shape either by mechanically stretching the polymer particles post-fabrication[168,169] or by fabricating nanoparticles within templates of the desired shape.[170,171]

In the stretching technique,[168,169] particles are suspended in a polymer matrix such as poly(vinyl alcohol). The matrix containing the particles is either immersed in a good solvent for the particles and not for the matrix, or heated above the T_g of the pristine polymer. Then the film is fixed to a stretching apparatus and pulled, and then cooled. The stretching of polystyrene (PS) nanoparticles has been documented in several studies. Some of the possible non-spherical geometries include rectangular disks, rods, and ellipsoids (See Figure 11). They were obtained from different combinations of heat and solvent annealing and 1D and 2D stretching. Studies are required to probe how this method can be applied to other polymers.

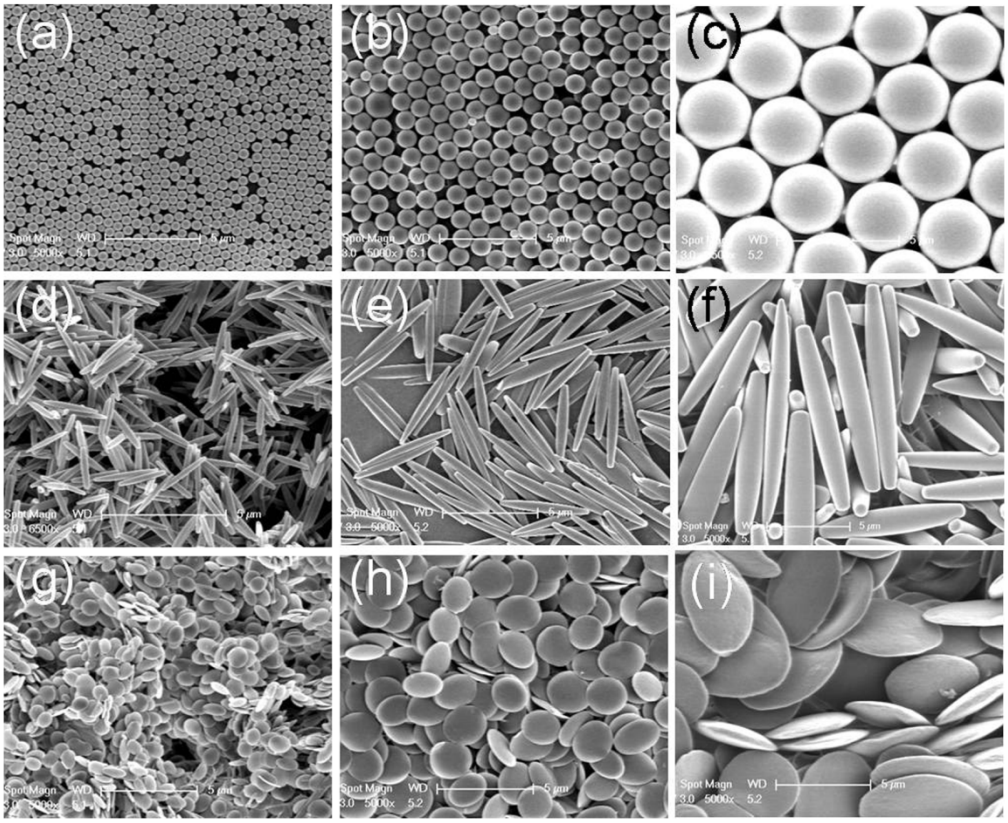

Figure 11: Possible polymer particle geometric shapes at different size scales: (a-c) spheres, (d-f) rods, and (g-i) ellipsoids. Reprinted by CC BY license from work by Mitragotri and coworkers.[168]

A more recent technique to obtain particles with different shapes is the Particle Replication in Non-wetting Templates (PRINT™) approach developed by DeSimone and co-workers.[170,171] In this approach, imprint lithography is used to design a perfluoropolyether (PFPE) template for the desired shape of nanoparticle prior to nanoparticle fabrication. A solution of the particle precursor is then spray- or drop-cast onto the template and the precursor is converted to a solid particle within the cavities through photocuring or by other methods. The particles can be physically removed from the template due to the low surface energy of the PFPE template, and redispersed in a solvent. The features of the lithographic mold dictate the size of the particle and

the prepared polymer particles have a uniform size distribution. Spheres, cylinders, disks, toroids, and cubes have been prepared by this method using the appropriate imprint lithography master for the template, each having near uniform size distribution. Mechanical stretching of the template has also been employed[171] to increase the catalog of shapes available by this method beyond those possible from the original, un-stretched templates alone. These include high aspect ratio nanorods, rectangular prisms, and various parallelepipeds. A variety of biologically relevant polymers—as this method was initially developed for the synthesis of drug delivery vehicles—have been molded into uniformly sized, shape-controlled polymer nanoparticles by this method. PRINT™ has yet to be exploited for polymer nanoparticle assemblies for functional polymer mesostructures, despite its great potential.

Non-spherical polymer particles have also been fabricated in a bottom-up fashion during seeded miniemulsion polymerization.[123] In this method, seed PS particles, cross-linked with divinylbenzene and coated on the surface with a hydrophilic polymer, are swelled and subjected to a second miniemulsion polymerization using fresh styrene monomer. The second polymerization creates a bulge of PS protruding from the cross-linked seed particle, and results in anisotropic, dumbbell-type particles. Bottom-up procedures for non-spherical polymer particle fabrication such as this are important for expanding the library of available shapes, and scaling up nanoparticle fabrication to industrial scales. In the aforementioned methods, the particles are typically >200 nm in at least one of the dimensions. The next challenge is to fabricate of polymer nanoparticles with desired shapes with size features < 100 nm.

2.1.1.5 Non-Spherical Particle Clusters.

Another approach to obtaining non-spherical geometries is to pack spherical polymer nanoparticles into geometric clusters of particles.[172] These clusters can then be treated as a

non-spherical moiety for self-assembly. The fabrication of stable colloidal clusters is more complex as it depends on the properties of the particle and on the properties of the dispersing solvent. They have been most successfully obtained by trapping multiple particles in an emulsion droplet (See Figure 12).[173] There have been many computational studies on the assembly of spheres into clusters.[174-176] These studies have unveiled multiple different geometries and symmetries that can exist in the clusters. The use of different cluster symmetries as seeds for crystallization of colloids has also been computationally explored but not experimentally verified.[177]

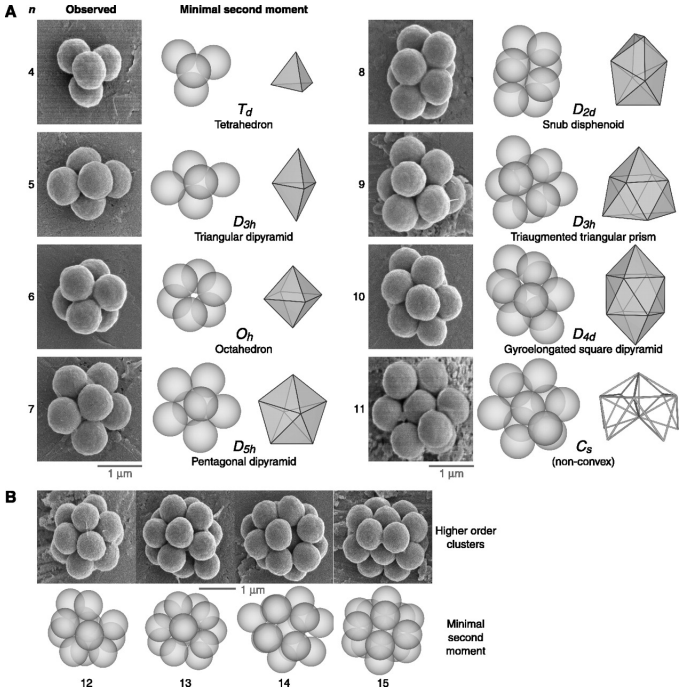

Figure 12: Polymer particle clusters obtained by trapping particles in emulsion droplet. (A) Cluster geometries with defined point groups, and (B) high order structures, along with predicted structures for particular point group. Reprinted with permission from work by Pine and coworkers.[173]

Another very interesting method for obtaining colloidal clusters is the combined utilization of DNA interactions and crystalline templates.[178] This work by Crocker and co-workers tunes

DNA interactions in order to obtain face-centered cubic (FCC) and body-centered cubic (BCC) lattices of fluorescent dye containing PS nanoparticles. 'Impurity' particles are incorporated into the crystalline assemblies and these particles have slightly different DNA sequences that can be reinforced with small segments of DNA. This reinforcement effectively connects all nearest neighbors to a single central particle. Then, all other contacts are melted, disassembling the crystalline assembly and releasing the DNA-reinforced clusters. The clusters released are the structure of the crystalline template and not the lowest energy configuration, such as cuboctahedron. When these clusters are fixed to the substrate through DNA interactions, the coordination and structure are dependent on the face and number of particles that lay on the glass. This rearrangement with a fixed face even results in ejection of particles in order to obtain the lowest energy configuration.

The self-assembly of micron-sized Janus charged particles has also been explored for the formation of well-defined clusters.[179] This approach, if extended to nanoparticles, may be a convenient method to fabricate well-defined clusters in large scale.

From isotropic nanoparticles to nanoparticles containing complex features, the array of available building blocks is large and offers exciting possibilities of mesoscale assemblies.[51,73,74] Yet, the two major challenges in the fabrication of polymer nanoparticles that need to be addressed are: (1) the lack of a general method to obtain nanoparticles with low size dispersity (<10%) for a wide variety of polymers in dispersing phase of choice, and (2) the lack of a bottom-up method to obtain nanoparticles for a wide variety of polymers with desired non-spherical shape.

2.1.2 Self-Assembly of Nanoparticles

2.1.2.1 Sphere Packing.

Since a sphere is the most common geometry in polymer nanoparticles, first, we discuss the packing of spherical nanoparticles into ordered and disordered structures for tunable polymer morphologies. We will then discuss the predictions for non-spherical shapes. The driving force for the packing of spheres, typically into ordered crystals, has long been studied by the physics community. It has been demonstrated that as the particle volume concentration exceeds ~55%,[98] the maximization of free volume entropy can alone drive the crystallization of spheres.[180] For single-sized spheres the purely entropically driven structure is the FCC lattice.[99] When different-sized spheres are allowed to assemble, the resulting structure depends on the radius ratio,[96,97,181] akin to structures of minerals and alloys.[182-184] Natural opals were one of the early examples studied in terms of mesoscale assemblies of particles[185] and more recently inorganic nanoparticle assemblies are receiving widespread attention.[53,92,102,186,187]

The common misconception is that spheres will pack into ordered assemblies all the time; however, there are routes that lead to kinetically trapped disordered assemblies. The phase pressure-density diagram for spherical assembly shows two paths for assembly (Figure 13).[188,189] One continuous pathway leads to a metastable ‘disordered’ assembly, so called random close-packed (RCP), sometimes also referred as maximally randomly jammed (MRJ) assembly.[188] The other pathway leads to the ordered, close-packed FCC assembly and involves a first order phase transition.[189] This arises from the difference in volume fraction for freezing (0.49) and melting (0.55).[188] Though ordered structures are the thermodynamic global minimum, a metastable local minimum exists for disordered structures. This was shown

computationally, where significant volume fluctuations are required to go from a disordered to ordered assembly.[189]

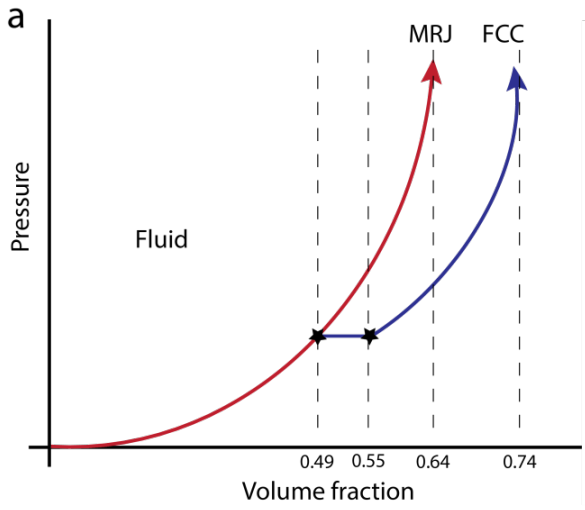

Figure 13: Phase diagram of hard spheres with respect to pressure and volume fraction showing a discontinuous path to ordered (FCC) structure and a continuous path to MRJ assemblies.[188]

The volume fraction of the initial dispersion has been shown to have an impact on the nature of assembly. This was best exemplified by Pusey et al. with mostly non-interacting (hard) PMMA micron-sized particles.[98] This work shows that homogeneous crystallization occurs at the hard-sphere melting volume fraction (found to be ~0.54) until ~0.57, where heterogeneous crystallization occurs. Glasses form at a hard-sphere volume fraction of ~0.61. Metastable disordered glasses form at high concentrations because particle diffusion is sufficiently disrupted, preventing the formation of thermodynamically favorable ordered structures, even after month long periods.[190] This is consistent with the phase diagram in Figure 13. The three-dimensional phase diagram of volume fraction, attraction, and stress for the 'jamming' of particles into disordered structures has been studied.[190] In this phase diagram, dispersed fluids form jammed assemblies on the three-dimensional plane of increasing volume fraction,

increasing attraction energy, and decreasing stress. Disordered structures are sometimes referred as gels or glasses.[191-194]

2.1.2.2 Interparticle Interactions

Interparticle forces are an important tool in engineering the assembly of nanoparticles. The DLVO (Derjaguin-Landau-Verwey-Overbeek) theory is used to model colloidal interactions in aqueous media.[104,195] The sum of the van der Waals, electrostatic, and depletion energies is termed DLVO energy: $\Phi_{DLVO} = \Phi_{vdw} + \Phi_{es} + \Phi_{dep}$. van der Waals energy ($\Phi_{vdw}$) is calculated by the equation in Table 1 and is proportional to the Hamaker constant (A). The Hamaker constant[104] is a material property that represents the strength of van der Waals interactions. The non-retarded Hamaker constant can be calculated by considering the refractive indices (n) and dielectric constant (ε) of two interacting bodies and the medium they are interacting across. The electrostatic interaction energy (Φ_{es}) is calculated by the equation in Table 1, and depends on the exponential $e^{-\kappa\delta}$ where κ^{-1} is the electrostatic screening length (Debye Length), and δ is the distance between the interacting bodies. The equation for κ^2 is given in Table 1; the Debye length depends solely on the properties of the solvent.[104] These interactions are well known and predictable in aqueous solutions, but they are not well understood in non-aqueous colloidal dispersions.[104,195,196] Much effort has focused on tuning the particle properties in order to tune the interparticle interactions and thus the assembly.[195] In comparison, the dispersing phase choice can be simple yet powerful tool to precisely tune the interactions between nanoparticles, and thus their assembly.

Table 1: Equations for estimating the interaction energies of colloidal solutions

$\Phi_{vdw} = \frac{-A}{6\delta}\left(\frac{r_1 r_2}{r_1+r_2}\right)$ van der Waals energy
$\Phi_{es} = 4\pi\varepsilon_0\varepsilon_s\left(\frac{r_1 r_2}{r_1+r_2}\right)\psi_1\psi_2 e^{-\kappa\delta}$ Electrostatic energy
$A \sim \frac{3}{4}kT\left(\frac{\varepsilon_1-\varepsilon_s}{\varepsilon_1+\varepsilon_s}\right)\left(\frac{\varepsilon_2-\varepsilon_s}{\varepsilon_2+\varepsilon_s}\right) + \frac{3h\nu_e}{8\sqrt{2}}\frac{(n_1^2-n_s^2)(n_2^2-n_s^2)}{\sqrt{(n_1^2+n_s^2)}\sqrt{(n_2^2+n_s^2)}\left(\sqrt{(n_1^2+n_s^2)}+\sqrt{(n_2^2+n_s^2)}\right)}$ Non-retarded Hamaker constant
$\kappa^2 = \frac{2N_\infty Z^2 e^2}{\varepsilon_0\varepsilon_s kT}$ Debye electrostatic screening length is κ^{-1}

van der Waals interactions can be tuned by solvent choice, and even made repulsive in specific circumstances.[197] For two particles with dielectric constants (over frequencies ξ) ε_1 and ε_2 interacting in a solvent with dielectric constant ε_s, the interaction goes as: $-(\varepsilon_1-\varepsilon_s)(\varepsilon_2-\varepsilon_s)$. In a typical colloidal solution, this term is negative, leading to attraction. However, when $\varepsilon_1 > \varepsilon_s > \varepsilon_2$, the aforementioned term is positive making the van der Waals interaction repulsive. This phenomenon has been experimentally confirmed by Parsegian and co-workers using force-probe measurements.[197]

Further, van der Waals interactions can be tuned using the refractive indices of the interacting materials. The concept of refractive index "matching" has been demonstrated in polymer nanoparticle assembly by Bartlett et al.[96] where PMMA spheres were dispersed in decalin/carbon disulfide and self-assembled into crystal structures: A, AB_2, AB_{13}, or B, at a radius ratio of 0.62 by varying the particle volume fraction. The refractive index-matched solvent screens attractive van der Waals interactions allowing the entropic maximization of particle free volume to dictate the assembly.

2.1.2.3 Ordered Assemblies.

Ordered nanoparticle assemblies are particularly attractive for the design of polymeric mesostructures because many of the predicted morphologies are akin to block co-polymer morphologies, except with greater versatility in polymer type and available morphologies.[198,199] There are myriad examples of ordered assemblies—Binary Nanoparticle Super Lattices (BNSLs)—from two types of inorganic nanoparticles. BNSL structures that have been realized with inorganic nanoparticles include NaCl, CsCl, NiAs, AlB_2, $MgZn_2$, $MgNi_2$, $NaZn_{13}$, and ZnS.[92,200-213] It is important to note that although the structures obtained from inorganic nanoparticle BNSLs are homeotypic with minerals, they often do not match the structures predicted by radius ratio rules.[92] Often, the obtained structures have packing densities lower than 0.74, essentially eliminating entropy as the principle driving force for the assembly of these building blocks. Murray and co-workers show that the Coulombic potential arising from the charge on the particles stabilizes the formation of BNSLs.[92]

Compared to inorganic nanoparticle BNSLs, examples of BNSL-type assemblies involving polymer nanoparticles are scant.[214-217] Most studies focus either on *micron-sized* particles for photonic crystals[218,219] or on micron-sized particles/nanoparticles where the size of the

nanoparticles was chosen so that the nanoparticles will not interfere with the assembly of micron-sized particles; the nanoparticles were designed to be larger than the interstitial voids in the assembly of micron-sized particle, but not too large (e.g. radius ratio ~ 0.2).[96,220,221]

One aspect of polymer nanoparticles that is important is the presence of surfactants to stabilize the nanoparticles through repulsive interactions at long distances. At short distances, two polymer nanoparticles can have strong van der Waals attractions as predicted by the DLVO theory for colloidal interactions.[104,195] If these van der Waals interactions are not screened, then strong interparticle interactions can lead to non-equilibrium, disordered, or jammed assemblies. Thus, we need the ability to disperse polymer nanoparticles in a dispersing phase with a refractive index that matches the polymers refractive index. As mentioned before, the challenge is to develop more nanoparticle fabrication methods with the capability to cross-link the polymer within the nanoparticles and disperse them in solvents of choice.

Ordered assemblies from soft colloidal micro-/nanogels have been explored in order to study the assembly behavior of soft colloids.[222-230] The most abundantly used polymer for microgel colloidal crystals is poly(*N*-isopropylacrylamide) (pNIPAm) and derivatives of pNIPAm. The size of pNIPAm particles decreases with increasing temperature. pNIPAm particles made in a typical synthesis have a slightly anionic surface, but their the electrophoretic mobility is ‘modest’. Therefore, electrostatic repulsion may not be a dominating factor to the pair potential. Moreover, swollen polymer networks are predicted to have a low Hamaker Constant, therefore the van der Waals forces will only be a small contributor to pair potential. These two conditions allow for entropy driven assembly.[227] pNIPAm particles cannot be sedimented by gravity like latex particles; therefore they are brought into close contact by ‘forced sedimentation’ via centrifugation. Rapid sedimentation leads to disordered phases because the

particles do not have time to access thermodynamically favored ordered structures. However, these disordered assemblies can be warmed up to shrink the size of the particles. Upon warming, the jammed assembly turns into a dense fluid, which upon cooling has sufficient diffusion in order to assemble into ordered crystalline assemblies.[227] The crystalline phase diagram for assemblies of microgels has been explored.[222,224] The phase diagram is different from a hard sphere diagram and has greater structural diversity.[92] It is another example how how polymer nanoparticles offer unique avenues for research in the area of particle assembly.

2.1.2.4 Directed Assembly.

Directed assembly of nanoparticles can be accomplished via hydrogen bonding,[231] DNA,[232,233] Coulombic interactions,[234] polymer-polymer interactions,[73,74,235-237] magnetic interactions,[238] and other supramolecular interactions.[56,239] This directed assembly is typically accomplished by functionalization of particles to impart chemical moieties that impose the aforementioned interactions between particles. We will discuss what we consider a few particularly interesting examples in this Chapter.

Functionalization of the particles with groups that can engage in interparticle interactions such as hydrogen bonding can help realize ordered polymer nanoparticle assemblies. This can be simply done by copolymerizing hydrogen bond acceptors on one type of nanoparticle and hydrogen bond donors on the other.[231] This technique does allow for some controlled assembly, however, it is quite limited to nanoparticles that are prepared by miniemulsion polymerization and are compatible with hydrogen bonding co-monomer. Recently DNA strands have been used to guide inorganic nanoparticle assemblies.[232] Crocker and co-workers have demonstrated the formation of ordered crystals or disordered assemblies of PS particles, which can be tuned by modulating the relative strength of the interaction (See Figure 14).[233] The

authors claim the ability to access morphologies that are kinetically inaccessible by simple nucleation alone, and can only be formed by controlling interparticle interactions. The authors provide a phase diagram of morphologies as a function of interaction energies. The use of DNA to engineer particle assemblies is a blossoming field, and holds much promise to access a wide variety of structures.

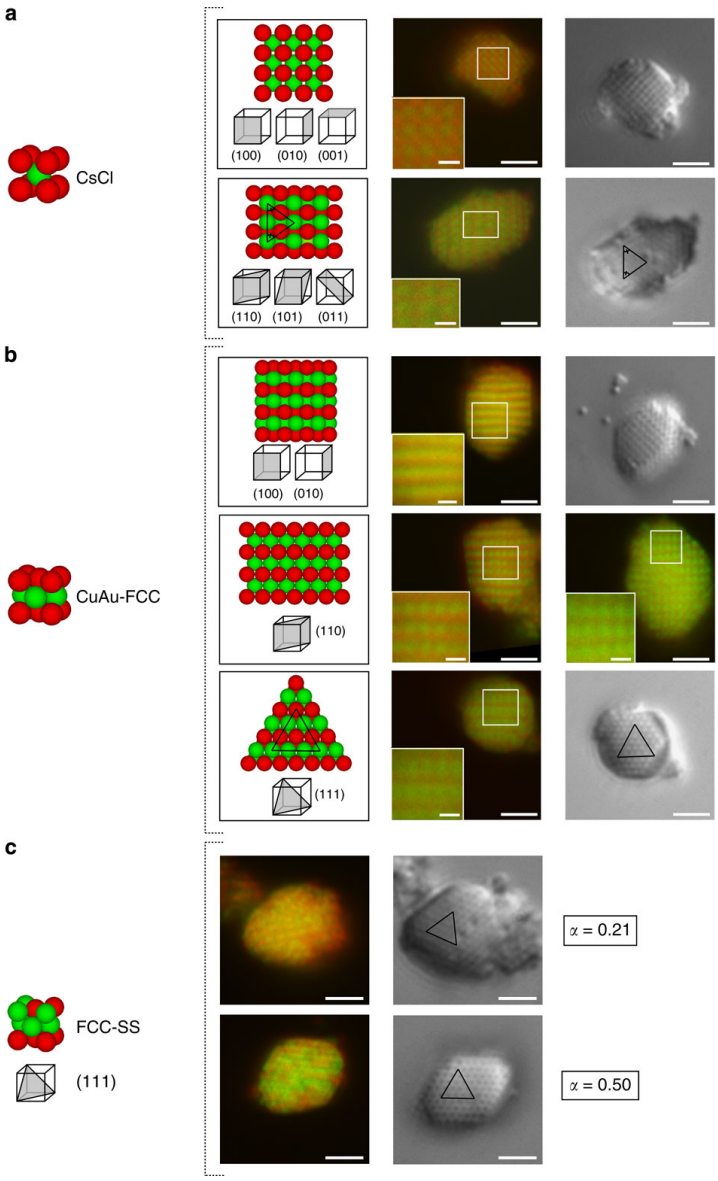

Figure 14: Polymer nanoparticle superlattices homeotypic with (a) CsCl, (b) CuAu-FCC, and disordered FCC; along with corresponding facet planes schematics, confocal microscopy images and differential interference contrast micrographs. Structures are made by changing particle interactions. Reprinted with permission from work by Crocker and coworkers.[233]

Another interesting way to direct the assembly of nanoscale macromolecular building blocks is through polymer-polymer interactions; this has been studied both experimentally and theoretically.[73,74,235-237] Through this method, the interactions between the polymer 'hairs' or corona on nanoparticles can direct the assembly of the nanoparticles into a variety of structures. The mechanism of assembly is akin to the diblock copolymer phase diagram where polymer interactions direct the assembly of the nanoscale building blocks.

It is important to note that if directional interparticle interactions exist, as in hydrogen bonding directed assembly, then the resulting structure will not always be the one predicted by the traditional radius ratio rules. Moreover, in inorganic particle assemblies, it has been shown that myriad attractive and repulsive forces compete with entropy resulting in structures not predicted by entropy maximization computations.[92] Thus, this is a rich area of collaboration between computation and experiments to systematically study how the interparticle interactions affect the particle assemblies.

2.1.2.5 Disordered Assemblies.

Most studies on particle assemblies have focused on ordered assemblies. Attraction at close interparticle distances can cause particles to jam together, which would prohibit the formation of some of the equilibrium, ordered structures mentioned previously. The result of these collectively jammed assemblies (as in Figure 15) is a disordered assembly.

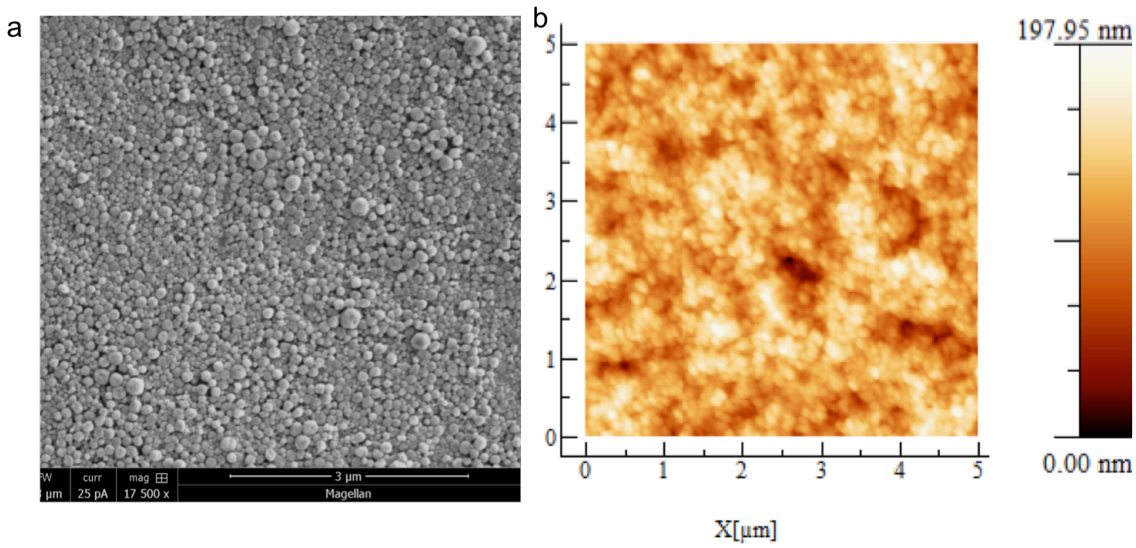

Figure 15: Disordered nanoparticle assemblies of different types of nanoparticles. (a) Scanning electron micrograph of donor and acceptor nanoparticles from work by Venkataraman and coworkers.[116] (b) Atomic force microscopy image of a disordered assembly of PS and poly(methyl methacrylate) (PMMA) nanoparticles.

Contrary to common perception, not only do binary disordered assemblies provide a valid route to functional mesoscale morphologies, but they also provide a surprising amount of tunability and control over the assembled structure. When considering a binary mixture of particles, there are two parameters that can be utilized to control its assembly, the number ratio and the radius ratio of the two types of particles.[240] In fact, ordered assemblies can be tuned by changing the radius ratio, but are restricted to very specific stoichiometry/number ratios, giving even more control in disordered assemblies. We recently demonstrated that disordered nanoparticle assemblies of donor and acceptor materials can be used to design a bicontinuous structure for photovoltaic applications which is discussed elsewhere.[116]

Thus far, disordered assemblies have remained largely unexplored, especially in the design of polymer binary mesoscale assembly. One of the possible reasons for this may be due to the difficulties in structurally characterizing these disordered assemblies. Confocal

microscopy[241,242] and electron tomography[243] have been utilized to characterize the structure of disordered assemblies, however, these techniques are not ideal for analyzing 3D assemblies of nanometer-sized particles. Moreover, structures derived from micron-sized and millimeter-sized particle assemblies may not map onto the structures of nanoparticle assemblies.[241] Electron tomography is emerging as a tool to probe 3D morphologies of thin films, but it is neither rapid nor routine. Therefore, structural analysis of disordered nanoparticle particle assemblies has thus far been elusive. We will demonstrate in an upcoming paper that conducting atomic force microscopy (cAFM) in conjunction with simple computation can be used to non-destructively probe the structure of disordered assemblies, provided that one of the particle types is conducting. This technique will be able to provide a morphology map of disordered assemblies by changing the number ratio and the radius ratio of the two types of particles.

Disordered nanoparticle assemblies have several advantages over ordered nanoparticle assemblies. First, they are ubiquitous, and scalable over large areas; secondly, they can be made using a variety of deposition[117] and roll-to-roll methods[244] and under ambient conditions. Lastly, they have two parameters (radius and number ratio) that can be independently tuned. Disordered assemblies—thus far largely unexplored—have potential to be a highly tunable and applicable method to realize functional polymer mesoscale morphologies.

2.1.2.6 Structures from Non-Spherical Shapes.

The self-assembly of non-spherical inorganic nanoparticles has been extensively studied.[245,246] Studies on the assembly of non-spherical polymer nanoparticles are limited, because very few non-spherical polymer nanoparticles have thus far been synthesized. Simulations of non-spherical, polyhedral structures indicate the presence of a rich diversity of

structures (See Figure 16).[247,248] Similar to the packing of spheres, the packing of polyhedra into these structures can be rationalized by the volume excluded from these packings, leading to entropy maximization by the surroundings.[249] Thus, based on the shape of the polyhedral structures, disordered, liquid crystalline, and crystalline structures have been predicted.[248] These predictions do not only outline many ordered assemblies waiting to be verified experimentally, but they also allow for the prediction of the packing structure for a given polyhedron based solely on its shape. These computations also illustrate the power of using geometry to get to various mesostructures. Directional interparticle interactions combined with shape can lead to exciting structures, but computing such structures will require input from experimental observations.

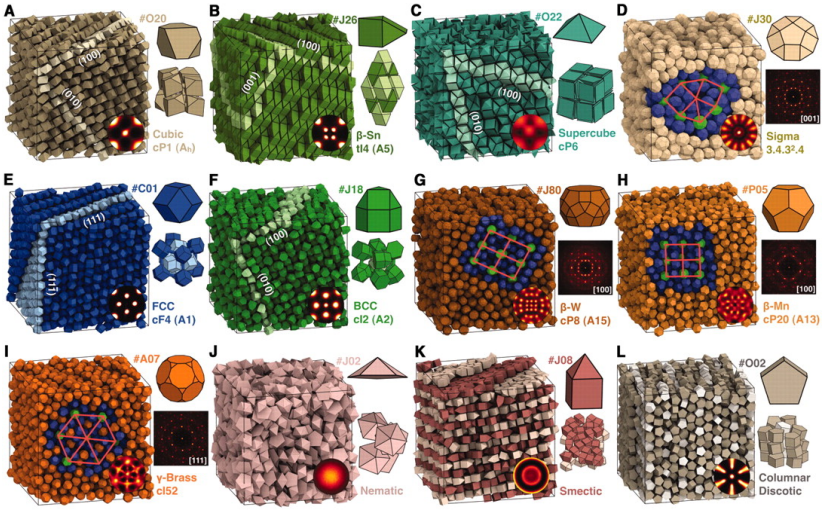

Figure 16: Simulation results for the packing of 2048 polyhedra. Simulated assemblies obtained are (A-D) crystals, (E-I) plastic crystals, and (I-J) liquid crystals. Each simulated assembly has a corresponding bond order diagram, polyhedron shape, small assembly of particles, and diffraction pattern. Reprinted with permission from work by Glotzer and coworkers.[248]

2.1.3 Impact on Functional Materials

Thus far, the field has focused on the physics of assembly and the resultant structures. However, we feel that the area of this field that requires further investigation is functional polymeric material from assembled polymer nanoparticles. The majority of functional materials from colloidal assembly are photonic or diffractive in nature, which means that their functionality is derived from the periodicity of the assembled structure and not necessarily from the materials that make up the structure.[250] We believe that the breadth of applications that can be accessed by the packing of two different polymer nanoparticles can be great if the right polymers are selected and the right structures are assembled. We will highlight here three examples of applications where we see the potential for incorporating function into assemblies of polymer nanoparticles. However, one can apply to any application that requires the assembly of multiple components in to hierarchical morphologies.

There are myriad functional materials where two or more polymeric materials (sometimes disparate) need to be arranged in specific molecular assemblies at the nanoscale and morphologies in the mesoscale and beyond (Figure 7). One such functional material is the donor-acceptor bulk heterojunction for organic photovoltaic (OPV) devices. We and others have demonstrated that individual organic donor and acceptor materials can be assembled into nanoparticles and assembled into working devices.[64,116,244,251-254] In these devices, particle-particle contacts are promoted, since the weakly bound surfactants can be dislodged by the strong van der Waals interactions between the particles. This leads to jammed, disordered assemblies with intimate contact between the nanoparticles and efficient charge transport.[255,256] In comparison, charge transport is unfavorable in inorganic nanoparticle assemblies due to the barrier created by non-conjugated ligands.[257] This is an *important and*

key difference between inorganic and organic nanoparticles. Also, the general expectation is that ordered structures, such as the bicontinuous AlB_2 packing are required for applications such as OPVs (Figure 17).[198,199] However, we have demonstrated that disordered structures can provide a bicontinuous structure with donor-acceptor interfaces for exciton splitting and efficient OPV devices.[116,255]

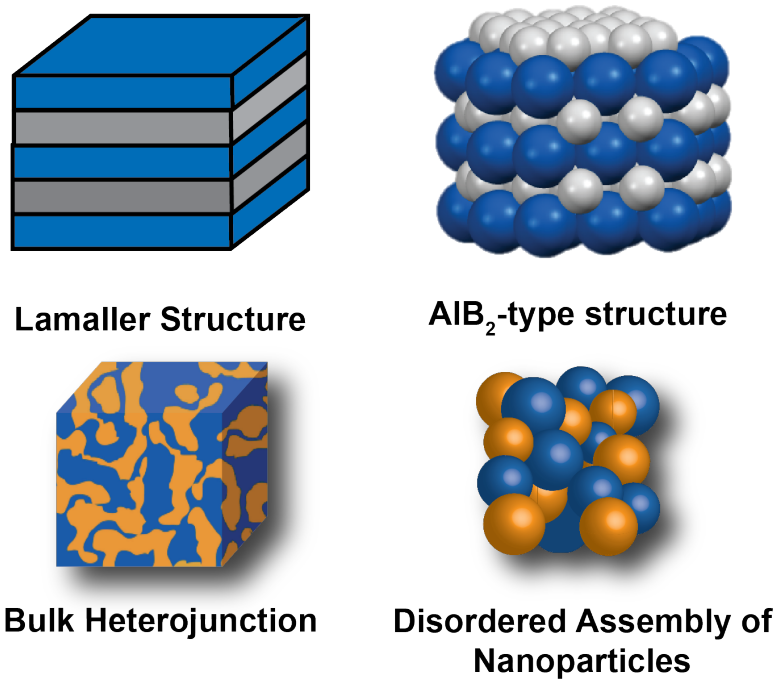

Figure 17: (top) Illustration of a lamellar structure seen in diblock copolymers and the alternating layered structure of AlB_2-type structures that can be obtained through ordered assemblies of two polymer nanoparticles and (bottom) illustration of the bulk heterojunction structure which can be obtained through a disordered assembly of nanoparticles. Reproduced with permission from Ref. [258].

Thermoelectric materials derived from polymers are another example that requires the assembly of multiple polymeric materials into specific morphologies. For example, it has been reported in mixtures of poly(3-butylthiophene)/polystyrene (P3BT/PS) for thermoelectric devices, that the figure of merit (*ZT*) is maximum when the two materials exist in an interpenetrating bicontinuous structure.[259] We believe that assemblies of P3BT and PS

polymer nanoparticles can provide an ideal platform to systematically tune morphologies and domain sizes for optimal performance. Nanoparticles also open up possibilities to explore thermal conductivity in polymer materials.[260,261]

Another potential application is materials for ionic conductivity. Ion transport materials such as Nafion^{TM} contain two domains, a fluorinated hydrocarbon, and an ion transporting hydrated sulfonic acid domain. The chemistry and the assembly of these two domains define its functionality. Recently, it has been shown that the bicontinuous gyroidal phase is the optimal phase for Li^+ ion conduction.[262] We envision achieving such bicontinuous structures through the assembly of polymer nanoparticles. For example, it has been shown that particle films derived from latex particles containing poly(styrenesulfonic acid) show superior proton conductivity compared to polymer membranes with similar charge content.[263] Particle assembly can also provide us straightforward pathways to combine nanoparticles for electronic transport with nanoparticles for ion transport to achieve structures with separate but continuous charge transport channels for concurrent electronic and ionic transport for battery and energy applications.[264]

Using polymer nanoparticles as building blocks is a simple yet powerful method to obtain mesoscale morphologies. This approach provides us the ability to obtain stable mesoscale structures in a single step, through self-assembly of two or more nanoscale moieties. We can independently pre-assemble the polymer domains with the desired packing within the nanoparticle. As we continue our progress in the fabrication and assembly of polymer nanoparticles with specific shape, size, and functionality, we will be able to develop a powerful bottom-up approach that provides control and tunabilty at each step of the self-assembly process to reliably obtain stable mesoscale (or nanostructured) morphologies. The field of polymer

nanoparticle assemblies opens up a pathway for the systematic study and tuning of functional materials with disparate components while exercising control of each of the components assembly at multiple length scales.

2.2 SELF-ASSEMBLY OF NANOPARTICLES

This chapter[**] reviews the various methods and techniques for the self-assembly of nanoparticles (organic and inorganic). Extending the concept of nanoparticle packing to create polymer-based nanostructures will allow us to (a) obtain stable nanoscale structures in a single step, through self-assembly from *any* two or more spherical moieties; (b) independently pre-assemble the polymer domains with the required molecular assembly *within* domain size dictated by the size of the particle; (c) systematically alter nanoscale morphology through changes in the size and shape of the nanoparticles or interparticle interactions or both: and (d) the ability to rationally design nanostructured materials using multiple polymer components in the assembly. The concept of spherical packing is a powerful bottom-up approach that provides hierarchal control and tunability in each step of the self-assembly process to reliably obtain stable nanoscale morphologies.

Inorganic nanoparticles/nanocrystals have been the focus of the assembly of nanoparticles into specific morphologies. The low size dispersity of inorganic nanoparticle samples is an important factor to obtaining ordered structures. Thus, a diverse number of techniques to obtain these structures have been established utilizing inorganic nanoparticles. Therefore, many of the techniques that will be discussed herein to self-assemble nanoparticles have only been employed using inorganic nanoparticles. It is the expectation that the same principles can be extended to organic nanoparticles.

[**] This chapter was adapted with permission from a book chapter: Renna, Lawrence A., Timothy S. Gehan, and D. Venkataraman. "Polymer Nanostructures through Packing of Spheres." *Optical Properties of Functional Polymers and Nano Engineering Applications* 1 (2014): 227.

There are numerous methods for the self-assembly of nanoparticles into colloidal crystals, glasses, and superlattices.[92,94,186,265,266] The methods in this chapter have been broken down into the following categories: self-assembly by evaporation, self-assembly at the liquid-air interface, self-assembly at the liquid-liquid interface, and other types of self-assembly that do not necessarily fit into the aforementioned classifications.

2.2.1 Self-Assembly by Evaporation

In this method the slow evaporation of the liquid phase of a colloidal dispersion on a substrate produces a self-assembled structure. Although the technique is relatively simple, there are myriad attractive, repulsive, and disruptive forces that complicate the self-assembly process. The solvent evaporation method has been used to obtain ordered arrays of spherical particles[92,96,267-269], nanorods[270] and nanotriangles.[271] One of the earliest examples using solvent evaporation to obtain an ordered binary nanoparticle assembly was reported by Bartlett et al.[96] They utilized the radius ratio of the particles and partial volume fraction to tune the morphology of the nanoparticle assembly. The authors demonstrated that PMMA nanospheres (186 nm and 321 nm) dispersed in decalin/carbon disulfide self-assemble into four different crystal structures: A, AB_2, AB_{13}, or B, at a radius ratio of 0.62 and varying the particle volume fraction. The dispersant was chosen to have the same refractive index as the nanoparticles, and therefore reduces the van der Waals interactions between nanoparticles. When such enthalpic forces are screened, as in this case, the system behaves similarly to the age-old physics problem of assembling hard spheres where the entropy gain in maximizing particle free volume is the dominant factor. Self-assembly of SiO_2 nanoparticles (200 nm – 700 nm) dispersed in ethanol have also been shown to assemble on a vertically aligned substrate into close-packed structures. The authors demonstrated that the film's thickness could be controlled from a single

monolayer of nanoparticles to hundreds of nanoparticle thick films by tuning the volume fraction and particle size.[272]

When a colloidal solution is allowed to dry unperturbed on a horizontal substrate, the "coffee ring effect" is often observed.[273] This effect is due to the non-equilibrium state of a drying droplet where different evaporation rates throughout the droplet and small temperature fluctuations result in capillary flows within the droplet. These forces move nanoparticles outward toward the droplet's contact line, causing a concentration gradient of nanoparticles in the film after drying is complete (Figure 18b and c). Recent work has shown that by simply changing the shape of the nanospheres to nanoellipsoids, the coffee ring effect can be suppressed (Figure 18a). This is due to the long-range interactions between particles that are generated by the anisotropic shape of the ellipsoids, resulting in non-close packed structures. Another interesting solution to avoid the coffee ring effect is to control the evaporation rate by placing the sample in an environment that contains some degree of saturation of the solvent. The saturation can be changed to tune the evaporation rate providing an additional tool to self-assemble nanoparticles.[274-277] By slowing the evaporation rate, the evaporation gradient in the droplet is reduced and thus the capillary force is reduced. Inorganic nanocubes and nanooctahedra have also been shown to self-assemble into different structures through controlled evaporation by placing the substrate with a droplet of colloidal solution in a desiccator at ambient, under vacuum, or saturated environments.[278]

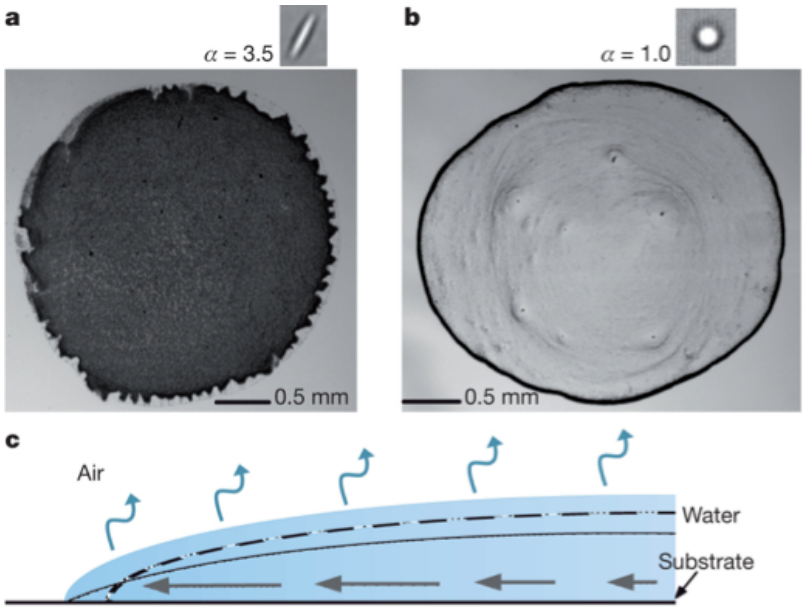

Figure 18: Image of film with ellipsoidal nanoparticles (a) and spherical nanoparticles (b), where the coffee ring effect can be clearly see due to the outward flow in the droplet (c). Reprinted with permission from Ref. [13].

It has been observed that solvent molecules can get occluded to result in non-close-packed assemblies.[279] It has also been shown that host-guest chemistry can be used to create non-close-packed nanostructures.[115] For example, PbSe nanoparticle dispersions mixed with guest molecules squalane, squalene, or polymers such as polyisoprene, were allowed to evaporate on substrate resulting in non-close-packed structures such as AB_{13}. Without the inclusion of guest molecules a close-packed crystal is obtained.

In order to prevent the coffee ring effect, the dispersion can be contained within a cavity and allowed to evaporate. An example of this procedure is to place a Teflon ring on a substrate, add a polymer nanoparticle dispersion inside the ring, and allow the solution to evaporate. Often, the result is a close-packed colloidal crystal.[280] Aside from typical polymer nanoparticles PS/PMMA, mesoporous silica particles filled with conjugated polymers can also be assembled via dispersant evaporation. The silica can be etched away leaving a polymeric nanostructured

material.[281] Using PS nanoparticles self-assembled on a substrate constrained by a ring, the effect of polydispersity on the order of the assembled colloidal crystals was demonstrated. When a colloidal solution has wide size dispersity, it was shown that there are "non-uniformities in the filling fraction."[282]

Solvent evaporation/capillary flow induced self-assembly of poly(9,9-di-n-octylfluorenyl-2,7-diyl) (PFO) and MEH-PPV and a blend of the two polymer nanoparticles has also been demonstrated in a confined well.[283] This was done in a 600 μm gap between two vertically aligned ITO substrates. The spacing between the two ITO substrates was filled with the nanoparticle dispersion (30 nm and 74 nm respectively) in 40% (v/v) ethylene glycol (EG)/H_2O. The surface tension gradient creates a Marangoni flow opposite and parallel to the capillary forces. The Marangoni force can be tuned by varying amount of EG such that it reduces the capillary flow, and thus circumvents the nanoparticle concentration gradient in dried films (Figure 19). The nanoparticles self-assemble due to particle-particle interactions, particle-ITO interactions, and due to entropic effects.

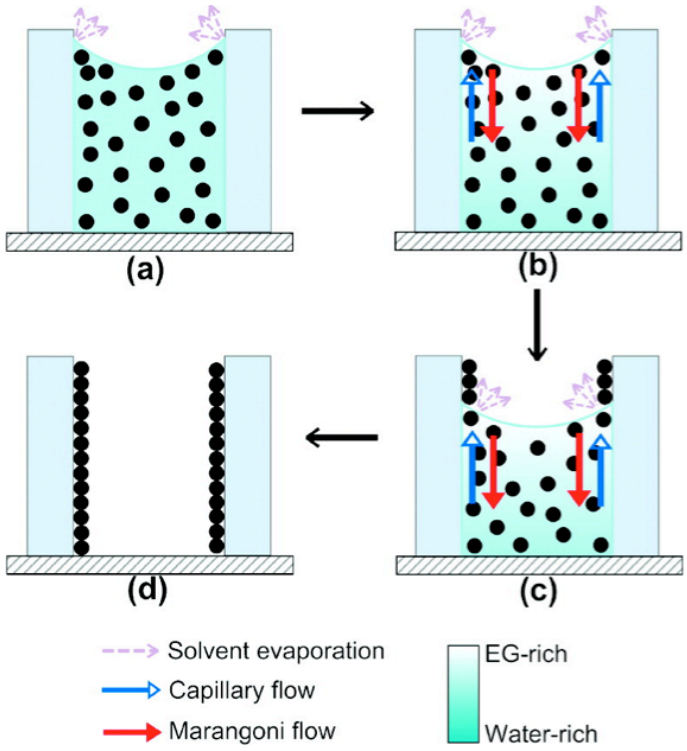

Figure 19: The formation of nanoparticle assemblies due to solvent evaporation, Marangoni and capillary flow in EG/H_2O dispersant. Reprinted with permission from Ref. [283].

Ordered structures have also been obtained using binary nanoparticle systems where the size of the small nanoparticle is less than or close to the size of the void created by the hexagonally packed large nanoparticles.[216,276] In this example, the horizontal deposition has been shown to produce large binary colloidal crystals of PS where the small nanoparticles fill in the voids of the packed large nanoparticles. Similar binary and ternary nanoparticle colloidal crystals have also been obtained through layer-by-layer assembly. In this method, a single nanoparticle solution of PS or SiO_2 in water was confined on a substrate and allowed to evaporate. Then a different size nanoparticle dispersion was directly applied onto the aforementioned assembly and allowed to evaporate.

Assembly of inorganic nanoparticles through solvent evaporation has been demonstrated to produce a diverse number of ordered structures (Figure 20) with natural analogues including but

not limited to: NaCl, CsCl, NiAs, CuAu, FeCr alloy, orth-AB, AlB_2, $MgZn_2$, $MgNi_2$, Cu_3Au, Fe_4C, $CaCu_5$, CaB_6, $NaZn_{13}$, CdSe, cub-AB_{13}, ico-AB_{13},[92,200-213,284] and A_6B_{19} which interestingly has no natural analogue.[285] The technique, most notably utilized by Murray, Talapin and co-workers, is the solvent evaporation of single, binary, or ternary nanoparticle dispersions on an angled substrate at elevated temperatures and reduced pressure (Figure 21). Murray and co-workers exemplified the effects of radius ratio, particle volume fractions, and the particles relative charge on the self-assembly of nanoparticles, by tuning these properties to obtain a large variety of structures. It was demonstrated that the superlattices formed by a colloidal dispersion could be changed by adding small amounts of carboxylic acids, trioctylphosphine oxide (TOPO), or dodecylamine. This result is another example of complexity of the interplay of various interactions, such as the van der Waals, electrostatic, steric repulsion, dipolar, and entropic forces that dictate the structure of nanoparticle assemblies.[92,203] Talapin and co-workers used temperature as a tool to control the ordering of nanoparticles into diverse structures.[200] This method has been consistently proven to be a versatile technique to self-assemble inorganic nanoparticles into a variety of ordered nanostructures, and has also been extended to organic nanoparticles.[231] Using this method it has been demonstrated that a binary dispersion of PS nanoparticles in $CHCl_3$, (radius ratio between 0.52 to 0.85) can self-assemble into ordered crystals. The charge on the nanoparticles is tuned by incorporating complementary functional groups during the synthesis of the nanoparticles to increase interparticle attraction.

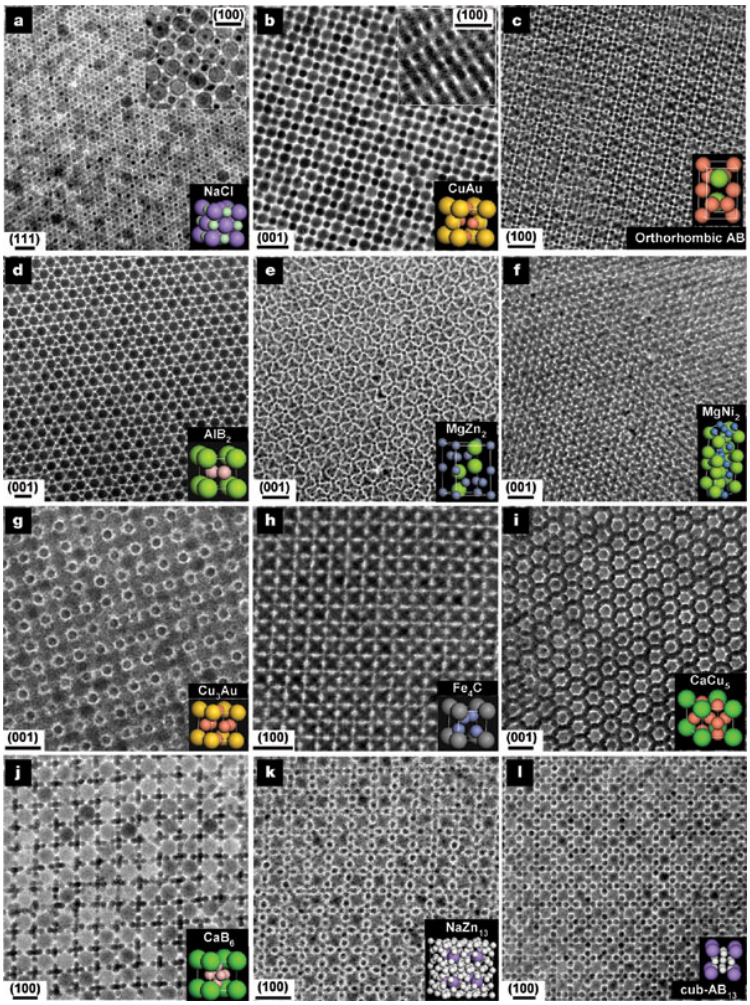

Figure 20: TEM images of binary nanoparticle assemblies, exemplifying the structural diversity. Reprinted with permission from Ref. [92].

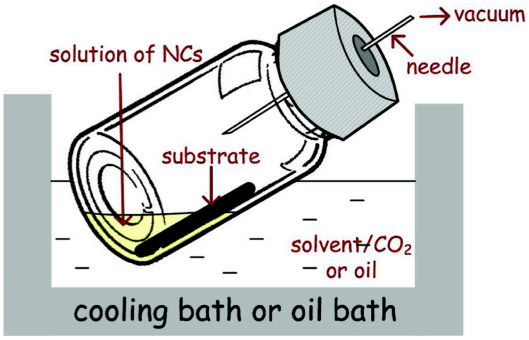

Figure 21: General apparatus setup for inorganic nanoparticle self-assembly. Reprinted with permission from Ref. [200].

Solvent composition plays a major role in determining whether nanoparticles self-assemble into glassy structures or ordered superlattices. The solvent plays an important role in mediating interparticle interactions.[186,286] Much like small molecule crystallization, the key to obtaining an ordered crystal is a slow transition to the destabilization of the colloidal dispersion to establish equilibrium for particles to form a nanocrystal. A common strategy is to use a multi-component dispersant with a low-boiling good dispersing solvent and a high-boiling bad dispersing solvent. As the good solvent evaporates, the weak dispersing solvent causes particles to aggregate and thus nucleate nanocrystal growth. This technique was demonstrated with CdSe nanoparticles, where 95% hexane and 5% octane mixture produced a glassy crystal, whereas 95% octane and 5% octanol produced ordered superlattices.[186,287,288] Another interesting use of multi-component dispersant was with PbS, CdSe, and $CoPt_3$ nanoparticles, where the colloidal solution in hexane was placed in a test tube with a vertically aligned substrate. i-PrOH was added carefully to prevent mixing. The slow "diffusional intermixing of the solvents" caused the growth of nanocrystals on the substrate.[289] The multi-component dispersant evaporation is a versatile technique and provides opportunity to easily tune interparticle interactions during self-assembly.

Another method that has been used to obtain colloidal crystals is the continuous motorized deposition technique developed by Nagayama and Dimitrov.[290] In this method, nanoparticles were assembled into hexagonal close-packed arrays by the convective force generated by dispersant evaporation. Polystyrene nano/sub-micron particles (79 nm to 2106 nm) were suspended in water with trace amounts of SDS, NaCl, octanol, and milk casein protein to tune the wetting properties of the dispersion. A glass slide was mechanically lifted with a gearbox vertically out of the nanoparticle dispersion at the same rate at which the array is formed, so that

the leading edge of the assembly is at a constant position with respect to the colloidal solution. The rate of convective assembly is described by the equation: $v_c = \frac{\beta l j_e \varphi}{h(1-\epsilon)(1-\varphi)}$ where v_c is the rate of crystal growth, β a constant from 0 to 1 that depends on particle interactions, j_e is the dispersant evaporation flux, φ is the product of the number of nanoparticles per volume and the volume occupied by a single particle, h is the thickness of the assembly or the size of the nanoparticle in a monolayer, and ϵ is the porosity of the packing of the assembly. (Figure 22). This technique has been used with PS and SiO_2 to make colloidal crystals and inverse structures.[291] This principle of rate of convective assembly was also demonstrated in experiments where a small volume of PS/Au nanoparticles are dragged horizontally across the substrate by a "deposition plate" controlled by a motor to create hexagonally packed lattices,[292] and in binary nanoparticle systems of PS nanoparticles (140 to 300 nm) in a vertically oriented confined convective assembly apparatus controlled by a motorized dipping machine (Figure 23). Depending on the radius ratio and particle volume fraction, ordered lattices of AB, AB_2, AB_3, AB_4, and AB_5 were obtained.[293]

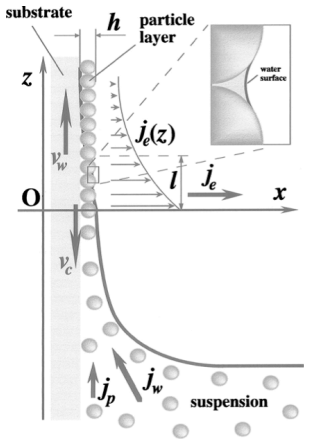

Figure 22: Schematic of continuous convective assembly where "v_w is the substrate withdrawal rate, v_c is the array growth rate, j_w is the water influx, j_p is the respective particle influx, j_e is the water evaporation flux, and h is the thickness of the array." Reprinted with permission from Ref. [290].

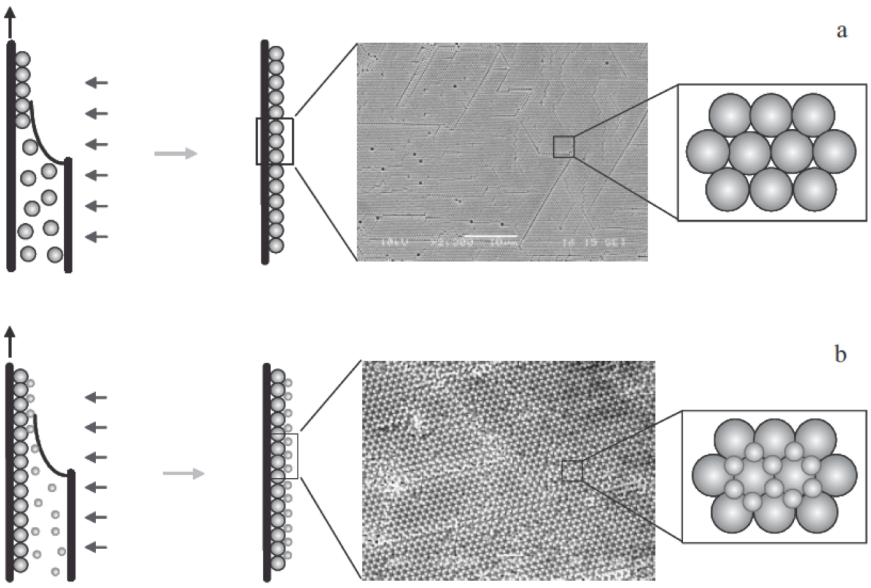

Figure 23: Schematic of confined assembly where a template is formed of larger particles (a) for the smaller particles to form binary assembly (b). Reprinted with permission from Ref. [293].

2.2.2 Self-Assembly at the Liquid-Air Interface

Self-assembly at the liquid-air interface has been widely used to obtain colloidal crystals and superlattices. This method circumvents the non-equilibrium droplet and coffee ring effect by moving nanoparticles to the liquid-air interface where equilibrium can be established.[294] The following will demonstrate some of the methods that have been utilized to migrate nanoparticles from solution to the liquid-air interface to self-assemble.

Experiments with Au nanoparticles revealed that by adding dodecanethiol to dispersions, the nanoparticles migrate to the liquid-air interface where islands self-assemble at the interface, merge, and form long-range ordered lattices (Figure 24). There are two important elements to this technique first, “rapid evaporation to segregate particles near the liquid–air interface”, and second an “attractive interaction between the particles and the liquid–air interface to localize them on the interface”.[294-296] This was further explored with various “alkanethiol/solvent

combinations using decanethiol or dodecanethiol as the coating agent and hexane, octane, decane, or dodecane as the solvent to disperse the nanocrystals" where decahedra, icosahedra, and cubooctahedra crystals were formed.[297]

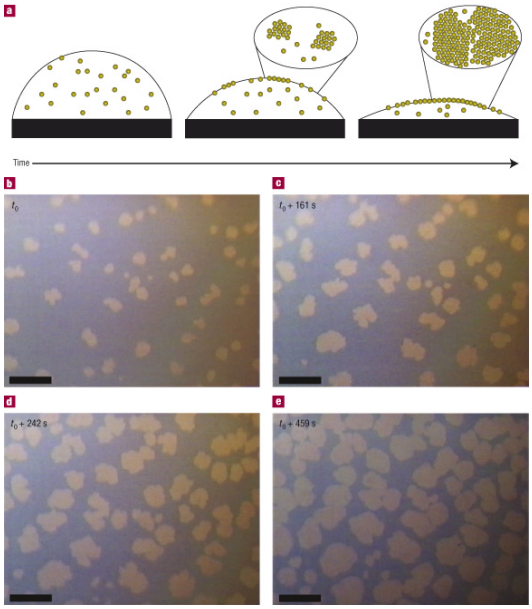

Figure 24: Schematic of migration of nanoparticles to the liquid-air interface during drying (a) and optical images of nanoparticle island growth (b-e). Reprinted with permission from Ref. [294].

Self-assembly at the liquid-air interface, when the liquid is a "bad" dispersant for the nanoparticles has proven to be an interesting method for colloidal crystal formation. This technique was utilized my Murray and co-workers, where Fe_3O_4 and FePt nanoparticles dispersed in hexane were applied on top of an immiscible diethylene glycol (DEG) layer. As the hexane evaporated the nanoparticles self-assembled at the DEG-air interface resulting in a large-scale AlB_2 superlattice that can be easily transferred from the interface to any substrate (Figure 25).[298] This technique has also been used to create additional binary and ternary superlattices,[299] binary assemblies of Au nanospheres, rods, wire,[297] CdSe nanoparticles,[288] and anisotropic nanocrystals.[300] Addition of a miscible solvent that is still

a bad solvent for the nanoparticles also results in self-assembly at the liquid-air interface.[301-303]

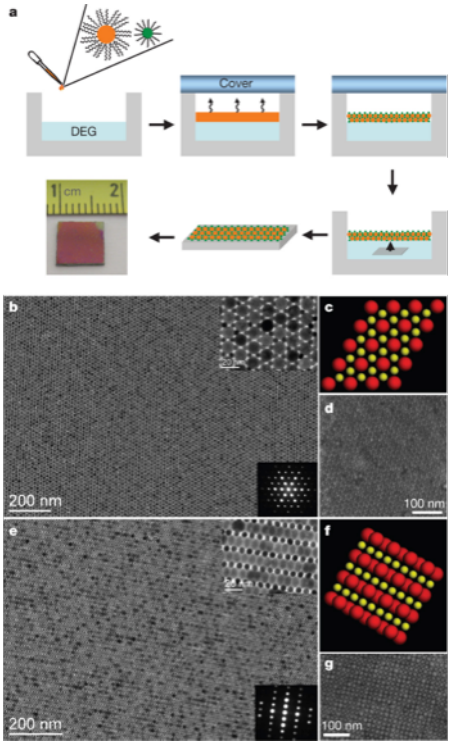

Figure 25: Schematic of nanoparticle assembly at the DEG-air interface (a), and AlB2-type BNSL membranes self-assembled from 15-nm Fe3O4 and 6-nm FePt nanocrystals (b-g). Reprinted with permission from Ref. [209].

Diverse binary assemblies at the air-dispersant interface have been obtained by Weiping Cai and co-workers using PS nanoparticles.[217] Convective forces generated by the evaporation of the ethanol/water dispersant are used to assemble the nanoparticles at the liquid-air interface. In this method, nanoparticle dispersions of 1:1 ethanol/water containing both the large and small nanoparticles is injected into a preformed water droplet on the substrate. The volatile alcohol carries the nanoparticles to the water-air interface where they self-assemble into ordered structures (AB_2, AB_6, AB_9, AB_{12}, AB_{17}, and hybrid combinations of two structures). The rapid evaporation of ethanol increases the convective forces in the droplet carrying nanoparticles to the

interface. The particles are confined to the interface due to hydrophobic effects and the surface tension of the dispersant (Figure 26 (top)). The structural diversity obtained through this method can be tuned with radius ratio, volume ratio, and concentration ratio of small to large nanoparticles (presented in a phase diagram in Figure 26 (bottom)). This is a useful and versatile technique, however the maximum radius ratio in the phase diagram is 0.2, and has yet to be validated when the nanoparticles are similar in size.

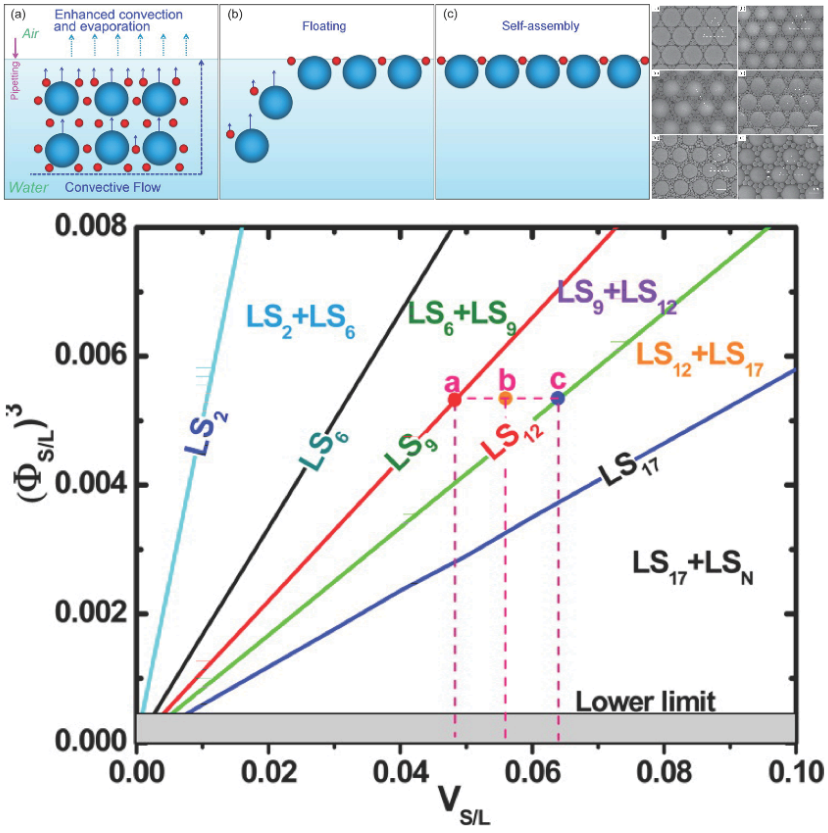

Figure 26: Scheme of ethanol assisted transfer of nanoparticles to the liquid-air interface (top left), and SEM image of binary assemblies (top right), and phase diagram of volume ratio vs. radius ratio cubed. Adapted with permission from Ref. [217].

The self-assembly of nanoparticles at the liquid-air interface is a versatile technique to obtain a wide-array of morphologies. The most attractive feature of this method is the exit from the non-equilibrium--almost chaotic and uncontrollable--droplet on a substrate, to the interface where

equilibrium can be established. A major concern is whether this concept can be extended to large-scale operations.

2.2.3 Self-assembly at Liquid-Liquid Interface

The liquid-liquid interface presents an interesting medium for nanoparticle self-assembly. Nanoparticles can quickly and easily assemble into the lowest free energy configuration due to the equilibrium accomplished by the high mobility of nanoparticles at the liquid-liquid interface, as demonstrated with CdSe nanoparticles at the water-toluene interface.[304,305] Thin films of Au nanoparticles were self-assembled at the water-toluene interface using this method.[306] Micelles of nanoparticle heterodimers (Fe_3O_4, Ag) were self-assembled at the interface between water and various organic solvents.[307]

Furst and co-workers demonstrated the 2D self-assembly and size-sorting of positively charged PS nanoparticles near a water-oil interface.[308] The authors reason that: "as the interface confines colloids dispersed in the aqueous phase against a solid substrate, the disjoining pressure generated by the electrostatic repulsion with the charged particles causes the interface to deform locally, in the normal direction. This deformation generates long-range lateral capillary forces between the particles, which drive their rapid self-assembly." The resulting structures are "defect free" and ordered.

2.2.4 Other Types of Self-Assembly

Talapin and co-workers have used a microfluidic method technique to assemble $CoFe_2O_4$, CdSe, PbS, Au, and Pd nanoparticles into single and binary nanoparticle superlattices.[309] In this technique, the nanoparticle dispersion along with more dispersant (toluene) and a precipitant (miscible bad solvent, ethanol, *i*-propanol, *n*-butanol) are injected into the microfluidic capillary tubing with an immiscible bad solvent (perfluoro-tri-*n*-butylamine, perfluoro-di-*n*-

butylmethylamine, or perfluoropentylamine) as the carrier fluid at a controlled injection rate. Nanoliter plugs are created in the tubing, and crystallization occurs either within the nanodroplet, or at the liquid-liquid interface depending on the system, to create fcc single particle size crystals, or AlB_2 binary crystals. The volumes of all three of the injected components can be varied to control the size of the plug, the NP concentration, and the amount of precipitant (Figure 27).

Template assisted assembly has also used to obtained ordered nanoparticle assemblies. Nanoparticle aggregates of PS and SiO_2 nanoparticles were made by forcing them into templates with capillary flow.[310] Also, inkjet printing colloidal poly(para-phenylene) or Au nanoparticle solutions into templates have been used to create ordered nanostructures.[311] Furthermore, CdSe and Fe_2O_3 nanoparticles have been shown to make up to 100 layer thick ordered crystals using a patterned microfluidic cell.[312,313]

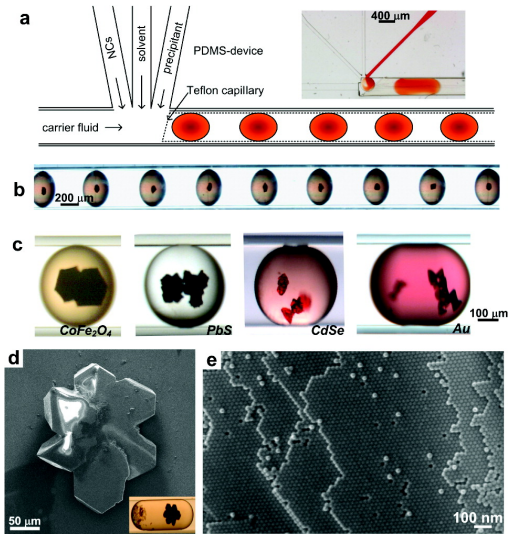

Figure 27: Apparatus for microfluidic self-assembly (a) in nanoliter plugs (b). Crystallization within the plugs (c) results in ordered assemblies (d and e). Reprinted with permission from Ref. [309].

Layer-by-layer spin coating is a simple technique that has been used for creating binary colloidal crystals. This technique was demonstrated with 222 nm to 891 nm silica nanoparticles and works by spin coating nanoparticle dispersions in ethanol/ethylene glycol, first the larger sized nanoparticles, and the then the smaller, and then repeat. This technique has been utilized to obtain AB_2 and AB_3 structures.[314] Another interesting nanoparticle self-assembly technique that also utilizes layer-by-layer is the alternatively dipping of the substrate into a polyelectrolyte, and then into an oppositely charged colloidal dispersion. This creates a nanoparticle polyelectrolyte sandwich,[315,316] and has also been conducted with magnetic nanoparticles with assistance of a magnetic field.[317]

The use of biological molecules covalently or coordinately bound to nanoparticles has also drawn considerable interest for nanoparticle assembly.[232,318-328] For example, work by Mirkin and co-workers self-assembled gold nanoparticle containing DNA oligonucleotide "sticky ends". Complementary pieces of DNA bind to each other and create nanoparticle aggregates, which can be reversibly assembled and disassembled with heat by forming and breaking hydrogen bonds.[232] One can imagine imparting functionality, which need not be biological, to rationally self-assemble nanoparticles.

2.3 Tunable Electrical Percolation in Binary Assemblies of Polymer Nanoparticles

This chapter[††] details the experimental and theoretical analysis of charge percolation through random assemblies of nanoparticles, so-called 'glasses'. Binary polymer nanoparticle glasses provide opportunities to realize the facile assembly of disparate components, with control over nanoscale and mesoscale domains, for the development of functional materials. This work demonstrates that tunable electrical percolation can be achieved through semiconducting/insulating polymer nanoparticle glasses by varying the relative percentages of equal-sized nanoparticle constituents of the binary assembly. Using time-of-flight charge carrier mobility measurements and conducting atomic force microscopy, we show that these systems exhibit power law scaling percolation behavior with percolation thresholds of ~24–30%. We develop a simple resistor network model, which can reproduce the experimental data, and can be used to predict percolation trends in binary polymer nanoparticle glasses. Finally, we analyze the cluster statistics of simulated binary nanoparticle glasses, and characterize them according to their predominant local motifs as (p_i, p_{1-i})-connected networks that can be used as a supramolecular toolbox for rational material design based on polymer nanoparticles.

The primary experimental tools used were TOF, and conducting atomic force microscopy (cAFM). Different concepts, across disciplines, were used to analyze the data, such as:

[††] This chapter was adapted, with permission, from Renna, Lawrence A., Monojit Bag, Timothy S. Gehan, Xu Han, Paul M. Lahti, Dimitrios Maroudas, and Dhandapani Venkataraman. "Tunable Percolation in Semiconducting Binary Polymer Nanoparticle Glasses." *The Journal of Physical Chemistry B* 120, no. 9 (2016): 2544-2556. I would like to acknowledge Dr. Xu Han for her numerical simulations of time-of-flight (TOF) mobility, Dr. Timothy S. Gehan for synthesizing the nanoparticles, and Prof. Monojit Bag for preparing devices, making TOF measurements, and many useful discussions.

percolation theory and network theory. Thus, these topics will be introduced here prior to presentation of the article.

2.3.1 Background

2.3.1.1 Time-of Flight Charge Carrier Mobility

Electrical conduction through semi-conducting polymers occurs through charge carriers, positively charged holes and negatively charged electrons. The conductivity (σ) of a material is $\sigma = n \times e \times \mu$, which is equivalent to $\frac{I}{E}$, where n is the number of charge carriers, e is the elementary charge, μ is the chare carrier mobility, I is current, and E is the applied field. The mobility is related to E, and the drift velocity of charge carriers (v_d) by the equation: $\mu = \frac{v_d}{E}$. Therefore, the charge carrier mobility, μ, is how fast charge individual carriers move through a material, with respect to E. On the other hand, conductivity, σ, describes the net speed of all charges through a material with respect to E.

To measure the mobility through the *bulk* of a material, Time-of-Flight (TOF) charge carrier mobility is employed. The TOF mobility is a good indication of how well a material transports charge carriers because it is independent of the number of carriers, and it is a bulk measurement, compared to field effect transistor (FET) mobility measurements which are dominated by interfacial charge carrier transport. The devices architecture for TOF experiments (Figure 28 left), in general, consists of a sandwich structure of a transparent electrode, the material of interest, and a top metal electrode. The sample is pulsed with a laser to generate charge carriers, and the current is measured as a function of time (Figure 28 right). The mobility is then calculated by $\mu = d^2 \times \tau^{-1} \times E^{-1}$, where τ is the transient time, and d is the thickness of the material being measured.

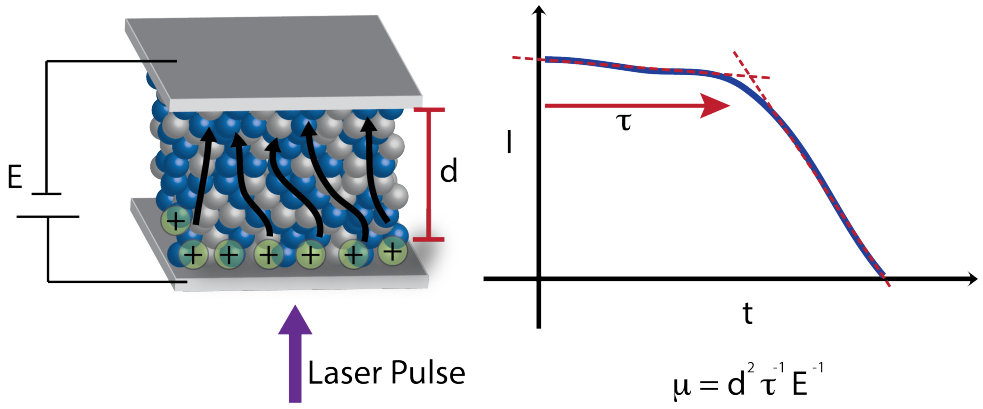

Figure 28: Depiction of TOF experiment and measurement.

While the charge carrier mobility is useful to describe the speed of charge carrier transport, there is even more information that can be gleaned from TOF experiments about the nature of charge carrier transport in the material. The shape of *I* vs *t* curve gives information about how dispersive the charge carrier transport is. A square curve indicates a uniform distribution of charge carriers, transporting through the material at similar times. A less square, slopped curve indicates dispersive charge carrier transport, where carriers are arriving at the top electrode at quantitatively different times.

2.3.1.2 Conducting Atomic Force Microscopy (cAFM)

Conductive atomic force microscopy (cAFM) is a useful tool to measure current profiles of films. Although it technically measures surface current, it is actually a *bulk measurement* because current has to travel through bulk film to the conductive AFM probe, akin to scanning tunneling microscopy (STM). In a typical cAFM experiment, the material is coated on top of an electrode, sometimes a charge selective transport layer is used as an interlayer/charge injection layer. An AFM probe with a metallic conducting coating is brought into contact with the top of the material, and raster scanned. Contact, with the same amount of force (controlled by applying a voltage to a piezoelectric stack)

cAFM can provide information on bulk morphology of conjugated polymer films. Dark hole current measurements by cAFM of poly(3-hexylthiophene-2,5-diyl) (P3HT) Phenyl-C_{61}-butyric acid methyl ester (PCBM) blends show an increase in overall current magnitude but also a widening current distribution with increased annealing time.[329] The authors attribute this broadening of current distribution to "heterogeneity of the morphology" in the film.[330] cAFM has also provided evidence of percolation networks in poly(ethylene oxide)-b-poly-triphenylamine (PEO-b-PTPA) within a TiO_2 matrix by measuring local conductive domains that carry current from the electrode.[331] Another investigation has shown the broadening of current distribution and increase in overall current when the size of P3HT crystallites is increased through solvent processing.[332] Their model is shown in Figure 29, where the P3HT crystallites provide the conductive pathway for charge collection at the cAFM probe.

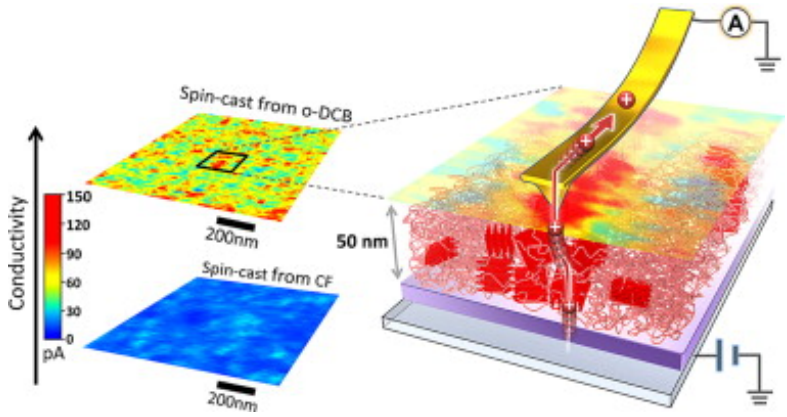

Figure 29: Speculated model of conducting pathways through P3HT crystallites measured by cAFM. Figure shows the experimentall higher and more heterogeneous surface current images obtained from o-dichlorobenzene (o-DCB) processed films as compared to chloroform (CF). Reprinted with permission.[332]

These studies mentioned here do not provide the desired amount of morphological information that would allow for a predictive model. This is because the systems studied lack the predefined nano-domains that nanoparticles provide that allow for adequate models of the

morphology. Therefore, nanoparticles provide a viable nanostructure that can be predicted with computer simulations and to use cAFM to accurately determine morphology.

2.3.1.3 Percolation Theory[‡‡]

Percolation theory is a useful tool to describe how the connectivity of a set of constituents effects its structure, its mechanical properties, and its transport properties. Percolation was first introduced in 1957 to describe the flow of a fluid through a structure with randomly open and closed passages, see Figure 30. This type of percolation is called bond-percolation, where the transport occurs through the connections of occupied sites in the structure. Conversely, site-percolation occurs through the constituent components of the network. Figure 31 illustrates the connectivity maps for bond-percolation networks (top) and site-percolation networks (bottom).[188]

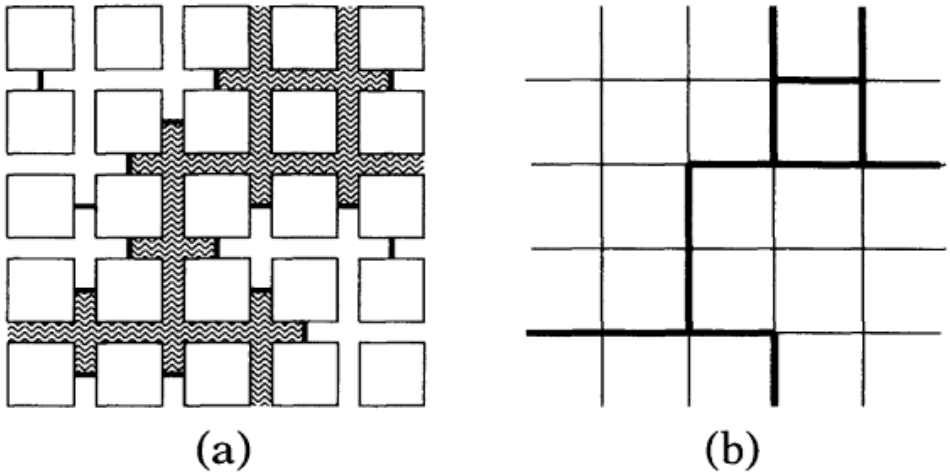

Figure 30: (a) Bond-percolation of a fluid through the open channels of a square lattice. (b) Connectivity map of percolation in (a). Reprinted with permission from Ref. [188]

[‡‡] I would like to acknowledge use of Torquato, Salvatore. *Random heterogeneous materials: microstructure and macroscopic properties*. Vol. 16. Springer Science & Business Media, 2013; which has been invaluable to my understanding of percolation theory, and its subsequent application to nanoparticle assemblies fabricated in our lab. This book has been the primary source of knowledge for the introduction to percolation theory provided here.

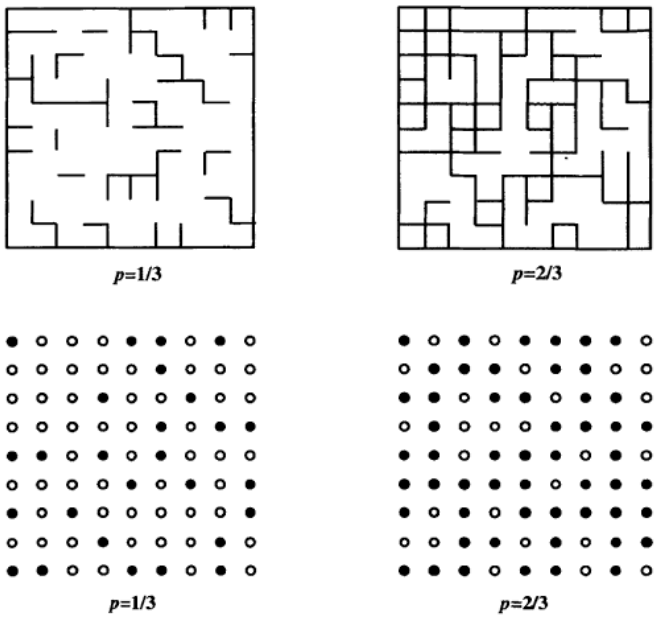

Figure 31: (top) Bond-percolation, and (bottom) site-percolation for a square lattice. Reprinted with permission from Ref. [188].

For any network, the percolation is determined by the number of 'open' bonds or sites (p). The percolation is zero below a percolation threshold (p_c), and is non-zero above p_c. Bond-percolation and site-percolation have inherently different p_c for the same structure. For example, the bond- p_c for a square lattice is $p_c = 50\%$, while for site percolation $p_c \approx 59\%$ (see Figure 31). We will focus on site-percolation from this point forward as it is most relevant to transport through nanoparticle assemblies.[188]

Open bonds or sites connect to create a network; the connectivity of a network is determined by the coordination number (Z) and the dimensionality (d) of the structure or lattice. This is shown in Table 2 for selected lattices, along with their respective p_c exact or numerical solutions. Generally, the higher the dimensionality d and coordination Z, the lower the p_c due to the higher connectivity of the network.[188]

Percolation in infinite ordered lattices is relevant to predicting macroscopic properties of heterogeneous (open or closed sites) materials. To predict p_c, we use the equation $p_c = {f_c}/{\phi}$, where ϕ is the packing fraction of, and f_c is the critical occupied volume fraction. Scher and Zallen have found that f_c is an approximate invariant for p_c.[333] For $d = 2$, $f_c \sim 45\%$, and for $d = 3$, $f_c \sim 16\%$. Using the above relation, we estimated p_c for various lattice types (see Table 2) with good correlation to exact or numerical solutions. For bicontinuous percolation, generally, the expression $p_c < p < 1- p_c$ should be satisfied, and thus p_c should be less than or equal to 50%. However, if a system has phase-inversion asymmetry, or next nearest-neighbor percolation, bicontinuous percolation can still be achieved when $p_c > 50\%$.[188]

Thus far we have only discussed ordered lattices with randomly occupied sites. Random assemblies of spheres are relevant system to study as they are good models for heterogeneous materials, and as we have mentioned previously, ubiquitously formed for functional materials. The number of nearest neighbors, Z is not a discrete number but rather a distribution in these types of assemblies. Thus, the network of open sites is not as intuitive to picture. The packing fraction of a random close packed assembly of spheres is $\phi = 64\%$, thus the p_c, can be predicted to be 25%.Continuum models have calculated 29% for maximally jammed random assemblies of non-overlapping spheres.[188] These results, to the best of our knowledge, have not been validated for random assemblies of nanometer sized particles until our study.[334]

Table 2: Dimensionality (d), coordination number (Z) and site-percolation thresholds for selected lattice types from exact results, and using the invariant f_c/ϕ. Adapted with permission from Ref. [188].

	Lattice			p_c	
Name	***d***	***Z***	$\boldsymbol{\phi}$	***exact/numerical solution*** [188]	f_c/ϕ
Hexagonal (Honeycomb)	2	3	64%	70%	74%
Square	2	4	78%	59%	57%
Triangular	2	6	91%	50%	50%
Diamond	3	4	34%	43%	47%
Simple Cubic	3	6	52%	31%	31%
Body-centered Cubic	3	8	68%	25%	24%
Face-centered Cubic	3	12	74%	20%	22%
Random Close Packed	3	~6	64%	29%	25%

Many bulk properties (i.e. transport) of heterogeneously percolating materials exhibit power law scaling. For example, the conductivity goes $\sigma \sim (p - p_c)^t$, for $p > p_c$, where t is the *independent* 'critical exponent'. Numerical simulations yield t = 1.3 and 2 for d = 2 and 3 respectively, although experimentally (for d = 3) t varies from 1.5 to 11.[335,336] One explanation for this variance invokes charge tunneling. In tunneling-percolation theory $\sigma \sim (p - p_c)^T$, where $T = {t + 1}/{1 - \alpha}$, and $\alpha = {1 - \xi}/{2(a - d)}$, where a is the interparticle distance, d is the particle diameter, and ξ is a tunneling factor.[336] Thus far, unfortunately to the detriment of material design and predictability, a rigorous correlation between t and

geometric exponents does not exist.[188] However, the power-law scaling can be used to predict bulk properties; which we will demonstrate in this chapter.[334]

2.3.1.4 Network/Graph Theory[§§]

It is useful to classify chemical/molecular networks by their geometries or topologies. Examples of describing connected chemical or molecular systems by their network or graph structure are found for ionic and inorganic lattices,[337,338] covalently bonds in molecules,[339] coordination networks[340], hydrogen-bond patterns,[341] polymer morphologies,[342] neural networks,[343] nanoparticle assemblies,[344,345] and more (see Figure 32).

The benefit of this approach is that no matter how complex a system is; it can be reduced to a system of *p*-connected points. For simple systems, the *p*-connectedness is the same for all points and can thus be described as a *p*-connected network. I will discuss later how to address more complex networks with non-discrete *p*-connectedness. The basic systems of connected points, as defined by A.F. Wells is: "$p = 1$: there is only one solution, a pair of connected points. $p = 2$: the only possibilities are closed rings or an infinite chain. $p \geq 3$ the possible systems now include finite groups (for example, polyhedral) and arrangements extending indefinitely in one, two or three dimension (*p*-connected nets)." Figure 33 illustrates the possible structures for each *p*-connected network (for $p \geq 3$).[337]

[§§] I would like to acknowledge use of the book, Wells, Alexander Frank. *Structural inorganic chemistry*. Oxford University Press, 1975; which has been invaluable to my understanding of network theory, and its subsequent application to nanoparticle assemblies fabricated in our lab. This book has been the primary source of knowledge for the introduction to network theory provided here.

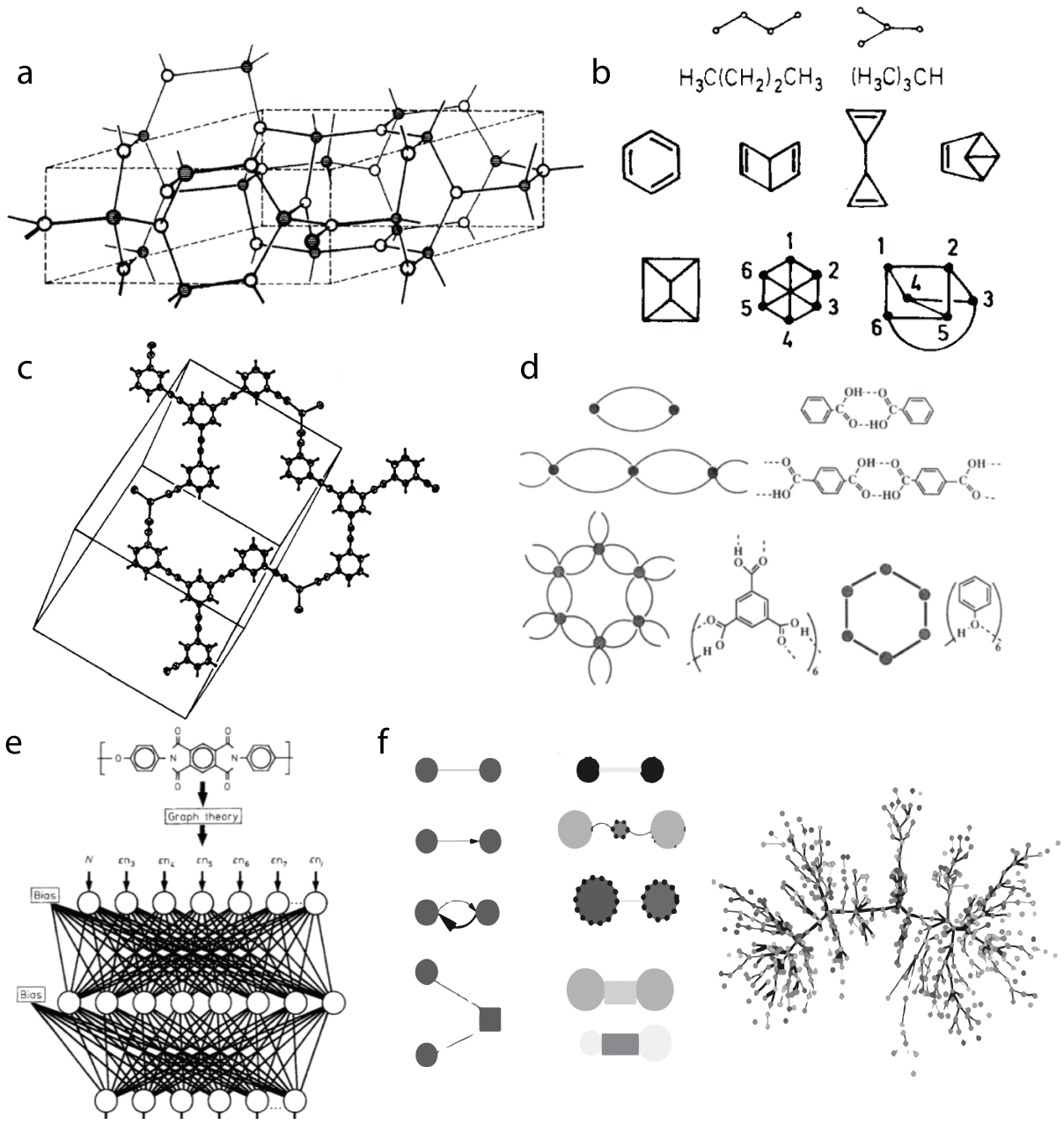

Figure 32: Network representations of chemical structures with increasing size scale (from atoms to molecules, to macromolecules, to nanoscale aggregates. (a) Ge_3N_4 structure represented as a (3, 4)-connected network.[337] (b) Chemical structure and network representation (top) C_4H_{10} isomers, and (bottom) $(CH)_n$ annulene isomers.[339] c) 3-connected network of coordination network Ag[1,3,5(4-ethynylbenzonitrile)benzene)CF_3SO_3] $2C_6H_6$.[346] d) Chemical structure and network representation of (top) 2-connected infinite repeating dimer hydrogen bond pattern of terephthalic acid, (bottom left) 3-connected hydrogen-bonded cyclic dimers of trimesic acid, and (bottom right) 2-connected cyclic phenol hydrogen bonding motif.[341] (e) Highly *p*-connected network representation of polymer Kapton.[342] (f) (left) elements of a network of nanoparticles (middle) types of nanoparticle interactions, and (right) maximum flow network.[344]

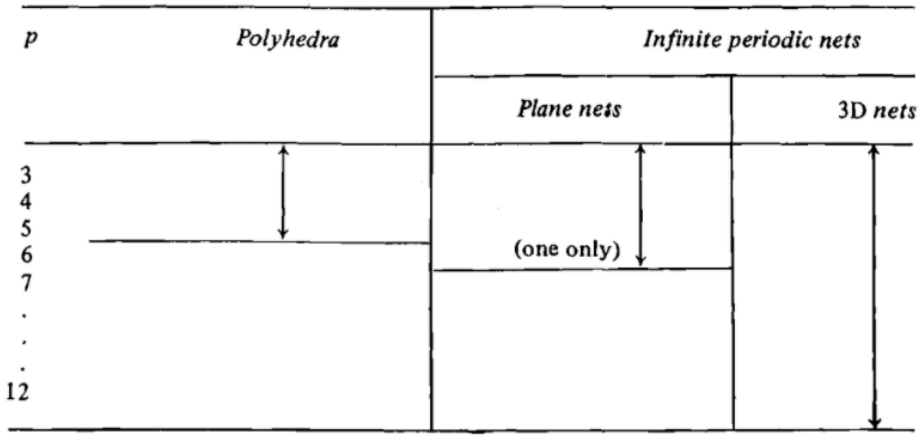

Figure 33: Possible structures for p-connected networks (for $p \geq 3$). Adapted from Ref. [337].

By applying network theory to real systems such as oxides and oxy-ions (where the tetrahedral MO_4 motif is the constituent component of the network), we can see that the structural rules illustrated by A.F. Wells for p-connected networks applies (see Figure 34). Thus, the general rules of a p-network can be used to determine or predict the structure of an assembly.[337]

p	*Oxy-ion*				*Oxide molecule*	
1	pyro	$Si_2O_7^{6-}$	$P_2O_7^{4-}$	$S_2O_7^{2-}$	Cl_2O_7	finite
2	meta	$(SiO_3)_n^{2n-}$	$(PO_3)_n^{n-}$	$(SO_3)_n$		cyclic or linear
3	infinite 2D	$(Si_2O_5)_n^{2n-}$	$(P_2O_5)_n$			polyhedral, 2D, or 3D
4	infinite 3D	$(SiO_2)_n$				infinite 3D

Figure 34: Chemical formulas of oxides and oxy-ions, their p-connectedness, and network structure. Adapted with permission from Ref. [337].

As mentioned previously, for $p \geq 3$, possible structures are polyhedral, plane nets, and three dimensional nets, thus it is useful to discuss these structures in more detail. The first class of polyhedral are called the regular (Platonic) solids, where the vertices are equivalent and the faces are all the same shape. Using Euler's relation for the number of vertices, edges, and faces,

equations can be derived to describe the structure of *p*-connected polyhedra. If x_n is the number of faces with *n* edges, then for *p* = 3, $3x_3 + 2x_4 + x_5 \pm 0x_6 - x_7 - 2x_8 - \cdots = 12$, thus a 3-connected regular-polyhedra can only being constructed with triangles, squares, or pentagons, *i.e.* the coefficients to x_3, x_4, x_5 are positive. There are three 'special' solutions (for regular Platonic solids) to the equation to describe the structure of a 3-connected polyhedra, they are x_3 = 4, x_4 = 6, and x_5 = 12, corresponding to tetrahedron, cube, and dodecahedron. For a 4-connected polyhedra, the derived equation is, $2x_3 + 0x_4 - 2x_5 - 4x_6 - \cdots = 16$, for a 5-connected polyhedra: $x_3 - 2x_4 - 5x_5 - 8x_6 - \cdots = 20$. Therefore, a 4-connected polyhedra will be composed of x_3 = 8 triangles (octahedron), and a 5-connected polyhedra will be constituted of x_3 = 20 triangles (icosahedron). Using this relationship, the five Platonic solids are derived. By truncating the Platonic solids, one can obtain semi-regular solids (Archimedean or Catalan), the resulting structure still must satisfy the derived equations for *p*-connected polyhedra derived above from Euler's relation. For example, for *p* = 3, the coefficient to x_6 is 0, therefore adding any number of hexagons will still satisfy the relation. One solution, x_4 = 6 and x_6 = 8 gives a truncated octahedron, which is related to Platonic solid, x_4 = 6, cube. Another non-trivial solution is x_3 = 2 and x_4 = 3, which is a trigonal prism.[337]

The structure of plane nets can be derived in a similar fashion to polyhedra. Where χ_n is the ratio of constituent polygons with *n* sides, the derived equations for *p*-connected plane nets is $3\chi_3 + 4\chi_4 + 5\chi_5 + 6\chi_6 + \cdots n\chi_n$ = 6, 4, 10/3, and 3 for 3-, 4-, 5-, and 6-connected nets respectively. Special solutions for for *p* = 3, 4, and 6 are χ_6 = 1, χ_4 = 1, and χ_3 = 1 respectively. The solutions correspond to the three regular networks, the hexagonal net, square net, and triangular net (Figure 35a). Of course, there are other solutions, which yield semi-regular nets, for example a 3-connected network where χ_4 = χ_4 = 0.5 is a solution for a plane net containing

squares and hexagons in equal ratios. Examples of semi-regular plane nets are shown in Figure 35b.[337]

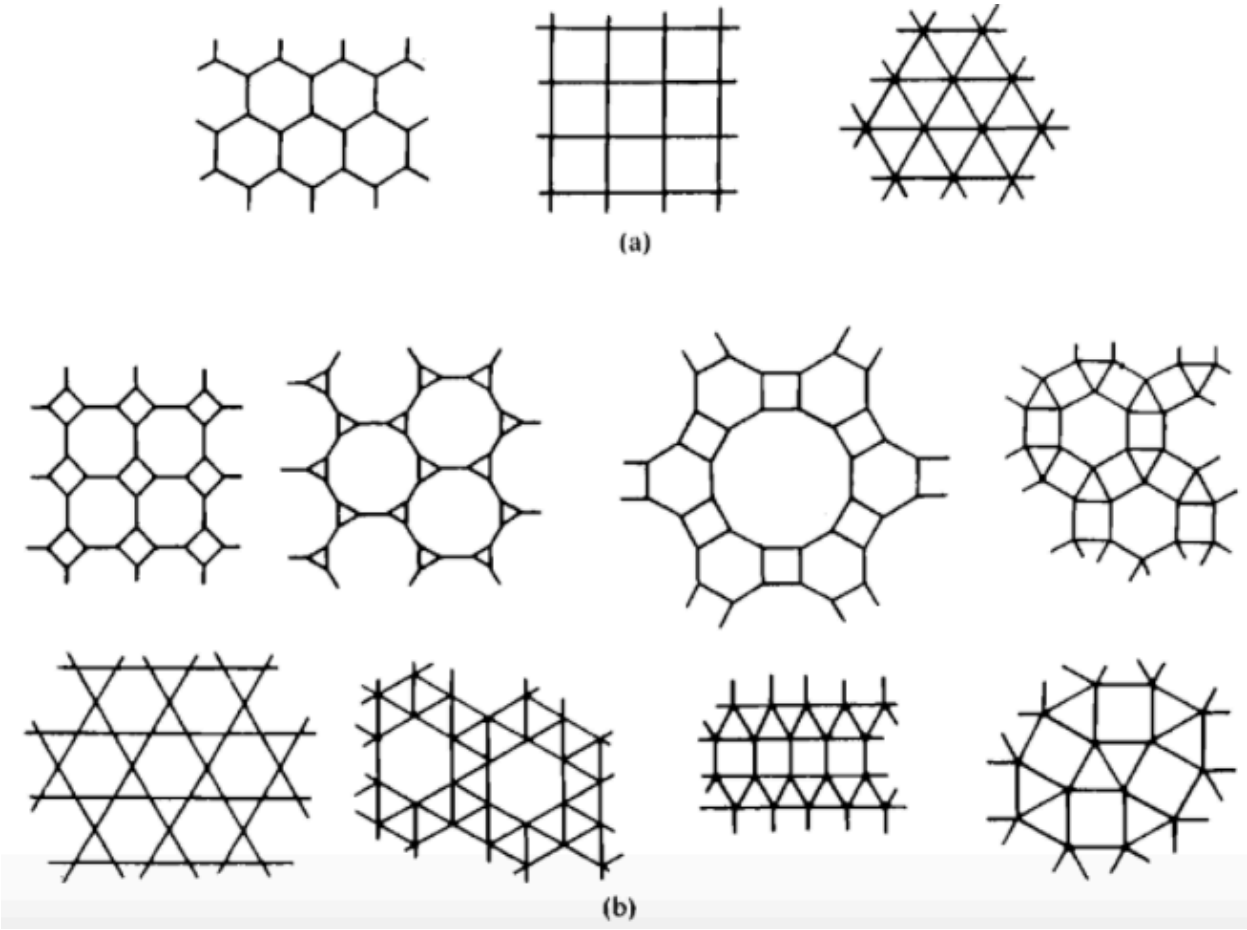

Figure 35: (a) regular plane nets and (b) semi-regular plane nets. Reprinted with permission from Ref. [337].

Networks can also be composed of multiple p_n,p_m-connected constituents, e.g. 3,4-connected network. A more general equation for the structure of p_n,p_m-connected nets is derived: $\sum n\chi_n = \frac{2(3R+4)}{(R+2)}$, where R is the ratio of p_n to p_m. The solutions of this equation range from 4 to 6 as R ranges from zero to infinity. For example, a 3,4-connected network, with a R = 2:1, $\sum n\chi_n$ = 5, a solution is χ_5 = 5. Thus the network is comprised of 5-sided constituents, containing points of 3 and 4 connectivity.[337]

Lastly, three dimensional networks do not have equations to represent their structures that polyhedra and plane nets have. Therefore, to develop a heuristic for understanding the structure of three dimensional network, we have to understand that in order to have three dimensional network, connections must be made in all 6 possible directions in Euclidean space. The simplest example is a 6-connected network, where each point makes 6 connections. For $p < 6$, points must be combined to form constituent repeat units containing N points that can make 6 connections. Constituent repeat units of a three dimensional net can consist of two $p = 4$ ($N = 2$) points, four $p = 3$ ($N = 4$) points, or a combination of two $p = 3$ and one $p = 4$ ($N = 3$) points (*i.e.* 3,4-connected net) (see Figure 36). When linkages are identical, the shapes that comprise the network can be calculated by $2(N + 1)$. Thus, a 3-connected net is made of 10 side polygons, a 3,4-connected net is made of eight sided polygons, a 4-connected network is constructed from 6 sided polygons (e.g. diamond structure), and a 6-connected network is comprised of 4 sided polygons.[337]

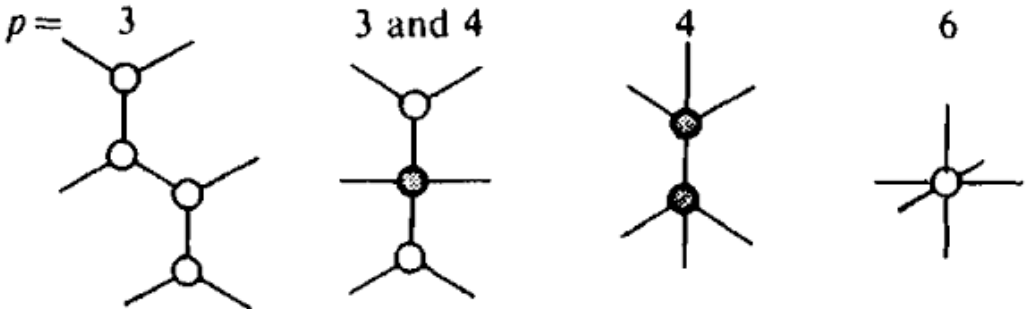

Figure 36: Constituent repeat units of three dimensional networks for (from left to right) p = 3-, 3,4-, 4- and 6-connected networks, consisting of N = 4, 3, 2, and 1 points respectively. Adapted with permission from Ref. [337].

2.3.2 Tunable Percolation in Semiconducting Binary Polymer Nanoparticle Glasses

Polymeric materials composed of two or more components with percolation pathways within each component are desired across materials science for numerous applications such as photovoltaics,[79,116,330,347] thermoelectrics,[259] ion transporting materials,[262,264]

porous catalysts,[348] membranes,[349] and conducting composites.[350] Percolation — whether it is for electrical,[264,330] thermal,[260] mass,[351] or ionic[262,264] transport — through bulk materials is determined by the *structure* and *connectivity* of a network comprised of the constituent polymer meso- or microstructure.[262,351-353] The most common method to prepare polymeric materials with percolating pathways is by blending two or more polymers in a common solvent and fabricating films or nanofibers.[79,89,116,259,330,347,354,355] Other methods employing conducting-fillers have also been explored to create polymer based percolation networks.[356] However, the morphology within these materials is dictated by several interdependent kinetic processes that cannot be independently controlled.[89,354-359] Thus, it is very difficult to control the assembly of each of the components in the nanoscale as well as the assembly of these nanoscale assemblies into a meso- or microstructure. Designing large-scale binary polymer blends with tunable percolation behavior is particularly challenging synthetically due to polymer processing conditions. Further, designing binary polymer morphologies can be very material specific.

Nanoparticles can assemble into ordered assemblies and disordered glasses.[188] Glasses are particularly exciting because of they contain much more structural diversity — they exhibit distributions of connectivity in number and type — than ordered assemblies.[360] Thus, by the paradigm: structure determines property, unique properties can arise from binary nanoparticle glasses. An analogy to this is in metallic glasses where it has been demonstrated that there exists average structural local motifs, despite the overall disorder, and tuning these motifs affects the properties of the material.[360,361] However, for polymer nanoparticle glasses the local nanoscale structure-property-relationship has not been extensively studied.

Forming nanoparticle glasses is quite simple, and occurs when equilibrium processes are disrupted.[188] This has been demonstrated for one type of polymer nanoparticle by simply increasing the particle concentration,[98,362] or by rapid film formation.[363] There are numerous examples of computational studies of binary particle glasses,[188,240,353,364-371] however very few experimental studies of binary nanoparticle glasses exist, on either structure or properties; we address both using experiment and computation.

We have been pursuing the use of polymer nanoparticle assemblies as a route to realize functional materials containing two or more components.[258] In this approach, each component is fabricated in nanoparticle form and these nanoparticles are assembled to create mesoscale structures.[258] The assembly of these nanoparticles is predominantly determined by the nanoparticle geometry and interparticle interactions. Polymer nanoparticle assemblies offer the ability to control the assembly of each component at the nanoscale as well as their structure at the mesoscale. Herein, we show that binary nanoparticle assemblies can be used to tune percolation pathways in polymer materials. As a proof-of-concept demonstration, we show that tunable electronic conduction in nanoparticle 'blends' of a semiconducting polymer, poly(3-hexylthiophene) (P3HT), and an insulating polymer, polystyrene (PS), is possible by changing the relative percentages of equal-sized nanoparticle constituents (η) in the binary blend. We have measured and modeled[256] the time-of-flight (TOF) charge carrier mobility of P3HT and PS nanoparticle assemblies[255] to probe bulk charge percolation, and used conducting atomic force microscopy (cAFM) to probe electrical percolation in the nanoscale. We fit data from TOF and cAFM experiments at various values of η to a power law scaling relation for percolation behavior.[240,261,353,372,373] Moreover, we have developed a simple resistor network model[352,374,375] to reproduce nanoscale percolation measurements by cAFM and make

further predictions. Using this model, we have analyzed the structure of percolating networks in binary polymer nanoparticle glasses in terms of their average or predominant local motifs, describing them as (p_i, p_{1-i})-connected networks. This connectivity map can be used as a supramolecular toolbox to create polymeric materials with disparate polymers assembled into functional morphologies with percolating pathways.

2.3.2.1 Experimental Methods

All chemicals were used as received from their suppliers. Nanoparticles were synthesized by post-polymerization miniemulsion via a known procedure.[116,251] P3HT from Rieke Metals Inc. with average molecular weight $\bar{M}_W$ = 36 kDa, regioregularity = 96%, and polydispersity Đ = 2.3, and PS from Sigma Aldrich with $\bar{M}_W$ = 35 kDa, were dissolved in $CHCl_3$ (Alpha Aesar) at 30 mg/mL, and 0.5 mL of the polymer solution was added to 3 mL of 10 mM sodium dodecyl sulfate (SDS, from Sigma Aldrich) in NanoPure H_2O. The resulting mixture was sonicated for 2 minutes at 20% maximum amplitude using a 1/8" probe tip sonicator (Misonix-3000). After sonication, the emulsion was heated at 70 °C for 40 minutes under constant stirring. Each nanoparticle solution was raised to 2.5 mL with NanoPure water. The various ratios of P3HT nanoparticles to PS nanoparticles were prepared by mixing the appropriate volume ratios of each nanoparticle solution. Excess surfactant was removed by centrifugal 5 times; the final reconstitution was to 0.5 mL with 20% EtOH and 80% H_2O. The molecular weight cut-off (MWCO) of the filter used was MWCO = 10 kDa; which has pore sizes large enough to allow surfactant to pass through, but small enough to prevent any nanoparticles from passing through. Nanoparticle size and size dispersity were determined by Nanoparticle Tracking Analysis (NTA) using Nano Sight NS500. Small angle X-ray scattering (SAXS) of a binary nanoparticle glass on

polyimide tape (Kapton®) was measured using Ganesha SAXS-Lab system using Cu K-alpha radiation (0.154 nm).

Cleaned indium tin oxide (ITO) substrates were treated under UV-O_3 prior to film deposition. For cAFM samples poly(3,4-ethylenedioxythiophene):poly(styrene sulfonate) (PEDOT:PSS) (Clevios P VP AI 4083) was spin coated on the ITO substrates at 2,500 rpm for 40 s, and then annealed for 20 min at 150 °C. The PEDOT:PSS layer was exposed to UV-O_3 for 3 min to increase hydrophilicity. Concentrated solutions of nanoparticle dispersions were spin coated at 1,000 rpm for cAFM samples and 600 rpm for TOF measurements on pre-heated ITO substrates; they were then kept as cast films in a vacuum chamber for 12 h. For TOF measurements, a thin layer (30 nm) of Al cathode was thermally deposited at a chamber pressure of 1×10^{-6} mbar with a deposition rate of 0.5 – 3 Å/s. Typical nanoparticle film thicknesses were ~200 nm for cAFM samples and 1 - 2 μm for TOF samples, as estimated using an Alpha Step IQ profilometer.

For TOF experiments, a 355 nm (Continuum) laser pulse (10 ns) was used as light source for photo-carrier generation. The resulting transient photocurrent was then measured under applied bias voltage (Agilent E3620A/E3612A) across a 500 Ω coupling resistance. A GHz oscilloscope (Tektronix TDS 3052C) was used to record the transient photocurrent.

cAFM mapping was done simultaneously with topographic height imaging on an Asylum Research MFP3D stand-alone microscope. The probe (AppNano ANSCM-PT) used was a Pt/Ir coated (~25 nm) Si probe with a spring constant of 1-5 N/m. Measurements were carried out in contact mode with constant deflection in order to maintain contact during raster scan. The obtained scans were 2.5 μm × 2.5 μm (512 pixel × 512 pixel) at a scan speed of 0.3 Hz. A bias of +2.00 V was applied between the Pt/Ir-coated probe and the ITO electrode; bias conditions were

such that hole current from the ITO substrate was measured at the probe. AFM measurements were analyzed with Asylum Research software in Igor Pro.

2.3.2.2 Theoretical Methods

Numerical simulations of TOF experiments were carried out using a previously reported deterministic drift-diffusion-reaction model that accounts for hole transport as well as trapping and detrapping kinetics.[256] The model has already been demonstrated to reproduce experimental TOF measurements of photocurrent evolution in P3HT nanoparticle assemblies. For more information on numerical simulation of TOF data, readers are directed to Han *et al*.[256]

Particle packing simulations were carried out using the algorithm developed by K. W. Desmond and E. R. Weeks.[364] The algorithm uses an alternating expansion and contraction of the particles (at an initially low packing fraction, $\phi = 0.25$), keeping the radius ratio constant, and decreasing the rate of expansion/contraction by a factor of two after each iteration. If an overlapping state occurs (according to the criterion that one minus the center to center distance divided by the average diameter of the two particles is less than the overlap threshold $\epsilon_r = 10^{-5}$), a nonlinear conjugate gradient method is used to adjust the position of the particles until the average force per particle is less than the threshold value of $\epsilon_E = 10^{-7}$. The simulation is terminated when the change in packing fraction ($\delta\phi$) is less than a threshold of $\delta\phi_{min} = 10^{-6}$. The alternating expansion and contraction, while minimizing overlap, produces a simulated assembly. The thresholds ϵ_r, ϵ_E, and $\delta\phi_{min}$ were determined in reference[364] in order to achieve reproducible results from reasonably fast simulations. Boundary conditions were fixed along x and y directions, and periodic along z direction, adjusting the surface boundary with each

iteration in order to keep *h* constant. Readers are referred to the work by Desmond *et al.*[364] for further details on simulated packings of spheres generated in this study.

The resistor network model calculations were carried out in MATLAB R2014a (MathWorks, Inc.). The details of the model are described later in the manuscript.

2.3.2.3 Nanoparticle Characterization

Semiconducting P3HT and insulating PS nanoparticles were synthesized following a reported method[116,251] with mode diameters of 85 nm (± ~ 13 nm) for both nanoparticle types as determined by NTA (see Figure 37a). We estimate that the nanoparticles have a size dispersity of about 15%. Reducing the dispersity to <10% will eliminate the shoulder in the curves of Fig. S1a. This dispersity in nanoparticle size may very well aid in the formation of glasses. However, literature reports[98,353,362] indicate that the processing conditions (concentrated solutions and spin-coating) provide the main driving force toward glass formation. A tapping mode AFM image of a nanoparticle assembly is shown in Figure 37b. Dispersions of the nanoparticles were spin coated on substrates from a solution of 20% ethanol and 80% water to fabricate assemblies. Spin-coated assemblies provided the optimal film smoothness (root mean square (rms) < 24 nm) for the best cAFM measurements.

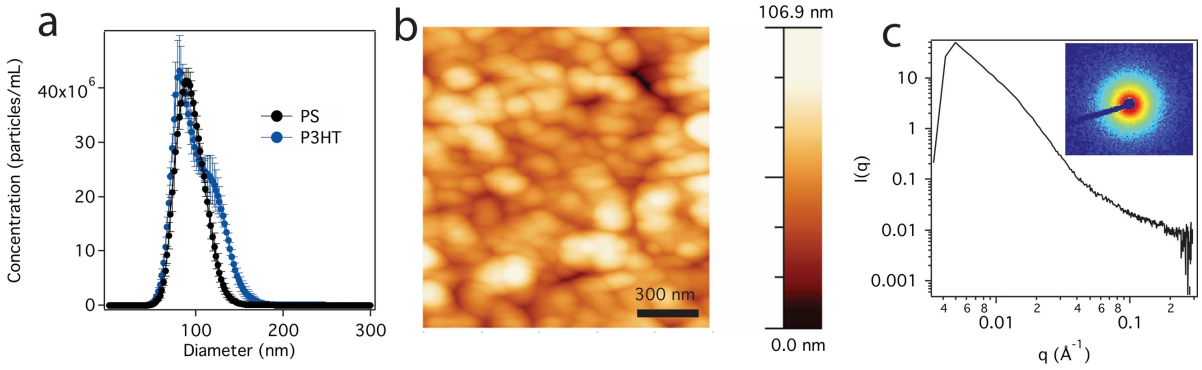

Figure 37: (a), NTA results showing the concentration (# nanoparticles /mL) vs. diameter (nm) of separate dispersions of post-polymerization miniemulsion prepared P3HT and PS nanoparticles. (b), Tapping mode AFM of P3HT and PS nanoparticles. (c) Average SAXS profile of drop-cast binary P3HT/PS polymer nanoparticle glass (η ~ 60%). The SAXS intensity pattern is shown in the inset.

2.3.2.4 Time-of-Flight Mobility

The photo-generated charge carrier mobility through binary nanoparticle glasses was measured by TOF. A graphical depiction of the TOF experimental setup is shown in Figure 38a. In a TOF experiment, the holes move through an interconnected network of P3HT nanoparticles (represented as blue spheres). From the TOF transient curves (see Figure 50a-c), we calculated the hole mobilities, and we found that the hole mobility decreased from ~4×10^{-4} cm^2/Vs to ~8×10^{-5} cm^2/Vs, to ~8×10^{-6} cm^2/Vs as the P3HT nanoparticle percentage (η) decreased from 80% to 60% to 40% (see Figure 38b). No significant hole transport was observed at η = 20%. This result is consistent with estimates from computation that the percolation threshold (p_c)[352,353] — the percent of 'connected' components required for the assembly to exhibit percolation behavior — is around 25% - 29% for random, glass-like assemblies.[353] In the inset in Figure 38b, we also show a semi-log plot demonstrating the smooth increase with increasing η in bulk charge carrier mobility in binary polymer nanoparticle glasses, indicating that the percolation behavior can be easily tuned by changing η.

We next used the hole mobility data to experimentally estimate the percolation threshold for the prepared semiconducting polymer nanoparticle glasses. For films with finite thickness,[261,372,373] p_c was calculated by fitting to the data the power law scaling relation

$$f(\eta) = a(\eta - p_c)^t \text{ for } \eta > p_c,$$

where a is a scaling factor and t is the critical exponent. The fit according to the power law scaling of equation is shown in Figure 38b with a dashed line for five different square root of applied fields from $E^{1/2} = 144$ $V^{1/2}cm^{-1/2}$ to 322 $V^{1/2}cm^{-1/2}$. The correlation coefficient, R^2, from this least-squares regression fit to the TOF mobility data is $R^2 = 0.98$ to 0.99, yielding as fitting parameters $a = 1.7 \times 10^{-3}$ to 3.1×10^{-3}, $p_c = 30\% \pm 0.4\%$, and $t = 2.99$ to 3.02. Figure 38c shows the virtually constant p_c with respect to the applied field.

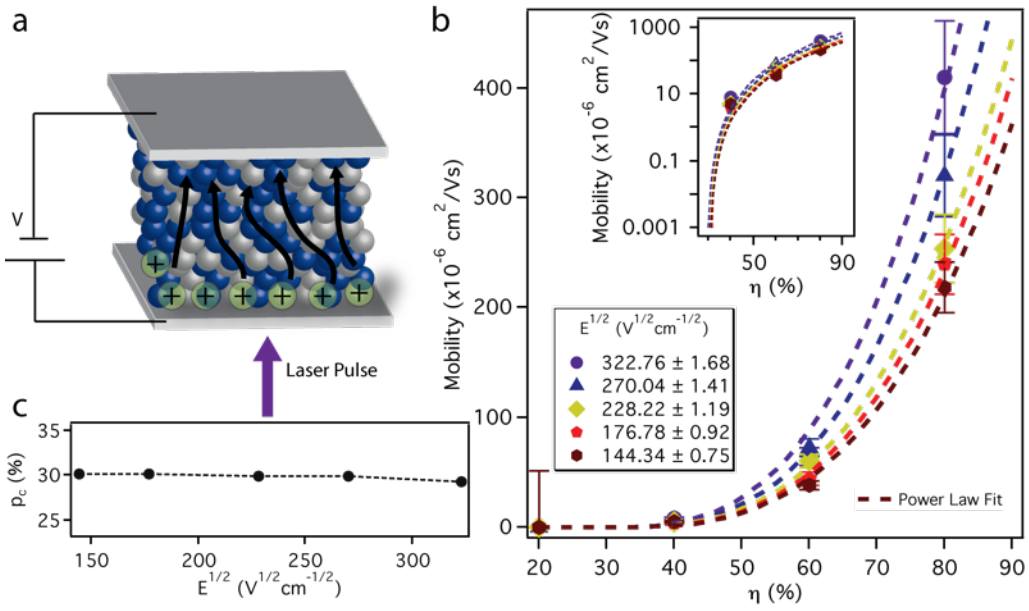

Figure 38: (a) Schematic representation of TOF charge carrier mobility experiment where holes travel through the network of P3HT spheres (blue). (b) Mobility as a function of η with power law scaling fit (dashed line), for five different applied fields, showing the ability to tune charge carrier mobility. Semi-log plot in the inset shows mobility in log scale to demonstrate tunability of hole mobility with η. (c) Percolation threshold (p_c) as a function of the square root of the applied field ($E^{1/2}$) in TOF experiment, showing virtually no dependence of p_c on $E^{1/2}$.

2.3.2.5 Conducting Atomic Force Microscopy

We then characterized nanoparticle films by cAFM in order to probe the electrical percolation behavior of the binary nanoparticle glasses on the nanoscale. A schematic depiction of the cAFM experimental setup is shown in Figure 39.

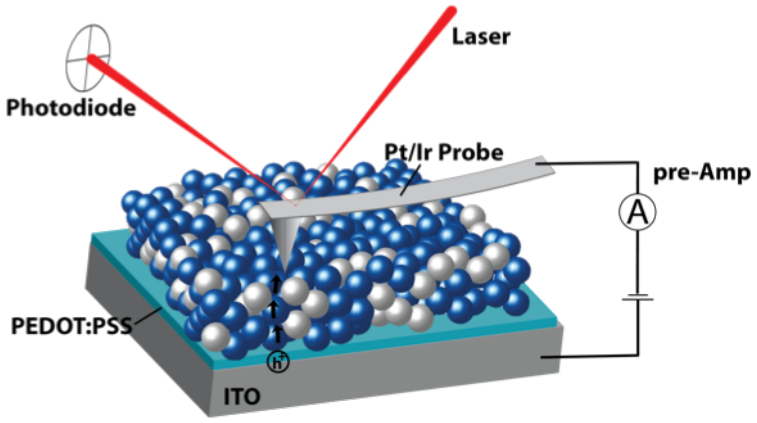

Figure 39: Schematic depiction of the cAFM experimental setup for investigation of electrical percolation in binary nanoparticle glasses, where holes travel from the PEDOT:PSS injection layer through a pathway of P3HT (blue) spheres to the conducting AFM probe.

It should be mentioned that cAFM is a widely available technique that has been used recently to probe percolation pathways in thin films containing semiconducting[116] or conducting spherical components.[376] In binary nanoparticle assemblies, where only one of the constituent particles is conducting, this path is composed of an interconnected network of conducting or semiconducting nanoparticles. The fact that the thin-film assemblies can be deconstructed into an interconnected network of spheres allows for a deeper, more detailed analysis of the underlying topology than in previous studies.[332,377-379] In our cAFM experiments, the sample was biased (+ 2.00 V) such that hole current flowed through the hole conducting P3HT polymer nanoparticle network from the hole injection PEDOT:PSS layer coated ITO electrode to the Pt/Ir

conducting probe. A single-pass scan provides information regarding the interconnected conducting particle network along which holes can travel through the film.

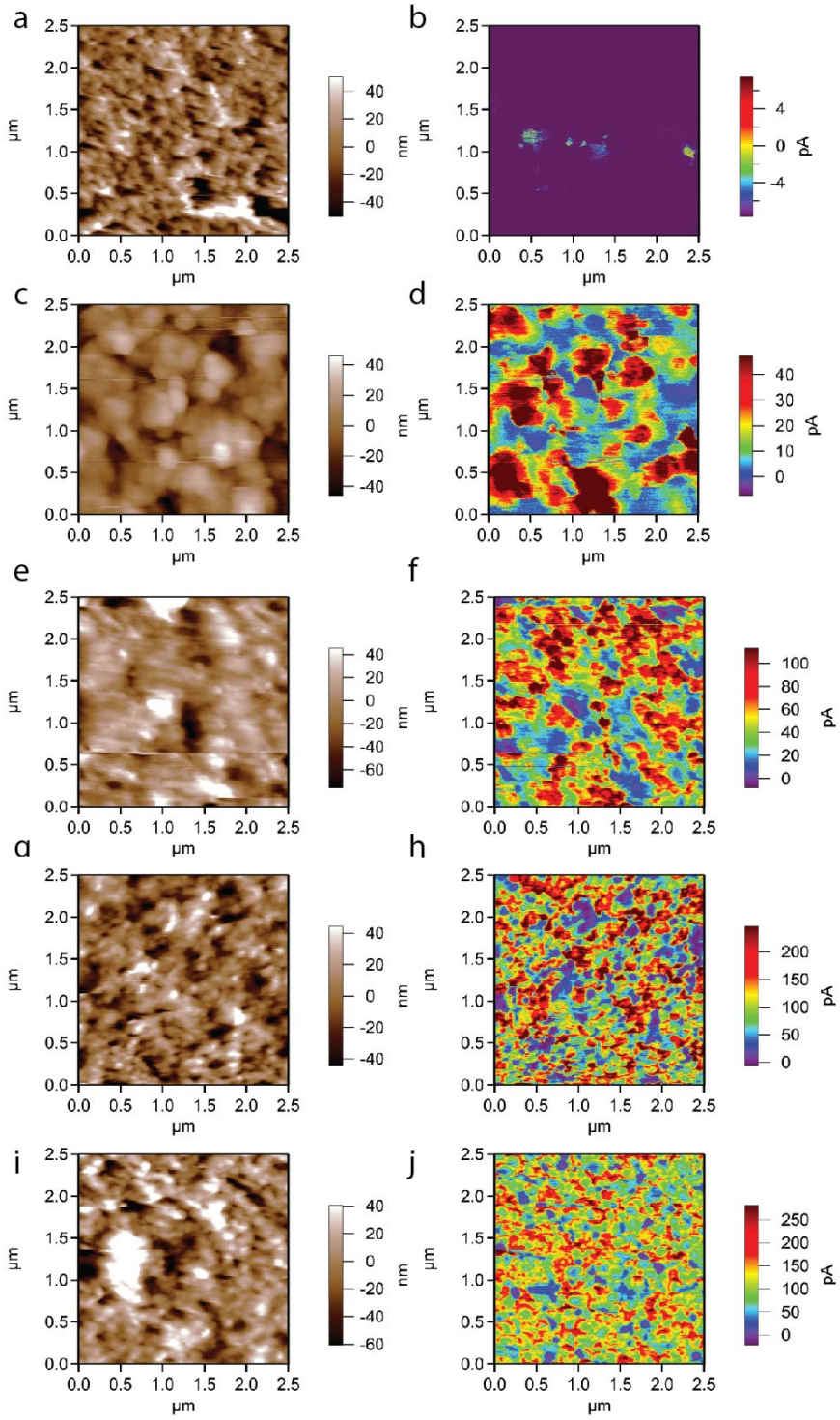

Figure 40: Height and current maps respectively for (a),(b), η = 20% (c),(d), η = 40% (e),(f), η = 60% (g),(h), η = 70% (i),(j), and η = 80%.

In Figure 41a-e, we show the cAFM maps of binary nanoparticle glasses with η = 20%, 40%, 60%, 70%, and 80%, respectively. The corresponding AFM height and current maps are shown in Figure 40a-j. The various samples had comparable topography. The measured rms roughness, from contact mode AFM, for the assemblies with η = 20%, 40%, 60%, 70%, and 80% were 23.4 nm, 14.8 nm, 23.2 nm, 23.5 nm, and 18.45 nm, respectively. From these maps, we generated histograms of pixel counts vs. current distributions (see Figure 41f). The plot of Figure 41f has two key characteristics. As η increases, (1) the overall current increases, and (2) the width of the current distribution also increases. We associate these characteristics with the decrease in the total resistance of the path measured at a particular point as the fraction of P3HT nanoparticles increases. An increase in conductance measured at a single nanoparticle at the surface of a film can be the result of the decrease in the path length or the increase in the number of paths or both. A plot of the mode current obtained from the distributions shown in Figure 41f as a function of η is shown in Figure 41g as closed circle symbols. There is little to no observed current for η = 20% (average current is zero), which is consistent with the predicted p_c of 25% - 29% (*vide supra*). The inherent randomness of these assemblies leads to reproducibility. To further highlight this, we show in Figure 41g, in open triangle symbols, the mode current of ten randomly sampled sub-selections of each cAFM map. Due to the randomness of the assemblies, there is little fluctuation in current for randomly sampled areas, and the averages are identical to the overall average current in full cAFM map.

Next, we used the cAFM current data to experimentally estimate the p_c for the prepared semiconducting polymer nanoparticles glasses. We calculated p_c by using the same power law scaling relation as we did to fit the TOF mobility data, and the resulting power law fit is shown in Figure 41g as a black dashed line. The R^2 coefficient for the fit to the cAFM current data is R^2

= 0.98, and gave the fitting parameters $a = 3.2 \times 10^{-10}$, $p_c = 24\%$, and $t = 1.89$. The p_c value obtained from the fit matches with the computed threshold for nanoparticle random, glass-like assemblies.[353] Further, the conductivity exponent t obtained from the fit closely matches the universal value of $t = 1.9$ predicted for a three-dimensional percolation when the "local microstructure is isotropic and contains only short-range correlations."[372] This indicates that the assembly is indeed random or a glass and has percolation pathways in three dimensions. A SAXS intensity pattern and average profile of drop-cast binary P3HT/PS polymer nanoparticle assembly at η ~ 60% (Figure 37c) shows a very broad peak over the scattering vector range q = 0.005 $Å^{-1}$ to 0.03 $Å^{-1}$ (the corresponding d-spacing ranges from 125.7 nm to 20.9 nm), and no defined peaks, which is also consistent with our conclusion that the assembly is a random glass.

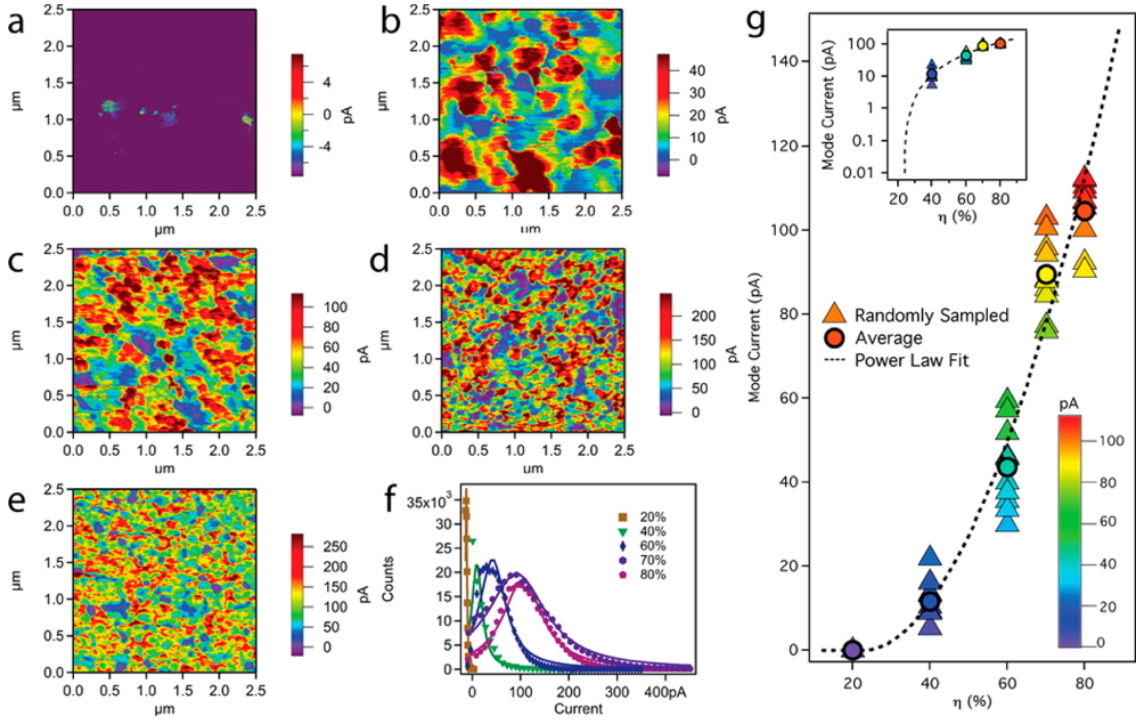

Figure 41: Conductive AFM maps of binary P3HT/PS nanoparticle films at values of η equal to (a) 20%, (b) 40%, (c) 60%, (d) 70%, and (e) 80%. (f) Pixel current histogram plots for the previous five cAFM maps. (g) Mode current from current distributions as a function of η (dashed line) for ten randomly sampled sub-selections of each cAFM map, in open triangle symbols, and the average in closed circle symbols. The semi-log plot in the inset shows log mode current as a function of η. The error bars from the fitting distributions are small and not visible on the plot.

For ordered spherical lattices (lattice percolation) and through 'off-lattice' heterogeneous packings of spheres (glasses), p_c has been computed *numerically*, and can be simply estimated by[353]

$$p_c = {}^{f_c}/_{\phi},$$

where the critical occupied volume fraction (f_c) is approximately 0.16 in 3-D.[333] Using the above equation, and a packing fraction $\phi = 0.644$, we can estimate that $p_c \approx 25\%$ in nanoparticle glasses, which matches well with the p_c value of 24% that we obtained from fitting the power law scaling relation to the cAFM data. More detailed continuum models that provide better numerical estimates of p_c have found $p_c \approx 29\%$ for identical overlapping spheres.[353,365] When we fit the TOF mobility data with the power law scaling relation, we obtained $p_c = 30\%$, which matches well with the theoretical estimates. The films used in the TOF experiments are considerably thicker (1-2 μm) than those used in the cAFM experiments (200 nm). We attribute the difference of 6% in the p_c according to the two methods to the difference in the sample thickness used in the two experimental procedures. To our knowledge, our study provides the first experimental validation of percolation behavior in polymer nanoparticle glasses.

2.3.2.6 Resistor Network Model

We next developed a resistor network model to analyze the conductivity behavior observed in cAFM. We hypothesized that if we consider each nanoparticle (and its interfaces/contacts with other nanoparticles) as a composite resistor then the nanoparticle assembly can be modeled as a system of resistors. The current at a particular point on the surface can then be calculated from the path length, or simply the number of interconnected nanoparticles along a particular path, and the number of continuous paths from the bottom electrode to the individual particle that meets

the cAFM probe. As shown in detail below, in spite of its simplicity, this model does reproduce the observed characteristics of the data presented in Figure 41f-g.

We first simulated disordered assemblies of spherical particles using an established algorithm[364] with particle interaction potentials described as 'soft repulsive linear springs'.[366] The radius ratio (ψ) of the two types of particles in the binary system was kept at $\psi = 1$ in all the simulations. The simulations were performed using simulation cells containing 5000, 10000, and 15000 particles. In order to avoid edge effects, the lateral dimensions of the simulation cell were chosen to be much larger than its vertical dimension. The height of the simulation box (film thickness) normalized by the diameter of the nanoparticle was equal to only a few nanoparticle diameters (h = 2.5, 3.0, 6.0, and 12.0) to best correlate with the experimentally measured thicknesses of the nanoparticle films. The final packing fraction (ϕ) of the simulated assemblies was 0.63 - 0.64, i.e., approximately equal to the maximum ϕ for maximally random jammed assemblies of hard spheres.[353,380] In the final configuration, the particles were labeled randomly as conducting or insulating. The percentage (η) of the conducting particles was varied from 10% to 90% in increments of 10%, and three configurations were generated for each value of η. Three-dimensional representations of the simulated particle assemblies for h = 2.5 at η = 40% and 60% of conducting nanoparticles (blue spheres) are shown in Figure 42a-b. Measuring the packing fraction ϕ of P3HT/PS nanoparticle glasses accurately has been challenging because of the difficulty in measuring the nanoparticle densities. An approximate measurement of ϕ in P3HT nanoparticle assemblies found $\phi \sim 0.57 \pm 10\%$, close to the expected value of 0.63 - 0.64.[381]

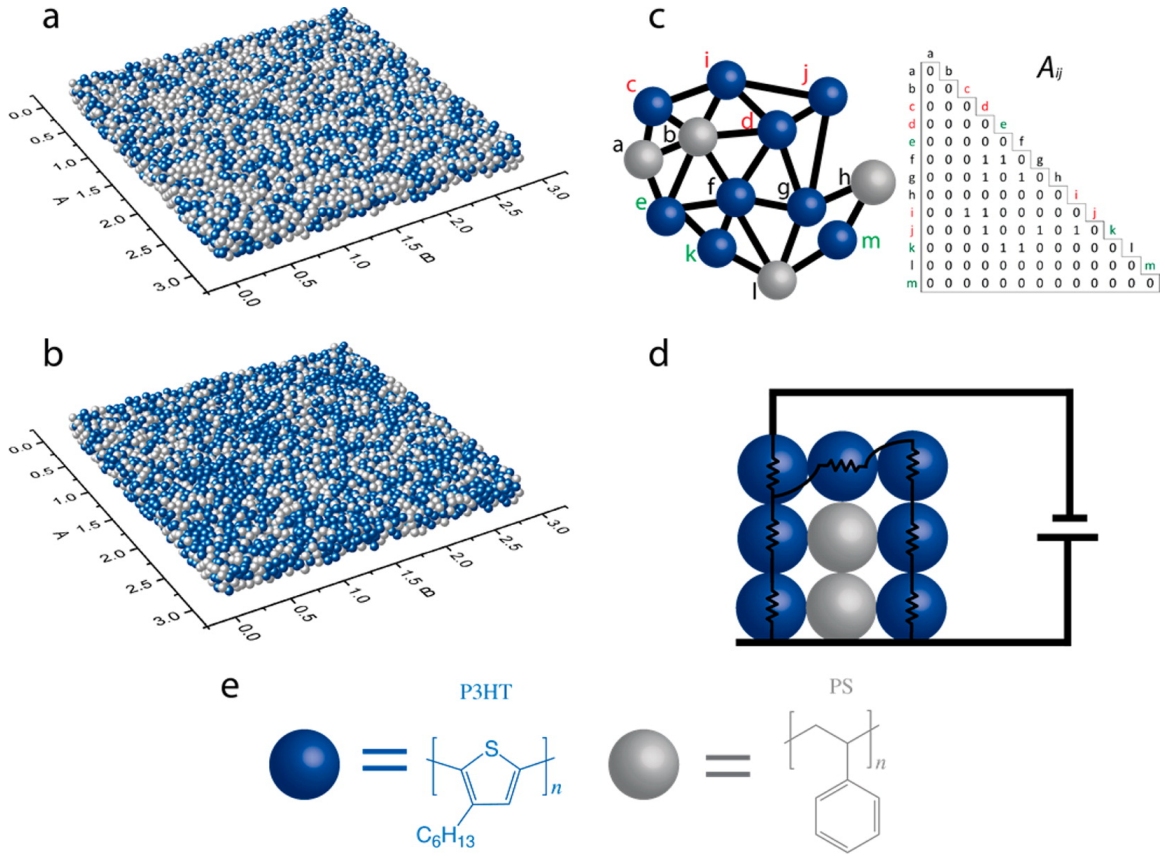

Figure 42: Configurations from simulations with 5,000 nanoparticles for films of thickness h = 2.5 nanoparticle diameters at values of η equal to (a) 40% and (b) 60%. (c) A representative connected network of nanoparticles and the adjacency matrix **A** with elements A_{ij} for the connected network of conducting particles; blue and grey spheres are used to denote conducting and insulating particles, respectively. Bottom/electrode particles, surface particles, and internal film particles are labeled with green, red, and black letters, respectively. (d) Schematic depiction of the resistor model proposed in this paper for predicting the way current flows through nanoparticle assemblies on an electrode as probed by cAFM. (e) Key indicating the chemical identity of the blue and grey spheres (P3HT and PS particles, respectively).

Using the simulated assemblies, we then calculated the center-to-center Euclidean distances between pairs of particles for all conducting particles in the simulation box. Two particles were considered to be in contact if the distance between their centers was less than the diameter (d) plus δ where $\delta = 0.045 \times d$). The value of $d + \delta$ was determined to only consider first neighbor contacts by using the pair correlation function (see Figure 44a). Using this information, a $n \times n$ adjacency matrix **A** with elements A_{ij}, is constructed, where $i, j \in \{1, \ldots, n\}$ and n is the number

of conducting nanoparticles in the simulation box. In this matrix, $A_{ij} = 1$ if conducting particles i and j are in contact, and $A_{ij} = 0$ otherwise (see Figure 42c). From the adjacency matrix, the shortest path from a bottom particle to a top particle in the simulation box is determined using Dijkstra's algorithm;[382] for initial simplicity, the edge weights for all nodes in **A** are set to unity. Using this algorithm, all shortest paths from each particle on a plane (the ITO electrode) through conducting particles to a single point at the surface (nanoparticle in contact with AFM probe) are evaluated. If each nanoparticle in the path is considered a resistor with the same resistance or edge weight (as a first-order approximation) for all paths, then the current at each particle can be calculated by treating the nanoparticle connections as resistors in series, and multiple paths as serial resistors in parallel (see Figure 42d). Therefore, the current at each surface nanoparticle is then calculated by

$$I = V \sum (RN_k)^{-1} ,$$

where I is the current, V is the voltage (taken equal to unity for this study), R is the resistance of a single particle set to unity, N_k is the number of particles of the shortest k^{th} unique path, and the sum is taken over all paths. This path analysis was done for three configurations at each value of η considered (from 10% to 90% conducting particles), at h = 2.5, 3.0, and 6.0. The distributions for their average binned effective simulated surface current with a Lorentzian fit for the h = 2.5 nanoparticles thick assembly is shown in Figure 43a; the current distributions for other thicknesses are shown in Figure 44g-i.

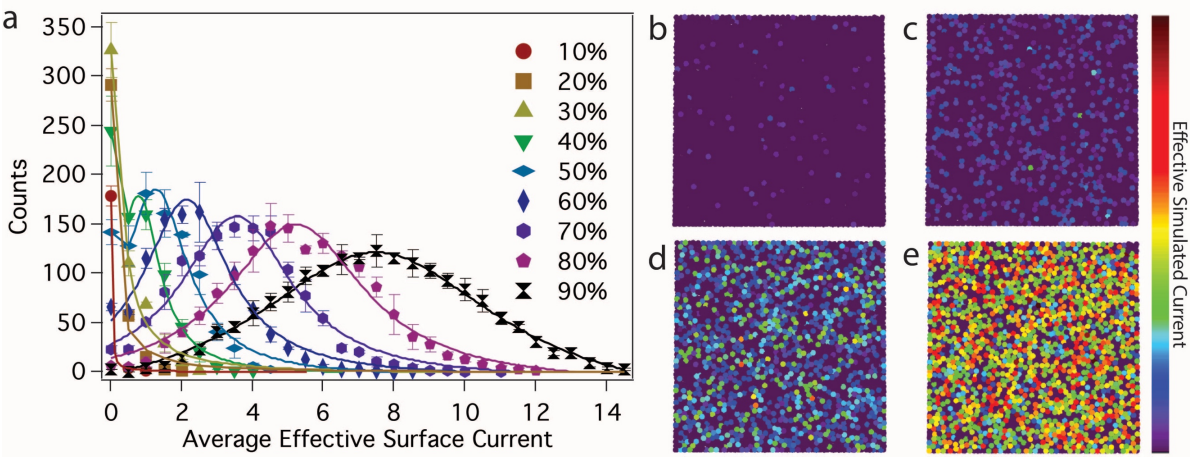

Figure 43: (a) Simulated average effective surface current from three independent computer simulations at $h = 2.5$ and increasing percentage η (from 10% to 90%) of conducting particles, with the corresponding Lorentzian fits (solid lines). Surface representation (map) of simulated effective current from simulations at values of η equal to (b) 20%, (c) 40%, (d) 60%, and (e) 80%.

The simulated effective surface current distributions in Figure 43a exhibit several interesting features: (1) as the percentage of conducting particles increases, the distribution shifts to higher effective current; (2) as the percentage of conducting particles increases, the Lorentzian distribution becomes broader; and (3) at low percentages of conducting particles, there is a significant zero-current contribution to the distribution. These are the same trends observed in the cAFM surface current distributions (as seen in Figure 41f). The fractions of conducting surface particles that have a continuous pathway to the bottom substrate are shown in Table 3. The number of conducting pathways increases in a sigmoidal fashion with increasing η (as seen in Figure 44b). The spatial distribution of the effective surface current for η = 20%, 40%, 60%, and 80% can be seen in the surface representation plots in Figure 43b-e. These observations are consistent with the increase in the number of conducting pathways from an individual particle on the ITO electrode to a surface particle.

To compare the cAFM distributions to the simulated ones (h = 2.5, to best correlate with experimental thicknesses as measured by profilometry) shown in Figure 45, common statistical analysis methods were used.[383] The distributions were fit according to the Lorentzian function

$$f(\eta) = \frac{A}{(\eta - x_0)^2 + B}$$

where x_0 represents the mode current of the distribution, A is the scaling parameter, and B is the width parameter. We then calculated the correlation coefficient (R^2), which determines how well the model represents the data. As R^2 approaches 1 the statistical model (distribution of above Lorentzian fit) provides an excellent representation of the data. Also, the Fisher correlation statistic (P-value) was determined with an *a priori* $P \leq 0.05$ to determine statistical significance; the P-value is a measure of the statistical significance against the null hypothesis or no correlation. As the P-value approaches 0, there is significant evidence against the null hypothesis.

Table 3: Fraction of particles on the surface of a simulated assembly that have at least one percolation pathway to the bottom planar electrode for h = 2.5, 3.0 and 6.0 with respect to η.

η	***h* = 2.5**	***h* = 3.0**	***h* = 6.0**
10 %	0.027 +/- 0.053	0.004 +/- 0.050	0.000 +/-0.048
20 %	0.206 +/- 0.046	0.121 +/- 0.062	0.000 +/- 0.026
30 %	0.402 +/- 0.051	0.281 +/- 0.035	0.037 +/- 0.041
40 %	0.666 +/- 0.048	0.607 +/- 0.042	0.380 +/- 0.018
50 %	0.846 +/- 0.013	0.822 +/- 0.011	0.738 +/- 0.029
60 %	0.941 +/- 0.003	0.938 +/- 0.011	0.914 +/- 0.019
70 %	0.982 +/- 0.003	0.980 +/- 0.005	0.971 +/- 0.001
80 %	0.995 +/- 0.000	0.993 +/- 0.002	0.989 +/- 0.003
90 %	0.999 +/- 0.000	0.998 +/- 0.001	0.999 +/- 0.000

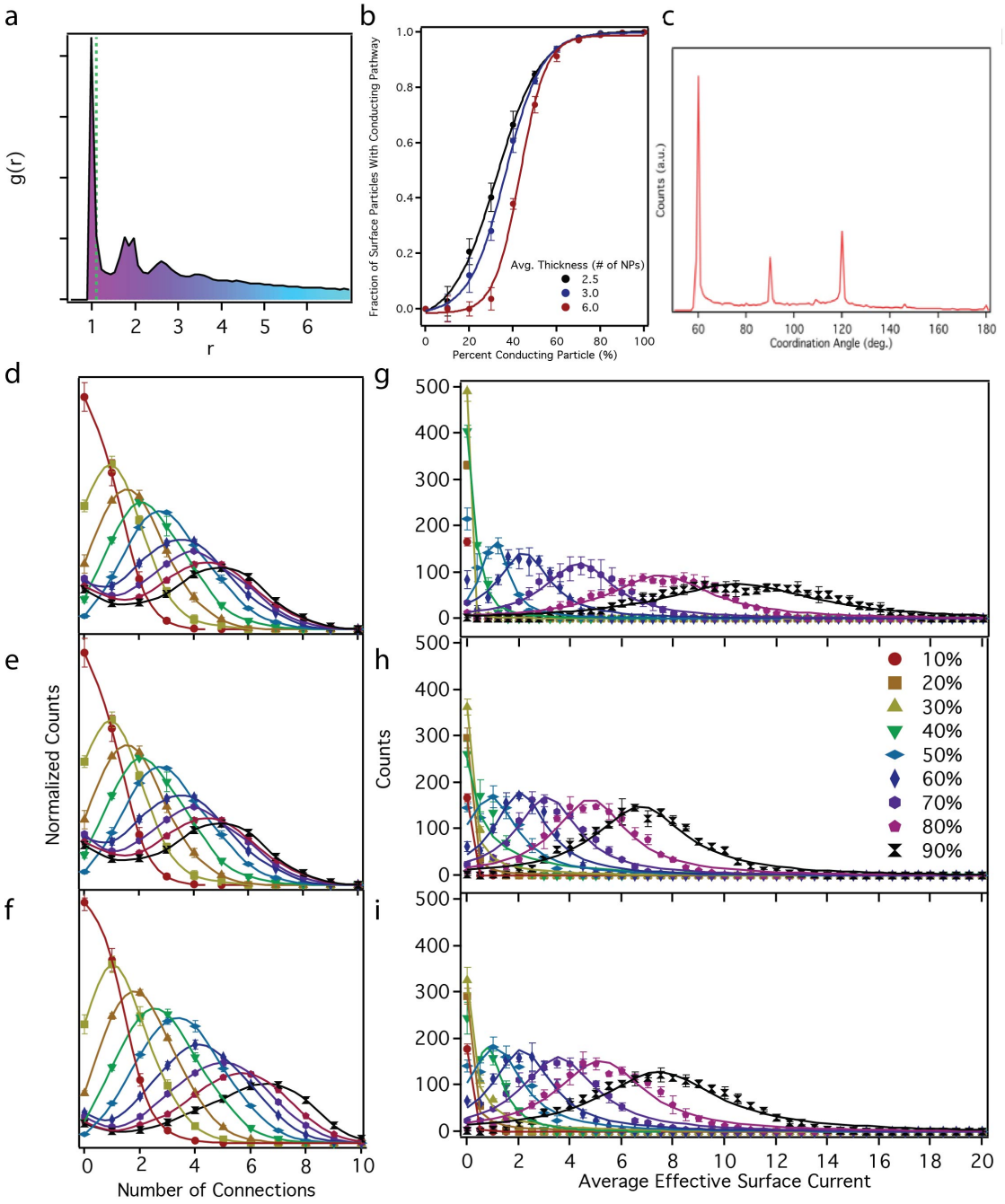

Figure 44: (a) Pair correlation function for simulated disordered nanoparticle network assemblies. The green dashed line marks $d + \delta$. (b) fraction of particles on the surface of a simulated assembly that have at least one percolation pathway to the planar electrode for $h = 2.5$, 3.0 and 6.0 with respect to η (c), common distribution for coordination angle between any three connected particles in a simulated nanoparticle network, the most common coordination angle is 60°, result is reproduced for all h and η. Distributions for number of contacts for (d) $h = 2.5$, (e) $h = 3.0$, (f) $h = 6.0$ for η = 10% - 90%. Simulated average effective surface current distributions for (g) $h = 6.0$, (h) $h = 2.5$, (i) $h = 3.0$ for η = 10% - 90%.

The Lorentzian fits of the simulated data had correlation coefficients $R^2 > 0.97$, and a Fisher correlation *P*-value of $< 1\times10^{-5}$. Lorentzian fits for cAFM current pixel maps had $R^2 > 0.88$, and the *P*-values were $< 1\times10^{-5}$. To examine whether there is an agreement between the average current measured in the cAFM experiments and that predicted in the simulations, the x_0 fitting parameters for both simulations and experiments were normalized by their respective x_0 counts at $\eta = 60\%$ for direct comparison. The data was normalized using $\eta = 60\%$ because it is the median η measured, and normalizing by extremes (min. or max. η) can be unstable. For all distributions, x_0 was set to be equal or greater than 0. The normalized fitting parameter x_0 from both cAFM and simulation distribution fits was determined with $R^2 = 0.98$ and a *P*-value of 5.16×10^{-4}. This indicates that the model is accurate at predicting the mode current differences between different samples (see inset in Figure 45), and at predicting the mode current of different samples given one known distribution fit, i.e., that at $\eta = 60\%$ in this study. Also, the simulated x_0 value follows the same power law scaling behavior (in p_c and t) as the cAFM current seen in the inset in Figure 45 inset represented with the black dashed line.

For direct comparisons of the entire current distributions from cAFM measurements with those from simulations, the distribution fits were normalized by the maximum number of counts at 60% and the x_0 value for $\eta = 60\%$ P3HT particles. Points were generated using the Lorentzian function with the fitting parameters ranging from 0 to $x_0 + 4B$ at 80% P3HT particles; 40 points were generated for all distribution fits. The generated points on the distribution fits for cAFM data were compared with those from simulation. The R^2 coefficients for $\eta = 20\%$, 40%, 60%, 70%, and 80% were equal to 0.93, 0.92, 0.98, 0.84, and 0.96, respectively, indicating that the model can account for at minimum 84% of the variance in the cAFM distribution. The *P*-value is

$< 1\times10^{-5}$ for all samples; this indicates that there is a strong correlation between the experimental data and the simulation predictions.

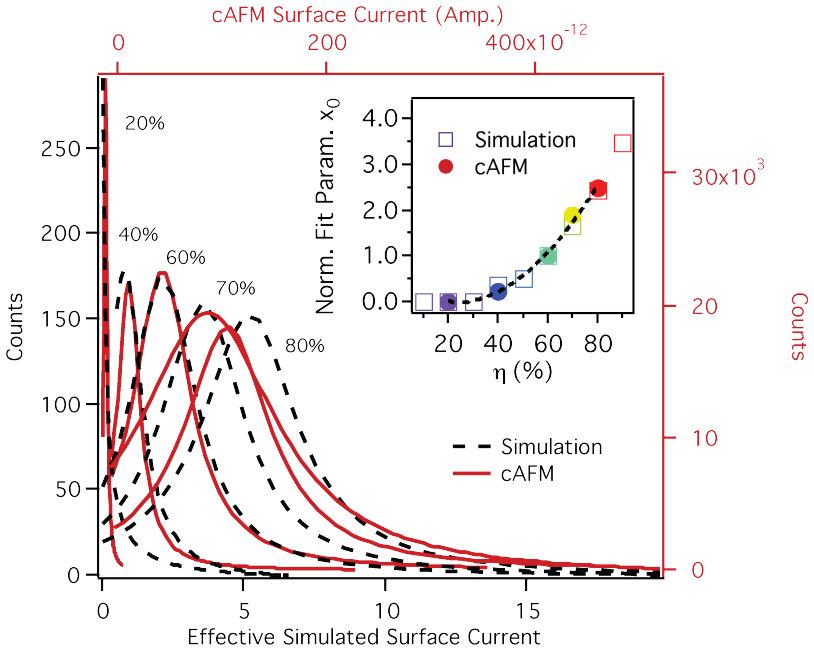

Figure 45: (a) Surface current distributions from simulation predictions (dashed black lines) and cAFM measurements (solid red lines) for η = 20%, 40%, 60%, 70%, and 80% P3HT nanoparticles. The inset shows the η dependence of the fitting parameter x_0 normalized by the value of x_0 at 60% P3HT particles for both simulation predictions and cAFM data. The dashed black lines represent power law scaling fits. All $x_0 < 0$ are set to 0 so that negative current is not allowed.

2.3.2.7 Substructure Analysis

Having verified that the model predictions match well with the cAFM measurements, we used cluster statistics to analyze the substructures present within the simulated assemblies. Ordered nanoparticle assemblies can be described as discrete *p*-connected networks, where each point (corresponding to a given particle center) is connected to *p* other points.[337,340] For disordered nanoparticles glasses, however, a discrete '*p*' is not valid but a mode *p*-connected network is valid. The distributions for the number of connections for conducting particles in assemblies with *h* = 2.5, 3.0, and 6.0 at conducting η = 10% - 90% are shown in Figure 44d-f. The mode of the

distributions was used to describe the connectedness of each assembly at a particular η. Consistent with our expectations, the results indicate that as η increases the degree of connectedness in each network also increases. The maximum connectedness for any single particle was found to be 12, which is consistent[337] with the closest-packing of hard spheres.

Using the number of connections or degree of coordination information, we then determined the coordination geometry of the assemblies by finding the most common coordination angle[338] (θ) between three connected particles. We found that, in all of the simulated disordered assemblies of equal-sized spheres, the most common coordination angle is $\theta = 60°$, followed by 120°, and 90° regardless of composition (see Figure 44c). A maximum distribution density at $\theta = 60°$ has been reported previously.[384] For $p = 6$, the two possible common coordination geometries are an octahedron and a trigonal prism. The prominence of $\theta = 60°$ and 120° suggest that the most likely structure that would corroborate our finding is a distorted trigonal prism. We, therefore, conclude that assemblies with $p < 6$ are predominantly defective trigonal prismatic substructures with approximately 6-p defects.

The dependence of the mode connections ('p-connected') on η for different thicknesses (h) is plotted in Figure 46. All of the mode connections found for all h examined can be found listed in Table 4. Also, for each 'p' the most-likely predicted substructures are isolated particles for $p = 0$, isolated dimers of particles for $p = 1$, 1-D chains for $p = 2$, chains with ~60° branch points (branched chains) for $p = 3$, trigonal prismatic structures with two missing points or defects for $p = 4$, trigonal prismatic structures with one defect for $p = 5$, and trigonal prismatic structures for $p = 6$. The mode connectedness of the assemblies never reaches $p \geq 7$; so, higher coordination substructures are not needed to define the morphologies in these disordered glasses. The degrees of connectedness of particles in disordered glasses are in fact distributions, and contain

combinations of the aforementioned substructure geometries; however, the predominant morphology can be defined by the mode *p*-connected substructure. Figure 46 shows that these substructures, and thus, the overall morphology can be easily tuned by simply changing the value of η in the equal-sized binary nanoparticle glasses. The structure of the disordered binary nanoparticle glassess can be simply described as a (p_i, p_{1-i})-connected network, where i = η ÷ 100% is the fraction of a certain particle type in the assembly. For example, using Figure 46, the morphology of a disordered nanoparticle assembly containing 60% of one particle type and 40% of the other can be described as a mode (3, 2)-connected network for h = 2.5. The predominant substructure of the 60% phase will be a branched chain, and the predominant substructure of the 40% phase will be a 1-D chain.

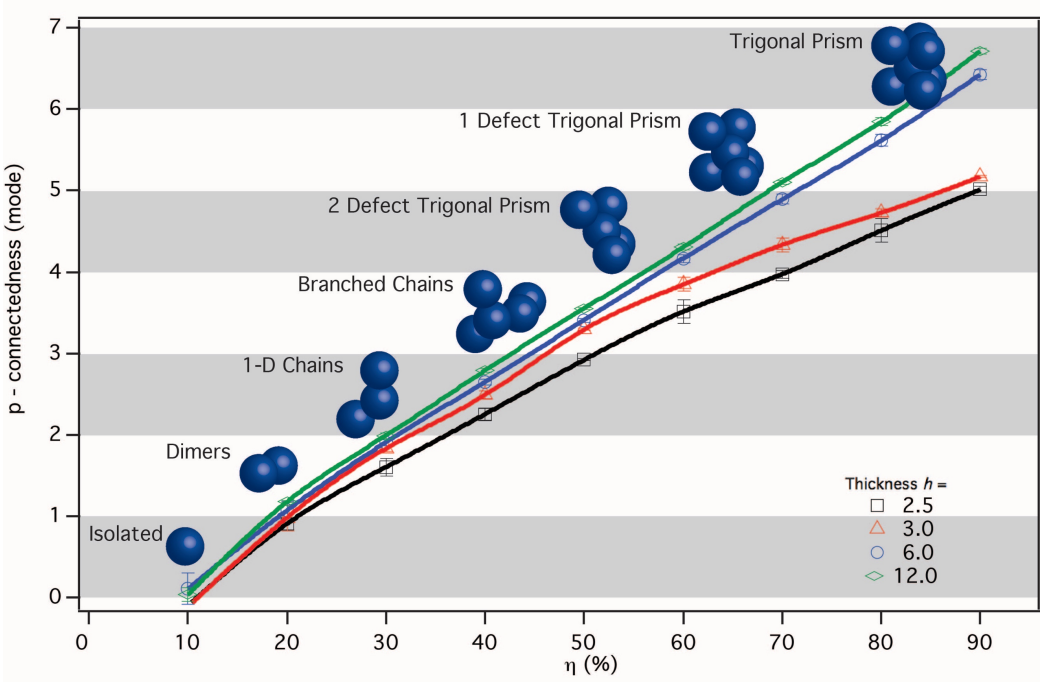

Figure 46: Predicted predominant substructures in disordered assemblies of binary nanoparticles. Mode number of connections (p) as a function of η for assemblies of thickness h = 2.5, 3.0, 6.0, and 12.0 nanoparticle diameters. Representations of the predominant nanoparticle substructure of one type of nanoparticle (denoted as a blue sphere) also are shown for different degrees of connectedness (p values).

Table 4: Mode number of connections of simulated disordered nanoparticle networks for nanoparticles for h = 2.5, 3.0 and 6.0 for η from 10% to 90%.

η	***h* = 2.5**	***h* = 3.0**	***h* = 6.0**
10 %	0.0	0.0	0.0
20 %	0.909 +/- 0.07	0.984 +/- 0.16	1.073 +/- 0.11
30 %	1.606 +/- 0.10	1.833 +/- 0.04	1.910 +/- 0.03
40 %	2.256 +/- 0.08	2.489 +/- 0.04	2.651 +/- 0.04
50 %	2.921 +/- 0.01	3.293 +/- 0.01	3.411 +/- 0.03
60 %	3.513 +/- 0.14	3.846 +/- 0.09	4.168 +/- 0.05
70 %	3.974 +/- 0.05	4.33 +/- 0.08	4.891 +/- 0.06
80 %	4.510 +/- 0.14	4.727 +/- 0.05	5.615 +/- 0.07
90 %	5.012 +/- 0.04	5.170 +/- 0.01	6.426 +/- 0.06

We have developed a definition of disordered binary polymer nanoparticle glass networks as (p_i, p_{1-i})-connected networks; but it bears further explanation of what this definition really means, as the networks of nanoparticles are disordered. Simulated disordered networks of particles do not give positional information of particles in experimental films. However, they do give information on the statistical structure of the network, and how such a network will perform. This is akin to neural networks,[385] where two unique brains of the same species will not have the exact same network of neurons, but the network structure (e.g., neural connectivity) and the way it communicates via electrical charge will be comparable.

2.3.2.8 Robustness Analysis of Random Nanoparticle Assemblies

After evaluating the connectedness, we analyzed the robustness of these networks using a modified network analysis toolbox.[386] Network robustness in general, is how well networks

"hold-up" or perform their desired task when a node (or several nodes) are removed, or the edge between two nodes is removed either randomly or through targeted attack. The robustness of physical networks such as nanoparticle networks is significant, particularly where mass or charge transfer is desired. It is important to know if the materials will remain functional despite failure at a particular point in the network. The robustness of a network is dependent on the structure of the network, i.e. a highly interconnected network will be robust.

To analyze network robustness for disordered films of assembled nanoparticles, we successively removed at random one node from the conducting particle network and monitored the size of the largest cluster in the network, as cluster size is a good indicator of a network that would allow for charge transport. A graph of the size of the largest cluster vs. the fraction of nodes/particles removed can be found in the Figure 47a-c for h = 2.5, 3.0 and 6.0. Networks containing η = 50% to 90% of the conducting particle were quite robust, with largest cluster sizes containing at least ~30% of the total number of particles in the simulation box up until a phase change, which occurs when ~35% to ~50% of the particles in the network were removed. When η = 40%, the network is still moderately robust having a gradual slope in the decrease in largest cluster size as particles are removed. Below η= 40% the size of the largest cluster is small before random removal, and shows only minor changes as removal progresses. Thicker films (h = 3.0 and 6.0) are even more robust, requiring a lower percentage of conducting particles, and having a phase change at a greater fraction of particles removed from the assembly. The robustness combined with the predicted predominant substructure provides useful design rules for disordered nanoparticle assemblies.

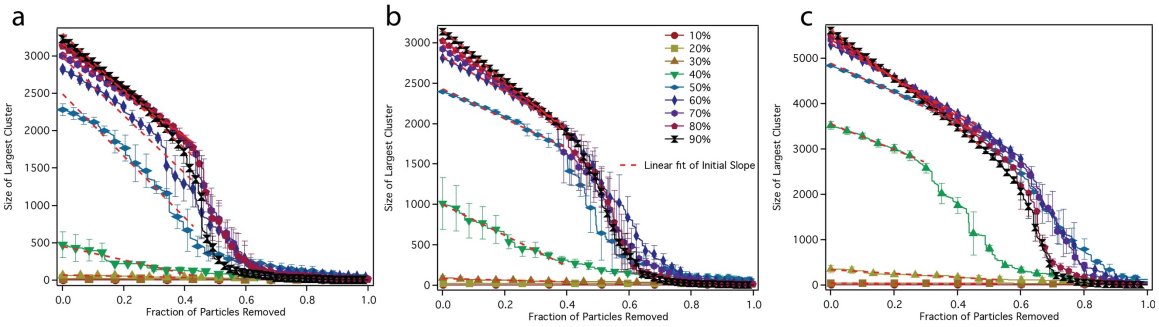

Figure 47: Robustness graphs of simulated disordered nanoparticle networks. The size (in number of nanoparticles connected by some pathway) of the largest interconnected cluster as a function of fraction of particles randomly removed successively for (a) h = 2.5, (b) h =3.0, and (c) h = 6.0. at η = 10% - 90%. The graphs show a phase shift at a greater fraction of particles removed as h increases.

2.3.2.9 Reproducibility in cAFM and Resistor Network Model

To illustrate this point, we show in Figure 48a-c three different cAFM area scans of a η = 70% sample. A cursory look at these images indicates that there is no pixel-to-pixel, or nanoparticle positional, correspondence. However, a current vs. pixel count histogram (Figure 48d) shows that the mode currents and the current distribution are similar.

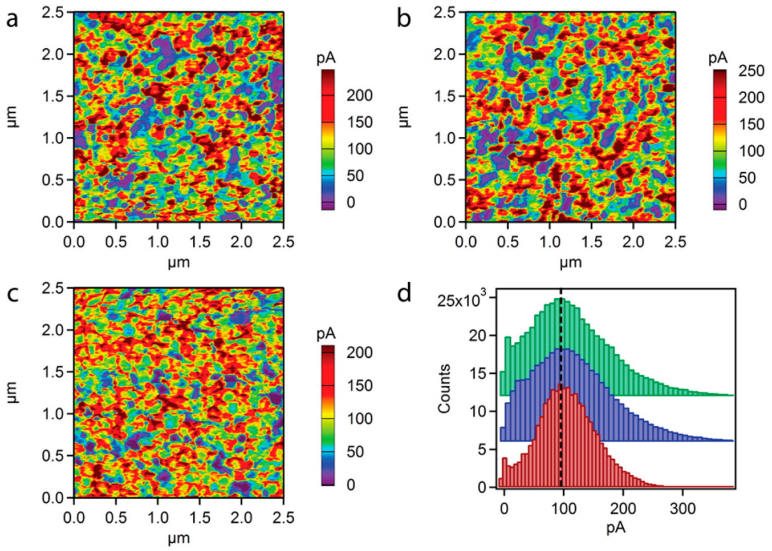

Figure 48: (a-c) cAFM maps at three different locations for η = 70%. (d) Current vs. pixel count histograms for (a-c), showing comparable current distributions and mode current Histograms are stacked for clarity.

We also simulated three *different* nanoparticle networks (h = 3 and η = 50%), by changing the particle position initialization for generating random configurations.[364] The assemblies are shown in Figure 49a, and there is no particle-to-particle correspondence. However, the *p*-connectedness (Figure 49b) and coordination angle (Figure 49c) distribution were found to be similar for the three simulated assemblies. Thus, we can conclude that these three *different* simulated disordered particle networks have comparable structure based on their connectedness and coordination angle. As done before, we calculated the effective surface current for these three *different* assemblies and plotted a histogram for each of the counts vs. effective surface current and Lorentzian fits in Figure 49d. The modes of the simulated effective surface currents are shown as vertical dashed lines in Figure 49d and they are comparable for all the distributions; the widths of the current distributions also are similar.

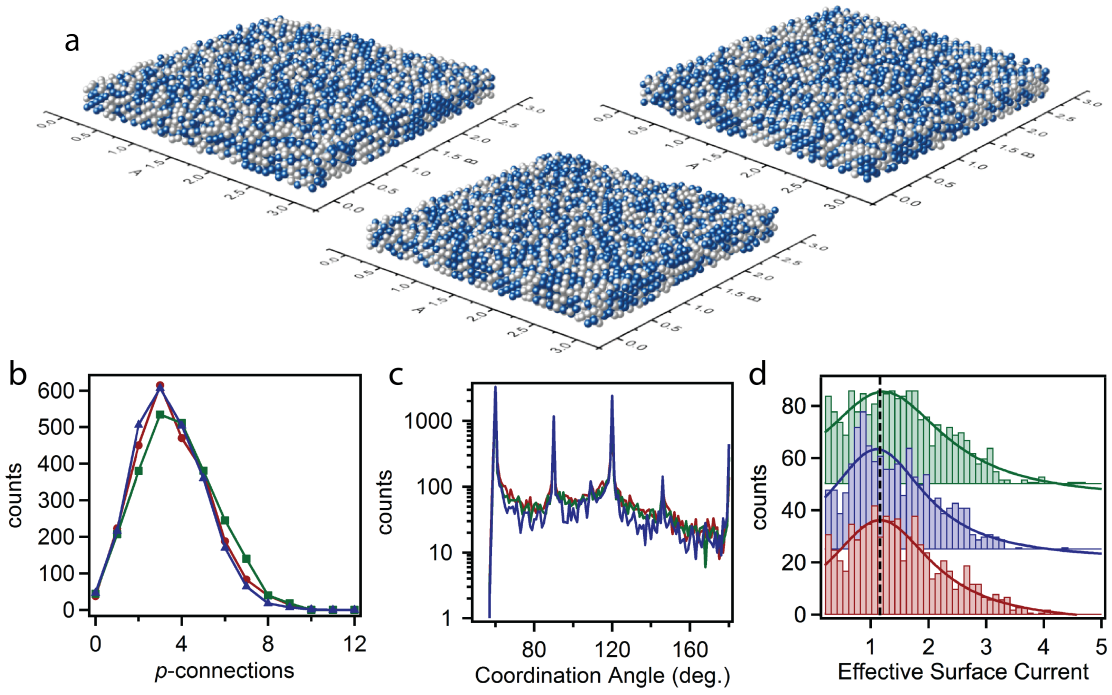

Figure 49: (a) Three *different* simulated disordered nanoparticle glasses at h = 3.0 nanoparticle diameters and η = 50%; different assemblies were obtained by using a different seed for the Mersenne Twister random number generator. Number of counts as a function of (b) *p*-connections, (c) coordination angle, and (d) effective surface current in histogram form with Lorentzian fits for the three different assemblies in (a). Histograms are stacked for clarity.

These two experiments demonstrate that though two disordered nanoparticle glass networks are not exactly the same, but for a given h, θ, and η, the network structures are comparable and the network functions are also comparable. Therefore, the simulated assembly is not *the unique* structure of the experimentally derived assembly with one-to-one particle correspondence, but it is *a* statistical representation of the structure that describes particle-to-particle connectedness and network connectivity. Further, since *different* binary nanoparticle glass networks have comparable average structure it is appropriate to define them as such, i.e., as (p_i, p_{1-i})-connected networks.

2.3.2.10 Numerical Simulations and Analysis of TOF Data

Having defined the particle networks in nanoparticle assemblies, we return to the TOF mobility data to understand the impact of network connectivity on the charge carrier mobility. Numerical simulations of the TOF experiments of hole transport through P3HT/PS nanoparticle assemblies were conducted (see Figure 50d-f) using a previously reported method.[256] Numerical simulations for η = 40%, 60%, and 80% were conducted at applied biases of 2 V and 3 V. Hole transport coefficients, kinetic parameters, and material properties derived from fitting modeling predictions to the TOF experimental data for transient photocurrents can be found in Figure 50g. The detrapping kinetic rate coefficient (C_{dt}) increases from 1.0×10^4 s^{-1} to 1.5×10^4 s^{-1} to 3.0×10^4 s^{-1} as the percentage of conducting particles η increases from 40% to 60% to 80%, respectively. The variation of C_{dt} with increasing η has certain implications for the structure of the assembly. The rate of positional detrapping increases as η increases because the *p*-connectedness of the network increases with increasing η and, thus, the number of available pathways that can be accessed for charge transport increases. This is represented graphically in Figure 51a, where for linear or less *p*-connected networks the probability of hopping (P_h)

between particles is low or zero in the presence of a positional trap state. On the other hand, for higher *p*-connected networks, the probability of finding an alternative path for the charge carrier to be detrapped is higher, and P_h is greater than zero. Combining our numerical simulations for charge transport and nanoparticle assembly structure indicates that highly *p*-connected networks provide alternate pathways for hole detrapping.

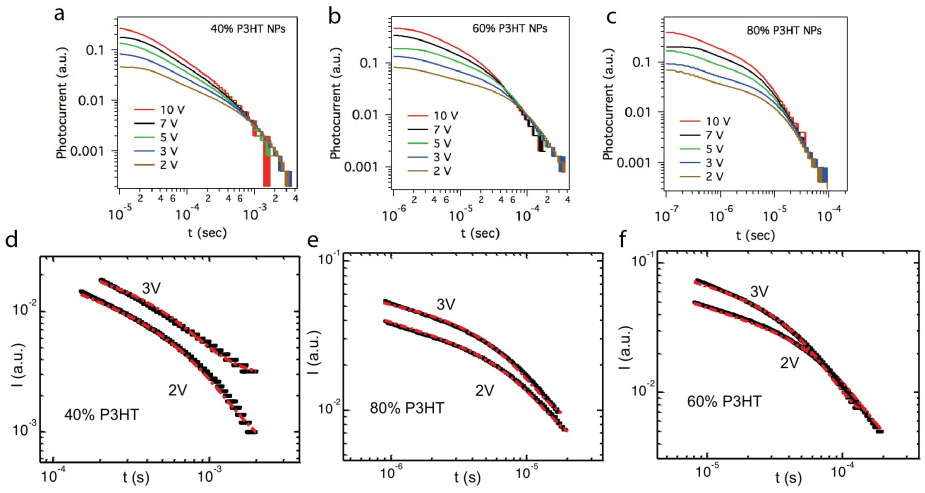

g

P3HT:PS =	80:20	60:40	40:60
Hole density P_0 ($\times 10^{26}$ m^{-3})	6-7.3	7.5-8.0	5.5-6.0
Hole mobility μ_0 ($\times 10^{-9}$ $m^2V^{-1}s^{-1}$)	9	1.3	0.05
E field dependence γ_p ($\times 10^{-4}$ $(V/m)^{-1/2}$)	-1	-1.4	-1.4
Hole trapping density P_t ($\times 10^{22}$ m^{-3})	2.5	2.4-3.0	3.9-4.3
Trapping coefficient C_t ($\times 10^{-17}m^3s^{-1}$)	**1.1**	**3.5**	**5**
Detrapping coefficient C_{dt} ($\times 10^4$ s^{-1})	**3**	**1.5**	**1.0**

Figure 50: TOF transients and results from numerical simulations of TOF data. TOF transients measured at 2V, 3V, 5V, 7V, and 10V for nanoparticle films with (a) η = 40%, (b) η = 60%, and (c) η = 80%. Numerical simulations (red dashed lines) of TOF transients (black markers) from deterministic hole transport model at 2V and 3V for (d) η = 40%, (e) η = 60%, and (f) η = 80%. (g) Table of hole transport coefficients, kinetic parameters, and material properties derived from fitting modeling predictions. Where $C_{dt} = C_0 \exp(-E_{tn}/k_BT)$ and E_{tn} is the trap energy depth.

In TOF experiments, a negative field dependence coefficient for non-zero-field charge carrier mobility is associated with positional disorder in the sample; when higher voltages are applied, paths that are not perfectly aligned with the external field become more difficult to travel.[387,388] This scenario is similar to the alternative pathway detrapping mechanism that we propose here from the C_{dt} calculations and, thus, we would expect to see the negative electric field dependence on the hole mobility in the TOF experiments. Indeed, in the field dependent TOF mobility data shown in Figure 51b we observe a negative field dependence on the measured charge mobility for all values of η examined, consistent with our hypothesis that as the degree of network connectedness increases, the probability of charge carrier detrapping will increase.

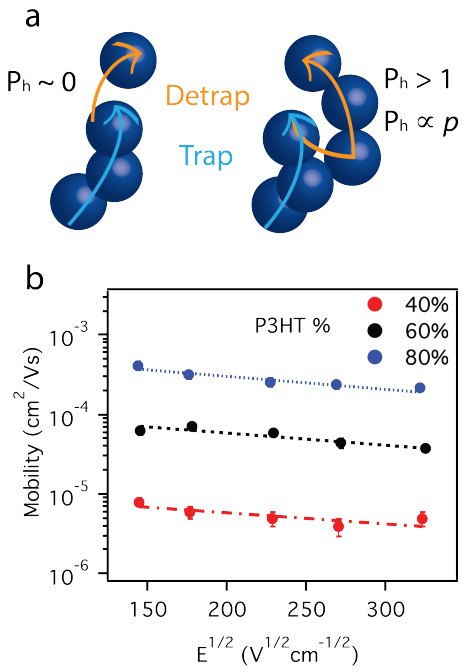

Figure 51: (a) Schematic depiction of positional trap states in low *p*-connected nanoparticle networks where the rate of hopping (P_h) is very low, implying that the predicted detrapping rate coefficient (C_{dt}) from numerical simulations of hole transport in these nanoparticle assemblies will be low. On the contrary, highly *p*-connected branched nanoparticle networks have alternative paths for detrapping available to access, thus P_h and C_{dt} in these assemblies will be higher with P_h being proportional to the degree of *p*-connectedness of the network. (b) Hole mobility for assemblies with η = 40%, 60%, and 80% P3HT nanoparticles as a function of the square root of the applied field, showing an increase in the mobility with an increase in the percentage η of P3HT nanoparticles, and a negative field dependence for all η values examined.

2.3.2.11 Conducting AFM of Polymer Blends

Finally, we compare the trends in our results from P3HT/PS nanoparticle assemblies with reported results for P3HT/polymer blends and P3HT nanofibers in a polymer matrix. In both, a low percolation threshold of ~1 wt.% was observed when the mobility was measured in a field-effect transistor (FET) configuration.[89,354,355,358,359,389] However, the mobility reached a maximum with ~3 wt.% of P3HT (~ 10^{-3} $cm^2V^{-1}s^{-1}$) and a mobility plateau was exhibited for a P3HT concentration higher than 3 wt.%. This is an indication that the path length and the number of paths of P3HT domains that charges travel through remain fairly constant, and is therefore not tunable, after the P3HT concentration reaches a level of ~3 wt.%. The morphologies in many polymer blends were found to be 'vertically stratified' with large, micron-sized features.[389] Vertically stratified structures are not characterized by bulk percolation pathways throughout the entire thickness of the film and, therefore, they cannot be studied using techniques such as TOF. It is also important to note that the mobility measured in a FET configuration can be different from mobility measured in a TOF configuration. In contrast, the nanoparticle assemblies that we focused on are characterized by formation of percolation pathways in the bulk and the charge carrier mobility change as a function of P3HT concentration (wt.%) follows a power law scaling relation. We conclude that using nanoparticle assemblies enables tunable and predictable percolation. Specifically, the nanoparticle assemblies afford the capability to tune the number of paths and the path lengths of connected conducting P3HT nanoparticles in the binary assembly that is not possible in polymer blends. Moreover, using nanoparticle assemblies allow us to control the domain sizes at the nanoscale for each of the components in the binary assembly.

To further validate this point, we fabricated P3HT/PS blends at 20, 40, 60, and 80 wt.% P3HT and analyzed them by cAFM. The resulting 15 μm × 15 μm cAFM maps are shown in Figure

52a-d. The maps are binarized in Figure 52e, in order to demonstrate the large-size features. In this experiment, we demonstrate that, in binary polymer blends, both the mesoscale morphology and the domain size change with increasing wt.% P3HT. However, in the *nanoparticle approach*, i.e., the use of binary nanoparticle assemblies (see Figure 53) instead of binary polymer blends, the mesoscale morphology can be *independently* tuned without changing the nanoscale domain size; this is the power of *the nanoparticle approach*.

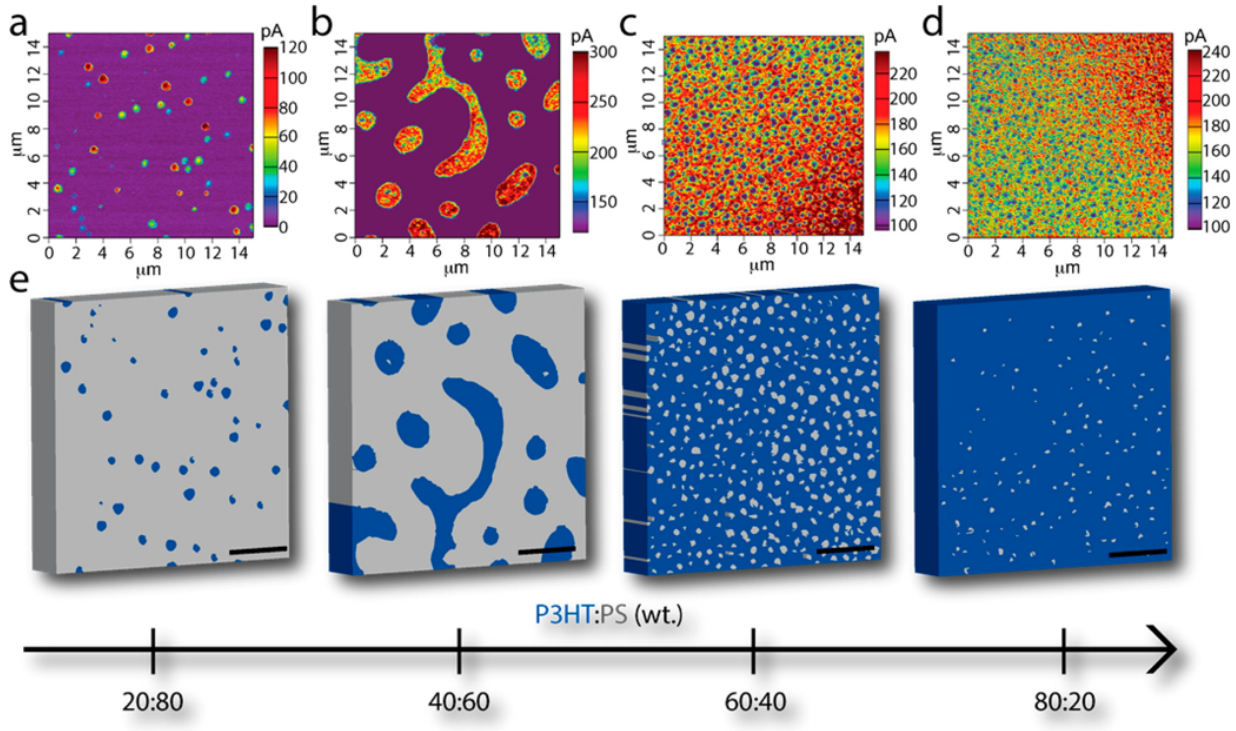

Figure 52: (a-d) 15 µm × 15 µm cAFM maps for P3HT:PS blends at weight ratios of 20:80, 40:60, 60:40, and 80:20 spin coated from chloroform. (e) Binarized cAFM map depicting P3HT (blue) and PS (grey) blend morphology; the scale bars are 2.5 µm.

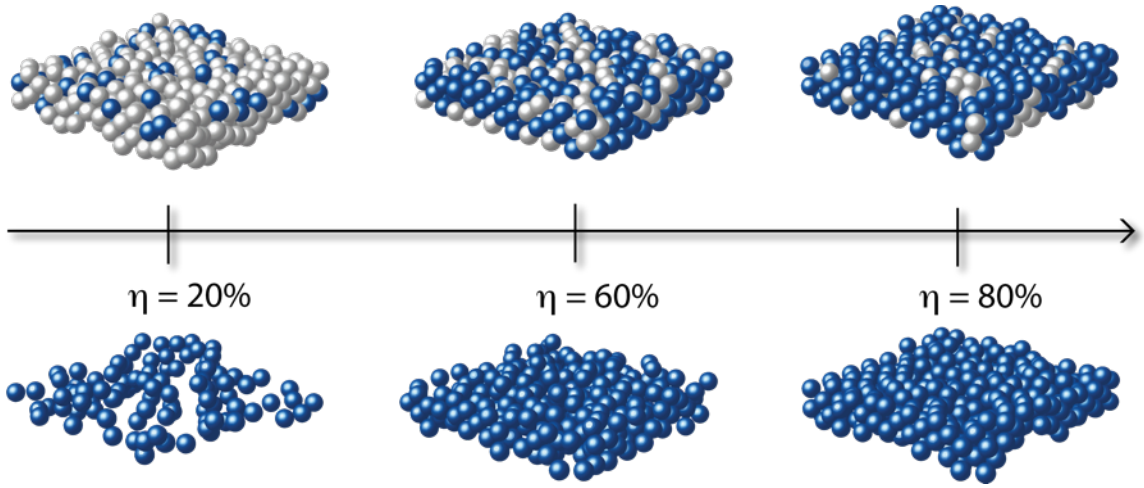

Figure 53: A visual representation of the tunability of percolation in binary polymer nanoparticle glasses. Top: Simulated assemblies of binary nanoparticle glasses at η = 20%, 60%, and 80%. Bottom: The insulating nanoparticles, colored grey on top, are removed to reveal the percolation network of conducting nanoparticles colored blue on top and bottom. This demonstrates how the structure of a polymer percolation network can be tuned by simply varying η

We have demonstrated tunable electronic transport in binary polymer nanoparticle glasses composed of nanoparticles of poly(3-hexylthiophene), a semiconducting polymer, and polystyrene, an insulating polymer. Using TOF mobility and cAFM current maps, we have also revealed that percolation in these systems follows a power law scaling behavior, with percolation thresholds of ~ 24% - 30%. A simple resistor network model was developed that accurately predicts current trends from cAFM maps, enabling the predictability of percolation behavior in these systems. We also performed cluster statistical analysis on simulated configurations of such binary nanoparticle glasses and developed a definition of the morphologies as (p_i, p_{1-i})-connected networks. We have shown that specific substructures in these morphologies can be predicted based on coordination, and be tuned by changing the percentage of one type of particle in the binary assembly, thus providing a design strategy for equal-sized binary particles at different η. The connectivity map can be used to create polymeric materials from disparate polymers

assembled into functional morphologies with desired percolation pathways. We conclude that using disordered nanoparticle assemblies provides a versatile and scalable approach toward tunable morphologies for a variety of functional materials. Our studies establish a new platform for creating mesoscale structures using disordered nanoparticle assemblies.

2.4 Resistor Network Model of Percolation in Randomly Conducting Disordered and Ordered Binary Nanoparticle Assemblies

In this section I present a resistor network model that incorporates the unique individual pathways for charge percolation in randomly conducting 1) equal-sized random assemblies of nanoparticles, 2) unequal-sized random assemblies of nanoparticles, and 3) binary nanoparticle super lattices. We next apply percolation theory to the resistor network results to calculate bulk percolation properties.

The concept of building electronic devices from nanomaterials such as nanoparticles, is increasingly being explored.[116,209,258,334,390,391] Nanomaterials allow for the assembly of disparate components with individually tailored properties on multiple length scales for the crucial control over device morphology. In order to understand how these materials will work as functional materials, it is important to first understand their percolation behavior, and how structure can be used to change percolation properties. In particular, binary assemblies of spherical nanoparticles where one type of particle form percolation pathways is of interest.[258,334] Herein, we introduce a resistor network model of percolation applied to several different models of randomly conducting binary assemblies of spheres. The results of the model are related to classical percolation theory[353] of random heterogeneous materials to describe percolation properties.

Binary nanoparticle assemblies can be generally characterized into two types: ordered assemblies, and disordered assemblies. Ordered assemblies can be classified by their ionic structural analogs, and are commonly referred to as binary nanoparticle superlattices (BNSLs).[92,198,209,233] Disordered assemblies can be classified by the size and number ratio of the two types of particles, as well as the volume packing fraction.[364,380,392] Disordered

assemblies can be loosely packed or maximally jammed (so called nanoparticle glass) and anything in between.

We have developed a resistor network[352,374,375] algorithm to compute the charge percolation through binary nanoparticle assemblies. The algorithm predicts the individual particle currents for assemblies lying on planar electrodes. The model is applicable to any assembly of spherical particles where the x, y, and z position and the size and identity of every particle are known. Here we explore three different types of assemblies using this algorithm. First, we show the effect of the percent of conducting particles to non-conducting particles (η), in equal-sized, binary nanoparticle glasses, on charge percolation. Next we demonstrate how the size ratio of conducting particles to non-conducting particles (γ) in random assemblies affects the charge percolation properties. And finally, we explore the effect of η on ten BNSL with different ionic crystal analogues. These examples demonstrate the power of nanoparticle assemblies to obtain tunable percolation behavior.

2.4.1 Resistor Network Model

The resistor network model to calculate charge percolation in binary assemblies of nanoparticles was first reported in Ref. [334]. Herein, we expand the use of the model to other systems. In our simulation device, the binary nanoparticle active layer is composed of either an insulating or conducting nanoparticle. This nanoparticle assembly can be random or ordered. The assembly is placed on a planar electrode where charges are injected into the assembly and then detected on an individual nanoparticle basis at the surface. In this model each nanoparticle in a particular path is considered a composite resistor, thus, a chain of nanoparticles is just a chain of serial resistors. Multiple unique paths are treated as parallel serial resistors. Therefore, the

current at a particular surface particle can be calculated by summation of Ohm's law using the equation:

$$I_S = V \sum (RN_k)^{-1}$$

where I_S is the simulated current, V is the applied field, R is the resistance of one nanoparticle, and N is the number of particles of the k^{th} path. For simplicity, all simulations were run at $V = 1$ V and $R = 1\ \Omega$.

To simulate current through a nanoparticle assembly, first, using the information of the assembly — x, y, and z position of every nanoparticle, and whether or not the particle is conducting — all of the non-conducting particles are removed from the assembly. Next, a $n \times n$ adjacency matrix **A** with elements A_{ij}, is composed, where $i, j \in \{1, ..., n\}$ and n is the number of particles in the assembly. In the matrix **A**, $A_{ij} = 1$ if particles i and j are in contact (the distance between i and j is less than the diameter of i plus the diameter of j plus δ) and z_j is greater than or equal to z_i, and if particles are not in contact $A_{ij} = 0$. Using **A**, and Dijkstra's algorithm,[382] each unique shortest path is solved for all bottom particles to each top particles. Essentially each particle at the surface has a a unique network of pathways extending to the bottom planar electrode. Then, using the Ohm's Law summation equation above, the current at every surface particle is calculated. For each assembly the current is binned (bin size = 0.1 A)

2.4.2 Percolation Through Equal-Sized Random Assemblies

The first type of assembly that we used to simulate charge percolation was a binary nanoparticle glass of equal-sized particles. These assemblies were simulated by an algorithm reported by Desmond and Weeks.[364] Assemblies contained a total of 5,000 particles, the simulated assemblies were 12 times larger in the x and y direction than in the z direction (~ 3 particles). Then, particles were randomly identified as conducting or not from $\eta = 10\%$ to 90% in

increments of 10%, where η is the percent conducting particles in the assembly. The assemblies are randomly identified in triplicate. The results of the resistor network model for the equal-sized binary nanoparticle glasses are shown in Figure 54 in open symbols. The data is fit with the following Lorentzian equation, shown in solid lines:

$$f(\eta) = \frac{A}{(\eta - x_0)^2 + B}$$

where A is a scaling parameter, x_0 is the mode current, and B is a width parameter. The inset of Figure 54 shows the plot of x_0 versus η. The plot shows the ability to tune current through the nanoparticle percolation network by changing η. The black dashed line is the fit to the data using typical power law scaling percolation[240,261,353,372,373] equation.

$$f(\eta) = a(\eta - p_c)^t \text{ for } \eta > p_c$$

where a is a scaling parameter, p_c is the percolation threshold, and t is the critical exponent. The critical exponent is a universal descriptor of the fractal properties of the assembly. p_c represents the critical concentration of conducting particles (η) required for the binary assembly to be conducting. The corresponding fitting parameters are a = 15.78, p_c = 24%, and t = 2.08, with a correlation coefficient to the fitting of R^2 = 0.99. We would like to note here that $t \sim 2$ is consistent with the critical exponent for 3D percolation, where the local structure is isotropic and has only short range correlations. Because p_c and t arise from a particular fractal structure, experimental properties can be measured, and parameters can be matched with computation, in order to understand the structure of real systems that have previously been too small to see.[334] However, unfortunately, a rigorous correlation between t and geometric scaling exponents has yet to be developed, thus a physical picture is hard to describe, particularly for truly non-random systems.[353]

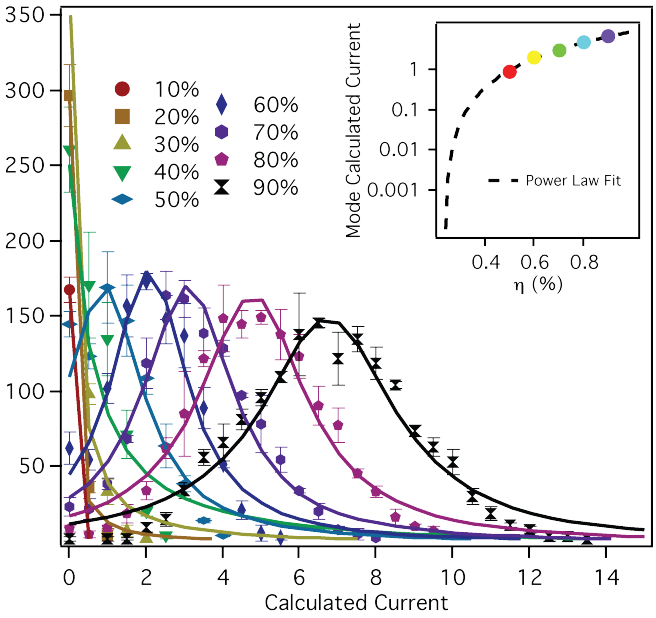

Figure 54: Counts vs calculated current for random assemblies of equal-sized spheres with increasing percentage of conducting spheres η; solid lines are Lorentzian distribution fits to the data. Inset shows the mode current from the Lorentzian fit vs. η, the black dashed line is the power law scaling percolation fit to the data.

2.4.3 Percolation Through Unequal-Sized Random Assemblies

We next explored the effect of radius ratio ($\gamma = r_{small}/r_{large}$) in random binary nanoparticle glasses on electrical percolation. Simulated nanoparticle glasses were again made using the algorithm reported by Desmond and Weeks.[364] We simulated assemblies at γ = 1.0, 0.8, 0.66, and 0.57 (where the larger particle is the conducting one), at η = 10%, 30%, 50%, 70%, and 90%; all assemblies were simulated in triplicate by changing the Mersenne Twister seed number for random particle identification. We next simulated current profiles using the Ohm's Law equation for all simulated assemblies.[364] The current profiles are fit with the Lorentzian distribution to extract the mode calculate current parameter x_0. Figure 55a shows the plot of x_0 versus η for all γ in closed symbols. The dashed lines are the corresponding power law scaling percolation fits using the previous equation. The corresponding fitting parameters and correlation

coefficients of the fits are shown in Table 5. A plot of p_c versus γ is shown in Figure 55b, demonstrating the exponential decline in p_c as you decrease γ. This result shows that if you increase the size of the conducting particle, the amount of it required for fabricating a percolating composite device drops off exponentially.

We can look at the pair correlation function (g(*r*)) of these assemblies to see how the connectedness of their percolation pathways changes with η. In Figure 56, we show a plot of pair correlation functions, where $r = r_{large,}$ of assemblies with γ = 0.66 at η = 10%, 30%, 50%, 70%, and 90%.The peak at low *r* correspond to small-small particle correlations, the peak at intermediate *r* correspond to small-large particle correlations, and the peak at high *r* (*i.e.* *r* = 1) correspond to large-large particle correlations. As a reminder, η corresponds to the percentage of the larger conducting spheres in the assembly, while 1- η corresponds to the percentage of smaller insulating spheres. At low η, there is predominantly correlation between small-small insulating particles. As η increases, both small-large, and large-large particle correlations increase, but small-large correlations do not result in percolation pathways. At high η, there is predominantly large-large conducting particle correlations in the assembly. At smaller γ, large-large correlations increase at lower η, thus the lower p_c.

We wish to note the decrease in the critical exponent *t* as γ decreases. As stated previously *t* is a value that describes the fractal properties of the assembly. Therefore, we can assume that the fractal properties in random binary assemblies change with radius ratio. It is generally accepted that *t* = 1 to 2 in three dimensions, we find *t* = 0.91 to 2.08. Others have attempted to connect *t* to geometric parameters, however a rigorous definition has yet to be developed.[353] Here, we do not connect physical structure with *t* but show that it can in fact be tuned by using radius ratio γ.

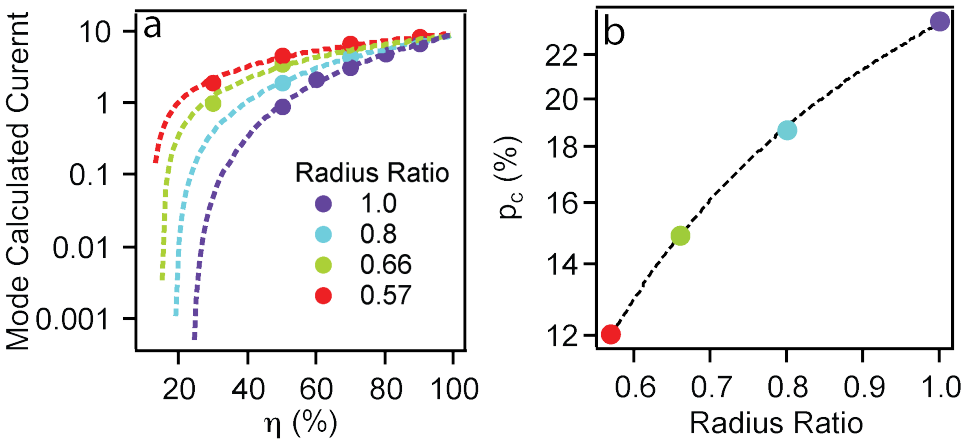

Figure 55: a) Mode calculated current vs η at different γ, dashed lines correspond to power law scaling percolation theory fits. b) Plot of p_c vs γ, showing exponential dependence in black dashed line.

Table 5: Percolation power law scaling fit parameters for different values of γ.

γ	**1.0**	**0.8**	**0.66**	**0.57**
a	15.78	12.12	10.59	10.44
p_c	24%	18%	15%	12%
t	2.08	1.56	1.12	0.91
$\mathbf{R^2}$	0.996	0.999	0.996	0.993

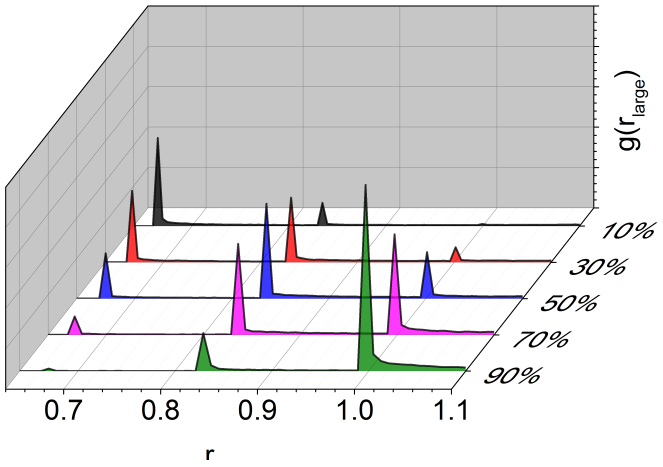

Figure 56: Pair correlation functions of assemblies with γ = 0.66 at η = 10%, 30%, 50%, 70%, and 90%.

2.4.4 Percolation Through Randomly Conducting Ordered Assemblies

We next used 25 × 25 × 1 super cells of crystalline structures in order to probe the resistor network model on BNSLs. In this simulation, any particle (big or small) was randomly identified as conducting or not at η = 10%, 30%, 50%, 70%, and 90% in triplicate, and then the percolation model was run on those assemblies. The structures used for this experiment and their corresponding γ, space groups, and crystal systems are shown in Table 6. The results of the simulations are shown in Figure 57 as counts versus calculated current plots, where the counts have been normalized by the total number of particles in the assembly. Also, the plots are stacked for clarity.

Table 6: Description of BNSLs used in this study.

Structure	γ	Space Group	Crystal System	Ref.
ZnS (Wurzite)	0.836	$P6_3mc$	Hexagonal	[393]
FeS_2	0.671	Pnnm	Orthorhombic	[394]
HgS	0.773	$P3_221$	Trigonal	[395]
AlB_2	0.686	P6/mmm	Hexagonal	[396]
CsCl	0.406	Pm-3m	Cubic	[397]
AuCu	0.971	P4/mmm	Tetragonal	[398]
NiAs	0.976	$P6_3/mmc$	Hexagonal	[399]
$CaCu_5$	0.750	P6/mmm	Hexagonal	[400]
$AuCu_3$	0.971	Pm-3m	Cubic	[397]

There are several observations about charge percolation in BNSLs that can be made. First, there is a clear discreteness in currents paths that are available for charge percolation; this is evident by the peaks, or the complete absence of peaks at particular current values for virtually all structures. ZnS-type structures show the emergence of peaks at calculated currents 0.3 A and 0.7 A with increasing η. FeS_2-type structures show peaks at calculated currents 0.5 A. 1.0 A, and 1.5 A. HgS-type structures show the appearance of a peak at calculated current 0.2 A. AlB_2-type structures shows calculated current peaks at 0.5 A, 0.7 A, a major peak at 1.0 A, and then a peaks at 1.3 A, 1.5 A, 1.7 A. 2.0 A, 2.3 A, 2.5 A, and 2.7 A. At high η, a peak at 0.2 A starts to dominate, when η = 90% the current extends from 0.2 A down to 3.4 A. NaCl-type structure have major peaks that increase with increasing η at 0.5 A, 1 A, 1.5 A, 2.0 A, and 2.5 A. Minor peaks at 0.8 A, 1.3 A, 1.8 A, 2.3 A, 2.8 and so on are also present. The CsCl-type structure has

peaks at 1.0 A, 1.5 A, 2.0 A, 2.5 A, 3.0 A, and 3.5 A. At higher η, there are more percolation pathways which are shown as distributions of current which have x_0 = 3.7 A, 6.8 A, and 15.8 A for η = 50%, 70% and 90% respectively. AuCu-type structures shows low counts of current from 0.2 A to 1 A at η = 10%, with no identifiable x_0. From η = 30%, 50%, and 70% x_0 = 0.24 A, 1.0 A, and 5.3 A respectively. Interestingly, when η = 90% the calculated current becomes bimodal, with individual x_0 = 6.1 A and 8.9 A, indicating two unique paths. NiAs-type structure has peaks at 0.3 A, 0.5 A, 0.7 A, 0.8 A, 1.0 A, 1.2 A, 1.4 A and so on. The peaks form current distributions with x_0 = 0.5 A, 0.89 A, 1.9 A, and 3.5 A for η = 30%, 50%, 70%, 90% respectively. CaCu5-type structure has peaks at 0.5 A, 1.0 A, 1.5 A, 3.0 A, 2.5 A, and 3.0 A; forming current distributions with x_0 = 2.8 A, 5.8 A, and >30 A for η = 50%, 70%, and 90% respectively. Lastly, AuCu3-type structure has a major peak at 0.3 A for η = 10% and 30% respectively; and current distributions of 0.92 A 4.1 A, 15.5 A, and >30 A for η = 30%, 50%, 70%, and 90% respectively.

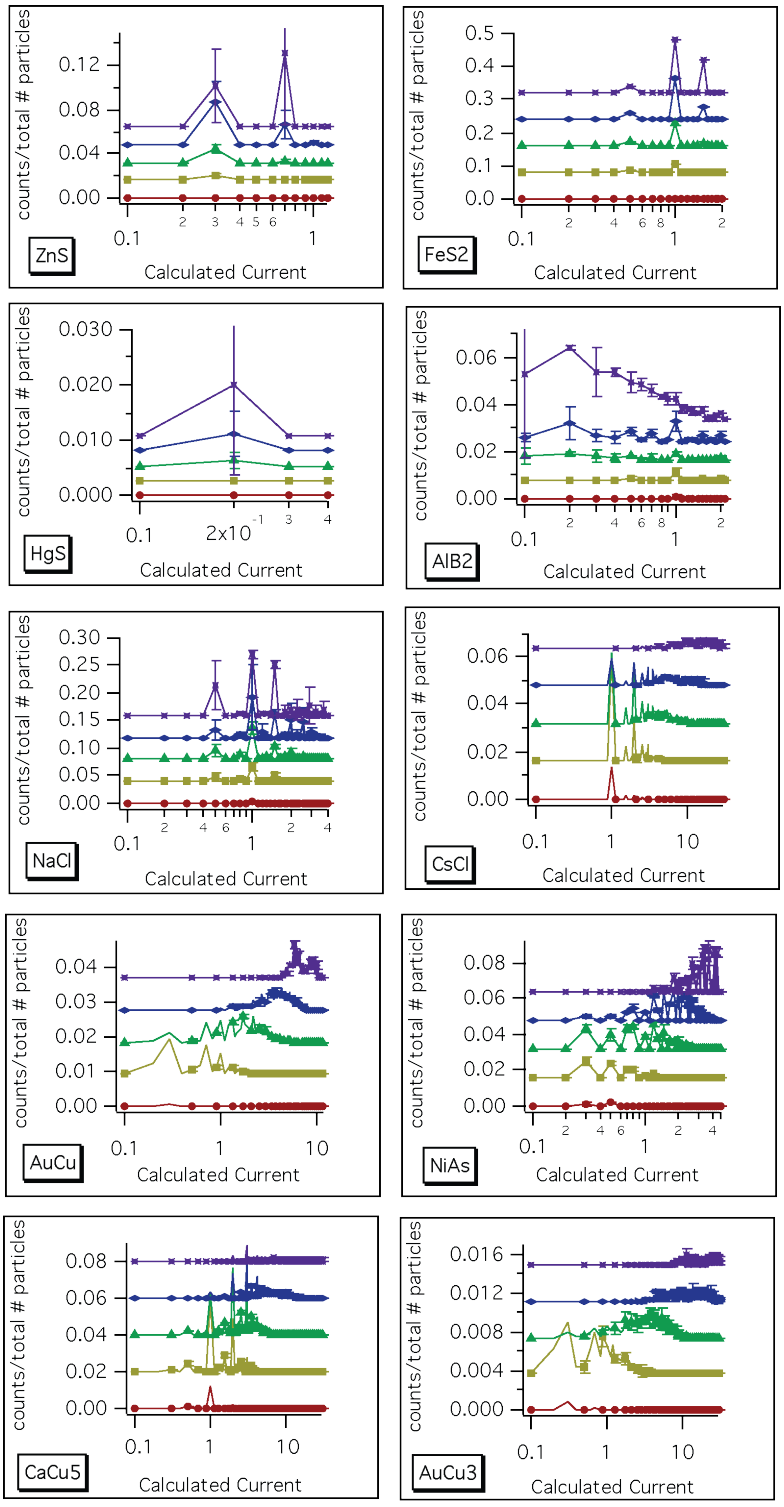

Figure 57: Surface current profiles of selected BNSL at η = 10% (red), 30% (yellow), 50% (green), 70% (blue), and 90% (purple).

To analyze the percolation, BNSLs do not have current distribution as in random assemblies, therefore we cannot use the Lorentzian distribution equation to find the mode current, rather we use a weighted average. Plot of weighted average current vs η is shown is Figure 58 for all BNSLs. The fit parameters for power law percolation fits are shown in Table 7. ZnS-type structure was calculated to have a p_c = 17.3%, and t = 1.97. The FeS2-type structure had a p_c = 13.9% and t = 0.84. HgS-type structure had a p_c = 21.0% and t = 1.77. AlB2-type structure had a p_c = 28.6%, and t = 2.99. NaCl-type structure had p_c = 23.5% and t = 1.18. CsCl-type structure had a p_c > 0% and t = 2.68. AuCu-type strucute had a p_c =14.2% and t = 1.74. NiAs-type structure has a p_c = 3.4% and t = 2.13. CaCu5-type structure had a p_c >0% and t = 2.93. Lastly, AuCu3-type structure had a p_c >0% and t =3.74. Percolation thresholds of p_c >0% are likely a result of the BNSL only being one unit cell in the z-direction.

Table 7: Power law scaling fit parameters for different BNSL structures.

Structure	***a***	p_c	***t***	$\mathbf{R^2}$
ZnS (Wurzite)	0.49	17.3 %	1.97	0.989
FeS_2	0.91	13.9 %	0.84	0.997
HgS	0.03	21.0 %	1.77	0.991
AlB_2	1.34	28.6 %	2.99	0.982
NaCl	1.85	23.5%	1.18	0.982
CsCl	21.26	> 0 %	2.68	0.995
AuCu	11.69	14.2 %	1.74	0.999
NiAs	4.48	3.4 %	2.13	0.999
$CaCu_5$	22.09	> 0 %	2.93	0.994
$AuCu_3$	59.0	> 0 %	3.74	0.999

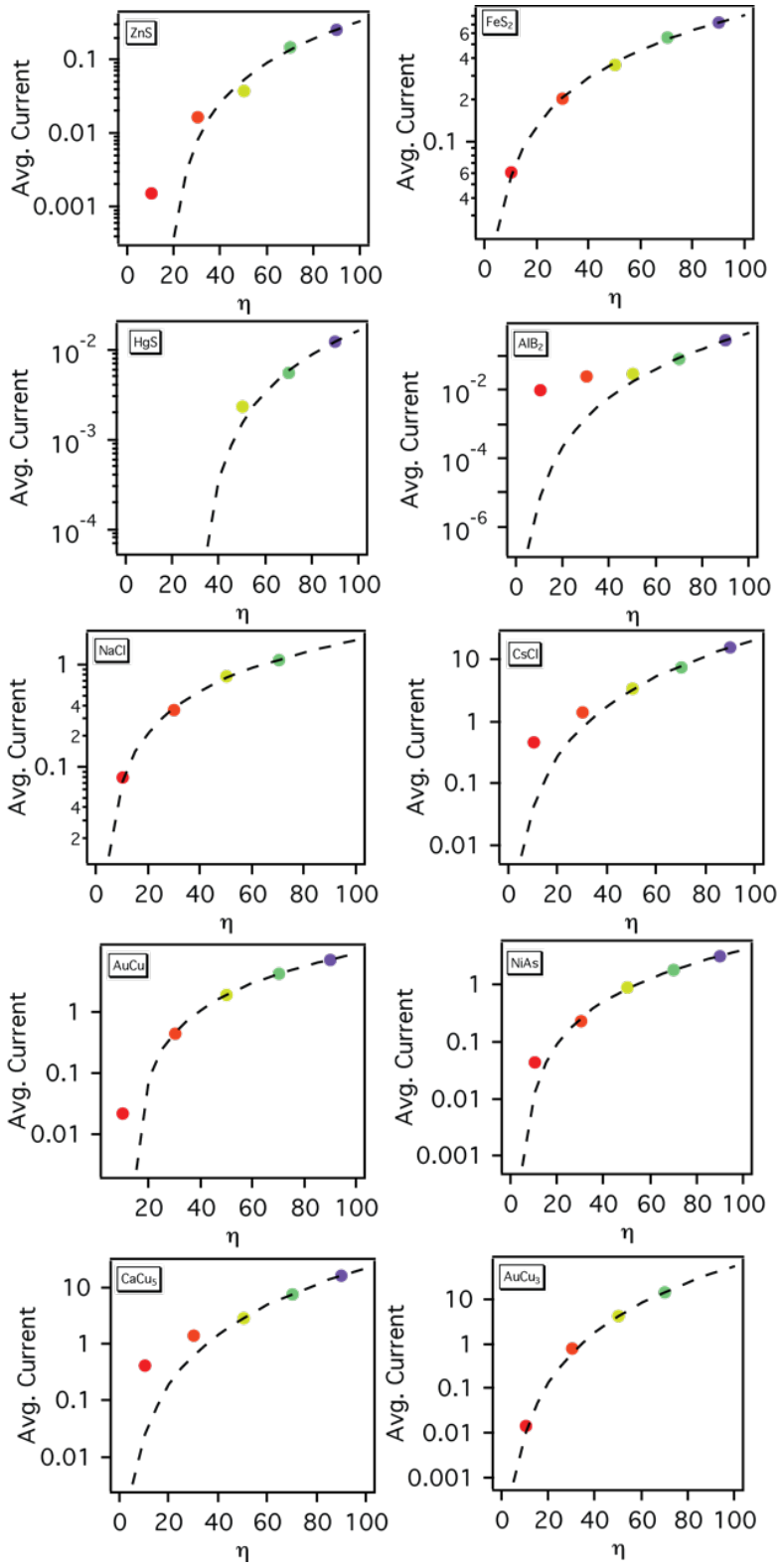

Figure 58: Weighted avg. current vs η for different BNSL structures with power law scaling percolation fits in black dashed lines.

To conclude, we have demonstrated a resistor network model utilizing a summation of Ohm's law percolation pathways in series and in parallel, for percolation through randomly conducting 1) equal-sized random assemblies of nanoparticles, 2) unequal-sized random assemblies of nanoparticles, and 3) binary nanoparticle super lattices. We demonstrate that for most assemblies, percolation (*i.e.* current) exhibits power law scaling with respect to the percentage of the conducting nanoparticle η. Further, we show that the 3 dimensional structure has implication on both the percolation threshold and the critical exponent. This model can be employed to predict percolation properties and utilized for rational material design of particular properties (*e.g.* charge percolation) where nanoparticles are the constituent building blocks.

2.5 Nanoparticle Assemblies for Organic Photovoltaics

This chapter[***] focuses on the use of binary nanoparticle assemblies to realize organic photovoltaics. I would particularly like to highlight the use of cAFM to probe charge transport through nanoparticle assemblies, and at charge selective transport layer interface. Herein, we address here the need for a general strategy to control molecular assembly over multiple length scales. Efficient organic photovoltaics require an active layer comprised of a mesoscale interconnected networks of nanoscale aggregates of semiconductors. We demonstrate a method, using principles of molecular self-assembly and geometric packing, for controlled assembly of semiconductors at the nanoscale and mesoscale. Nanoparticles of poly(3-hexylthiophene) (P3HT) or [6,6]-phenyl-C_{61}-butyric acid methyl ester (PCBM) were fabricated with targeted sizes. Nanoparticles containing a blend of both P3HT and PCBM were also fabricated. The active layer morphology was tuned by the changing particle composition, particle radii, and the ratios of P3HT:PCBM particles. Photovoltaic devices were fabricated from these aqueous nanoparticle dispersions with comparable device performance to typical bulk-heterojunction devices. Our strategy opens a revolutionary pathway to study and tune the active layer morphology systematically while exercising control of the component assembly at multiple length scales.

There is a need for a general strategy to control molecular assembly over multiple length scales. This need is most evident in the area of organic photovoltaics (OPVs) wherein active layers

---

[***] This chapter is adapted from Gehan, Timothy S., Monojit Bag, Lawrence A. Renna, Xiaobo Shen, Dana D. Algaier, Paul M. Lahti, Thomas P. Russell, and Dhandapani Venkataraman. "Multiscale active layer morphologies for organic photovoltaics through self-assembly of nanospheres." *Nano Letters* 14, no. 9 (2014): 5238-5243. I would like to acknowledge Dr. Timothy S. Gehan for synthesizing the nanoparticles and preparing ‘inks’ for devices, Dr. Dana D. Algaier and Dr. Xiaobo Shen for SEM, and Prof. Monojit Bag for making TOF and solar-cell measurements.

comprise mesoscale interconnected networks of nanoscale aggregates of semiconductors.[401-404] Consistently achieving and tuning this structure has been challenging due to the interplay of multiple kinetic processes during fabrication.[109,110] Herein we show that the fundamental concept of sphere packing[96,198] can be exploited to fabricate multi-scale hierarchical structures reliably through self-assembly. We fabricated efficient OPVs through the self-assembly of separate spherical nanoparticles (NPs) comprised of either poly(3-hexylthiophene) (P3HT) or [6,6]-phenyl-C_{61}-butyric acid methyl ester (PCBM). Devices of blend nanospheres comprised of both P3HT and PCBM were also fabricated. We demonstrate multi-scale control over morphology (Figure 59) by changing the particle size, ratio, and composition.

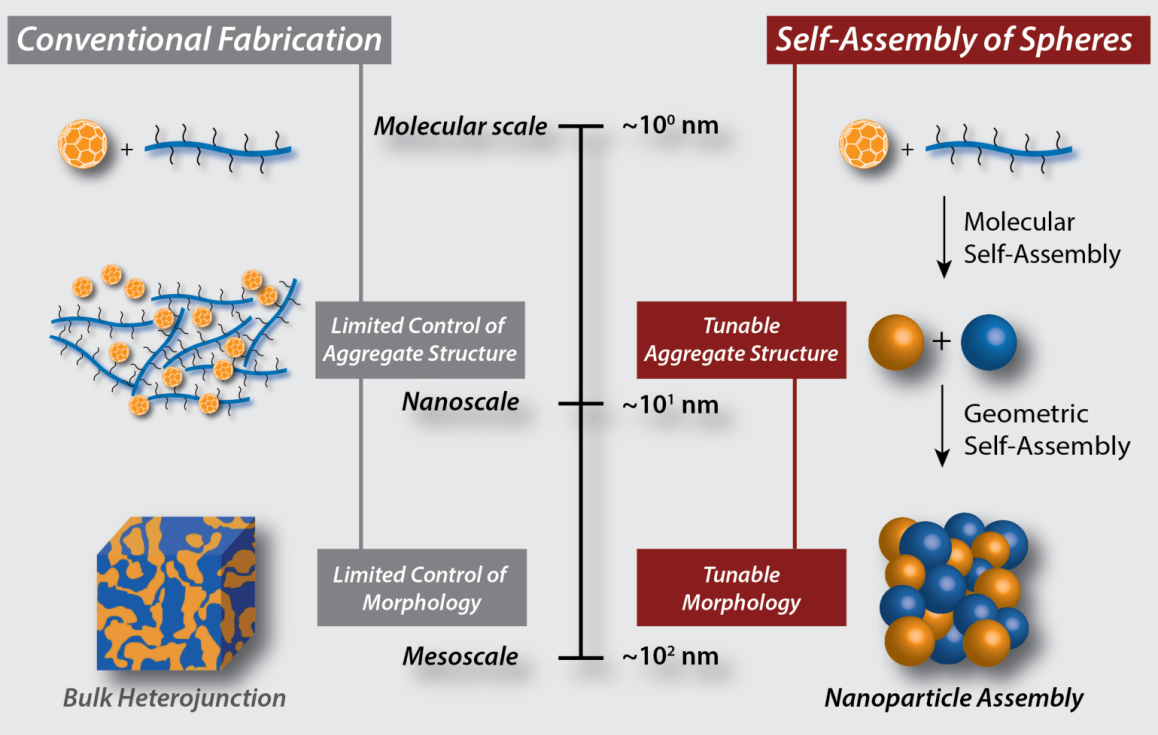

Figure 59: Schematic comparison of morphology control with the conventional method and the nanoparticle assembly method for the fabrication of organic photovoltaic active layers.

Spheres can assemble into ordered or randomly packed assemblies, depending on sphere-sphere interactions, size dispersity, and size ratios.[92,198,405] Both assemblies can provide morphologies with interfaces for charge transfer and continuous pathways for charge transport—two key requirements for organic photovoltaic devices—when sphere-to-sphere contacts are present. In inorganic nanoparticle assemblies, particle-particle contacts are actually *prevented* by the ligands strongly bound to the surface of the nanoparticles, leading to poor charge transport.[406] We found that in organic nanoparticle assemblies, particle-particle contacts are easily established because the weakly bound surfactants can be dislodged by strong van der Waals interactions between the nanoparticles, leading to jammed disordered assemblies with intimate nanoparticle contacts and efficient charge transport.[255,256] Computations indicate that jammed co-assemblies, like ordered binary superlattices, can also provide co-continuous structures where the morphology is dictated by the ratio of the sphere radii.[240] Thus, jammed assembly of single and binary conjugated polymer nanospheres provides a new strategy to achieve and tune morphologies required for effective active layer charge transport in organic photovoltaic devices.

Conjugated polymer nanoparticles have been investigated as active layer materials in OPVs, albeit with limited success.[64,407,408] We show that efficient OPVs can be fabricated with blend nanoparticles and with separate nanoparticles using P3HT and PCBM, the archetypical active layer materials in OPVs,[409] by combining the principles of sphere packing with improved fabrication methods. Blend nanoparticles have electron- and hole transporters in the same nanoparticle, offering a unique pathway to create bulk heterojunction (BHJ) structures within a single nanoparticle,[408,410,411] and to propagate this structure to the mesoscale through self-assembly. On the other hand, formulating active layer materials into *separate* nanoparticles prior to their co-assembly allows the control of their size, their internal structure and ordering, and their surface

properties. These attributes enable the formation of domains having *pre-defined* sizes, *independently* tailored ordering, and *well-defined* contacts (interfaces) between the electron and hole conducting domains.

2.5.1 Nanoparticle Synthesis and Characterization

The blend nanoparticles and separate nanoparticles were fabricated using a modified mini-emulsion method.[135,412] The diameter of the blend nanoparticles was determined to be 80±9 nm using nanoparticle-tracking analysis. The diameter of P3HT nanoparticles was 79±20 nm and PCBM nanoparticles was 71±24 nm. The diameter of a 1:1 mixture of P3HT and PCBM nanoparticles was 74±11 nm indicating that there is no aggregation of the nanoparticles in the dispersion. The molecular packing of P3HT in aqueous nanoparticle suspensions was probed using electronic spectroscopy. The UV-vis spectrum of P3HT can be deconvoluted into absorption arising from aggregate P3HT and from amorphous P3HT.[135] Using this method, we estimated that in P3HT:PCBM blend *and* in separate P3HT nanoparticles, the ratio of aggregate to amorphous P3HT was 70:30 (Figure 60). We attribute the amorphous component to P3HT within the nanoparticle and not to free P3HT, because P3HT is insoluble in water. As blend and separate nanoparticles show similar ratios of aggregate to amorphous P3HT, we conclude that PCBM does not significantly affect P3HT aggregation in the blend nanoparticles. As in BHJ, the PCBM is expected to concentrate in the amorphous or non-aggregated domains of P3HT or to phase separate from P3HT.[107,401] The UV-vis spectra of both blend nanoparticle and separate nanoparticle dispersions having similar particle sizes and concentrations show features similar to those of annealed thin films of P3HT and PCBM cast from chlorobenzene, indicating that the same aggregation features desired in thin films can be captured in the nanoparticles. X-ray diffraction

(XRD) of blend and separate nanoparticle assemblies show similar results indicating crystalline P3HT within the nanoparticles (Figure 61).

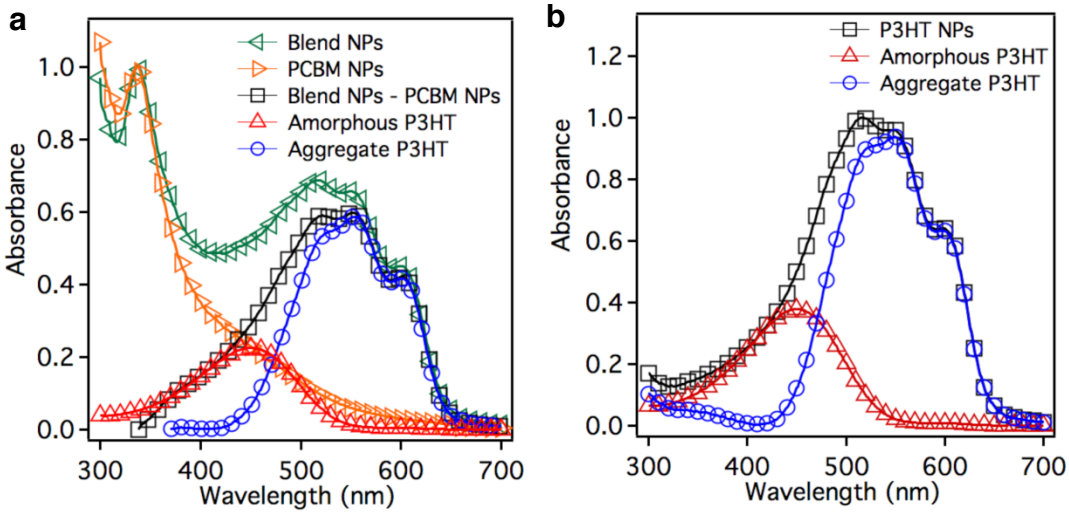

Figure 60: (a) P3HT:PCBM blend nanoparticles. PCBM nanoparticles absorption was subtracted from the blend absorption spectrum to estimate P3HT (amorphous and aggregate) absorption. P3HT aggregate in the blend nanoparticles is 70.22%. (b) P3HT nanoparticles. P3HT aggregate in the nanoparticles is estimated to be 71.25%.

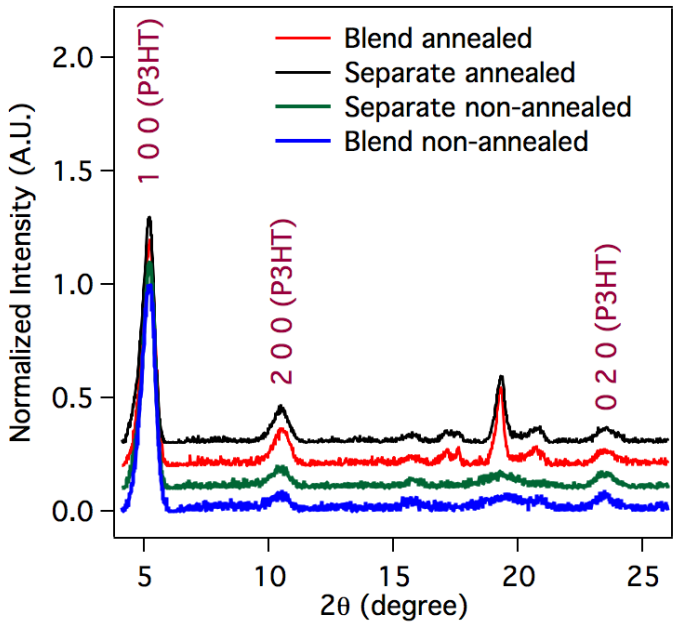

Figure 61: X-ray diffraction data for P3HT and PCBM blend and separate nanoparticles film drop casted under infrared lamp. Enhanced PCBM peak is observed after ramp heating (annealing) from 30°C to 150°C temperature under nitrogen environment. A strong 100 P3HT peak is observed in all samples.

Scanning electron microscopy (SEM) images of spin-coated assemblies of blend nanoparticles and co-assemblies of separate P3HT and PCBM nanoparticles (1:1) on silicon substrates show that the nanoparticles form jammed assemblies with particle-particle contacts (Figure 62c and Figure 63). A simulation[364] of a random close packed co-assembly of two types of hard spheres (Figure 62a) having the same radii in a 1:1 number ratio shows interconnected pathways for both types of particles. These interconnected pathways are clearly seen in Figure 62b where all the spheres of one type from Figure 62a are omitted. To differentiate experimentally between P3HT and PCBM nanoparticles, the same film from Figure 62c was dipped into dichloromethane for 15 min to remove the PCBM selectively; SEM of the resultant film is shown in Figure 62d. The binary images in Figure 62e-f of Figure 62c-d, respectively, show removal of approximately half of the nanoparticles. After the removal of PCBM, the void spaces in the film are visible, demonstrating that the films are a jammed *co-assembly* of P3HT and PCBM nanoparticles. Cross sectional SEM of a thin film of P3HT:PCBM blend nanoparticles confirms that the nanoparticles are closely packed throughout the film. Similar results were also observed for separate nanoparticle co-assembled active layers.

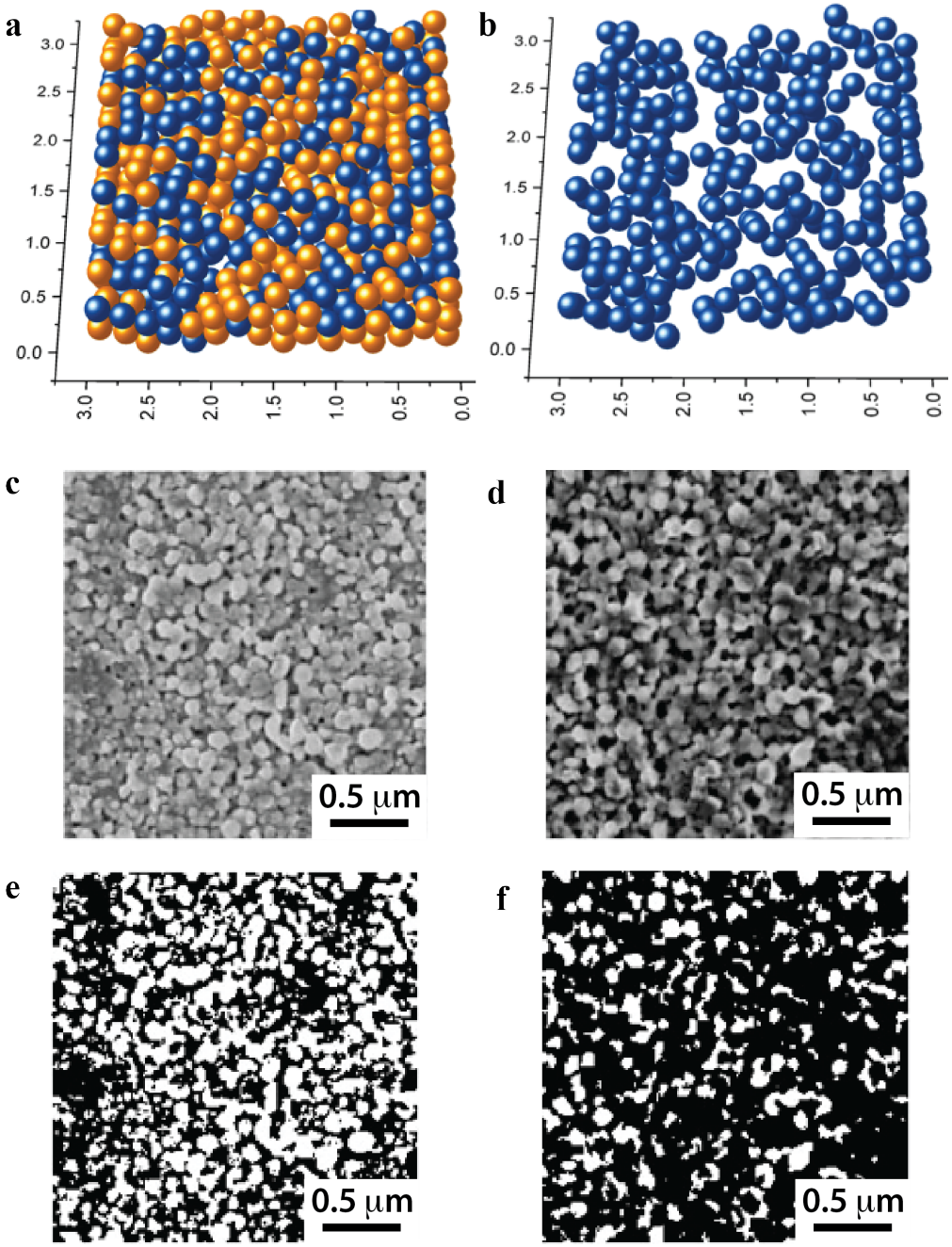

Figure 62: (a) Simulated packing of a 1:1 number ratio of two types of particles showing random, jammed assembly. (b) Simulated packing of a 1:1 number ratio of two types of particles showing conducting pathways for one set of particles (other type is omitted). (c) Top view SEM of P3HT and PCBM separate nanoparticles. (d) Top view SEM of P3HT and PCBM separate nanoparticles after being dipped in DCM for 15 min. (e) A binary scale image of the SEM image in c. (f) A binary scale image of the SEM image in d.

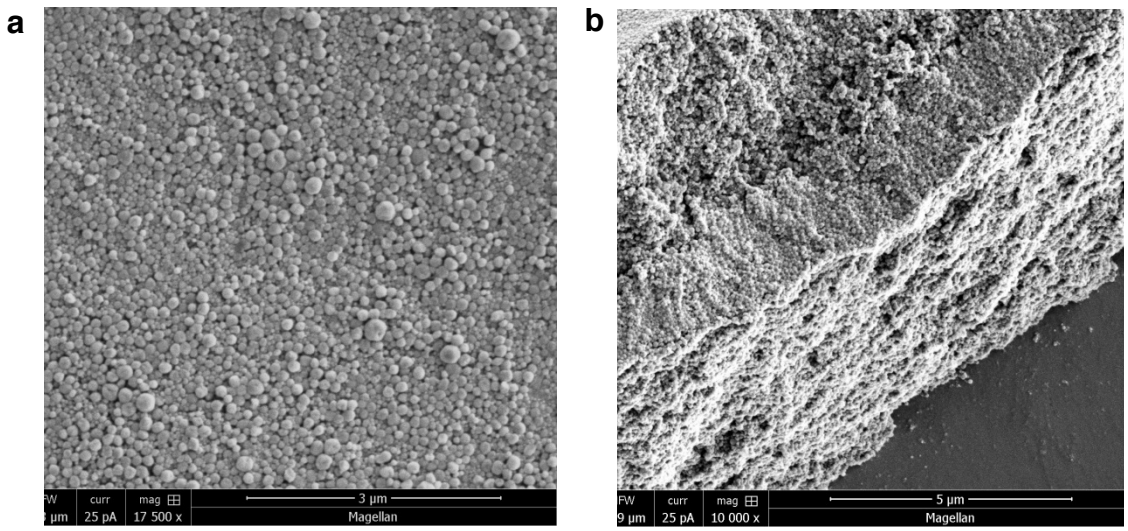

Figure 63: (a) TOP SEM image of P3HT and PCBM blend nanoparticle sample spin coated on PEDOT:PSS coated Si substrate. (b) Cross sectional SEM image of P3HT and PCBM blend (1:1) nanoparticle sample spin coated on Si substrate.

2.5.2 cAFM of Nanoparticle Assemblies

Conducting AFM (cAFM) was used to probe the conducting pathways in the active layer. cAFM images of assemblies of blend nanoparticles and co-assemblies of separate nanoparticles (~240 nm thick films) on ITO/PEDOT:PSS are shown in Figure 64, and with corresponding height images in Figure 65. Based on the applied bias conditions, the measured current is a result of the movement of holes to the platinum probe. The dark red regions in the images are areas of high hole conductivity and the blue regions are areas of low conductivity. Both Figure 64a (blend nanoparticles) and Figure 64b (separate nanoparticles) show the presence of conductive pathways for hole transport through the nanoparticle films to the platinum probe. In control testing, cAFM of films composed only of P3HT nanoparticles or PCBM nanoparticles show uniformly high conductivity throughout the film for the former, and uniformly low conductivity for the latter; this corresponds to high and low hole transport in the respective films (Figure 66). Therefore, we

conclude that the areas of low current are regions with either a high concentration of PCBM or regions surrounded by PCBM. All of these results show that there are continuous pathways for hole transport in random assemblies of both blend and separate nanoparticles.

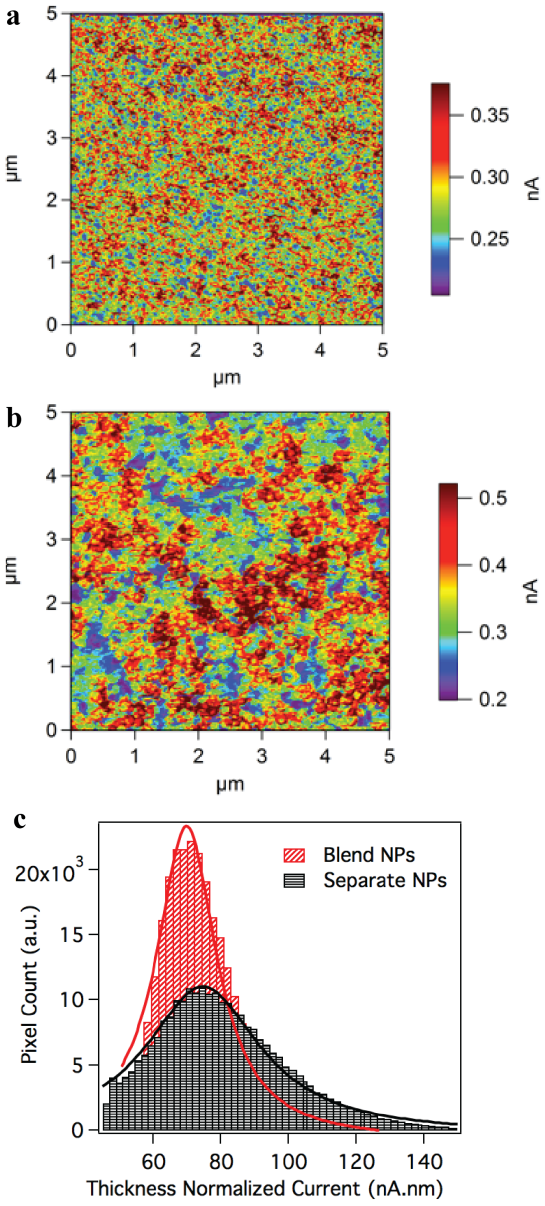

Figure 64: (a) cAFM image of P3HT and PCBM blend nanoparticles (1:1 by wt. ratio.) without a PCBM top layer. (b) cAFM image of separate P3HT nanoparticles and PCBM nanoparticles (1:1 by No. ratio) without a PCBM top layer. (c) Histogram plot depicting normalized pixel count with associated currents measured for blend nanoparticles, and separate nanoparticles.

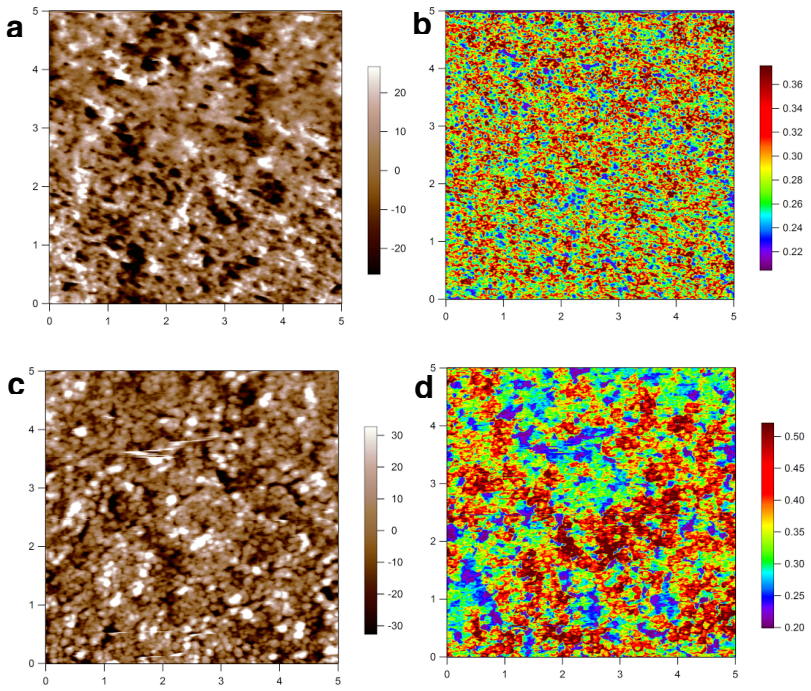

Figure 65: (a) Topological image and (b) c-AFM of P3HT and PCBM blend NPs film of 250 nm thickness. Bias voltage of 2 V was applied between ITO electrode and conducting AFM tip. (c) topological image and (d) c-AFM image of P3HT and PCBM separate NPs film of 225 nm thickness. 2V bias voltage was applied between ITO substrate and conducting AFM tip. xy scale bar is in μm, z-scale bar is in nm for topological image and nA for c-AFM image.

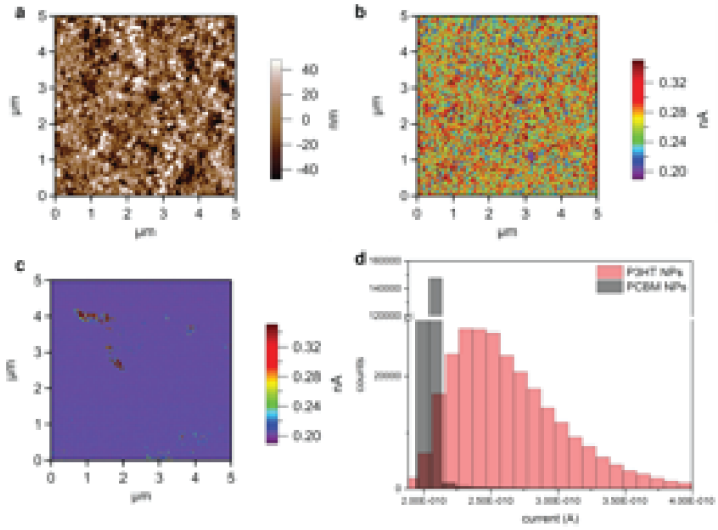

Figure 66: (a) Height AFM image of only P3HT nanoparticle film (b) corresponding c-AFM image of a P3HT only nanoparticle film in image a. (c) c-AFM image of a PCBM only nanoparticle film. 2V bias voltage was applied between ITO substrate and conducting AFM tip. (d) Current mapping histogram of the c-AFM images in a and b.

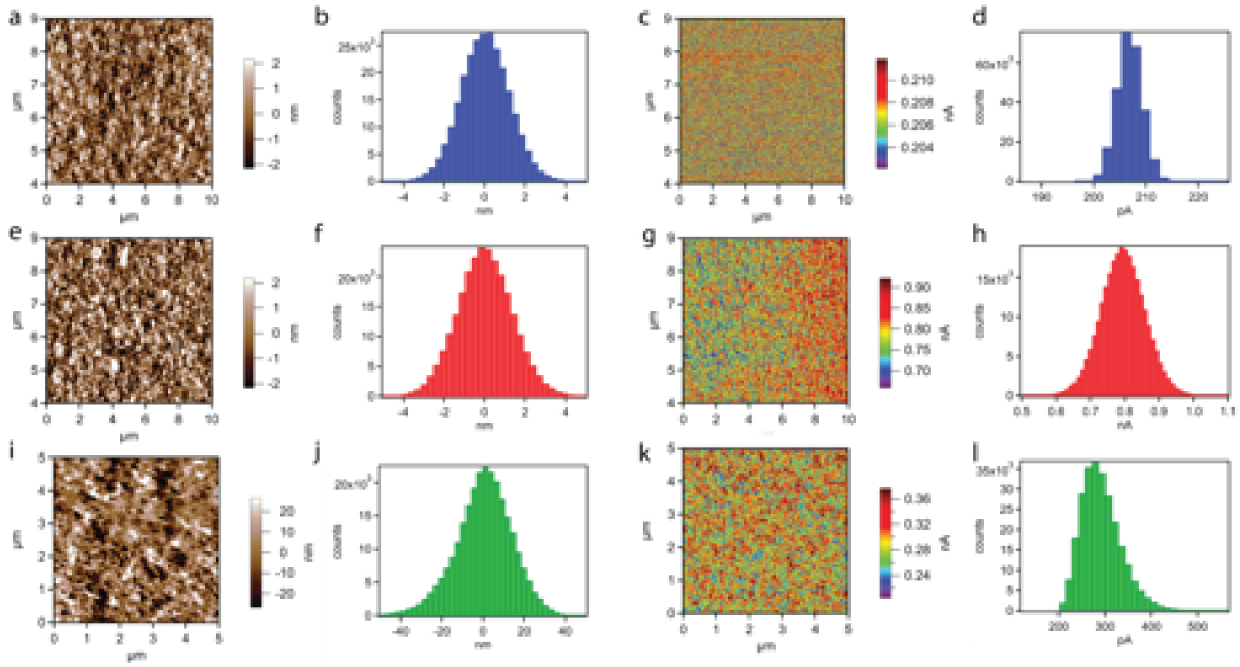

Figure 67: (a) AFM height image of a 1:1 P3HT to PCBM BHJ device spin coated from chlorobenzene and annealed. (b) Corresponding height count histogram of a. (c) cAFM image of the surface of the BHJ device described in a. (d) Corresponding current mapping histogram for the image in c. (e) AFM height image of a 1:1 P3HT to PCBM BHJ device spin coated from chlorobenzene, annealed and dipped in DCM to remove PCBM from the surface. (f) Corresponding height count histogram of e. (g) cAFM image of the surface of the DCM dipped BHJ device described in e. (h) Corresponding current mapping histogram for the image in g. (i) AFM height image of a 1:1 P3HT to PCBM blend nanoparticle device. (j) Corresponding height count histogram of i. (k) cAFM image of the surface of the DCM dipped BHJ device described in i. (l) Corresponding current mapping histogram for the image in k.

Histograms of the current mapping provide clues to the underlying device morphology; the number of counts is directly proportional to the number of available paths in the film for hole conduction, and the current is related to path length from a given particle to the ground electrode. The histogram analysis (Figure 64c) of Figure 64a-b show the morphological difference between the blend and separate nanoparticle films. They also show that the separate nanoparticle film has a slightly larger average normalized current than the blend nanoparticle film. The current distribution peak width is larger for separate nanoparticles than it is for blend nanoparticles, indicating a wider distribution of pathways including more short pathways having low resistance.

The cAFM results show that (a) there are conductive pathways for holes through the bulk of both blend and separate nanoparticle films, and (b) there are morphological differences between active layers derived from blend and from separate nanoparticles. A comparison of cAFM for BHJ and nanoparticle films is shown in Figure 67.

2.5.3 Time-of-Flight Mobility

Time of Flight (TOF) mobility measurements of P3HT, P3HT:PCBM blend, and P3HT and PCBM separate nanoparticle films were carried out to determine the effectiveness of their charge conduction pathways. P3HT nanoparticle films have a hole mobility ~2×10^{-4} $cm^2V^{-1}s^{-1}$, the same order of magnitude as seen for pristine P3HT films. A 1:1 mixture of separate P3HT nanoparticles and PCBM nanoparticles shows a hole mobility of ~8×10^{-5} $cm^2V^{-1}s^{-1}$. In both cases, the mobility has only a weak field dependence. Blend nanoparticles comprised of 1:1 weight ratio of P3HT to PCBM has a hole mobility comparable to a P3HT-only nanoparticle film at a low-field regime, but the mobility decreases with increasing field. This behavior is attributed to positional disorder in the Bässler model for charge transport in disordered solids.[413] The cAFM and TOF data indicate fundamental differences in the conductive pathways between blend and separate nanoparticle films.

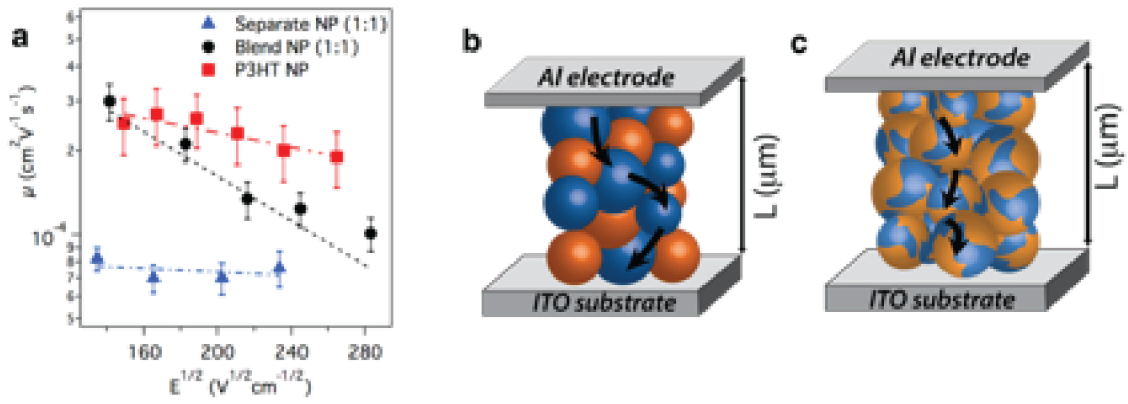

Figure 68: (a) Electric field dependent TOF mobility of P3HT nanoparticles, P3HT and PCBM blend nanoparticles and P3HT and PCBM separate nanoparticles film. (b) schematic diagram of P3HT and PCBM separate nanoparticles film showing hole conduction pathway. (c) schematic diagram of P3HT and PCBM blend nanoparticle film showing hole conduction pathway.

2.5.4 Photovoltaics

2.5.4.1 Device Fabrication

For fabricating OPV devices, aqueous dispersions of blend nanoparticles or separate nanoparticles were spin coated onto ITO substrates coated with PEDOT:PSS, which acts as a hole transporting layer. Except for electrode deposition, all the fabrication steps were done in ambient atmosphere. The PEDOT:PSS layer was treated with UV-O_3 for 3 min to increase surface hydrophilicity, which was found to be critical for achieving uniform films of nanoparticle assemblies as seen in optical microscopy images. AFM analysis of surface roughness of nanoparticle films with a typical thickness of ~240 nm decreased from ~70 nm to ~10 nm upon UV-O_3 treatment. Immediately after treatment, an aqueous dispersion of blend nanoparticles or separate nanoparticles was spin coated on top, under illumination by a commercial infrared (IR) lamp. After drying at room temperature in a vacuum chamber for 12 h, a thin layer of PCBM as

an electron transporting layer (ETL) was spin coated from an orthogonal solvent on top of the nanoparticle film, followed by vapor deposition of cathode (Ca/Al).

2.5.4.2 cAFM of Electron Transport Layer

Use of the ETL was critical for achieving a high fill factor. cAFM images of a thin film of P3HT:PCBM blend nanoparticles with a thin coating of PCBM on top is shown in Figure 69. The corresponding height image indicates that the PCBM top layer reduces surface roughness of the nanoparticle film, and Figure 69 indicates the PCBM top layer blocks many pathways for holes to reach the top electrode thus reducing leakage current. We found similar results for a thin film of co-assembled separate nanoparticles with a PCBM top layer.

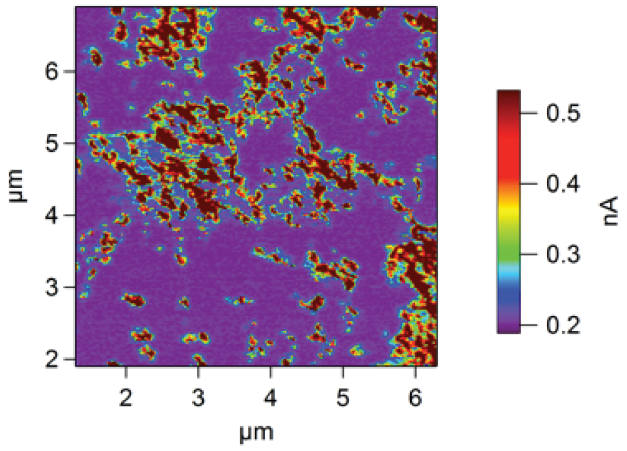

Figure 69: cAFM image of P3HT:PCBM blend nanoparticle-OPV devices with PCBM buffer layer.

2.5.4.3 Photovoltaic Performance

The highest efficiency was achieved when the nanoparticle dispersion solvent was changed to 20% ethanol by volume in water. These dispersions led to the highest device performance for both blend (2.15%) and separate (1.84%) nanoparticles; the current-voltage device performance is shown in Figure 70a.

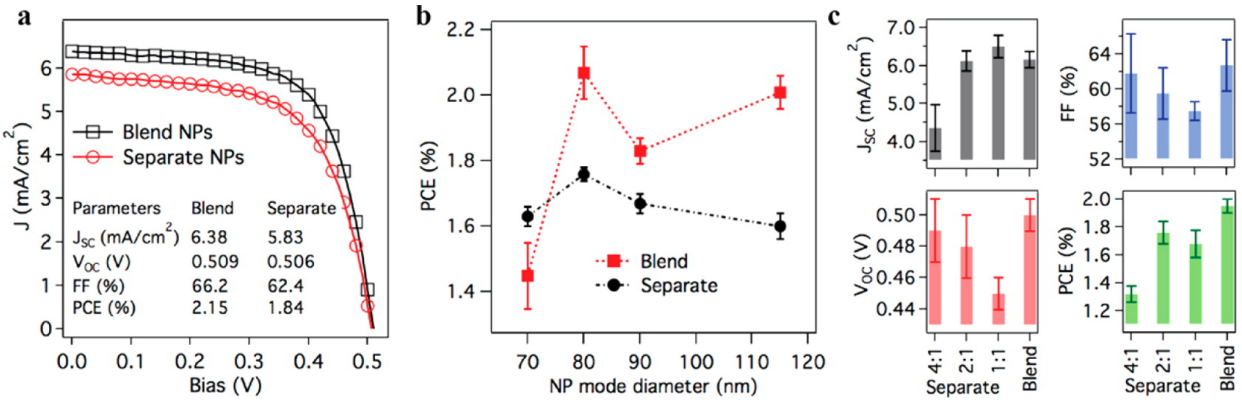

Figure 70: (a) nanoparticle OPV device performance of P3HT:PCBM blend (1:1 by wt. ratio) nanoparticles and P3HT and PCBM separate (2:1 by No. ratio) nanoparticles. (b) P3HT and PCBM separate (1:1 by No. ratio) nanoparticles size dependent PCE, and P3HT:PCBM blend (1:1 by wt. ratio) nanoparticles size dependent PCE. (c) Device performance of P3HT and PCBM blend and separate nanoparticles devices at different ratio of P3HT nanoparticle to PCBM nanoparticle. All particles are ~ 80 nm (mode diameter).

2.5.5 Tunable Morphologies Through Nanoparticle Assemblies

The power of using sphere packing for OPV applications is the ability to independently tune the domain size while keeping the morphology constant and vice versa, which thus far has been elusive. To probe the effect of domain size on OPV performance, devices from separate and blend nanoparticles were prepared using nominal particle mode diameters of 115 nm, 90 nm, 80 nm, and 70 nm. The concentration of P3HT to PCBM was held constant (1:1 weight ratio) for the devices prepared with either blend or separate nanoparticles. The expectation for blend nanoparticles is that the domain size for each component is similar for all particle sizes; therefore particle size should have a minimal impact on efficiency. The expectation for separate nanoparticles is that the efficiency will increase with decreasing particle size until the size approaches the exciton diffusion length. Four sets of devices were prepared using each particle size, keeping the sizes of P3HT and PCBM separate nanoparticles the same within each set. The impact of particle size on power

conversion efficiency (PCE) for blend and separate nanoparticles is shown in Figure 70b. Contrary to expectation, both blend and separate nanoparticle devices showed an optimal domain size at 80 nm. This supports the increasing belief that optimal domain size can be larger than 10 nm.[414]

To probe the impact of morphology with constant domain size, OPV devices were fabricated by changing the ratio of the number of p-type (P3HT) domains to the number of n-type (PCBM) domains (Figure 71). Upon increasing the ratio of P3HT nanoparticles to PCBM nanoparticles from 1:1 to 4:1 the PCE drops from 1.78% to 1.38%, as seen in Figure 70c. The most efficient ratio of P3HT to PCBM nanoparticles was 2:1 with a maximum efficiency of 1.84%. By controlling the relative ratio of separate nanoparticles, we can control the morphology of the active layer. The cAFM images of 1:1 and 2:1 P3HT nanoparticles to PCBM nanoparticles (Figure 72a-b respectively) indicates that the morphologies are different. As the ratio of P3HT nanoparticles to PCBM nanoparticles increases (from 1:1 to 2:1 to 1:0, Figure 72a-c), the number of hole conducting pathways also increases leading to increased current. This increase in current is clearly seen in in Figure 72d. This method provides a general approach that now enables the independent optimization of the domain size and morphology for enhanced device performance.

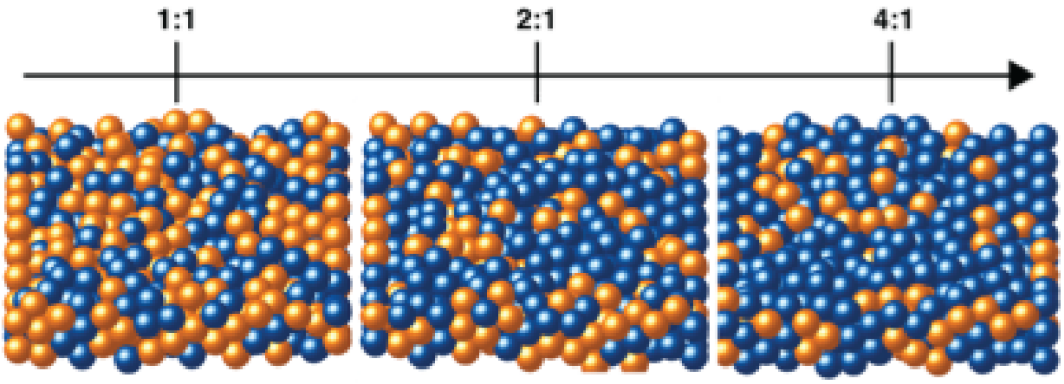

Figure 71: Simulated random packing of two types of particles with 1:1, 2:1, and 4:1 number ratio of blue particles to orange particles.

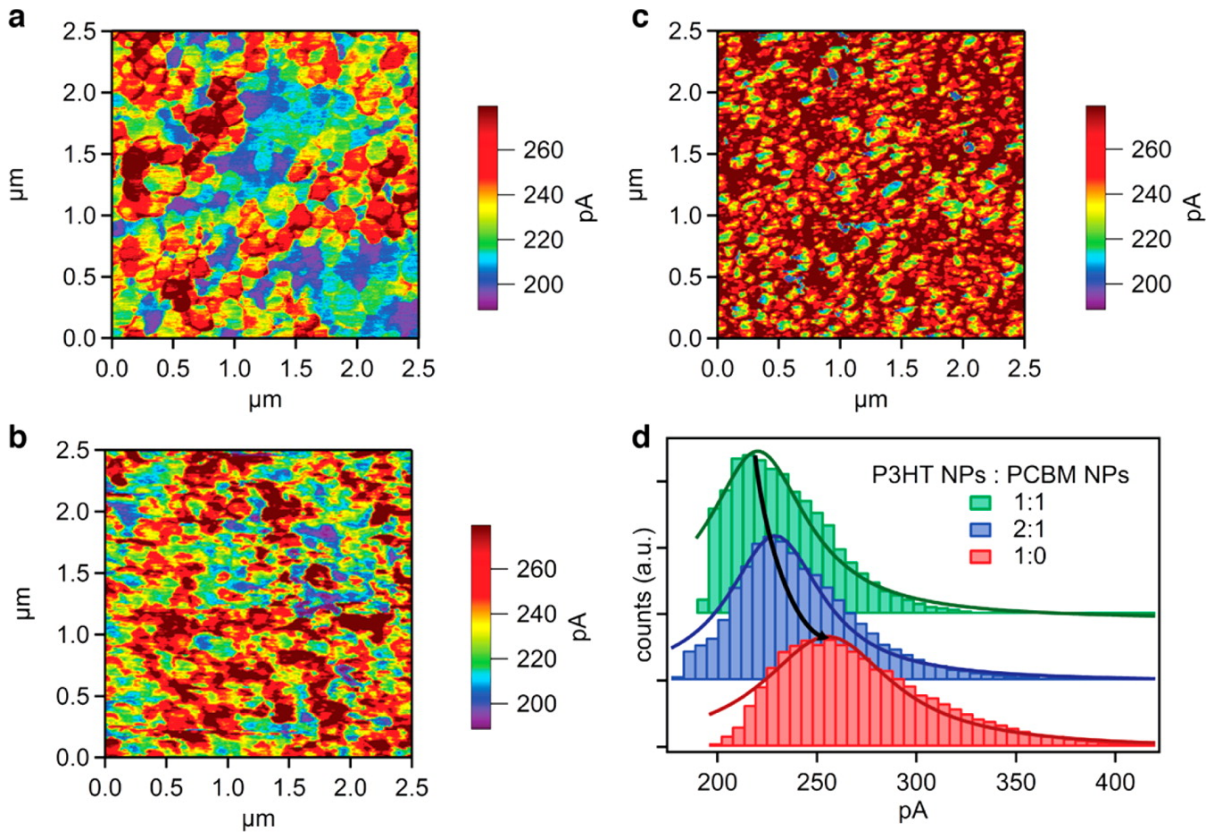

Figure 72: (a) cAFM image of a 1:1 number ratio of P3HT nanoparticles to PCBM nanoparticles without a PCBM top layer. (b) cAFM image of a 2:1 number ratio of P3HT nanoparticles to PCBM nanoparticles without a PCBM top layer. (c) cAFM image of only P3HT nanoparticles (1:0 number ratio) without a PCBM top layer. (d) Histogram plot depicting the pixel count with associated currents measured for the cAFM images in a, b, and c.

We have used the concept of sphere packing to control the hierarchical active layer morphology of OPV cells by pre-formed each active layer component as nanospheres and fabricating uniform nanosphere assemblies. In contrast to conventional methods of controlling active layer morphologies, this approach affords the ability to (a) pre-tailor the semiconductor domains with the required internal packing and size; (b) obtain stable co-continuous structures that are controlled from the nanoscale to mesoscale, through self-assembly into equilibrium or kinetically-trapped morphologies in a single step; (c) use multiple hole conductors to broaden the absorption spectrum; (d) systematically elucidate the optimal structure for an efficient OPVs and

(e) use environmentally benign solvents such as water for device fabrication. Controlling each active layer component at multiple length scales using sphere packing not only offers a method for developing next generation OPVs, but also opens a revolutionary pathway for the systematic study and tuning of functional materials while exercising control of the component assembly at multiple length scales

2.6 Tunable Concurrent Electronic and Ionic Transport in Binary Polymer Nanoparticle Assemblies

This chapter[†††] details a route to binary polymer morphologies with co-continuous pathways for simultaneous electronic and ionic transport by the assembly of poly(3-hexylthiphene) and lithium ion-doped poly(vinylpyridine) nanoparticles. By using AC impedance spectroscopy and DC steady-state conductivity measurements, we demonstrate that binary nanoparticle assemblies provide concurrent electronic and ionic conduction. By changing the percentage of one type of particle to the other, we exhibit excellent tunability of both the electronic and ionic conductivities. The simplicity of fabrication combined with the versatility in obtainable properties illustrate the power of using nanoparticle assemblies as a means to realize functional polymer mesoscale morphologies.

Co-continuous binary polymer morphologies with percolation pathways that pervade in three dimensions for two types of charge carriers is desired for many applications such as photovoltaics,[116,347,415] and electrochemical energy storage, *i.e.* batteries.[264,416] Co-continuous morphologies are observed as metastable phases during the spinodal decomposition in polymer blends.[9] Therefore, various strategies such as thermal quenching[10] and jamming of particles at the interface[11,12] have been studied to kinetically trap these morphologies in polymer blends. Co-continuous morphologies can also be realized in thin films through the self-assembly of diblock copolymers[14,417] but requires the chemical synthesis of the polymers, and the well-known phase diagram is valid only for random coil-coil diblock copolymers.[14]

[†††] This chapter was adapted, with permission, from Renna, Lawrence A., Julia D. Lenef, Monojit Bag, and D. Venkataraman. "Tunable Concurrent Electronic and Ionic Conductivity in Binary Polymer Nanoparticle Assemblies". *Under Review* (2016). I would like to acknowledge Julia D. Lenef for FTIR, and Nanoparticle Tracking Analysis.

Inorganic solid state materials with conducting pathways for ionic and electronic transport are well-established.[30,418] Yet, achieving such concurrent percolation pathways in polymer films have not been straightforward. Some examples include imbibing ionic fluids in polymer films,[419] incorporating ion conducting side chains on conjugated polymers,[420-422] and ion-doped[423-426]/oxidized[427] conjugated polymers. However, these methods do not afford separate and systematic control over the morphology and properties of the electronic and ionic conducting phases. More recently, Balsara and co-workers have utilized the lamellar and nanowire morphologies of a diblock copolymers, *i.e.* poly(3-hexylthiophene)-*b*-poly(ethylene oxide) (P3HT-*b*-PEO), to realize concurrent electronic and lithium ion conduction.[264,416]

We have been pursuing the strategy of using binary polymer nanoparticle assemblies to create hierarchical mesoscale structures with control of molecular assembly over multiple length scales.[116,258,334] In this strategy, polymer components are first assembled as nanoparticles that are then used as building blocks for further assembly to create mesoscale structures. Nanoparticle assemblies provides a unique and modular pathway to generate complex structures and co-assemblies under non-equilibrium processing conditions with macroscopic homogeneity and compositional flexibility. In earlier work, we have shown tunable percolation in binary nanoparticles assemblies composed of a semiconductor nanoparticle and an insulating nanoparticles.[334] We have also demonstrated that co-continuous percolating pathways can be obtained for binary nanoparticles assemblies composed of electron transporting nanoparticles and hole transporting nanoparticles.[116] In this Letter, we demonstrate the fabrication of binary nanoparticle assemblies composed of electronically conducting and ionically conducting nanoparticles (see Figure 73a). We also show that the electronic conduction and ionic conduction can be tuned by mixing the nanoparticles at various ratios.

2.6.1 Nanoparticle Synthesis and Device Fabrication

Since we have already established the use of P3HT (Rieke Metals, $\bar{M}_W$ = 36 kDa, regioregularity = 96%, and polydispersity Đ = 2.3) nanoparticles for electronic conduction,[116,334] we sought to fabricate polymer nanoparticles that could conduct Li ions. We explored this by using four different poly(vinylpyridine)-based (PVP) polymers, which has been shown to be a good solid-state Li ion conductor.[428-431] Copolymers containing styrene units were used to decrease the solubility in water and increase the solubility of the polymer in chloroform for the synthesis of stable dispersions. We observed that polymer nanoparticle dispersions of poly(4-vinylpyridine) were not as stable as nanoparticles of copolymers containing styrene units. We used the following commercially available polymers, poly(2-vinylpyridine-*co*-styrene) with 30% styrene content [P($2VP_{0.7}$-*co*-$S_{0.3}$), Scientific Polymer Products, $\bar{M}_W$ = 200 kDa], poly(4-vinylpyridine-*co*-styrene), with 10% and 50% styrene content [P($4VP_{0.9}$-*co*-$S_{0.1}$), $\bar{M}_v$ = 140,000 kDa and P($4VP_{0.5}$-*co*-$S_{0.5}$), $\bar{M}_W$ = 400 kDa, Scientific Polymer Products], and poly(2-vinylpyridine-*b*-styrene), 50% styrene content [P($4VP_{0.5}$-*b*-$S_{0.5}$), Polymer Source, $\bar{M}_W$ = 8.2 kDa-b-8.3 kDa]. All polymer structures are shown in Figure 73b.

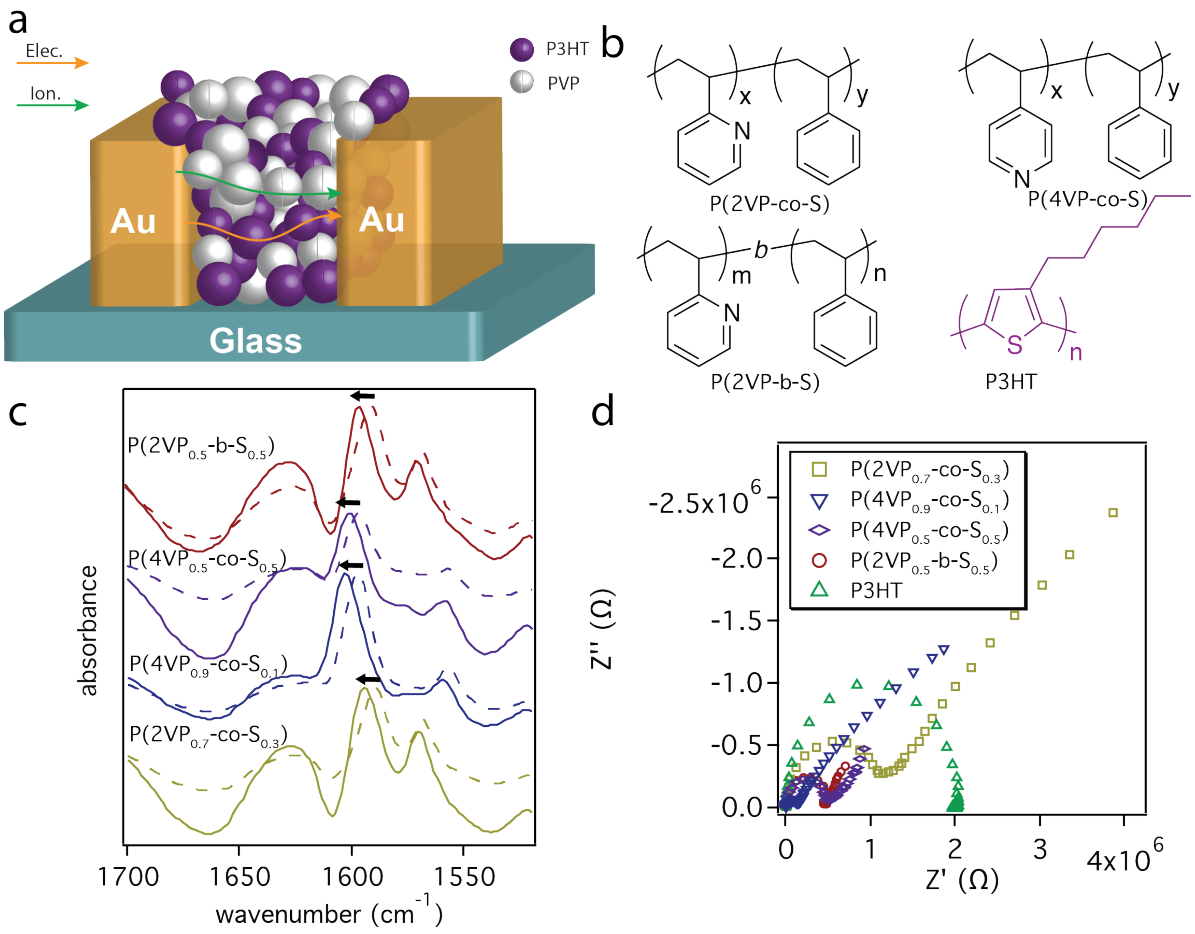

Figure 73: a) Scheme depicting the co-continuous electronic and ionic transport in binary assemblies of P3HT and PVP-based polymer nanoparticles. This scheme also represents the device configuration used in this study for electronic measurements, not drawn to scale. b) Chemical structure of polymers used in this study; from top left to right, P(2VP-*co*-S), P(4VP-*co*-S), from bottom left to right, P(2VP-*b*-S), and P3HT. c) FTIR of Li ion doped (solid line) and undoped (dashed line) PVP-based nanoparticles. The shift in the pyridine ring stretching mode at ~1600 cm^{-1} due to Li ion coordination is indicated with an arrow. d) Nyquist plots of unary polymer nanoparticle assemblies in Au|nanoparticle|Au architecture.

Polymer nanoparticles were fabricated via a previously reported method of post-polymerization miniemulsion.[116,334] Briefly, a 0.5 mL of a 30 mg/mL solution of polymer in chloroform was added to 3 mL of 10 mM sodium dodecyl sulfate (SDS) in NanoPure water. Then a miniemulsion was formed by sonication for 2 min at 20% maximum amplitude using a probe-tip ultrasonicator. Next, chloroform is removed by stirring in an open vessel at 75 °C for

40 min. To dope PVP-based polymers with Li ions, 2.5 mg/mL (50% wt. to polymer) of lithium trifluoromethane sulfonate (LiOTf) was included in the aqueous solution prior to sonication. Particle size was determined using Nanoparticle Tracking Analysis (NTA, see Figure 74 and Table 8 for results). Particle diameters were 73 nm – 128 nm. Fourier Transform infrared spectroscopy (ATR-FTIR) showed a shift in the pyridine ring stretching mode at ~1600 cm^{-1}, consistent with the coordination of pyridine with Li ions,[432] see Figure 73c. Devices for electronic and ionic transport measurements (see Figure 73a) of solid nanoparticle assemblies were fabricated by repeated drop-casting of nanoparticle dispersions on to heated glass substrates, which were maintained at 75 °C, with thermally evaporated gold electrodes, (100 nm high) separated by a 165 μm gap. Thus, all electronic measurements made on polymer nanoparticle assemblies throughout this study were performed across this 165 μm gap between gold electrodes.

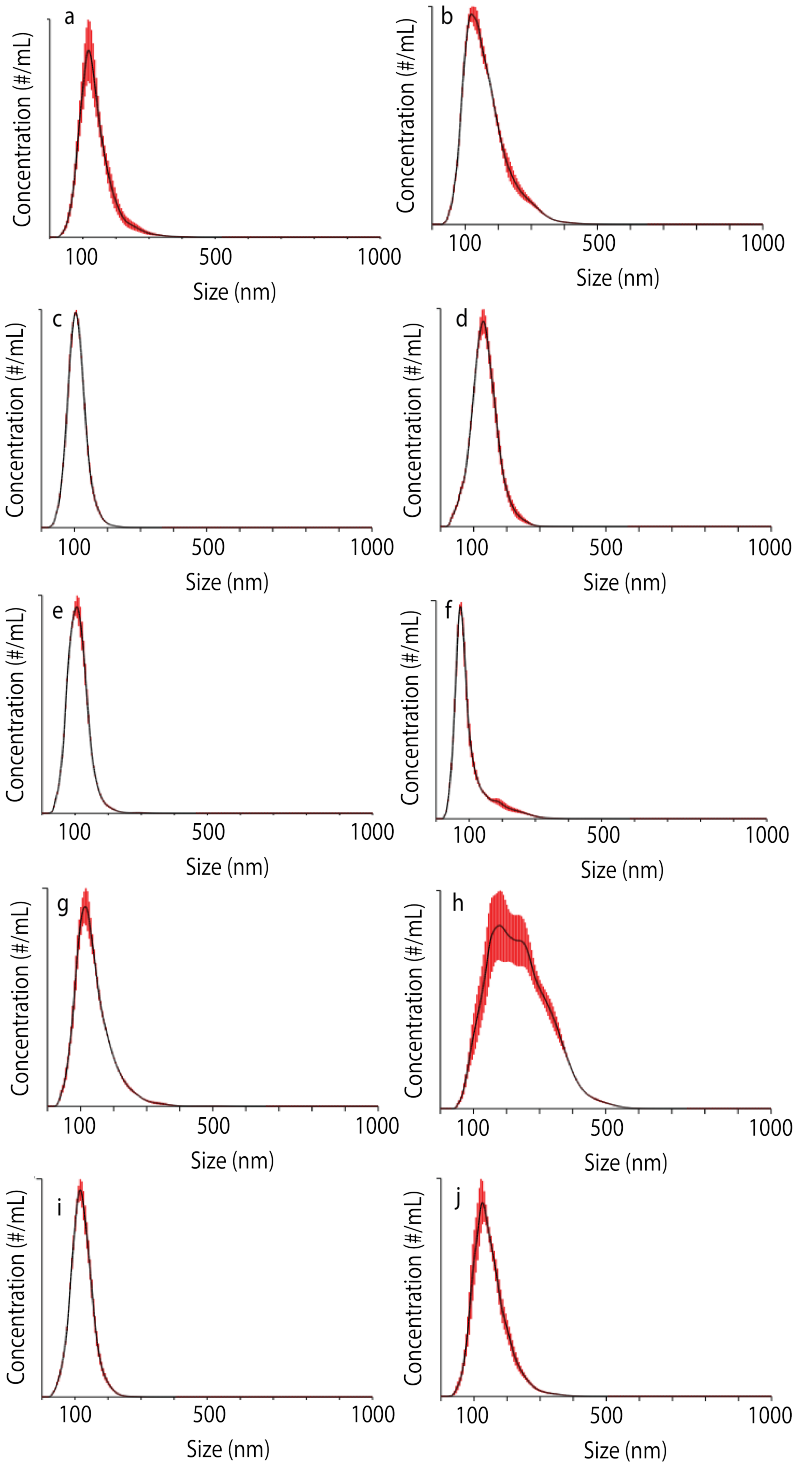

Figure 74: Average concentration vs particle size from NTA of a) P(2VP$_{0.7}$-*co*-S$_{0.3}$), b) P(2VP$_{0.7}$-*co*-S$_{0.3}$) + LiOTf, c) P(4VP$_{0.5}$-*co*-S$_{0.5}$), d) P(4VP$_{0.5}$-*co*-S$_{0.5}$) + LiOTf, e) P(4VP$_{0.9}$-*co*-S$_{0.1}$), f) P(4VP$_{0.9}$-*co*-S$_{0.1}$) + LiOTf, g) P(2VP$_{0.5}$-*b*-S$_{0.5}$), h) P(2VP$_{0.5}$-*b*-S$_{0.5}$)+ LiOTf, i) P3HT, and j) 50% P3HT + 50% P(4VP$_{0.9}$-*co*-S$_{0.1}$) + LiOTf. Red bars represent one standard deviation from three measurements. Summarized in Table 8.

Table 8: Average mode diameter of nanoparticles from NTA.

Nanoparticle	Avg. Mode Diameter
P(2VP$_{0.7}$-*co*-S$_{0.3}$)	116 nm ± 1.7 nm
P(2VP$_{0.7}$-*co*-S$_{0.3}$) + LiOTf	121 nm ± 4.3 nm
P(4VP$_{0.5}$-*co*-S$_{0.5}$)	103 nm ± 0.3 nm
P(4VP$_{0.5}$-*co*-S$_{0.5}$)+ LiOTf	128 nm ± 0.7 nm
P(4VP$_{0.9}$-*co*-S$_{0.1}$)	103 nm ± 2.9 nm
P(4VP$_{0.9}$-*co*-S$_{0.1}$) + LiOTf	73 nm ± 0.7 nm
P(2VP$_{0.5}$-*b*-S$_{0.5}$)	113 nm ± 2.2 nm
P(2VP$_{0.5}$-*b*-S$_{0.5}$) + LiOTf	199 nm ± 31.3 nm
P3HT	115 nm ± 1.7 nm
50% P3HT + 50% P(4VP$_{0.9}$-*co*-S$_{0.1}$) + LiOTf	126 nm ± 4.6 nm

2.6.2 Probing Lithium Ion Conduction in Nanoparticles by EIS

We next turned to AC electrochemical impedance spectroscopy (EIS) to probe the Li ion conduction in unary polymer nanoparticle assemblies, and the results are shown as Nyquist plots in Figure 73d. Impedance was measured from 1×10^6 Hz to 0.1 Hz (V_{AC} = 1.0 V, V_{DC} = 0 V) at ambient conditions. All PVP-based polymer nanoparticles displayed Nyquist plots with an initial high frequency semicircle, which is attributed to conduction of Li ions, followed by a low frequency 'linear' part of the spectra due the blocking nature of the gold electrodes for Li ions. On the other hand, the Nyquist plot for P3HT nanoparticles displayed a single semicircle, indicative of electronic transport. For unary nanoparticle assemblies, the intersection of the

semicircle with the real axis (*x*-axis) can be taken as the resistance to ionic transport for PVP-based polymers, or the resistance to electronic transport for P3HT nanoparticles. We find that P(2VP$_{0.7}$-*co*-S$_{0.3}$) had the highest ionic resistance of 1.17 MΩ, P(4VP$_{0.5}$-*b*-S$_{0.5}$) had a resistance of 0.50 MΩ, P(4VP$_{0.5}$-*co*-S$_{0.5}$) had a resistance of 0.49 MΩ, and P(4VP$_{0.9}$-*co*-S$_{0.1}$) had the lowest ionic resistance of 0.15 MΩ. For comparison, sodium polystyrene sulfonate has an ionic resistance of 0.42 MΩ.[‡‡‡][433] We concluded that polymer nanoparticles with 4-vinylpyridine groups have a lower ionic resistance than polymer nanoparticles with 2-vinylpyridine groups. We also found that increasing the ratio of pyridine to styrene units decreased the ionic resistance. Unary P3HT nanoparticle assemblies had an electronic resistance of 2.04 MΩ. Based on these results we used P3HT and P(4VP$_{0.9}$-*co*-S$_{0.1}$) nanoparticles to fabricate binary assemblies for concurrent electronic and ionic conduction.

2.6.3 Binary Assemblies: Steady-State Current Measurements

To realize co-continuous electronic and ionic conduction pathways we mixed P3HT nanoparticles with P(4VP$_{0.9}$-co-S$_{0.1}$) nanoparticles and fabricated films by drop-casting as before. We fabricated binary nanoparticle assemblies with 80%, 75%, 66%, 50%, 33%, and 25% P3HT to P(4VP$_{0.9}$-*co*-S$_{0.1}$), by weight percent of polymer. We first determined the electronic resistance of these mixed assemblies by steady-state DC measurements.[416] A small DC bias (E) was applied, and the current was measured for ~180 s, collecting 2,500 data points. An applied bias of E = -50 mV bias was applied, followed by -30 mV, -20 mV, 20 mV, 30 mV, and finally 50 mV. When only P3HT nanoparticles were used, see Figure 75a, steady-state current was obtained within 1 sec. For mixed conductor assemblies, the steady-state current was obtained

‡‡‡ Data extracted from Figure 5b in G. Casalbore-Miceli, M. Yang, N. Camaioni, C.-M. Mari, Y. Li, H. Sun, and M. Ling, *Solid State Ion*. **131**, 311 (2000) using WebPlotDigitizer.

after ~ 100 sec. The initial current is high due to combined electronic and ionic current, however, over time, the Li ions stop moving and the steady-state electronic current is measured. Representative current vs time plots for binary assemblies of P3HT and P(4VP$_{0.9}$-*co*-S$_{0.1}$) nanoparticles are shown in Figure 75b-d. We calculated the steady-state current by taking the average current in the last ~ 14 s, 200 data points. An Ohm's Law fit of E vs I gives the electronic resistance of the assembly (see Figure 75e); electronic resistances ranged from ~ 2 MΩ to ~ 260 MΩ. In general, we observe an increase in conductance (G) with an increase in the percentage of P3HT to P(4VP$_{0.9}$-*co*-S$_{0.1}$) nanoparticles, see Figure 75f. This finding is consistent with our previous results on tunable electronic transport in binary conducting/insulating polymer nanoparticle assemblies.[334]

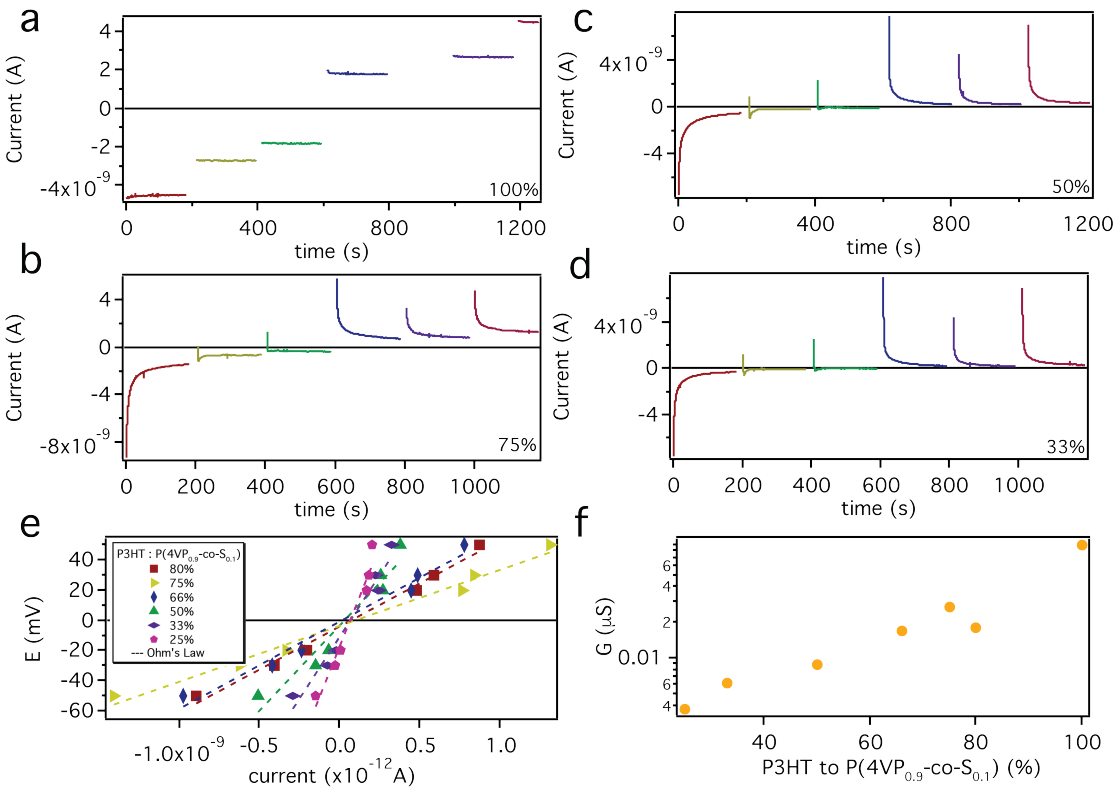

Figure 75: Current vs. time, in Au|nanoparticle|Au architecture, for a)100%, b) 75%, c) 50%, and d) 33% P3HT to P(4VP$_{0.9}$-*co*-S$_{0.1}$) nanoparticles. e) Plot of E vs I and Ohm's law fit of steady-state current values. F) Plot of electronic G vs percentage of P3HT to P(4VP$_{0.9}$-*co*-S$_{0.1}$) nanoparticles.

2.6.4 Binary Assemblies: EIS Measurements

We next did EIS of the binary nanoparticle assemblies, shown in Figure 76a-f. The Nyquist plots (black markers) show a semicircle followed by a linear component, followed by more interfacial capacitance. The resistance associated with the semicircle decreases with increasing humidity and temperature (see Figure 78and Figure 79), which indicates that resistance is predominantly from ionic conduction. From the steady-state electronic current measurements, we measured large resistances in the mixed assemblies compared to the ionic resistance. To extract ionic resistance, we used an equivalent circuit modeling of the data using the circuit shown in Figure 76g. The circuit model contains a geometric capacitance element (C_{μ}), in parallel with an electronic resistance ($R_{elec.}$), also in parallel with a serial ionic resistance ($R_{ion.}$) and Warburg ion diffusion element (W).

The parallel circuit was used to model the semicircle and the initial linear part of the Nyquist plots, because attempts at modeling very low frequencies reveals it is not simple Debye layer capacitance. However, the low frequency data is not needed to calculate the ion transport resistance in these systems. Modeling was done in an iterative fashion, and $R_{elec.}$ was fixed to the value obtained from steady-state measurements. The results of the modeling are shown in Table 9, and as solid lines overlaid on impedance spectra in Figure 76a-f. Similar to the electronic conductance, the ionic conductance (G) increased as the percentage of P($4VP_{0.9}$-*co*-$S_{0.1}$) nanoparticles to P3HT nanoparticles increased, as seen in Figure 76h. The dependence of ionic conductance on the percentage of P($4VP_{0.9}$-*co*-$S_{0.1}$) nanoparticles confirms that ionic transport indeed moves through the PVP-based nanoparticles, and not within the voids of the nanoparticle assembly. This result shows that the ionic transport can be tuned by changing the relative percentages of the two types of nanoparticles in the assembly.

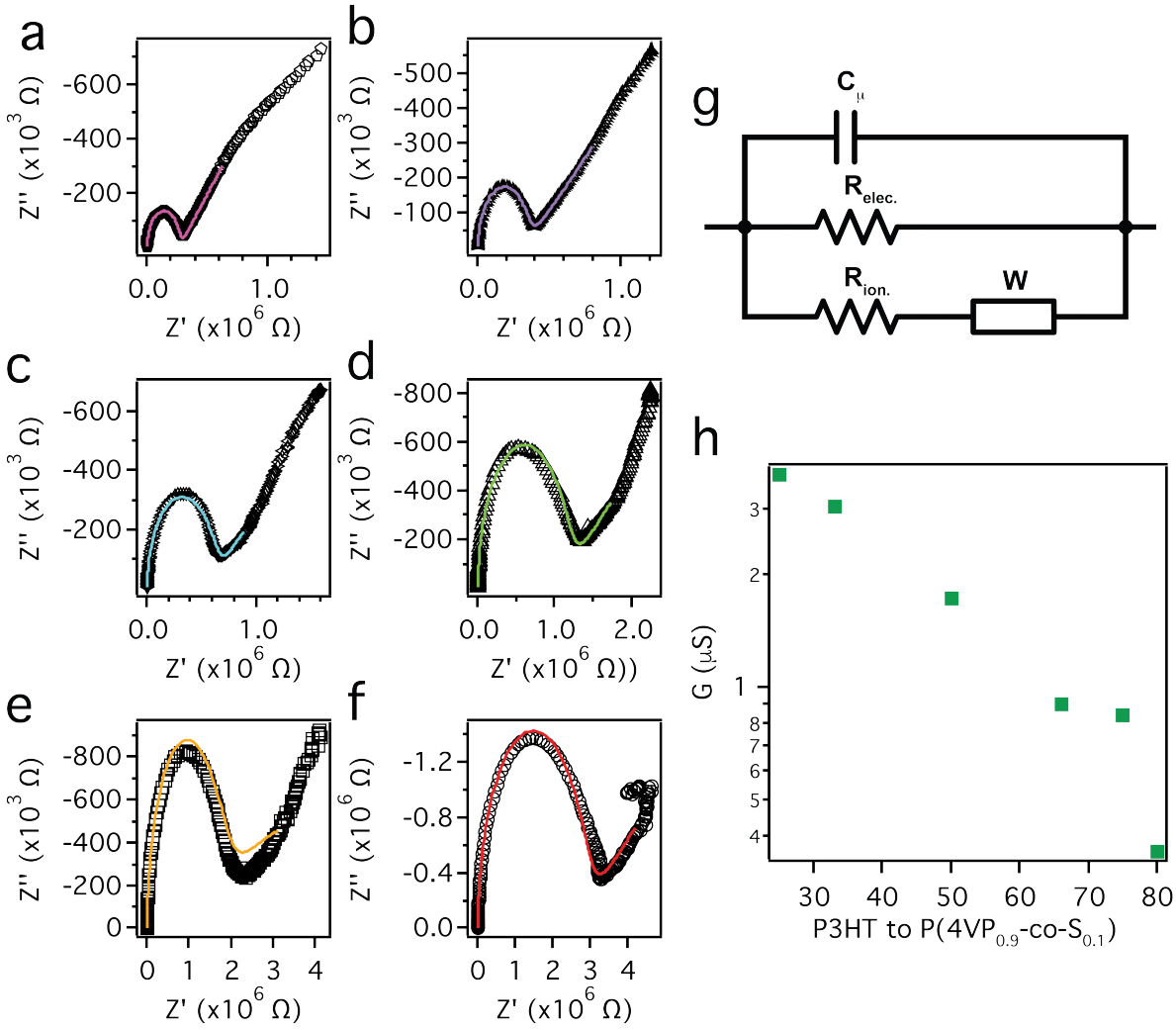

Figure 76: EIS of Au|nanoparticle|Au architecture, data is presented in Nyquist plots (data in black markers) of a) 25%, b) 33%, c) 50%, d) 66%, e) 75%, and f) 80% P3HT to P(4VP$_{0.9}$-*co*-S$_{0.1}$) nanoparticles, with corresponding equivalent circuit model fits in solid lines. g) Equivalent circuit model containing parallel electronic and ionic conduction pathways used in this study. h) Plot of ionic G vs percentage of P3HT to P(4VP$_{0.9}$-*co*-S$_{0.1}$) nanoparticles.

Table 9: Results from equivalent circuit modeling of EIS measurements of binary mixed P3HT and P(4VP$_{0.9}$-*co*-S$_{0.1}$) nanoparticle assemblies. *Indicates the resistance was determined from steady-state current measurements, and fixed during the modeling procedure. The Warburg model of interfacial ionic diffusion is calculated by the equation: $W = A_W \frac{\tanh(j\omega T_W)^P}{(j\omega T_W)^P}$ where A_W is the Warburg impedance, j is $\sqrt{-1}$, T_W is the Warburg time constant, and P is the power, which is equivalent to P = 0.5 for perfect 1-D diffusion.

P3HT: P(4VP$_{0.9}$-*co*-S$_{0.1}$)	**C_μ**	**$R_{elec.}$***	**$R_{ion.}$**	**A_W**	**T_W**	**P**	**χ^2**
80%	26.6 pF	57.05 MΩ	2.78 MΩ	7.4 MΩ	10.36 s	0.28	0.004
75%	25.9 pF	37.1 MΩ	1.19 MΩ	5.2 MΩ	6.69 s	0.17	0.006
66%	25.1 pF	57.7 MΩ	1.11 MΩ	5.37 MΩ	6.89 s	0.33	0.002
50%	25.3 pF	113.0 MΩ	0.58 MΩ	5.25 MΩ	6.90 s	0.36	0.002
33%	25.9 pF	162.2 MΩ	0.33 MΩ	3.02 MΩ	4.32 s	0.35	0.001
25%	26.2 pF	267.6 MΩ	0.27 MΩ	3.5 MΩ	3.44 s	0.45	0.004

2.6.5 Binary Assemblies: Concurrent Conductivity

We calculated electronic and ionic conductivities ($\sigma_{elec.}$ and $\sigma_{ion.}$) of the mixed conductor binary nanoparticle assemblies from EIS and steady-state DC resistances. We measured the film thickness by profilometry, and the film width by optical microscopy, the channel length was taken as the 165 μm gap between the gold electrodes. The conductivities, $\sigma_{elec.}$ and σ_{ion} are plotted in Figure 77a. For mixed conductor binary nanoparticle assemblies we found $\sigma_{elec.}$ = 6.2 × 10^{-7} S/cm to 1.0 × 10^{-6} S/cm, and $\sigma_{ion.}$ = 2.1 × 10^{-5} S/cm to 6.1 × 10^{-4} S/cm by varying the nanoparticle ratios. These values, obtained at ambient temperatures, are comparable to those obtained at 90 °C in the diblock copolymer work.[264,416] We also found that the ratio, $\sigma_{elec.}/\sigma_{ion}$ vs percentage of P3HT to P(4VP$_{0.9}$-*co*-S$_{0.1}$) nanoparticles follows a predictable trend,

which was not observed in diblock copolymer work, see Figure 77b. Thus, nanoparticle assemblies can be used to fabricate materials with predictable electronic and ionic transport properties.

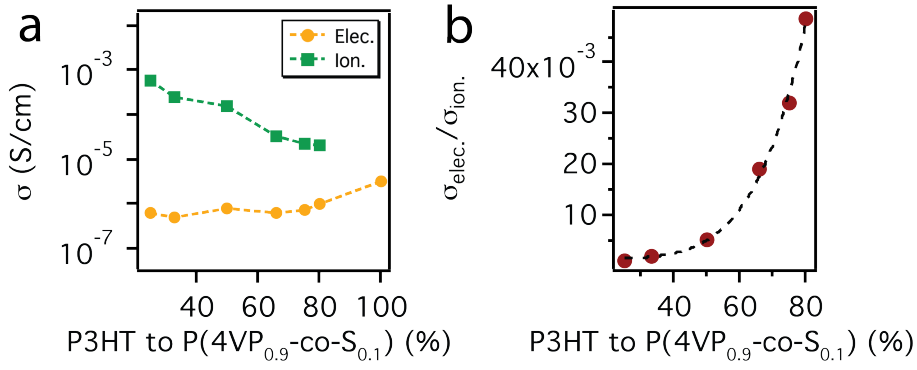

Figure 77: a) Plot of $\sigma_{elec.}$ and $\sigma_{ion.}$ vs percentage of P3HT to P(4VP$_{0.9}$-*co*-S$_{0.1}$) nanoparticles, dashed lines are guides for the eye. b) Plot of $\sigma_{elec.}/\sigma_{ion.}$ vs percentage of P3HT to P(4VP$_{0.9}$-*co*-S$_{0.1}$) nanoparticles, the dashed line is a power-law fit to the data.

2.6.6 Binary Assemblies: Humidity and Temperature Dependent EIS

Lastly, we performed humidity and temperature dependent EIS studies on a binary assembly of 80% P3HT to P(4VP$_{0.9}$-*co*-S$_{0.1}$) nanoparticles (Figure 78 and Figure 79 respectively), the data is summarized in Table 10. Humidity dependent measurements were made at 60 °C, by varying the relative humidity from RH = 35% to 95% in steps of 10%. The Nyquist plots can be seen in Figure 78. We assume again, that the resistance of the semicircle arises predominantly from ionic conduction. As the humidity was increased from RH = 35% to 95% the conductivity increased from $\sigma_{ion.} = 5.33 \times 10^{-5}$ S/cm to 6.42×10^{-2} S/cm. Temperature dependent EIS measurements were made at 40 °C, 50 °C, 60 °C, and 80 °C at RH = 60%, and are shown in Figure 79a,b. As the temperature is increased, the ionic conductivity increased from $\sigma_{ion.} = 3.85 \times 10^{-6}$ S/cm to 7.74×10^{-4} S/cm. An Arrhenius analysis (see Figure 79c) yields an activation energy $E_a \approx 0.1$ eV, assuming the resistance observed is predominantly from ionic transport. This value is

comparable to E_a measured for ionic conduction in P4VP complexed with Li salts of E_a = 0.10 eV to 0.16 eV.[428] In comparison, P3HT-*b*-PEO polymers were shown to have an E_a = 0.03 eV to 0.07 eV for Li ion transport.[416]

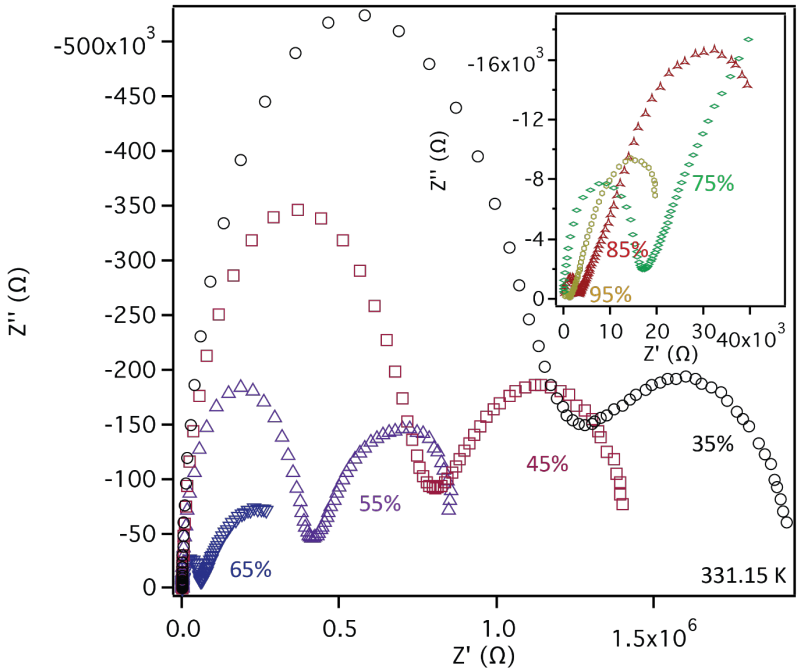

Figure 78: Humidity dependent EIS for 80% P3HT to P(4VP$_{0.9}$-*co*-S$_{0.1}$) nanoparticles.

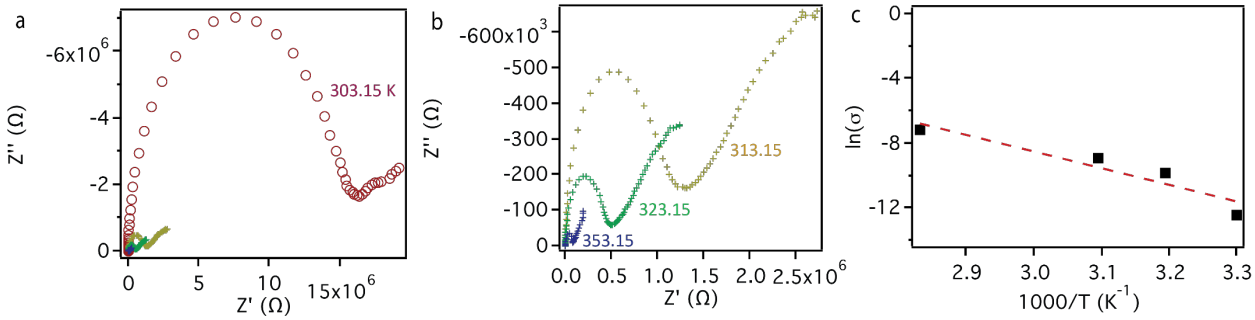

Figure 79: (a,b) Temperature dependent EIS for 80% P3HT to P(4VP$_{0.9}$-*co*-S$_{0.1}$) nanoparticles. (c) Arrhenius plot of ln(conductivity) vs 1000/T, with linear fit (red dashed line). Activation energy extracted from fit is E_a = 0.1 eV.

Table 10: Humidity and temperature dependent conductivity for an assembly of 80% P3HT to P(4VP$_{0.9}$-*co*-S$_{0.1}$) nanoparticles.

RH (%)	**T** (°C)	$\sigma_{ion.}$ (S/cm)
35	**60**	5.33×10^{-5}
45	**60**	8.06×10^{-5}
55	**60**	1.53×10^{-4}
65	**60**	1.02×10^{-3}
75	**60**	3.58×10^{-3}
85	**60**	1.96×10^{-2}
95	**60**	6.42×10^{-2}
60	**40**	3.85×10^{-6}
60	**50**	5.38×10^{-5}
60	**60**	1.36×10^{-4}
60	**80**	7.74×10^{-4}

In this chapter, we have demonstrated that binary polymer nanoparticle assemblies can be used to fabricate tunable co-continuous polymer morphologies for concurrent electronic and ionic transport. We demonstrate that PVP-based polymer nanoparticles can be used for solid-state Li ion conduction, with high ionic conductivities reaching $\sigma_{ion} = 6.42 \times 10^{-2}$ S/cm in mixed assemblies. We also show that by varying the percentage of electronic conducting (P3HT) and ionic conducting [P(4VP$_{0.9}$-*co*-S$_{0.1}$)] polymer nanoparticles we can tune both the $\sigma_{elec.}$ and σ_{ion}, in a predictable manner. Our work opens the pathway to fabricate and optimize polymer-based materials for battery applications.

CHAPTER 3

ELECTRONIC AND IONIC TRANSPORT IN HYBRID ORGANIC/INORGANIC PEROVSKITES

3.1 Introduction to Hybrid Organic/Inorganic Lead Triiodide Perovskites

Hybrid organic/inorganic lead triiodide perovskites, simply called perovskites in the field, are a class of materials with the chemical formula AMX_3, where A is typically an organic cation methylammonium (MA^+) or formamidinium (FA^+) or alkali metal Cs^+; M is Pb(II) or Sn(II); and X is I^-, Br^-, or Cl^-. The structure of these materials, in general, consists of metal-halide octahedral with the organic cation occupying the octahedral void, but will be discussed in more detail later on. These materials have surged through the photovoltaic community in recent years due to its ease of fabrication (*i.e.* solution possessed) and high photovoltaic power conversion efficiencies (PCE);[31-34] however, they have also been demonstrated to have application in field effect transistors,[35] thermoelectrics,[36] piezoelectrics,[37] lasing,[38] LEDs,[39] memory storage,[40] and more.

For photovoltaics, the current certified maximum PCE is an impressive 22.1%.[440] Perovskites have actually surpassed PCEs in just a few years that it took other technologies decades of research to obtain, see Figure 80. A unique combination of material properties makes this class of materials highly suitable to photovoltaic applications. The band gap and energy levels of perovskites can be easily tuned by changing the A, M, or X (see Figure 81).[32,441] $MAPbI_3$, for example, has a direct band gap of ~ 1.55 eV, and adsorbs over most of the visible spectrum. Further, the exciton binding energy is remarkably low, 0.030 eV, allowing holes and electrons tor readily dissociate.[31] They also demonstrate relatively high charge carrier mobility for both charge carriers, and very long carrier diffusion lengths (100 nm to 1 μm).[31,34]

Although perovskites have displayed remarkable photovoltaic performance, there are, of course, issues that need to be addressed before commercialization can be possible. The most striking is their inherent instability under ambient conditions[31,41] and their degradation upon prolonged exposure to heat and sunlight.[43]

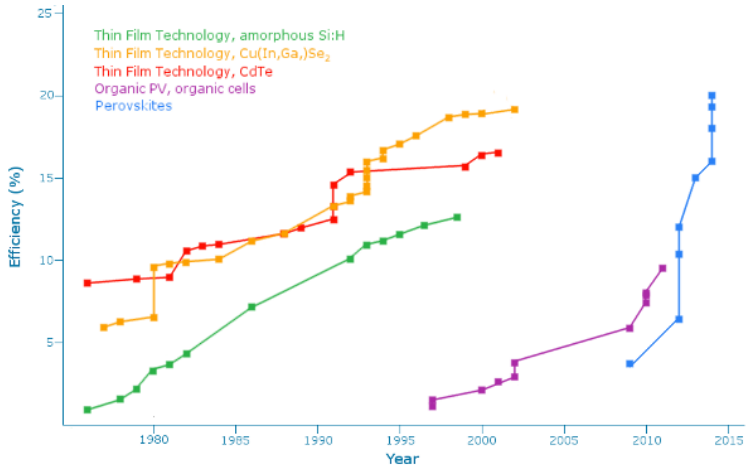

Figure 80: Power conversion efficiencies of photovoltaic technologies over time. Adapted from Ossila.com.

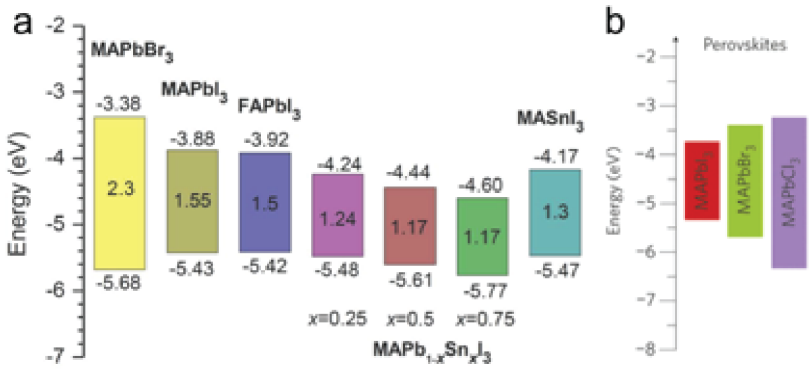

Figure 81: Band gap and energy level tuning by changing chemical composition of AMX_3 perovskites. (a) adapted from from Ref. [32]. (b) adapted from Ref. [441]

3.1.1 Structure of Perovskites

Although there is a high degree of structural and chemical diversity in "perovskite" structures,[442] including three dimensional and lower dimensional structures,[442] double

perovskites ($A_2MM'X_6$) containing Bi and Ag,[443] and Ruddleson-Popper-type layered perovskites;[444] I will focus on the structure of MA/FAPbI$_3$, as it is one of the most research and best performing perovskites.[31,33,445] The ions that make up the perovskite structure are dictated by radius ratio rules established by Linus Pauling which dictates the stability of possible structures with N-coordination based on the ratio of the ionic radii.[182] For perovskites, the structure can be predicted based on the Goldchmidt tolerance factor (*t*)[446,447]:

$$t = \frac{r_A + r_x}{\sqrt{2}(r_B + r_x)}$$

This number (*t*) could be used to determine if a particular ion would form a stable perovskite, and what the structure would be. When *t* is between 0.8 and 1, a cubic or pseudo-cubic structure tends to form, when *t* is less than 0.8 the orthorhombic phase predominates, and when *t* is greater than 1the layered hexagonal phase forms.[447] Figure 82 shows the dependence of the tolerance factor on the ionic radii of the A ion in AMX_3 perovskite alloys, and how the crystal structure changes from orthorhombic to cubic to hexagonal. It should be noted that only the cubic phase shows good photovoltaic performance.[447]

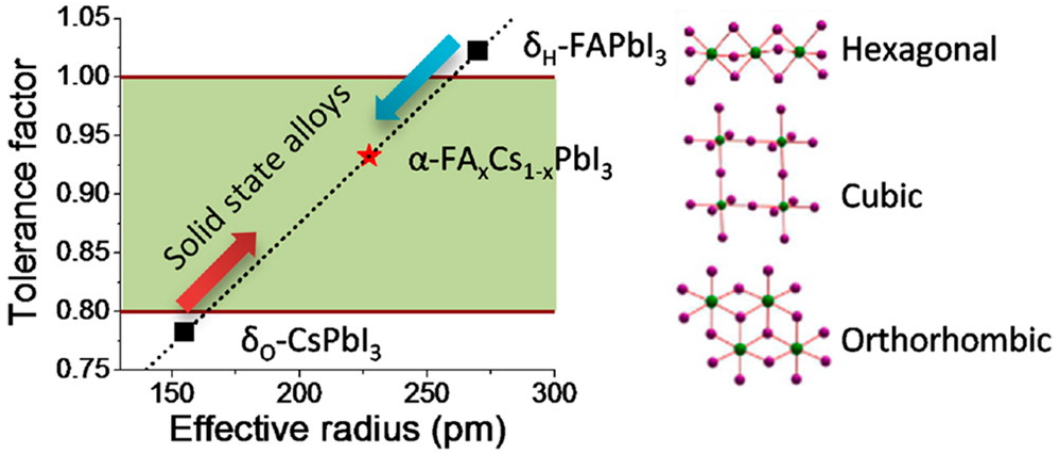

Figure 82: Tolerance factor vs. effective radius of A ion in AMX_3 perovskite, showing dependence of crystal structure on ionic radii. Used with permission from Ref. [447].

The structure of perovskites is temperature dependent. For example, $MAPbI_3$ goes from orthorhombic (*Pnma*) to tetragonal (*I4cm* or *I4/mcm*, pseudo-cubic) at ~-112 °C, followed by a discontinuous (see Figure 83 for change in lattice parameters vs temperature)[448] phase change to cubic (*Pm-3m*) at ~ 45 °C.[445] This second phase transition can be hard to detect due to many overlapping peaks in x-ray diffraction (XRD, see Figure 84), however the peak attributed to the tetragonal (211) plane can be used to track the phase change.[445] This readily accessible tetragonal to cubic phase change has implications on the electronic[445] and ionic properties of the material that will be discussed in the following chapter.

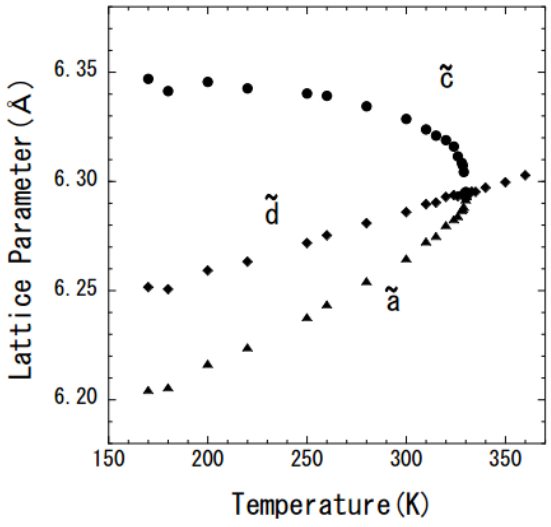

Figure 83 Discontinuous temperature dependence of lattice parameters in $MAPbI_3$ during phase change. Phase change occurs at ~45 °C (318.15 K). From Ref. [448]

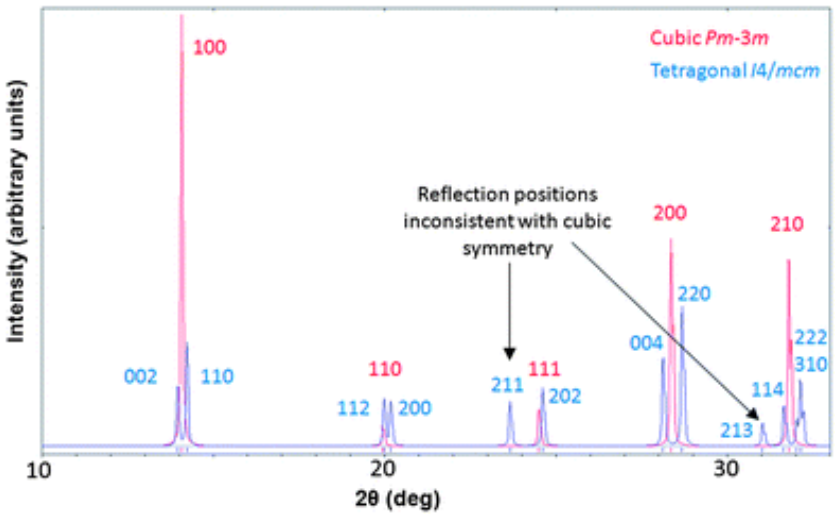

Figure 84 Calculated XRD pattern for cubic and tetragonal phases of $MAPbI_3$. From Ref. [445]

3.1.2 Electronic and Ionic Transport at Perovskite Interfaces

The following chapters deal with electronic and ionic transport in perovskite materials, specifically, how interfacial materials can be used to characterize these materials. First, I detail the discovery of mixed electronic and ionic transport in perovskite, some of the contributing factors that affect ionic transport, and its implications on device stability. Next, I discuss the use of a functionalized fullerene as a work function modifier to improve perovskite-based device photovoltaic efficiency. Then I will talk about the use of a hole-transport layer which has a lower work function than traditionally used polymer hole transport layers, resulting in a higher built in potential in the device; the material also has the added benefit of being water-processable. Subsequently, I will discuss the use of a three material graded work function recombination layer for connection perovskite-based and polymer-based solar cells in a tandem-cell configuration. Next, I will discuss the use of KFPM to probe the photo-generated-charge extraction and polarization in perovskite charge transport material bilayers. Then, I will detail the use of carbon nanotubes as charge extractors from perovskite layers, resulting in lower recombination losses.

And finally, I will talk about the use of hole transport polymers with ionic functionality, and how the ionic groups play a role in photovoltaic performance, and how they can be used to arise interesting properties for memristors.

3.2 Mixed Electronic and Ionic Transport in Hybrid Organic/Inorganic Perovskites

This chapter[§§§] focuses on the peculiar behaviour observed in perovskite solar cells where the degrade why operated under solar simulator irradiation. Solar cells fabricated using alkyl ammonium metal halides as light absorbers have the right combination of high power conversion efficiency and ease of fabrication to realize inexpensive but efficient thin film solar cells. However, they degrade under prolonged exposure to sunlight. Herein, we show that this degradation is quasi-reversible, and that it can be greatly lessened by simple modifications of the solar cell operating conditions. We studied perovskite devices using electrochemical impedance spectroscopy (EIS) with methylammonium (MA)-, formamidinium (FA)-, and MA_xFA_{1-x} lead triiodide as active layers. From variable temperature EIS studies, we found that the diffusion coefficient using MA ions was greater than when using FA ions. Structural studies using powder X-ray diffraction (PXRD) show that for MAPbI3 a structural change and lattice expansion occurs at device operating temperatures. On the basis of EIS and PXRD studies, we postulate that in MAPbI3 the predominant mechanism of accelerated device degradation under sunlight involves thermally activated fast ion transport coupled with a lattice-expanding phase transition, both of which are facilitated by absorption of the infrared component of the solar spectrum. Using these findings, we show that the devices show greatly improved operation lifetimes and stability under white-light emitting diodes, or under a solar simulator with an infrared cutoff filter or with cooling.[449]

[§§§] This chapter is adapted, with permission, from Bag, Monojit, Lawrence A. Renna, Ramesh Y. Adhikari, Supravat Karak, Feng Liu, Paul M. Lahti, Thomas P. Russell, Mark T. Tuominen, and Dhandapani Venkataraman. "Kinetics of ion transport in perovskite active layers and its implications for active layer stability." *Journal of the American Chemical Society* 137, no. 40 (2015): 13130-13137. I would like to acknowledge Prof. Monojit Bag for device characterization, and Prof. Ramesh Y. Adhikari for discussions on EIS.

Lead halide-based perovskite solar cells[34,450-458] have drawn considerable interest because of their high efficiency and low temperature solution processability.[459] But, a major practical limitation of these systems is their poor stability under ambient conditions[31,41] and their degradation upon prolonged exposure to heat and sunlight.[43] Previous reports have focused on degradation pathways attributed to moisture and temperature effects.[43,460,461] But thus far, the origin and nature of *photo-induced* degradation is largely unexplored.

In inorganic-organic hybrid lead iodide perovskites an organic counterion — typically alkyl ammonium — occupies voids within a 3D framework created by vertex-shared PbI_6 octahedra. Migration of ions within the 3D framework has been speculated to be an important factor leading to device instability and hysteresis in device current-voltage (J-V) profiles.[42] Some reports have explored ionic drift/transport in the perovskite active layer.[28,29,44-48] But, there is no clear understanding of the factors that facilitate undesired ion transport in the materials. Toward clarifying the possible role of ion transport in the degradation of perovskite solar cells, we studied them *in operando,* by electrochemical impedance spectroscopy (EIS)[462-464] combined with structural analysis of active layers by powder x-ray diffraction (PXRD), using varied illumination and temperature conditions.

3.2.1 Material/Device Fabrication

Methyl ammonium iodide (MAI) was synthesized by the following procediure. Methylamine (24 mL, 33%) was dissolved in EtOH (100mL) under $Ar_{(g)}$. HI (5 mL, 55%) was added drop-wise to stirred methylamine solution. After ca. 15 minutes, the solution was concentrated *in vacuo*. The yellow solid was washed several times with diethyl ether, recrystallized from diethyl ether/EtOH to form a white solid and then dried *in vacuo* at 70 °C.

Formamidinium iodide (FAI) was synthesized by the following procedure. Formamidine acetate (2.5g) was dissolved in EtOH (100 mL) under $Ar_{(g)}$. HI (10.77 mL, 57%) was added drop-wise to stirred formamidine acetate solution. After ca. 2 h at ~50 °C, the solution was concentrated *in vacuo*. The yellow solid was washed several times with diethyl ether, recrystallized from diethyl ether/EtOH to form a white solid and then dried *in vacuo* at 70 °C.

Devices were fabricated as follows. ITO substrates (~20 $\Omega \cdot sq^{-1}$) were cleaned by ultrasonication of the substrates submerged in soap solution, then acetone, and then isopropyl alcohol followed by drying in a hot air oven at 140 °C for 2 h. poly(3,4-ethylenedioxythiophene) polystyrene sulfonate (PEDOT:PSS) (Clevios PVP AI 4083) was filtered through a 0.45 micron polyvinylidene fluoride (PVDF) filter (Wilkem Scientific), then spin coated onto the substrates at 3000 rpm for 30 s The PEDOT:PSS coated ITO substrates were then annealed at 140 °C for 20 min in a hot air oven. PbI_2 (40 wt. %) was dissolved in dry N,N-dimethylformamide (DMF) and filtered through a 0.45 micron polytetrafluoroethylene (PTFE) (Wilkem Scientific) filter. The hot solution (~80 °C) was then spin coated at 6000 rpm onto a hot substrate (~80 °C) for 60 s The PbI_2 coated film was then kept on a hot plate (90 °C) to dry for 1 h. MAI, FAI and mixtures of MAI and FAI (1:1 by wt.) were dissolved in isopropyl alcohol (40 $mg \cdot mL^{-1}$) and spin coated on the PbI_2 coated substrates at 6000 rpm for 60 s at room temperature. $MAPbI_3$ and $MA_xFA_{1-x}PbI_3$ samples were annealed on a hot plate (85 °C) for 1 h. $FAPbI_3$ samples were annealed at 160 °C for 10 min. The devices were then kept in the dark for over 12 h. [6,6]-phenyl-C_{61}-butyric acid methyl ester (PCBM) in chlorobenzene (20 mg mL^{-1}) as an electron-transporting layer was then spin coated atop the devices at 1000 rpm for 60 s inside a glove box. Next, a 15 nm thick Ca electrode was thermally deposited at a rate of 0.5 $Å \cdot s^{-1}$ followed by 100 nm of Al electrode deposited at a rate of 1 – 3 $Å \cdot s^{-1}$, all at a chamber pressure of 1×10^{-6} mbar.

3.2.2 Current-Voltage and EIS Measurements

Current-voltage (*J-V*) curves of the perovskite solar cells were tested under an AM 1.5G solar simulator at 100 $mV \cdot cm^{-2}$ light intensity inside a N_2 filled glove box, at time intervals over 70 h. Impedance was measured using an Agilent 4294A Precision Impedance Analyzer at different bias voltages after each efficiency measurement, using a frequency analyzer under AM 1.5G simulated illumination, as well as under dark condition. Temperature dependent study was conducted using a thermoelectric heater/cooler with a thermocouple attached to measure in-situ temperature. *J-V* measurements were made without a photomask to compare with EIS experiments were a photomask cannot be used. Device stability experiments were performed using a cool white-LED array (12V, 10 W) light source and an AM 1.5G solar simulator at 100 $mWcm^{-2}$ light intensity and the same solar simulator with an infrared cut off, Newport-Oriel KG5 filter.

J-V curves of planar heterostructure (Figure 85a inset) perovskite solar cells shown in Figure 85a were measured under inert atmosphere inside a glove box by scanning the voltage from the short circuit current (J_{SC}) to the open circuit voltage (V_{OC}) at a scan rate of 250 $mV \cdot s^{-1}$. We obtained an average power conversion efficiency (PCE) of 10.3% over 32 $MAPbI_3$ devices with a maximum PCE of 13.6% (without using a photo-mask) under an AM 1.5G solar simulator at 100 $mW \cdot cm^{-2}$ light intensity. The average over 32 devices and maximum efficiency obtained using perovskite having *both* counterions ($MA_xFA_{1-x}PbI_3$) were 11.6% and 13.3%, respectively. By comparison, the maximum efficiency obtained from $FAPbI_3$ devices was 8.9%. Low PCE in $FAPbI_3$ devices has been attributed to their weak near-IR absorption.[465] The *J-V* characteristics, reproducibility, and device crystallinity of these devices are given in Figure 86.

For the main discussion below, we focus on results from $MAPbI_3$ and $MA_xFA_{1-x}PbI_3$ devices because of their high PCEs and reproducibility compared to $FAPbI_3$ devices.

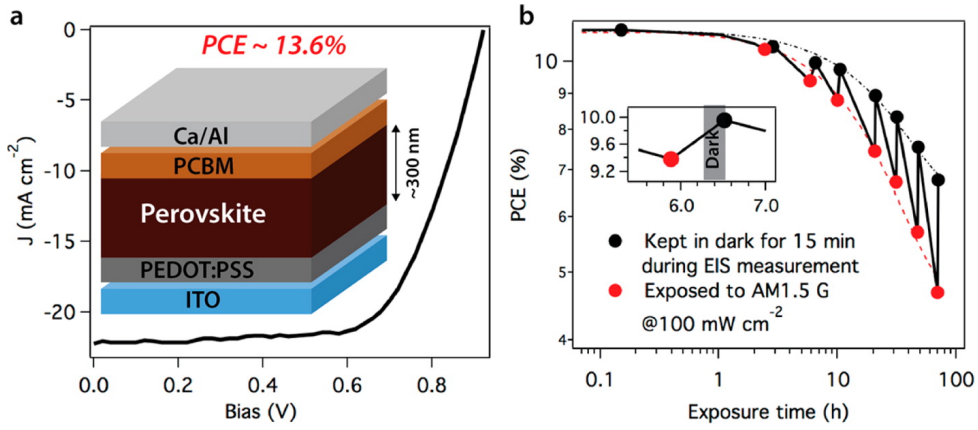

Figure 85: (a) $MAPbI_3$ perovskite solar cell light *J-V* characteristics for best cell without photomask. Inset: Device architecture. (b) Device efficiency as a function of light exposure time. EIS was carried out at each points represented as red circle. Black circle represents the efficiency just after the device was kept in dark for 15 min during dark impedance measurement.

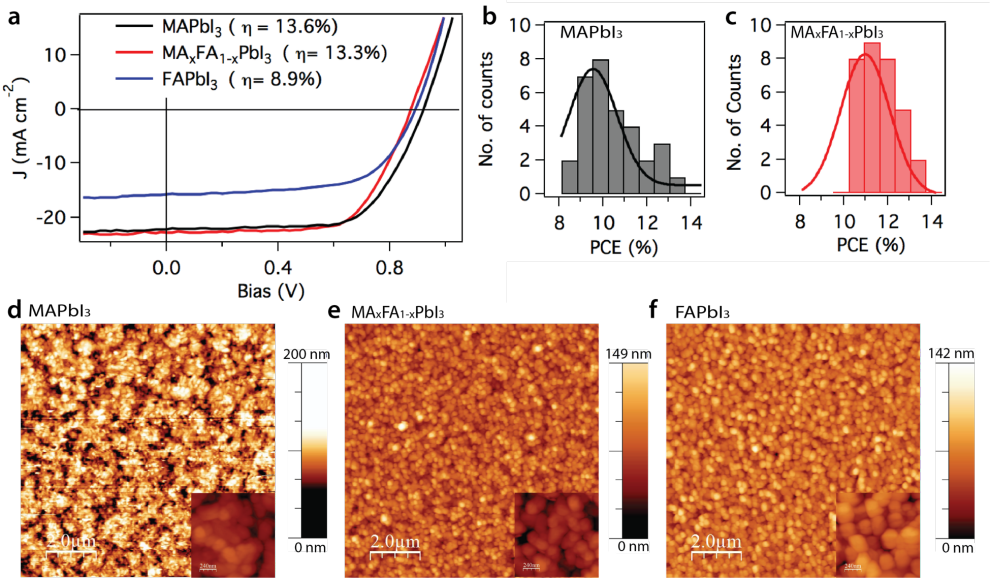

Figure 86: (a) *J-V* characteristics of $MAPbI_3$, $FAPbI_3$ and $MA_xFA_{1-x}PbI_3$ samples (best device efficiency). Statistical distribution on the reproducibility of (b) $MAPbI_3$ (c) $MA_xFA_{1-x}PbI_3$ perovskite solar cells. AFM height image of (d) $MAPbI_3$ (e) $MA_xFA_{1-x}PbI_3$ (f) $FAPbI_3$ perovskite solar cell. Scale bar is 2 μm. Inset: magnified image of perovskite nano-crystal.

Under prolonged illumination, the overall PCE of the devices decreased over time (Figure 85b), with the $MAPbI_3$ devices degrading faster than $MA_xFA_{1-x}PbI_3$ devices. In 20 h, $MAPbI_3$ device PCEs dropped by 40%, whereas the $MA_xFA_{1-x}PbI_3$ device PCEs dropped only by 15% (see Figure 87). Surprisingly, when a previously illuminated $MAPbI_3$ device was kept in the dark for ~15 min and then re-illuminated, much of the lost PCE was recovered, indicating that the device degradation was quasi-reversible (Figure 85b). After being kept in the dark under inert atmosphere inside a glove box for 70 h, the PCE of $MAPbI_3$ devices dropped only marginally. Much more impressively, from a similar dark-storage test *for 30 days*, $MA_xFA_{1-x}PbI_3$ device shows *no* appreciable loss in PCE (Figure 88). $MAPbI_3$ devices did show degradation (see Figure 88), which can be attributed to the exposure to light and applied bias when making *J-V* measurements. Compared to $MAPbI_3$ devices, we also observed a reduced *J-V* hysteresis in $MA_xFA_{1-x}PbI_3$ devices (Figure 89). Based on these data, we conclude that (a) the device degradation is accelerated by the AM1.5G illumination of the device and *not* by trace oxygen or moisture inside the glove box (Table 11), and (b) the mixed counterion $MA_xFA_{1-x}PbI_3$ devices exhibit greatly improved stability under dark and under illumination conditions, compared to the corresponding single-counterion devices.

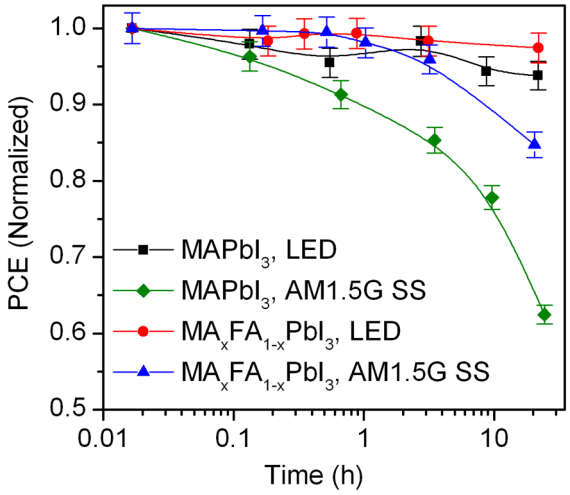

Figure 87: Photo-stability of $MAPbI_3$ and $MA_xFA_{1-x}PbI_3$ perovskite solar cells under AM1.5G solar simulator 100 $mWcm^{-2}$ light intensity and under white-LED (20 $mWcm^{-2}$). Devices were continuously kept under light at 0 applied bias. 3% Error bar represents measurement variability (multiple measurement) due to hysteresis. Device efficiency was normalized with respect to the initial (at t = 0 h) efficiency of the device.

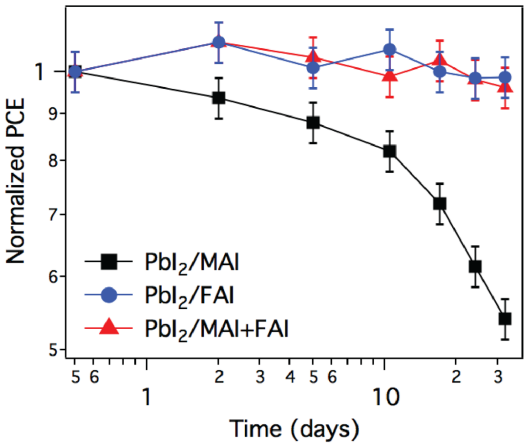

Figure 88: Device stability of three types of solar cells in dark under N_2 atmosphere inside glove box. Error bar represents 5% tolerance level accounted for the measurement error on each day. However, devices were exposed to AM1.5G solar simulator at 100 $mW.cm^{-2}$ optical power during *J-V* measurement under applied bias which could also promote the photo-degradation of $MAPbI_3$.

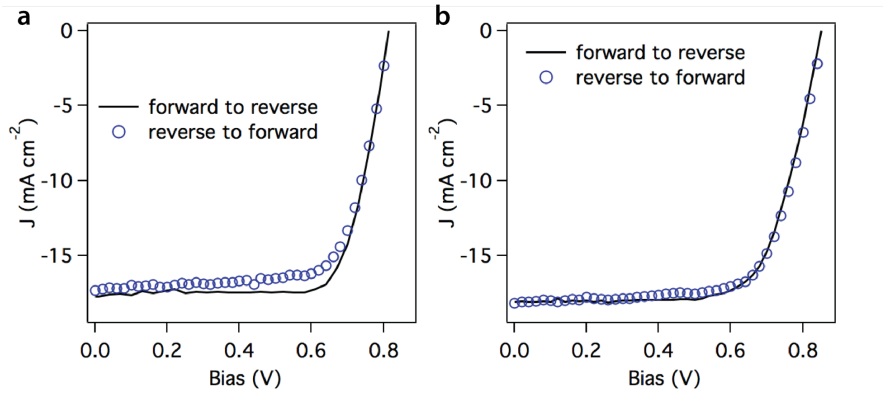

Figure 89: Typical device *J-V* characteristics under AM1.5G solar simulator at 100 mWcm^{-2} optical power with forward and reverse voltage-scan direction at a scan rate of 250 mV.s^{-1} showing hysteresis in measurement. (a) $MAPbI_3$ samples (b) $MA_xFA_{1-x}PbI_3$ samples. Average device efficiency was 10% – 11%.

Table 11: $MAPbI_3$ perovskite solar cell metrics.

Device Condition	J_{SC} (mA·cm^{-2})	V_{OC} (V)	FF (%)	η (%)	R_s (Ω·cm^2)	R_{sh} (kΩ·cm^2)
Sample 1, as prepared	18.85	0.865	70.2	11.45	5.8	0.857
After 70 h in light	8.66	0.929	58.1	4.68	11.8	0.328
After 15 min in dark	12.67	0.851	62.8	6.78	9.2	0.330
Sample 2, as prepared	17.57	0.983	66.4	11.47	7.5	0.896
After 5 days	17.55	0.970	61.5	10.48	10.6	0.686

To understand the origin of photo-induced, yet quasi-reversible degradation in the perovskite films, we carried out EIS measurements on devices under dark conditions as well as under

AM1.5G illumination in a nitrogen-filled glove box. In these EIS measurements, the device impedance was measured by applying 20 mV

AC voltage whose frequency (ω) is swept from 100 Hz to 1 MHz in 100 equal steps on a logarithmic scale. EIS results are conventionally presented as a Nyquist plot, with the real component of the impedance (Z') as the abscissa and the imaginary part (Z'') as the ordinate.[466] Nyquist plots of a $MAPbI_3$ sample under dark conditions (Figure 90a) versus AM 1.5G solar simulator conditions at 100 $mWcm^{-2}$ light intensity (Figure 90b) show different characteristics. The plots under dark conditions showed a single charge transport regime[466] at low forward bias voltages (V_{app}) with an estimated transit time (τ_d) of ~90 μs (Figure 90a). When V_{app} was increased, a single recombination semicircle was observed, *indicating only one type of charge transport (electronic) is predominant under dark conditions*. The Nyquist plot from a device under illumination shows *two* distinct charge transport regimes, with two semicircles associated with different time constants (τ). The semicircle closest to the origin is associated with the higher frequency spectrum and is attributed predominantly to impedance arising from the electronic transport. The second semicircle is associated with the low frequency spectrum and is attributed to the impedance arising either from charge or mass transfer at the interface or Warburg ion diffusion.[467] Additional data, including light intensity dependence and dark measurements, are shown in Figure 91. As a control experiment, we measured the EIS of a bulk heterojunction organic solar cell having no ions in the active layer, a cell fabricated from poly(3-hexylthiophene) and PCBM. The EIS of this system — as expected — shows only one semicircle in the high frequency regime, under *both* dark and illuminated conditions (Figure 92c & d). Based on these results, and literature precedent describing the impedance spectroscopy of systems with two types of charge carriers,[264,468,469] we assert that the low frequency EIS

component *arising only in the illuminated* perovskite is predominately associated with the diffusion of ions.

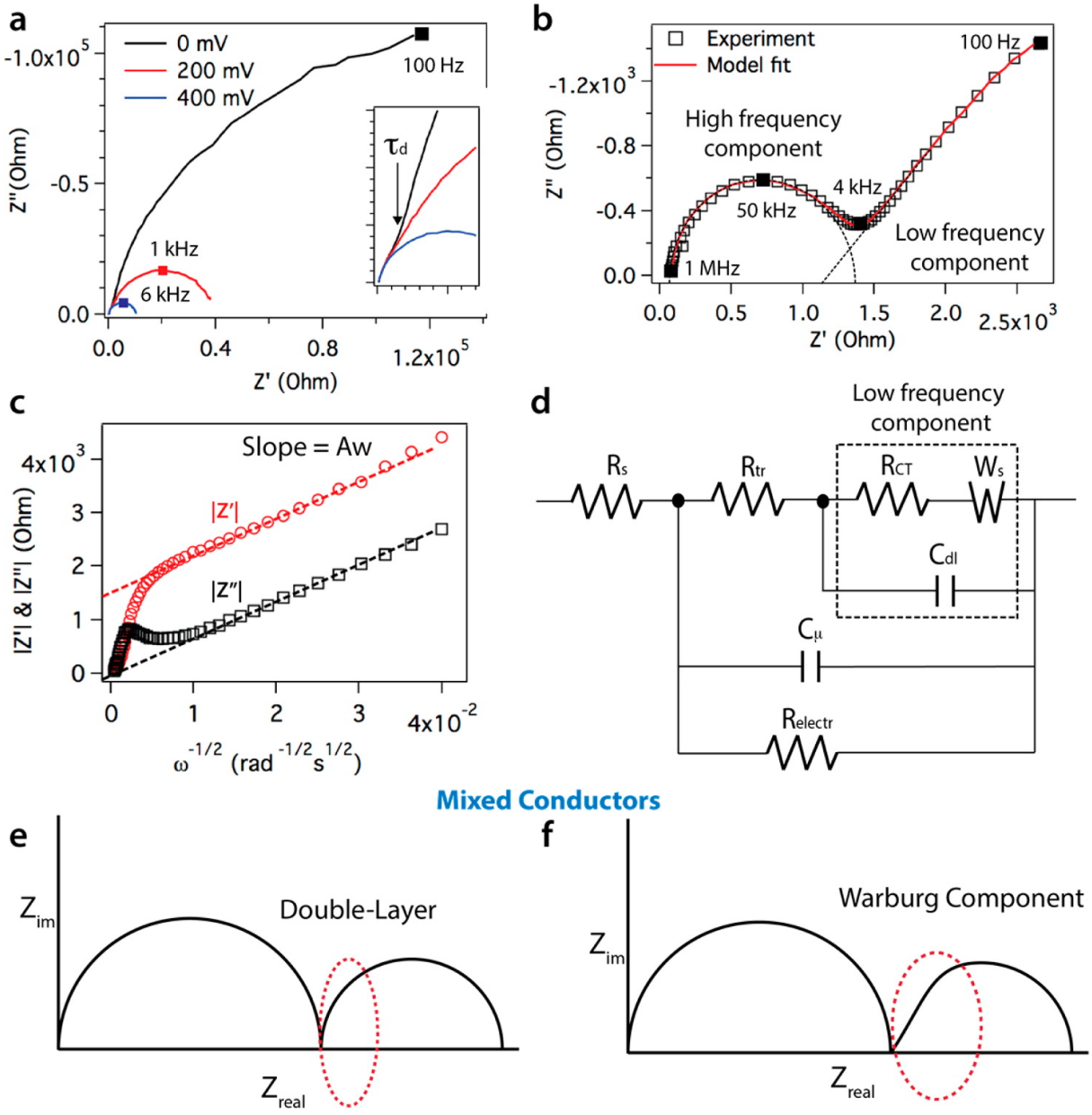

Figure 90: (a) Nyquist plot of $MAPbI_3$ samples under dark. Data was taken from 100 Hz to 1 MHz oscillation frequency at 20 mV AC amplitude and 0 V DC bias. Inset: High frequency component showing transport regime. (b) EIS plot of $MAPbI_3$ sample at 45 °C at 100 $mW \cdot cm^{-2}$ light intensity and 0 V applied bias. (c) Warburg impedance plot of same data. (d) Equivalent circuit diagram of perovskite solar cells showing combined charge and ion transport impedance. (e) Typical Nyquist plot for mixed conductor system with double-layer capacitance showing semi-circular feature in low frequency regime. (f) Typical Nyquist plot for mixed conductor system with Warburg diffusion as evidence by the linear portion of the low frequency regime.

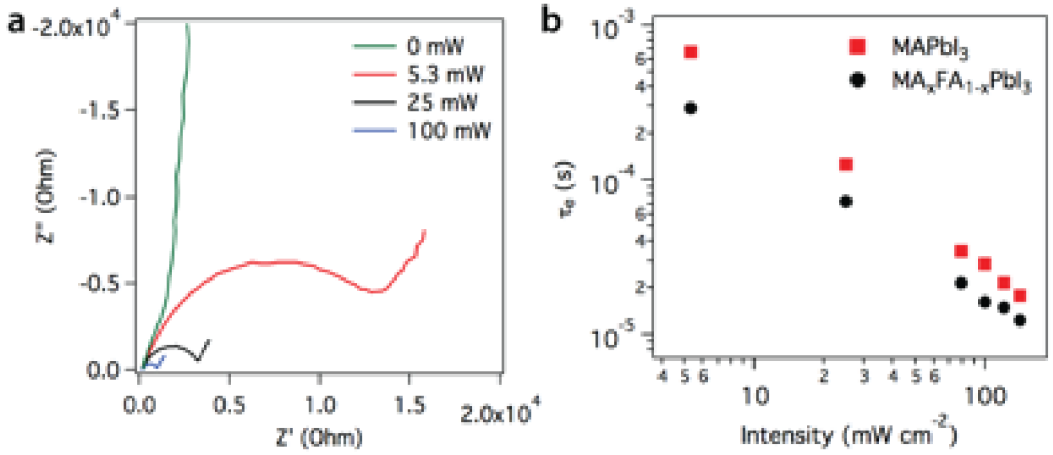

Figure 91: Light intensity dependent impedance measurements. (a) Nyquist plot of $MAPbI_3$ perovskite sample under different light intensity at 0 V bias. (b) Carrier lifetime (τ_e) calculated from the high frequency component of the Nyquist plot as a function of light intensity.

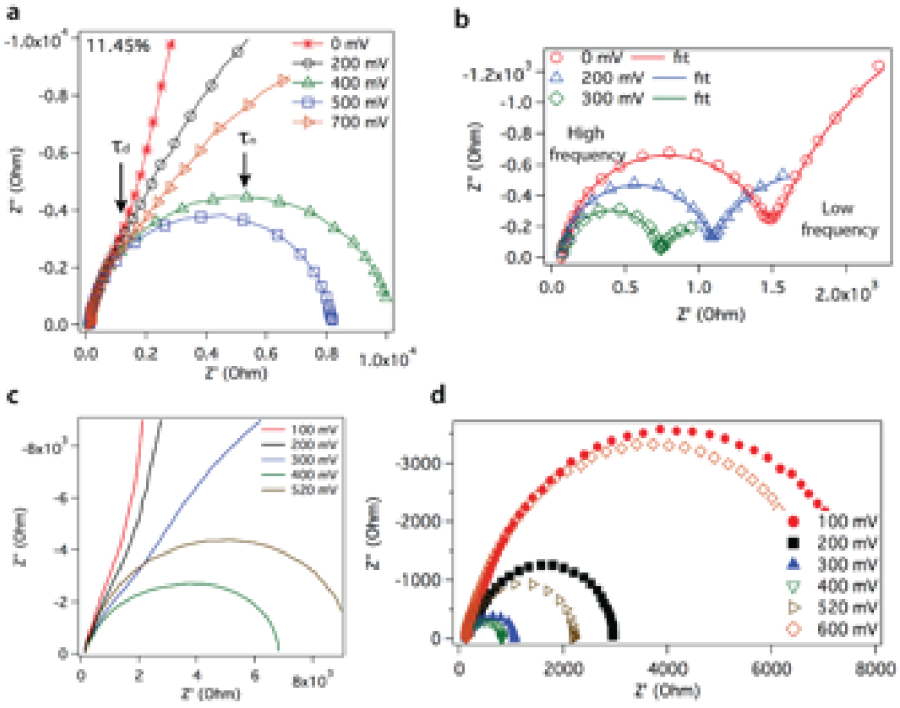

Figure 92: (a) Nyquist plot of perovskite solar cells under dark at different bias voltages. (b) Nyquist plot of perovskite solar cells under AM1.5G solar simulator at different bias voltages. (c) Nyquist plot of P3HT:PCBM bulk heterojunction (BHJ) solar cells under dark. (d) Nyquist plot of BHJ solar cells under AM1.5G solar simulator.

3.2.3 EIS Analysis

Prior EIS studies of perovskite-based solar cells attribute the low frequency component to double layer capacitance due to charge accumulation at the interface, not to ion migration.[44,470-476] To account for charge accumulation at the interface in these studies, ion migration to the interface can be invoked. But, this low frequency component can also arise from ion diffusion or Warburg diffusion. The tell-tale signature of ion/Warburg diffusion is the presence of a linear region as in Figure 90f in the Nyquist plot instead of just a semicircle as in Figure 90e that indicates double-layer capacitance. A close examination of the published EIS spectra from which charge accumulation effects were concluded, shows the presence of a linear component in low frequency Nyquist plot region.[****] This feature is just what we obtained in our *in operando* EIS measurements.

To support our ion diffusion degradation mechanism hypothesis further, we modelled the ionic diffusion in the low frequency regime as a Warburg element (W_S),[477] whose impedance is represented by the equation:

$$W_S = A_W \frac{\tanh\left(j\omega T_W\right)^P}{\left(j\omega T_W\right)^P}$$

where A_W is the Warburg impedance, T_W is the Warburg time constant and exponent P is ~0.5.[469,478] A detailed explanation of the model derivation is given in the Supporting Information. Plots of |Z'| and |Z"| as functions of $\omega^{-1/2}$ show linear behavior in the low frequency

[****] For example in Figure 3b,c of Ref. [470] A. R. Pascoe, N. W. Duffy, A. D. Scully, F. Huang, and Y.-B. Cheng, Insights into Planar $CH_3NH_3PbI_3$Perovskite Solar Cells Using Impedance Spectroscopy, *J. Phys. Chem. C* **119**, 4444 (2015)., we can see Warburg-like linear component in the low frequency regime. However, the equivalent circuit shown in Figure 3a of this reference does not include Warburg component.

regime, with the slope of both lines being equal to A_W (Figure 90c). The imaginary component line intersects the ordinate at zero. This observation is unequivocal proof that this sort of low frequency component arises from Warburg *ion* diffusion.[477]

To evaluate the kinetics of the photo-induced ion transport, the Nyquist plots were modelled as mixed conductor systems based on the equivalent circuit model in Figure 90d, which contains both high frequency electronic elements and low frequency ionic elements.[467,468] In the model circuit, the high frequency component consists of charge and ion transport resistance (R_{tr}) coupled with interfacial charge transfer resistance (R_{CT}). Any ion accumulation at the interface is modelled as an interfacial Debye-layer capacitance (C_{dl}), while chemical capacitance (C_μ) represents the stored charge in the bulk perovskite layer. Free carrier recombination/transport (electrons and holes both) is modelled using another resistance term (R_{electr}) in parallel with the ion diffusion term. Series resistance (R_s) represents contact resistance arising from the electron and hole transport layers, as well as contributions from the measurement apparatus itself. The details of the modelling are provided in the supporting information.

Using ZView version 3.4c (Scribner Associates Inc.), we fit the impedance spectra in Figure 90b and all other Nyquist plots to the circuit model shown in Figure 90d, and obtained R_{tr}, R_{CT}, C_{dl}, C_μ, R_{electr}, R_s, A_w, T_w, and P. From the value of T_W, we calculated the effective chemical diffusion coefficient (D) using the equation:

$$D = \frac{L_D^2}{T_W}$$

where L_D is the effective ion diffusion length. In our study, a maximum diffusion length was assumed to be equal to the perovskite film thickness (~300 nm) measured by profilometry. At the 45 °C (318 K) operating temperature of the device, under AM1.5G illumination, D was calculated to be ~3.6×10^{-12} $cm^2 \cdot s^{-1}$ for $MAPbI_3$, ~2×10^{-12} $cm^2 \cdot s^{-1}$ for $MA_xFA_{1-x}PbI_3$, and ~$3\times10^{-}$

^{13} $cm^2 \cdot s^{-1}$ for $FAPbI_3$. The ionic diffusion coefficient follows the order $MA > MA_xFA_{1-x} >> FA$, decreasing with increasing size of the ions and being about an order of magnitude higher for the increased stability MA and mixed counterion materials. While some recently reported studies on $MAPbI_3$ perovskite solar cells conclude that iodide[46,47] anion may be the mobile ion other studies indicate that alkyl ammonium counterion[28,29,48] is mobile. Recent first principles, state-of-the-art computational analysis indicated that the time scale associated with iodide ion mobility is < 1μs, but for methyl ammonium ions to be tens of ms.[28] Given the fast time scale predicted for iodide transport, evidence of iodide transport in EIS would be hidden under the first semicircle, which is dominated by electronic processes. From our EIS measurements, the time constant associated with the Nyquist semicircle that only appears during illumination is on the order of tens of ms. Moreover, we find that diffusion coefficient obtained in $MAPbI_3$ devices ions is greater than that in $FAPbI_3$ devices. Both these observations are consistent with the computational studies reported by De Angelis and co-workers,[28] with all of these results supporting our hypothesis that the mobile ion in illuminated perovskite solar cells of this type is the alkyl ammonium counterion.

3.2.4 Arrhenius-type Analysis of Ionic Transport

The activation energy (E_a) for ionic diffusion can be calculated by its relationship to T_w shown in the equation:

$$\frac{1}{T_W} = \frac{kT}{h}\frac{a^2\alpha}{L_D^2}\exp\left(\frac{-E_a}{kT}\right)$$

where a is the lattice parameter for the perovskite, α (alpha) is the coordination factor, h is Planck's constant and E_a is the activation energy.[469] By measuring impedance spectra at various temperatures (Figure 93) and plotting $\ln[1/(T \cdot T_W)]$ vs. T^{-1} as shown in Figure 94, we calculated for $MAPbI_3$ that E_a = ~56 $kJ \cdot mol^{-1}$ (~0.58 eV) in the low temperature regime (<320

K). Interestingly, De Angelis and co-workers calculated E_a = ~0.5 eV[28] and Tateyama and co-workers calculated E_a = 0.57 eV[48] for MA^+ ion migration in a tetragonal $MAPbI_3$ supercell. In the high temperature regime (>320 K), we calculate that E_a drops significantly to ~22 $kJ \cdot mol^{-1}$. We speculate this discontinuity in Arrhenius-like behavior of ionic transport in $MAPbI_3$ arises from a discontinuous volume change induced by a phase transition,[445] as is discussed below. For $MA_xFA_{1-x}PbI_3$ the E_a = ~61 $kJ \cdot mol^{-1}$ was obtained at all temperatures. $MA_xFA_{1-x}PbI_3$ exhibits continuous Arrhenius-like ionic transport because a phase transition does *not* occur as in $MAPbI_3$, again as shown below. The E_a = ~21 $kJ \cdot mol^{-1}$ for $FAPbI_3$ samples at operating temperatures, rising to ~76 $kJ \cdot mol^{-1}$ at higher temperature. These combined results show that under device operating conditions, the activation energy for ion diffusion is higher for MA_xFA_{1-x}, consistent with our observation that devices with mixed ions have a higher stability than those with MA ions alone. $FAPbI_3$ devices also shows improved stability (see Figure 88) compared to compared to $MAPbI_3$ devices despite a low E_a; however the D is also very low, which can explain the enhanced stability.

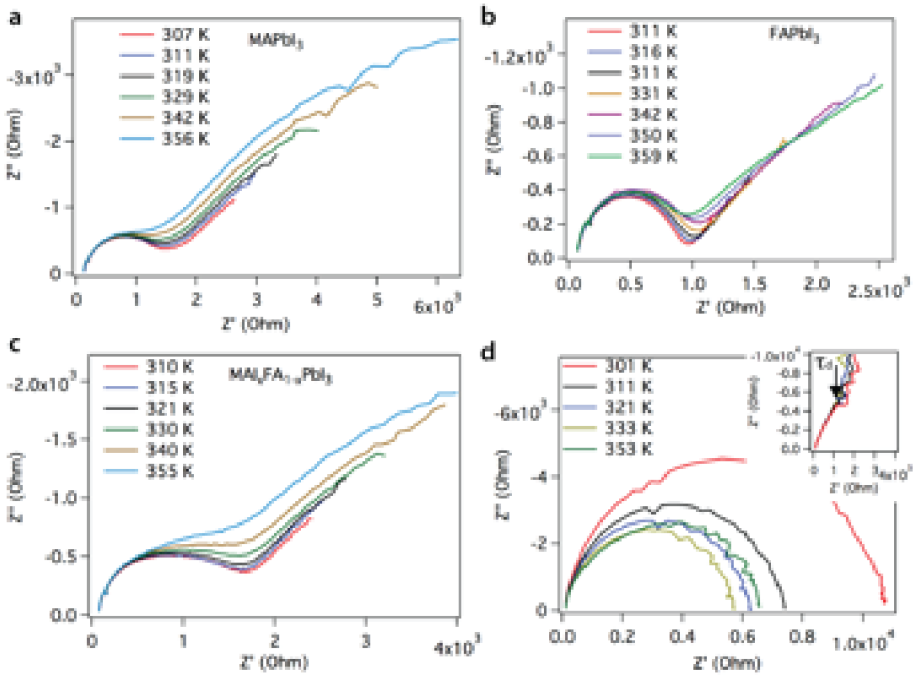

Figure 93: Temperature dependent impedance of perovskite solar cells. Impedance plot of perovskite sample under 100 mW.cm^{-2} light intensity and at different temperature at 0 V applied bias for (a) $MAPbI_3$ (b) $FAPbI_3$ (c) $MA_xFA_{1-x}PbI_3$. (d) Temperature dependent dark impedance plot of $MA_xFA_{1-x}PbI_3$ at 800 mV bias. Inset: Dark impedance at 0 V DC bias.

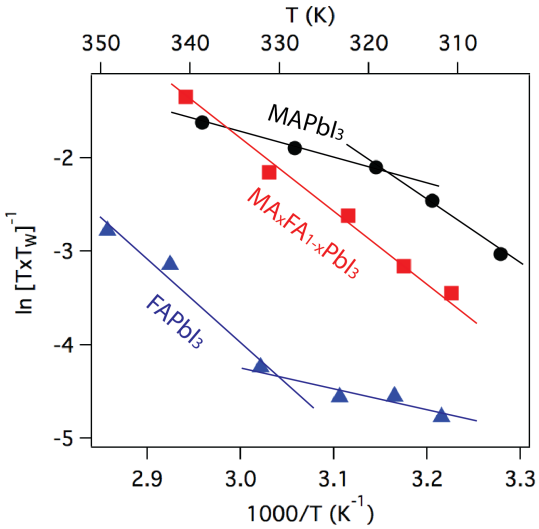

Figure 94: Arrhenius-like plot of $1/(T \cdot T_W)$ vs T^{-1} for $MAPbI_3$, $FAPbI_3$ and $MA_xFA_{1-x}PbI_3$.

Activation energy barrier, E_a, is also related to the ionic conductivity (σ_{ion}) through the equation:

$$\sigma_{ion} = n \frac{e^2 a^2 \alpha}{h} \exp\left(\frac{-E_a}{kT}\right)$$

where n is the number of ions and e is the ionic charge. The temperature dependent ionic conductivity (σ_{ion}) is independently obtained from the Warburg impedance (A_W). A plot of $\ln(\sigma_{ion})$ vs. $1/T$ is linear as seen in Figure 95, the plot shows *decreasing* conductivity with increasing temperature for $MAPbI_3$. However from the diffusion coefficient measurement, we have observed E_a ~56 kJ.mol^{-1}. This may be due to the trapping of ions at interfaces or loss of ions through chemical degradation. From the conductivity measurements, we estimate the ratio of charge carriers present at 306 K and at 318 K to be (n_{306}:n_{318}) ~4:1.The temperature dependent ionic conductivity (σ_{ion}) can also be independently obtained from the Warburg impedance (A_W). A plot of $\ln(\sigma_{ion})$ vs. $1/T$ and its derivation are shown in Figure 95. Despite varying temperatures from 301K to 353K, Nyquist plots of devices under dark conditions showed only high frequency charge transport regime behavior (Figure 93d), consistent with electronic-only transport. *No* measurable dark performance ion transport regime was observed, unlike for devices under illumination (Figure 93a-c), indicating that the *ion transport is indeed induced by light*.

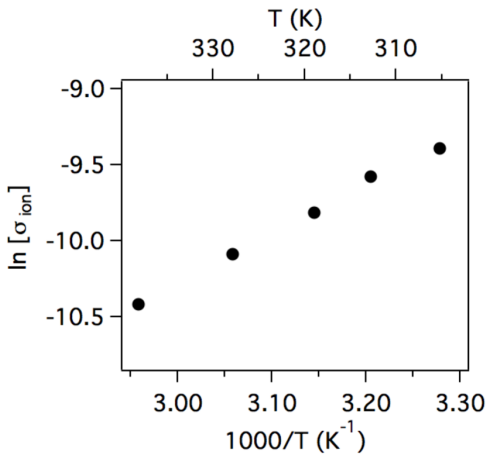

Figure 95: Temperature dependent conductivity of $MAPbI_3$ sample at 0 V applied bias under AM1.5G solar simulator at 100 mW cm^{-2} light intensity.

3.2.5 Irradiation Source Effect

In order to identify the regions in the AM 1.5G solar simulator spectrum that induce the destabilizing ion transport, we first measured EIS for devices operating under a commercial white-LED that does not emit IR or UV components (Figure 96). The EIS Nyquist plots for $MAPbI_3$ devices comparing white-LED versus AM1.5G illuminated performance at 79 mW·cm^{-2} light intensity, show significant decrease in the low frequency ion-transport regime under white-LED illumination, indicating slower ion transport compared to the device illuminated by the solar simulator (Figure 97). The ion diffusion coefficient under white-LED was 1.4×10^{-12} $cm^2\cdot s^{-1}$, compared to 3×10^{-12} $cm^2\cdot s^{-1}$ under AM1.5G solar simulation. This difference in the diffusion coefficient is consistent with differences in the operating temperatures of the devices, 301 K under LED and 320 K under AM1.5G solar simulator. It further indicates that the ion transport is induced and accelerated *by visible light*: the IR illumination component seems to contribute only to thermal activation of the visible-light induced ion transport.

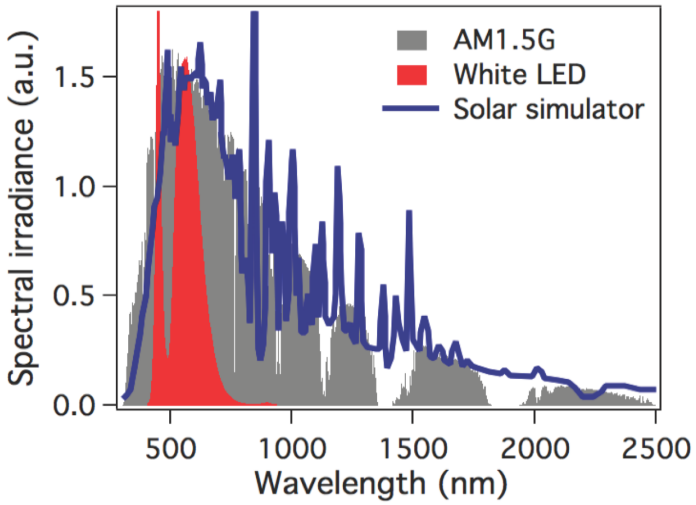

Figure 96: White-LED, solar simulator, and AM1.5G solar spectrum. Solar simulator and AM1.5G spectra data were adopted from the Newport and NREL website.

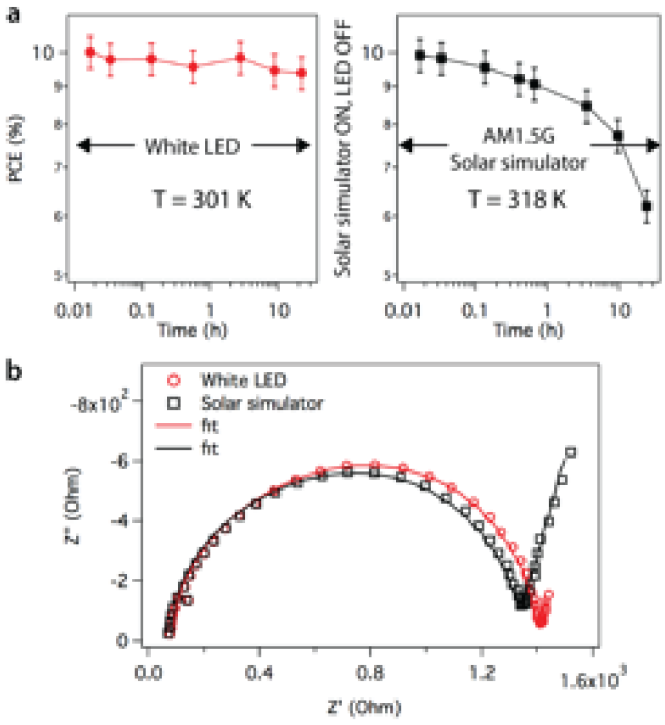

Figure 97: (a) Device stability under commercial white-LED array of 20 $mWcm^{-2}$ light intensity and under AM1.5G solar simulator at 79 $mWcm^{-2}$ light intensity. (b) EIS plot of $MAPbI_3$ perovskite solar cells under white-LED (red circle) and under AM1.5G solar simulator (black square). Symbols represent impedance at 0 mV applied.

3.2.6 Structural Analysis

We examined perovskite samples (glass/PEDOT:PSS/perovskite/PCBM) by powder X-ray diffraction (PXRD) under different light and temperature conditions, to gauge the effects of visible versus IR illumination components. The PXRD of $MAPbI_3$ device after solar simulator illumination for 15 min showed an increase in lattice dimensions (Figure 98). No such structural lattice change was observed when the sample was exposed to white-LED light alone at a measured operating temperature of 28 °C (301 K). A similar lattice expansion to that induced under AM1.5G solar simulator illumination, was also observed for illumination with an IR-only source (150 W commercial IR lamp), as shown in Figure 99a. The tetragonal (*I4cm*) $MAPbI_3$ perovskite (211) PXRD peak[445] at $2\theta = 23.48°$ actually disappears as the temperature rises above 45 °C (see Figure 100), while peaks showing a transition to cubic perovskite (*Pm3m*) are observed. However, this transition reverses when the IR lamp is switched off. PXRD of both $MA_xFA_{1-x}PbI_3$ and $FAPbI_3$ show the PXRD peaks of a trigonal (*P3m1*) structure at 45 °C, consistent with the literature.[479] These show no phase transitions, but they do show an increase in lattice parameters with IR illumination, similar to $MAPbI_3$.

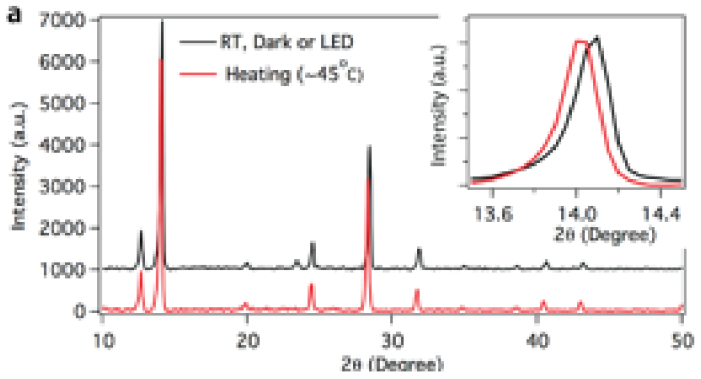

Figure 98: (a) PXRD of $MAPbI_3$ sample at room temperature (~25 °C) and after 15 min in AM1.5G solar simulator. Substrate temperature is ~45 °C.

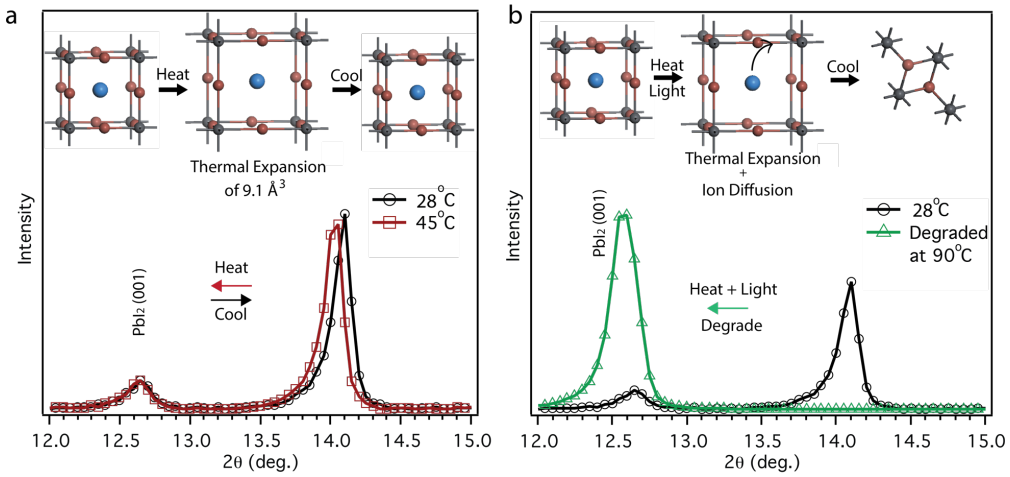

Figure 99: (a) PXRD of $MAPbI_3$ sample at room temperature (28 °C) and after heating with infrared lamp (~45 °C) in dark. The process is reversible once the device gets cooled. (b) PXRD pattern of perovskite sample after prolonged heating in presence of visible light, showing degradation of perovskite to PbI_2 structure.

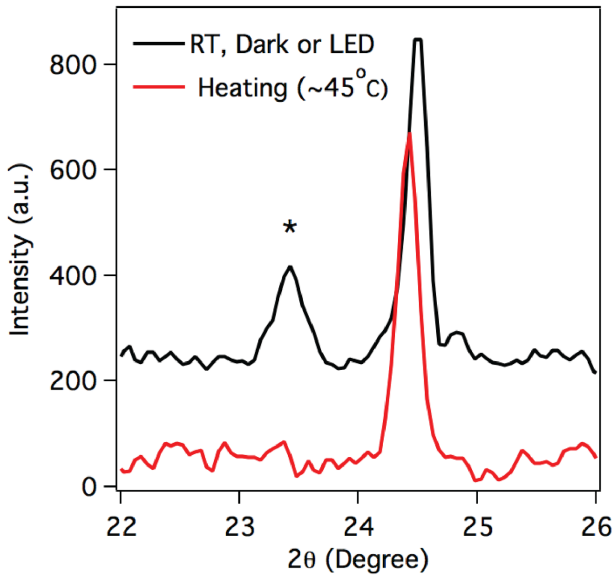

Figure 100: XRD of $MAPbI_3$ sample at room temperature (~25 °C) and after heating (~45 °C substrate temperature measured by a thermocouple). Perovskite peak at $2\theta = 23.48°$ is marked with the asterisk (*) and indicates a tetragonal phase.

To extract lattice parameters and unit cell volumes before and after heating, the PXRD data was refined using the Rietveld method using known structures[448,480] as starting points. Upon

heating with the IR lamp (~45 °C, 318 K), the volume change observed in $MAPbI_3$ was 9.1 $Å^3$ per unit cell, a 3.66% relative expansion. These observations indicate reversible perovskite lattice expansion under IR heating that correlates with the quasi-reversible thermal/IR PCE cycling that we observed in these solar cells (Figure 85b). The volume increase that accompanies the tetragonal to cubic structural phase change in $MAPbI_3$, has been reported to occur discontinuously,[445] which also correlates with the ion transport activation energy barrier discontinuity from 56 $kJ \cdot mol^{-1}$ to 22 $kJ \cdot mol^{-1}$ that we find at ~320 K. The PXRD analyses for $MA_xFA_{1-x}PbI_3$ and $FAPbI_3$ indicate 4.6 $Å^3$ and 2.2 $Å^3$ per unit cell volume increases upon heating, which are relative expansions of 0.63% and 0.23%, respectively (Figure 101). $MA_xFA_{1-x}PbI_3$ does *not* undergo a structural phase transition, and its thermal expansion is quite low compared to that of $MAPbI_3$: thus, ionic diffusion in this mixed system follows continuous Arrhenius behavior. There was no observed phase change for $FAPbI_3$, nor is there any literature evidence of structural changes at high temperatures, so the increase in E_a observed for $FAPbI_3$ samples requires further investigation

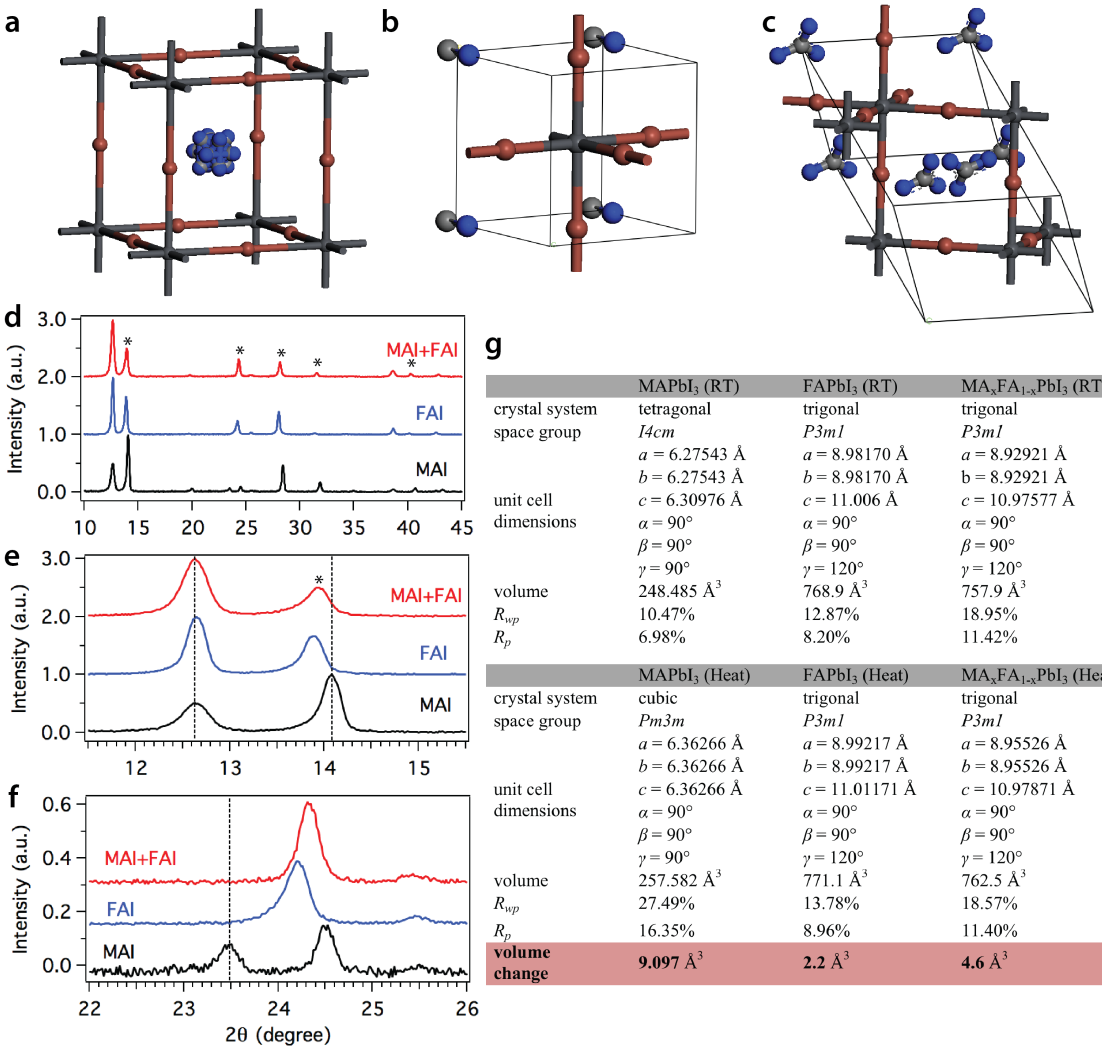

	$MAPbI_3$ (RT)	$FAPbI_3$ (RT)	$MA_xFA_{1-x}PbI_3$ (RT)
crystal system	tetragonal	trigonal	trigonal
space group	*I4cm*	*P3m1*	*P3m1*
unit cell dimensions	a = 6.27543 Å b = 6.27543 Å c = 6.30976 Å α = 90° β = 90° γ = 90°	a = 8.98170 Å b = 8.98170 Å c = 11.006 Å α = 90° β = 90° γ = 120°	a = 8.92921 Å b = 8.92921 Å c = 10.97577 Å α = 90° β = 90° γ = 120°
volume	248.485 Å^3	768.9 Å^3	757.9 Å^3
R_{wp}	10.47%	12.87%	18.95%
R_p	6.98%	8.20%	11.42%

	$MAPbI_3$ (Heat)	$FAPbI_3$ (Heat)	$MA_xFA_{1-x}PbI_3$ (Heat)
crystal system	cubic	trigonal	trigonal
space group	*Pm3m*	*P3m1*	*P3m1*
unit cell dimensions	a = 6.36266 Å b = 6.36266 Å c = 6.36266 Å α = 90° β = 90° γ = 90°	a = 8.99217 Å b = 8.99217 Å c = 11.01171 Å α = 90° β = 90° γ = 120°	a = 8.95526 Å b = 8.95526 Å c = 10.97871 Å α = 90° β = 90° γ = 120°
volume	257.582 Å^3	771.1 Å^3	762.5 Å^3
R_{wp}	27.49%	13.78%	18.57%
R_p	16.35%	8.96%	11.40%
volume change	**9.097** Å^3	**2.2** Å^3	**4.6** Å^3

Figure 101: (a) Cubic (*Pm3m*) perovskite structure showing disorder in the MA counterion. (b) Tetragonal (*I4cm*) perovskite structure. (c) Trigonal (*P3m1*) perovskite structure showing disorder in FA. (d-f) PXRD of 3 perovskite samples fabricated from sequential deposition of MAI, FAI and mixture of MAI and FAI (1:1 by wt.) on PbI_2 film. FAI sample was annealed at 160 °C for 10 min and other two samples were annealed at 85 °C for 30 min. Some of the perovskite peaks are highlighted with the asterisk (*) symbol to distinguish from PbI_2 peaks. (g) Crystallographic data for perovskite samples from Reitveld refinement of PXRD spectra to known structures.

The EIS and PXRD results correlated with device performance in this study provide a comprehensive and revised picture of the origin of the photo-induced degradation of perovskites. The EIS studies show that that ion diffusion is associated with the degradation, and that the diffusion is light induced and thermally activated, and that the alkyl ammonium-type counterions

are the diffusion ions. PXRD proves that the perovskite lattices expand on heating, but that this process is reversible. There is a strong correlation between the ionic diffusion coefficient and the activation energy barrier for ion transport with device stability. In $MAPbI_3$, lower activation energy barrier coupled with a higher diffusion coefficient of ions leads to poor device stability under light and dark. Moreover, the $MAPbI_3$ activation energy decreases at high temperature, further promoting ion transport. By contrast, in mixed $MA_xFA_{1-x}PbI_3$ devices, a higher activation energy barrier coupled with the lower diffusion coefficient of ions leads to a better stability under light and dark. This last finding has important practical consequences in the search for more stable perovskite solar cell formulations.

3.2.7 Improving Device Stability

Since the ion diffusion is light induced but thermally activated, we hypothesized that the device stability would be further increased if the devices were operated under conditions that do not increase the device temperature. Indeed, with $MA_xFA_{1-x}PbI_3$, the PCE under white-LED light (*sans* IR component) illumination was stable over the full 20 h duration of an experiment, as shown in Figure 87. The device stability was also vastly improved when a KG5 filter was used to block the near-IR component of the AM1.5G illuminator. Finally, the device was also stable under standard AM 1.5G illumination when the device was air-cooled with a fan (Figure 103). Devices kept at 45 °C for 17 h under dark showed a 5% decrease in PCE when re-illuminated with an AM 1.5G illuminator. After 17 h at 45 °C, PCE of devices showed a 19% decrease under white-LED light and a 23% decrease with AM1.5G solar simulator (Figure 102a). All the device *J-V* characteristics were averaged over 4 samples and are shown in Figure 102b-d. These results conclusively show that *a combination of heat and light facilitates rapid ion diffusion and device degradation*. The enhanced stability under white LED along with the decrease in ion diffusion

coefficient (*vide supra*) indicates that perovskite active layer degradation is indeed correlated with alkyl ammonium transport. This may be due to accumulation of vacancies, which may destabilize the lattice, and causes collapse to PbI_2.

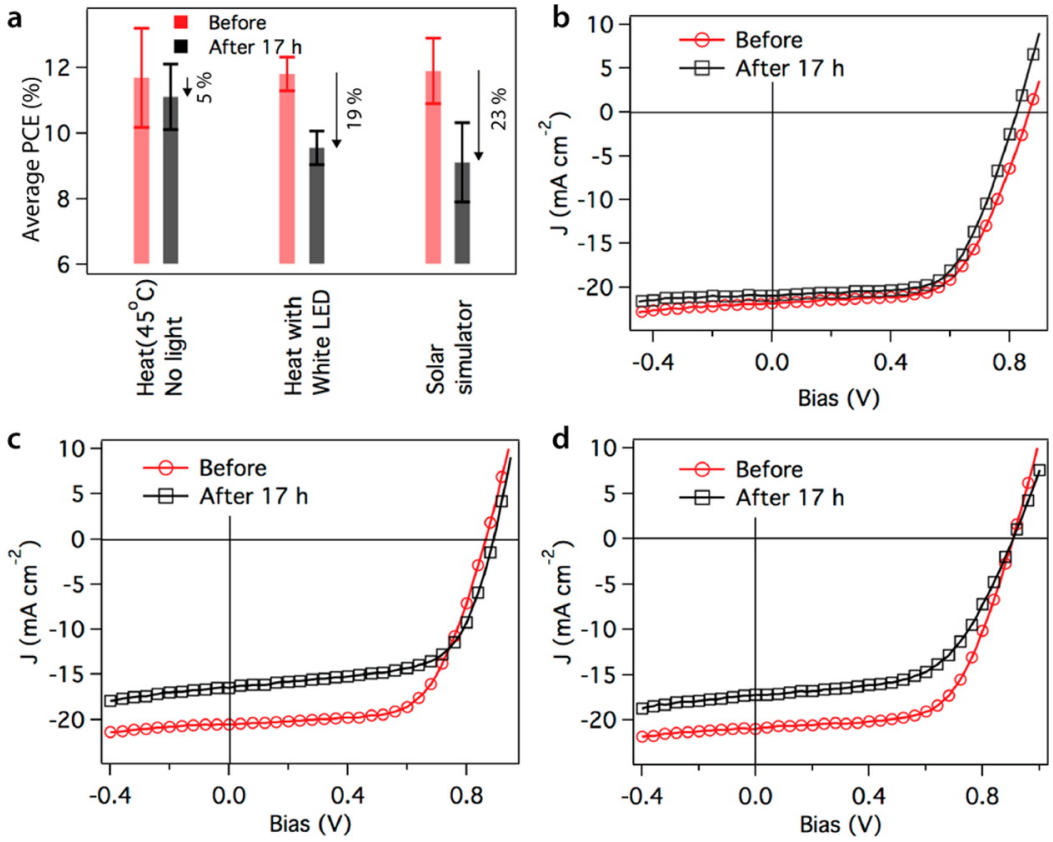

Figure 102: (a) Mixed counterions perovskite solar cell stability after 17 h continually under dark at 45 °C, white-LED light at 45 °C, and AM1.5G solar simulator at 100 $mW \cdot cm^{-2}$ light intensity. *J-V* curves averaged over 4 devices before and after (b) heating in dark at 45 °C, (c) heating at 45 °C under white-LED, and (d) AM1.5G solar simulator.

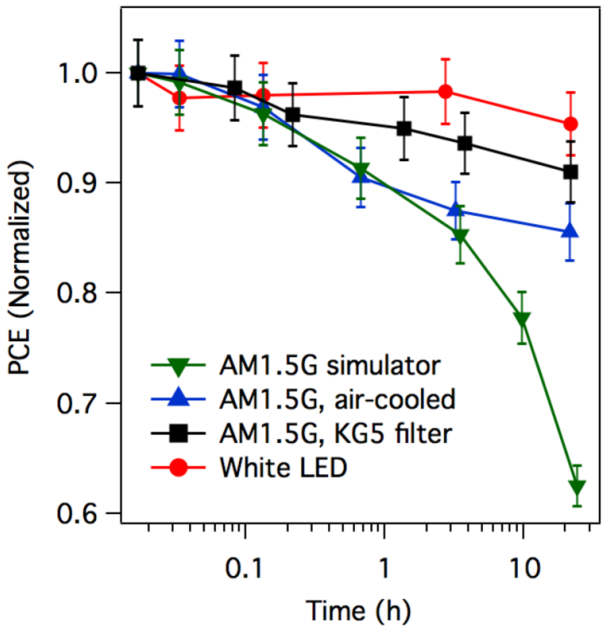

Figure 103: $MAPbI_3$ perovskite device stability (normalized PCE) under AM1.5G solar simulator at 79 $mW \cdot cm^{-2}$ and under AM1.5G solar simulator at 100 $mW \cdot cm^{-2}$ light intensity with a KG5 IR cut off filter, AM1.5G solar simulator with a fan cooler, and white-LED at 20 $mW \cdot cm^{-2}$. 3% error is accounted for J-V measurement hysteresis and lamp power fluctuation.

If perovskite-based photovoltaics are truly the future of cheap and efficient solar energy, they cannot degrade under sunlight. It is therefore imperative to develop a fundamental understanding of the light induced degradation pathways in perovskite active layers so that this problem can be solved. In this communication we have clarified the degradation mechanism of alkyl ammonium lead triiodide-based perovskite solar cells under continuous photo-illumination. We find that the degradation of perovskite solar cells under sunlight requires *both* an IR and a visible component of the solar spectrum. Further, the quasi-reversibility of the photo-induced degradation phenomenon is observed for the first time in these systems. EIS measurements provide evidence of fast ion transport of the ammonium counterions in the perovskite thin film, which for $MAPbI_3$ can be facilitated by lattice expansion accompanied with a phase transition under simulated solar spectrum containing infrared component. Thus, the photo-stability can be improved by reducing

the infrared component incident on the perovskite solar cells. Mixing a larger counterion (FA) with MA provides the right balance between device performance and stability by circumventing the phase change and increasing the activation energy barrier for ion transport.

3.3 Work Function Modification Using Functionalized Fullerenes for Enhanced Photovoltaic Performance

This chapter[††††] described the use of a functionalized fullerene molecule as an interlayer in perovskite-based solar cells between the electron transport layer and the anode. Interface engineering is critical for achieving efficient solar cells, yet a comprehensive understanding of the interface between a metal electrode and electron transport layer (ETL) is lacking. Here, a significant power conversion efficiency (PCE) improvement of fullerene/perovskite planar heterojunction solar cells from 7.5% to 15.5% is shown by inserting a fulleropyrrolidine interlayer between the silver electrode and ETL. The interface between the metal electrode and ETL is carefully examined using a variety of electrical and surface potential techniques. Electrochemical impedance spectroscopy (EIS) measurements demonstrate that the interlayer enhances recombination resistance, increases electron extraction rate, and prolongs free carrier lifetime. Kelvin probe force microscopy (KPFM) is used to map the surface potential of the metal electrode and it indicates a uniform and continuous work function decrease in the presence of the fulleropyrrolidine interlayer. Additionally, the planar heterojunction fullerene/perovskite solar cells are shown to have good stability under ambient conditions.

Perovskite solar cells have attracted extensive attention since the breakthrough in late 2012.[453,454,481-485] This emerging photovoltaic technology has been regarded as a promising path to cost-effective solar cells.[32,34,450,455,486-493] Typically, perovskite solar cells are

---

[††††] This chapter was adapted, with permission, from Liu, Yao, Monojit Bag, Lawrence A. Renna, Zachariah A. Page, Paul Kim, Todd Emrick, D. Venkataraman, and Thomas P. Russell. "Understanding Interface Engineering for High- Performance Fullerene/Perovskite Planar Heterojunction Solar Cells." *Advanced Energy Materials* 6, no. 2 (2016). I would like to acknowledge Dr. Yao Liu and Prof . Monojit Bag for device preparation and characterization, Dr. Zachariah page for material synthesis, and Paul Kim for electron microscopy.

fabricated with a mesoscopic or planar heterojunction active layer. In mesoscopic devices, perovskite is deposited onto a microporous scaffold (*e.g.* titanium dioxide (TiO_2), zinc oxide (ZnO), aluminum oxide (Al_2O_3)).[457] Planar heterojunctions have perovskite active layer sandwiched between charge selective transport layers.[457] Due to the high absorption coefficient,[480] low exciton binding energy[457,480] and long carrier-diffusion length,[480,494,495] metal halide perovskites with organic counterions have enabled both mesoscopic and planar solar cells to achieve power conversion efficiencies (PCEs) > 18%,[458,496-500] with state-of-the-art mesocopic devices reaching certified PCE of 20.1%.[498] To date, perovskite solar cells with planar heterojunction structures are slightly less efficient than their mesoscopic counterparts, but their fabrication is straightforward and compatible with well-established solution-based low temperature fabrication roll-to-roll procedures used for the production of polymer solar cells.[458,496-498]

The incorporation of charge selective transport layers at the electrode/active layer junctions has often been regarded as a prerequisite to realize efficient charge extraction in planar perovskite solar cells.[501] Thus, great effort has been focused on the development and understanding of interfacial engineering between perovskite and electron transport layers (ETLs) or hole transport layers (HTLs) for effective charge carrier separation.[23,502-505] In perovskite solar cells, the diffusion length of electrons is shorter than holes and it is regarded as a major limitation associated with these devices.[506,507] To address this limitation, compact semiconducting metal oxide (e.g., ZnO, TiO_2) ETLs have been used to facilitate electron transport in planar heterojunction devices.[452,454,489,508] In addition to the use of metal oxide layers, electrode work function modification by an interlayer can further improve the performance of perovskite solar cells.[458,509-516] For example, Yang et al. incorporated polyethyleneimine ethoxylated

(PEIE) between indium tin oxide (ITO) electrode and TiO_2 to significantly increase the PCE of planar heterojunction perovskite solar cells, identifying that reduction of ITO's work function (Φ) by PEIE, due to the presence of a negative interfacial dipole, was a leading contributor to the observed device performance improvement.[458] Phenyl-C_{61}-butyric acid methyl ester ($PC_{61}BM$) has been used as an alternative ETL to metal oxide layers in planar heterojunction devices, providing more efficient charge injection from perovskite,[497] while allowing for low-temperature solution processing that precludes ITO's use as an electron-extracting electrode.[497,517,518] In addition, the deposition of $PC_{61}BM$ on perovskite film[473] or making perovskite-$PC_{61}BM$ hybrid active layer[519] is effective to passivate charge trap states and defects on the surface and grain boundaries of the perovskite materials, which is beneficial for electron extraction from the perovskite active layer and eliminating the notorious photocurrent hysteresis. It is also found that the electron transfer from perovskite to TiO_2 can be promoted by modification of the TiO_2 contact layer using a C_{60} self-assembled monolayer and consequently the adverse effect of photocurrent hysteresis can be addressed.[520] Utilizing ITO as a hole-extracting electrode in perovskite-based solar cells (described in the literature as inverted devices) has only been studied since 2013.[517] However, there is almost equal evidence to support that both high work function metal cathode[497,521] and low work function meal cathode[496,518] and metal cathode with surface modification[510-516] can be used to achieve excellent device performance. Hence, the interface between cathode and PCBM has not been fully understood in inverted perovskite solar cells. For example, several groups have reported fullerenes,[510,512,516,522] other small molecules[513,517,523] or polymers[514] as interfacial modifiers of high work function metal cathode (e.g., Ag) in inverted perovskite solar cells. A noteworthy example was recently reported by Azimi et al.[512] where perovskite solar

cell efficiency was improved from 9.4% to 13.4% upon reducing the work function of silver electrode due to the interfacial dipoles produced by a fullerene interlayer.

Interface modification layers can lower the electrode Φ due to the presence of a negative interfacial dipole, causing an increase in the electrostatic potential across the device.[524] The strengthened electric field increases free charge generation and extraction efficiency to enhance the short-circuit current density (J_{SC}) and fill factor (*FF*). The interfacial dipole moreover increases the Φ offset between the two electrodes of the device, thus maximizing open-circuit voltage (V_{OC}).[525,526] However, the influence of interface modification on electronic transport and recombination kinetics in perovskite solar cells has not been fully investigated, though it is critical to understand interface engineering to further enhance device performance. We recently developed a fulleropyrrolidine based interface modification layer (C_{60}-N, Figure 104) that forms a large negative interfacial dipole (-0.8 eV) on Ag electrodes as measured by ultraviolet photoelectron spectroscopy (UPS).[525] Therefore, C_{60}-N is an ideal interfacial modification material for the investigation of interface engineering in inverted perovskite solar cells. Herein, we show that high performance and air stable fullerene/perovskite planar heterojunction solar cells can be fabricated with C_{60}-N as an interlayer between $PC_{61}BM$ and silver (Ag) electrode, achieving a maximum PCE of 15.48%. Electrochemical impedance spectroscopy (EIS) and Kelvin probe force microscopy (KPFM) measurements were utilized to fully understand how the interface between metal electrode and ETL influence device performance.

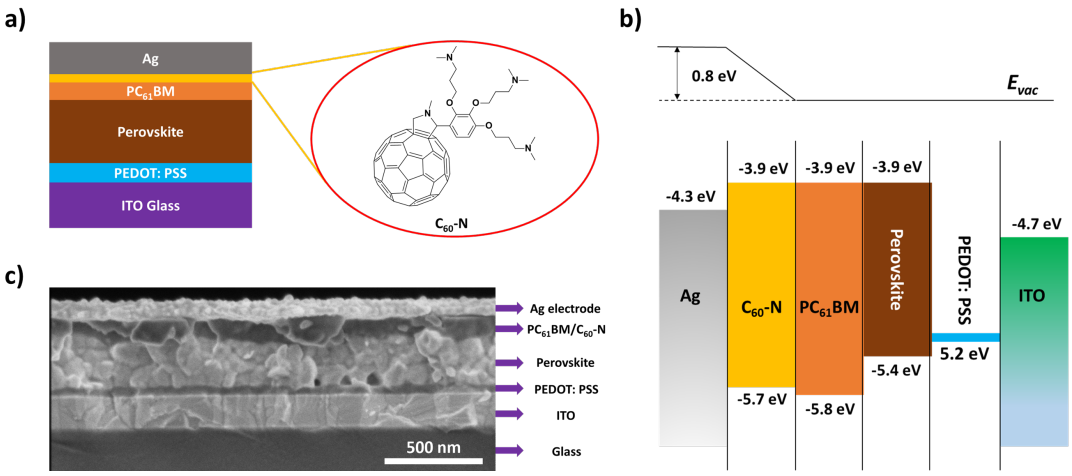

Figure 104: a) Device architecture and the molecular structure of C_{60}-N; b) energy level diagram of the device (interfacial dipole value is obtained by UPS measurement[525]); c) cross-sectional SEM image of the device.

3.3.1 Photovoltaic Performance

Fullerene/perovskite planar heterojunction solar cells shown in Figure 104were fabricated by a sequential deposition process starting from ITO (hole extracting electrode).[450] The conducing polymer poly(3,4-ethylenedioxythiophene):poly(styrenesulfonate) (PEDOT:PSS), which is widely applied in polymer solar cells as a HTL, was coated onto ITO to provide a high Φ electrode (Figure 104). The PbI_2 solution was then spin coated onto PEDOT: PSS modified ITO substrates, followed by thermal annealing, which is critical to promote the crystallization of the as-spun PbI_2 film. A mixture of MAI and FAI (1:1 by wt.) was drop coated from isopropanol onto the crystallized PbI_2 film, followed by spin coating to remove excess solution. Thermal annealing was used to promote the reaction of MAI and FAI with PbI_2 to form perovskite crystals (Figure 105). Shown in Figure 104c, the uniform perovskite crystals (~150 nm) form condensed packing with a film thickness of ~300 nm. $PC_{61}BM$ (ETL) was then spin coated onto the perovskite active layer from chlorobenzene, followed by C_{60}-N (interface modification layer) from 2,2,2-trifluoroethanol (TFE) and finally Ag electrode (100 nm) was deposited by thermal evaporation.

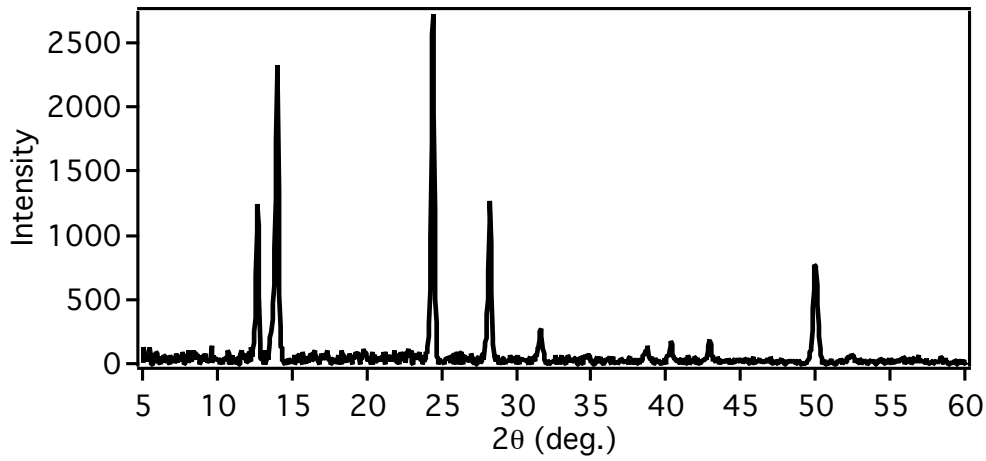

Figure 105: XRD of mixed counterion perovskite crystals formed by combining MAI and FAI with PbI_2.

As shown in Figure 106a, the devices without C_{60}-N interlayers gave maximum PCEs of 7.50%, noting the presence of an S-shaped *J-V* curve, which arises from carrier accumulation inside of the device.[527] The insertion of C_{60}-N interlayers led to good rectification with a maximum PCE of 15.48%, indicating enhanced carrier extraction from the active layer after surface modification with interlayer. PCE histogram shown in Figure 106b indicates that the average efficiency is ~13%, which is calculated from 85 devices (Table 12, Figure 104). Additionally, no *J-V* hysteresis was observed upon forward and reverse device sweeping, suggesting that the perovskite active layer and interfaces have a negligible number of defects (Figure 106c).[528] The lack of hysteresis is important from a device characterization standpoint, since it removes variability arising from active layer imperfections, allowing emphasis to be given to the effects of interfacial engineering on device performance. External quantum efficiency (EQE) profile shown in Figure 106d demonstrates a broad photo-response extending to ~ 800 nm with a peak EQE value of ~ 91 %.

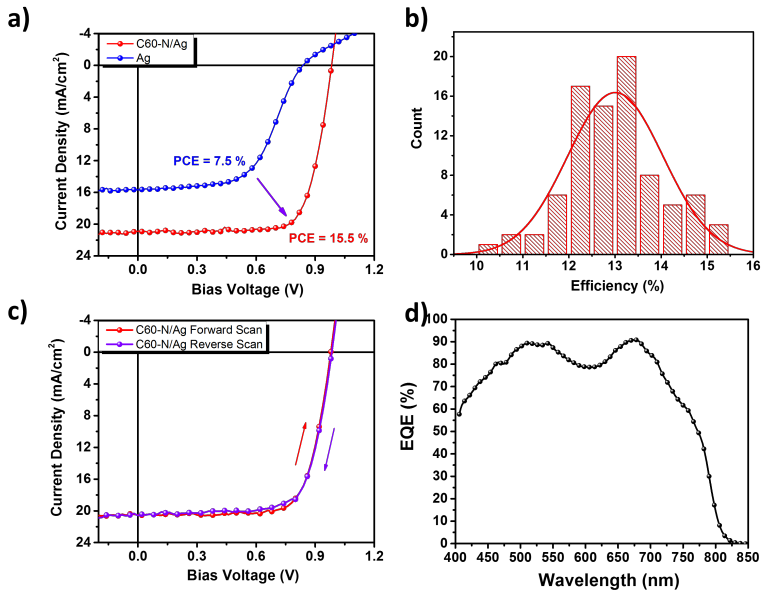

Figure 106: a) J-V curve of the devices with and without a C_{60}-N modification layer; b) PCE histogram of 85 devices containing C_{60}-N interlayers; c) hysteresis investigation of the device with C_{60}-N interlayer and d) it is corresponding EQE profile.

Table 12: Device Performance

Device Structure	Device Amount	V_{OC} (V)	J_{SC} (mA/cm^2)	FF (%)	PCE (%)
Bare Ag cathode	12	0.87 ± 0.01	15.93 ± 0.82	52.2 ± 4.1	7.17 ± 0.27
Ag/C_{60}-N cathode	85	0.98 ± 0.03	18.95 ± 1.06	70.4 ± 3.1	13.00 ± 1.04

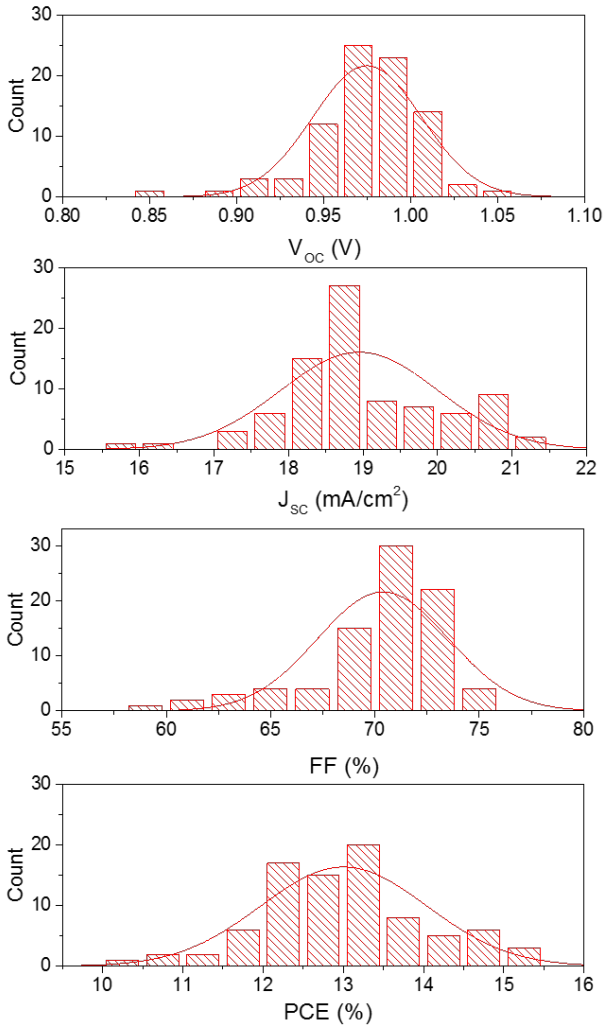

Figure 107: VOC, JSC, FF and PCE histogram of 85 devices containing a C60-N interlayer.

3.3.2 Electrochemical Impedance Spectroscopy (EIS) Characterization

We carried out EIS characterization to understand the recombination losses and charge transport properties upon introducing a C_{60}-N interlayer between the ETL and Ag electrode. In the EIS measurement, a small AC voltage of 20 mV is applied under constant illumination to measure device impedance as a function of frequency (ω), sweeping from 100 Hz to 1 MHz. The Nyquist plot shown in Figure 108a has two distinct charge transport regimes; a low frequency component

(<2.5 kHz) that arises predominantly from the slow relaxation/diffusion of ions, and a high frequency component (> 2.5 kHz), originating from the electronic transport and recombination kinetics. At 0 V applied DC bias the high frequency impedance is associated with the recombination resistance (R_{rec}). We observed that the R_{rec} increased (shown as dotted lines in Figure 108a) for devices containing a C_{60}-N interlayer compared to bare Ag devices, which leads to reduced recombination losses.[471] Additionally, the lifetime (τ_n) of free carriers increased from 12 μs to 16 μs for bare Ag to C_{60}-N/Ag devices, as calculated from the Nyquist plot. EIS measurements were also used to generate Mott-Schottky (MS) plots for bare Ag and C_{60}-N/Ag devices, where the interfacial charge density is inversely proportional to the slope of the MS plot, assuming an equivalent dielectric constant for both devices. The slope of the C_{60}-N/Ag devices is two orders of magnitude higher than bare Ag devices, indicating low interfacial charge density and thus excellent charge extraction at the metal electrode interface for the devices containing C_{60}-N. Additionally, the high charge accumulation at the $PC_{61}BM$/Ag interface for devices without an interlayer helps to explain the observed S-shaped J-V curve and low V_{OC} for the bare Ag device. These EIS measurements demonstrate the importance of an interlayer at the electron extracting electrode/ETL interface in planar heterojunction perovskite solar cells to reduce recombination losses and prevent interfacial charge build-up by assisting electron transport.

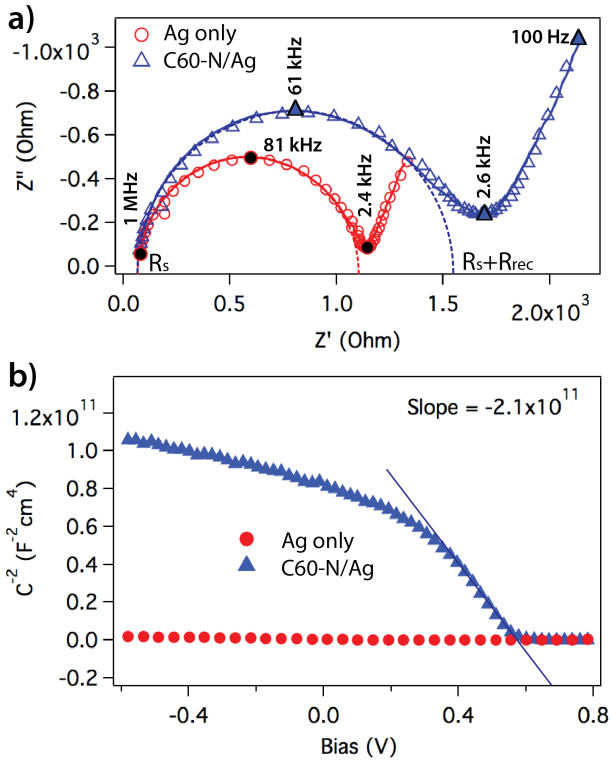

Figure 108: a) Nyquist plot of planar heterojunction perovskite solar cells. Dashed lines represent the recombination semicircle. Characteristic frequencies are highlighted with solid symbols; b) Mott-Schottky plot of two perovskite samples measured at 10 kHz probe frequency.

3.3.3 Kelvin Probe Force Microscopy (KPFM) Measurements

KPFM is an effective technique to understand the working mechanism of perovskite solar cells.[529,530] To further understand the interface modification in our devices, we carried out KPFM measurements to determine the contact potential differences (V_{CPD}) between the atomic force microscopy (AFM) probe and bare Ag electrode, Ag/$PC_{61}BM$, or Ag/C_{60}-N. In a typical KPFM experiment, a first pass scan is done in mechanically driven tapping mode to measure topography, and then a second pass scan is done — so called nap mode — at Δz above the surface, where the cantilever is driven at its AC voltage resonant frequency to determine V_{CPD}. Potential differences between the Pt/Ir probe and the sample cause mechanical oscillations in the probe and are offset by an applied voltage (V_{DC}) via a potential feedback loop; therefore $V_{DC} = V_{CPD}$.[531]

The samples for KPFM were prepared by evaporating Ag (70 nm) onto a clean Si wafer, followed by spin coating $PC_{61}BM$ from chlorobenzene or C_{60}-N from TFE. Potential maps (Figure 109a-c, Figure 110) were measured at three different locations on the sample, and the Si wafer was kept grounded throughout all measurements. Potential histograms were made and fit with Gaussian curves to find the mean V_{CPD} for the sample. Representative V_{CPD} histograms for Ag electrode, Ag/ $PC_{61}BM$, and Ag/C_{60}-N are shown in Figure 109d, where the V_{CPD} of bare silver is offset to 0 V in order to represent the change in V_{CPD} for $PC_{61}BM$ and C_{60}-N coated samples. By this method we found ΔV_{CPD} between bare Ag and Ag/$PC_{61}BM$ to be $0.14 \pm 0.01 V$, and between bare Ag and Ag/C_{60}-N to be $0.62 \pm 0.03 V$. By the equation:[531] $V_{CPD} \approx (\Phi_{probe} - \Phi_{sample})/-e$ we estimated a 0.62 eV Φ decrease when C_{60}-N is coated on Ag relative to bare Ag and 0.47 eV Φ decrease for C_{60}-N/Ag relative to $PC_{61}BM$/Ag. This apparent decrease in Ag Φ arises from the presence of a negative interfacial dipole between Ag and C_{60}-N, and explains the improved V_{OC} and rectification for devices containing C_{60}-N interlayers. Additionally we measured ΔV_{CPD} of as-prepared devices by peeling off the silver electrodes of the devices using Scotch® tape and making KPFM measurements on the underside of the electrodes for solar cells with and without C_{60}-N interlayers (Figure 111). V_{CPD} histograms of potential maps at three different locations are shown in Figure 109e for samples with and without C_{60}-N interlayer, showing a $\Delta V_{CPD} = 0.27 \pm 0.01$ V (decreasing Φ) for devices with C_{60}-N interlayers relative to those without ($PC_{61}BM$/Ag). Although a discrepancy exists between ΔV_{CPD} measured for freshly cast (0.47 V) *vs.* peeled (0.27 V) Ag substrates, the overall result (decreased Ag Φ) correlates well with the observed gain in V_{OC} for perovskite solar cells that have C_{60}-N interlayers.

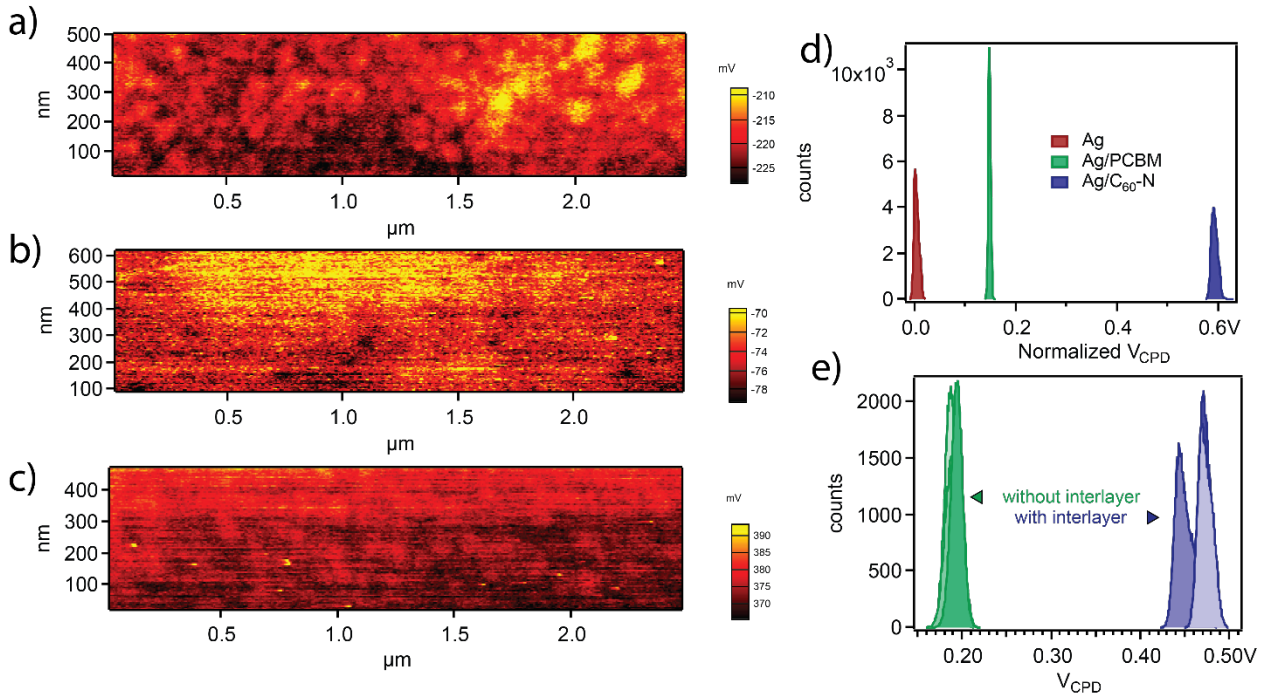

Figure 109: Surface potential maps from KPFM measurements for a) bare Ag, b) PCBM/Ag, and c) Ag/C_{60}-N. d) Representative V_{CPD} histograms of surface potential maps offset to put V_{CPD} of Ag at 0 V to better show ΔV_{CPD} with PCBM and C_{60}-N. e) V_{CPD} histograms of surface potential maps of Ag electrodes peeled from as-prepared devices with and without C_{60}-N interlayer at three different locations each.

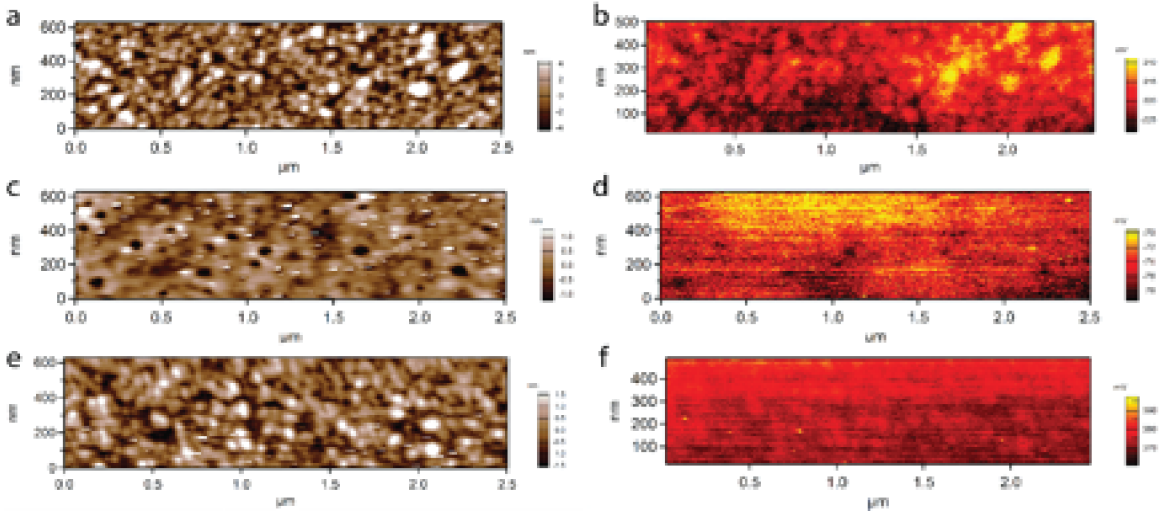

Figure 110: Topographic AFM and KPFM surface potential maps for (a,b) Ag, (c,d) Ag/PCBM, and (e,f) Ag/C60-N respectively.

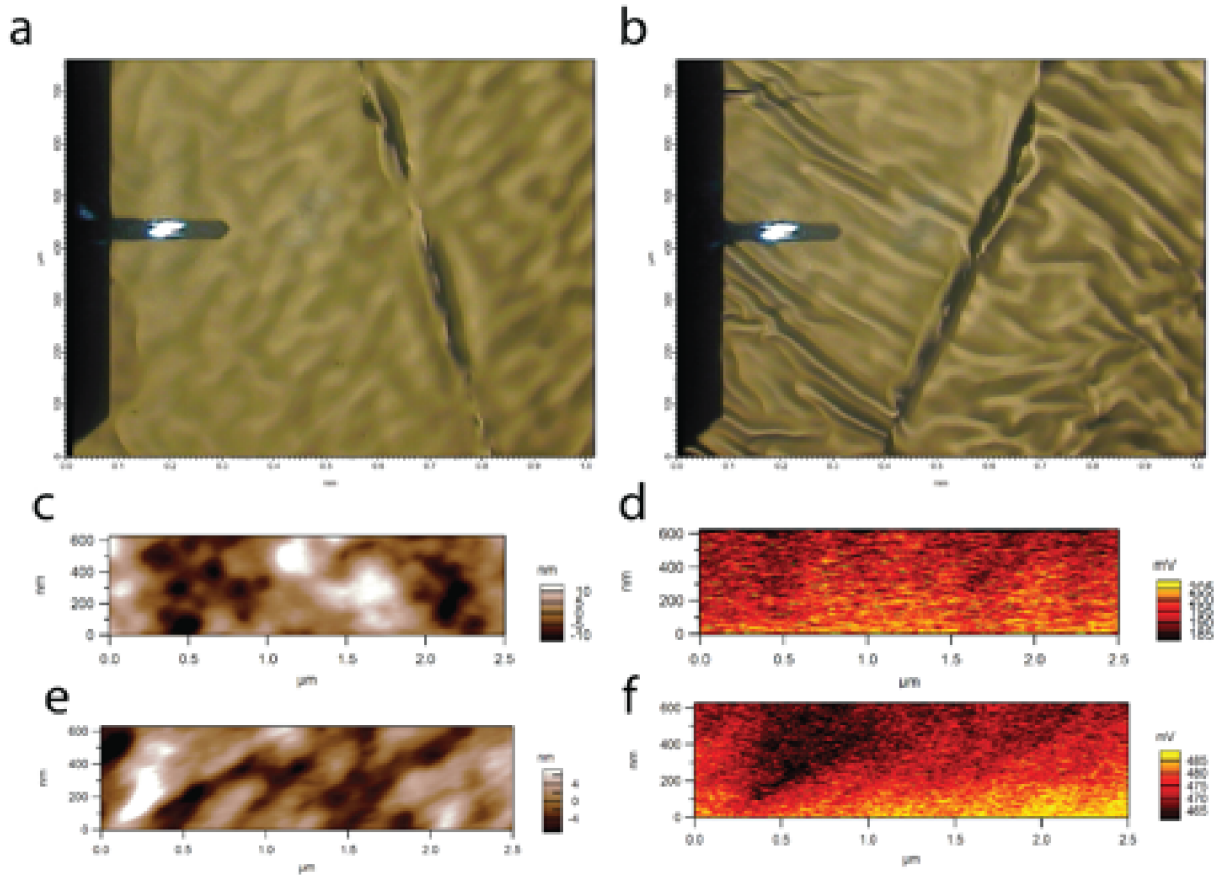

Figure 111: (a,b) Optical micrographs with AFM probe for scale of the underside of Ag electrodes peeled off of devices without and with C_{60}-N interlayers respectively. Topographic AFM and KPFM surface potential maps for (c,d) Ag electrodes from devices without C_{60}-N interlayers and (e,f) with C_{60}-N interlayers respectively.

3.3.4 Device Stability Investigation

It has been shown that the half-life time of some perovskite solar cells with planar heterojunction architecture cannot surpass 2 days under ambient atmosphere.[458,532] We are also interested in the ambient stability of our devices (Figure 112). We found that the PCEs of these devices drop rapidly in the initial ~30 hours, ~ 12% decrease on average. However, after storing for ~30 hours in air, the PCEs of these devices remained relatively stable even up to ~80 hours. After 2 months of storage in air it was found that these devices still maintained an average PCE of 6.50%. Though the reason for the stability of these devices is not clear, we speculate that the cover layer (C_{60}-N

and $PC_{61}BM$) is more hydrophobic than perovskite layer (Figure 113) and works like an encapsulation layer that blocks the penetration of humidity.[497]

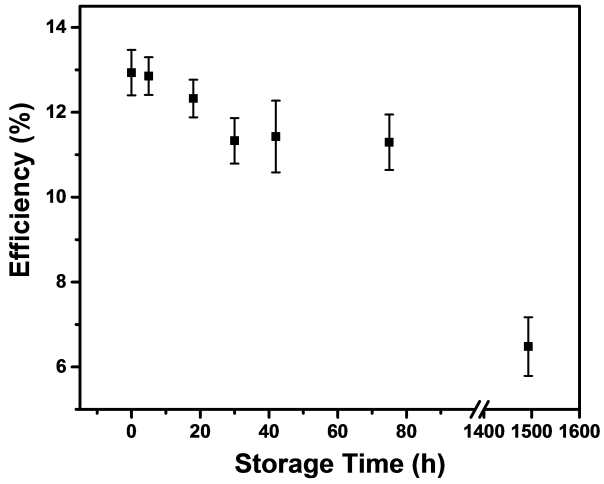

Figure 112: Stability investigation performed by storing 6 unencapsulated devices in air and in the absence of light.

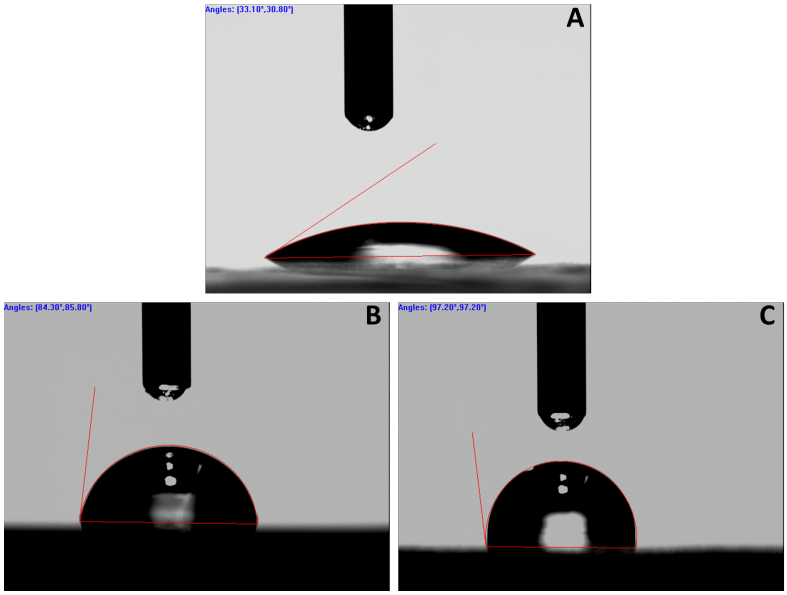

Figure 113: Contact angle measurement of (a) perovskite film; (b) C_{60}-N thin film and (c) $PC_{61}BM$ thin film (the water droplet is 100 µL).

We have demonstrated a significant improvement in PCEs of fullerene/perovskite inverted planar heterojunction solar cells from 7.50% to 15.48% by inserting C_{60}-N as interlayer between metal electrode and ETL. A variety of electrical and surface potential characterization techniques were used to understand the interface between metal electrode and ETL. With the aid of these measurements, we answer three basic questions about the role of interface engineering in inverted perovskite solar cells: first, optimizing interface between metal electrode and ETL can enhance recombination resistance and reduce recombination loss; second, lowering work function of electron extracting electrode can increase electron extraction rate at perovskite/ETL interface; finally, a longer lifetime of the free careers can be achieved by modification of this interface. KPFM characterization successfully mapped the surface potential of Ag electrode with and without surface modification, indicating a uniform and continuous work function decrease after surface modification. The mapping results of the Ag electrode surface directly contacted with ETL in real devices show an apparent work function decrease after the insertion of C_{60}-N interlayer, which correlates well with the V_{OC} gain seen in actual devices. Besides clarifying these important issues, the stability investigation of these devices indicates that interface engineering is a promising method for achieving high performance and air stable inverted perovskite solar cells.

3.4 An Aqueous Processed Polymer Hole Extraction Layer with Increased Work Function Compared to PEDOT:PSS

This chapter[‡‡‡‡] discusses the use of hole transport material for perovskite-based solar cells which can be processed from water. We show that this material improves device performance compared to the standard transport material, as a result of the increased built in field through the device. The increased built in field manifests due to the higher work function of the polymer as measured by KPFM.

Inverted planar perovskite solar cells are of considerable interest[33,41,485,491,497,500,522,533-536] since the discovery of bipolar transport properties in perovskites[451,455] and the report on the perovskite/fullerene planar heterojunction structure in 2013.[517] Compared to titanium dioxide (TiO_2) based planar perovskite solar cells that usually require high-temperature (>450 °C) treatment,[33,498-500,537-542] inverted perovskite solar cells are more compatible with facile solution processing techniques used for producing organic solar cells.[29,33,500,543-545] Optimization of perovskite film morphology on poly(3,4-ethylenedioxythiophene):poly(styrenesulfonic acid) (PEDOT:PSS) coated substrates has enabled inverted perovskite solar cells to achieve power conversion efficiencies (PCEs)[496,497] approaching the record values obtained by their TiO_2-based counterparts.[498]

---

‡‡‡‡ This chapter was adapted, with permission, from Liu, Yao, Lawrence A. Renna, Zachariah A. Page, Hilary B. Thompson, Paul Y. Kim, Michael D. Barnes, Todd Emrick, Dhandapani Venkataraman, and Thomas P. Russell. "A Polymer Hole Extraction Layer for Inverted Perovskite Solar Cells from Aqueous Solutions." *Advanced Energy Materials* 6, no. 20 (2016). I would like to acknowledge Dr. Yao Liu for device preparation, Dr. Zachariah A. Page for material synthesis, Hilary B. Thompson for photoluminescence measurements, and Paul Y. Kim for electron microscopy.

Particularly, inverted perovskite/fullerene planar heterojunction solar cells effectively eliminate or suppress photocurrent hysteresis associated with perovskites.[473,519]

In an inverted architecture, the perovskite film is deposited on top of a hole extraction layer (HEL), typically PEDOT:PSS.[33] However, the acidity of PEDOT:PSS is often detrimental to device performance and stability.[357,546] Several solution processable inorganic substitutes for PEDOT:PSS, such as vanadium oxide (V_2O_5),[543] nickel oxide (NiO_X),[35,547,548] and copper iodide (CuI),[549] have been examined as HELs in inverted perovskite solar cells; unfortunately, their processing methods are more complicated and less environmentally friendly than PEDOT:PSS cast from aqueous solutions. To maximize device efficiency, high-temperature annealing is required for V_2O_5 (500 °C)[543] and NiO_X (300 °C),[502,550] and CuI is cast from volatile organic solvents (e.g., acetonitrile).[549] Hence, novel organic HELs have emerged as promising alternatives to PEDOT:PSS,[551-554] in particular polyelectrolytes due to their wettability by the perovskite precursor solution.[555] For example, Choi et al. reported a water/methanol-processed polyelectrolyte as a hole extraction material in inverted perovskite solar cells, affording a maximum PCE of 12.5%,[555] while Li et al. developed a water soluble polyelectrolyte for inverted perovskite solar cells that required thermal annealing at 140 °C for 30 min to achieve a maximum PCE of 16.6%.[556]

To efficiently extract holes from perovskite active layer and generate large built-in potential (V_{bi}) across the devices, we sought a material that possesses relatively high work function (W) and simplifies the preparation of high-quality perovskite layers. Recently, we found that poly(arylene-vinylene) (PAVs) with polar side chains can be synthesized by the Horner–Wadsworth–Emmons coupling/polymerization in water without using toxic reagents/catalysts.[557] This method provides an avenue to produce PAVs with a broad

backbone modification, especially to facilitate the introduction of electron-deficient monomers into the polymer backbone, which lowers the highest occupied molecular orbital (HOMO) energy level of the resulting conjugated polymer and thus increases the work function of the material.[557] Also, this new method provides a route to fabricate PAVs with reasonably high molecular weight and a high degree of *trans*-vinylene linkages that promote planarization of the polymer backbone by removing torsional interactions between aryl-rings, thus extending conjugation. Here, we show that a PAV-based conjugated polyelectrolyte (PVBT-SO_3) developed through this polymerization strategy can be used as a hole extraction material for efficient inverted perovskite solar cells that can be cast from aqueous solutions and used without thermal annealing.

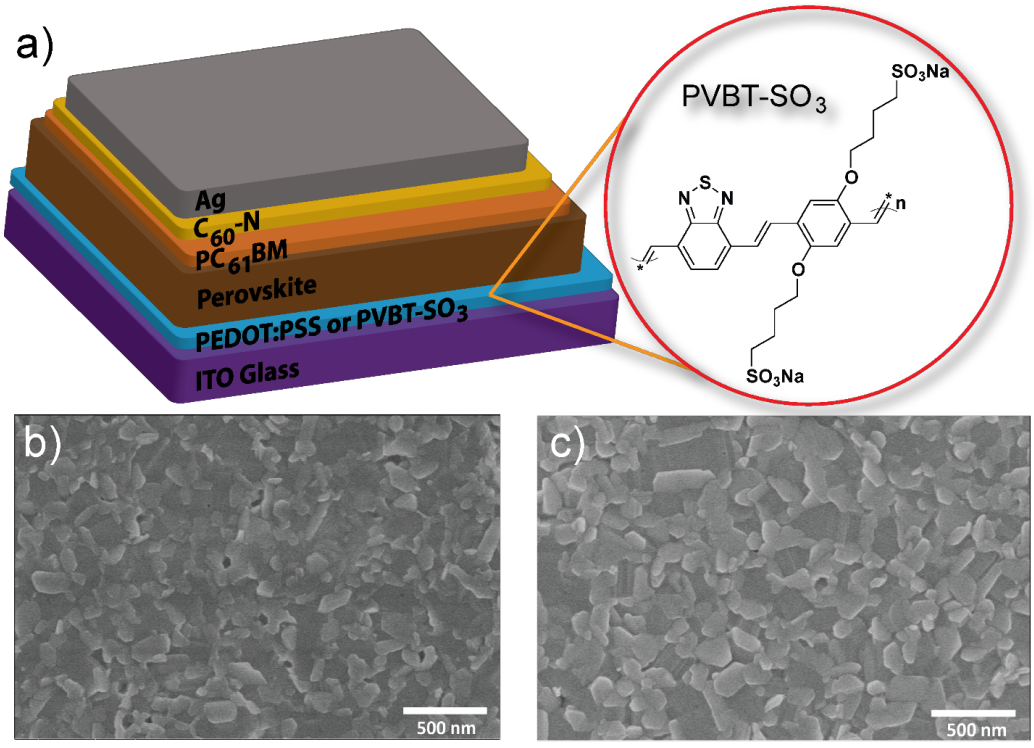

Figure 114: a) Device architecture and molecular structure for PVBT-SO_3; scanning electron microscopy (SEM) images of perovskite film on b) ITO/PEDOT:PSS substrate and c) ITO/PVBT-SO_3 substrate.

3.4.1 Device Structure and Characterization

Fullerene/perovskite planar heterojunction solar cells, shown in Figure 114a, were fabricated by a one-step deposition process starting from indium tin oxide (ITO) substrates (hole extracting electrode). Aqueous solutions of PEDOT:PSS or PVBT-SO_3 were spin-coated onto ITO substrates to serve as the HEL. PVBT-SO_3 formed uniform films on ITO substrates, even for films 5 nm in thickness, with no aggregation observable by optical microscopy (Figure 115). The perovskite precursor solution ($Pb(OAc)_2$ and methylammonium iodide (MAI)) was spin-coated onto an ITO/HEL substrate, followed by mild thermal annealing (at 90 °C for 5 min) to form the photoactive layer. As shown in Figure 114b-c, uniform and continuous perovskite films formed on the ITO/HEL substrates. Notably, perovskite films on ITO/PVBT-SO_3 substrate had larger crystallites (crystal size ≤200 nm) and were free of pinholes when compared to films on ITO/PEDOT:PSS substrates. Powder X-ray diffraction (Figure 116) showed peaks attributable to (100), (111), (200), and (220) planes of the tetragonal phase of the perovskite on both glass/PEDOT:PSS and glass/PVBT-SO_3 substrates. To facilitate selective electron extraction from the perovskite, phenyl-C_{61}-butyric acid methyl ester ($PC_{61}BM$) was spin-coated onto the perovskite layer from chlorobenzene. This was followed by spin-coating an interface modification layer of C_{60}-N[525] (Figure 117) from 2,2,2-trifluoroethanol (TFE). Silver electrodes were then thermally evaporated onto the C_{60}-N layer for electron extraction as shown in Figure 114a.

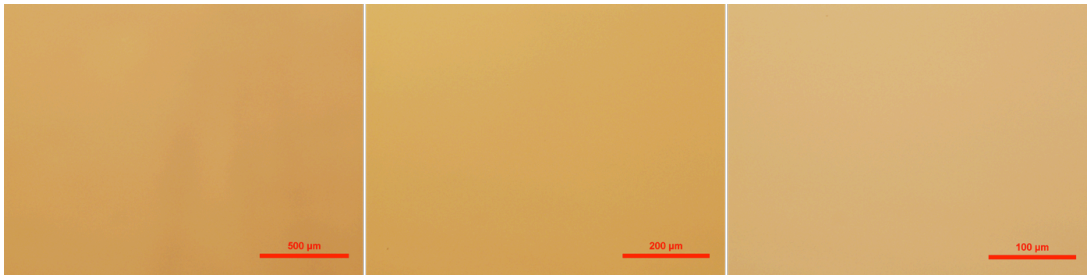

Figure 115: Optical microscopy images of PVBT-SO_3 thin film (5 nm) on ITO/Glass substrates.

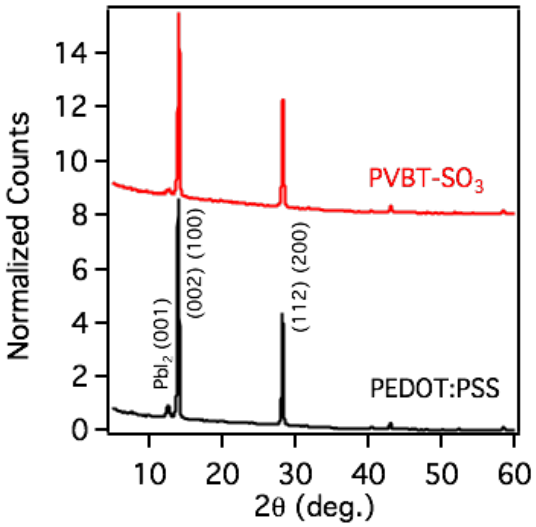

Figure 116: X-ray diffraction of the perovskite films on PVBT-SO_3/glass and PEDOT:PSS/glass substrates. Spectra are normalized by their respective PbI_2 (001) peaks.

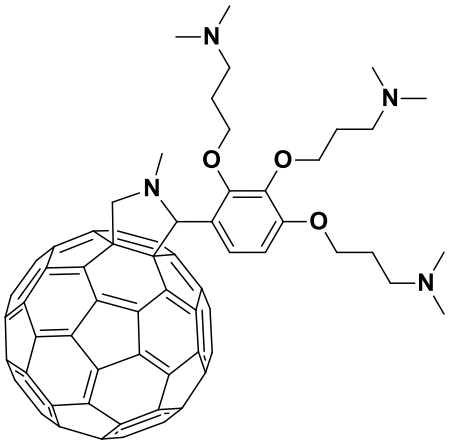

Figure 117: Molecular structure of C_{60}-N

3.4.2 Photovoltaic Performance

As shown in Figure 118a, devices utilizing the conventional PEDOT:PSS HEL gave a maximum PCE of 12.6% with an open circuit voltage (V_{OC}) of 0.89 V, a short circuit current density (J_{SC}) of 19.6 mA cm^{-2}, and a fill factor (FF) of 72.0%. This PCE is comparable to that reported by Bolink and co-workers using the same perovskite precursor and mild thermal

treatment (90 °C for 5 min).[558] For devices with a PVBT-SO_3 HEL, the influence of the HEL thickness was probed. Devices with a thin HEL (5 nm) show a slightly higher J_{SC}, but a relatively lower FF, while with a thickness of 20 nm, both the J_{SC} and FF of the devices decease (see Figure 119 and Table 13). Space charge limited current measurements yielded a hole mobility of $2.67 \times 10^{-3} cm^2\ V^{-1}\ s^{-1}$ for PVBT-SO_3 (Figure 120), which may not provide sufficient hole transport for the thicker films (20 nm). Hence, we found 10 nm to be an optimum thickness for the PVBT-SO_3 HEL. The use of PVBT-SO_3 as the HEL (10 nm) afforded a maximum PCE of 15.9% with a V_{OC} of 0.97 V, a J_{SC} of 21.2 mA cm^{-2}, and a FF of 77.4%. Thus, PCEs achieved by the as-spun PVBT-SO_3 layer are 26% higher than the device based on PEDOT:PSS (where the HEL required more extensive thermal annealing). Notably, the PVBT-SO_3 containing devices show significantly less hysteresis than devices with PEDOT:PSS layers.

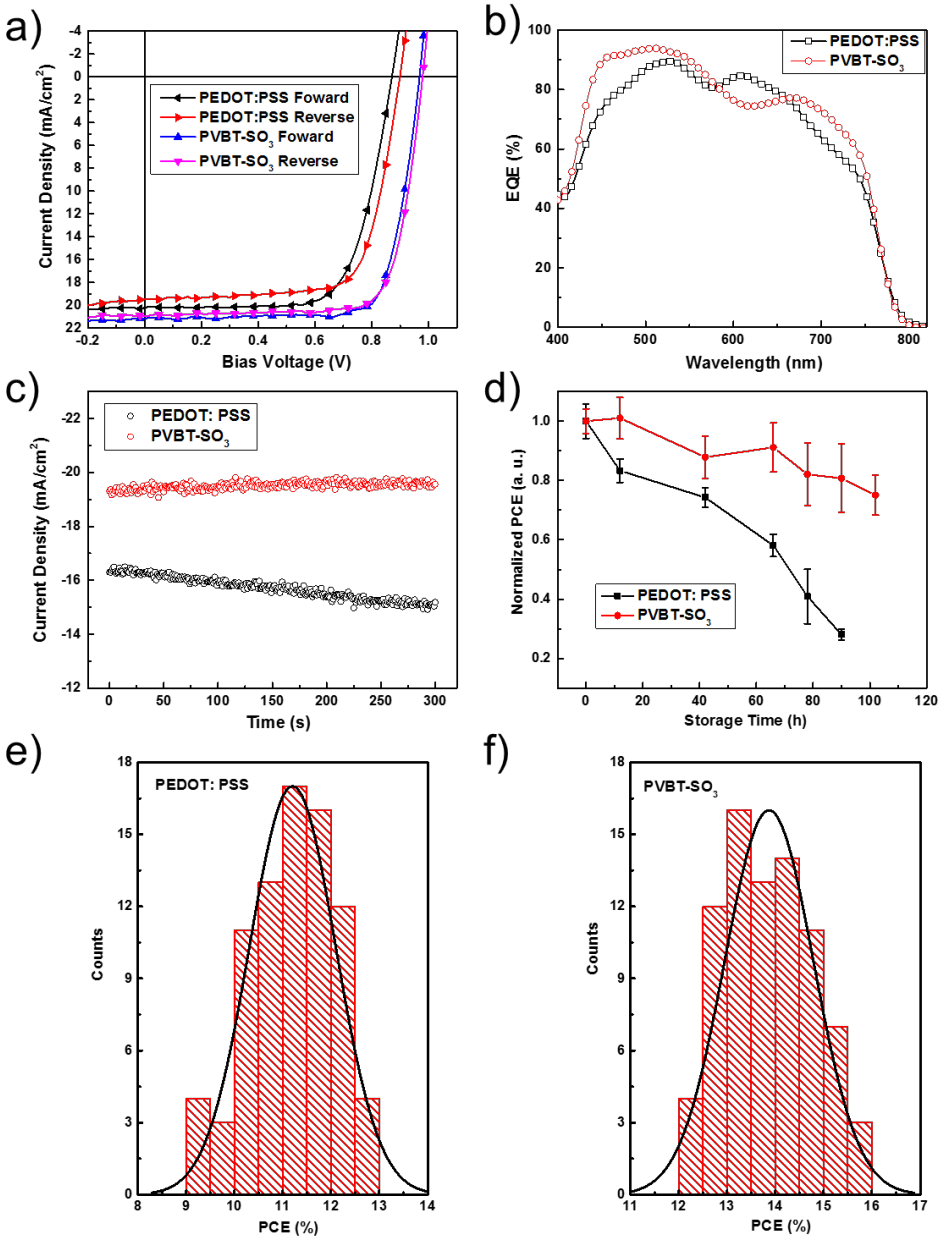

Figure 118: a) Current density (*J*)-voltage (V) curves of devices based on PEDOT:PSS and PVBT-SO_3 HELs; b) EQE profiles of the devices based on PEDOT:PSS and PVBT-SO_3; c) steady-state measurement of the encapsulated devices held at the maximum power point (the PEDOT: PSS device was biased at 0.7 V and the PVBT-SO_3 device was biased at 0.8 V); d) long term stability measurement of the unencapsulated devices (5 devices of each type) stored under ambient atmosphere at 20-30% relative humidity; PCE histograms generated from 80 device measurements for e) PEDOT:PSS and f) PVBT-SO_3 containing devices.

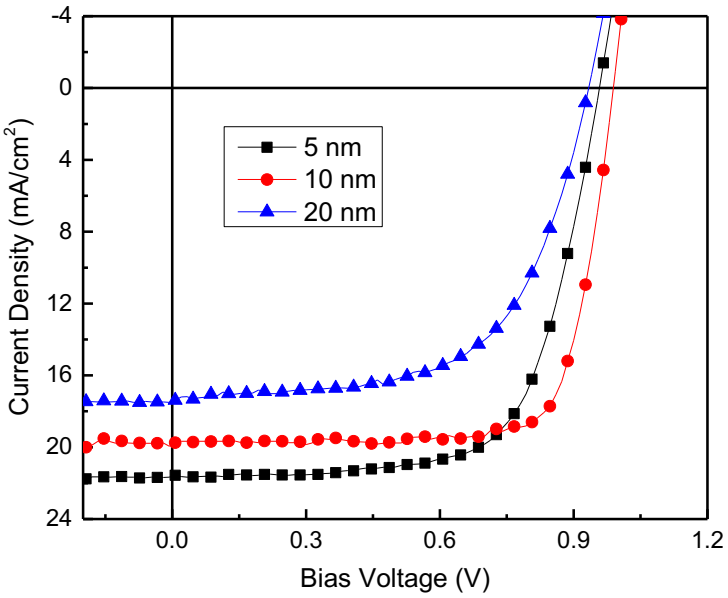

Figure 119: J-V curves of perovskite solar cells containg PVBT-SO_3 HEL with different thickness (5nm, 10 nm, and 20 nm).

Table 13: Device parameters of perovskite solar cells containg PVBT-SO_3 HEL with different thickness (Standard deviation for averages obtained from six devices and all the devices are fabricated using the same batch precursor).

HEL Thickness	V_{OC} (V)	J_{SC} (mA/cm^2)	FF (%)	PCE (%)
5 nm	0.97 ± 0.02	21.00 ± 1.70	67.2 ± 4.8	13.60 ± 1.11
10 nm	0.98 ± 0.01	20.84 ± 1.08	73.6 ± 2.1	14.94 ± 0.52
20 nm	0.93 ± 0.01	16.97 ± 0.62	62.0 ± 2.8	9.82 ± 0.74

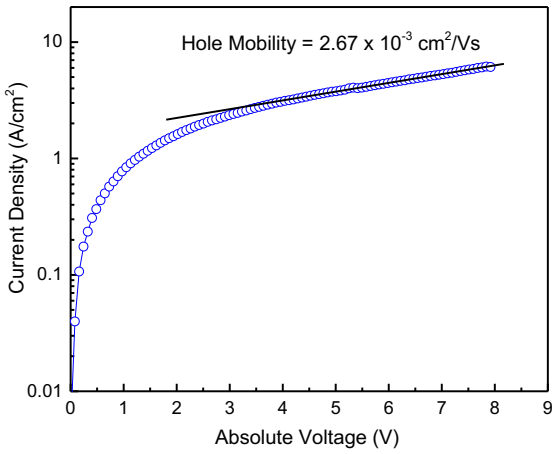

Figure 120: Hole-only diodes were fabricated using the architectures: ITO/ PVBT-SO_3 (120 nm)/Au. Hole mobility was extracted by fitting the current density–voltage curves using the Mott–Gurney relationship (space charge limited current).

External quantum efficiency (EQE) measurements shown in Figure 118b confirm the improved J_{SC} of the devices employing PVBT-SO_3 as the HEL. We performed steady-state measurements for the two best performing devices containing either PEDOT:PSSS or PVBT-SO_3 (Figure 118c). Under simulated AM1.5G radiation (100 mW cm^{-2}) and bias voltage at the maximum power point, the PVBT-SO_3 based device produced a more stable output current than the PEDOT:PSS based device, with the latter showing a diminished current over time. Long-term air stability was tested by storing five separate devices of each type (PEDOT:PSS and PVBT-SO_3) in the absence of light (Figure 118d), then returning the devices to the glovebox for testing. Over 10 h storage, the PVBT-SO_3 devices showed no degradation, while the average PCE of PEDOT:PSS devices decreased by ≈20%. During the first ≈40 h, the PEDOT:PSS devices degraded slightly faster than PVBT-SO_3 devices. However, after ≈40 h, the PEDOT:PSS devices degraded rapidly, with the average PCE decreasing by 70% after ≈90 h of storage. In contrast, the average PCE for the PVBT-SO_3 devices decreased by only ≈20% during the same

timeframe. Since the acidity of PEDOT:PSS is detrimental to long-term device performance and stability,[555] the pH neutrality (Figure 121) of PVBT-SO_3 may assist with the improved device stability. To test the reproducibility, 80 devices of each type were fabricated and tested, as shown in Figure 118e-f. The PEDOT:PSS devices afforded an average PCE of ≈11%, while PVBT-SO_3 based devices gave an average PCE of ≈14%, attesting to the reliable and reproducible device performance improvement when using PVBT-SO_3 as the HEL.

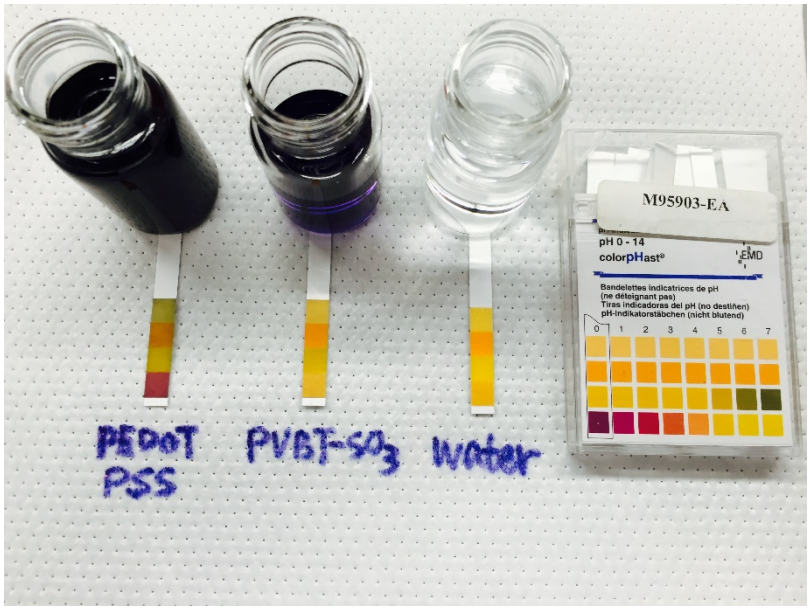

Figure 121: A comparison of PH value between PVBT-SO_3 and PEDOT:PSS

3.4.3 EIS Measurements

Electrochemical impedance spectroscopy (EIS) measurements were performed to understand the recombination losses and charge transport properties in devices with different HELs. In the EIS measurement, a small applied AC voltage (20 mV) measures device impedance as a function of frequency (ω), sweeping from 100 Hz to 1 MHz under simulated AM1.5G irradiation (100 mW cm^{-2}) inside an N_2-filled glovebox. As shown in Figure 122a, the Nyquist plot for each device type shows two semicircles associated with different time constants (τ), representing two

distinct charge transport regimes. The semicircle closest to the origin, associated with the higher frequency spectrum, is attributed to impedance arising predominantly from the electronic transport and recombination kinetics. The second semicircle, associated with the low frequency regime, is attributed to the impedance from slow relaxation/diffusion of ions.[449,559] At 0 V applied DC bias, the first semicircle (high-frequency region) of the Nyquist plot is associated with the recombination resistance (R_{rec}).[559] The PVBT-SO_3 containing devices show higher R_{rec}values compared to PEDOT:PSS containing devices, as shown in Figure 122a, which corresponds to a reduced recombination loss and correlates with the superior device performance observed when using PVBT-SO_3. Shown in Figure 122b are Mott–Schottky (MS) plots for each type of devices obtained by EIS characterization. The interfacial charge density is inversely proportional to the slope of the MS plot assuming an equivalent dielectric constant for both devices.[559] A steeper slope was found for PVBT-SO_3 containing devices (-1.0×10^{13}) relative to PEDOT:PSS containing devices (-9.4×10^{10}), indicating a lower interfacial charge density for the PVBT-SO_3 case by over two orders of magnitude, and thus more efficient charge extraction for PVBT-SO_3. Therefore, PVBT-SO_3 acts as a more efficient HEL relative to PEDOT:PSS, due to reduced recombination losses and interfacial charge density within the devices.

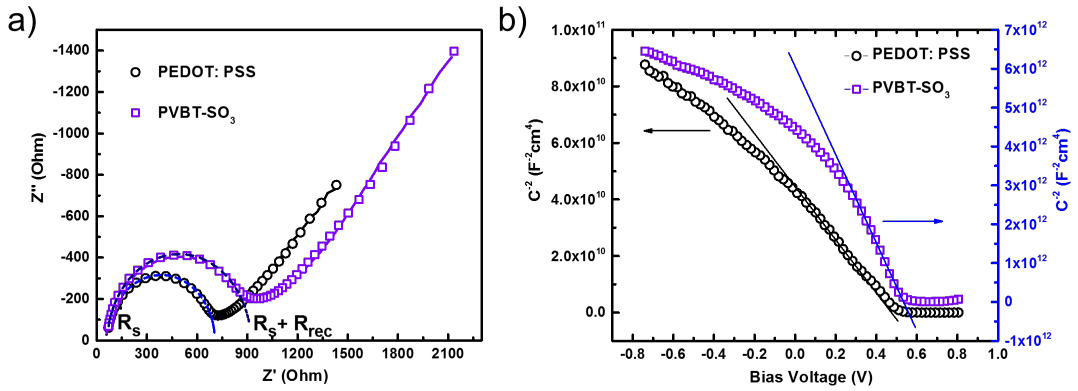

Figure 122: a) Nyquist plot of the device with PEDOT:PSS or PVBT-SO_3 (Dashed lines represent the recombination semicircle); b) Mott-Schottky plot of the device measured at 10 kHz probe frequency.

3.4.4 Photoluminescence Measurements

Time-resolved photoluminescence (TRPL) measurements were performed on perovskite/HEL samples to assess the efficiency of charge separation in the PVBT-SO_3 versus PEDOT:PSS samples. Figure 123a–c shows PL images obtained from identically prepared perovskite films on a) clean glass, b) glass/PEDOT:PSS, and c) glass/PVBT-SO_3. The three images show a similar polycrystalline structure of the luminescent perovskite film, but the PL is strongly quenched in the presence of the PVBT-SO_3 HEL. This effect is seen clearly in Figure 123d, showing that the perovskite spectra are similar for the different samples but generate only ≈1/20 the PL intensity. Figure 123e shows representative PL decay traces from the three different perovskite samples. Interestingly, the presence of the HEL perturbs the fluorescence decay rate only slightly; single-exponential fits to the PL decay provide decay constants of 0.034 and 0.029 ns^{-1} for the PEDOT:PSS and PVBT-SO_3 interlayers, respectively. This counterintuitive result can be

understood by considering that the PL emission in perovskites does not typically arise from a simple radiative decay of optically generated excitons. Kamat and co-workers[560] showed that excitons in perovskites undergo dissociation into free carriers on a time scale of a few picoseconds; the PL emission on longer timescales arises from exciton regeneration from mobile carriers. The HEL decreases local hole concentration by extraction, thus decreasing PL intensity without significantly affecting PL decay rate. Thus the combined wavelength and time-resolved PL measurements support the EIS and other measurements that the PVBT-SO_3 interlayer acts as an efficient charge extractor, reducing the perovskite PL intensity by efficient extraction of holes into the interlayer.

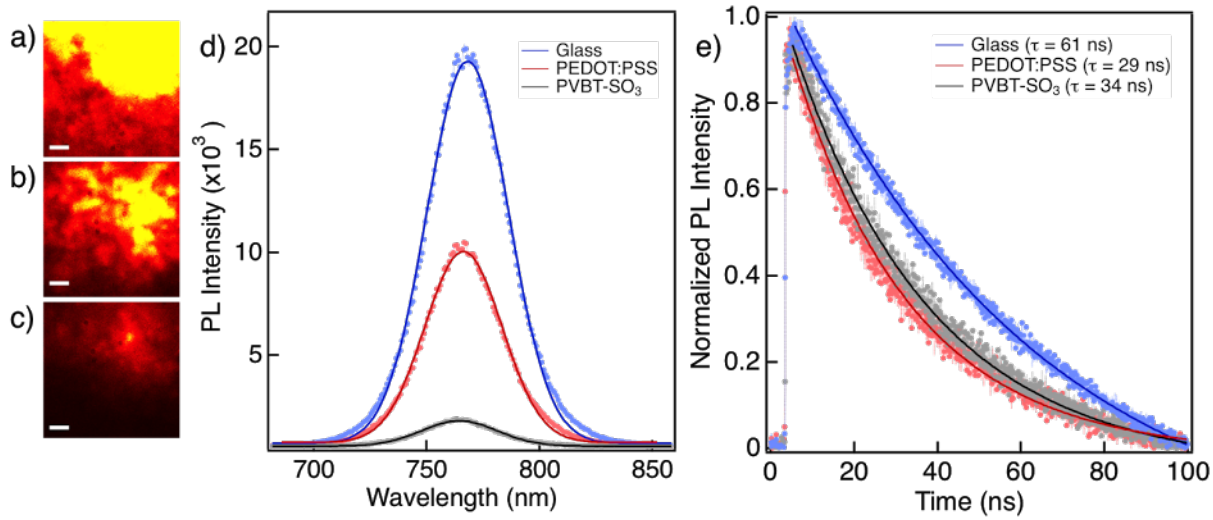

Figure 123: Photoluminescence (PL) and time-resolved photoluminescence (TRPL) for a) glass/perovskite, b) glass/PEDOT:PSS/perovskite, and c) glass/PVBT-SO_3/perovskite; scale bar represents 300 nm. d) PL spectra showing quenching effects for the three films e) TRPL decay lifetimes.

3.4.5 KPFM Measurements

Kelvin probe force microscopy (KPFM) was used to evaluate the work function (W) of different architectures with PEDOT:PSS or PVBT-SO_3 (Figure 124). We use the relationship: $q \cdot V_{CPD} = (W_{probe} - W_{sample})$ to calculate W from measured contact potential differences between the sample and the probe (V_{CPD}). HELs were introduced by spin-coating onto Au-coated Si substrates, and KPFM measurements were conducted. Tapping mode atomic force microscopy (AFM) images for PEDOT:PSS and PVBT-SO_3 are shown in Figure 124a-b, respectively. Color maps of work function, overlaid on height images, for PEDOT:PSS and PVBT-SO_3 are shown in Figure 124c. Figure 124d shows the corresponding counts versus work function distributions for the two HELs. The measured $W$for PEDOT:PSS was 4.99 eV ± 13.28 meV, while for PVBT-SO_3 it was 5.09 eV ± 6.51 meV. PEDOT:PSS and PVBT-SO_3 films have a comparable roughness, as indicated by tapping mode AFM. Consequently, the difference in W is attributed to the electronic properties of the polymer. Ultraviolet photoelectron spectroscopy was used to determine the ionization potential (IP) from the low-binding energy onset. The IP of PVBT-SO_3 was found to be 5.19 eV, which corresponds to the HOMO level of the polymer.[557] Since the HOMO level of PEDOT:PSS is ≈5.0 eV,[561,562] the deeper HOMO level of PVBT-SO_3 (5.19 eV) contributes to the higher work function of the bulk film. Since all devices contain exactly the same electron transport layer (ETL), the work function offset of the HEL and ETL determines the magnitude of the built-in-potential (V_{bi}) across the active layer. This ≈0.1 eV increase in W of PVBT-SO_3 film affords devices with a larger V_{bi}, which is crucial for solar cell devices with a higher V_{oc}, J_{sc}, and FF.[23] The deeper HOMO level of PVBT-SO_3 HEL may contribute to the improved V_{oc} of the device.[561-563]

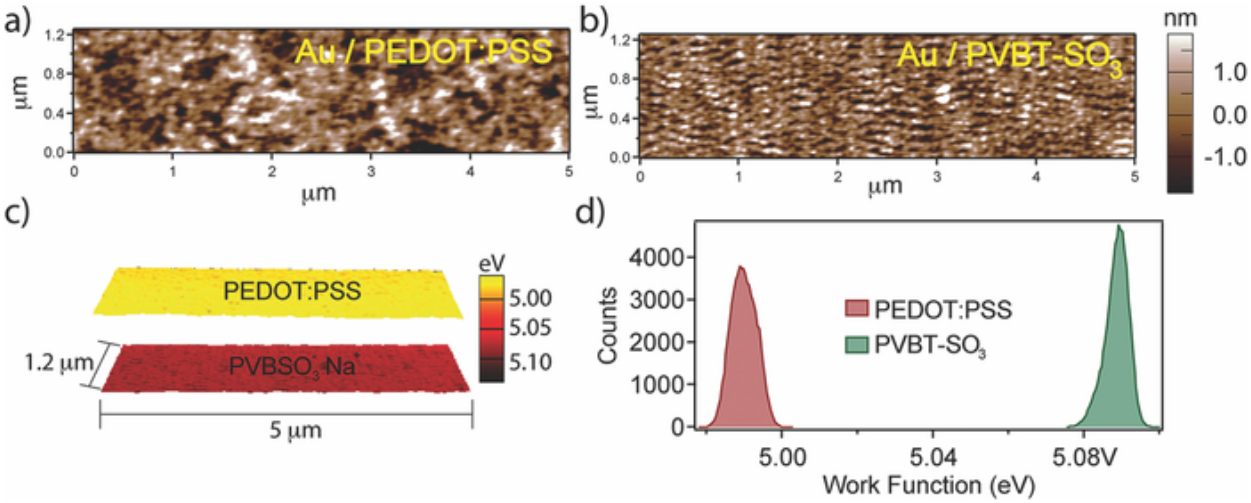

Figure 124: Tapping mode AFM height images for a) PEDOT:PSS and b) PVBT-SO_3 on Au substrates. c) Color work function maps overlaid on height AFM images, and d) counts vs work function distributions.

In summary, a water-processable HEL that requires no thermal annealing was developed as an alternative to the widely used PEDOT:PSS for the fabrication of high performance inverted perovskite solar cells. A maximum PCE of 15.9% was achieved by using PVBT-SO_3 as the HEL, representing an ≈26% improvement over the PEDOT:PSS containing devices. PVBT-SO_3 based devices also showed substantially improved stability and long-term air stability. EIS measurements suggest that PVBT-SO_3 containing devices have larger recombination resistance and more efficient charge extraction relative to those with PEDOT:PSS. KPFM characterization confirms that PVBT-SO_3 films show higher work function than that of PEDOT:PSS, which provides a larger V_{bi} in devices containing PVBT-SO_3 and thus a better performance, while time-resolved PL measurements further confirmed an efficient charge extraction of PVBT-SO_3 interlayers from perovskite. The results presented here for PVBT-SO_3 as a new hole extraction material to improve solution processed perovskite solar cells indicates conjugated polyelectrolytes may possess superior charge extraction properties and their modification on

electrodes is an additional advantage for generating large V_{bi} across the devices, which will encourage the design and utility of new polymers that advance photovoltaic technology.

3.5 Tandem Thin-Perovskite/Polymer Solar Cells with Graded Recombination Layer

This chapter[§§§§] discusses the fabrication and analysis of a tandem solar cell, containing a perovskite front subcell and a polymer:fullerene bulk heterojunction back subcell connected by a graded recombination layer. Perovskite-containing tandem solar cells are attracting attention for their potential to achieve high efficiencies. We demonstrate a series connection of a ~90 nm thick perovskite front subcell and a ~100 nm thick polymer:fullerene blend back subcell that benefits from an efficient graded recombination layer containing a zwitterionic fullerene, silver (Ag), and molybdenum trioxide (MoO_3). This methodology eliminates the adverse effects of thermal annealing or chemical treatment that occurs during perovskite fabrication on polymer-based front subcells. The record tandem perovskite/polymer solar cell efficiency of 16.0%, with low hysteresis, is 75% greater than that of the corresponding ~90 nm thick perovskite single-junction device and 65% greater than that of the polymer single-junction device. The high efficiency of this hybrid tandem device, achieved using only a ~90 nm thick perovskite layer, provides an opportunity to substantially reduce the lead content in the device, while maintaining the high performance derived from perovskites.

Perovskite solar cells have recently emerged as a promising photovoltaic technology[34,450,454,455,481-483,489,496,499,516,522,537,538,564-567] with reported power conversion efficiencies (PCEs) approaching crystalline silicon solar cells.[440,498] In

---

[§§§§] This chapter was adapted, with permission, from Liu, Yao, Lawrence A. Renna, Monojit Bag, Zachariah A. Page, Paul Kim, Jaewon Choi, Todd Emrick, Dhandapani Venkataraman, and Thomas P. Russell. "High Efficiency Tandem Thin-Perovskite/Polymer Solar Cells with a Graded Recombination Layer." *ACS applied materials & interfaces* 8, no. 11 (2016): 7070-7076. I would like to acknowledge Dr. Yao Liu and Prof. Monojit Bag for device fabricvation and characterization, and Dr. Zachariah A. Page for material synthesis.

pursuit of optimal efficiency, perovskite-containing tandem solar cells are especially attractive.[568-575] However, the overwhelming majority of research has been focused on combining perovskite solar cells with copper indium gallium diselenide (CIGS) or silicon based devices.[569-571,573,574] Polymer-based solar cells, which share similar processing and architecture characteristics, are promising candidates for integration with perovskite solar cells to form hybrid tandem devices.[572] Such devices would have enhanced mechanical flexibility, while maintaining solution processability.[572,576] Moreover, recently developed perovskite solar cells with planar heterojunction structures are compatible with well-established solution-based, low temperature, roll-to-roll fabrication procedures used for the production of polymer-based solar cells.[453,484,485,491,492,497,500,534,565,577]

The one reported polymer/perovskite hybrid tandem solar cell gave a maximum PCE of 10.2%, consisting of a polymer front sub-cell and a perovskite back sub-cell.[572] The preparation of perovskite/polymer tandem solar cells faces two primary limitations: 1) if the perovskite was prepared as back sub-cell on top of the polymer front sub-cell in the layer-by-layer deposition procedures, the thermal/chemical treatment typically used during perovskite fabrication is not compatible with polymer-based sub-cell, and 2) conversely, if the perovskite was prepared as front sub-cell, the thick perovskite active layer (hundreds of nanometers) generally used to capture incident light prevents light from reaching the back sub-cell. Recently, ultrathin[578] or semitransparent[567,579] perovskite films were utilized in devices showing high efficiency and a perovskite thickness of 80 nm can afford a PCE of 10.1%,[580] which represents an avenue towards tandem solar cells with a thin perovskite active layer comprising the front sub-cell. While there is currently no environmentally friendly alternative for lead in perovskite devices,[581] thinner active layer can reduce the amount of lead within a perovskite-containing

solar cell. However, reducing the thickness of the perovskite active layer comes at the cost of reduced light absorption, resulting in an overall lower efficiency than their thicker counterparts. We mitigate this issue by implementing a new design strategy that combines a thin perovskite layer with a low band gap conjugated polymer showing a similar optical absorption to supplement light absorption and boost efficiency. We specifically demonstrate the facile solution-based fabrication of high performance tandem perovskite/polymer solar cells containing a ~90 nm thick perovskite front sub-cell and a ~100 nm thick polymer-based back sub-cell connected with a graded recombination layer. A record maximum PCE of 16.0% was achieved for these tandem perovskite/polymer solar cells with low hysteresis, demonstrating excellent synergy between the perovskite and polymer components. These hybrid tandem devices show impressive device metrics, including a maximum open circuit voltage (V_{OC}) of 1.80 V and a maximum fill factor (FF) of 77%.

3.5.1 Solar Cell Fabrication

The indium tin oxide (ITO)-coated glass substrates (20 ± 5 ohms/square) were obtained from Thin Film Devices Inc., and were cleaned through ultrasonic treatment in detergent, deionized water, acetone, and isopropyl alcohol and then dried in an oven (100 °C) for 6 hours. Poly(3,4-ethylenedioxythiophene):poly(styrenesulfonate) (PEDOT:PSS) as hole transport layer was spin coated on pre-cleaned ITO substrates at 2500 rpm for 40 s and annealed at 150 for 30 min. The perovskite layer was formed by spin-coating a solution of lead acetate ($Pb(OAc)_2$) and methylammonium iodide (MAI) (1:3 molar ratio) in *N,N*-dimethylformamide (DMF) onto the hot PEDOT: PSS/ ITO substrates (~ 100 °C) at a spin-speed of 6000 rpm for 60 s inside a glove box (N_2 atmosphere, < 1 ppm O_2, <1 ppm H_2O). As-cast films were then annealed in dark at 100 °C for 2 min in glove box. To achieve perovskite with different film thickness, we prepared

perovskite precursor solution with a concentration of 600 mg/mL, 450 mg/mL, 300 mg/mL and 200 mg/mL, respectively. The corresponding perovskite film thickness is ~ 160 nm, ~ 110 nm, ~ 90 nm, ~ 70 nm as determined by profilometry. For perovskite single junction devices, after the preparation of perovskite film, a thin layer of phenyl-C_{61}-butyric acid methyl ester ($PC_{61}BM$) (60-70 nm) was then spin coated inside a glove box (N_2 atmosphere, < 1 ppm O_2, <1 ppm H_2O) from a solution in chlorobenzene (20 mg/mL) at 1000 rpm for 60 s. Then fulleropyrrolidine with tertiary amine (C_{60}-N) in 2,2,2-trifluoroethanol (TFE) (3 mg/mL) was spin coated onto $PC_{61}BM$ surface with a thickness of ~10 nm. Finally, 100 nm Ag cathode was deposited (area 6 mm^2 defined by metal shadow mask) on the active layer under high vacuum (1×10^{-6} mbar) using a thermal evaporator. For polymer single junction devices, a mixture of a low energy gap polymer (PCE-10): [6,6]-phenyl C_{71}-butyric acid methyl ester ($PC_{71}BM$) (1:1.8 weight ratio, molecular structures are shown in Figure 126) in chlorobenzene:1,8-diiodoocatane (3 v% DIO) was stirred at 55 °C for ~1 day. The photoactive layers were deposited by spin-coating the solution onto the PEDOT:PSS/ ITO substrates. The thickness of the active layer film was ~100 nm (determined by profilometry). DIO was removed under vacuum, followed by spin-coating of C_{60}-N (15 nm). 100 nm Ag cathode was deposited (area 6 mm^2 defined by metal shadow mask) on the active layer under high vacuum (1×10^{-6} mbar) using a thermal evaporator. For tandem perovskite/polymer devices, after the preparation of perovskite film, a thin layer of $PC_{61}BM$ (60 nm-70 nm) was then spin coated from chlorobenzene. Then tris(sulfobetaine)-substituted fulleropyrrolidine (C_{60}-SB) in TFE (6 mg/mL) was spin coated onto $PC_{61}BM$ surface with a thickness of ~30 nm. 10 nm silver and 10 nm molybdenum trioxide (MoO_3) were deposited onto C_{60}-SB film sequentially by thermal evaporation. The polymer bulk heterojunction (BHJ) layer (~100 nm) were spin-coated onto the bottom layer. DIO was removed under vacuum, followed by spin-coating of C_{60}-N (15

nm). 100 nm Ag cathode was deposited (area 6 mm^2 defined by metal shadow mask) on the active layer under high vacuum (1×10^{-6} mbar) using a thermal evaporator.

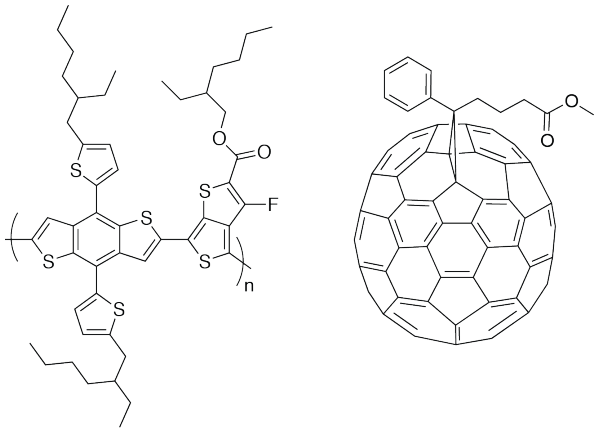

Figure 125: Molecular structure of PCE-10 and $PC_{71}BM$.

3.5.2 Solar Cell Characterization

The current-voltage (I-V) characteristics of the devices were measured under simulated AM1.5G irradiation (100 $mWcm^{-2}$) using a Xe lamp-based Newport 91160 300-W Solar Simulator. A Xe lamp equipped with an AM1.5G filter was used as the white light source. The light intensity was adjusted with an NREL-calibrated Si solar cell with a KG-5 filter. The QE-PV-SI Measurement Kit (Newport/Oriel Instruments) with 150 W Xe arc lamp, monochromator, and calibrated silicon reference cell with power meter, are used for Quantum efficiency (QE)/Incident Photon to Charge Carrier Efficiency (IPCE) measurement for solar cells over a 400–1100 nm spectral range. To avoid overestimating the photocurrent, we isolated each device completely by scratching the surrounding films around the device using steel blade carefully and a metal photo mask with an aperture area of 5.5 mm^2 was used during device measurement.

The preparation of thin and high quality perovskite films hinges on rapid crystal growth, as recently reported by Snaith et al. for lead acetate ($Pb(OAc)_2$) on mesoporous titanium dioxide-coated substrates.[542] To use this procedure to fabricate thin perovskite films (< 200 nm) on ITO/PEDOT:PSS substrates, it was necessary to increase the rate of crystal growth further and decrease crystal size, which is crucial for obtaining tightly packed, continuous, and pinhole-free perovskite layers. Thus, the substrates were pre-heated to 100 °C immediately prior to spin-coating, and during the coating process films darkened, indicating the formation of perovskite crystals. Additionally, a fast spin-coating speed (6000 rpm) produced high quality uniform perovskite films with excellent reproducibility. By using spin-coating at high temperature and varying the concentration of the perovskite precursor solution, the layer thickness was tuned from ~70 nm to ~160 nm. Thinner perovskite films (~70 nm, ~90 nm and ~110 nm) had a transmittance exceeding 50% for wavelengths larger than 600 nm (Figure 126a), while thicker films (~160 nm) had lower transmittance (< 40%) from 500 nm to 740 nm (Figure 126a), indicating that perovskite film thicknesses of ~100 nm are suitable for use as front sub-cells in tandem photovoltaic devices. Power X-ray diffraction (PXRD) (Figure 126b) demonstrates the efficient conversion of $Pb(OAc)_2$/MAI mixtures into polycrystalline methylammonium lead triiodide ($MAPbI_3$) perovskite using spin-coating at high temperature. The red dashed-lines (from left to right) in the PXRD pattern indicate the tetragonal perovskite peaks attributable to (100), (111), (200), and (220).[480] Scanning electron microscopy (SEM) and atomic force microscopy (AFM) revealed the surface profiles of the perovskite films as a function of thickness. The SEM images (Figure 126c and Figure 127) show homogeneous and pinhole-free films, with grain sizes of approximately 100 nm irrespective of the perovskite film thickness (Figure 127). Additionally, AFM (Figure 126d and Figure 128) confirms the homogeneity of the

surface and reveals a smooth, (root mean square (RMS) roughness: Rq < 10 nm) tightly packed surface across the film. These results demonstrate that $MAPbI_3$ can be fabricated through a single step solution deposition approach to provide thin perovskite films with continuous coverage on ITO/PEDOT:PSS substrates. In addition, the tunability of the perovskite film thickness from ~70 nm - ~160 nm allows for a precise adjustment of transmission and ensures that photons are absorbed by the back sub-cell.

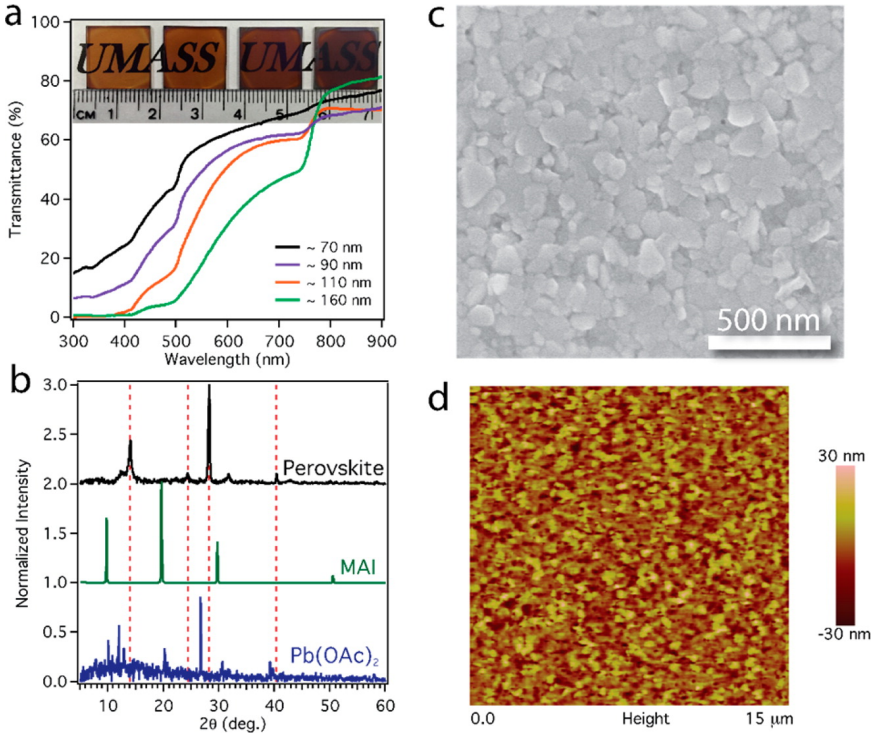

Figure 126: (a) Transmittance measurement of the perovskite films with different thicknesses (inset: the film thickness increases from left to right); (b) PXRD for precursors and perovskite, where red lines show perovskite only peaks; Representative SEM image (c) of a perovskite film ($MAPbI_3$) with a thickness of ~ 90 nm and (d) its corresponding AFM image.

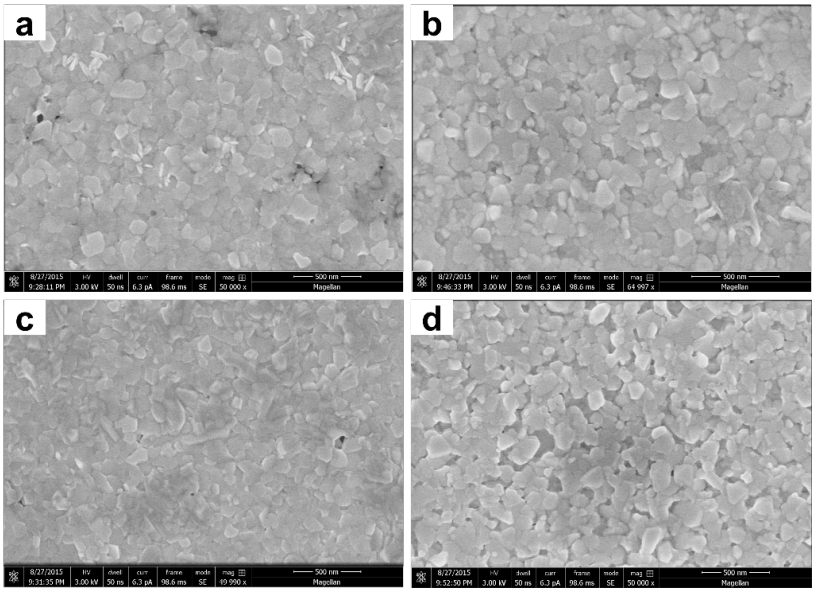

Figure 127: SEM images of perovskite films on ITO/PEDOT:PSS substrates with different film thickness. (a) ~ 70 nm. (b) ~ 90 nm. (c) ~ 110 nm. (d) ~ 160 nm.

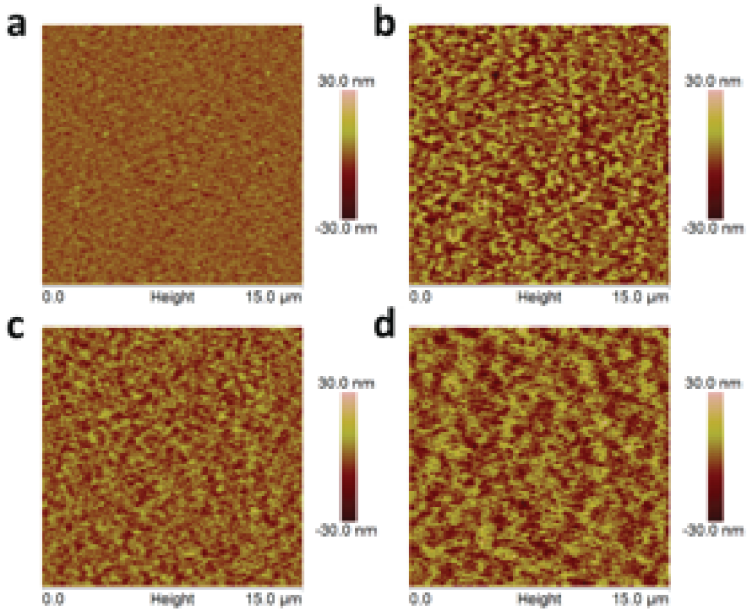

Figure 128: AFM images of perovskite films on ITO/PEDOT:PSS substrates with different film thickness. (a) ~ 70 nm. (b) ~ 90 nm. (c) ~ 110 nm. (d) ~ 160 nm.

The photovoltaic properties of the perovskite thin films were first investigated using a single junction device architecture of ITO/PEDOT:PSS/perovskite/$PC_{61}BM$/C_{60}-N/Ag. The thickness of

the perovskite layer significantly influenced the V_{OC} and short-circuit current density (J_{SC}), as shown in Figure 129a. Increasing the perovskite layer thickness from 70 nm to 160 nm raised the V_{OC} from 0.82 V to 1.03 V, and J_{SC} from 10.6 mA/cm^2 to 15.6 mA/cm^2 (Figure 129a, Table 14). Correspondingly, the maximum PCEs of these single junction perovskite devices were improved from 6.1% to 11.4%. Single junction polymer-based solar cells were also fabricated using a PCE-10:$PC_{71}BM$ BHJ active layer, where the optimal layer thickness was ~100 nm.[525,582] Figure 129b shows the J-V curve for champion single junction devices with an architecture of ITO/PEDOT:PSS/PCE-10:$PC_{71}BM$/C_{60}-N/Ag, resulting in a V_{OC} of 0.77 V, J_{SC} of 17.8 mA/cm^2, fill factor (FF) of 70.9%, and a maximum PCE of 9.7%. The strong UV-visible attenuation coefficients (α, cm^{-1}) (Figure 129c) for perovskite and polymer BHJ films are complementary and afford excellent absorption over 400 nm - 800 nm. External quantum efficiency (EQE) profiles of single junction devices (Figure 129d) show that below ~600 nm the perovskite single junction devices have a strong photo-response, while above ~600 nm the photo-response of the polymer single junction device dominates, which corresponds well with the UV-visible absorption spectra.

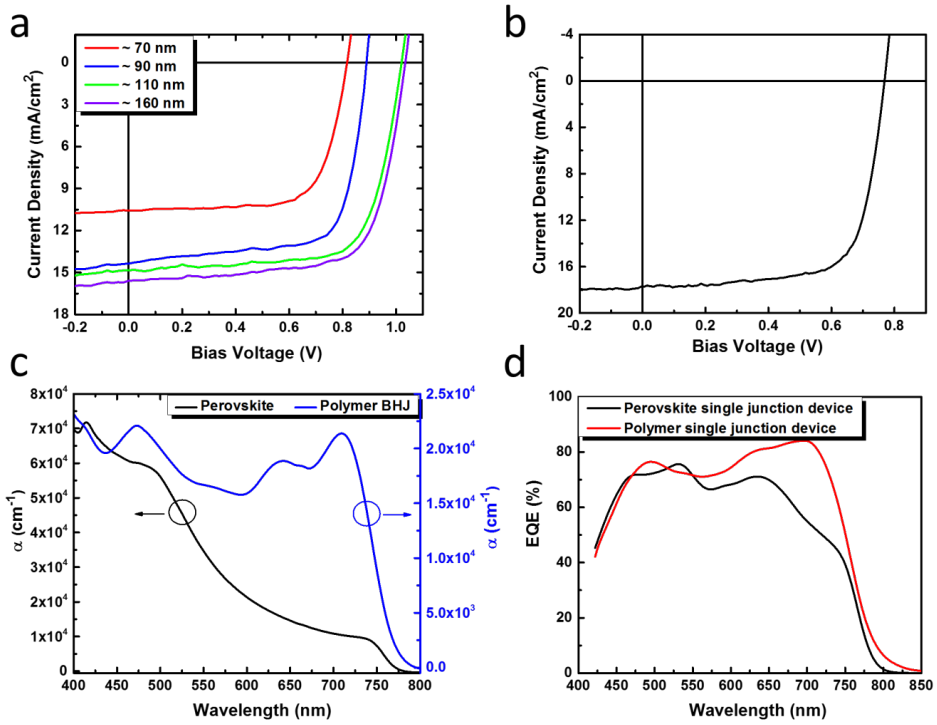

Figure 129: (a) J-V curves of perovskite single junction solar cells (ITO/PEDOT:PSS/Perovskite/$PC_{61}BM$/C_{60}-N/Ag) with different perovskite layer thickness. (b) J-V curve of a polymer single junction solar cell (ITO/PEDOT:PSS/Polymer BHJ/C_{60} N/Ag) with a BHJ layer thickness of ~100 nm. (c) UV-visible absorption of perovskite and polymer BHJ films. (d) EQE profiles of the optimal perovskite and polymer single junction solar cells in this work.

Table 14: Photovoltaic performance of the optimal perovskite single junction devices with variable perovskite thickness.

Perovskite thickness	Efficiency (%)	V_{OC} (V)	J_{SC} (mA/cm^2)	FF (%)
~70 nm	6.1	0.82	10.6	70.8
~90 nm	9.1	0.89	14.3	71.6
~110 nm	10.8	1.02	14.9	71.3
~160 nm	11.4	1.03	15.6	70.6

The solar cell device architecture and composition used in this work are provided in Figure 130a. The front sub-cell consists of a $PC_{61}BM$/perovskite planar heterojunction solar cell fabricated on an ITO/PEDOT:PSS substrate. The perovskite layer was prepared as for the single junction devices. The recombination layer in this sub-cell was a 30 nm film of C_{60}-SB as an electron transport layer (ETL), 10 nm silver as a recombination center, and 10 nm molybdenum trioxide (MoO_3) as a hole transport layer (HTL). The back sub-cell is comprised of a BHJ active layer (~100 nm) containing a blend of PCE-10:$PC_{71}BM$. This layer was coated onto the recombination layer, followed by C_{60}-N (15 nm) as an ETL and silver (100 nm) as metal cathode. C_{60}-SB was cast from TFE, while common solvents for polymer solar cell fabrication (chloroform, toluene, chlorobenzene and dichlorobenzene) neither removed the films nor modified their electronic signature.[526] The orthogonal solubility of C_{60}-SB relative to $PC_{61}BM$ makes it suitable for sequential solution processing, while providing robust protection for the front sub-cell, and an ideal platform for solution deposition of the polymer BHJ back sub-cell that is cast from chlorobenzene. Cross-sectional SEM (Figure 130b and Figure 131) distinguish each layer of the device, with little-to-no observable interdiffusion between layers. SEM provides evidence that the three-component recombination layer (C_{60}-SB/ultrathin Ag/MoO_3) effectively protects the perovskite front sub-cell and provides good contact between the two sub cells. Figure 130c shows the energy band diagram of each material utilized in the device, highlighting the ability of both C_{60}-SB and C_{60}-N to generate large negative interfacial dipoles (Δ) on silver, as determined by ultraviolet photoelectron spectroscopy (UPS).[525]

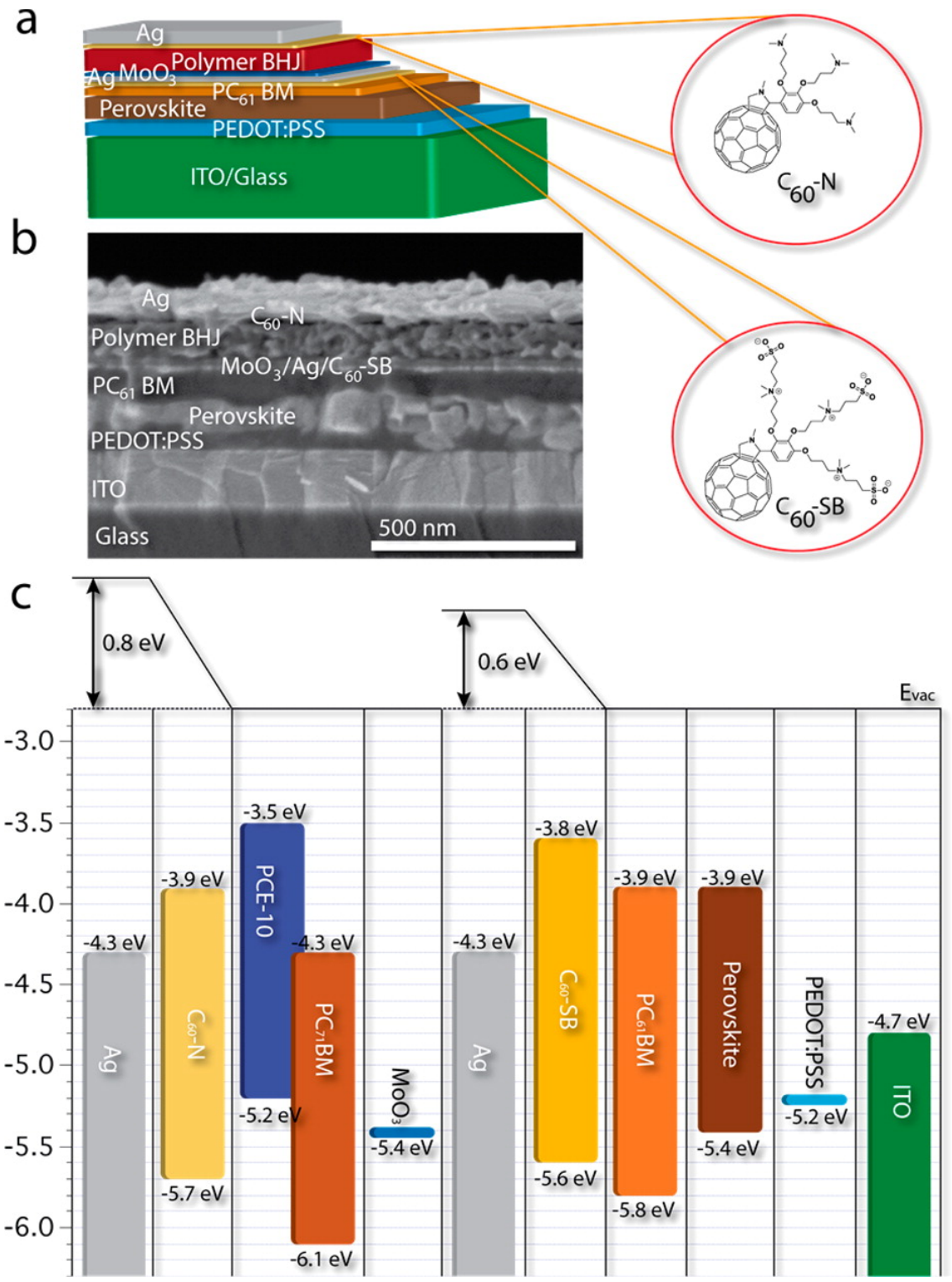

Figure 130: (a) Device structure of tandem perovskite/polymer solar cells, and the fullerene interlayer materials (C_{60}-N, C_{60}-SB). (b) False-color cross-sectional SEM image of a tandem device with a perovskite layer thickness of ~90 nm. (c) Energy level diagram of the device (interfacial dipole values obtained by UPS). [525]

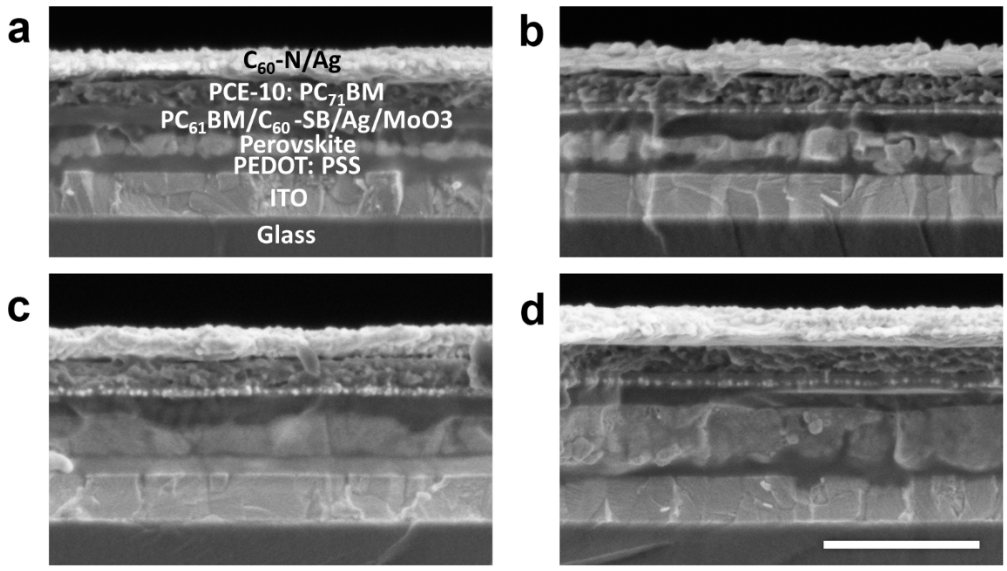

Figure 131: Cross-sectional SEM images of the tandem devices with different perovskite layer thickness. (a) ~ 70 nm. (b) ~ 90 nm. (c) ~ 110 nm and (d) ~ 160 nm (The scale bar is 500 nm).

Given the demonstrated effect of perovskite thickness on V_{OC}, J_{SC}, and FF of single junction devices, it was of interest to investigate how the thickness of a perovskite front sub-cell influenced the performance of tandem perovskite/polymer solar cells (Table 15and Figure 132a). For each device, the polymer-based BHJ layer thickness was kept constant, ~100 nm, which was the optimized film thickness for single junction devices. Thinner perovskite layers (< ~100 nm) afford a higher J_{SC} relative to thicker layers, which is attributed to an enhanced transmittance (Figure 126a), allowing for improved absorption of the polymer back sub-cell. EQE measurements confirmed an increased photo-response in the range where PCE-10 absorbs most strongly (600 nm - 740 nm) (Figure 1325b) when thinner perovskite layers (< ~100 nm) were used in the tandem devices. Increasing the perovskite thickness beyond 100 nm results in a decrease in J_{SC} of the tandem devices, in contradiction to that observed for single-junction perovskite solar cells. Figure 133a shows the current density-voltage (J-V) curve of the champion tandem device with low hysteresis. The corresponding EQE profile shown in Figure

133b gives a broad photo-response extending to 800 nm. A maximum PCE of 16.0% was achieved, representing a ~75% improvement over the corresponding single junction ~90 nm thick perovskite (PCE = 9.1%) and a 65% improvement over the single junction polymer (PCE = 9.7%) solar cells. To confirm the viability of this protocol, 63 independent hybrid tandem devices were fabricated using ~90 nm thick perovskite front sub-cells, with the majority of devices showing PCE values between 13% and 16% (Figure 134). The presented methodology for the fabrication of tandem perovskite/polymer solar cells provides a platform to integrate state-of-the-art polymer BHJs with perovskite devices, since the pre-annealed perovskite front sub-cell has no influence on the polymer back sub-cell during the fabrication process. The high V_{OC} (maximum of 1.80 V) and FF (maximum of 77%) values achieved by these hybrid tandem solar cells (Figure 132and Figure 134) are comparable to, or exceed, current perovskite/silicon hybrid systems,[570,574,583] indicating an efficient union of the two sub cells by the three-component recombination layer.

Table 15: Optimal photovoltaic performance of tandem perovskite/polymer devices with different perovskite layer thickness fabricated in the same batch.

Perovskite thickness	Efficiency (%)	V_{OC} (V)	J_{SC} (mA/cm^2)	FF (%)
~70 nm	10.3	1.55	9.7	68.9
~90 nm	15.9	1.62	12.9	76.1
~110 nm	14.1	1.76	11.0	72.9
~160 nm	12.1	1.77	9.9	69.1

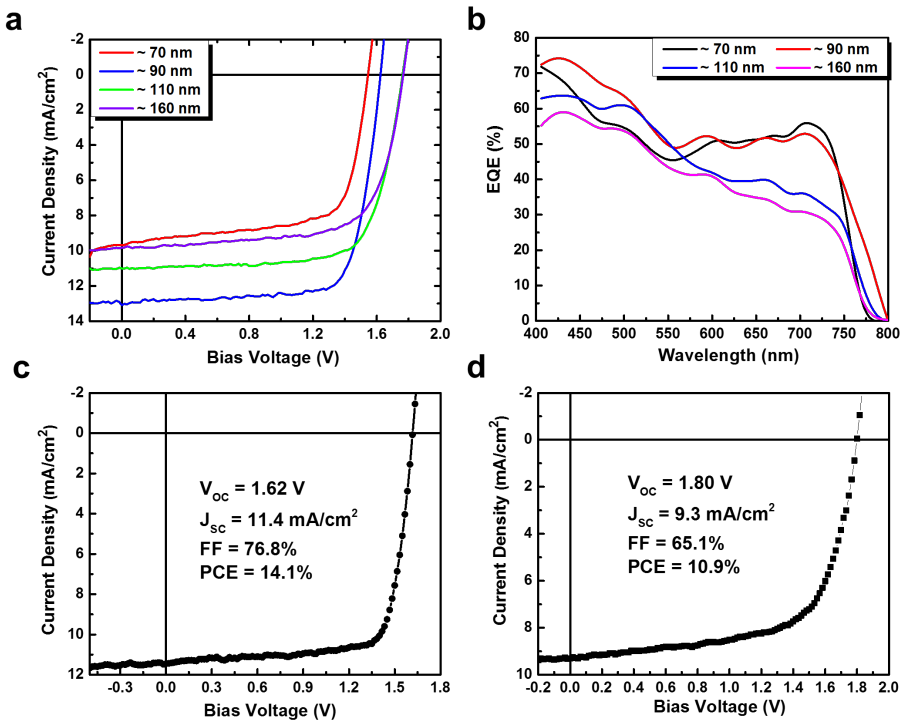

Figure 132: Device performance of perovskite/polymer tandem solar cells. (a) J-V curves of polymer/ perovskite hybrid tandem solar cells with different perovskite layer thickness. (b) EQE profiles of polymer/ perovskite hybrid tandem solar cells with different perovskite layer thickness. (c) J-V curve of polymer/ perovskite hybrid tandem solar cells with the best FF value. (d) J-V curve of polymer/ perovskite hybrid tandem solar cells with the best V_{OC} value.

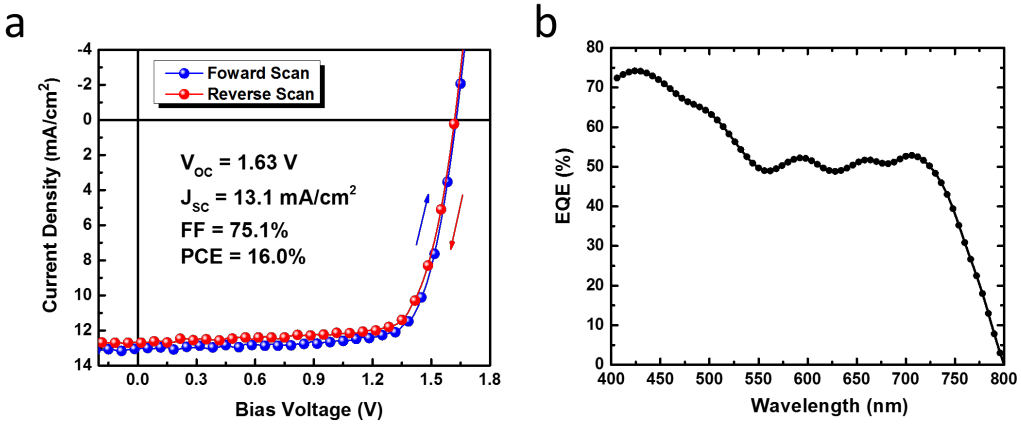

Figure 133: (a) J-V curves and device metrics of the optimal polymer/perovskite hybrid tandem solar cell (ITO/PEDOT:PSS/Perovskite/$PC_{61}BM$/C_{60}-SB/Ag/MoO_3/Polymer BHJ/C_{60}-N/Ag) under both forward and reverse scans and corresponding (b) EQE profile.

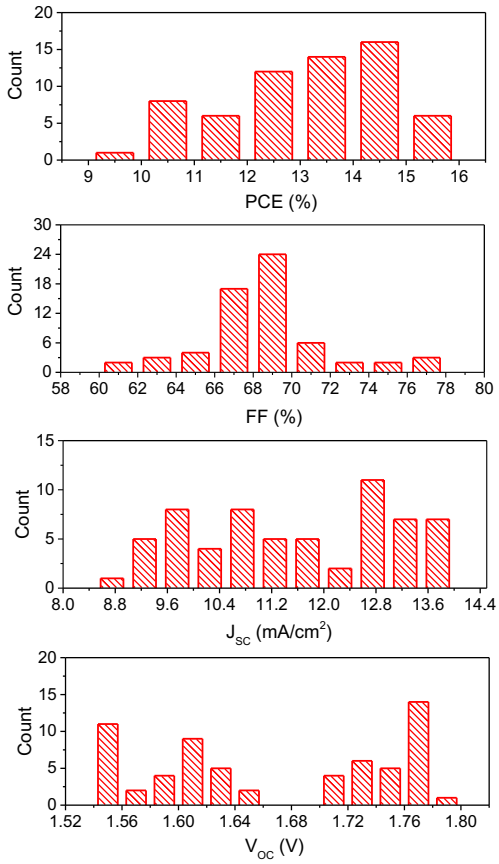

Figure 134: Histograms of PCE, FF, J_{SC} and V_{OC} based on 63 independent tandem devices.

3.5.3 KPFM Measurements

Kelvin probe force microscopy (KPFM) measurements were performed to analyze the C_{60}-SB/Ag/MoO_3 recombination layer (Figure 135). We designed the recombination layer to efficiently extract electrons from the perovskite front sub-cell, and holes from the polymer-based back sub-cell. In KPFM, we measure the contact potential difference (V_{CPD}) between the sample and the Pt/Ir coated Si atomic force microscopy (AFM) probe.[531] Two types of surface potential measurements were made by KPFM: 1) on top of layers in a standard architecture, and 2) under the layers by peeling off the Ag layer using Scotch® tape, and measuring the underside.

The surface potential at the top of the recombination layer, where the surface is composed of MoO_3, was V_{CPD} ~ -100 meV, as shown in Figure 135 sample A. Without MoO_3, the Ag surface showed a V_{CPD} ~ -16 meV, as shown in Figure 135 sample B. These results show that MoO_3 increases the work function toward the polymer back sub-cell by ~ 84 meV. When the Ag layer is peeled off of a C_{60}-SB layer (there is still C_{60}-SB left on the Ag film as evidenced by the X-ray photoelectron spectroscopy (XPS) data shown in Figure 136), the measured surface potential is V_{CPD} ~ +151 meV, as seen in Figure 135 sample C. This result shows that the C_{60}-SB layer decreases the work function of silver by ~ 167 meV at the perovskite front sub-cell, and is consistent with UPS results.[46] There is a total difference of ~ 251 meV between the top and the bottom of our recombination architecture. This asymmetric work-function throughout the recombination layer, as measured by KPFM, is evidence of a graded architecture with a low work-function toward the perovskite front sub-cell for efficient electron extraction, and an increased work-function toward the polymer-based back sub-cell for efficient hole extraction. We also measured the surface potential in the opposite direction, as shown in Figure 137. Surface potential measurements were made on MoO_3, then Ag on MoO_3, and then C_{60}-SB on Ag on MoO_3; all on grounded Au substrates as done previously. Here, we also show the same graded potential difference through the recombination architecture as in Figure 135. In this configuration we measured an even larger total difference of ~ 671 meV across the three layers. This difference is attributed to the lessened handling time of MoO_3 in air.

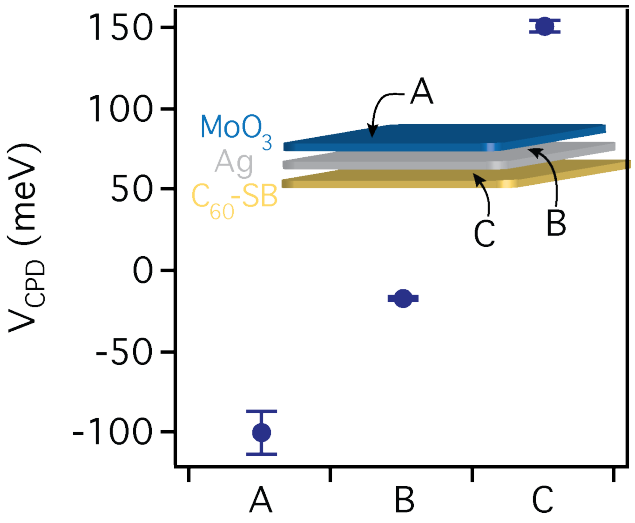

Figure 135: Surface potential (V_{CPD}) of the recombination layers (C_{60}-SB (30 nm)/Ultrathin Ag (10 nm)/MoO_3 (10 nm)).

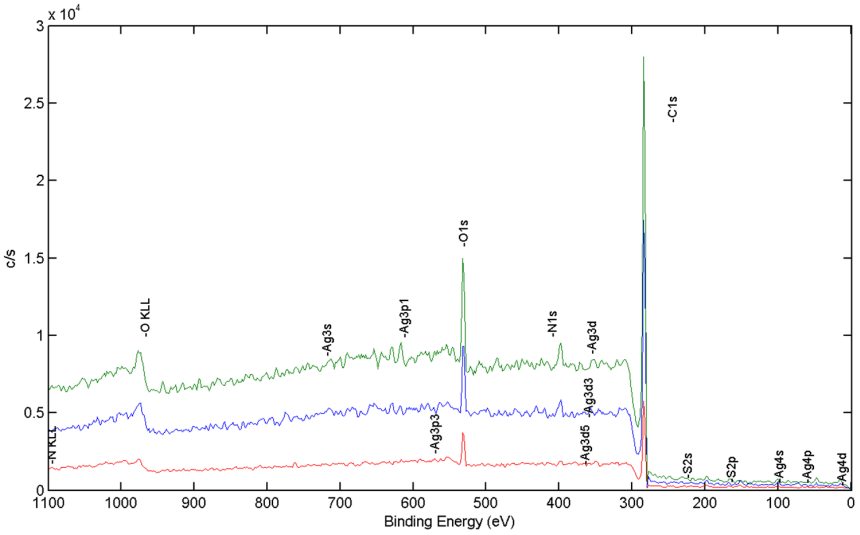

Figure 136: XPS of the Ag film surface peeled from the C_{60}-SB layer. The angle dependent measurements show the signals of nitrogen, sulfur and oxygen coming from C_{60}-SB. Confirming ist presence on the peeled Ag electrode.

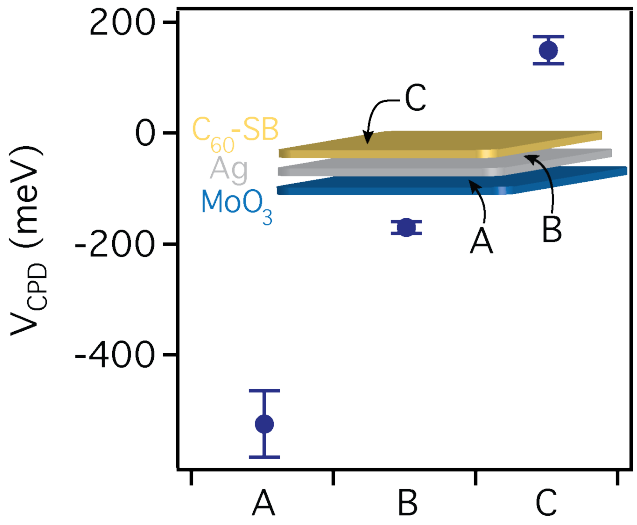

Figure 137: Surface potentials (V_{CPD}) from MoO_3, Ag, to C_{60}-SB of the graded recombination layer on gold substrates. The surface potential difference from MoO_3, Ag, to C_{60}-SB (here) is even larger than that from C_{60}-SB, Ag, to MoO_3 as shown in the main text, which further confirmed the graded potential property of the recombination layer.

In summary, this contribution established a record efficiency to date for a tandem perovskite/polymer solar cell fabricated by a facile solution deposition approach. The maximum efficiency of 16.0% achieved by this hybrid tandem device is 75% higher than the corresponding ~90 nm thick perovskite single junction device and 65% higher than the polymer single junction device. An efficient graded recombination layer, as confirmed by KPFM measurement, was developed for the series connection of the two sub-cells to achieve a very high V_{OC} of 1.80 V and a high FF of 77%. AFM and SEM characterization confirm smooth and continuous thin perovskite layers, making the presented methodology an excellent platform for the preparation of tandem perovskite/polymer solar cells by solution deposition. Our design demonstrates the synergistic benefit of combining these two previously competing materials, paving the way for ultrathin perovskite films to achieve high efficiency. Additionally, the presented methodology

provides an alternative to substantially reduce the amount of toxic lead within a high performance perovskite-containing solar cell.

3.6 Observation of Large-Scale and Charge Transport Material Dependent Light-Induced Polarization of Perovskite Layers

This chapter[*****] details the use of Photo-Kelvin Probe Force Microscopy (photo-KPFM) to observe light-induced polarization across 200 nm thick polycrystalline methylammonium lead triiodide ($MAPbI_3$) perovskite films in $MAPbI_3$/charge transport material (CTM) bilayers. Polarization of up to ~600 mV was observed for some $MAPbI_3$/CTM bilayers. We discern that the sign of polarization is dependent on the predominate charge carrier properties of the CTM used. Thus, the observed effect is due selective extraction of either holes or electrons from the $MAPbI_3$ layer, leaving behind an excess of charge of the opposite sign. Surprisingly, the reported extremely high dielectric phenomenon in perovskites does not screen these excess charges, as the polarization is measured through the entire perovskite layer. We also propose this experiment as a method to evaluate the efficacy of CTMs, revealing the effect of interfacial work function modification

Hybrid organic-inorganic perovskite-based devices are increasingly being explored for a variety of advanced electronic materials, particularly as active layers in solar cells.[31,33,34,454,481,584-586] This class of materials has achieved record power conversion efficiencies due to its unique set of properties, such as ambipolar transport,[587] μm-scale free carrier diffusion lengths,[588] and spontaneous polarizability.[589]

In this work we fabricated methylammonium lead triiodide ($MAPbI_3$) perovskite/CTM bilayers on ITO electrodes. We report here, the direct observation of large-scale ambipolar transport, and spontaneous polarization using Photo-Kelvin Probe Force Microscopy (photo-

---

[*****] I would like to acknowledge Dr. Yao Liu for device fabrication, and Dr. Zachariah A. Page for materials synthesis.

KPFM).[29,530,590,591] We find that charge extraction of photo-generated free charge carriers by the CTM/electrode interface causes fast polarization of the 200 nm thick polycrystalline perovskite film. The polarization is directly detected by measuring the surface potential of the $MAPbI_3$/air interface opposite the $MAPbI_3$/CTM interface under illumination at increasing photon flux. Moreover, we find that the sign of polarization is CTM-dependent. CTMs that extract holes leave an excess of negative charges, which accumulate at the opposite interface. Oppositely, CTMs that extract electrons from the $MAPbI_3$ layer show an accumulation of positive charges at the $MAPbI_3$/air interface.

3.6.1 Device Fabrication

We chose several CTMs to investigate how the surface potential of perovskite layers is affected by illumination. They are poly(3,4-ethylenedioxythiophene): polystyrene sulfonate (**PEDOT:PSS**), [6,6]-phenyl-C_{61}-butyric acid methyl ester (**$PC_{61}BM$**), polyethylenimine, ethoxylated (**PEIE**), poly(benzothiadiazole vinylene-*alt*-2,5-bis(4-sodium sulfonate)butoxy)-1,4-phenylenevinylene) (**PVBT-SO_3**),[24,557] 2,3,4-tris(3-(dimethylamino)propoxy)fulleropyrrolidine (**C_{60}-N**),[559] 2,3,4-tris(3-(sulfobetaine)propoxy)fulleropyrrolidine (**C_{60}-SB**),[525] and **PSS**; see Figure 138 for structures. CTMs were chosen based on if they were hole or electron transporters, or insulators, and if they are known to form interfacial dipoles at electrode interfaces.

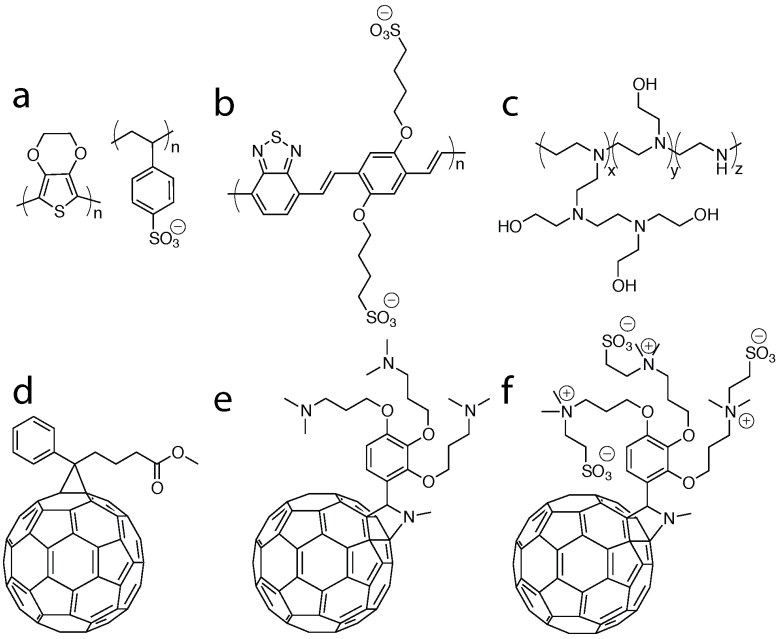

Figure 138: Chemical structure of charge transport materials. a) PEDOT:PSS, b) PVBT-SO_3, c) PEIE, d) $PC_{61}BM$, e) C_{60}-N, and f) C_{60}-SB.

Indium tin oxide (ITO)-coated glass substrates, 20 ± 5 ohms/sq, were cleaned by ultrasonic treatment in detergent, deionized water, acetone, and isopropyl alcohol, and then dried in an oven for 6 hours. Then CTM were spin coated onto ITO substrates. PEDOT:PSS, PVBT-SO_3 and PSS were spin coat from water. $PC_{61}BM$ was spin coat from chlorobenzene. C_{60}-N and C_{60}-SB were spin coat from trifluoroethanol. $MAPbI_3$ was prepared on top of CTM by spin-coating a solution of lead acetate ($Pb(OAc)_2$) and methylammonium iodide (MAI), 1:3 molar ratio, in *N*,*N*-dimethylformamide on to heated substrates.

3.6.2 photo-KPFM

KPFM measurements were made using an Asylum Research MFP3D stand-alone instrument with a Pt/Ir coated silicon AFM probe (used as received from AppNano ANSCM-PT). Measurements were made in a two-pass approach; the first pass measures topography and the probe is mechanically driven, and in the second pass the surface potential is measured while the

probe is driven at its AC voltage resonant frequency at height of ΔH = 30 nm above the surface. Potential differences between the probe and the sample cause mechanical oscillations of the AFM probe, which are cancelled by an applied DC bias by a feedback loop. The applied bias is thus equal to the potential difference between sample and probe. Three scans of 5 μm × 1.25 μm (512 pixel × 128 pixel) at 0.5 Hz. Histogram plots of counts vs. potential are made for each scan, and fit with a Gaussian distribution to obtain the average and standard deviation of the potential for a particular scan.

We measured the change in surface potential of photo-excited $MAPbI_3$ perovskite/CTM bilayers on ITO/glass using photo-KPFM. The experiment is depicted in Figure 139, where the perovskite-interlayer bilayer is on top of a grounded ITO/glass substrate. A 532 nm pulse-diode laser is used to illuminate the sample, with a spot size of ~ 40 um. A neutral density filter is used tune the intensity of illumination. The photon flux (ϕ, $10^{21}/m^{-2}s^{-1}$) is calculated using the 40 μm illumination spot. A range of photon flux from $1.66 \times 10^{21}/m^{-2}s^{1}$ to $3260.77 \times 10^{21}/m^{-2}s^{-1}$ is used.

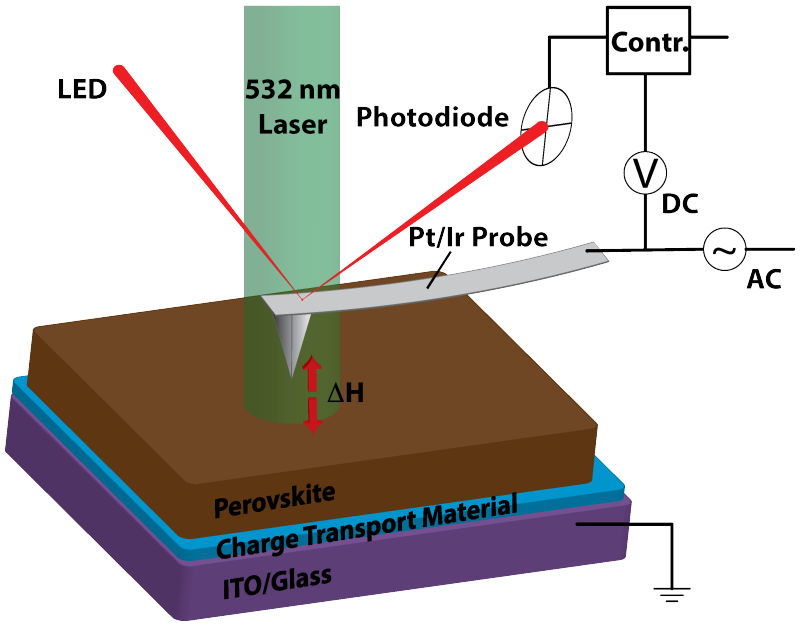

Figure 139: Depiction of photo-KPFM experiment. Device architecture is glass/ITO/CTM/$MAPbI_3$.

Tapping mode AFM images revealed < 100 nm $MAPbI_3$ grains. A representative height plot for $MAPbI_3$ on PEDOT:PSS is shown in Figure 140a. In Figure 140b-d we show surface potential plots for $MAPbI_3$ on PEDOT:PSS at $\phi = 0/m^{-2}s^{-1}$, $867.41 \times 10^{21}/m^{-2}s^{-1}$, and $3260.77 \times 10^{21}/m^{-2}s^{-1}$ respectively. When the sample contained PEDOT:PSS, we observed a rapid decrease in surface potential with respect to photon flux from +206.79 mV ± 1207 mV to -18.75 mV ± 8.64 mV.

PEDOT:PSS is commonly used as a hole transporter, therefore we expect that photo-generated holes will be almost exclusively extracted from the perovskite layer. As positively charged holes are extracted from the bottom of the perovskite layer through the CTM to the ITO electrode, an excess of negatively charged electrons. We posit that the ability for MAPbI3 to spontaneously polarize cause an accumulation of negative charges at the top perovskite interface. This sea of electrons is easily detected by KPFM. As we increase the photon flux, more excitons are formed and subsequently separated, and thus holes extracted, leaving behind even more negatively charged electrons.

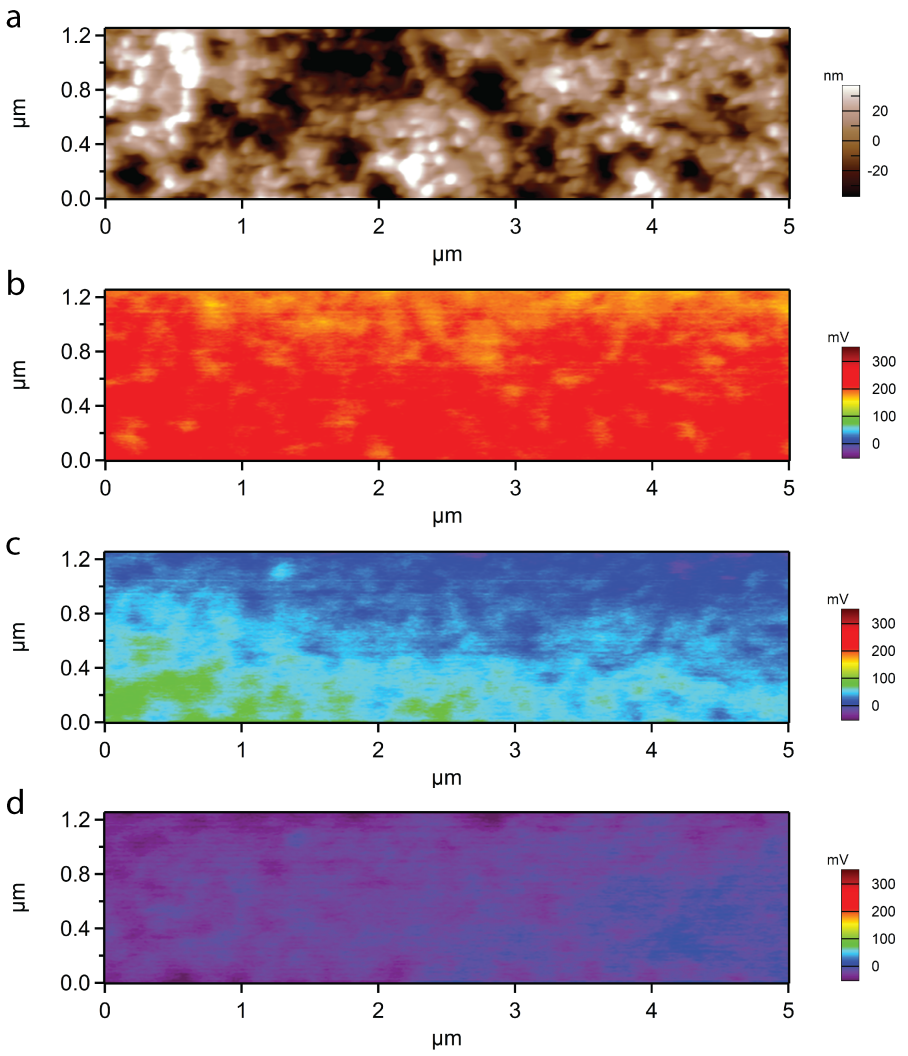

Figure 140: AFM and KPFM of $MAPbI_3$ on PEDOT:PSS. a) tapping mode height image. Surface potential maps in a) dark, b) illumination of $\phi = 867.41 \times 10^{21}/m^{-2}s^{-1}$, and $\phi = 3260.77 \times 10^{21}/m^{-2}s^{-1}$. Surface potential scale is the same for b-d.

To further test the photo-induced polarization due to specific charge extraction we conducted photo-KPFM on $MAPbI_3$ samples on a variety of CTMs. To directly compare measurements, we report the change in surface potential during illumination compared to dark, $V_{ill} - V_{dark}$ (mV). A plot of $V_{ill} - V_{dark}$ (mV) vs ϕ for samples containing different CTMs are shown in Figure 141. The hole transporters PEDOT:PSS and PVBT-SO_3 both showed a decrease in potential with ϕ, indicating an excess of negatively charged electrons are being detected. PEIE is an insulator, but

is also a known electrode work function modifier.[592] Previous studies have found that PEIE reduces the work function of ITO by ~ 1eV. The relatively low work function electrode should selectively extract electrons; however, we observe that the sign of polarization at the $MAPbI_3$/air interface is negative. In fact, the work function modification of ITO performed as well as holt transporter PVBT-SO_3.

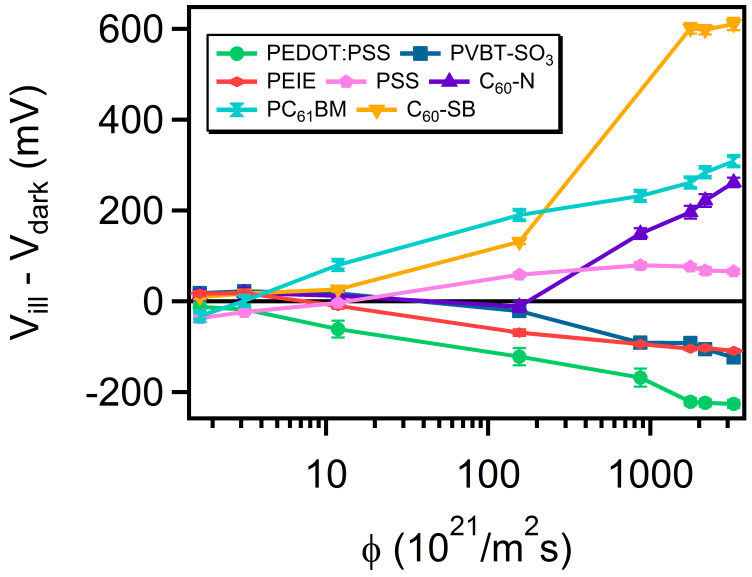

Figure 141: Plot of change in surface potential, $V_{ill} - V_{dark}$ (mV) vs photon flux (ϕ, $10^{21}/m^{-2}s^{-1}$) for $MAPbI_3$/CTM bilayers on grounded ITO electrodes.

We next tested $MAPbI_3$/CTM bilayers using electron transporting materials. Using $PC_{61}BM$ an increase in surface potential was observed with increasing ϕ, opposite of what was observed for hole CTM. As with PEDOT:PSS, however in an opposite fashion, negatively charged electrons are primarily extracted from the perovskite by $PC_{61}BM$, leaving an excess of positively charged holes. The $MAPbI_3$ layer is quickly polarized, leaving a positively polarized interface measured by KPFM.

C_{60}-N and C_{60}-SB are electron CTMs, but are also known to form interfacial dipoles with Ag electrodes of 0.8 eV and 0.6 eV respectively,[525,545,559,592] effectively lowering the work function of the electrode. C_{60}-N was also demonstrated to pin the work function of ITO to a very low 3.65 eV,[525] essentially making hole transport impossible. We observe that the sign of polarization of the $MAPbI_3$/air interface is positive upon irradiation, indicating that electrons are indeed extracted by C_{60}-N and C_{60}-SB to the ITO electrode. C_{60}-SB contains a dipole in its sulfobetaine groups, which form an interfacial dipole with ITO; this results in a large polarization of the perovskite/air interface of ~ 600 mV at illumination of $3260.77 \times 10^{21}/m^{-2}s^{-1}$. Finally, we used insulating PSS as a CTM. Polystyrene has been demonstrated to be a tunneling contact for hole transport to Spiro-OMeTAD/Au in perovskite-based solar cells.[593] When PSS is used a contact with ITO, we observe a slight positive polarization, although significantly less than other electron transport materials $PC_{61}BM$, C_{60}-N, and C_{60}-SB. Thus, we observe that in the $MAPbI_3$/PSS/ITO architecture, PSS acts as an electron tunneling layer, albeit a relatively ineffective one. The results are summarized in Figure 142, displaying the approximate energy levels of the device architectures used in this study, and which charge carrier is extracted and which one is accumulated in the perovskite layer and detected by KPFM.

Polarization in perovskite layers has been ascribed to electronic and/or ionic processes. However, the spontaneous polarization under light in combination with the unbalanced architecture used lend its self to a predominantly electronic mechanism. Further, the observation of the effect of hole or electron transport properties of the CTM on the sign of polarization also suggest a principally electronic phenomenon.

As charges are extracted through the CTM interface, it may be expected that opposite charges will either quickly recombine, or be screened by the reportedly high dielectric[594] perovskite.

However, we observe that the perovskite layer is highly polarizable, as excess charges accumulate at the interface opposite the CTM as detected by surface potential measurements. We also report two surprising results, the first that low work function PEIE/ITO extracted holes. This suggests that the processing conditions of PEIE used were not sufficient to lower the ITO work function to conduct electrons. The second is that insulating PSS/ITO provides a tunneling contact for electrons, however not as good as other electron transporters.

Finally, we suggest that this method of measuring the magnitude and sign of polarization of perovskite layers can be utilized to analyze the efficacy of CTM/electrode interfaces. The sign of polarization is related to the type of charge carrier (hole or electron) extracted, while the magnitude is related to the number of charges extracted. For example, this work suggests that C_{60}-SB/ITO may be a good electron transport interface, with a highest surface potential of ~600 mV measured in these experiments

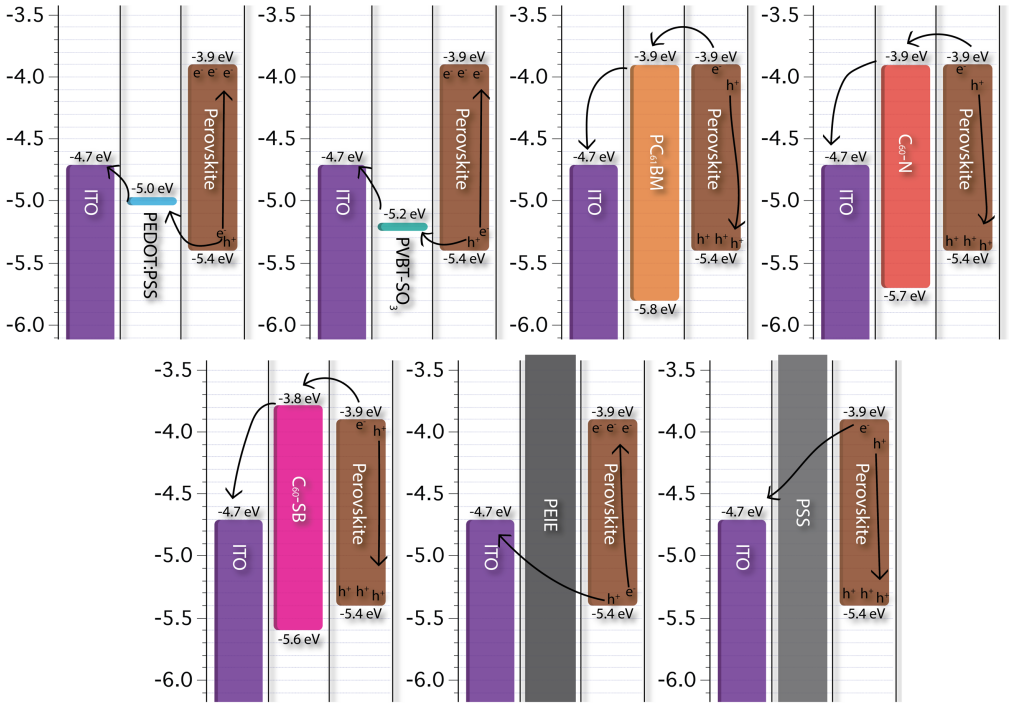

Figure 142: Energy diagrams for perovskite/CTM/ITO architectures, demonstrating the accumulation of specific charge carriers, from KPFM, depending on the CTM.

3.7 Reduced Charge Recombination in Carbon Nanotube/Perovskite Active Layers

In this chapter[†††††] we discuss the use of carbon nanotubes, incorporated into the bulk perovskite active layer, as a means to enhance charge extraction and reduce charge recombination. Using impedance spectroscopy and computation, we show that incorporation of multi-walled carbon nanotubes (MWCNTs) in the bulk of the active layer of perovskite-based solar cells reduces charge recombination and increases the open circuit voltage. An ~87% reduction in recombination was achieved when MWCNTs were introduced in the planar-heterostructure perovskite solar cell containing mixed counterions. The open circuit voltage (V_{oc}) of perovskite/MWCNTs devices was increased by 70 mV, while the short circuit current density (Jsc) and fill factor (FF) remained unchanged.

Lead halide-based perovskite solar cells[33,34,451-456,595] have garnered widespread attention because of their high efficiency[458,496] and low-temperature solution processing.[459] Over the past few years there have been numerous reports on perovskite solar cells, especially on materials processing[450,453] and interface engineering[458,515], to enhance device efficiency. A key feature of lead tri-halide-based perovskites is that they are ambipolar charge transporters.[454,596] Upon photo-illumination, photo-generated carriers, *i.e.*, electrons and holes, get transported through the same active layer. Thus, although the mobilities of the charge carriers are high in the perovskite layer, inefficient charge extraction out of the

---

[†††††] This chapter was adapted, with permission, from Bag, Monojit, Lawrence A. Renna, Seung Pyo Jeong, Xu Han, Christie L. Cutting, Dimitrios Maroudas, and D. Venkataraman. "Evidence for reduced charge recombination in carbon nanotube/perovskite-based active layers." *Chemical Physics Letters* 662 (2016): 35-41. I would like to acknowledge Prof. Monojit Bag and Christie L. Cutting for device fabrication, Seung Pyo Jeong for synthesizing polymer material for dispersing carbon nanotubes, and Dr. Xu Han for current voltage simulations using drift-diffusion model.

active layer leads to charge recombination[597,598] in the bulk, which lowers the open circuit voltage (V_{oc}). Theoretical calculations predict that the open circuit voltage can be increased by 60 mV if the charge recombination losses are reduced by an order of magnitude[599] Thus, perovskite solar cells require either an electron- or a hole-transporting layer or both for selective charge extraction at the perovskite/electrode interfaces.[471] In a conventional device, a compact or a nanostructured/mesoporous TiO_2 layer is used as the electron transporting material (ETM), which extracts the electrons from the perovskite layer and reduces the charge recombination.[591,597,600] 2,2′,7,7′-tetrakis(N,N-di-*p*-methoxyphenylamine)-9,9′-spirobifluorene (spiro-OMeTAD) is commonly used as the hole transporting material (HTM).[482] In an inverted device architecture, a thin layer of poly(3,4-ethylenedioxythiophene) polystyrene sulfonate (PEDOT:PSS) is placed between the ITO electrode and the active layers to extract the holes. A [6,6]-phenyl-C_{61}-butyric acid methyl ester (PCBM) layer is placed between the metal electrode and the perovskite layer to extract the electrons.[459,496] Except for mesoporous TiO_2, all other methods focus on the extraction of charges at the interface and not in the bulk. Moreover, the electron and hole mobilities in PCBM and PEDOT:PSS, respectively, are very low compared to those in the perovskite active layer. Modifications to PCBM[518] or PEDOT:PSS layers[601] are necessary to increase the electron or hole extraction rate. Nanostructured carbon,[602] including CNTs and graphene based systems, has been used for a variety of energy applications particularly transparent electrodes and charge transport layers.[603] CNTs have been used in composite materials as electrodes for perovskite devices.[34,604] Also, CNTs have been incorporated at the perovskite-electrode interface,[504,605-609] which helps with hole extraction at the interface. In principle, one can extend this concept to extract holes from the bulk also if CNTs are incorporated with the active

layer. However, this has been a challenge because in has been difficult to obtain stable CNT dispersions in solvents that are compatible with perovskite active layer fabrication. Herein, we show the facile incorporation of MWCNTs in the bulk of the perovskite layer and the reduction in recombination losses by 87%. We also demonstrate that the introduction of MWCNTs in the bulk of the perovskite layer reduces the charge accumulation at the perovskite/ PEDOT:PSS interface and leads to improved V_{oc} and thus higher power conversion efficiency (PCE).

3.7.1 Fabrication of MWCNT/Perovskite Active Layers

Stable dispersions of MWCNTs were prepared in DMF as shown in Figure 143. For this study, we used MWCNTs that have outer diameters of 40-60 nm and lengths of 1-2 μm. First, MWCNTs were added to DMF (0.1 $mg \cdot mL^{-1}$) along with poly(methyl methacrylate) (PMMA)-functionalized hexabenzocoronene (HBC). The HBC moiety was placed specifically at the PMMA chain-end such that the polymer chain-end can interact with the MWCNT through strong π-π interactions.[610] The dispersion was then ultrasonicated for a few minutes and was allowed to settle for 24 h before use. MWCNTs that were not attached to the polymer settled at the bottom of the vial and were separated from the dispersion by decantation. The dispersion is stable over 30 days under ambient conditions (see Figure 144).

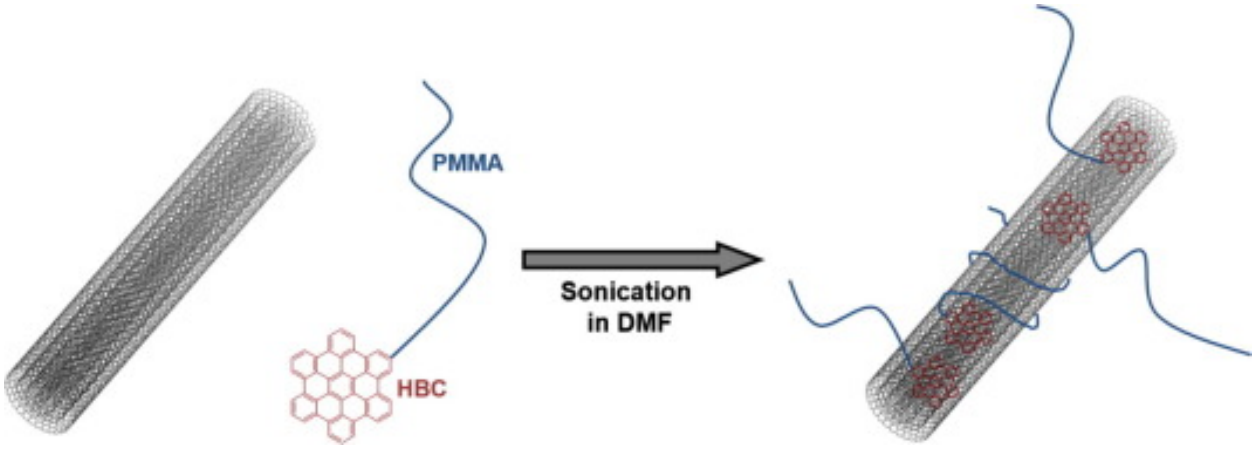

Figure 143: Schematic representation of HBC-PMMA-grafted MWCNT.

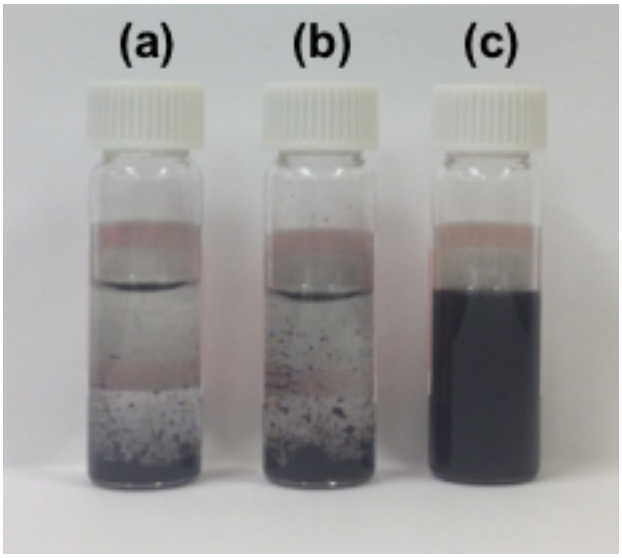

Figure 144: Dispersion test of (a) MWCNTs (0.1 mg/mL) in toluene, (b) MWCNTs (0.1mg/mL) with PMMA only (1 mg/mL) in toluene, and (c) MWCNTs (0.1 mg/mL) with HBC functionalized with PMMA (0.1 mg/mL) in toluene.

Planar heterojunction perovskite solar cells were fabricated in air by sequential deposition[450] of organic counterions onto the PbI_2 thin film. 50 μL of hot solution (400 $mg \cdot mL^{-1}$) of lead iodide in DMF was spin coated on a pre-heated (85 °C) PEDOT:PSS-coated ITO substrate at 6000 rpm for 35 s. PbI_2-coated substrates were then annealed at 85 °C for 45 min. Mixed counterions (1:1 by wt. ratio) of methylammonium iodide (MAI) and formamidinium iodide (FAI) were dissolved in isopropanol (40 $mg \cdot mL^{-1}$). 50 μL of this solution was spin coated on top of PbI_2 films at 6000 rpm for 35 s at room temperature. Devices were then annealed at 85 °C for 45 min in the dark. MWCNT/perovskite composite devices were prepared from the PbI_2 solution containing 0.005% and 0.01% of MWCNTs (by wt. to PbI_2) in DMF keeping the PbI_2 concentration approximately 400 $mg \cdot mL^{-1}$. Powder x-ray diffraction (PXRD) revealed (see Figure 145) complete conversion to a trigonal (*P3m1*) perovskite phase for films fabricate with or without MWCNTs. A thin layer of PCBM was spin coated from a solution in chlorobenzene

(20 mg·mL^{-1}) at room temperature at 1000 rpm for 60 s inside a N_2-filled glove box. Finally, 15 nm of Ca at a deposition rate of 0.5 Å·s^{-1} followed by 100 nm of Al electrode at a deposition rate of 1-3 Å·s^{-1} were thermally deposited using a shadow mask of 6 mm^2 active area at 1×10^{-6} mbar.

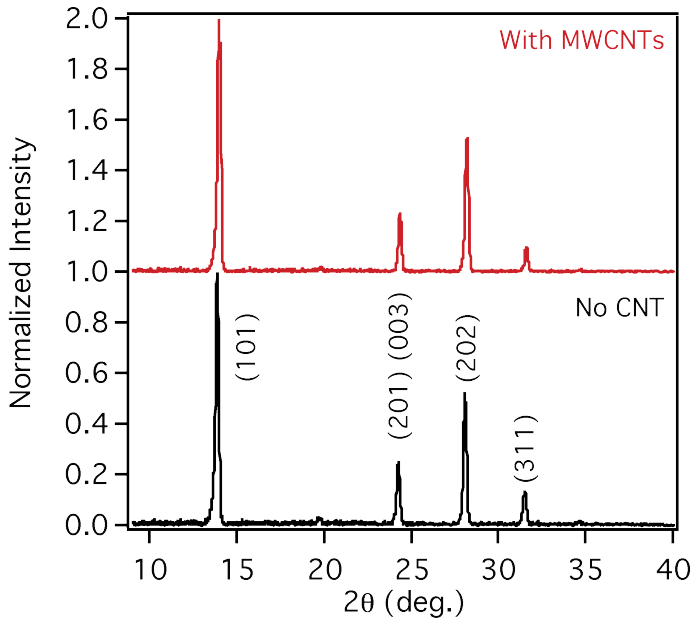

Figure 145: Background subtracted and intensity normalized PXRD of perovskite films fabricated with and without MWCNTs. Both films showed complete conversion to the trigonal (*P3m1*) perovskite phase with peaks attributed to the (101), (2001)/(003), (202), and (311) planes.

CNT bundles are often dispersed in a solvent using covalent chemical modification of the surface, conjugated polymers, or polymeric surfactants.[611,612] Perovskite active layers are fabricated from solutions of lead and organic ammonium halide salts in polar solvents such as isopropanol or *N*,*N*-dimethylformamide (DMF). Thus, to incorporate MWCNTs in the bulk of the active layers, we needed MWCNT dispersions in polar solvents that are compatible with the active layer fabrication conditions. Moreover, the MWCNTs should preserve their electronic properties, and the interface between the MWCNT/perovskite should facilitate charge transfer. We recently reported a supramolecular strategy that uses π-π interactions to non-covalently

attach the chain end of a polymer to MWCNT.[610] Using this method, we were able to incorporate 0.005% and 0.01% of MWCNTs in the bulk of the perovskite layer. We chose MWCNTs because they are predominantly metallic and have high electrical conductivity compared to single-wall CNTs.[613,614] We verified the presence of MWCNTs in the PbI_2 film using scanning electron microscopy (SEM) and conducting atomic force microscopy (cAFM) (see Figure 146). Most of the MWCNTs were expected to be in the bulk with no preferential orientation and only a few of them were expected to be oriented perpendicular to the film, thus spanning the entire film thickness. The presence of conducting MWCNTs in the film was detected by bright contrast due to charging in SEM. In cAFM, we observed higher current regions in the non-conducting PbI_2 matrix indicating the presence of percolating pathways from the bottom electrode to the cAFM probe. Both observations are consistent with presence of MWCNTs in the PbI_2 matrix. Further, the presence of MWCNTs in the films after conversion was confirmed with SEM. Figure 147 shows MWCNTs are in the grain boundaries of large perovskite grains, which are on the order of 1 μm.

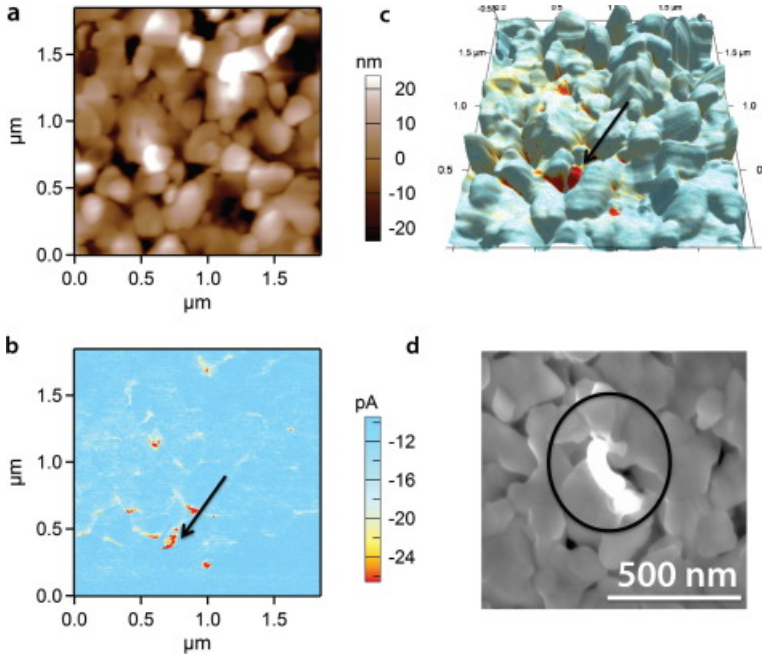

Figure 146: (a) AFM topographic image of PbI_2/MWCNT composite film on PEDOT:PSS-coated ITO substrate. (b) cAFM image of the same area. (c) Topographic image superimposed onto current mapping from cAFM. High current regions are from MWCNTs. (d) SEM image of PbI_2/MWCNTs composite film on Si substrate. A MWCNT is highlighted with a circle.

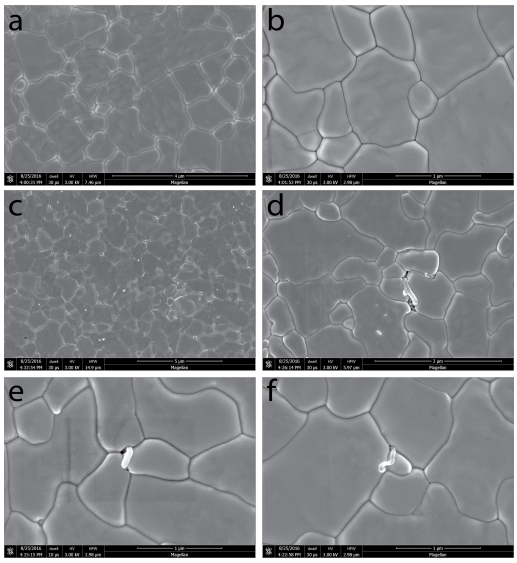

Figure 147: SEM of perovskite films fabricated (a-b) without MWCNTs and (c-f) with MWCNTs. SEM reveals large grains, on the order of 1 µm, with MWCNTs in the grain boundaries.

3.7.2 MWCNT/Perovskite Current-Voltage Measurements

Current density-voltage (J-V) measurements (Figure 148) were carried out in the dark as well as under AM1.5G solar simulator at 100 $mW \cdot cm^{-2}$ intensity of light in a N_2-filled glove box. Dark J-V measurements were carried out at a scan rate of 50 $mV \cdot s^{-1}$ from reverse to forward bias as well as forward to reverse bias. No hysteresis was observed for devices containing 0.005% and 0.01% MWCNTs. However, perovskite solar cells containing no MWCNTs showed a small hysteresis in dark measurements (see Figure 149). J-V measurements under light were conducted by scanning the voltage from the forward bias to the reverse bias direction at a scan rate of 250 $mV \cdot s^{-1}$. J-V curves under light were averaged over 9 devices containing MWCNTs at concentrations of 0%, 0.005% and 0.01%, the averaged measurements are shown in Figure 148a. We focused on mixed counterions of MAI and FAI instead of $MAPbI_3$ because they are reported to have superior photovoltaic performance.[615] Average and best device parameters are given in Table 16 for all three samples. The V_{oc} (~0.95 V) was higher in devices containing MWCNTs compared to the reference (0% MWCNTs) solar cell V_{oc} (0.88 V). The maximum PCE of 12.9% was obtained from devices containing 0.005% MWCNTs. Further increase in MWCNTs in the perovskite matrix led to reduced current density and fill factor. Device performance histograms for 22 devices containing 0.005% MWCNT are shown in Figure 148c.

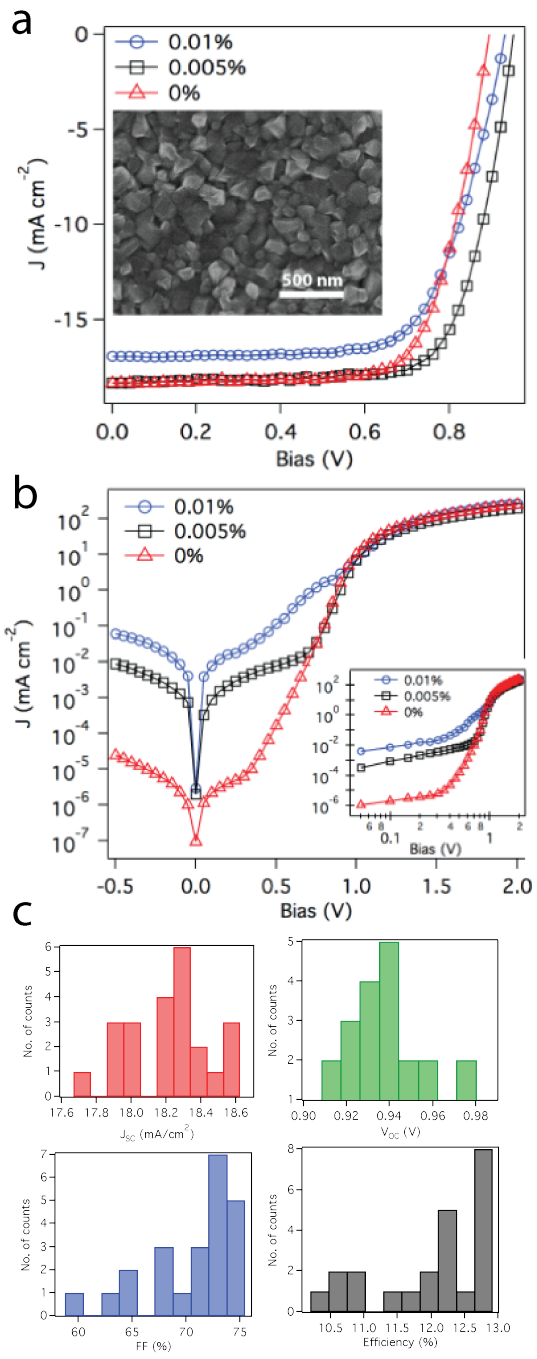

Figure 148: (a) J-V curves from steady exposure to light of three lead tri-iodide-based perovskite photovoltaic devices with active layers containing 0%, 0.005% and 0.01% MWCNTs (by wt. to PbI_2) averaged over 9 samples from different substrates of the same batch of experiments. Inset: Top SEM image of perovskite sample containing no CNTs. (b) Dark J-V characteristics of perovskite photovoltaic devices with active layers containing 0% (red triangles), 0.005% (black squares) and 0.01% (blue circles) of MWCNTs. The inset shows a log-log plot of the dark J-V curves. (c) Device performance histograms for 22 devices containing 0.005% MWCNT.

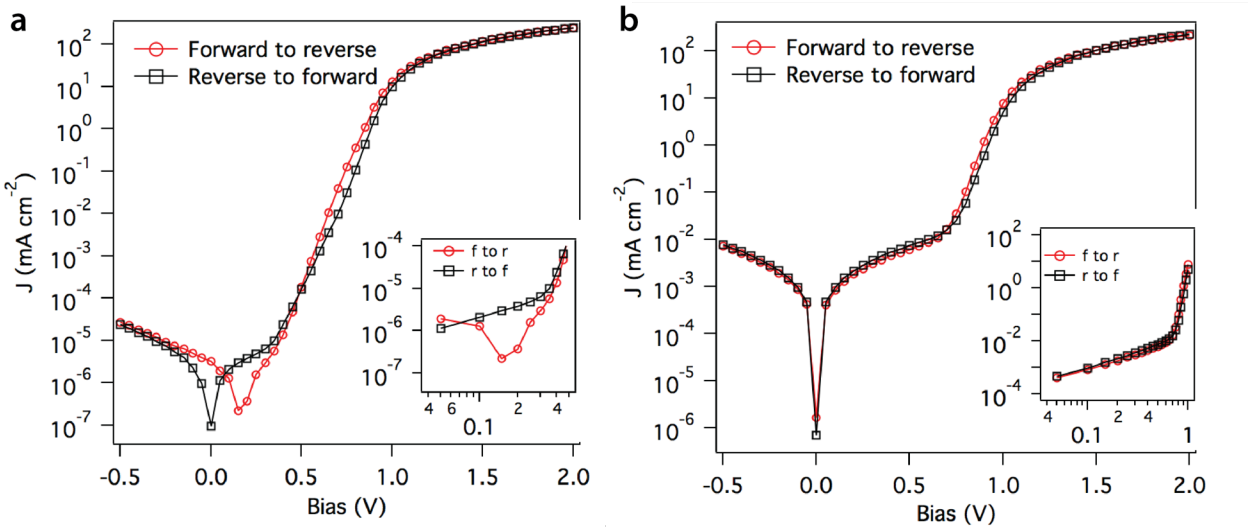

Figure 149: (a) Dark J-V curve for a perovskite device containing no MWCNTs in the active layer. Inset: log-log plot of the same J-V curve in the low-field regime. (b) Dark J-V curve for a perovskite device containing MWCNTs in the active layer at a concentration of 0.005% (by wt. to PbI_2). Inset: log-log plot of the same J-V curve in the low-field regime.

Table 16: Performance of lead tri-iodide-based perovskite solar cells containing 0%, 0.005% and 0.01% MWCNTs in the active layer. Average values are reported from 9 best devices of multiple substrates.

Device condition	J_{sc} *(mA-cm^{-2})*	V_{oc} *(V)*	*FF (%)*	η *(%)*
0.0% CNT (Avg.)	18.15 ± 0.5	0.885 ± 0.005	72.6 ± 1	11.7 ± 0.4
Best cell	18.66	0.883	73.3	12.09
0.005 % CNT (Avg.)	18.27 ± 0.2	0.95 ± 0.02	73.0 ± 2	12.7 ± 0.4
Best cell	18.28	0.97	72.8	12.91
0.01% CNT (Avg.)	16.82 ±0.3	0.92 ± 0.02	69.0 ± 2	10.7 ± 0.2
Best cell	16.84	0.934	69.6	10.96

2.6.3 MWCNT/Perovskite EIS Measurements

We first investigated the recombination losses in the perovskite films using electrochemical impedance spectroscopy (EIS).[616,617] Figure 150 shows the Nyquist plot for samples containing 0%, 0.005%, and 0.01% MWCNTs at applied bias voltages (V_{app}) of 0 mV and 900 mV under AM1.5G solar simulator at 100 mW·cm^{-2} light intensity. Nyquist plots in the dark are

shown in Figure 151. The Nyquist plots were analyzed using an equivalent electronic circuit model (Figure 150c).[616,617] To separate the ionic component from the electronic component, we introduced a Warburg diffusion element along with a charge transfer resistance (R_{CT}) and a Debye layer capacitance (C_{dl}) to the circuit model (Figure 150c).[449] The electronic component is represented by resistive (R_{elect}) and chemical capacitance (C_{μ}) elements. Three distinct regimes are observed in the Nyquist plots under light: (1) a high-frequency regime related to the interfacial resistance and capacitance, (2) an intermediate-frequency regime related to charge transport and recombination, and (3) and a low-frequency regime related to charge accumulation and/or ion diffusion.[29,449,616,618] To analyze the recombination and charge transport, we focused our analysis on the intermediate frequency regime of the Nyquist plots. When $V_{app} = 0$ V, the built-in internal electric field is high because it is not compensated by an applied voltage.[619] Under this condition, the dominant charge transport mode is drift and the measured resistance, R_{elect}, is dominated by charge recombination resistance (R_{rec}).[620] As seen in Figure 150a, as the concentration of MWCNTs increase, R_{rec} also increases consistent with reduced recombination and efficient charge collection.[470] At $V_{app} = 900$ mV, the applied voltage is close to the V_{oc}. Under this condition, the internal electric field decreases and the charge transport is dominated by diffusion. The measured resistance, R_{elect} is dominated by charge transport resistance (R_{tr}) as shown in Figure 150b. R_{tr} decreases as the percentage of MWCNTs is increased in the perovskite matrix, indicating better charge transport (Figure 150b). In active layer containing 0.01% MWCNTs, the hole mobility is expected to be higher than the electron mobility due to the high hole mobility in MWCNTs.[621] These experimental results are also consistent with our simulation results that predict high hole mobility in devices containing 0.01% MWCNTs.

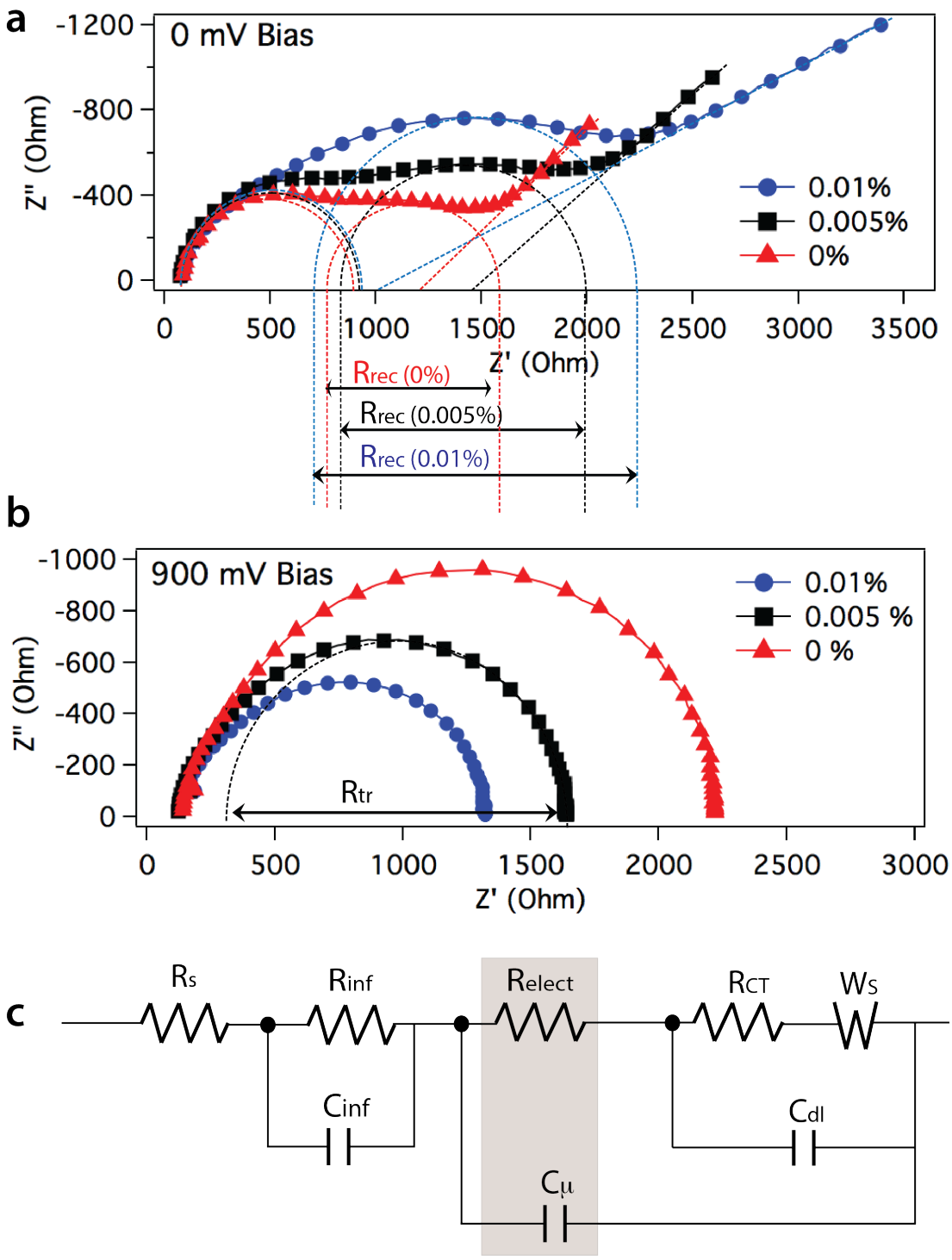

Figure 150: EIS plot of perovskite solar cells under AM1.5G solar simulator at 100 mW·cm^{-2} light intensity at a bias voltage of (a) 0 V and (b) 900 mV. The frequency range is from 100 Hz to 1 MHz at 20 mV AC amplitude. (c) Equivalent circuit diagram for the perovskite solar cell. R_{elect} represents the electronic transport component and W_S represents the Warburg diffusion element. The shaded area represents the intermediate-frequency component of the Nyquist plot.

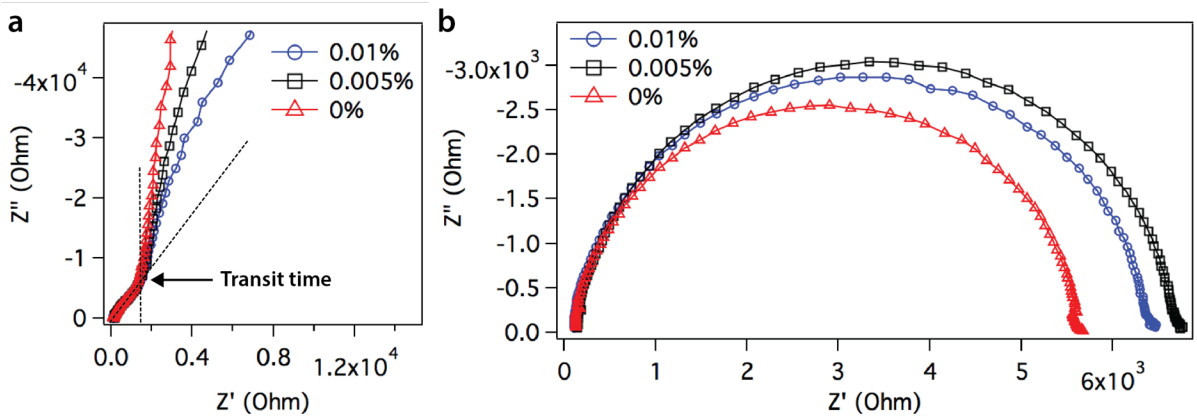

Figure 151: Dark impedance measurement of perovskite solar cells containing MWCNTs in the active layer at concentrations of 0%, 0.005% and 0.01% (by wt. to PbI_2) at an applied DC bias of (a) 0 V and (b) 0.8 V. By applying a DC bias, we show that devices containing 0.005%wt. MWCNTs have the largest recombination resistance in the dark, and thus the most efficient charge extraction.

2.6.4 MWCNT/Perovskite Mott-Schottkey Analysis

We then examined the charge carrier concentration of the three samples at the perovskite/HTM interface from the slope of the Mott-Schottky (M-S) plot as shown in Figure 152 under AM1.5G solar simulator at 100 $mW \cdot cm^{-2}$ light intensity. The photo-generated charge carrier concentration at the perovskite/HTM interface is inversely proportional to the slope of the linear regime of the M-S plot assuming the dielectric constant is the same for all three samples. The ratio of the slopes of the linear regime of the M-S plot was 1:1.8:2.3 for 0%, 0.005% and 0.01% MWCNTs respectively indicating that the photo-generated charge accumulation is reduced by a factor of two at the perovskite/HTM interface when the MWCNT content was increased to 0.005%. These results are consistent with the EIS results and the simulation that showed that charge extraction rate at the perovskite/PEDOT:PSS interface was improved upon introduction of MWCNTs.

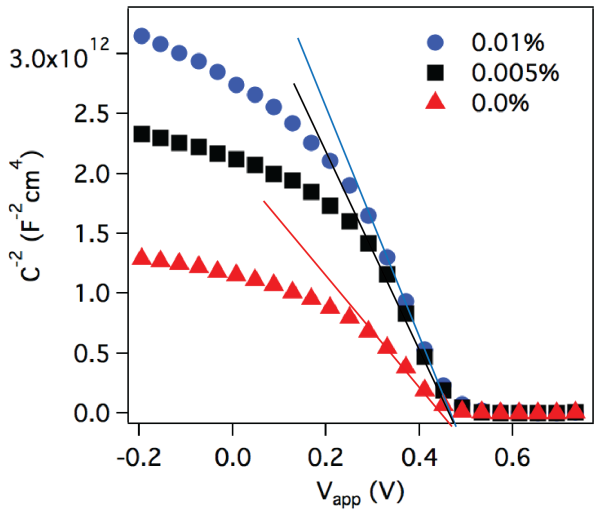

Figure 152: Mott-Schottky plot of lead tri-halide perovskite solar cells containing MWCNTs at concentrations of 0%, 0.005% and 0.01% (by wt. to PbI_2) in the bulk of the perovskite films at 100 $mW \cdot cm^{-2}$ light intensity. Capacitance was measured at a 10 kHz oscillation frequency with 20 mV AC amplitude.

2.6.5 MWCNT/Perovskite Current-Voltage Simulations Using Drift-Diffusion Model

To understand the origin of the increase in V_{oc} in the presence of MWCNTs in perovskite solar cells, we first carried out charge transport simulations in the devices examined by implementing a drift-diffusion-reaction model that is detailed in SI of Ref.[622] The parameter values obtained in the simulations are given in Table 17and discussed in SI of Ref.;[622] the simulation results are compared with the experimental J-V measurements in Figure 153. We assumed a comparable electron and hole mobility (~ 1×10^{-4} $m^2V^{-1}s^{-1}$) in perovskite solar cells without any MWCNTs introduced in the active layer,[588,623] whereas the mobility of electrons and holes in PCBM[473] and PEDOT:PSS,[624] respectively, were taken to be at least four orders of magnitude lower than in the perovskite active layer. We observed a significant reduction (at least 87%) in recombination loss in active layers containing MWCNTs. The simulation indicated that the hole mobility was four times higher than the electron mobility for devices containing 0.01%

MWCNTs whereas the mobilities are comparable in devices containing 0% and 0.005% MWCNTs. Moreover, the bulk defect density was calculated to be about 9 times higher in devices containing 0.01% MWCNTs compared to devices with 0% MWCNTs. Our simulations also indicated that the charge extraction rate at the perovskite/PEDOT:PSS interface was improved upon introduction of MWCNTs in the active layer.

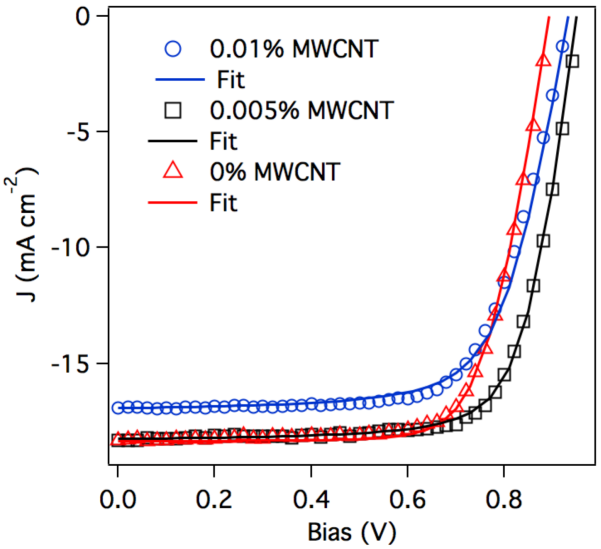

Figure 153: (a) Best fitting of simulation predictions according to the drift-diffusion-reaction model (solid lines) to the experimentally measured J-V characteristics (open symbols) in perovskite photovoltaic devices for 0%, 0.005% and 0.01% (by wt. to PbI_2) concentration of MWCNTs in the active layer.

Table 17: Optimal parameter values obtained from fitting the simulation predictions according to the drift-diffusion-reaction model to the experimental *J-V* data for perovskite samples containing 0%, 0.005% and 0.01% MWCNTs in the active layer. All of the parameters are defined in SI of Ref. [622], where the drift-diffusion-reaction model is described in detail.

Parameters		*0%*	*0.005%*	*0.01%*
Charge generation	G_0 ($\times 10^{27}$ $m^{-3}s^{-1}$)	3.8	3.8	3.53
Perovskite relative permittivity	$\varepsilon_{perovskite}$	6.5	6.5	6.5
Electron mobility in PCBM	μ_n ($\times 10^{-8}$ $m^2V^{-1}s^{-1}$)	2.4	2.4	2.4
Hole mobility in PEDOT:PSS	μ_p ($\times 10^{-8}$ $m^2V^{-1}s^{-1}$)	2.4	2.4	2.4
Electron mobility in perovskite	μ_n ($\times 10^{-4}$ $m^2V^{-1}s^{-1}$)	1.0	1.0	1.0
Hole mobility in perovskite	μ_p ($\times 10^{-4}$ $m^2V^{-1}s^{-1}$)	1.0	1.0	**4.0**
Intrinsic carrier density	n_i ($\times 10^{15}$ m^{-3})	6.5	6.5	6.5
Recombination coefficient at PCBM/perovskite interface	$C_{PCBM/Perovskite}$	1.0	1.0	1.0
Recombination coefficient at PEDOT:PSS/perovskite interface	$C_{PEDOT:PSS/Perovskite}$	**1.0**	**0.5**	**0.2**
Bulk recombination coefficient in perovskite layer	$C_{perovskite}$ ($\times 10^{-8}$)	**4.5**	**0.57**	**0.5**
Bulk defect density	N_t ($\times 10^{24}$ m^{-3})	**0.14**	**1.05**	**1.28**

2.6.6 MWCNT/Perovskite Defect/Trap Density Analysis

Next, we probed the impact of MWCNTs on defect or trap state densities by analyzing the J-V device characteristics under dark. The dark J-V device characteristics for the three samples containing 0%, 0.005% and 0.01% MWCNTs are shown in Figure 148b. We found that the dark current in the reverse voltage bias regime increased with MWCNT concentration and is consistent with increasing leakage current. A fit of the dark J-V curves to a diode equation indicates all samples show a non-ideal behavior (ideality factor, $n > 1$) (see Figure 154 and Table 18). The ideality factor was calculated to be 1.71, 1.73 and 5.32 for samples containing 0%,

0.005% and 0.01% MWCNTs respectively. Both the increase in the leakage current and the ideality factor result from the increase of trap states introduced by the incorporation of MWCNTs. In the high forward voltage regime, the current densities for the three samples are comparable, indicating that the serial resistances of these devices are comparable and are not affected by the incorporation of the MWCNTs into the perovskite bulk.

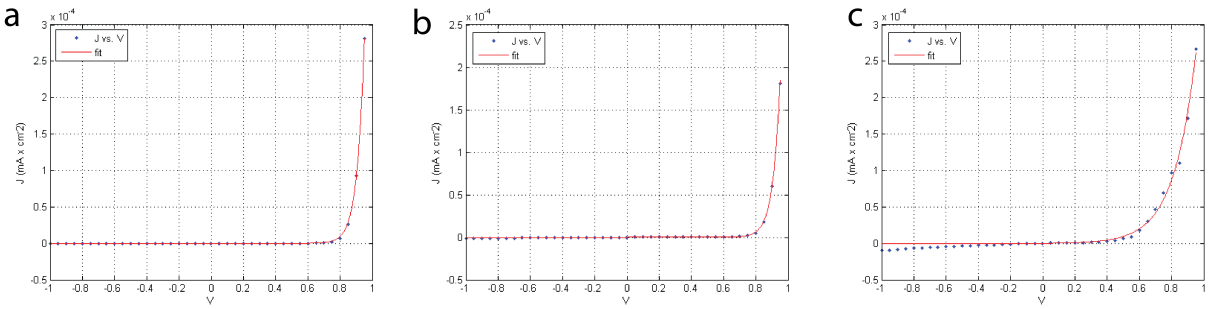

Figure 154: Dark J-V curve and fits with general diode equation for (a) 0.0%, (b) 0.005%, and (c) 0.01% MWCNT; measured J-V data points are shown with blue diamonds and fits with red line. J-V curves were fit from -1 V to 1 V (space-charge-limited regime) using the equation: $J(V) = a \cdot \left(e^{-q \cdot V / k_B \cdot T \cdot n} - 1\right)$. Where a is a prefactor, q is the elementary charge (1.6×10^{-19} C), k_B is Boltzmann's constant (1.38×10^{-23} $m^2 \cdot kg \cdot s^{-2} \cdot K^{-1}$), T is 298.15 K, and n is the ideality factor; where $n = 1$ is ideal diode behavior. a and n were refined using non-linear least squares regression analysis in the MATLAB curve fitting toolbox. Fit results are shown in Table 18.

Table 18: Summary of dark *J-V* fit parameters with diode equation.

% MWCNT	*a*	*n*	R-squared
0.0%	1.2e-13	1.71	0.9974
0.005%	9.6e-14	1.73	0.9990
0.01%	2.5e-7	5.32	0.9905

Our simulations and experiments indicate that introduction of MWCNTs in the bulk of perovskite active layers leads to (1) reduction in charge recombination, (2) improved charge extraction at the electrode/HTL interface, and (3) increase in the trap states leading to increased leakage current and ideality factor. We also find that that the presence of 0.005% MWCNTs

provided the best overall device performance. The device performance improves with reduced charge recombination and improved charge extraction, but may diminish with increase in the trap states. For example, an increase in trap states leads to increase in both J_{SC} and *n*. Increase in *n* will lead to higher V_{oc} whereas increase in J_{SC} will lead to lower V_{oc}.[625] Therefore, we conclude that a MWCNT concentration of 0.005% by wt. is a reasonable estimate of the optimal MWCNT concentration for a planar inverted perovskite device architecture that provides a balanced hole and electron transport with reduced bulk recombination loss and minimal introduction of trap states. Only a low concentration (0.005%) of MWCNTs is required to reduce the recombination rate as the hole diffusion length is significantly high in perovskite materials.[588] Efficient charge collection at the interface and reduced recombination loss increases V_{oc} and the overall PCE.[598] Our results are also consistent with a recent observation that the incorporation of CNTs in the active layers improves photoluminescence lifetime and thus device performance.[626]

In this chapter, we have demonstrated a facile route for the synthesis of perovskite/MWCNT materials for high efficiency photovoltaics. MWCNTs introduced into the perovskite active layer not only facilitate charge transport, but also reduce charge carrier recombination losses by >87% in the bulk due to separation of charges at the perovskite/MWCNT interfaces. The reduction in recombination losses due to selective charge transport in the bulk generates opportunities for further material engineering towards higher PCE. This approach of CNT incorporation into the perovskite matrix is compatible to both conventional and inverted device geometries. It also opens up future directions to tune electron and hole mobility in CNT/perovskite composite nanomaterials.

3.8 Role of Interfacial Ionic Functional Groups on Ionic Transport in Perovskite Solar Cells, and its Application Towards Memristors

This chapter[‡‡‡‡‡] details the role that ionic functional groups on hole transporting layers plays on the ionic transport at perovskite interfaces. Many perovskite solar cells show an undesirable current-voltage (*I-V*) hysteresis in their forward and reverse voltage scans, to the detriment of device characterization and performance. This hysteresis is likely due to slow ion migration in the bulk of perovskite active layer. We show the interfacial chemistry between the perovskite and charge transport layer plays a critical role on the ion transport and subsequent *I-V* hysteresis in perovskite based devices. Three phenylene vinylene polymers containing cationic, zwitterionic, and anionic pendent groups were utilized to fabricate charge transport layers with diverse interfacial ionic functionalities. The interfacial-adsorbing boundary induced by the polymer zwitterion at the interface traps mobile ions, responsible for the *I-V* hysteresis in these perovskite-based devices. Further, we exploit the ion adsorbing nature of the interface to fabricate perovskite-based memristors. Here, we examine a new chemical mechanism fundamental to *I-V* hysteresis in perovskite-based devices and introduces a novel paradigm of interfacial ion adsorption to induce memristive behavior.

Hybrid lead halide perovskite solar cells are rapidly advancing the pace of photovoltaic research.[33,34,454,481,530,584-586] Over the past several years, the power conversion efficiencies (PCEs) of perovskite solar cells increased from 3.8% to a certified value of

---

‡‡‡‡‡ This chapter was adapted, with permission, from Liu, Yao, Lawrence A. Renna, Hilary B. Thomson, Zachariah A. Page, Todd Emrick, Michael D. Barnes, Monojit Bag, Dhandapani Venkataraman, and Thomas P. Russell. "Role of Ionic Functional Groups on Ion Transport at Perovskite Interfaces." *Under Review* (2016). I would like to acknowledge Dr. Yao Liu for fabricating devices, Hilary B. Thomson for photoluminescence measurements, and Dr. Zachariah A. Page for synthesizing materials.

22.1%.[450,455,458,482,491,496,516,538,627-629] However, for these materials to be incorporated into commercial devices, lingering questions must be addressed.[28,29,46,48,616,630,631] One critical issue pertains to the origin of current density (*J*)-voltage (*V*) hysteresis often encountered in perovskite solar cell measurements that makes device characterization difficult.[42,44,45,501,528,632-635] The prevailing hypothesis on the origin of *J-V* hysteresis is the relatively slow vacancy aided migration of ions through perovskite films during device operation.[27,449,528,636-638] Thus, two approaches aim to eradicate *J-V* hysteresis in perovskite solar cell: 1) to reduce/eliminate ion migration by grain boundary passivation or chemical means,[449,473,519,639,640] and 2) to accelerate ion migration to time-scale corresponding to device measurements.[42,45,641]

Most studies addressing the influence of ion migration on *J-V* hysteresis of perovskite solar cells focus on the active layer (perovskite),[27,47,449,636,642] with little consideration about ion migration at the interface between the charge selective transport layer and perovskite. Cahen and co-workers recently showed that ion migration is affected by interfacial dependent polarization through the device,[643] while Correa-Baena *et al*. demonstrated a reduction in *J-V* hysteresis using mesoporous titanium dioxide (TiO_2) as an interfacial layer to increase perovskite crystallite size and thus accelerate ion (MA^+) migration.[641] Moreover, it has been shown that different charge selective transport layers lead to various levels of *J-V* hysteresis, which suggests that interface engineering as a suitable avenue to suppress this unfavorable effect.[42,528,559,644-647] However, since ion migration appears to occur throughout perovskite devices, it is challenging to identify its influence at a particular interface on *J-V* hysteresis. Recently, Shao *et al*.[473] and Xu *et al*.[519] reported a trap-passivation effect of fullerene on perovskite bulk films, which affords the fullerene/perovskite heterojunction solar

cells with little-to-no *J-V* hysteresis. Perovskite trap-passivation with fullerene thus provides a channel to selectively investigate the influence of ion migration at the interface on *J-V* hysteresis in perovskite solar cells, simply by sequentially coating a fullerene electron transport layer (ETL) onto perovskite bulk film.[33,485,497,640,648]

In this chapter, we fabricated fullerene/methylammonium lead triiodide ($MAPbI_3$) perovskite planar heterojunction solar cells on a series of substituted poly(phenylene vinylene) (PPVs, Figure 155)[557] including the cationic poly(benzothiadiazole vinylene-*alt*-2,5-bis(5-(*N*,*N*,*N*-trimethylammonium bromide)hexyloxy)-1,4-phenylenevinylene) (PVBT-TMA), anionic poly(benzothiadiazole vinylene-*alt*- 2,5-bis(4-sodium sulfonate)butoxy)-1,4-phenylenevinylene) ($PVBT\text{-}SO_3$), and zwitterionic poly(benzothiadiazole vinylene-*alt*-2,5-bis((*N*-(3-sulfonato-1-propyl)-*N*,*N*-dimethylammonium)hexyloxy)-1,4-phenylenevinylene) (PVBT-SB). These polymers possess identical phenylene vinylene backbones, but have different hydrophilic pendent groups. By utilizing these polymers as hole transport layers (HTLs), intermediate between $MAPbI_3$ and indium-tin oxide (ITO), we were able to vary the intrinsic bulk and surface ionic species, and thus interactions. The diverse functionalities of these PPVs impacted the electronic and ionic properties of the perovskite-based devices. Most strikingly, we observed comparable ion diffusion when any of the three PPVs were used, but *J-V* hysteresis was found only in the fullerene/perovskite planar heterojunction devices using the zwitterionic PPV (PVBT-SB) as the HTL. Electrochemical impedance spectroscopy (EIS) and conductive atomic force microscopy (cAFM) characterization showed that PVBT-SB provides an adsorbing boundary for mobile MA^+ that migrate to the interface during device operation. MA^+ adsorbs onto the PVBT-SB interface under forward bias conditions, and, therefore, causes hysteresis when the reverse bias conditions are applied. Kelvin probe force microscopy (KPFM) showed

that the ion adsorbing nature of PVBT-SB arises from the zwitterionic side chains, which form an electric double layer. These studies uncover the origin of *J-V* hysteresis at the interface in perovskite solar cells. The ion adsorbing PVBT-SB interface is also shown to introduce memristive behavior in perovskite-based devices.

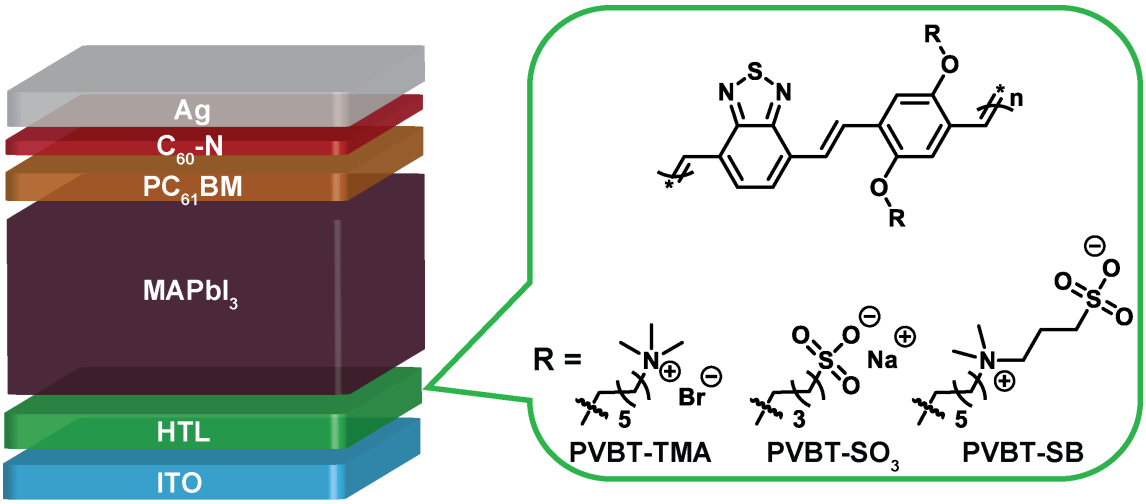

Figure 155: A schematic of the device architecture: ITO/HTL/$MAPbI_3$/$PC_{61}BM$/C_{60}-N/Ag. The PPV HTL are shown on the right.

3.8.1 Device Fabrication

C_{60}-N (molecular structure in Figure 156) is prepared according to previous procedures.[525] Methylammonium iodide (MAI) was purchased from 1-Material. Phenyl-C_{61}-butyric acid methyl ester ($PC_{61}BM$) was purchased from Nano-C. All the solvents and Lead acetate used in this research were purchased from Sigma Aldrich and used without further purification.

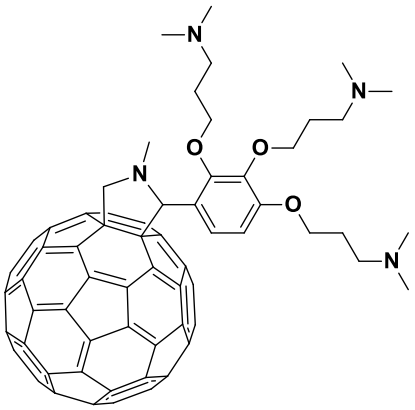

Figure 156: Molecular structure of C_{60}-N.

The indium tin oxide (ITO)-coated glass substrates (20 ± 5 ohms/square) were obtained from Thin Film Devices Inc., and were cleaned through ultrasonic treatment in detergent, deionized water, acetone, and isopropyl alcohol and then dried in an oven for 6 hours. HTLs (PVBT-TMA, PVBT-SO_3, and PVBT-SB) were spin coated onto pre-cleaned ITO substrates. For control devices with double-lay HTL, the PVBT-SB solution in 2,2,2-trifluoroethanol (TFE) was first spin-coated onto ITO, then PVBT-SO_3 solution in water was spin coated onto PVBT-SB/ITO substrate. The perovskites were prepared by spin-coating a perovskite precursor in *N,N*-dimethylformamide (DMF) onto the HTL/ITO substrates inside a glove box (N_2 atmosphere, < 1 ppm O_2, <1 ppm H_2O). As-cast films were then annealed in dark at 90 °C for 5 min in glove box. For perovskite solar cells, a thin layer of $PC_{61}BM$ (60-70 nm) as ETL was then spin coated inside a glove box (N2 atmosphere, < 1 ppm O_2, <1 ppm H_2O) from a solution in chlorobenzene (20 mg/mL) at 1000 rpm for 60 s. Then C_{60}-N in TFE (3 mg/mL) was spin coated onto $PC_{61}BM$ surface with a thickness of ~10 nm. Finally, 100 nm Ag cathode was deposited (area 6 mm^2 defined by metal shadow mask) on the active layer under high vacuum (1×10^{-6} mbar) using a thermal evaporator. For perovskite memristors, 100 nm Au electrode was deposited (area 6 mm^2 defined by metal shadow mask) on the perovskite layer directly.

3.8.2 Device characterization

The *J-V* characteristics of the devices were measured under simulated AM1.5G irradiation (100 $mWcm^{-2}$) using a Xe lamp-based Newport 91160 300-W Solar Simulator. A Xe lamp equipped with an AM1.5G filter was used as the white light source. The light intensity was adjusted with an NREL-calibrated Si solar cell with a KG-5 filter. A metal photo mask with an aperture area of 5.5 mm^2 was used during device measurement.

Topographic image contrast was enhanced using Contrast Limited Adaptive Histogram Equalization[649] in ImageJ, then marker-based watershed segmentation[650,651] was performed in MATLAB R2015B to identify individual grains, and then grain perimeters were calculated by a Region Morphometry analysis in ImageJ.[652]

PL spectra were obtained using 405 nm pulsed excitation and collection through a 1.4 N.A. oil objective and long pass filter (405 nm), and focusing the PL on the entrance slit of an ACTON 3160a imaging spectrograph. TRPL was taken with 405 nm pulsed excitation, and imaging onto an avalanche photodiode (ID Quantique ID100) and routed into a PicoQuant TimeHarp 300 time-to-digital converter (~ 50 ps full width at half max (FWHM) instrument response function). Samples were prepared on clean glass or ITO/glass coverslips for optical interrogation, with careful attention to uniform film thickness between the different samples. The thicknesses of HTLs is ~10 nm and the perovskite layer thickness is ~ 300 nm.

EIS was measured using an Agilent 4294A Precision Impedance Analyzer under 100 mWcm-2 light intensity at 20 mV applied AC amplitude. DC bias voltage was kept at 0 V. Frequency was swept from 40 Hz to 1 MHz.

Measurements were made in air using Asylum Research MFPD-SA instrument and Pt/Ir coated silicon probe, used as receive from AppNano (ANSCM-PT). Tapping mode scans were 2 μm × 2

μm (512 pixel × 512 pixel) at 1.0 Hz. cAFM measurements were made at selected $MAPbI_3$ grains in the topographic AFM image. The probe was brought into contact with the surface with a set point = 0.2 V for all measurements. A three-cycle triangle bias wave was applied between the conducting probe and the ITO electrode with amplitude of 4.0 V, at a rate of 0.4 Hz.

KPFM was measured in air using Asylum Research MFPD-SA instrument and Pt/Ir coated silicon probe, used as receive from AppNano (ANSCM-PT). Measurements were carried out in a two-pass manner; the first pass measures topography and the probe is mechanically driven, in the second pass surface potential is measured and the probe is driven at its AC voltage resonant frequency at height of 30 nm above the surface. Potential differences between the probe and the sample induce mechanical oscillations of the probe, which are nulled by an applied DC bias by a feedback loop. The applied bias is thus equal to the potential difference between sample and probe. Three scans of 5 μm × 1.25 μm (512 pixel × 128 pixel) at 0.5 Hz, at different locations, were made for each sample. Histogram plots of counts vs. potential are made for each scan, and fit with a Gaussian distribution to obtain the average and standard deviation of the potential for a particular scan. The potentials reported in the text are the averages and standard deviations of the three independent scan averages.

3.8.3 The Influence of PPVs on Device Performance

Fullerene/$MAPbI_3$ perovskite planar heterojunction solar cells, shown in Figure 155, were fabricated on ITO substrates.[559] Solutions of PVBT-SO_3 in water, PVBT-SB in TFE and PVBT-TMA in TFE[557] were spin-coated onto ITO substrates to serve as the HTLs (~10 nm). The $MAPbI_3$ precursor solution ($Pb(OAc)_2$ and MAI in DMF was spin-coated onto an ITO/HTL substrate, followed by mild thermal annealing (90 ºC for 5 min) to form the perovskite layer. $PC_{61}BM$ was spin-coated onto the perovskite layer from chlorobenzene and the samples were

stored in a sealed petri dish for 6 hours. This was followed by spin-coating an interfacial modification layer of C_{60}-N from TFE. Silver (Ag) electrodes were thermally evaporated onto the C_{60}-N layer for electron extraction. Figure 157 shows *J-V* characteristics of devices containing different PPV HTLs (corresponding device parameters in Table 19). The devices containing cationic or anionic PPVs showed negligible *J-V* hysteresis during forward and reverse scans even at different scanning speeds (142 – 258 mV/s), whereas the devices with zwitterionic PPV exhibited serious *J-V* hysteresis under identical conditions.

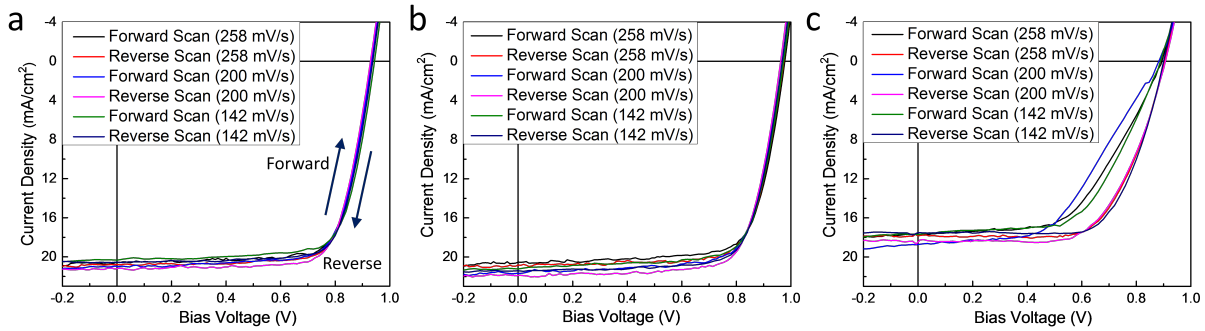

Figure 157: Typical *J-V* curves of the perovskite solar cells containing a HTL of (**a**) PVBT-TMA, (**b**) PVBT-SO_3, and (**c**) PVBT-SB.

Table 19: Device parameters of *J-V* curves in main text Figure 2

HTL	Scan Conditions (mV/s)		Efficiency (%)	V_{OC} (V)	J_{SC} (mA/cm^2)	FF (%)
PVBT-TMA	142	Forward	15.6	0.94	22.3	74.5
		Reverse	15.8	0.93	22.5	75.3
	200	Forward	15.7	0.93	22.8	73.7
		Reverse	16.0	0.93	22.9	74.9
	258	Forward	15.5	0.94	22.0	74.7
		Reverse	15.8	0.94	22.2	76.0
PVBT-SO_3	142	Forward	14.9	0.98	20.6	74.0
		Reverse	15.2	0.97	20.9	74.6
	200	Forward	15.3	0.97	21.6	73.1
		Reverse	15.7	0.96	21.9	74.5
	258	Forward	15.1	0.97	21.1	73.6
		Reverse	15.4	0.97	21.4	74.5
PVBT-SB	142	Forward	8.7	0.89	17.7	55.5
		Reverse	10.8	0.90	17.9	66.8
	200	Forward	8.3	0.88	18.7	50.4
		Reverse	10.7	0.91	18.4	64.2
	258	Forward	9.2	0.89	17.6	59.0
		Reverse	11.0	0.90	17.5	69.6

Surface and cross-sectional scanning electron microscopy (SEM) images show a similar morphology of $MAPbI_3$ films on different HTLs (Figure 158), while powder X-ray diffraction (PXRD) (Figure 159) has the same peaks attributable to the (002), (100), (112), and (200) planes of the perovskite tetragonal phase on all glass/HTL substrates. To confirm the similar $MAPbI_3$ morphologies on all HTLs, we performed a marker-based watershed segmentation[650,651] grain analysis of tapping-mode atomic force microscopy (AFM) images. The segmentation overlays on AFM images are shown in Figure 160a-c along with grain perimeter histograms (Figure 160d). We found that for PVBT-TMA, the average grain perimeter (p_{grain}) was p_{grain} = 231 ± 79 nm, for PVBT-SO_3, p_{grain} = 233 ± 80 nm, and for PVBT-SB, p_{grain} = 250 ± 90 nm. Therefore, we can conclude that the grain structure is generally unaltered regardless of the HTLs used, and is unlikely to contribute to the *J-V* hysteresis in the devices containing PVBT-SB.

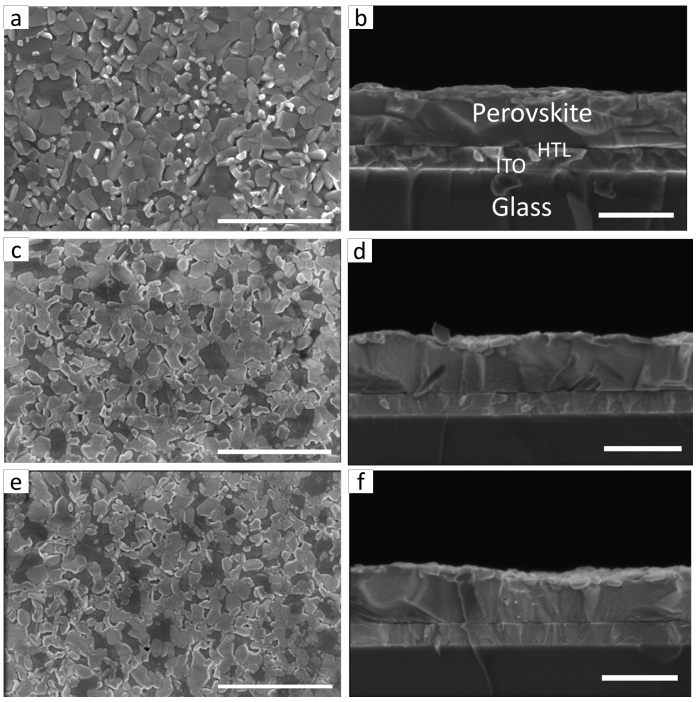

Figure 158: SEM images of perovskite films on different HTLs. (**a, b**) PVBT-TMA. (**c, d**) PVBT-SO_3. (**e, f**) PVBT-SB. Scale bar in a, c, and e is 1 μm; Scale bar in b, d, and f is 500 nm.

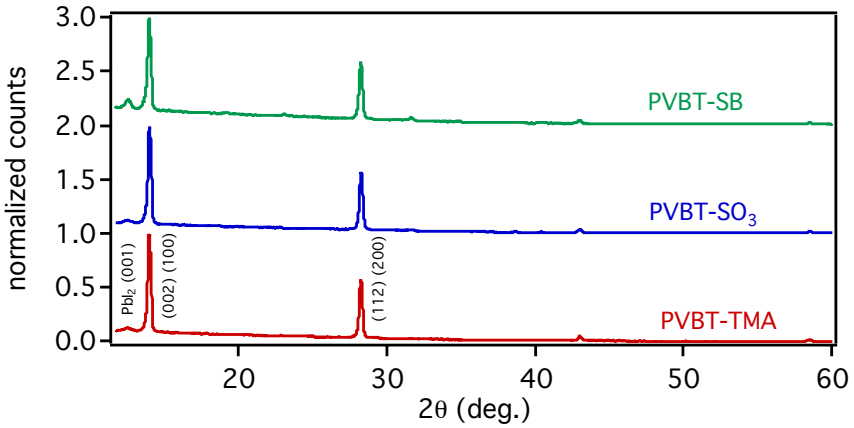

Figure 159: PXRD of perovskite films on different HTLs. Normalized PXRD spectra for $MAPbI_3$ on PVBT-TMA, PVBT-SO_3, and PVBT-SB showing the same crystal structure regardless of HTLs.

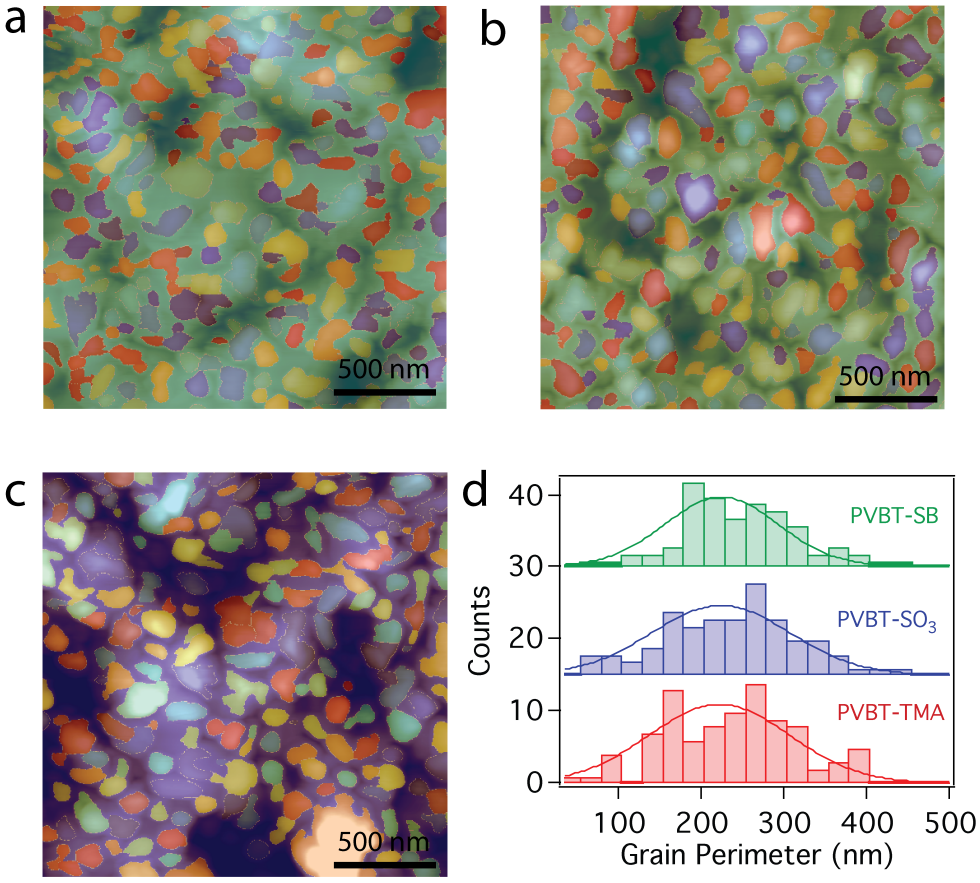

Figure 160: AFM topographic image of perovskite film on (**a**) PVBT-TMA/ITO substrate, (**b**) PVBT-SO_3/ITO substrate, and (**c**) PVBT-SB/ITO substrate. (**d**) Grain perimeter histograms with Gaussian fits, plots are stacked for clarity.

To identify the origin of *J-V* hysteresis for zwitterion containing devices, we did a control experiment, as shown in Figure 161. The solar cell devices were fabricated on ITO/PVBT-SB and ITO/PVBT-SB:PVBT-SO_3 substrates, separately. The *J-V* hysteresis was significantly suppressed by decoupling the PVBT-SB film from the $MAPbI_3$ layer. Since all the HTLs share the same backbone compositions, we conclude that the zwitterionic side chains should induce this *J-V* hysteresis. Previously we found that conjugated polymer zwitterions as cathode interlayers in polymer solar cells do not cause *J-V* hysteresis. Thus, it is unlikely that the zwitterions trap charges or the *J-V* hysteresis comes from the electronic process of the devices.[653] Hence, another mobile component (e.g. ion migration) at the perovskite/PVBT-SB interface contributes to this substantial difference in *J-V* characteristics.

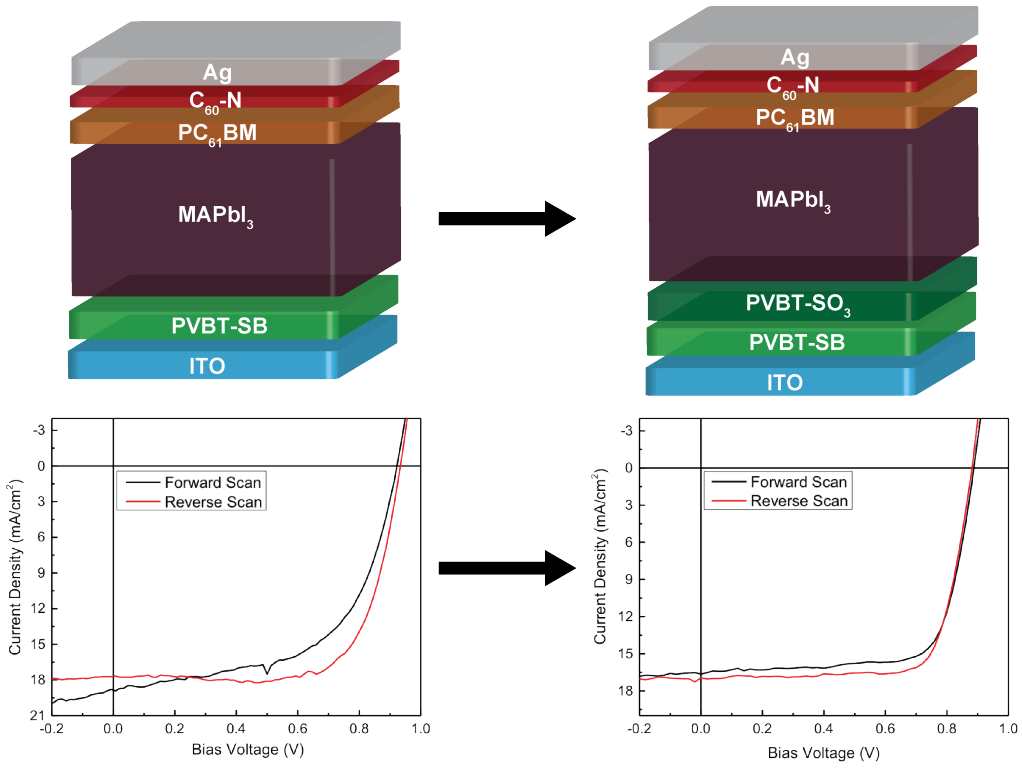

Figure 161: The left shows a typical device architecture containing zwiterionic PVBT-SB as the HTL with its *J-V* curve displaying hysteresis. When the interface is decoupled by PVBT-SO_3, right, the device *J-V* curve hysteresis is significantly reduced.

3.8.4 Photoluminescence (PL) measurements

Figure 162 shows typical wavelength and time-resolved photoluminescence (TRPL) measurements designed to compare charge extraction efficiency of HTLs from perovskite. Figure 162a-b shows the TRPL decay traces and PL spectra of the three HTLs spin-coated on glass with perovskite films spin-coated on top, prepared with identical perovskite film thickness as the working solar cell devices. The perovskite/interlayer samples were assayed over multiple regions of the film with identical exposure time and laser excitation power. PL measurements on similar perovskite/PVBT-SB interlayer samples were also made by coating on ITO substrates (Figure 163), which showed no significant changes in PL characteristics in comparison to the glass-only substrates. Both the PVBT-TMA and PVBT-SO_3 showed single exponential decay (Figure 162a), characteristics of $MAPbI_3$ films, with lifetimes of τ = 47 ns and τ = 34 ns, respectively, whereas the PVBT-SB interlayer displayed a pronounced power law decay (μ = -3.55), indicative of a two-body recombination of dilute polaron pairs.[654,655] The PVBT-SB interlayer also showed strongly quenched PL (Figure 162b), suggesting efficient charge extraction. The improved charge extraction arises from interfacial polarization, which is discussed later in this manuscript.

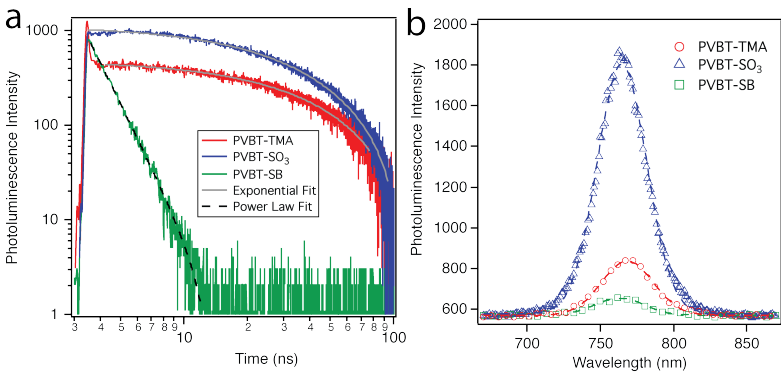

Figure 162: Time-resolved photoluminescence (TRPL) and photoluminescence (PL) characterizations of perovskite films with different HTLs. TRPL **(a)** and PL **(b)** of glass/HTL/perovskite films.

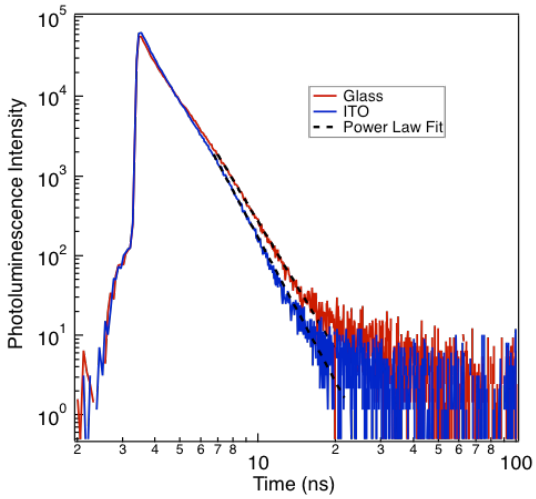

Figure 163: Time-resolved photoluminescence (TRPL) characterization of perovskite films with PVBT-SB HTLs on ITO versus glass. Both ITO and glass showed power law decays (μ = -5.04 and μ = -4.39, respectively), which is characteristic of two-body recombination of dilute polaron pairs.

3.8.5 Electrochemical impedance spectroscopy (EIS) measurements

We used EIS to analyze the different processes (and their respective time scales) that occur in devices containing different HTLs. Impedance was measured by applying a 20 mV AC voltage and scanning a frequency range of 1 MHz to 40 Hz under illumination from an AM1.5G solar simulator. The EIS Nyquist plots are shown in Figure 164a-d, where the real component of the impedance (Z') is the abscissa and the imaginary part (Z") is the ordinate. The Nyquist plots are fit with equivalent circuit models (Figure 164e-f) as discussed below. The Nyquist plots can be divided into the high frequency semicircle (closest to the origin) that represents predominately electronic transport, and the low frequency regime which arises from MA^+ ion transport.[449]

All devices showed an initial semicircular behavior at high frequency. At low frequency, for devices with cationic PVBT-TMA and anionic PVBT-SO_3 HTLs (Figure 164a-b), impedance is represented by linear semi-infinite ion diffusion.[25,477] We have modeled these impedance spectra with the equivalent circuit, model A (Figure 164e),[449] which combines high frequency

charge and low frequency ionic transport. The impedance is modeled with a charge transport/recombination resistance (R_{tr}) in series with an interfacial charge transfer resistance (R_{CT}). The ion diffusion is modeled with a constant phase Warburg element (W_s). Charge accumulation at the interface is modeled with a Debye-layer capacitance (C_{DL}), while charge stored in the perovskite is modeled as chemical capacitance (C_{μ}). Contact resistance between layers and in the contacts is modeled with a series resistance (R_s). All calculated fit parameters are shown in Table 20.

Table 20: EIS model fit parameters

	PVBT-TMA	**PVBT-SO3**	**PVBT-SB**	**PVBT-SB/ PVBT-SO3**	**PVBT-SB/ PVBT-SO3**
Model	Fit Model A	Fit Model A	Fit Model B	Fit Model A	Fit Model B
χ^2	0.0136	0.0134	0.0133	0.0158	0.0158
R_s **(Ω)**	67.43	65.44	69.65	70.31	70.19
R_{tr} **(Ω)**	567.9	661.3	771.6	587.2	582.4
R_{CT} **(Ω)**	35.36	183.8	61.06	130.9	115.2
A_W **(Ω)**	4259	2791	763.5	1387	2686
T_W **(s)**	0.037	0.022	0.030	0.023	0.055
P_W	0.66	0.56	0.74	0.51	0.61
C_{DL} **(μs/ Ω)**	0.719	0.137	0.109	0.063	0.062
C_μ **(nF)**	2.83	3.24	2.76	3.46	3.45
R_{int} **(Ω)**	N/A	N/A	547.2	N/A	54.42
CPE_{int} **($s^{0.8}$/Ω)**	N/A	N/A	1.26×10^{-5}	N/A	7.44×10^{-6}

For devices containing zwitterionic PVBT-SB, there is a clear linear part of the spectra followed by a semicircle bending towards the real axis (Figure 164c). In mass transport, there are two scenarios where this type of behavior arises.[25] First, the ions diffuse to a reflecting but reactive boundary where the resistance for reaction is several orders of magnitude less than

resistance to ion diffusion. In this case the ions react much more rapidly than they diffuse to the interface and effectively do not experience the boundary, due to rapid decay in ion concentration near the interface. The second scenario is that the ions diffuse to an adsorbing boundary, in which the Nyquist plot will appear as a linear component followed by a semicircular approach to the real axis irrespective of whether the boundary is reactive. A reversible electrochemical reaction at the perovskite/PVT-SB interface is not expected nor would this account for the semi-reversible device *J-V* hysteresis. Therefore, the results suggest that the PVBT-SB provides an adsorbing boundary for mobile MA^+ to diffuse through the $MAPbI_3$ active layer. To test this hypothesis, we decoupled the $MAPbI_3$/PVBT-SB interface with an additional layer of PVBT-SO_3. The EIS spectrum of this device is shown in Figure 164d as the control sample, which appears to behave similarly to the PVBT-SO_3-only device, with a linear Warburg component at low frequencies representative of semi-infinite diffusion. In addition, we fit the EIS spectra of the devices containing PVBT-SB with model B (Figure 164f). This model is model A with an additional *RC* component to represent the electric double layer formed by the combination of the zwitterionic dipole with the formation of an inner Helmholtz layer from adsorbed ions, which are represented as R_{int} and CPE_{int}, respectively. Due to the heterogeneity of the interface, we use an imperfect capacitor CPE (constant phase element)[25] with an exponent ~ 0.8, where an exponent of 1.0 is characteristic of a perfect capacitor.

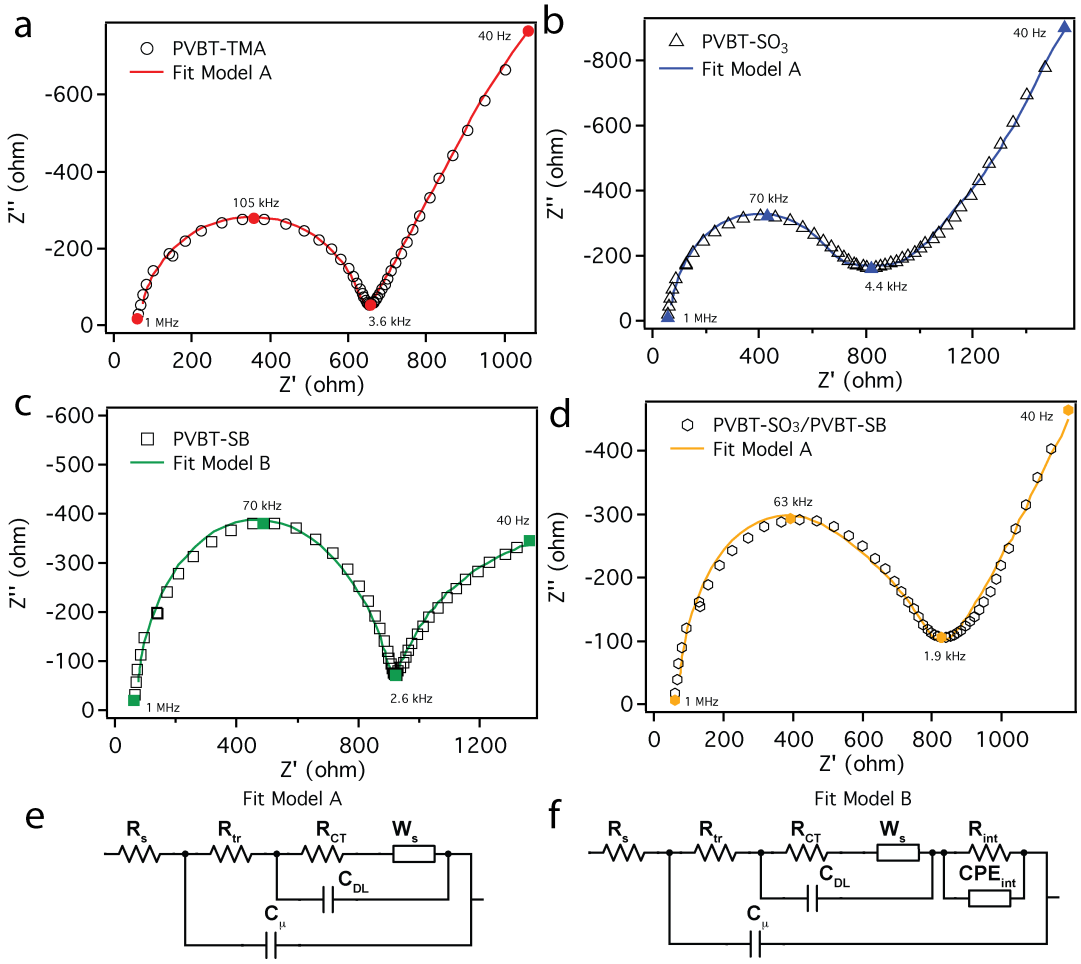

Figure 164: Nyquist plots for devices with HTLs of (**a**) PVBT-TMA, (**b**) PVBT-SO_3, (**c**) PVBT-SB, and (**d**) PVBT-SB covered with PVBT-SO_3 (open symbols are EIS data, colored symbols designate specific frequencies, and solid lines are equivalent circuit fit models.) model A (**e**) was used to fit Nyquist plots in **a**, **b** and **d**, while model B (**f**) was used to fit Nyquist plot in **c**.

We calculated R_{tr} for these devices, which represents charge recombination resistance.[559] For devices containing PVBT-TMA, R_{tr} ~ 578 Ω, PVBT-SO_3, R_{tr} ~ 661 Ω, and PVBT-SB, R_{tr} ~ 772 Ω. These results agree with the outcome of PL quenching experiments. Therefore, PVBT-SB should theoretically function optimally as an HTL, if the high frequency electronic components of the impedance spectra were the only factors influencing device performance. It is now evident that the slow low frequency processes occurring at the interface in the perovskite solar cells are crucial and this understanding provides valuable insight into device performance.

The low frequency normalized Bode imaginary plot for all three devices is shown in Figure 166a, where the peak position, in Hz, is characteristic of the timescale of ionic photo-response due to an applied AC bias. Here, we show that devices containing PVBT-SB HTL have the slowest response due to ions. Recent work by Correa-Baena *et al.*[641] has shown that increasing the ionic response time by increasing crystal size reduces device *J-V* hysteresis. However, in that work, the increase in response time was approximately two orders of magnitude. Conversely, in this study, the response due to ions is of the same order of magnitude and the $MAPbI_3$ grains are all of comparable sizes, suggesting that the response time alone cannot account for the hysteresis, further substantiating that interfacial phenomena plays a critical role.

The low frequency Warburg ion transport impedance element is calculated by the equation:[449,469]

$$W_s = A_W \frac{\tanh\,(j\omega T_W)^P}{(j\omega T_W)^P}$$

Where A_W is the Warburg resistance, T_W is Warburg time constant, and P is the exponent which is ~0.5 for perfect Warburg mass diffusion. Using the fit models we calculate A_W for devices containing different HTLs. For devices containing PVBT-TMA, $A_W \sim 4259\ \Omega$, PVBT-SO_3, $A_W \sim 2791\ \Omega$, and PVBT-SB, $A_W \sim 764\ \Omega$. A confirmation of Warburg-like ion diffusion is a plot of $|Z'|$ and $|Z''|$ versus $\omega^{-1/2}$, where in the low frequency regime the slope for both is $\sim A_W$, the lines are parallel, and the imaginary component intersects the ordinate at ~ 0 Ω.[477] These are shown for all three HTLs containing devices in Figure 165, confirming Warburg ion diffusion in the devices. We show that the Warburg ion transport resistance (A_W) is the lowest for devices containing PVBT-SB. It has been reported in CeO_x ionic conductors, that as A_W approaches infinity the boundary is fully blocking, and as A_W approaches 0 Ω, the boundary is ideally adsorbing.[469]

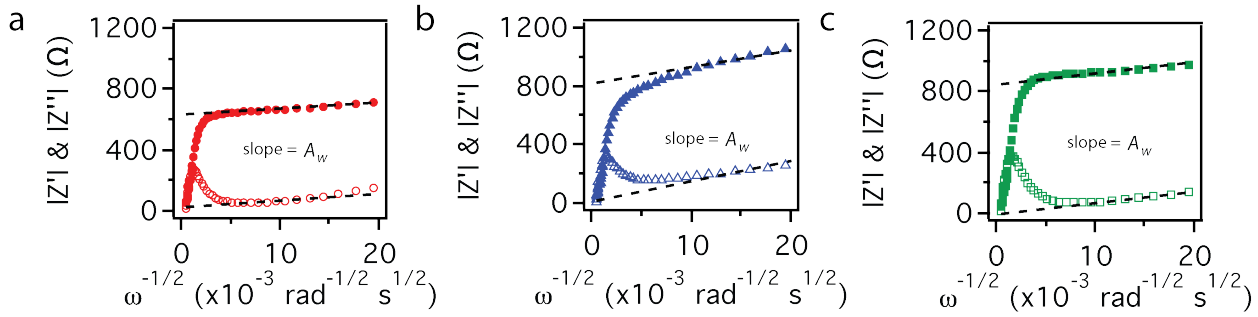

Figure 165: Warburg impedance plots. A plot of |Z'| (closed symbols) and |Z''| (open symbols) versus $\omega^{-1/2}$, for perovskite devices containing (a) PVBT-TMA, (b) PVBT-SO3, and (c) PVBT-SB. Dashed lines show linear fits with slope = A_W. The fit of the imaginary component intersects the ordinate at ~0 Ω.

To probe the effect of A_W on these systems, we conducted an impedance spectra simulation experiment[469] using model B. In the simulation all parameters are held constant, and, relevant to the experimental systems studied above, except for A_W that was varied from 0 Ω to 1×10^{20} Ω. In the simulation, the initial (high frequency) semicircle attributed to predominantly electronic processes is, as expected, unchanged by A_W. However, A_W heavily influences the second component of the simulated Nyquist plot, which in the model is attributable to slower ionic transport. The relationship between A_W and the behavior at the boundary can be seen in the simulated impedance spectra in Figure 166b. When $A_W = 0$ Ω, the boundary is perfectly adsorbing, as evidenced by the semicircle dropping toward the real axis. When $A_W = 1\times10^{20}$ Ω, the boundary is perfectly blocking, which is shown in the simulated Nyquist plot as a capacitive (phase = 90°) line. For $A_W \approx 100$ - 1000 Ω, the boundary is partially adsorbing, where the second (low frequency) semicircle bends towards the real axis. When $A_W \approx 3000$ - 10000 Ω, the simulated Nyquist plots show semi-infinite Warburg diffusion. The experimental values of A_W for devices with PVBT-TMA and PVBT-SO_3 fall within the simulated range for a semi-infinite diffusion model, which is indeed observed in the experimental impedance spectra. The

experimental A_W derived for PVBT-SB devices falls within the range for an adsorbing boundary, and is observed experimentally. These studies thus show how A_W can be used as a metric to describe the adsorbing or blocking nature of the boundary.

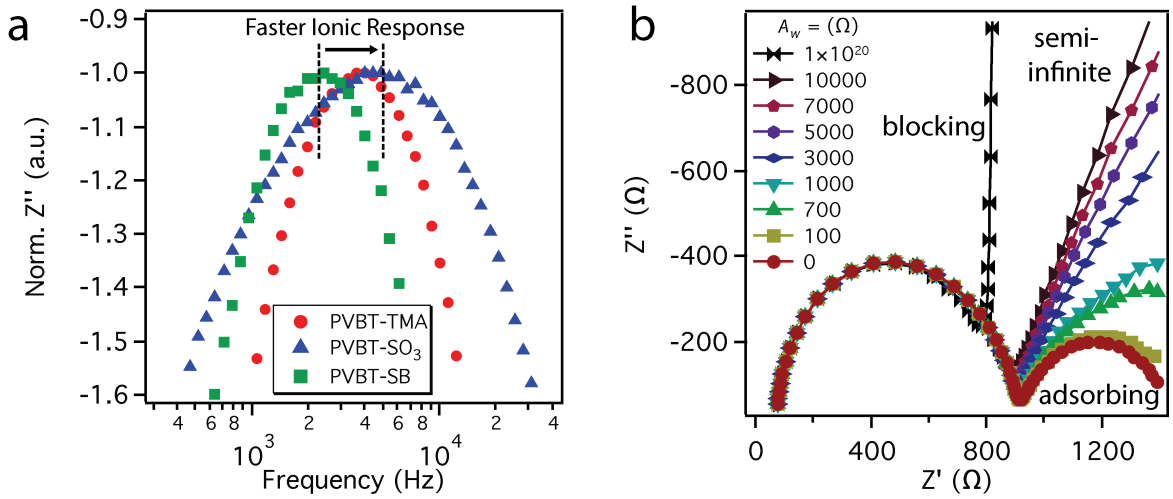

Figure 166: Ionic response analysis and the simulated Nyquist plot. (**a**) Normalized imaginary Bode plots, in the low-frequency ionic response regime, for devices containing all three HTLs. (**b**) Simulated Nyquist impedance spectra plots using fit model B shown in Figure 164f, modulating A_W and keeping all other fit parameters constant.

We also estimate the diffusion coefficient D for ion migration in these samples using the equation:[469]

$$D \approx \frac{L_D^2}{T_W}$$

Where L_D is the maximum diffusion length, taken to be the perovskite thickness (~300 nm). For devices containing PVBT-TMA, $D \sim 2.43 \times 10^{-8}$ cm^2 s^{-1}, PVBT-SO$_3$, $D \sim 4.08 \times 10^{-8}$ cm^2 s^{-1}, and for PVBT-SB, $D \sim 2.98 \times 10^{-8}$ cm^2 s^{-1}. For our control device containing PVBT-SO$_3$ between perovskite and PVBT-SB, we obtained $D \sim 3.98\times 10^{-8}$ cm^2 s^{-1}. These differences in D are inconsequential, thus the rate of ion diffusion is not a contributing factor to *J-V* hysteresis in PVBT-SB containing devices, and more likely due to effects of the ion adsorbing boundary.

3.8.6 Kelvin Probe Force Microscopy (KPFM) Measurements

We hypothesized that the zwitterionic PVBT-SB induces an adsorbing boundary for moving ions in $MAPbI_3$ based solar cells. The hydrophilic DMF solvent used for perovskite fabrication selectively dissolves zwitterionic pendent groups at the HTL surface, holding the potential to facilitate the orientation of zwitterionic dipoles at the interface with $MAPbI_3$ upon deposition from DMF. To experimentally probe this hypothesis, we turned to KPFM, which has the capability to sensitively detect changes in surface potential as a result of permanent electrostatic dipole orientation.[656,657] Figure 167a-b show representative AFM topographic and KPFM surface potential maps, respectively, for PVBT-SB spin coated on ITO/glass substrates. We performed three independent scans and calculated an average potential of 684.09 ± 40.05 mV. We next took a similarly prepared PVBT-SB film on ITO/glass, spin coated DMF on top, and removed residual solvent in vacuum. Figure 167c-d show representative topographic and surface potential maps for this DMF-washed sample, respectively. The results show that, despite similar topographies, there is a drastically different surface potential. The average potential measured, over three scans, for the DMF-washed PVBT-SB film was 465.71± 2.50 mV. This large decrease in surface potential suggests a greater percentage of sulfonate groups orienting outward the polymer film surface. Further, there is a ~93% decrease in the error over multiple measurements for samples after DMF washing, suggesting a more ordered surface. Based on the KPFM results, we propose the model shown in Figure 167e, where DMF aligns the zwitterionic side chains of PVBT-SB toward the $MAPbI_3$. This orientation creates an effective double layer capacitance that can trap mobile MA^+ migrating to the interface.[658]

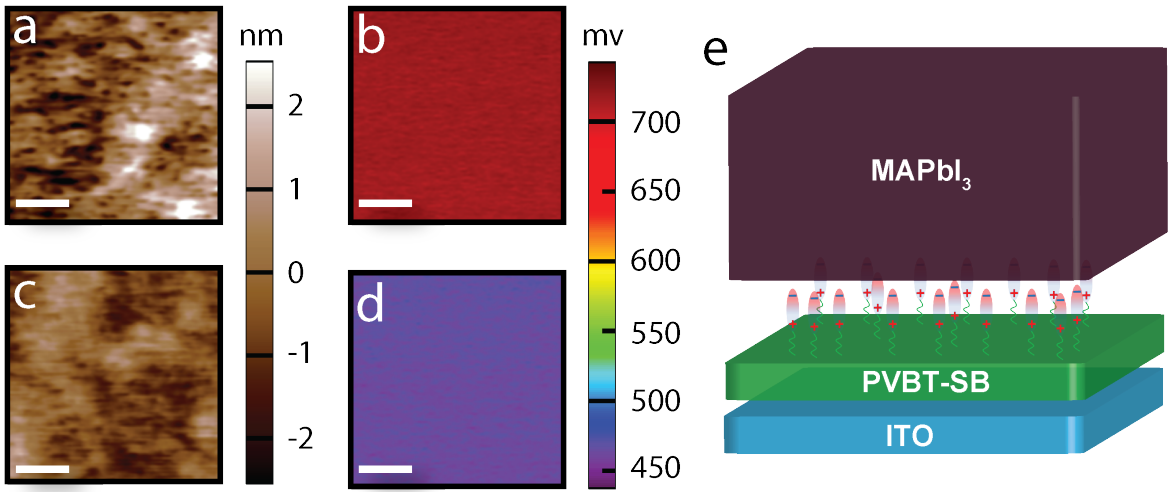

Figure 167: AFM and KPFM characterization of PVBT-SB thin films. Topographic AFM (**a**) and KPFM surface potential (**b**) maps for PVBT-SB on ITO/glass. Topographic AFM (**c**) and KPFM surface potential (**d**) maps for DMF-washed PVBT-SB on ITO/glass. Scale bar is 250 nm. (**e**) Proposed model of zwitterion orientation at interface between perovskite and HTL.

3.8.7 Conductive Atomic Force Microscopy (cAFM) Measurements

We next used cAFM to analyze the dark current-voltage (*I-V*) characteristics of individual $MAPbI_3$ grains on the three different HTLs. In this experiment, $MAPbI_3$ polycrystalline films were deposited on HTL/ITO/glass substrates as in device fabrication. Using ITO as the bottom electrode and a Pt/Ir coated AFM probe as the top electrode, a bias voltage was applied and the current measured. To study the time and bias direction dependent *I-V* dynamics, a triangle bias wave was applied at a rate of 0.4 Hz, with a maximum bias of +4.0 V and a minimum of -4.0 V. We analyzed the *I-V* characteristics from 0 V to +4.0 V since this produced more consistent results than the negative applied fields.

The topographic AFM image of $MAPbI_3$ on PVBT-TMA is shown in Figure 168a, and the three selected grains for current-voltage analysis are expanded next to the image. Semi-log *I-V* plots for the three individual grains are shown in Figure 169a-c. 'Grain 1' shows *I-V* hysteresis on all three forward and reverse biases. However, after three cycles the current measured at the

maximum voltage was still comparable. ‘Grain 2’ shows slight *I-V* hysteresis on the first two cycles, thereafter, the current decreased on the last cycle. ‘Grain 3’ shows limited hysteresis over all three cycles and maintained comparable current throughout the cycling. Figure 168d shows a plot of current and bias triangle wave *vs.* time for ‘Grains 1-3’.

The topographic AFM image and zoomed areas of interest of $MAPbI_3$ on PVBT-SO_3 are shown in Figure 168b. Semi-log *I-V* plots for the three individual grains are shown in Figure 169d-f. ‘Grain 4’ shows minimal *I-V* hysteresis, and maintains a maximum current throughout the three bias voltage cycles. ‘Grain 5’ shows minimal *I-V* hysteresis in the first cycle, significant *I-V* hysteresis in the second cycles, followed by a loss of current in the third cycle. ‘Grain 6’ shows *I-V* hysteresis in all three voltage cycles with incremental decrease in current over those cycles. Figure 168e shows a plot of current and bias as a function of time for ‘Grains 4-6’.

Figure 168c shows the topographic AFM image as well as zoomed-in areas for $MAPbI_3$ on PVBT-SB. Semi-log *I-V* plots for the three individual grains are shown in Figure 169g-i. Interestingly, all three analyzed grains on PVBT-SB showed significantly higher current than PVBT-TMA and PVBT-SO_3 on the first cycle, albeit with significant *I-V* hysteresis. This higher current is presumably due to the current associated with ion movement and the formation of a *p-i-n* polarity. Further, all three grains showed a dramatic decrease in current upon further *I-V* cycles. We hypothesize that this is due to the trapping of mobile ions in the PVBT-SB layer. Figure 168f shows a decrease in current for ‘Grains 7-9’ over time as the triangle bias wave is applied.

To conclude the cAFM studies, individual $MAPbI_3$ grains on different HTLs demonstrated heterogeneous *I-V* characteristics. Grains on PVBT-TMA and PVBT-SO_3 did however demonstrate markedly less *I-V* hysteresis than grains on PVBT-SB. Furthermore, the slight *I-V*

hysteresis observed for PVBT-TMA and PVBT-SO_3 can be attributed to lack of passivation by $PC_{61}BM$ ETL, which is present in devices. Grains on PVBT-TMA and PVBT-SO_3 showed consistent currents over multiple *I-V* cycles compared to PVBT-SB, which decreased over cycling, this is due to the adsorbing nature of PVBT-SB on MA^+ vacancies. Moreover, the *I-V* hysteresis for grains on PVBT-TMA and PVBT-SO_3 is quite different from the hysteresis for grains on PVBT-SB. Upon close examination of the first *I-V* cycle, in the reverse bias direction, grains on PVBT-TMA and PVBT-SO_3 showed an initial increase in current compared to the forward bias direction, while grains on PVBT-SB all demonstrated a decrease in current. We speculate that the slow, yet *reversible*, dynamics of ion transport in $MAPbI_3$ grains on PVBT-TMA and PVBT-SO_3 are the cause of this increasing current in *I-V* hysteresis. On the other hand, PVBT-SB interface provides a more *irreversible* trapping of ions, therefore the current decreases in the reverse bias direction.

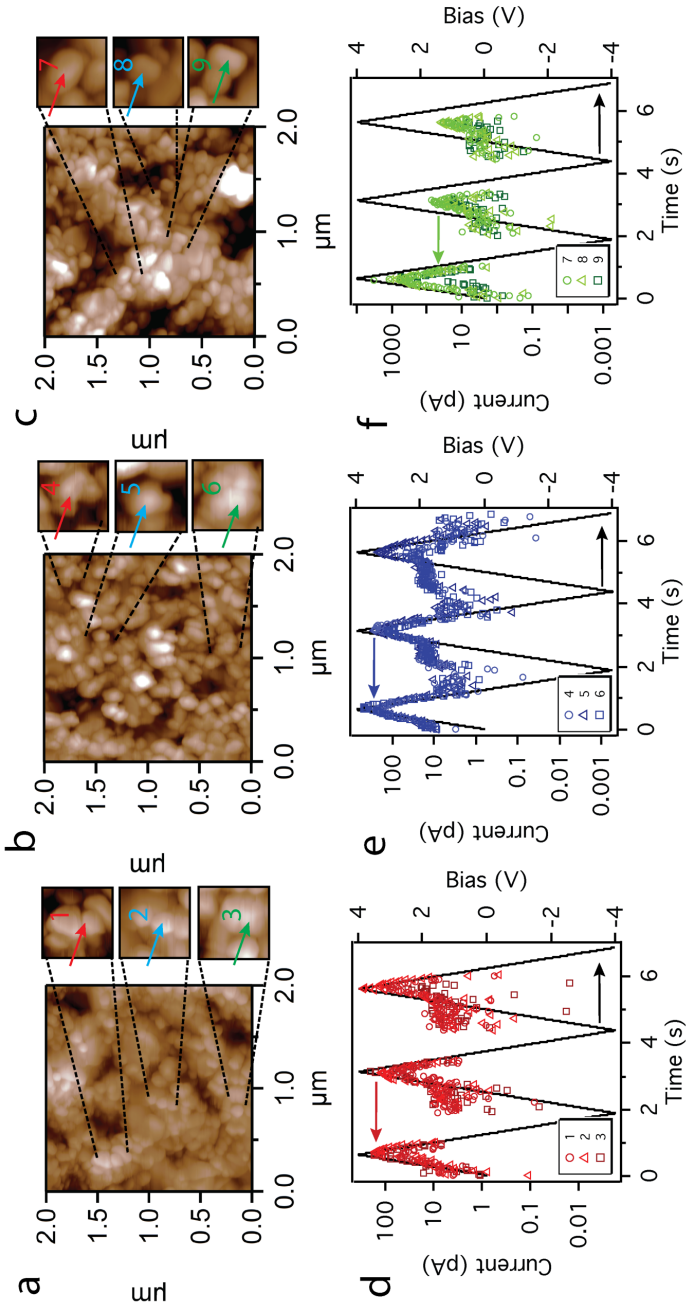

Figure 168: cAFM characterizations of perovskite films on different HTLs. Tapping mode AFM images of $MAPbI_3$ on (**a**) PVBT-TMA, (**b**) PVBT-SO_3, and (**c**) PVBT-SB. Expanded AFM images are shown for each for the specific grains where *I-V* measurements were made. Current vs time graphs for (**d**) PVBT-TMA, (**e**) PVBT-SO_3, and (**f**) PVBT-SB, showing current response to triangle bias wave.

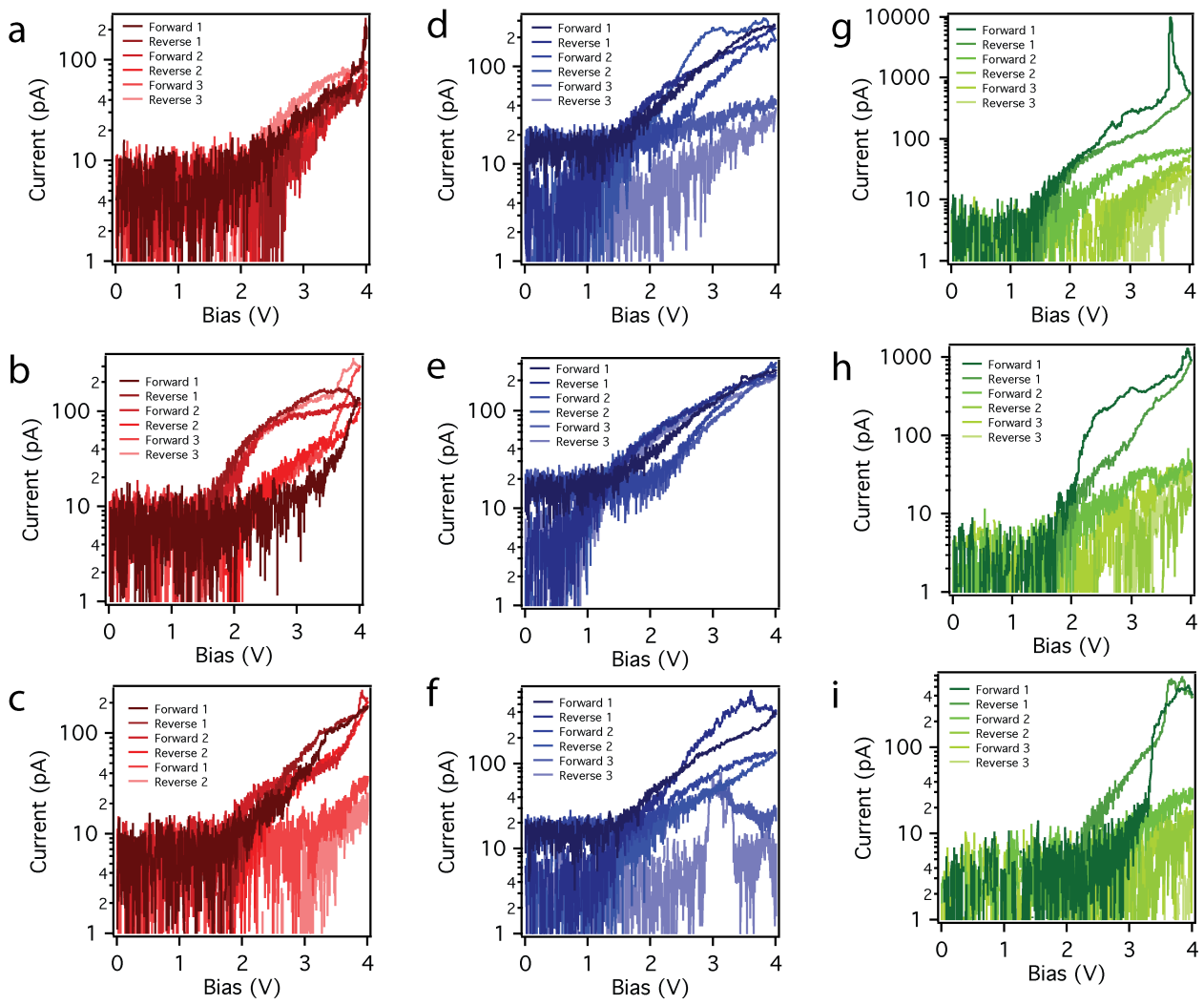

Figure 169: Semi-log *I-V* curves over three forward/reverse bias cycles for individual $MAPbI_3$ on (**a-c**) 'Grains 1-3' PVBT-TMA, (**d-f**) 'Grains 4 -6' PVBT-SO_3, and (**g-i**) 'Grains 7- 9' PVBT-SB.

3.8.8 Memristic Characterization

Memristors are circuit elements in which the resistance is not constant but depends on "memory" of prior *I-V* scanning cycles. The device memory is realized by gradual tuning of resistance in consecutive voltage sweeps. Memristor research has focused primarily on metal-oxide-semiconductors containing regions with a high percentage of dopants and coupled electronic and ionic transport.[659] An applied electric field shifts the edge between doped and

undoped regions in the *bulk*, altering the composite resistance.[660] While ion migration-generated *I-V* hysteresis is undesirable for photovoltaics, it is of use in memristors. In a recent research on perovskite-based memristors, memristic properties were obtained by changing the "speed" of ion migration through the bulk grain boundaries.[642,661] Here, we introduce a new concept to obtain memristic properties by trapping ions at the *interface*. Two-terminal devices were fabricated with an architecture of ITO/ PVBT-SO_3 or PVBT-SB/$MAPbI_3$/Au (Figure 170a an d). In the dark, consecutive positive and negative voltage sweeps, 0 V to 1.5 V, and 0 V to -1.5 V or 0 V to -1.9 V, respectively, were performed at a constant scanning speed of 140 mV/s. Here, we again demonstrate the role of interfacial ionic functionalities on ion transport. Devices containing PVBT-SO_3 showed negligible *I-V* hysteresis (Figure 170b-c). Devices containing PVBT-SB showed characteristic memristor behavior: *I-V* hysteresis accompanied with the tuning of the dark current under consecutive bias sweeps (Figure 170e-f). Under the voltage sweeps from 0 V to 1.5 V, the holes injected from ITO/PVBT-SB into the devices and the MA^+ ions trapped at the PVBT-SB layer should be continually pushed out, inducing the gradually increased current (Figure 170e). Under the voltage sweeps from 0 V to -1.5 V, the moving MA^+ ions were trapped by PVBT-SB and accumulated at the interface between perovskite and PVBT-SB, which generated a reverse electric field and impeded the further injection of holes from Au. Thus, a decrease of the current was found in the continually negative voltage scans.

We utilized the ion adsorption/desorption, arising from chemical functionality at the interface, to demonstrate memory write, read, and erase capabilities. As shown in Figure 171a, we can use a positive voltage scan as the writing process. A small constant voltage of 0.5 V was then applied as the reading voltage and the output current (high level) can be defined as the ON state. After that, the negative voltage scan was used as the erasing process and the same reading voltage (0.5

V) only gave a low level output current, which can be defined as the OFF state. Another writing-reading-erasing-reading cycle was shown in Figure 171b, where the constant writing (3 V) and erasing (-3 V) voltages were applied. We still found after the writing process by positive voltage, the 0.5 V reading voltage gave a high level output current (ON state). Then constant negative voltage scan was applied as erasing process, inducing a low level output current (OFF state) under the small reading voltage of 0.5 V. Thus, we can realize the simplest case of 0-1storage (two states) in perovskite devices. As the current can be tuned with successive voltage sweeps, higher order computing logic could be implemented with these types of devices. This is, to the best of our knowledge, the first example of using interfacial chemistry to obtain memristic behavior in perovskite-based devices, and opens new avenues to future non-volatile memory applications.

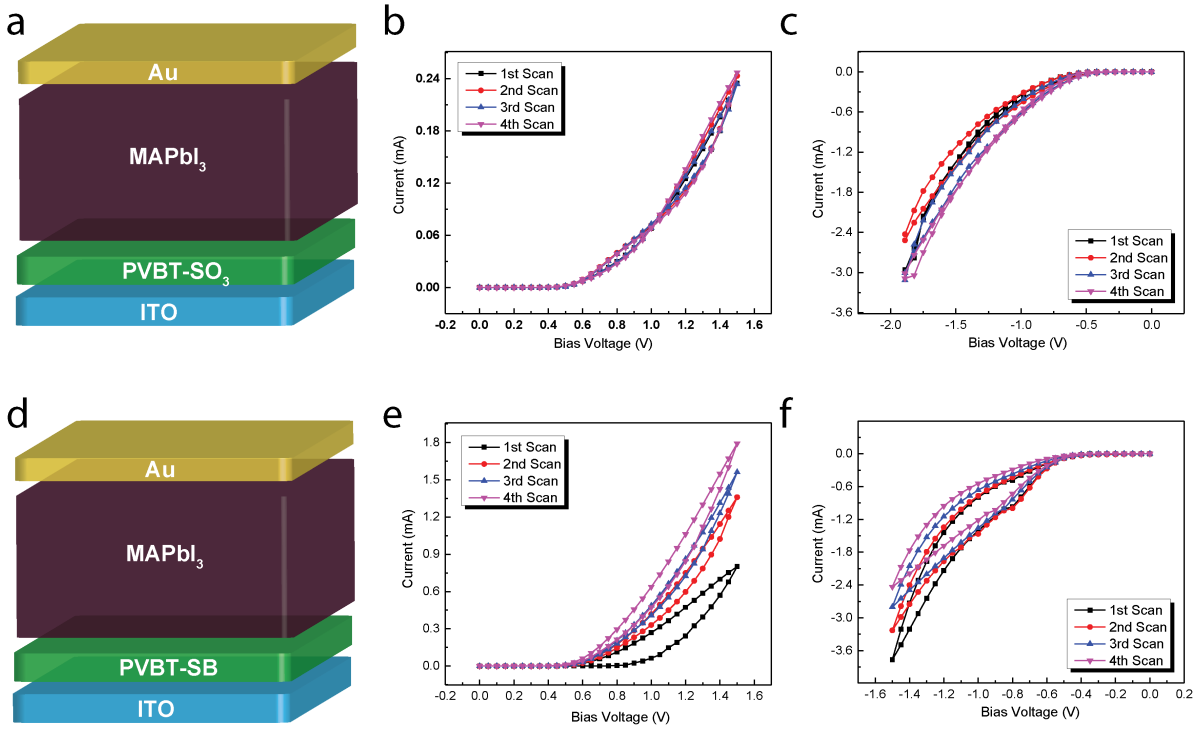

Figure 170: Characterizations of perovskite memristors. Perovskite diode device containing PVBT-SO_3 and its typical *I-V* curves (**a-c**). Perovskite diode device containing PVBT-SB and its typical *I-V* curves (**d-f**).

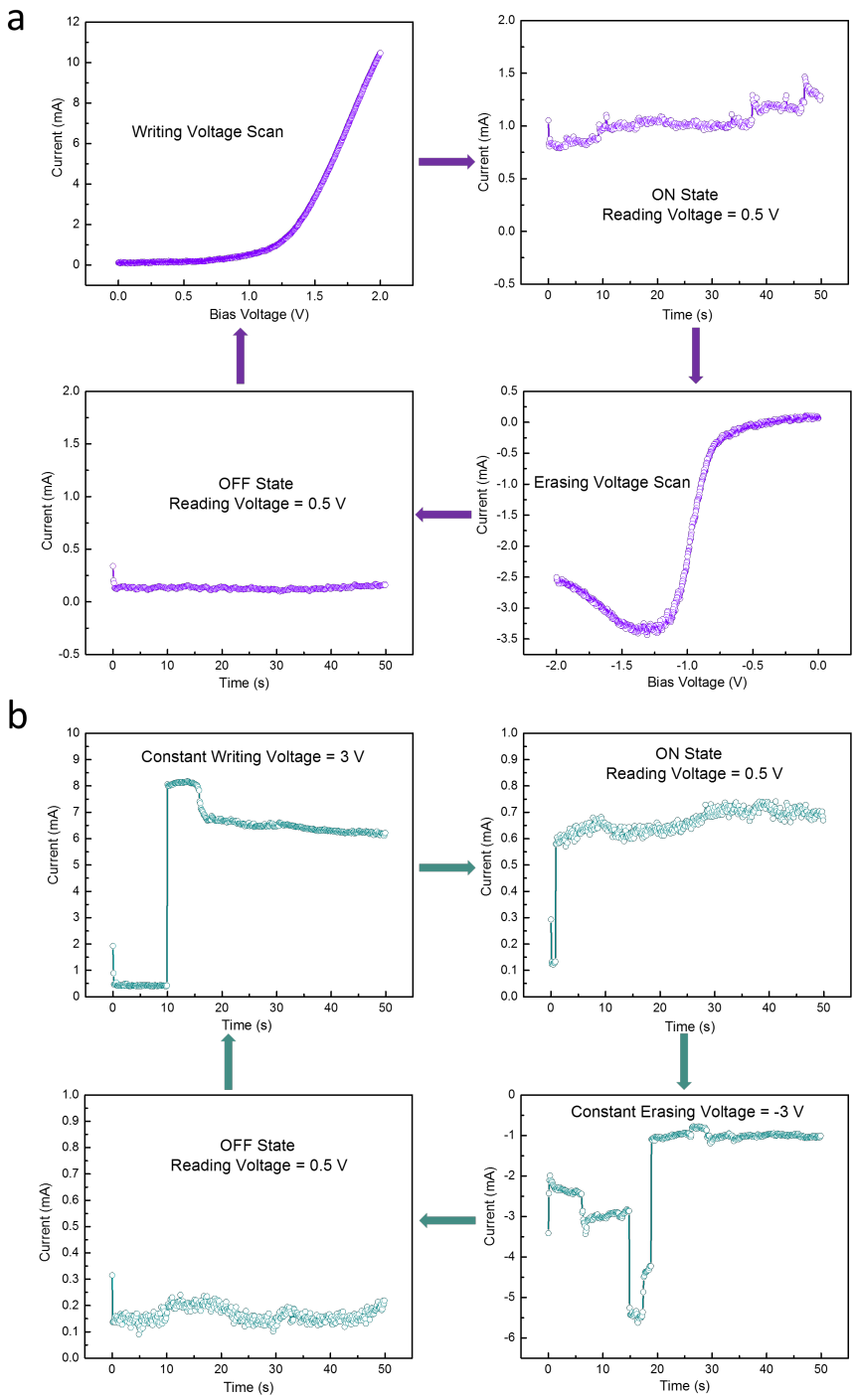

Figure 171: Perovskite devices containing PVBT-SB HTL showing non-volatile memory write, read, and erase capabilities. (a) The writing and erasing process were realized by continuously increased bias voltage; (b) the writing and erasing process were realized by constant bias voltage.

We have demonstrated the significant impact that ionic processes, influenced by interface engineering, can have on the *J-V* hysteresis in inverted planar heterojunction perovskite solar cells and how this can be used for perovskite-based memristors. By varying the surface properties of HTLs with different ionic characteristics (anionic, zwitterionic and cationic), we addressed a critical question concerning ion migration at the interface in perovskite solar cells and the impact on *J-V* hysteresis. For anionic and cationic HTLs, ions are able to move freely to and from the interface, resulting in only minor *J-V* hysteresis. For a zwitterionic HTL, EIS and cAFM characterization confirmed that the zwitterionic pendent groups interacted with the moving ions during device operation, inducing a serious *J-V* hysteresis. Hence, we confirmed that one of the origins of *J-V* hysteresis in perovskite solar cells is the trapping of ions at the interface between the perovskite layer and charge selective transport layer. We also proposed a model, based on KPFM measurements, to explain how oriented zwitterionic pendent groups trap ions at the interface *via* an effective electric double layer. The concept of ion trapping at the interface was also used to develop perovskite-based memristors, taking advantage of ionic process in perovskites. This research clarifies the influence of ion migration on interface engineering in perovskite solar cells, provides guidelines on performing perovskite device optimization at the interface, and provides an avenue for developing multifunctional perovskite devices through interface engineering.

APPENDICES

APPENDIX A

CONDUCTING ATOMIC FORCE MICROSCOPY (cAFM) – DETAILED EXPERIMENTAL PROCEDURE

cAFM was performed in Orca mode on the Oxford Instruments Asylum Research MFP3d stand-alone instrument. Probes used were either a Cr/Pt coated Si probe (Budget Sensors ContE-G, Force Constant = 0.2 N/m) or an Ir/Pt coated Si probe (AppNano ANSCM-PT, Force Constant = 1-5 N/m)

1. Samples for cAFM are prepared on some electrode, generally ITO.

2. The sample is fixed to the ORCA sample holder using double sided tape.

3. Using a razor blade, a small section, in the corner of the substrate, is scraped away to expose electrode.

4. Contact is made to the electrode using the provided clip on the ORCA sample holder.

5. The conducting AFM probe is loaded into the ORCA cantilever holder, and a small wire is connected to the POGO Out on the holder.

6. The cantilever holder is connected to the scanning head, and the sample holder is affixed to the stage magnetically. Also, the POGO Out wire is connected to the ORCA sample stage.

7. The LED is turned on and aligned on the cantilever (maximum sum), centered horizontally, and towards the end of the cantilever vertically.

8. The deflection of the LED light off the cantilever is adjusted so that it is centered on the photodiode.

9. Using the autotune protocol, the resonant oscillation frequency is found. In general, a target amplitude of 1 V, and target percent of -5% (repulsive regime) are used

10. Click Engage, the piezo is fully extended, and the feedback set point is set (generally to 0.05 V), then the AFM head is manually lowered towards the sample using the scroll wheels which lower the legs on the head.

11. By monitoring the z-voltage applied to the piezo, the height is manually set at where the piezo is retracted halfway. A bubble level is used to ensure that the AFM head is level.

12. To make a current map of the sample, set the imaging mode to contact.

13. set the desired scan size, rate, angle and resolution. I find that scan sizes of 2.5 μm -5 μm at a rate of 0.3 Hz produce the best scans.

14. In the AR do IV panel check 'Use' sample voltage, and set the voltage. Engage the probe to the sample and zero the current sensor. Then click 'Do Scan'.

15. To do current-voltage measurements, (cAFM spectroscopy). First, set the imaging mode to AC mode, set the desired scan size, rate, angle and resolution.

16. Click 'Do Scan' and make a topographic map in tapping mode.

17. In the AR do IV panel check click DoIV pick point, and pick spot on AFM map, then click DoIV go there.

18. Set the IV amplitude, frequency, function (wave shape), number of cycles, average (or not), and whether to apply bias to probe or electrode ('drives what?'). The make measurement by clicking 'Do it'.

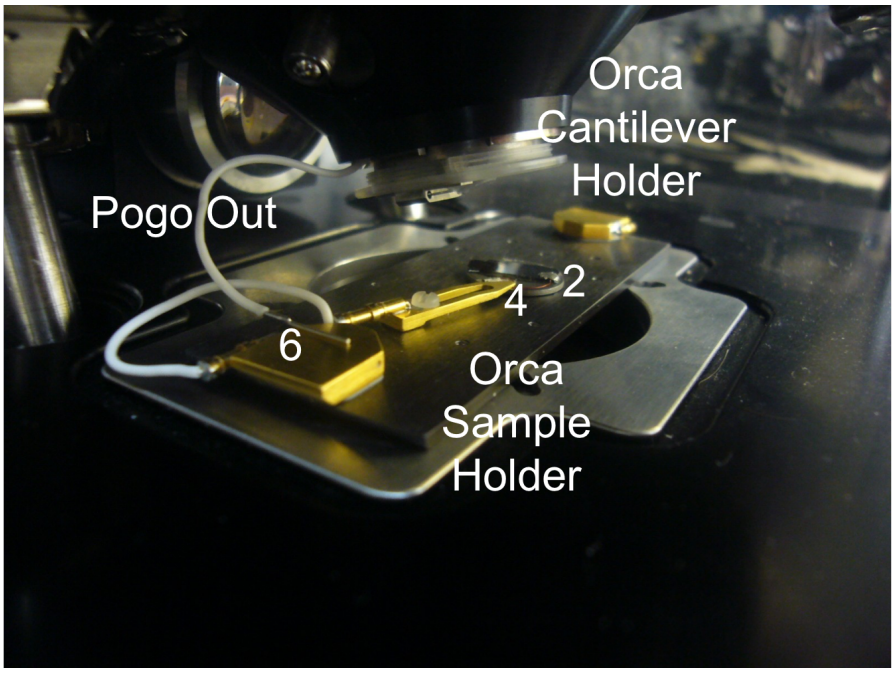

Figure 172: cAFM setup, from Ref. [662].

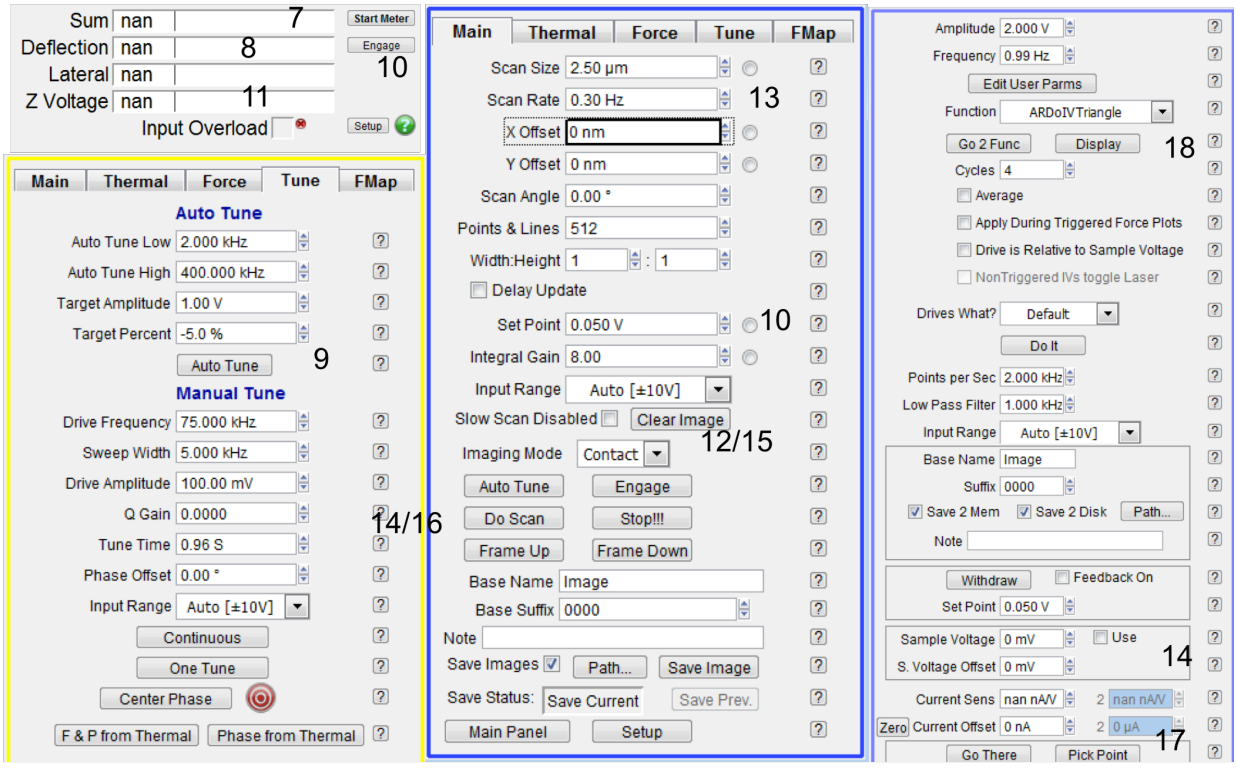

Figure 173: cAFM software panels.

APPENDIX B

KELVIN PROBE FORCE MICROSCOPY (KPFM) – DETAILED EXPERIMENTAL PROCEDURE

KPFM was performed on the Oxford Instuments Asylum Research MFP3d stand-alone instrument. Probes used were Ir/Pt coated Si probe (AppNano ANSCM-PT, Force Constant = 1-5 N/m).

1. Samples for KPFM are prepared on some electrode, generally ITO.

2. The sample is fixed to the ORCA sample holder using double sided tape.

3. Using a razor blade, a small section, in the corner of the substrate, is scraped away to expose electrode.

4. Contact is made to the electrode using the provided clip on the ORCA sample holder.

5. The conducting AFM probe is loaded into the standard cantilever holder.

6. The cantilever holder is connected to the scanning head, and the sample holder is affixed to the stage magnetically.

7. A BNC cable is connected to any port on the BNC panel on the ARC2 Controller The outer shell of the BNC cable (ground) is connected to the the sample to ground the substratre/electrode.

8. The LED is turned on and aligned on the cantilever (maximum sum), centered horizontally, and towards the end of the cantilever vertically.

9. The deflection of the LED light off the cantilever is adjusted so that it is centered on the photodiode.

10. Using the autotune protocol, the resonant oscillation frequency is found. In general, a target amplitude of 1 V, and target percent of -5% (repulsive regime) are used

11. Click Engage, the piezo is fully extended, and the feedback set point is set (generally to 0.05 V), then the AFM head is manually lowered towards the sample using the scroll wheels which lower the legs on the head.

12. By monitoring the z-voltage applied to the piezo, the height is manually set at where the piezo is retracted halfway. A bubble level is used to ensure that the AFM head is level.

13. Engage the piezo, and in the Electric Tune Panel do single force measurement.

14. Click the arrow between normal tune and electric tune.

15. Click electric tune.

16. In the electric tune panel, you can also set a bias to be applied to the sample, to do this experiment, instead of grounding the substrate to the outer shell of the BNC cable, run a wire from the POGO out on the cantilever holder to the electrode.

17. In the Nap Panel, set the Nap height, I generally use 30 nm.

18. Click ‘Do Scan’ and make a topographic map in tapping mode and a surface potential map in Nap mode.

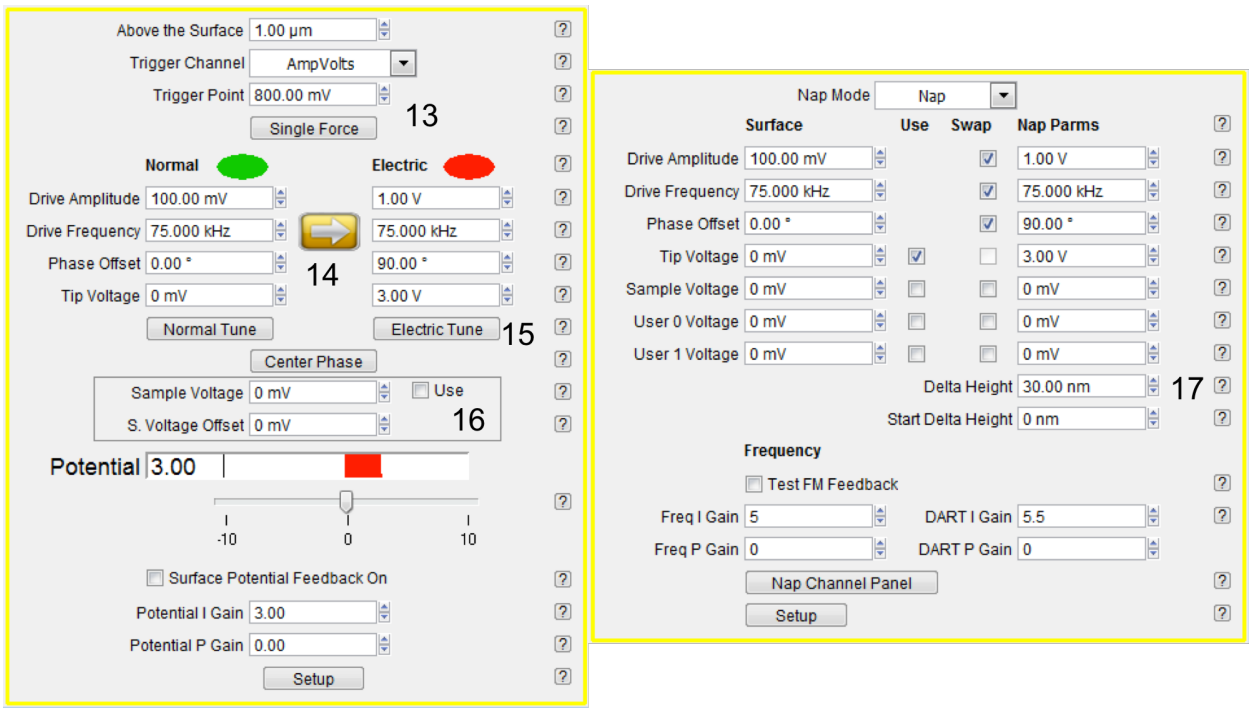

Figure 174: KPFM software panels.

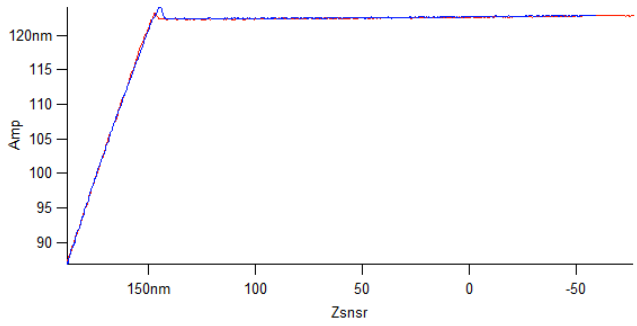

Figure 175: Typical force curve

APPENDIX C

MATLAB – RESISTOR NETWORK ALGORITHM

```
%%% Lawrence A. Renna %%%
%%% University of Massachusetts Amherst %%%
%%% lrenna.com %%%
%%% larryrenna@gmail.com %%%
%%% Last Edit 03/31/2016 09:23 %%%

%%% Please Cite LA Renna et al J. Phys. Chem. B, 2016, 120 (9), pp 2544ñ2556 DOI:
10.1021/acs.jpcb.5b11716

%%
number=1;

Data=FinalConfig;


if number==1;
VarR=system(5,1);
else
   VarR=system(6,1);
end

promptA = 'Fraction Conducting Particle 1?:';
percentparticle = input(promptA);
percentotherparticle= 1-percentparticle;

VarR2=system(6,1);

%Delta
LittleDelta=0.09*VarR;

Zmax=system(7,6);
% Input Constants
tic
%% Add Radius and Delta to Data
for i=1:length(Data)
   if Data(i,4)==2;
      Data(i,5)=VarR2;
    else Data(i,5)=VarR;
   end
end
for i=1:length(Data)
   Data(i,6)= Data(i,5)*LittleDelta;
```

```
end
%% Random ID
numElements = length(Data);
letters2use = {1 2};
percentages = [percentparticle percentotherparticle];
numEach = round(percentages*numElements);
while sum(numEach) < numElements
  [~,idx] = max(mod(percentages*numElements,1));
  numEach(idx) = numEach(idx) + 1;
end
while sum(numEach) > numElements
  [~,idx] = min(mod(percentages*numElements,1));
  numEach(idx) = numEach(idx) - 1;
end
indices = randperm(numElements);
output = cell(size(indices));
lower = [0,cumsum(numEach(1:end-1))]+1;
upper = cumsum(numEach);
for i = 1:numel(lower)
   [output{indices(lower(i):upper(i))}] = deal(letters2use{i});
end
o=cell2mat(output');
%% Separate Raw Data
RawX = Data(:, 1) ;
RawY = Data(:, 2) ;
RawZ = Data(:, 3) ;
RawRad = Data(:,5);
RawDelta = Data (:,6);
DataNew=[RawX, RawY, RawZ, o, RawRad, RawDelta];
%% Remove Data (ID = 2)
DataN=NaN*zeros*Data;
for n=1:length(Data);
   if DataNew(n,4)==number;
      DataN(n,1)=DataNew(n,1);
      DataN(n,2)=DataNew(n,2);
      DataN(n,3)=DataNew(n,3);
      DataN(n,4)=DataNew(n,4);
      DataN(n,5)=DataNew(n,5);
      DataN(n,6)=DataNew(n,6);
   end
end
% Remove data of other particle type
%% Sort and Extract Data

SortedData = sortrows(DataN,3);
% This sorts the data in Data by the third column/z value
```

```
BigX = SortedData(:, 1) ;
BigY = SortedData(:, 2) ;
BigZ = SortedData(:, 3) ;
BigR = SortedData(:,5) ;
BigDelta = SortedData(:,6);
% This extracts the X, Y, and Z values from the sorted data.
%% Distance Matrix

DistanceMatrix=NaN*zeros(length(BigX), length(BigX));
for i=1:length(BigX);
   for j=0:length(BigX);
      if i+j<=length(BigX)
      DistanceX=(BigX(i)-BigX(i+j))^2;
      DistanceY=(BigY(i)-BigY(i+j))^2;
      DistanceZ=(BigZ(i)-BigZ(i+j))^2;
      DistanceMatrix(i,j+1)=sqrt(DistanceX+DistanceY+DistanceZ);
      end
   end
end
% This generates the distance matrix for each point to every other point
%% Path Matrix (1 = connected, 0 = not)

PathMatrix=NaN*zeros(length(BigX), length(BigX));
for x=1:length(BigX);
   for y=1:length(BigX);
   if DistanceMatrix(x,y)<(2*((BigR(x)+BigR(y))/2))+((BigDelta(x)+BigDelta(y))/2);
      PathMatrix(x,y)=1;
   else PathMatrix(x,y)=0;
   end
   end
end
% This find all the path distances that are considered connected and
% assigns it a 1, all non-connected points are assigned a 0
%% Assemble Connected Pts

[Row,Column]=find(PathMatrix==1);
PathCoordinates=horzcat(Row, Column +Row-1);
PathCoordinatesSort=sortrows(PathCoordinates);
% This finds all the 1's and assembles them into an x,y matrix for each two
% point connections; and then sorts them by first point in a connection
%% Sparse Matrix

column1 = PathCoordinatesSort(:, 1) ;
column2 = PathCoordinatesSort(:, 2) ;
% These make the coordinate matrix into two columns
```

```
DG = sparse(column1,column2,1);
% This makes an array of connected pairs all with same path length of 1

%% Start and End Pts

StartPts=NaN*zeros(length(BigZ));
for z=1:length(BigZ);
      if BigZ(z)-BigR(z) <=0 ;
        StartPts(z) = BigZ(z);
      else StartPts(z) =NaN ;
      end
end
% This finds the starting points

EndPts=NaN*zeros(length(BigZ));
for z=1:length(BigZ);
      if Zmax -BigZ(z) <BigR(z) ;
        EndPts(z) = BigZ(z);
      else EndPts(z) =NaN ;
      end
end
% This Finds the end points.

[startz]=find(StartPts>=0);
[endz]=find(EndPts>=0);
STARTz=startz';
ENDz=endz';
% This gives the point ID for start and end points,then flips rows to columns
%% Shortest Path

ConnectedPathsMatrix=NaN*zeros(length(STARTz), length(ENDz));
for i=1 : length(STARTz);
   for j=1 : length(ENDz);
      ConnectedPathsMatrix(i,j)= graphshortestpath(DG, STARTz(i), ENDz(j));
   end
end
% This finds the shortest path from each starting point to each end point

ConnectedPathsMatrixInverse=NaN*zeros(length(STARTz), length(ENDz));
for i=1 : length(STARTz);
   for j=1 : length(ENDz);
      if ConnectedPathsMatrix(i,j)>length(DataN);
         ConnectedPathsMatrixInverse(i,j)=0;
      else ConnectedPathsMatrixInverse(i,j)= inv(ConnectedPathsMatrix(i,j));
      end
   end
```

```
end
% This takes the inverse of each path distance

S=sum(ConnectedPathsMatrixInverse,1);
% This sums the inverse distances to get the effective current
%% Surface Current

SurfaceCurrent=[endz,S'];
% This combines the end pt ID and the effective current, to give the
% effective current for each surface pt.

SC1=SurfaceCurrent';
% Transposes the surface current matrix


toc
%% Histogram


binsize=0.1;
hlength=50;
xsize=0:binsize:hlength;
hist(S,xsize);
H=hist(S,xsize);
HT1=[xsize',H'];
sc1=SC1';
% number of bins in histogram of current vs. counts, and plots.
```

APPENDIX D

MATLAB – CONNECTIVITY ANALYSIS

```
%%% Lawrence A. Renna %%%
%%% University of Massachusetts Amherst %%%
%%% lrenna.com %%%
%%% lrenna@umass.edu %%%
%%% Last Edit 11/04/2014 9:06 %%%

%%% Number of connections and angle analysis %%%
%%
Data=FinalConfig;
 prompt1 = 'Particle 1 or 2?:';
 number=input(prompt1);
%
%prompt2 = 'Radius?:';
if number==1;
VarR=system(5,1);
else
   VarR=system(6,1);
end

%prompt3 = 'Delta?:';
LittleDelta=0.09*VarR;

%prompt4 = 'Zmax?:';
Zmax=system(7,6);
% Input Constants
tic
%%

DataN=NaN*zeros*Data;
for n=1:length(Data);
   if Data(n,4)==number;
      DataN(n,1)=Data(n,1);
      DataN(n,2)=Data(n,2);
      DataN(n,3)=Data(n,3);
      DataN(n,4)=Data(n,4);
   end
end
% Remove data of other particle type
%%

SortedData = sortrows(DataN,3);
% This sorts the data in Data by the third column/z value
```

```
BigX = SortedData(:, 1) ;
BigY = SortedData(:, 2) ;
BigZ = SortedData(:, 3) ;
% This extracts the X, Y, and Z values from the sorted data.
%%

DistanceMatrix=NaN*zeros(length(BigX), length(BigX));
for i=1:length(BigX);
   for j=0:(length(BigX)-1);
      if i+j<=length(BigX)
      DistanceX=(BigX(i)-BigX(j+1))^2;
      DistanceY=(BigY(i)-BigY(j+1))^2;
      DistanceZ=(BigZ(i)-BigZ(j+1))^2;
      DistanceMatrix(i,j+1)=sqrt(DistanceX+DistanceY+DistanceZ);
      end
   end
end
% This generates the distance matrix for each point to every other point
%%

PathMatrix=NaN*zeros(length(BigX), length(BigX));
for x=1:length(BigX);
   for y=1:length(BigX);
   if DistanceMatrix(x,y)<(2*VarR)+LittleDelta;
      PathMatrix(x,y)=1;
   else PathMatrix(x,y)=0;
   end
   end
end
% This find all the path distances that are considered connected and
% assigns it a 1, all non-connected points are assigned a 0
%%

[Row,Column]=find(PathMatrix==1);

HH=hist(Column,max(Column));
%%
NUMBCONNECT=NaN*zeros(1,length(HH));
for i=1 : length(HH);
   NUMBCONNECT(i)= HH(i)-1;
end
%%
NCHist=hist(NUMBCONNECT,0:1:25);
hist(NUMBCONNECT,0:1:25)
connections = NCHist';
```

```
%%
%%
mm=horzcat(Column,Row);
X = SortedData(:, 1) ;
Y = SortedData(:, 2) ;
Z = SortedData(:, 3) ;
%%
XDist=NaN*zeros*length(Column);
YDist=NaN*zeros*length(Column);
ZDist=NaN*zeros*length(Column);
for i=1:length(Column);
   XDist(i)= X(Row(i))-X(Column(i));
   YDist(i)= Y(Row(i))-Y(Column(i));
   ZDist(i)= Z(Row(i))-Z(Column(i));
end

XD=XDist';
YD=YDist';
ZD=ZDist';
%%
aa=[Column,XD(:),YD(:),ZD(:)];
theta=NaN*zeros*length(XD);
CosTheta=NaN*zeros*length(XD);
for i=1:length(XD);
   for j=1:25;
      if i+j<= length(XD);
         if aa(i,1)==aa(i+j,1);
   u=[aa(i,2) aa(i,3) aa(i,4)];
   v=[aa(i+j,2) aa(i+j,3) aa(i+j,4)];
    CosTheta(i) = dot(u,v)/(norm(u)*norm(v));
     theta(i) = acos(CosTheta(i))*180/pi;
         end
      end
   end
end
Angle=theta';
%%
flipColumn=flipud(Column);
flipRow=flipud(Row);
mm2=horzcat(flipColumn,flipRow);
XDist2=NaN*zeros*length(flipColumn);
YDist2=NaN*zeros*length(flipColumn);
ZDist2=NaN*zeros*length(flipColumn);
for i=1:length(flipColumn);
   XDist2(i)= X(flipRow(i))-X(flipColumn(i));
   YDist2(i)= Y(flipRow(i))-Y(flipColumn(i));
```

```
    ZDist2(i)= Z(flipRow(i))-Z(flipColumn(i));
end

XD2=XDist2';
YD2=YDist2';
ZD2=ZDist2';
%%
aa2=[flipColumn,XD2(:),YD2(:),ZD2(:)];
theta2=NaN*zeros*length(XD2);
CosTheta2=NaN*zeros*length(XD2);
for i=1:length(XD2);
    for j=1:25;
        if i+j<= length(XD2);
            if aa2(i,1)==aa2(i+j,1);
    u2=[aa2(i,2) aa2(i,3) aa2(i,4)];
    v2=[aa2(i+j,2) aa2(i+j,3) aa2(i+j,4)];
     CosTheta2(i) = dot(u2,v2)/(norm(u2)*norm(v2));
       theta2(i) = acos(CosTheta2(i))*180/pi;
            end
        end
    end
end
Angle2=theta2';
%%
angles=hist(Angle,0:1:180);
angles2=hist(Angle2,0:1:180);
anglescombo=angles+angles2;
bar(0:1:180,anglescombo)
degrees=0:1:180;
CoordinationAngle=[degrees' anglescombo'];
%%
```

APPENDIX E

MATLAB – WATERSHED ALGORITHM

```
%%% Lawrence A. Renna %%%
%%% University of Massachusetts Amherst %%%
%%% lrenna.com %%%
%%% larryrenna@gmail.com %%%
%%% Last Edit 11/21/2016 15:37 %%%

%%% Adapted from S. Eddins, Cell Segmentation, The MathWorks, Inc., 2006.
%%% Watershed algorithm for segmentation of grains in AFM image
 %%
figure
imshow(orig)

figure
imshow(test)
% Original image (orig) and contrast enhanced image (test)
%%
I_eq = adapthisteq(test);
figure
imshow(I_eq)
% Further Contrast enhancement
%%
bw = im2bw(I_eq, graythresh(I_eq));
figure
imshow(bw)
% Apply Threshold
%%
bw2 = imfill(bw,'holes');
bw3 = imopen(bw2, ones(5,5));
bw4 = bwareaopen(bw3, 40);
bw4_perim = bwperim(bw4);
overlay = imoverlay(I_eq, bw4_perim, [.3 1 .3]);
figure
imshow(overlay)
% Clean image and overlay perim.
%%
mask_em = imextendedmax(I_eq, 30);
figure
imshow(mask_em)
% ID maxima
%%
```

```
mask_em = imclose(mask_em, ones(5,5));
mask_em = imfill(mask_em, 'holes');
mask_em = bwareaopen(mask_em, 40);
overlay2 = imoverlay(I_eq, bw4_perim | mask_em, [.3 1 .3]);
figure
imshow(overlay2)
% Clean and overlay
%%
I_eq_c = imcomplement(I_eq);

I_mod = imimposemin(I_eq_c, ~bw4 | mask_em);

L = watershed(I_mod);
figure
imshow(label2rgb(L))
LL= label2rgb(L, 'jet', 'w', 'shuffle');
figure
imshow(LL)

figure
imshow(orig)
hold on
himage = imshow(LL);
himage.AlphaData = 0.3;
% Watershed and final image
```

REFERENCES

[1] T. Aida, E. W. Meijer, and S. I. Stupp, Functional Supramolecular Polymers, *Science* **335**, 813 (2012).
[2] F. S. Bates, M. A. Hillmyer, T. P. Lodge, C. M. Bates, K. T. Delaney, and G. H. Fredrickson, Multiblock Polymers: Panacea or Pandora's Box?, *Science* **336**, 434 (2012).
[3] P. T. Hammond, Form and function in multilayer assembly: New applications at the nanoscale, *Adv. Mater.* **16**, 1271 (2004).
[4] P. T. Hammond, Building biomedical materials layer-by-layer, *Mater. Today* **15**, 196 (2012).
[5] C. J. Hawker and T. P. Russell, Block copolymer lithography: Merging "bottom-up" with "top-down" processes, *MRS Bull.* **30**, 952 (2005).
[6] O. Ikkala and G. ten Brinke, Hierarchical self-assembly in polymeric complexes: Towards functional materials, *Chem. Commun.*, 2131 (2004).
[7] L. C. Palmer and S. I. Stupp, Molecular Self-Assembly into One-Dimensional Nanostructures, *Acc. Chem. Res.* **41**, 1674 (2008).
[8] M. Ramanathan and S. B. Darling, Mesoscale morphologies in polymer thin films, *Prog. Polym. Sci.* **36**, 793 (2011).
[9] F. S. Bates, Polymer-Polymer Phase-Behavior, *Science* **251**, 898 (1991).
[10] G. R. Strobl, Structure Evolution during Spinodal Decomposition of Polymer Blends, *Macromolecules* **18**, 558 (1985).
[11] H.-j. Chung, K. Ohno, T. Fukuda, and R. J. Composto, Self-Regulated Structures in Nanocomposites by Directed Nanoparticle Assembly, *Nano Lett.* **5**, 1878 (2005).
[12] S. Huang, L. Bai, M. Trifkovic, X. Cheng, and C. W. Macosko, Controlling the Morphology of Immiscible Cocontinuous Polymer Blends via Silica Nanoparticles Jammed at the Interface, *Macromolecules* **49**, 3911 (2016).
[13] M. Muthukumar, Commentary on theories of polymer crystallization, *Eur. Phys. J. E Soft Matter* **3**, 199 (2000).
[14] M. W. Matsen and F. S. Bates, Unifying weak- and strong-segregation block copolymer theories, *Macromolecules* **29**, 1091 (1996).
[15] X. H. Cheng, M. K. Das, S. Diele, and C. Tschierske, Influence of semiperfluorinated chains on the liquid crystalline properties of amphiphilic polyols: Novel materials with thermotropic lamellar, columnar, bicontinuous cubic, and micellar cubic mesophases, *Langmuir* **18**, 6521 (2002).
[16] R. G. E. Kimber, A. B. Walker, G. E. Schroder-Turk, and D. J. Cleaver, Bicontinuous minimal surface nanostructures for polymer blend solar cells, *Phys. Chem. Chem. Phys.* **12**, 844 (2010).
[17] M. Lee, B. K. Cho, Y. G. Jang, and W. C. Zin, Spontaneous organization of supramolecular rod-bundles into a body-centered tetragonal assembly in coil-rod-coil molecules, *J. Am. Chem. Soc.* **122**, 7449 (2000).
[18] S. H. Lin, C. C. Ho, and W. F. Su, Cylinder-to-gyroid phase transition in a rod-coil diblock copolymer, *Soft Matter* **8**, 4890 (2012).
[19] A. J. Liu and G. H. Fredrickson, Phase separation kinetics of rod/coil mixtures, *Macromolecules* **29**, 8000 (1996).
[20] J. H. Ryu and M. Lee, in *Liquid Crystalline Functional Assemblies and Their Supramolecular Structures*, edited by T. Kato (Springer-Verlag Berlin, Berlin, 2008), pp. 63.

[21] I. Riess, Solid State Electrochemistry, *Isr. J. Chem.* **48**, 143 (2008).
[22] G. Yang, H. Tao, P. L. Qin, W. J. Ke, and G. J. Fang, Recent progress in electron transport layers for efficient perovskite solar cells, *J. Mater. Chem. A* **4**, 3970 (2016).
[23] K. G. Lim, H. B. Kim, J. Jeong, H. Kim, J. Y. Kim, and T. W. Lee, Boosting the power conversion efficiency of perovskite solar cells using self-organized polymeric hole extraction layers with high work function, *Adv Mater* **26**, 6461 (2014).
[24] Y. Liu, L. A. Renna, Z. A. Page, H. B. Thompson, P. Y. Kim, M. D. Barnes, T. Emrick, D. Venkataraman, and T. P. Russell, A Polymer Hole Extraction Layer for Inverted Perovskite Solar Cells from Aqueous Solutions, *Adv. Energy Mater.*, 1600664 (2016).
[25] V. F. Lvovich, *Impedance spectroscopy: applications to electrochemical and dielectric phenomena* (John Wiley & Sons, Hoboken, NJ, USA, 2012), p.^pp. 87-94.
[26] J. Maier, Ionic conduction in space charge regions, *Prog. Solid State Chem.* **23**, 171 (1995).
[27] S. Meloni *et al.*, Ionic polarization-induced current-voltage hysteresis in CH3NH3PbX3 perovskite solar cells, *Nat. Commun.* **7** (2016).
[28] J. M. Azpiroz, E. Mosconi, J. Bisquert, and F. De Angelis, Defect migration in methylammonium lead iodide and its role in perovskite solar cell operation, *Energy Environ. Sci.* **8**, 2118 (2015).
[29] Z. Xiao, Y. Yuan, Y. Shao, Q. Wang, Q. Dong, C. Bi, P. Sharma, A. Gruverman, and J. Huang, Giant switchable photovoltaic effect in organometal trihalide perovskite devices, *Nat. Mater.* **14**, 193 (2015).
[30] J. B. Goodenough, Electronic and ionic transport properties and other physical aspects of perovskites, *Rep. Prog. Phys.* **67**, 1915 (2004).
[31] M. Grätzel, The light and shade of perovskite solar cells, *Nat. Mater.* **13**, 838 (2014).
[32] H. S. Jung and N. G. Park, Perovskite solar cells: from materials to devices, *Small* **11**, 10 (2015).
[33] L. Meng, J. You, T. F. Guo, and Y. Yang, Recent Advances in the Inverted Planar Structure of Perovskite Solar Cells, *Acc. Chem. Res.* **49**, 155 (2016).
[34] M. A. Green, A. Ho-Baillie, and H. J. Snaith, The emergence of perovskite solar cells, *Nat. Photonics* **8**, 506 (2014).
[35] X. Y. Chin, D. Cortecchia, J. Yin, A. Bruno, and C. Soci, Lead iodide perovskite light-emitting field-effect transistor, *Nat. Commun.* (2015).
[36] Y. He and G. Galli, Perovskites for Solar Thermoelectric Applications: A First Principle Study of CH3NH3AI3(A = Pb and Sn), *Chem. Mater.* **26**, 53945400 (2014).
[37] Y.-J. Kim *et al.*, Piezoelectric properties of CH 3 NH 3 PbI 3 perovskite thin films and their applications in piezoelectric generators, *J. Mater. Chem. A* **4** (2015).
[38] G. Xing, N. Mathews, S. Lim, N. Yantara, X. Liu, D. Sabba, M. Grätzel, S. Mhaisalkar, and T. Sum, Low-temperature solution-processed wavelength-tunable perovskites for lasing, *Nat. Mater.* **13**, 476 (2014).
[39] Z.-K. Tan *et al.*, Bright light-emitting diodes based on organometal halide perovskite, *Nat. Nanotechnol.* **9**, 687 (2014).
[40] E. J. Yoo, M. Lyu, J. H. Yun, C. J. Kang, Y. J. Choi, and L. Wang, Resistive Switching Behavior in Organic-Inorganic Hybrid CH3 NH3 PbI3-x Clx Perovskite for Resistive Random Access Memory Devices, *Adv. Mater.* **27**, 6170 (2015).
[41] G. Niu, X. Guo, and L. Wang, Review of recent progress in chemical stability of perovskite solar cells, *J. Mater. Chem. A* **3**, 8970 (2015).

[42] E. L. Unger, E. T. Hoke, C. D. Bailie, W. H. Nguyen, A. R. Bowring, T. Heumuller, M. G. Christoforo, and M. D. McGehee, Hysteresis and transient behavior in current-voltage measurements of hybrid-perovskite absorber solar cells, *Energy Environ. Sci.* **7**, 3690 (2014).
[43] R. K. Misra, S. Aharon, B. Li, D. Mogilyansky, I. Visoly-Fisher, L. Etgar, and E. A. Katz, Temperature- and Component-Dependent Degradation of Perovskite Photovoltaic Materials under Concentrated Sunlight, *J. Phys. Chem. Lett.* **6**, 326 (2015).
[44] A. Dualeh, T. Moehl, N. Tétreault, J. Teuscher, P. Gao, M. K. Nazeeruddin, and M. Grätzel, Impedance Spectroscopic Analysis of Lead Iodide Perovskite-Sensitized Solid-State Solar Cells, *ACS Nano* **8**, 362 (2014).
[45] W. Tress, N. Marinova, T. Moehl, S. M. Zakeeruddin, M. K. Nazeeruddin, and M. Grätzel, Understanding the rate-dependent J-V hysteresis, slow time component, and aging in CH3NH3PbI3 perovskite solar cells: the role of a compensated electric field, *Energy Environ. Sci.* **8**, 995 (2015).
[46] C. Eames, J. M. Frost, P. R. Barnes, B. C. O'Regan, A. Walsh, and M. S. Islam, Ionic transport in hybrid lead iodide perovskite solar cells, *Nat. Commun.* **6**, 7497 (2015).
[47] T. Y. Yang, G. Gregori, N. Pellet, M. Gratzel, and J. Maier, The Significance of Ion Conduction in a Hybrid Organic-Inorganic Lead-Iodide-Based Perovskite Photosensitizer, *Angew. Chem. Int. Ed. Engl.* **54**, 7905 (2015).
[48] J. Haruyama, K. Sodeyama, L. Han, and Y. Tateyama, First-Principles Study of Ion Diffusion in Perovskite Solar Cell Sensitizers, *J. Am. Chem. Soc.* **137**, 10048 (2015).
[49] G. W. Crabtree and J. L. Sarrao, Opportunities for mesoscale science, *MRS Bull.* **37**, 1079 (2012).
[50] P. S. Weiss, Mesoscale Science: Lessons from and Opportunities for Nanoscience, *ACS Nano* **8**, 11025 (2014).
[51] A. J. Liu, G. S. Grest, M. C. Marchetti, G. M. Grason, M. O. Robbins, G. H. Fredrickson, M. Rubinstein, and M. O. de la Cruz, Opportunities in theoretical and computational polymeric materials and soft matter, *Soft Matter* **11**, 2326 (2015).
[52] A. Klug, The tobacco mosaic virus particle: structure and assembly, *Phil. Trans. R. Soc. B* **354**, 531 (1999).
[53] D. V. Talapin, LEGO materials, *ACS Nano* **2**, 1097 (2008).
[54] Z. H. Nie, A. Petukhova, and E. Kumacheva, Properties and emerging applications of self-assembled structures made from inorganic nanoparticles, *Nat. Nanotechnol.* **5**, 15 (2010).
[55] Z. L. Zhang, M. A. Horsch, M. H. Lamm, and S. C. Glotzer, Tethered nano building blocks: Toward a conceptual framework for nanoparticle self-assembly, *Nano Lett.* **3**, 1341 (2003).
[56] P. Akcora *et al.*, Anisotropic self-assembly of spherical polymer-grafted nanoparticles, *Nat. Mater.* **8**, 354 (2009).
[57] V. Pryamtisyn, V. Ganesan, A. Z. Panagiotopoulos, H. J. Liu, and S. K. Kumar, Modeling the anisotropic self-assembly of spherical polymer-grafted nanoparticles, *J. Chem. Phys.* **131**, 221102 (2009).
[58] H. Koerner, L. F. Drummy, B. Benicewicz, Y. Li, and R. A. Vaia, Nonisotropic Self-Organization of Single-Component Hairy Nanoparticle Assemblies, *ACS Macro Lett.* **2**, 670 (2013).
[59] Z. H. Nie, D. Fava, E. Kumacheva, S. Zou, G. C. Walker, and M. Rubinstein, Self-assembly of metal-polymer analogues of amphiphilic triblock copolymers, *Nat. Mater.* **6**, 609 (2007).

[60] X. B. Zeng, G. Ungar, Y. S. Liu, V. Percec, S. E. Dulcey, and J. K. Hobbs, Supramolecular dendritic liquid quasicrystals, *Nature* **428**, 157 (2004).
[61] M. Peterca *et al.*, Self-Assembly of Hybrid Dendrons into Doubly Segregated Supramolecular Polyhedral Columns and Vesicles, *J. Am. Chem. Soc.* **132**, 11288 (2010).
[62] C. Z. Li, Y. Matsuo, and E. Nakamura, Octupole-like Supramolecular Aggregates of Conical Iron Fullerene Complexes into a Three-Dimensional Liquid Crystalline Lattice, *J. Am. Chem. Soc.* **132**, 15514 (2010).
[63] M. J. Huang *et al.*, Selective assemblies of giant tetrahedra via precisely controlled positional interactions, *Science* **348**, 424 (2015).
[64] T. Kietzke, D. Neher, K. Landfester, R. Montenegro, R. Guntner, and U. Scherf, Novel approaches to polymer blends based on polymer nanoparticles, *Nat. Mater.* **2**, 408 (2003).
[65] S. Abbas and T. P. Lodge, Superlattice formation in a binary mixture of block copolymer micelles, *Phys. Rev. Lett.* **97**, 097803 (2006).
[66] S. Abbas and T. P. Lodge, Superlattice formation in binary mixtures of block copolymer micelles, *Langmuir* **24**, 6247 (2008).
[67] A. H. Gröschel, F. H. Schacher, H. Schmalz, O. V. Borisov, E. B. Zhulina, A. Walther, and A. H. Müller, Precise hierarchical self-assembly of multicompartment micelles, *Nat. Commun.* **3**, 710 (2012).
[68] Z. C. Sun, F. Bai, H. M. Wu, S. K. Schmitt, D. M. Boye, Z. Jiang, J. Wang, and H. Y. Fan, Cooperative Self-Assembly-Assisted Formation of Monodisperse Optically Active Spherical and Anisotropic Nanoparticles, *Chem. Eur. J.* **15**, 11128 (2009).
[69] S. Lee, M. J. Bluemle, and F. S. Bates, Discovery of a Frank-Kasper sigma Phase in Sphere-Forming Block Copolymer Melts, *Science* **330**, 349 (2010).
[70] W. Kung, P. Ziherl, and R. D. Kamien, Foam analogy in charged colloidal crystals, *Phys. Rev. E* **65**, 050401 (2002).
[71] P. Ziherl and R. D. Kamien, Soap froths and crystal structures, *Phys. Rev. Lett.* **85**, 3528 (2000).
[72] P. Ziherl and R. D. Kamien, Maximizing entropy by minimizing area: Towards a new principle of self-organization, *J. Phys. Chem. B* **105**, 10147 (2001).
[73] M. A. Glaser, G. M. Grason, R. D. Kamien, A. Kosmrlj, C. D. Santangelo, and P. Ziherl, Soft spheres make more mesophases, *EPL* **78**, 46004 (2007).
[74] H. M. Shin, G. M. Grason, and C. D. Santangelo, Mesophases of soft-sphere aggregates, *Soft Matter* **5**, 3629 (2009).
[75] C. Tschierske, Liquid crystal engineering - new complex mesophase structures and their relations to polymer morphologies, nanoscale patterning and crystal engineering, *Chem. Soc. Rev.* **36**, 1930 (2007).
[76] S. Mann, Self-assembly and transformation of hybrid nano-objects and nanostructures under equilibrium and non-equilibrium conditions, *Nat. Mater.* **8**, 781 (2009).
[77] G. Yu, J. Gao, J. C. Hummelen, F. Wudl, and A. J. Heeger, POLYMER PHOTOVOLTAIC CELLS - ENHANCED EFFICIENCIES VIA A NETWORK OF INTERNAL DONOR-ACCEPTOR HETEROJUNCTIONS, *Science* **270**, 1789 (1995).
[78] R. Gangopadhyay and A. De, Conducting polymer nanocomposites: A brief overview, *Chem. Mater.* **12**, 608 (2000).
[79] G. Li, V. Shrotriya, J. S. Huang, Y. Yao, T. Moriarty, K. Emery, and Y. Yang, High-efficiency solution processable polymer photovoltaic cells by self-organization of polymer blends, *Nat. Mater.* **4**, 864 (2005).

[80] A. C. Balazs, T. Emrick, and T. P. Russell, Nanoparticle polymer composites: Where two small worlds meet, *Science* **314**, 1107 (2006).
[81] F. Hussain, M. Hojjati, M. Okamoto, and R. E. Gorga, Review article: Polymer-matrix nanocomposites, processing, manufacturing, and application: An overview, *J. Compos. Mater.* **40**, 1511 (2006).
[82] D. R. Paul and L. M. Robeson, Polymer nanotechnology: Nanocomposites, *Polymer* **49**, 3187 (2008).
[83] B. C. Thompson and J. M. J. Frechet, Organic photovoltaics - Polymer-fullerene composite solar cells, *Angew. Chem. Int. Ed. Engl.* **47**, 58 (2008).
[84] T. Kuilla, S. Bhadra, D. H. Yao, N. H. Kim, S. Bose, and J. H. Lee, Recent advances in graphene based polymer composites, *Prog. Polym. Sci.* **35**, 1350 (2010).
[85] H. Qian, E. S. Greenhalgh, M. S. P. Shaffer, and A. Bismarck, Carbon nanotube-based hierarchical composites: a review, *J. Mater. Chem.* **20**, 4751 (2010).
[86] M. C. Orilall and U. Wiesner, Block copolymer based composition and morphology control in nanostructured hybrid materials for energy conversion and storage: solar cells, batteries, and fuel cells, *Chem. Soc. Rev.* **40**, 520 (2011).
[87] D. Feldman, Polyblend Nanocomposites, *J. Macromol. Sci., Pure Appl. Chem.* **52**, 648 (2015).
[88] P. Sengodu and A. D. Deshmukh, Conducting polymers and their inorganic composites for advanced Li-ion batteries: a review, *RSC Advances* **5**, 42109 (2015).
[89] A. D. Scaccabarozzi and N. Stingelin, Semiconducting:insulating polymer blends for optoelectronic applications—a review of recent advances, *J. Mater. Chem. A* **2**, 10818 (2014).
[90] Z. Starý, in *Characterization of Polymer Blends*, edited by S. Thomas, Y. Grohens, and P. Jyotishkumar (Wiley-VCH Verlag GmbH & Co. KGaA, Weinheim, Germany, 2015), pp. 93.
[91] R. Shenhar and V. M. Rotello, Nanoparticles: Scaffolds and building blocks, *Acc. Chem. Res.* **36**, 549 (2003).
[92] E. V. Shevchenko, D. V. Talapin, N. A. Kotov, S. O'Brien, and C. B. Murray, Structural diversity in binary nanoparticle superlattices, *Nature* **439**, 55 (2006).
[93] S. A. Claridge, A. W. Castleman, S. N. Khanna, C. B. Murray, A. Sen, and P. S. Weiss, Cluster-Assembled Materials, *ACS Nano* **3**, 244 (2009).
[94] M. Grzelczak, J. Vermant, E. M. Furst, and L. M. Liz-Marzan, Directed Self-Assembly of Nanoparticles, *ACS Nano* **4**, 3591 (2010).
[95] K. Thorkelsson, P. Bai, and T. Xu, Self-assembly and applications of anisotropic nanomaterials: A review, *Nano Today* **10**, 48 (2015).
[96] P. Bartlett, R. H. Ottewill, and P. N. Pusey, Superlattice formation in binary mixtures of hard-sphere colloids, *Phys. Rev. Lett.* **68**, 3801 (1992).
[97] P. Bartlett, R. H. Ottewill, and P. N. Pusey, Freezing of Binary-Mixtures of Colloidal Hard-Spheres, *J. Chem. Phys.* **93**, 1299 (1990).
[98] P. N. Pusey and W. Vanmegen, Phase-Behavior of Concentrated Suspensions of Nearly Hard Colloidal Spheres, *Nature* **320**, 340 (1986).
[99] P. N. Pusey, W. van Megen, P. Bartlett, B. J. Ackerson, J. G. Rarity, and S. M. Underwood, Structure of crystals of hard colloidal spheres, *Phys. Rev. Lett.* **63**, 2753 (1989).
[100] B. Pelaz *et al.*, The State of Nanoparticle-Based Nanoscience and Biotechnology: Progress, Promises, and Challenges, *ACS Nano* **6**, 8468 (2012).
[101] M. V. Kovalenko *et al.*, Prospects of Nanoscience with Nanocrystals, *ACS Nano* **9**, 1012 (2015).

[102] D. V. Talapin, J.-S. Lee, M. V. Kovalenko, and E. V. Shevchenko, Prospects of colloidal nanocrystals for electronic and optoelectronic applications, *Chem. Rev.* **110**, 389 (2009).
[103] A. Travesset, Binary nanoparticle superlattices of soft-particle systems, *Proc. Natl. Acad. Sci. U. S. A.* (2015).
[104] J. N. Israelachvili, *Intermolecular and Surface Forces* (Academic Press, 2011).
[105] D. Chen, F. Liu, C. Wang, A. Nakahara, and T. P. Russell, Bulk Heterojunction Photovoltaic Active Layers via Bilayer Interdiffusion, *Nano Lett.* **11**, 2071 (2011).
[106] B. A. Collins, J. R. Tumbleston, and H. Ade, Miscibility, Crystallinity, and Phase Development in P3HT/PCBM Solar Cells: Toward an Enlightened Understanding of Device Morphology and Stability, *J. Phys. Chem. Lett.* **2**, 3135 (2011).
[107] N. D. Treat, M. A. Brady, G. Smith, M. F. Toney, E. J. Kramer, C. J. Hawker, and M. L. Chabinyc, Interdiffusion of PCBM and P3HT Reveals Miscibility in a Photovoltaically Active Blend, *Adv. Energy Mater.* **1**, 82 (2011).
[108] H. P. Chen, R. Hegde, J. Browning, and M. D. Dadmun, The miscibility and depth profile of PCBM in P3HT: thermodynamic information to improve organic photovoltaics, *Phys. Chem. Chem. Phys.* **14**, 5635 (2012).
[109] F. Liu, Y. Gu, X. Shen, S. Ferdous, H.-W. Wang, and T. P. Russell, Characterization of the morphology of solution-processed bulk heterojunction organic photovoltaics, *Prog. Polym. Sci.* **38**, 1990 (2013).
[110] D. Venkataraman, S. Yurt, B. H. Venkatraman, and N. Gavvalapalli, Role of molecular architecture in organic photovoltaic cells, *J. Phys. Chem. Lett.* **1**, 947 (2010).
[111] X. Yang and J. Loos, Toward high-performance polymer solar cells: The importance of morphology control, *Macromolecules* **40**, 1353 (2007).
[112] R. Gaudiana, Organic photovoltaics: Challenges and opportunities, *J. Polym. Sci., Part B: Polym. Phys.* **50**, 1014 (2012).
[113] S. B. Darling and F. Q. You, The case for organic photovoltaics, *RSC Advances* **3**, 17633 (2013).
[114] R. A. Segalman, B. McCulloch, S. Kirmayer, and J. J. Urban, Block Copolymers for Organic Optoelectronics, *Macromolecules* **42**, 9205 (2009).
[115] Y. Nagaoka, O. Chen, Z. Wang, and Y. C. Cao, Structural Control of Nanocrystal Superlattices Using Organic Guest Molecules, *J. Am. Chem. Soc.* **134**, 2868 (2012).
[116] T. S. Gehan, M. Bag, L. A. Renna, X. Shen, D. D. Algaier, P. M. Lahti, T. P. Russell, and D. Venkataraman, Multiscale Active Layer Morphologies for Organic Photovoltaics Through Self-Assembly of Nanospheres, *Nano Lett.* **14**, 5238 (2014).
[117] L. A. Renna, T. S. Gehan, and D. Venkataraman, in *Optical Properties of Functional Polymers and Nano Engineering Applications*, edited by V. Jain, and A. Kokil (CRC Press, Boca Raton, FL USA, 2014), pp. 227.
[118] Y. Xia, B. Gates, Y. Yin, and Y. Lu, Monodispersed colloidal spheres: old materials with new applications, *Adv. Mater.* **12**, 693 (2000).
[119] J. P. Rao and K. E. Geckeler, Polymer nanoparticles: preparation techniques and size-control parameters, *Prog. Polym. Sci.* **36**, 887 (2011).
[120] D. Crespy and K. Landfester, Miniemulsion polymerization as a versatile tool for the synthesis of functionalized polymers, *Beilstein J. Org. Chem.* **6**, 1132 (2010).
[121] K. Landfester, N. Bechthold, F. Tiarks, and M. Antonietti, Miniemulsion polymerization with cationic and nonionic surfactants: A very efficient use of surfactants for heterophase polymerization, *Macromolecules* **32**, 2679 (1999).

[122] B. R. Saunders and B. Vincent, Microgel particles as model colloids: theory, properties and applications, *Adv. Colloid Interface Sci.* **80**, 1 (1999).
[123] E. B. Mock, H. De Bruyn, B. S. Hawkett, R. G. Gilbert, and C. F. Zukoski, Synthesis of anisotropic nanoparticles by seeded emulsion polymerization, *Langmuir* **22**, 4037 (2006).
[124] K. Landfester, The generation of nanoparticles in miniemulsions, *Adv. Mater.* **13**, 765 (2001).
[125] J. W. Kim and K. D. Suh, Monodisperse polymer particles synthesized by seeded polymerization techniques, *Ind. Eng. Chem. Res.* **14**, 1 (2008).
[126] A. J. C. Kuehne, M. C. Gather, and J. Sprakel, Monodisperse conjugated polymer particles by Suzuki-Miyaura dispersion polymerization, *Nat. Commun.* **3**, 1088 (2012).
[127] H. B. Li, X. F. Wu, B. W. Xu, H. Tong, and L. X. Wang, Solution-processible hyperbranched conjugated polymer nanoparticles with tunable particle sizes by Suzuki polymerization in miniemulsion, *RSC Advances* **3**, 8645 (2013).
[128] D. Muenmart, A. B. Foster, A. Harvey, M. T. Chen, O. Navarro, V. Promarak, M. C. McCairn, J. M. Behrendt, and M. L. Turner, Conjugated Polymer Nanoparticles by Suzuki-Miyaura Cross-Coupling Reactions in an Emulsion at Room Temperature, *Macromolecules* **47**, 6531 (2014).
[129] J. B. ten Hove, J. Appel, J. M. van den Broek, A. J. C. Kuehne, and J. Sprakel, Conjugated Polymer Shells on Colloidal Templates by Seeded Suzuki- Miyaura Dispersion Polymerization, *Small* **10**, 957 (2014).
[130] M. C. Baier, J. Huber, and S. Mecking, Fluorescent Conjugated Polymer Nanoparticles by Polymerization in Miniemulsion, *J. Am. Chem. Soc.* **131**, 14267 (2009).
[131] R. Haschick, M. Klapper, K. B. Wagener, and K. Mullen, Nanoparticles by ROMP in Nonaqueous Emulsions, *Macromol. Chem. Phys.* **211**, 2547 (2010).
[132] M. F. Cunningham, Controlled/living radical polymerization in aqueous dispersed systems, *Prog. Polym. Sci.* **33**, 365 (2008).
[133] P. B. Zetterlund, Y. Kagawa, and M. Okubo, Controlled/living radical polymerization in dispersed systems, *Chem. Rev.* **108**, 3747 (2008).
[134] S. R. S. Ting, E. H. Min, and P. B. Zetterlund, Reversible Addition-Fragmentation Chain Transfer (RAFT) Polymerization in Miniemulsion Based on In Situ Surfactant Generation, *Aust. J. Chem.* **64**, 1033 (2011).
[135] G. Nagarjuna, M. Baghgar, J. A. Labastide, D. D. Algaier, M. D. Barnes, and D. Venkataraman, Tuning Aggregation of Poly(3-hexylthiophene) within Nanoparticles, *ACS Nano* **6**, 10750 (2012).
[136] K. Landfester, Miniemulsions for nanoparticle synthesis, *Colloid Chem. II* **227**, 75 (2003).
[137] R. Potai and R. Traiphol, Controlling chain organization and photophysical properties of conjugated polymer nanoparticles prepared by reprecipitation method: The effect of initial solvent, *J. Colloid Interface Sci.* **403**, 58 (2013).
[138] N. Kurokawa, H. Yoshikawa, N. Hirota, K. Hyodo, and H. Masuhara, Size-dependent spectroscopic properties and thermochromic behavior in poly(substituted thiophene) nanoparticles, *ChemPhysChem* **5**, 1609 (2004).
[139] K. Landfester, Miniemulsion polymerization and the structure of polymer and hybrid nanoparticles, *Angew. Chem. Int. Ed. Engl.* **48**, 4488 (2009).
[140] D. Tuncel and H. V. Demir, Conjugated polymer nanoparticles, *Nanoscale* **2**, 484 (2010).

[141] B. S. Ong, Y. Wu, P. Liu, and S. Gardner, Structurally ordered polythiophene nanoparticles for high-performance organic thin-film transistors, *Adv. Mater.* **17**, 1141 (2005).
[142] F. Wang, M.-Y. Han, K. Y. Mya, Y. Wang, and Y.-H. Lai, Aggregation-driven growth of size-tunable organic nanoparticles using electronically altered conjugated polymers, *J. Am. Chem. Soc.* **127**, 10350 (2005).
[143] L. Seok Ho, L. Yong Baek, P. Dong Hyuk, K. Mi Suk, C. Eun Hei, and J. Jinsoo, Tuning optical properties of poly(3-hexylthiophene) nanoparticles through hydrothermal processing, *Sci. Tech. Adv. Mater.* **12**, 025002 (2011).
[144] J. Pecher and S. Mecking, Nanoparticles of Conjugated Polymers, *Chem. Rev.* **110**, 6260 (2010).
[145] K. L. Wooley, Shell crosslinked polymer assemblies: nanoscale constructs inspired from biological systems, *J. Polym. Sci., Part A: Polym. Chem.* **38**, 1397 (2000).
[146] B. A. G. Hammer, M. A. Reyes-Martinez, F. A. Bokel, F. Liu, T. P. Russell, R. C. Hayward, A. L. Briseno, and T. Emrick, Reversible, Self Cross-Linking Nanowires from Thiol-Functionalized Polythiophene Diblock Copolymers, *ACS Appl. Mater. Interfaces* **6**, 7705 (2014).
[147] R. K. O'Reilly, C. J. Hawker, and K. L. Wooley, Cross-linked block copolymer micelles: functional nanostructures of great potential and versatility, *Chem. Soc. Rev.* **35**, 1068 (2006).
[148] A. Walther and A. H. E. Müller, Janus Particles: Synthesis, Self-Assembly, Physical Properties, and Applications, *Chem. Rev.* **113**, 5194 (2013).
[149] F. X. Liang, C. L. Zhang, and Z. Z. Yang, Rational Design and Synthesis of Janus Composites, *Adv. Mater.* **26**, 6944 (2014).
[150] R. H. Deng, S. Q. Liu, F. X. Liang, K. Wang, J. T. Zhu, and Z. Z. Yang, Polymeric Janus Particles with Hierarchical Structures, *Macromolecules* **47**, 3701 (2014).
[151] T. Higuchi, A. Tajima, K. Motoyoshi, H. Yabu, and M. Shimomura, Frustrated phases of block copolymers in nanoparticles, *Angew. Chem. Int. Ed. Engl.* **47**, 8044 (2008).
[152] T. Higuchi, A. Tajima, H. Yabu, and M. Shimomura, Spontaneous formation of polymer nanoparticles with inner micro-phase separation structures, *Soft Matter* **4**, 1302 (2008).
[153] J. P. Xu, K. Wang, J. Y. Li, H. M. Zhou, X. L. Xie, and J. T. Zhu, ABC Triblock Copolymer Particles with Tunable Shape and Internal Structure through 3D Confined Assembly, *Macromolecules* **48**, 2628 (2015).
[154] H. Yabu, T. Higuchi, and H. Jinnai, Frustrated phases: polymeric self-assemblies in a 3D confinement, *Soft Matter* **10**, 2919 (2014).
[155] A. O. Moughton, M. A. Hillmyer, and T. P. Lodge, Multicompartment Block Polymer Micelles, *Macromolecules* **45**, 2 (2012).
[156] R. Vyhnalkova, A. H. E. Müller, and A. Eisenberg, Control of morphology and corona composition in aggregates of mixtures of PS-b-PAA and PS-b-P4VP diblock copolymers: effects of solvent, water content, and mixture composition, *Langmuir* **30**, 13152 (2014).
[157] R. Novoa-Carballal, A. Pfaff, and A. H. E. Müller, Interpolyelectrolyte complexes with a polysaccharide corona from dextran-block-PDMAEMA diblock copolymers, *Polym. Chem.* **4**, 2278 (2013).
[158] I. Cho and K. W. Lee, Morphology of latex particles formed by poly (methyl methacrylate)-seeded emulsion polymerization of styrene, *J. Appl. Polym. Sci.* **30**, 1903 (1985).
[159] T. Kietzke, D. Neher, M. Kumke, O. Ghazy, U. Ziener, and K. Landfester, Phase separation of binary blends in polymer nanoparticles, *Small* **3**, 1041 (2007).

[160] Y. C. Chen, V. L. Dimonie, O. L. Shaffer, and M. S. El-Aasser, Development of morphology in latex particles: the interplay between thermodynamic and kinetic parameters, *Polym. Int.* **30**, 185 (1993).
[161] B. Yu, B. Li, Q. Jin, D. Ding, and A.-C. Shi, Self-assembly of symmetric diblock copolymers confined in spherical nanopores, *Macromolecules* **40**, 9133 (2007).
[162] H. Yabu, K. Motoyoshi, T. Higuchi, and M. Shimomura, Hierarchical structures in AB/AC type diblock-copolymer blend particles, *Phys. Chem. Chem. Phys.* **12**, 11944 (2010).
[163] A. H. Gröschel, A. Walther, T. I. Löbling, F. H. Schacher, H. Schmalz, and A. H. E. Müller, Guided hierarchical co-assembly of soft patchy nanoparticles, *Nature* **503**, 247 (2013).
[164] H.-X. Lin, Z.-C. Lei, Z.-Y. Jiang, C.-P. Hou, D.-Y. Liu, M.-M. Xu, Z.-Q. Tian, and Z.-X. Xie, Supersaturation-dependent surface structure evolution: from ionic, molecular to metallic micro/nanocrystals, *J. Am. Chem. Soc.* **135**, 9311 (2013).
[165] M. L. Personick and C. A. Mirkin, Making sense of the mayhem behind shape control in the synthesis of gold nanoparticles, *J. Am. Chem. Soc.* **135**, 18238 (2013).
[166] A. R. Tao, S. Habas, and P. D. Yang, Shape control of colloidal metal nanocrystals, *Small* **4**, 310 (2008).
[167] G. Odian, *Principles of Polymerization* (John Wiley & Sons, Hoboken, NJ USA, 2004), 4th edn., p.^pp. 24.
[168] N. Doshi and S. Mitragotri, Macrophages recognize size and shape of their targets, *PLoS One* **5**, e10051 (2010).
[169] J. A. Champion, Y. K. Katare, and S. Mitragotri, Making polymeric micro- and nanoparticles of complex shapes, *Proc. Natl. Acad. Sci. U. S. A.* **104**, 11901 (2007).
[170] S. E. A. Gratton, P. D. Pohlhaus, J. Lee, J. Guo, M. J. Cho, and J. M. DeSimone, Nanofabricated particles for engineered drug therapies: A preliminary biodistribution study of PRINT™ nanoparticles, *J. Controlled Release* **121**, 10 (2007).
[171] Y. Wang, T. J. Merkel, K. Chen, C. A. Fromen, D. E. Betts, and J. M. DeSimone, Generation of a library of particles having controlled sizes and shapes via the mechanical elongation of master templates, *Langmuir* **27**, 524 (2010).
[172] C. S. Pluisch and A. Wittemann, Shape-Tailored Polymer Colloids on the Road to Become Structural Motifs for Hierarchically Organized Materials, *Macromol. Rapid Commun.* **34**, 1798 (2013).
[173] V. N. Manoharan, M. T. Elsesser, and D. J. Pine, Dense Packing and Symmetry in Small Clusters of Microspheres, *Science* **301**, 483 (2003).
[174] N. Arkus, V. N. Manoharan, and M. P. Brenner, Minimal energy clusters of hard spheres with short range attractions, *Phys. Rev. Lett.* **103**, 118303 (2009).
[175] N. Arkus, V. N. Manoharan, and M. P. Brenner, Deriving Finite Sphere Packings, *SIAM J. Discrete Math* **25**, 1860 (2011).
[176] G. Meng, N. Arkus, M. P. Brenner, and V. N. Manoharan, The free-energy landscape of clusters of attractive hard spheres, *Science* **327**, 560 (2010).
[177] Z. Zeravcic and M. P. Brenner, Self-replicating colloidal clusters, *Proc. Natl. Acad. Sci. U. S. A.* **111**, 1748 (2014).
[178] J. T. McGinley, I. Jenkins, T. Sinno, and J. C. Crocker, Assembling colloidal clusters using crystalline templates and reprogrammable DNA interactions, *Soft Matter* **9**, 9119 (2013).
[179] L. Hong, A. Cacciuto, E. Luijten, and S. Granick, Clusters of charged Janus spheres, *Nano Lett.* **6**, 2510 (2006).
[180] D. Frenkel, Order through disorder: entropy strikes back, *Physics world* **6**, 24 (1993).

[181] S. Hachisu and S. Yoshimura, Optical demonstration of crystalline superstructures in binary mixtures of latex globules, *Nature* **283**, 188 (1980).
[182] L. Pauling, The principles determining the structure of complex ionic crystals, *J. Am. Chem. Soc.* **51**, 1010 (1929).
[183] F. C. Frank and J. S. Kasper, Complex alloy structures regarded as sphere packings. I. Definitions and basic principles, *Acta Cryst.* **11**, 184 (1958).
[184] F. C. Frank and J. S. Kasper, Complex alloy structures regarded as sphere packings. II. Analysis and classification of representative structures, *Acta Cryst.* **12**, 483 (1959).
[185] J. V. Sanders and M. J. Murray, Ordered arrangements of spheres of two different sizes in opal, *Nature* **275**, 201 (1978).
[186] C. B. Murray, C. R. Kagan, and M. G. Bawendi, Synthesis and characterization of monodisperse nanocrystals and close-packed nanocrystal assemblies, *Annu. Rev. Mater. Sci.* **30**, 545 (2000).
[187] B. L. V. Prasad, C. M. Sorensen, and K. J. Klabunde, Gold nanoparticle superlattices, *Chem. Soc. Rev.* **37**, 1871 (2008).
[188] S. Torquato, *Random Heterogeneous Materials: Microstructure and Macroscopic Properties* (Springer Science & Business Media, Harrisonburg, VA USA, 2002), Interdisciplinary Applied Mathematics, 16 p.^pp. 76-77.
[189] Y. Jin and H. A. Makse, A first-order phase transition defines the random close packing of hard spheres, *Physica A* **389**, 5362 (2010).
[190] V. Trappe, V. Prasad, L. Cipelletti, P. N. Segre, and D. A. Weitz, Jamming phase diagram for attractive particles, *Nature* **411**, 772 (2001).
[191] H. Z. Cummins, Liquid, glass, gel: The phases of colloidal Laponite, *J. Non-Cryst. Solids* **353**, 3891 (2007).
[192] F. Sciortino, Disordered materials: One liquid, two glasses, *Nat. Mater.* **1**, 145 (2002).
[193] E. Zaccarelli, Colloidal gels: Equilibrium and non-equilibrium routes, *J. Phys.: Condens. Matter* **19**, 323101 (2007).
[194] H. Tanaka, Viscoelastic phase separation in soft matter and foods, *Faraday Discuss.* **158**, 371 (2012).
[195] D. Velegol, Assembling colloidal devices by controlling interparticle forces, *J. Nanophoton.* **1**, 012502 (2007).
[196] B. Siffert, A. Jada, and J. Eleli-Letsango, Stability Calculations of TiO2 Nonaqueous Suspensions: Thickness of the Electrical Double Layer, *J. Colloid Interface Sci.* **167**, 281 (1994).
[197] J. N. Munday, F. Capasso, and V. A. Parsegian, Measured long-range repulsive Casimir-Lifshitz forces, *Nature* **457**, 170 (2009).
[198] J. A. Labastide, M. Baghgar, I. Dujovne, Y. Yang, A. D. Dinsmore, B. G. Sumpter, D. Venkataraman, and M. D. Barnes, Polymer Nanoparticle Super lattices for Organic Photovoltaic Applications, *J. Phys. Chem. Lett.* **2**, 3085 (2011).
[199] G. Nagarjuna and D. Venkataraman, Strategies for controlling the active layer morphologies in OPVs, *J. Polym. Sci., Part B: Polym. Phys.* **50**, 1045 (2012).
[200] M. I. Bodnarchuk, M. V. Kovalenko, W. Heiss, and D. V. Talapin, Energetic and Entropic Contributions to Self-Assembly of Binary Nanocrystal Superlattices: Temperature as the Structure-Directing Factor, *J. Am. Chem. Soc.* **132**, 11967 (2010).
[201] M. I. Bodnarchuk, E. V. Sheychenko, and D. V. Talapin, Structural Defects in Periodic and Quasicrystalline Binary Nanocrystal Superlattices, *J. Am. Chem. Soc.* **133**, 20837 (2011).

[202] J. Chen, X. Ye, and C. B. Murray, Systematic Electron Crystallographic Studies of Self-Assembled Binary Nanocrystal Superlattices, *ACS Nano* **4**, 2374 (2010).
[203] Z. Chen, J. Moore, G. Radtke, H. Sirringhaus, and S. O'Brien, Binary nanoparticle superlattices in the semiconductor-semiconductor system: CdTe and CdSe, *J. Am. Chem. Soc.* **129**, 15702 (2007).
[204] M. V. Kovalenko, M. I. Bodnarchuk, and D. V. Talapin, Nanocrystal Superlattices with Thermally Degradable Hybrid Inorganic-Organic Capping Ligands, *J. Am. Chem. Soc.* **132**, 15124 (2010).
[205] S. Pichler, M. I. Bodnarchuk, M. V. Kovalenko, M. Yarema, G. Springholz, D. V. Talapin, and W. Heiss, Evaluation of Ordering in Single-Component and Binary Nanocrystal Superlattices by Analysis of Their Autocorrelation Functions, *ACS Nano* **5**, 1703 (2011).
[206] F. X. Redl, K. S. Cho, C. B. Murray, and S. O'Brien, Three-dimensional binary superlattices of magnetic nanocrystals and semiconductor quantum dots, *Nature* **423**, 968 (2003).
[207] E. V. Shevchenko, J. B. Kortright, D. V. Talapin, S. Aloni, and A. P. Alivisatos, Quasi-ternary nanoparticle superlattices through nanoparticle design, *Adv. Mater.* **19**, 4183 (2007).
[208] E. V. Shevchenko, M. Ringler, A. Schwemer, D. V. Talapin, T. A. Klar, A. L. Rogach, J. Feldmann, and A. P. Alivisatos, Self-assembled binary superlattices of CdSe and Au nanocrystals and their fluorescence properties, *J. Am. Chem. Soc.* **130**, 3274 (2008).
[209] E. V. Shevchenko, D. V. Talapin, C. B. Murray, and S. O'Brien, Structural characterization of self-assembled multifunctional binary nanoparticle superlattices, *J. Am. Chem. Soc.* **128**, 3620 (2006).
[210] D. V. Talapin, E. V. Shevchenko, M. I. Bodnarchuk, X. Ye, J. Chen, and C. B. Murray, Quasicrystalline order in self-assembled binary nanoparticle superlattices, *Nature* **461**, 964 (2009).
[211] J. J. Urban, D. V. Talapin, E. V. Shevchenko, C. R. Kagan, and C. B. Murray, Synergismin binary nanocrystal superlattices leads to enhanced p-type conductivity in self-assembled PbTe/Ag-2 Te thin films, *Nat. Mater.* **6**, 115 (2007).
[212] X. C. Ye, J. Chen, and C. B. Murray, Polymorphism in Self-Assembled AB(6) Binary Nanocrystal Superlattices, *J. Am. Chem. Soc.* **133**, 2613 (2011).
[213] W. H. Evers, B. De Nijs, L. Filion, S. Castillo, M. Dijkstra, and D. Vanmaekelbergh, Entropy-Driven Formation of Binary Semiconductor-Nanocrystal Superlattices, *Nano Lett.* **10**, 4235 (2010).
[214] H. L. Cong and W. X. Cao, Array patterns of binary colloidal crystals, *J. Phys. Chem. B* **109**, 1695 (2005).
[215] Z. C. Zhou, Q. F. Yan, Q. Li, and X. S. Zhao, Fabrication of binary colloidal crystals and non-close-packed structures by a sequential self-assembly method, *Langmuir* **23**, 1473 (2007).
[216] L. Wang, Y. Wan, Y. Li, Z. Cai, H. L. Li, X. S. Zhao, and Q. Li, Binary colloidal crystals fabricated with a horizontal deposition method, *Langmuir* **25**, 6753 (2009).
[217] Z. Dai, Y. Li, G. Duan, L. Jia, and W. Cai, Phase diagram, design of monolayer binary colloidal crystals, and their fabrication based on ethanol-assisted self-assembly at the air/water interface, *ACS Nano* **6**, 6706 (2012).
[218] T. Okubo, POLYMER COLLOIDAL CRYSTALS, *Prog. Polym. Sci.* **18**, 481 (1993).
[219] J. H. Zhang, Z. Q. Sun, and B. Yang, Self-assembly of photonic crystals from polymer colloids, *Curr. Opin. Colloid Interface Sci.* **14**, 103 (2009).
[220] N. Hunt, R. Jardine, and P. Bartlett, Superlattice formation in mixtures of hard-sphere colloids, *Phys. Rev. E* **62**, 900 (2000).

[221] P. Bartlett and A. I. Campbell, Three-dimensional binary superlattices of oppositely charged colloids, *Phys. Rev. Lett.* **95**, 128302 (2005).
[222] S. Nayak and L. A. Lyon, Soft nanotechnology with soft nanoparticles, *Angew. Chem. Int. Ed. Engl.* **44**, 7686 (2005).
[223] J. D. Debord and L. A. Lyon, Thermoresponsive photonic crystals, *J. Phys. Chem. B* **104**, 6327 (2000).
[224] D. Gottwald, C. N. Likos, G. Kahl, and H. Löwen, Phase behavior of ionic microgels, *Phys. Rev. Lett.* **92**, 068301 (2004).
[225] T. Hellweg, C. D. Dewhurst, E. Brückner, K. Kratz, and W. Eimer, Colloidal crystals made of poly (N-isopropylacrylamide) microgel particles, *Colloid Polym. Sci.* **278**, 972 (2000).
[226] Z. Hu, X. Lu, and J. Gao, Hydrogel opals, *Adv. Mater.* **13**, 1708 (2001).
[227] L. A. Lyon, J. D. Debord, S. B. Debord, C. D. Jones, J. G. McGrath, and M. J. Serpe, Microgel colloidal crystals, *J. Phys. Chem. B* **108**, 19099 (2004).
[228] H. Senff and W. Richtering, Temperature sensitive microgel suspensions: Colloidal phase behavior and rheology of soft spheres, *J. Chem. Phys.* **111**, 1705 (1999).
[229] J. M. Weissman, H. B. Sunkara, S. T. Albert, and S. A. Asher, Thermally switchable periodicities and diffraction from mesoscopically ordered materials, *Science* **274**, 959 (1996).
[230] S. Xu, J. Zhang, C. Paquet, Y. Lin, and E. Kumacheva, From hybrid microgels to photonic crystals, *Adv. Funct. Mater.* **13**, 468 (2003).
[231] F. M. Bayer, K. Hiltrop, and K. Huber, Hydrogen-Bond-Induced Heteroassembly in Binary Colloidal Systems, *Langmuir* **26**, 13815 (2010).
[232] C. A. Mirkin, R. L. Letsinger, R. C. Mucic, and J. J. Storhoff, A DNA-based method for rationally assembling nanoparticles into macroscopic materials, *Nature* **382**, 607 (1996).
[233] M. T. Casey, R. T. Scarlett, W. B. Rogers, I. Jenkins, T. Sinno, and J. C. Crocker, Driving diffusionless transformations in colloidal crystals using DNA handshaking, *Nat. Commun.* **3**, 1209 (2012).
[234] M. E. Leunissen, C. G. Christova, A.-P. Hynninen, C. P. Royall, A. I. Campbell, A. Imhof, M. Dijkstra, R. Van Roij, and A. Van Blaaderen, Ionic colloidal crystals of oppositely charged particles, *Nature* **437**, 235 (2005).
[235] C. I. Mendoza and E. Batta, Self-assembly of binary nanoparticle dispersions: From square arrays and stripe phases to colloidal corrals, *EPL* **85**, 56004 (2009).
[236] N. J. Fernandes, H. Koerner, E. P. Giannelis, and R. A. Vaia, Hairy nanoparticle assemblies as one-component functional polymer nanocomposites: Opportunities and challenges, *MRS Commun.* **3**, 13 (2013).
[237] R. Erhardt, M. Zhang, A. Böker, H. Zettl, C. Abetz, P. Frederik, G. Krausch, V. Abetz, and A. H. E. Müller, Amphiphilic Janus micelles with polystyrene and poly (methacrylic acid) hemispheres, *J. Am. Chem. Soc.* **125**, 3260 (2003).
[238] A. Snezhko and I. S. Aranson, Magnetic manipulation of self-assembled colloidal asters, *Nat. Mater.* **10**, 698 (2011).
[239] Y. Zhao *et al.*, Small-molecule-directed nanoparticle assembly towards stimuli-responsive nanocomposites, *Nat. Mater.* **8**, 979 (2009).
[240] D. He and N. N. Ekere, Effect of particle size ratio on the conducting percolation threshold of granular conductive-insulating composites, *J. Phys. D: Appl. Phys.* **37**, 1848, Pii s0022-3727(04)76454-2 (2004).
[241] R. Kurita and E. R. Weeks, Experimental study of random-close-packed colloidal particles, *Phys. Rev. E* **82**, 011403 (2010).

[242] M. Clusel, E. I. Corwin, A. O. N. Siemens, and J. Brujic, A granocentric model for random packing of jammed emulsions, *Nature* **460**, 611 (2009).
[243] P. M. Jenneson, R. D. Luggar, E. J. Morton, O. Gundogdu, and U. Tüzün, Examining nanoparticle assemblies using high spatial resolution x-ray microtomography, *J. Appl. Phys.* **96**, 2889 (2004).
[244] T. R. Andersen *et al.*, Aqueous processing of low-band-gap polymer solar cells using roll-to-roll methods, *ACS Nano* **5**, 4188 (2011).
[245] S. C. Glotzer and M. J. Solomon, Anisotropy of building blocks and their assembly into complex structures, *Nat. Mater.* **6**, 557 (2007).
[246] P. R. Sajanlal, T. S. Sreeprasad, A. K. Samal, and T. Pradeep, Anisotropic nanomaterials: structure, growth, assembly, and functions, *Nano Rev.* **2**, 5883_1 (2011).
[247] U. Agarwal and F. A. Escobedo, Mesophase behaviour of polyhedral particles, *Nat. Mater.* **10**, 230 (2011).
[248] P. F. Damasceno, M. Engel, and S. C. Glotzer, Predictive Self-Assembly of Polyhedra into Complex Structures, *Science* **337**, 453 (2012).
[249] D. Frenkel, Entropy-driven phase transitions, *Physica A* **263**, 26 (1999).
[250] O. D. Velev and S. Gupta, Materials Fabricated by Micro-and Nanoparticle Assembly–The Challenging Path from Science to Engineering, *Adv. Mater.* **21**, 1897 (2009).
[251] M. Bag, T. S. Gehan, L. A. Renna, D. D. Algaier, P. M. Lahti, and D. Venkataraman, Fabrication conditions for efficient organic photovoltaic cells from aqueous dispersions of nanoparticles, *RSC Advances* **4**, 45325 (2014).
[252] X. Zhou, W. Belcher, and P. Dastoor, Solar Paint: From Synthesis to Printing, *Polymers* **6**, 2832 (2014).
[253] H. F. Dam *et al.*, The effect of mesomorphology upon the performance of nanoparticulate organic photovoltaic devices, *Sol. Energy Mater. Sol. Cells* **138**, 102 (2015).
[254] S. Gärtner *et al.*, Eco-Friendly Fabrication of 4% Efficient Organic Solar Cells from Surfactant-Free P3HT: ICBA Nanoparticle Dispersions, *Adv. Mater.* **26**, 6653 (2014).
[255] M. Bag, T. S. Gehan, D. D. Algaier, F. Liu, G. Nagarjuna, P. M. Lahti, T. P. Russell, and D. Venkataraman, Efficient charge transport in assemblies of surfactant-stabilized semiconducting nanoparticles, *Adv Mater* **25**, 6411 (2013).
[256] X. Han, M. Bag, T. S. Gehan, D. Venkataraman, and D. Maroudas, Analysis of hole transport in thin films and nanoparticle assemblies of poly (3-hexylthiophene), *Chem. Phys. Lett.* **610**, 273 (2014).
[257] J. Y. Kim and N. A. Kotov, Charge Transport Dilemma of Solution-Processed Nanomaterials, *Chem. Mater.* **26**, 134 (2014).
[258] L. A. Renna, C. J. Boyle, T. S. Gehan, and D. Venkataraman, Polymer Nanoparticle Assemblies: A Versatile Route to Functional Mesostructures, *Macromolecules* **48**, 6353 (2015).
[259] G. Lu, L. Bu, S. Li, and X. Yang, Bulk Interpenetration Network of Thermoelectric Polymer in Insulating Supporting Matrix, *Adv. Mater.* **26**, 2359 (2014).
[260] G. H. Kim, D. Lee, A. Shanker, L. Shao, M. S. Kwon, D. Gidley, J. Kim, and K. P. Pipe, High thermal conductivity in amorphous polymer blends by engineered interchain interactions, *Nat. Mater.* **14**, 295 (2015).
[261] X.-G. Liang, J. R. Lukes, and C.-L. Tien, Anisotropic thermal conductance in thin layers of disordered packed spheres, *Heat transfer* **7**, 33 (1998).

[262] I. Villaluenga, X. C. Chen, D. Devaux, D. T. Hallinan, and N. P. Balsara, Nanoparticle-Driven Assembly of Highly Conducting Hybrid Block Copolymer Electrolytes, *Macromolecules* **48**, 358 (2015).
[263] J. Gao, Y. Yang, D. Lee, S. Holdcroft, and B. J. Frisken, Self-Assembly of Latex Particles into Proton-Conductive Membranes, *Macromolecules* **39**, 8060 (2006).
[264] A. E. Javier, S. N. Patel, D. T. Hallinan, V. Srinivasan, and N. P. Balsara, Simultaneous Electronic and Ionic Conduction in a Block Copolymer: Application in Lithium Battery Electrodes, *Angew. Chem. Int. Ed. Engl.* **50**, 9848 (2011).
[265] L. Xu, W. Ma, L. Wang, C. Xu, H. Kuang, and N. A. Kotov, Nanoparticle assemblies: dimensional transformation of nanomaterials and scalability, *Chem. Soc. Rev.* **42**, 3114 (2013).
[266] J. Zhang, Y. Li, X. Zhang, and B. Yang, Colloidal Self-Assembly Meets Nanofabrication: From Two-Dimensional Colloidal Crystals to Nanostructure Arrays, *Adv. Mater.* **22**, 4249 (2010).
[267] V. F. Puntes, K. M. Krishnan, and A. P. Alivisatos, Colloidal nanocrystal shape and size control: The case of cobalt, *Science* **291**, 2115 (2001).
[268] S. H. Sun, C. B. Murray, D. Weller, L. Folks, and A. Moser, Monodisperse FePt nanoparticles and ferromagnetic FePt nanocrystal superlattices, *Science* **287**, 1989 (2000).
[269] H. Zeng, J. Li, J. P. Liu, Z. L. Wang, and S. H. Sun, Exchange-coupled nanocomposite magnets by nanoparticle self-assembly, *Nature* **420**, 395 (2002).
[270] M. Zanella, G. Bertoni, I. R. Franchini, R. Brescia, D. Baranov, and L. Manna, Assembly of shape-controlled nanocrystals by depletion attraction, *Chem. Commun.* **47**, 203 (2011).
[271] D. A. Walker, K. P. Browne, B. Kowalczyk, and B. A. Grzybowski, Self-Assembly of Nanotriangle Super lattices Facilitated by Repulsive Electrostatic Interactions, *Angew. Chem. Int. Ed. Engl.* **49**, 6760 (2010).
[272] P. Jiang, J. F. Bertone, K. S. Hwang, and V. L. Colvin, Single-crystal colloidal multilayers of controlled thickness, *Chem. Mater.* **11**, 2132 (1999).
[273] P. J. Yunker, T. Still, M. A. Lohr, and A. G. Yodh, Suppression of the coffee-ring effect by shape-dependent capillary interactions, *Nature* **476**, 308 (2011).
[274] K. Bian, J. J. Choi, A. Kaushik, P. Clancy, D.-M. Smilgies, and T. Hanrath, Shape-Anisotropy Driven Symmetry Transformations in Nanocrystal Superlattice Polymorphs, *ACS Nano* **5**, 2815 (2011).
[275] T. Hanrath, J. J. Choi, and D.-M. Smilgies, Structure/Processing Relationships of Highly Ordered Lead Salt Nanocrystal Superlattices, *ACS Nano* **3**, 2975 (2009).
[276] G. Singh, S. Pillai, A. Arpanaei, and P. Kingshott, Electrostatic and capillary force directed tunable 3D binary micro- and nanoparticle assemblies on surfaces, *Nanotechnol.* **22**, 225601 (2011).
[277] Y. Xie *et al.*, Controllable Two-Stage Droplet Evaporation Method and Its Nanoparticle Self-Assembly Mechanism, *Langmuir* **29**, 6232 (2013).
[278] Z. Quan and J. Fang, Superlattices with non-spherical building blocks, *Nano Today* **5**, 390 (2010).
[279] B. W. Goodfellow, R. N. Patel, M. G. Panthani, D.-M. Smilgies, and B. A. Korgel, Melting and Sintering of a Body-Centered Cubic Superlattice of PbSe Nanocrystals Followed by Small Angle X-ray Scattering, *J. Phys. Chem. C* **115**, 6397 (2011).
[280] X. T. Peng and A. D. Dinsmore, Light propagation in strongly scattering, random colloidal films: The role of the packing geometry, *Phys. Rev. Lett.* **99**, 143902, 143902 (2007).

[281] T. L. Kelly, Y. Yamada, S. P. Y. Che, K. Yano, and M. O. Wolf, Monodisperse poly(3,4-ethylenedioxythiophene)-silica microspheres: Synthesis and assembly into crystalline colloidal arrays, *Adv. Mater.* **20**, 2616 (2008).
[282] L. Cerdán, A. Costela, E. Enciso, and I. García-Moreno, Random Lasing in Self-Assembled Dye-Doped Latex Nanoparticles: Packing Density Effects, *Adv. Funct. Mater.* **23**, 3916 (2013).
[283] C. Zheng, X. Xu, F. He, L. Li, B. Wu, G. Yu, and Y. Liu, Preparation of High-Quality Organic Semiconductor Nanoparticle Films by Solvent-Evaporation-Induced Self-Assembly, *Langmuir* **26**, 16730 (2010).
[284] D. V. Talapin, E. V. Shevchenko, C. B. Murray, A. V. Titov, and P. Král, Dipole−Dipole Interactions in Nanoparticle Superlattices, *Nano Lett.* **7**, 1213 (2007).
[285] M. P. Boneschanscher, W. H. Evers, W. Qi, J. D. Meeldijk, M. Dijkstra, and D. Vanmaekelbergh, Electron Tomography Resolves a Novel Crystal Structure in a Binary Nanocrystal Superlattice, *Nano Lett.* **13**, 1312 (2013).
[286] J. H. Fendler and I. Dekany, in *NATO Advanced Research Workshop on Nanoparticles in Solids and Solutions - An Integrated Approach to their Preparation and Characterization* (Springer Publishing Company, Szeged, Hungary, 1996), p. 580.
[287] C. B. Murray, Synthesis and characterization of II-VI quantum dots and their assembly into 3D quantum dot superlattices., *Abstr. Pap. Am. Chem. Soc.* **213**, 246 (1997).
[288] C. B. Murray, C. R. Kagan, and M. G. Bawendi, Self-Organization of CdSe Nanocrystallites into Three-Dimensional Quantum Dot Superlattices, *Science* **270**, 1335 (1995).
[289] P. Podsiadlo, G. Krylova, B. Lee, K. Critchley, D. J. Gosztola, D. V. Talapin, P. D. Ashby, and E. V. Shevchenko, The Role of Order, Nanocrystal Size, and Capping Ligands in the Collective Mechanical Response of Three-Dimensional Nanocrystal Solids, *J. Am. Chem. Soc.* **132**, 8953 (2010).
[290] A. S. Dimitrov and K. Nagayama, Continuous convective assembling of fine particles into two-dimensional arrays on solid surfaces, *Langmuir* **12**, 1303 (1996).
[291] Z. Cai, J. Teng, Y. Wan, and X. S. Zhao, An improved convective self-assembly method for the fabrication of binary colloidal crystals and inverse structures, *J. Colloid Interface Sci.* **380**, 42 (2012).
[292] B. G. Prevo and O. D. Velev, Controlled, rapid deposition of structured coatings from micro- and nanoparticle suspensions, *Langmuir* **20**, 2099 (2004).
[293] M. H. Kim, S. H. Im, and O. O. Park, Fabrication and structural analysis of binary colloidal crystals with two-dimensional superlattices, *Adv. Mater.* **17**, 2501 (2005).
[294] T. P. Bigioni, X. M. Lin, T. T. Nguyen, E. I. Corwin, T. A. Witten, and H. M. Jaeger, Kinetically driven self assembly of highly ordered nanoparticle monolayers, *Nat. Mater.* **5**, 265 (2006).
[295] J. He, X.-M. Lin, H. Chan, L. Vukovic, P. Kral, and H. M. Jaeger, Diffusion and Filtration Properties of Self-Assembled Gold Nanocrystal Membranes, *Nano Lett.* **11**, 2430 (2011).
[296] Z. Jiang, X.-M. Lin, M. Sprung, S. Narayanan, and J. Wang, Capturing the Crystalline Phase of Two-Dimensional Nanocrystal Superlattices in Action, *Nano Lett.* **10**, 799 (2010).
[297] A. Sanchez-Iglesias, M. Grzelczak, J. Perez-Juste, and L. M. Liz-Marzan, Binary Self-Assembly of Gold Nanowires with Nanospheres and Nanorods, *Angew. Chem. Int. Ed. Engl.* **49**, 9985 (2010).

[298] A. G. Dong, J. Chen, P. M. Vora, J. M. Kikkawa, and C. B. Murray, Binary nanocrystal superlattice membranes self-assembled at the liquid-air interface, *Nature* **466**, 474 (2010).
[299] A. G. Dong, X. C. Ye, J. Chen, and C. B. Murray, Two-Dimensional Binary and Ternary Nanocrystal Superlattices: The Case of Monolayers and Bilayers, *Nano Lett.* **11**, 1804 (2011).
[300] X. Ye, J. E. Collins, Y. Kang, J. Chen, D. T. N. Chen, A. G. Yodh, and C. B. Murray, Morphologically controlled synthesis of colloidal upconversion nanophosphors and their shape-directed self-assembly, *Proc. Natl. Acad. Sci. U. S. A.* **107**, 22430 (2010).
[301] A. Dong, X. Ye, J. Chen, Y. Kang, T. Gordon, J. M. Kikkawa, and C. B. Murray, A Generalized Ligand-Exchange Strategy Enabling Sequential Surface Functionalization of Colloidal Nanocrystals, *J. Am. Chem. Soc.* **133**, 998 (2011).
[302] K. Miszta *et al.*, Hierarchical self-assembly of suspended branched colloidal nanocrystals into superlattice structures, *Nat. Mater.* **10**, 872 (2011).
[303] T. Wang *et al.*, Self-Assembled Colloidal Superparticles from Nanorods, *Science* **338**, 358 (2012).
[304] S. Kutuzov, J. He, R. Tangirala, T. Emrick, T. P. Russell, and A. Boeker, On the kinetics of nanoparticle self-assembly at liquid/liquid interfaces, *Phys. Chem. Chem. Phys.* **9**, 6351 (2007).
[305] Y. Lin, H. Skaff, T. Emrick, A. D. Dinsmore, and T. P. Russell, Nanoparticle assembly and transport at liquid-liquid interfaces, *Science* **299**, 226 (2003).
[306] H. W. Duan, D. Y. Wang, D. G. Kurth, and H. Mohwald, Directing self-assembly of nanoparticles at water/oil interfaces, *Angew. Chem. Int. Ed. Engl.* **43**, 5639 (2004).
[307] H. W. Gu, Z. M. Yang, J. H. Gao, C. K. Chang, and B. Xu, Heterodimers of nanoparticles: Formation at a liquid-liquid interface and particle-specific surface modification by functional molecules, *J. Am. Chem. Soc.* **127**, 34 (2005).
[308] B. J. Park and E. M. Furst, Fluid-interface templating of two-dimensional colloidal crystals, *Soft Matter* **6**, 485 (2010).
[309] M. I. Bodnarchuk, L. Li, A. Fok, S. Nachtergaele, R. F. Ismagilov, and D. V. Talapin, Three-Dimensional Nanocrystal Superlattices Grown in Nanoliter Microfluidic Plugs, *J. Am. Chem. Soc.* **133**, 8956 (2011).
[310] M. Lisunova, N. Holland, O. Shchepelina, and V. V. Tsukruk, Template-Assisted Assembly of the Functionalized Cubic and Spherical Microparticles, *Langmuir* **28**, 13345 (2012).
[311] E. Fisslthaler, A. Bluemel, K. Landfester, U. Scherf, and E. J. W. List, Printing functional nanostructures: a novel route towards nanostructuring of organic electronic devices via soft embossing, inkjet printing and colloidal self assembly of semiconducting polymer nanospheres, *Soft Matter* **4**, 2448 (2008).
[312] A. Akey, C. Lu, L. Yang, and I. P. Herman, Formation of Thick, Large-Area Nanoparticle Superlattices in Lithographically Defined Geometries, *Nano Lett.* **10**, 1517 (2010).
[313] J. Liao, X. Li, Y. Wang, C. Zhang, J. Sun, C. Duan, Q. Chen, and L. Peng, Patterned Close-Packed Nanoparticle Arrays with Controllable Dimensions and Precise Locations, *Small* **8**, 991 (2012).
[314] D. Y. Wang and H. Mohwald, Rapid fabrication of binary colloidal crystals by stepwise spin-coating, *Adv. Mater.* **16**, 244 (2004).
[315] N. A. Kotov, I. Dekany, and J. H. Fendler, Layer-by-Layer Self-Assembly of Polyelectrolyte-Semiconductor Nanoparticle Composite Films, *J. Phys. Chem.* **99**, 13065 (1995).

[316] S. Srivastava and N. A. Kotov, Composite Layer-by-Layer (LBL) Assembly with Inorganic Nanoparticles and Nanowires, *Acc. Chem. Res.* **41**, 1831 (2008).
[317] M. Suda and Y. Einaga, Sequential Assembly of Phototunable Ferromagnetic Ultrathin Films with Perpendicular Magnetic Anisotropy, *Angew. Chem. Int. Ed. Engl.* **48**, 1754 (2009).
[318] L. M. Demers, S. J. Park, T. A. Taton, Z. Li, and C. A. Mirkin, Orthogonal assembly of nanoparticle building blocks on dip-pen nanolithographically generated templates of DNA, *Angew. Chem. Int. Ed. Engl.* **40**, 3071 (2001).
[319] H. D. Hill and C. A. Mirkin, The bio-barcode assay for the detection of protein and nucleic acid targets using DTT-induced ligand exchange, *Nat. Protoc.* **1**, 324 (2006).
[320] R. C. Jin, G. S. Wu, Z. Li, C. A. Mirkin, and G. C. Schatz, What controls the melting properties of DNA-linked gold nanoparticle assemblies?, *J. Am. Chem. Soc.* **125**, 1643 (2003).
[321] M. R. Jones, R. J. Macfarlane, B. Lee, J. Zhang, K. L. Young, A. J. Senesi, and C. A. Mirkin, DNA-nanoparticle superlattices formed from anisotropic building blocks, *Nat. Mater.* **9**, 913 (2010).
[322] M. A. Kostiainen, P. Hiekkataipale, A. Laiho, V. Lemieux, J. Seitsonen, J. Ruokolainen, and P. Ceci, Electrostatic assembly of binary nanoparticle superlattices using protein cages, *Nat. Nanotechnol.* **8**, 52 (2013).
[323] J. W. Liu and Y. Lu, A colorimetric lead biosensor using DNAzyme-directed assembly of gold nanoparticles, *J. Am. Chem. Soc.* **125**, 6642 (2003).
[324] H. Noh, C. Choi, A. M. Hung, S. Jin, and J. N. Cha, Site-Specific Patterning of Highly Ordered Nanocrystal Super lattices through Biomolecular Surface Confinement, *ACS Nano* **4**, 5076 (2010).
[325] S. J. Park, A. A. Lazarides, C. A. Mirkin, P. W. Brazis, C. R. Kannewurf, and R. L. Letsinger, The electrical properties of gold nanoparticle assemblies linked by DNA, *Angew. Chem. Int. Ed. Engl.* **39**, 3845 (2000).
[326] S. J. Park, A. A. Lazarides, C. A. Mirkin, and R. L. Letsinger, Directed assembly of periodic materials from protein and oligonucleotide-modified nanoparticle building blocks, *Angew. Chem. Int. Ed. Engl.* **40**, 2909 (2001).
[327] S. Y. Park, A. K. R. Lytton-Jean, B. Lee, S. Weigand, G. C. Schatz, and C. A. Mirkin, DNA-programmable nanoparticle crystallization, *Nature* **451**, 553 (2008).
[328] S. I. Stoeva, F. W. Huo, J. S. Lee, and C. A. Mirkin, Three-layer composite magnetic nanoparticle probes for DNA, *J. Am. Chem. Soc.* **127**, 15362 (2005).
[329] L. S. C. Pingree, O. G. Reid, and D. S. Ginger, Imaging the Evolution of Nanoscale Photocurrent Collection and Transport Networks during Annealing of Polythiophene/Fullerene Solar Cells, *Nano Lett.* **9**, 2946 (2009).
[330] C. Groves, O. G. Reid, and D. S. Ginger, Heterogeneity in Polymer Solar Cells: Local Morphology and Performance in Organic Photovoltaics Studied with Scanning Probe Microscopy, *Acc. Chem. Res.* **43**, 612 (2010).
[331] M. C. Lechmann, S. A. L. Weber, J. Geserick, N. Huesing, R. Berger, and J. S. Gutmann, Investigating morphology and electronic properties of self-assembled hybrid systems for solar cells, *J. Mater. Chem.* **21**, 7765 (2011).
[332] M. Osaka, H. Benten, L.-T. Lee, H. Ohkita, and S. Ito, Development of highly conductive nanodomains in poly(3-hexylthiophene) films studied by conductive atomic force microscopy, *Polymer* **54**, 3443 (2013).
[333] H. Scher and R. Zallen, Critical density in percolation processes, *J. Chem. Phys.* **53**, 3759 (1970).

[334] L. A. Renna, M. Bag, T. S. Gehan, X. Han, P. M. Lahti, D. Maroudas, and D. Venkataraman, Tunable Percolation in Semiconducting Binary Polymer Nanoparticle Glasses, *J. Phys. Chem. B* **120**, 2544 (2016).
[335] S. Vionnet-Menot, C. Grimaldi, T. Maeder, S. Strässler, and P. Ryser, Tunneling-percolation origin of nonuniversality: Theory and experiments, *Phys. Rev. B* **71**, 064201 (2005).
[336] M. Cattani and M. C. Salvadori, Insulator-Conductor Transition: A Brief Theoretical Review, *arXiv preprint arXiv:0903.3587* (2009).
[337] A. F. Wells, *Structural Inorganic Chemistry* (Oxford University Press, New York, NY, USA, 1975), 4th edn., p.^pp. 57-64.
[338] D. Venkataraman, Y. Du, S. R. Wilson, K. A. Hirsch, P. Zhang, and J. S. Moore, A Coordination Geometry Table of the d-Block Elements and Their Ions, *J. Chem. Educ.* **74**, 915 (1997).
[339] A. T. Balaban, Applications of Graph-Theory in Chemistry, *J. Chem. Inf. Comput. Sci.* **25**, 334 (1985).
[340] D. Venkataraman, S. Lee, J. S. Moore, P. Zhang, K. A. Hirsch, G. B. Gardner, A. C. Covey, and C. L. Prentice, Coordination networks based on multitopic ligands and silver(I) salts: A study of network connectivity and topology as a function of counterion, *Chem. Mater.* **8**, 2030 (1996).
[341] M. C. Etter, Encoding and Decoding Hydrogen-Bond Patterns of Organic-Compounds, *Acc. Chem. Res.* **23**, 120 (1990).
[342] B. G. Sumpter and D. W. Noid, Neural networks and graph theory as computational tools for predicting polymer properties, *Macromol. Theory Simul.* **3**, 363 (1994).
[343] E. Bullmore and O. Sporns, Complex brain networks: graph theoretical analysis of structural and functional systems, *Nat. Rev. Neurosci.* **10**, 186 (2009).
[344] J. Živkovic and B. Tadic, Nanonetworks: The graph theory framework for modeling nanoscale systems, *Nanoscale Syst. Math. Model. Theory Appl.* **2**, 30 (2013).
[345] M. Suvakov and B. Tadic, Modeling collective charge transport in nanoparticle assemblies, *J. Phys. Condens. Matter.* **22**, 163201 (2010).
[346] D. Venkataraman, G. B. Gardner, S. Lee, and J. S. Moore, Zeolite-Like Behavior of a Coordination Network, *J. Am. Chem. Soc.* **117**, 11600 (1995).
[347] B. C. Thompson and J. M. Frechet, Polymer-fullerene composite solar cells, *Angew. Chem. Int. Ed. Engl.* **47**, 58 (2008).
[348] Q. Sun, Z. Dai, X. Meng, and F. S. Xiao, Porous polymer catalysts with hierarchical structures, *Chem. Soc. Rev.* **44**, 6018 (2015).
[349] O. D. Velev and A. M. Lenhoff, Colloidal crystals as templates for porous materials, *Curr. Opin. Colloid Interface Sci.* **5**, 56 (2000).
[350] G. P. Moriarty, J. H. Whittemore, K. A. Sun, J. W. Rawlins, and J. C. Grunlan, Influence of polymer particle size on the percolation threshold of electrically conductive latex-based composites, *Journal of Polymer Science Part B: Polymer Physics* **49**, 1547 (2011).
[351] J. Sax and J. M. Ottino, Modeling of Transport of Small Molecules in Polymer Blends - Application of Effective Medium Theory, *Polym. Eng. Sci.* **23**, 165 (1983).
[352] I. Balberg, in *Semiconducting Polymer Composites: Principles, Morphologies, Properties and Applications*, edited by X. Yang (Wiley-VCH Verlag GmbH & Co. KGaA, Weinheim, Germany, 2012), pp. 145.

[353] S. Torquato, *Random heterogeneous materials: microstructure and macroscopic properties* (Springer Science & Business Media, Harrisonburg, VA, USA, 2013), Vol. 16, Interdisciplinary Applied Mathematics.
[354] Y. D. Park, H. S. Lee, Y. J. Choi, D. Kwak, J. H. Cho, S. Lee, and K. Cho, Solubility-Induced Ordered Polythiophene Precursors for High-Performance Organic Thin-Film Transistors, *Adv. Funct. Mater.* **19**, 1200 (2009).
[355] C. C. Chou, H. C. Wu, C. J. Lin, E. Ghelichkhani, and W. C. Chen, Morphology and Field-Effect Transistor Characteristics of Electrospun Nanofibers Prepared From Crystalline Poly(3-hexylthiophene) and Polyacrylate Blends, *Macromol. Chem. Phys.* **214**, 751 (2013).
[356] H. Pang, L. Xu, D.-X. Yan, and Z.-M. Li, Conductive polymer composites with segregated structures, *Prog. Polym. Sci.* **39**, 1908 (2014).
[357] L. M. Chen, Z. R. Hong, G. Li, and Y. Yang, Recent Progress in Polymer Solar Cells: Manipulation of Polymer: Fullerene Morphology and the Formation of Efficient Inverted Polymer Solar Cells, *Adv. Mater.* **21**, 1434 (2009).
[358] L. Qiu, W. H. Lee, X. Wang, J. S. Kim, J. A. Lim, D. Kwak, S. Lee, and K. Cho, Organic Thin-film Transistors Based on Polythiophene Nanowires Embedded in Insulating Polymer, *Adv. Mater.* **21**, 1349 (2009).
[359] L. Qiu, X. Wang, W. H. Lee, J. A. Lim, J. S. Kim, D. Kwak, and K. Cho, Organic Thin-Film Transistors Based on Blends of Poly(3-hexylthiophene) and Polystyrene with a Solubility-Induced Low Percolation Threshold, *Chem. Mater.* **21**, 4380 (2009).
[360] E. Ma, Tuning order in disorder, *Nat. Mater.* **14**, 547 (2015).
[361] J. Ding, S. Patinet, M. L. Falk, Y. Cheng, and E. Ma, Soft spots and their structural signature in a metallic glass, *Proc. Natl. Acad. Sci. U. S. A.* **111**, 14052 (2014).
[362] P. N. Pusey and W. van Megen, Observation of a glass transition in suspensions of spherical colloidal particles, *Phys. Rev. Lett.* **59**, 2083 (1987).
[363] D. T. Toolan, S. Fujii, S. J. Ebbens, Y. Nakamura, and J. R. Howse, On the mechanisms of colloidal self-assembly during spin-coating, *Soft Matter* **10**, 8804 (2014).
[364] K. W. Desmond and E. R. Weeks, Random close packing of disks and spheres in confined geometries, *Phys. Rev. E* **80**, 051305, 051305 (2009).
[365] M. D. Rintoul and S. Torquato, Precise determination of the critical threshold and exponents in a three-dimensional continuum percolation model, *J. Phys. A: Math. Gen.* **30**, L585 (1997).
[366] N. Xu, J. Blawzdziewicz, and C. S. O'Hern, Random close packing revisited: Ways to pack frictionless disks, *Phys. Rev. E* **71**, 061306 (2005).
[367] A. Donev, F. H. Stillinger, and S. Torquato, Configurational entropy of binary hard-disk glasses: nonexistence of an ideal glass transition, *J. Chem. Phys.* **127**, 124509 (2007).
[368] R. Seyboldt, D. Hajnal, F. Weysser, and M. Fuchs, Shear moduli of two dimensional binary glasses, *Soft Matter* **8**, 4132 (2012).
[369] R. O. Rosenberg, D. Thirumalai, and R. D. Mountain, Liquid, Crystalline and Glassy States of Binary Charged Colloidal Suspensions, *J. Phys. Condens. Matter* **1**, 2109 (1989).
[370] A. Donev, F. H. Stillinger, and S. Torquato, Do binary hard disks exhibit an ideal glass transition?, *Phys. Rev. Lett.* **96**, 225502 (2006).
[371] B. Coluzzi, M. Mezard, G. Parisi, and P. Verrocchio, Thermodynamics of binary mixture glasses, *J. Chem. Phys.* **111**, 9039 (1999).

[372] S.-I. Lee, Y. Song, T. W. Noh, X.-D. Chen, and J. R. Gaines, Experimental observation of nonuniversal behavior of the conductivity exponent for three-dimensional continuum percolation systems, *Phys. Rev. B* **34**, 6719 (1986).
[373] A. V. Neimark, Electrophysical Properties of a Finite Thickness Percolation Layer, *Sov. Phys. JETP* **98**, 611 (1990).
[374] A. Abbaspour, J.-L. Luo, and K. Nandakumar, Three-dimensional random resistor-network model for solid oxide fuel cell composite electrodes, *Electrochim. Acta* **55**, 3944 (2010).
[375] B. Zeimetz, B. A. Glowacki, and J. E. Evetts, Resistor network model for simulation of current and flux percolation in granular coated conductors, *Physica C* **372-376**, 767 (2002).
[376] D. Toker, D. Azulay, N. Shimoni, I. Balberg, and O. Millo, Tunneling and percolation in metal-insulator composite materials, *Phys. Rev. B* **68**, 041403 (2003).
[377] A. Alexeev, J. Loos, and M. M. Koetse, Nanoscale electrical characterization of semiconducting polymer blends by conductive atomic force microscopy (C-AFM), *Ultramicroscopy* **106**, 191 (2006).
[378] R. Viswanathan and M. B. Heaney, Direct imaging of the percolation network in a three-dimensional disordered conductor-insulator composite, *Phys. Rev. Lett.* **75**, 4433 (1995).
[379] R. Giridharagopal and D. S. Ginger, Characterizing Morphology in Bulk Heterojunction Organic Photovoltaic Systems, *J. Phys. Chem. Lett.* **1**, 1160 (2010).
[380] S. Torquato, T. M. Truskett, and P. G. Debenedetti, Is Random Close Packing of Spheres Well Defined?, *Phys. Rev. Lett.* **84**, 2064 (2000).
[381] Y. Yang, PhD Thesis, University of Massachusetts, 2015.
[382] G. Nagib and W. G. Ali, Network Routing Protocol using Genetic Algorithms, *IJECE* **10**, 36 (2010).
[383] E. Whitley and J. Ball, Statistics review 3: Hypothesis testing and P values, *Critical Care* **6**, 222 (2002).
[384] G. D. Scott and D. L. Mader, Angular Distribution of Random Close-packed Equal Spheres, *Nature* **201**, 382 (1964).
[385] P. A. Getting, Emerging Principles Governing the Operation of Neural Networks, *Annu. Rev. Neurosci.* **12**, 185 (1989).
[386] L. Muchnik, Complex Networks Package for MatLab (Version 1.6), 2013.
[387] A. J. Mozer and N. S. Sariciftci, Negative electric field dependence of charge carrier drift mobility in conjugated, semiconducting polymers, *Chem. Phys. Lett.* **389**, 438 (2004).
[388] P. M. Borsenberger, Hole transport in tri-p-tolylamine-doped bisphenol-A-polycarbonate, *J. Appl. Phys.* **68**, 6263 (1990).
[389] S. Goffri *et al.*, Multicomponent semiconducting polymer systems with low crystallization-induced percolation threshold, *Nat. Mater.* **5**, 950 (2006).
[390] J. H. Choi *et al.*, Exploiting the colloidal nanocrystal library to construct electronic devices, *Science* **352**, 205 (2016).
[391] X. Yu and V. M. Rotello, Nanoparticle devices: Going with the electron flow, *Nat Nano* **6**, 693 (2011).
[392] D. He, N. N. Ekere, and L. Cai, Computer simulation of random packing of unequal particles, *Phys. Rev. E* **60**, 7098 (1999).
[393] G. Aminoff, XI. Untersuchungen über die Kristallstrukturen von Wurtzit und Rotnickelkies, *Z. Kristallogr.* **58**, 203 (1923).
[394] M. J. Buerger, Interatomic distances in marcasite and notes on the bonding in crystals of loellingite, arsenopyrite, and marcasite types, *Z. Kristallogr.* **97**, 504 (1937).

[395] P. Auvray, F. Genet, and C. Lab01atoire, Affinement de la structure cristalline du cinabre oc-HgS, *Bull. Soc. Fr. Mineral. Cdstallogr.* **96**, 218 (1973).
[396] S. A. B.G. Hyde, *Inorganic Crystal Structures* (Wiley, New York, USA, 1989).
[397] R. W. G. Wyckoff, *Crystal Structures 1* (John Wiley & Sons, 1963), New York.
[398] C. H. Johansson and J. O. Linde, Röntgenographische und elektrische Untersuchungen des CuAu-Systems, *Annalen der Physik* **417**, 1 (1936).
[399] N. Alsén, Röntgenographische Untersuchung der Kristallstrukturen von Magnetkies, Breithauptit, Pentlandit, Millerit und verwandten Verbindungen, *Gff* **47**, 19 (1925).
[400] M. De Graef and M. E. McHenry, *Structure of materials: an introduction to crystallography, diffraction and symmetry* (Cambridge University Press, 2007).
[401] D. Chen, A. Nakahara, D. Wei, D. Nordlund, and T. P. Russell, P3HT/PCBM Bulk Heterojunction Organic Photovoltaics: Correlating Efficiency and Morphology, *Nano Lett.* **11**, 561 (2011).
[402] G. J. Hedley, A. J. Ward, A. Alekseev, C. T. Howells, E. R. Martins, L. A. Serrano, G. Cooke, A. Ruseckas, and I. D. W. Samuel, Determining the optimum morphology in high-performance polymer-fullerene organic photovoltaic cells, *Nat. Commun.* **4**, 1 (2013).
[403] Y. Huang, E. J. Kramer, A. J. Heeger, and G. C. Bazan, Bulk Heterojunction Solar Cells: Morphology and Performance Relationships, *Chem. Rev.*, DOI: 10.1021/cr400353v (2014).
[404] M. T. Dang, L. Hirsch, G. Wantz, and J. D. Wuest, Controlling the Morphology and Performance of Bulk Heterojunctions in Solar Cells. Lessons Learned from the Benchmark Poly(3-hexylthiophene): 6,6 -Phenyl-C-61-butyric Acid Methyl Ester System, *Chem. Rev.* **113**, 3734 (2013).
[405] C. L. Phillips and S. C. Glotzer, Effect of nanoparticle polydispersity on the self-assembly of polymer tethered nanospheres, *J. Chem. Phys.* **137**, 104901 (2012).
[406] J.-Y. Kim and N. A. Kotov, Charge Transport Dilemma of Solution-Processed Nanomaterials, *Chemistry of Materials* **26**, 134 (2014).
[407] T. Kietzke, D. Neher, M. Kumke, R. Montenegro, K. Landfester, and U. Scherf, A nanoparticle approach to control the phase separation in polyfluorene photovoltaic devices, *Macromolecules* **37**, 4882 (2004).
[408] N. Nicolaidis *et al.*, Solution processable interface materials for nanoparticulate organic photovoltaic devices, *Appl. Phys. Lett.* **104**, 043902, 043902 (2014).
[409] D. Minh Trung, L. Hirsch, and G. Wantz, P3HT:PCBM, Best Seller in Polymer Photovoltaic Research, *Adv. Mater.* **23**, 3597 (2011).
[410] J. J. Richards, C. L. Whittle, G. Shao, and L. D. Pozzo, Correlating Structure and Photocurrent for Composite Semiconducting Nanoparticles with Contrast Variation Small-Angle Neutron Scattering and Photoconductive Atomic Force Microscopy, *ACS Nano* **8**, 4313 (2014).
[411] S. Chambon, C. Schatz, V. Sebire, B. Pavageau, G. Wantz, and L. Hirsch, Organic semiconductor core-shell nanoparticles designed through successive solvent displacements, *Mater. Horiz.* **1**, 431 (2014).
[412] K. Landfester, R. Montenegro, U. Scherf, R. Guntner, U. Asawapirom, S. Patil, D. Neher, and T. Kietzke, Semiconducting polymer nanospheres in aqueous dispersion prepared by a miniemulsion process, *Adv. Mater.* **14**, 651 (2002).
[413] P. M. Borsenberger, L. Pautmeier, and H. Bässler, Charge transport in disordered molecular solids, *J. Chem. Phys.* **94**, 5447 (1991).
[414] M.-H. Ham, G. L. C. Paulus, C. Y. Lee, C. Song, K. Kalantar-zadeh, W. Choi, J.-H. Han, and M. S. Strano, Evidence for High-Efficiency Exciton Dissociation at Polymer/Single-Walled

Carbon Nanotube Interfaces in Planar Nano-heterojunction Photovoltaics, *ACS Nano* **4**, 6251 (2010).
[415] Y. J. Kim, W. Jang, D. H. Wang, and C. E. Park, Structure–Property Correlation: A Comparison of Charge Carrier Kinetics and Recombination Dynamics in All-Polymer Solar Cells, *J. Phys. Chem. C* **119**, 26311 (2015).
[416] S. N. Patel, A. E. Javier, G. M. Stone, S. A. Mullin, and N. P. Balsara, Simultaneous conduction of electronic charge and lithium ions in block copolymers, *ACS Nano* **6**, 1589 (2012).
[417] G. H. Fredrickson and F. S. Bates, Dynamics of block copolymers: Theory and experiment, *Annu. Rev. Mater. Sci.* **26**, 501 (1996).
[418] I. Riess, Mixed ionic-electronic conductors - material properties and applications, *Solid State Ion.* **157**, 1 (2003).
[419] A. Sreeram, S. Krishnan, S. J. DeLuca, A. Abidnejad, M. C. Turk, D. Roy, E. Honarvarfard, and P. J. G. Goulet, Simultaneous electronic and ionic conduction in ionic liquid imbibed polyacetylene-like conjugated polymer films, *RSC Adv.* **5**, 88425 (2015).
[420] N. Costantini, G. Wegner, M. Mierzwa, and T. Pakula, Simultaneous Ionic and Electronic Conductivity in Polymeric Materials, *Macromol. Chem. Phys.* **206**, 1345 (2005).
[421] D. Witker and M. D. Curtis, Lithium ion and electronic conductivity in 3-(oligoethylene oxide)thiophene comb-like polymers, *J. Power Sources* **156**, 525 (2006).
[422] K. S. Schanze and A. H. Shelton, Functional Polyelectrolytes, *Langmuir* **25**, 13698 (2009).
[423] X. M. Ren and P. G. Pickup, Ionic and Electronic Conductivity of Poly-(3-Methylpyrrole-4-Carboxylic Acid), *J. Electrochem. Soc.* **139**, 2097 (1992).
[424] X. M. Ren and P. G. Pickup, Coupling of Ion and Electron-Transport during Impedance Measurements on a Conducting Polymer with Similar Ionic and Electronic Conductivities, *J. Chem. Soc. Faraday Trans.* **89**, 321 (1993).
[425] P. Ferloni, M. Mastragostino, and L. Meneghello, Impedance analysis of electronically conducting polymers, *Electrochim. Acta* **41**, 27 (1996).
[426] J. Plocharski and H. Wycislik, Mixed conductivity in poly(p-phenylene) doped with iron chloride, *Solid State Ion.* **127**, 337 (2000).
[427] S. H. Glarum and J. H. Marshall, The Impedance of Poly(Aniline) Electrode Films, *J. Electrochem. Soc.* **134**, 142 (1987).
[428] H. Uramoto and N. Kawabata, Ionic conductivity of poly(4-vinylpyridine) complexed with lithium salts, *Electrochim. Acta* **39**, 2181 (1994).
[429] P. Atorngitjawat and J. Runt, Ion conduction and polymer dynamics of poly(2-vinylpyridine)-lithium perchlorate mixtures, *J. Phys. Chem. B* **111**, 13483 (2007).
[430] B. Kim, H. Ahn, J. H. Kim, D. Y. Ryu, and J. Kim, Transition behavior and ionic conductivity of lithium perchlorate-doped polystyrene-b-poly (2-vinylpyridine), *Polymer* **50**, 3822 (2009).
[431] S. Oh, D. W. Kim, C. Lee, M.-H. Lee, and Y. Kang, Poly(vinylpyridine-co-styrene) based in situ cross-linked gel polymer electrolyte for lithium-ion polymer batteries, *Electrochim. Acta* **57**, 46 (2011).
[432] A. L. Santana, L. K. Noda, A. T. N. Pires, and J. R. Bertolino, Poly (4-vinylpyridine)/cupric salt complexes: spectroscopic and thermal properties, *Polym. Test.* **23**, 839 (2004).

[433] G. Casalbore-Miceli, M. Yang, N. Camaioni, C.-M. Mari, Y. Li, H. Sun, and M. Ling, Investigations on the ion transport mechanism in conducting polymer films, *Solid State Ion.* **131**, 311 (2000).
[434] V. N. Manoharan and D. J. Pine, Building materials by packing spheres, *MRS Bull.* **29**, 91 (2004).
[435] G. R. Yi, V. N. Manoharan, E. Michel, M. T. Elsesser, S. M. Yang, and D. J. Pine, Colloidal clusters of silica or polymer microspheres, *Adv. Mater.* **16**, 1204 (2004).
[436] R. Mehra, Application of refractive index mixing rules in binary systems of hexadecane and heptadecane withn-alkanols at different temperatures, *J. Chem. Sci.* **115**, 147 (2003).
[437] D. Subbaramaiya, in *Proceedings of the Indian Academy of Sciences-Section A* (Springer, 1934), pp. 355.
[438] C. J. Chin, S. Yiacoumi, C. Tsouris, S. Relle, and S. B. Grant, Secondary-minimum aggregation of superparamagnetic colloidal particles, *Langmuir* **16**, 3641 (2000).
[439] M. P. Taylor and J. E. G. Lipson, Effects of solvent on polymer chain dimensions: a Born-Green-Yvon integral equation study, *Fluid Phase Equilib.* **150**, 641 (1998).
[440] http://www.nrel.gov/pv/assets/images/efficiency_chart.jpg.
[441] B. R. Sutherland and E. H. Sargent, Perovskite photonic sources, *Nat. Photonics* **10**, 295 (2016).
[442] B. Saparov and D. B. Mitzi, Organic–Inorganic Perovskites: Structural Versatility for Functional Materials Design, *Chem. Rev.* **116**, 4558 (2016).
[443] A. H. Slavney, T. Hu, A. M. Lindenberg, and H. I. Karunadasa, A Bismuth-Halide Double Perovskite with Long Carrier Recombination Lifetime for Photovoltaic Applications, *J. Am. Chem. Soc.* **138**, 2138 (2016).
[444] C. C. Stoumpos, D. H. Cao, D. J. Clark, J. Young, J. M. Rondinelli, J. I. Jang, J. T. Hupp, and M. G. Kanatzidis, Ruddlesden–Popper Hybrid Lead Iodide Perovskite 2D Homologous Semiconductors, *Chem. Mater.* **28**, 2852 (2016).
[445] T. Baikie, Y. N. Fang, J. M. Kadro, M. Schreyer, F. X. Wei, S. G. Mhaisalkar, M. Graetzel, and T. J. White, Synthesis and crystal chemistry of the hybrid perovskite (CH3NH3) PbI3 for solid-state sensitised solar cell applications, *J. Mater. Chem. A* **1**, 5628 (2013).
[446] V. M. Goldschmidt, Die gesetze der krystallochemie, *Naturwissenschaften* **14**, 477 (1926).
[447] Z. Li, M. Yang, J.-S. Park, S.-H. Wei, J. J. Berry, and K. Zhu, Stabilizing Perovskite Structures by Tuning Tolerance Factor: Formation of Formamidinium and Cesium Lead Iodide Solid-State Alloys, *Chem. Mater.* **28**, 284 (2016).
[448] H. Mashiyama, Y. Kurihara, and T. Azetsu, Disordered cubic perovskite structure of CH3NH3PbX3 (X = Cl, Br, I), *J. Korean Phys. Soc.* **32**, S156 (1998).
[449] M. Bag, L. A. Renna, R. Y. Adhikari, S. Karak, F. Liu, P. M. Lahti, T. P. Russell, M. T. Tuominen, and D. Venkataraman, Kinetics of Ion Transport in Perovskite Active Layers and Its Implications for Active Layer Stability, *J. Am. Chem. Soc.* **137**, 13130 (2015).
[450] J. Burschka, N. Pellet, S. J. Moon, R. Humphry-Baker, P. Gao, M. K. Nazeeruddin, and M. Gratzel, Sequential deposition as a route to high-performance perovskite-sensitized solar cells, *Nature* **499**, 316 (2013).
[451] L. Etgar, P. Gao, Z. Xue, Q. Peng, A. K. Chandiran, B. Liu, M. K. Nazeeruddin, and M. Gratzel, Mesoscopic CH3NH3PbI3/TiO2 heterojunction solar cells, *J. Am. Chem. Soc.* **134**, 17396 (2012).

[452] J. H. Heo *et al.*, Efficient inorganic-organic hybrid heterojunction solar cells containing perovskite compound and polymeric hole conductors, *Nat. Photonics* **7**, 487 (2013).
[453] N. J. Jeon, J. H. Noh, Y. C. Kim, W. S. Yang, S. Ryu, and S. I. Seok, Solvent engineering for high-performance inorganic-organic hybrid perovskite solar cells, *Nat. Mater.* **13**, 897 (2014).
[454] M. M. Lee, J. Teuscher, T. Miyasaka, T. N. Murakami, and H. J. Snaith, Efficient hybrid solar cells based on meso-superstructured organometal halide perovskites, *Science* **338**, 643 (2012).
[455] M. Liu, M. B. Johnston, and H. J. Snaith, Efficient planar heterojunction perovskite solar cells by vapour deposition, *Nature* **501**, 395 (2013).
[456] M. D. McGehee, Perovskite solar cells: Continuing to soar, *Nat. Mater.* **13**, 845 (2014).
[457] H. J. Snaith, Perovskites: The Emergence of a New Era for Low-Cost, High-Efficiency Solar Cells, *J. Phys. Chem. Lett.* **4**, 3623 (2013).
[458] H. Zhou *et al.*, Photovoltaics. Interface engineering of highly efficient perovskite solar cells, *Science* **345**, 542 (2014).
[459] J. You *et al.*, Low-temperature solution-processed perovskite solar cells with high efficiency and flexibility, *ACS Nano* **8**, 1674 (2014).
[460] J. A. Christians, P. A. Miranda Herrera, and P. V. Kamat, Transformation of the Excited State and Photovoltaic Efficiency of CH3NH3PbI3 Perovskite upon Controlled Exposure to Humidified Air, *J. Am. Chem. Soc.* **137**, 1530 (2015).
[461] J. Yang, B. D. Siempelkamp, D. Liu, and T. L. Kelly, Investigation of CH3NH3PbI3 Degradation Rates and Mechanisms in Controlled Humidity Environments Using in Situ Techniques, *ACS Nano* **9**, 1955 (2015).
[462] V. Freger and S. Bason, Characterization of ion transport in thin films using electrochemical impedance spectroscopy. I. Principles and theory, *J. Membr. Sci.* **302**, 1 (2007).
[463] Q.-C. Zhuang, T. Wei, L.-L. Du, Y.-L. Cui, L. Fang, and S.-G. Sun, An Electrochemical Impedance Spectroscopic Study of the Electronic and Ionic Transport Properties of Spinel LiMn2O4, *J. Phys. Chem. C* **114**, 8614 (2010).
[464] M. Li, M. J. Pietrowski, R. A. De Souza, H. Zhang, I. M. Reaney, S. N. Cook, J. A. Kilner, and D. C. Sinclair, A family of oxide ion conductors based on the ferroelectric perovskite Na0. 5Bi0. 5TiO3, *Nat. Mater.* **13**, 31 (2014).
[465] M. Hu, L. Liu, A. Mei, Y. Yang, T. Liu, and H. Han, Efficient hole-conductor-free, fully printable mesoscopic perovskite solar cells with a broad light harvester NH2CH=NH2PbI3, *J. Mater. Chem. A* **2**, 17115 (2014).
[466] J. Bisquert, I. Mora-Sero, and F. Fabregat-Santiago, Diffusion–Recombination Impedance Model for Solar Cells with Disorder and Nonlinear Recombination, *ChemElectroChem* **1**, 289 (2014).
[467] J. Jamnik and J. Maier, Treatment of the Impedance of Mixed Conductors Equivalent Circuit Model and Explicit Approximate Solutions, *J. Electrochem. Soc.* **146**, 4183 (1999).
[468] W. Lai and S. M. Haile, Impedance Spectroscopy as a Tool for Chemical and Electrochemical Analysis of Mixed Conductors: A Case Study of Ceria, *J. Am. Ceram. Soc.* **88**, 2979 (2005).
[469] P. Jasinski, V. Petrovsky, T. Suzuki, and H. U. Anderson, Impedance Studies of Diffusion Phenomena and Ionic and Electronic Conductivity of Cerium Oxide, *J. Electrochem. Soc.* **152**, J27 (2005).

[470] A. R. Pascoe, N. W. Duffy, A. D. Scully, F. Huang, and Y.-B. Cheng, Insights into Planar CH3NH3PbI3Perovskite Solar Cells Using Impedance Spectroscopy, *J. Phys. Chem. C* **119**, 4444 (2015).
[471] E. J. Juarez-Perez, M. Wubetaler, F. Fabregat-Santiago, K. Lakus-Wollny, E. Mankel, T. Mayer, W. Jaegermann, and I. Mora-Sero, Role of the Selective Contacts in the Performance of Lead Halide Perovskite Solar Cells, *J Phys Chem Lett* **5**, 680 (2014).
[472] A. Pockett, G. E. Eperon, T. Peltola, H. J. Snaith, A. Walker, L. M. Peter, and P. J. Cameron, Characterization of Planar Lead Halide Perovskite Solar Cells by Impedance Spectroscopy, Open-Circuit Photovoltage Decay, and Intensity-Modulated Photovoltage/Photocurrent Spectroscopy, *J. Phys. Chem. C* **119**, 3456 (2015).
[473] Y. Shao, Z. Xiao, C. Bi, Y. Yuan, and J. Huang, Origin and elimination of photocurrent hysteresis by fullerene passivation in CH3NH3PbI3 planar heterojunction solar cells, *Nat. Commun.* **5**, 5784 (2014).
[474] O. Almora, I. Zarazua, E. Mas-Marza, I. Mora-Sero, J. Bisquert, and G. Garcia-Belmonte, Capacitive Dark Currents, Hysteresis, and Electrode Polarization in Lead Halide Perovskite Solar Cells, *J. Phys. Chem. Lett.* **6**, 1645 (2015).
[475] H. S. Kim, I. Mora-Sero, V. Gonzalez-Pedro, F. Fabregat-Santiago, E. J. Juarez-Perez, N. G. Park, and J. Bisquert, Mechanism of carrier accumulation in perovskite thin-absorber solar cells, *Nat. Commun.* **4**, 2242 (2013).
[476] J. A. Christians, R. C. Fung, and P. V. Kamat, An inorganic hole conductor for organo-lead halide perovskite solar cells. Improved hole conductivity with copper iodide, *J. Am. Chem. Soc.* **136**, 758 (2014).
[477] C. Ho, I. D. Raistrick, and R. A. Huggins, Application of A-C Techniques to the Study of Lithium Diffusion in Tungsten Trioxide Thin Films, *J. Electrochem. Soc.* **127**, 343 (1980).
[478] W. Sugimoto, H. Iwata, K. Yokoshima, Y. Murakami, and Y. Takasu, Proton and Electron Conductivity in Hydrous Ruthenium Oxides Evaluated by Electrochemical Impedance Spectroscopy: The Origin of Large Capacitance, *J. Phys. Chem. B* **109**, 7330 (2005).
[479] A. Binek, F. C. Hanusch, P. Docampo, and T. Bein, Stabilization of the Trigonal High-Temperature Phase of Formamidinium Lead Iodide, *J. Phys. Chem. Lett.* **6**, 1249 (2015).
[480] C. C. Stoumpos, C. D. Malliakas, and M. G. Kanatzidis, Semiconducting Tin and Lead Iodide Perovskites with Organic Cations: Phase Transitions, High Mobilities, and Near-Infrared Photoluminescent Properties, *Inorg. Chem.* **52**, 9019 (2013).
[481] H. S. Kim *et al.*, Lead iodide perovskite sensitized all-solid-state submicron thin film mesoscopic solar cell with efficiency exceeding 9%, *Sci Rep* **2**, 591, 591 (2012).
[482] N. J. Jeon, H. G. Lee, Y. C. Kim, J. Seo, J. H. Noh, J. Lee, and S. I. Seok, o-Methoxy Substituents in Spiro-OMeTAD for Efficient Inorganic-Organic Hybrid Perovskite Solar Cells, *J. Am. Chem. Soc.* **136**, 7837 (2014).
[483] J. W. Lee, D. J. Seol, A. N. Cho, and N. G. Park, High-efficiency perovskite solar cells based on the black polymorph of HC(NH2)2 PbI3, *Adv Mater* **26**, 4991 (2014).
[484] C. H. Chiang, Z. L. Tseng, and C. G. Wu, Planar heterojunction perovskite/PC71BM solar cells with enhanced open-circuit voltage via a (2/1)-step spin-coating process, *J. Mater. Chem. A* **2**, 15897 (2014).
[485] Z. G. Xiao, C. Bi, Y. C. Shao, Q. F. Dong, Q. Wang, Y. B. Yuan, C. G. Wang, Y. L. Gao, and J. S. Huang, Efficient, high yield perovskite photovoltaic devices grown by interdiffusion of solution-processed precursor stacking layers, *Energy Environ. Sci.* **7**, 2619 (2014).

[486] P. Docampo, S. Guldin, T. Leijtens, N. K. Noel, U. Steiner, and H. J. Snaith, Lessons Learned: From Dye-Sensitized Solar Cells to All-Solid-State Hybrid Devices, *Adv. Mater.* **26**, 4013 (2014).
[487] P. Gao, M. Graetzel, and M. K. Nazeeruddin, Organohalide lead perovskites for photovoltaic applications, *Energy Environ. Sci.* **7**, 2448 (2014).
[488] S. Kazim, M. K. Nazeeruddin, M. Graetzel, and S. Ahmad, Perovskite as Light Harvester: A Game Changer in Photovoltaics, *Angew. Chem. Int. Ed. Engl.* **53**, 2812 (2014).
[489] D. Liu and T. L. Kelly, Perovskite solar cells with a planar heterojunction structure prepared using room-temperature solution processing techniques, *Nat. Photonics* **8**, 133 (2014).
[490] M. Xiao *et al.*, A Fast Deposition-Crystallization Procedure for Highly Efficient Lead Iodide Perovskite Thin-Film Solar Cells, *Angew. Chem. Int. Ed. Engl.* **53**, 9898 (2014).
[491] Z. Xiao, Q. Dong, C. Bi, Y. Shao, Y. Yuan, and J. Huang, Solvent annealing of perovskite-induced crystal growth for photovoltaic-device efficiency enhancement, *Adv Mater* **26**, 6503 (2014).
[492] Y. Z. Wu, A. Islam, X. D. Yang, C. J. Qin, J. Liu, K. Zhang, W. Q. Peng, and L. Y. Han, Retarding the crystallization of PbI2 for highly reproducible planar-structured perovskite solar cells via sequential deposition, *Energy Environ. Sci.* **7**, 2934 (2014).
[493] P. P. Boix, K. Nonomura, N. Mathews, and S. G. Mhaisalkar, Current progress and future perspectives for organic/inorganic perovskite solar cells, *Mater. Today* **17**, 16 (2014).
[494] J. H. Noh, S. H. Im, J. H. Heo, T. N. Mandal, and S. I. Seok, Chemical Management for Colorful, Efficient, and Stable Inorganic-Organic Hybrid Nanostructured Solar Cells, *Nano Lett.* **13**, 1764 (2013).
[495] F. Hao, C. C. Stoumpos, R. P. H. Chang, and M. G. Kanatzidis, Anomalous Band Gap Behavior in Mixed Sn and Pb Perovskites Enables Broadening of Absorption Spectrum in Solar Cells, *J. Am. Chem. Soc.* **136**, 8094 (2014).
[496] W. Nie *et al.*, Solar cells. High-efficiency solution-processed perovskite solar cells with millimeter-scale grains, *Science* **347**, 522 (2015).
[497] J. H. Heo, H. J. Han, D. Kim, T. K. Ahn, and S. H. Im, Hysteresis-less inverted CH3NH3PbI3 planar perovskite hybrid solar cells with 18.1% power conversion efficiency, *Energy Environ. Sci.* **8**, 1602 (2015).
[498] W. S. Yang, J. H. Noh, N. J. Jeon, Y. C. Kim, S. Ryu, J. Seo, and S. I. Seok, High-performance photovoltaic perovskite layers fabricated through intramolecular exchange, *Science* **348**, 1234 (2015).
[499] N. Ahn, D. Y. Son, I. H. Jang, S. M. Kang, M. Choi, and N. G. Park, Highly Reproducible Perovskite Solar Cells with Average Efficiency of 18.3% and Best Efficiency of 19.7% Fabricated via Lewis Base Adduct of Lead(II) Iodide, *J. Am. Chem. Soc.* **137**, 8696 (2015).
[500] C. G. Wu, C. H. Chiang, Z. L. Tseng, M. K. Nazeeruddin, A. Hagfeldt, and M. Gratzel, High efficiency stable inverted perovskite solar cells without current hysteresis, *Energy Environ. Sci.* **8**, 2725 (2015).
[501] Y. Zhang *et al.*, Charge selective contacts, mobile ions and anomalous hysteresis in organic-inorganic perovskite solar cells, *Mater. Horiz.* **2**, 315 (2015).
[502] J. Y. Jeng *et al.*, Nickel oxide electrode interlayer in CH3 NH3 PbI3 perovskite/PCBM planar-heterojunction hybrid solar cells, *Adv Mater* **26**, 4107 (2014).

[503] B. Conings, L. Baeten, C. De Dobbelaere, J. D'Haen, J. Manca, and H.-G. Boyen, Perovskite-Based Hybrid Solar Cells Exceeding 10% Efficiency with High Reproducibility Using a Thin Film Sandwich Approach, *Adv. Mater.* **26**, 2041 (2014).
[504] S. N. Habisreutinger, T. Leijtens, G. E. Eperon, S. D. Stranks, R. J. Nicholas, and H. J. Snaith, Carbon Nanotube/Polymer Composites as a Highly Stable Hole Collection Layer in Perovskite Solar Cells, *Nano Lett.* **14**, 5561 (2014).
[505] E. Edri, S. Kirmayer, S. Mukhopadhyay, K. Gartsman, G. Hodes, and D. Cahen, Elucidating the charge carrier separation and working mechanism of CH3NH3PbI3-xClx perovskite solar cells, *Nat. Commun.* **5**, 3461 (2014).
[506] K. Wang, C. Liu, P. Du, J. Zheng, and X. Gong, Bulk heterojunction perovskite hybrid solar cells with large fill factor, *Energy Environ. Sci.* **8**, 1245 (2015).
[507] C. S. Ponseca, Jr. *et al.*, Organometal Halide Perovskite Solar Cell Materials Rationalized: Ultrafast Charge Generation, High and Microsecond-Long Balanced Mobilities, and Slow Recombination, *J. Am. Chem. Soc.* **136**, 5189 (2014).
[508] A. K. Chandiran, A. Yella, M. T. Mayer, P. Gao, M. K. Nazeeruddin, and M. Graetzel, Sub-Nanometer Conformal TiO2 Blocking Layer for High Efficiency Solid-State Perovskite Absorber Solar Cells, *Adv. Mater.* **26**, 4309 (2014).
[509] L. Zuo, Z. Gu, T. Ye, W. Fu, G. Wu, H. Li, and H. Chen, Enhanced Photovoltaic Performance of CH(3)NH(3)Pbl(3) Perovskite Solar Cells through Interfacial Engineering Using Self-Assembling Monolayer, *J. Am. Chem. Soc.* **137**, 2674 (2015).
[510] P. W. Liang, C. C. Chueh, X. K. Xin, F. Zuo, S. T. Williams, C. Y. Liao, and A. K. Y. Jen, High-Performance Planar-Heterojunction Solar Cells Based on Ternary Halide Large-Band-Gap Perovskites, *Adv. Energy Mater.* **5**, 1400960 (2015).
[511] C.-C. Chueh, C.-Z. Li, and A. K. Y. Jen, Recent progress and perspective in solution-processed Interfacial materials for efficient and stable polymer and organometal perovskite solar cells, *Energy Environ. Sci.* **8**, 1160 (2015).
[512] H. Azimi *et al.*, A Universal Interface Layer Based on an Amine-Functionalized Fullerene Derivative with Dual Functionality for Efficient Solution Processed Organic and Perovskite Solar Cells, *Adv. Energy Mater.* **5**, 1401692 (2015).
[513] H. Zhang, H. Azimi, Y. Hou, T. Ameri, T. Przybilla, E. Spiecker, M. Kraft, U. Scherf, and C. J. Brabec, Improved High-Efficiency Perovskite Planar Heterojunction Solar Cells via Incorporation of a Polyelectrolyte Interlayer, *Chem. Mater.* **26**, 5190 (2014).
[514] Q. Xue *et al.*, Highly efficient fullerene/perovskite planar heterojunction solar cells via cathode modification with an amino-functionalized polymer interlayer, *J. Mater. Chem. A* **2**, 19598 (2014).
[515] J. Seo, S. Park, Y. C. Kim, N. J. Jeon, J. H. Noh, S. C. Yoon, and S. I. Sang, Benefits of very thin PCBM and LiF layers for solution-processed p-i-n perovskite solar cells, *Energy Environ. Sci.* **7**, 2642 (2014).
[516] P. W. Liang, C. Y. Liao, C. C. Chueh, F. Zuo, S. T. Williams, X. K. Xin, J. Lin, and A. K. Jen, Additive enhanced crystallization of solution-processed perovskite for highly efficient planar-heterojunction solar cells, *Adv Mater* **26**, 3748 (2014).
[517] J. Y. Jeng, Y. F. Chiang, M. H. Lee, S. R. Peng, T. F. Guo, P. Chen, and T. C. Wen, CH3NH3PbI3 perovskite/fullerene planar-heterojunction hybrid solar cells, *Adv Mater* **25**, 3727 (2013).
[518] C. Kuang *et al.*, Highly Efficient Electron Transport Obtained by Doping PCBM with Graphdiyne in Planar-Heterojunction Perovskite Solar Cells, *Nano Lett.* **15**, 2756 (2015).

[519] J. Xu *et al.*, Perovskite-fullerene hybrid materials suppress hysteresis in planar diodes, *Nat. Commun.* **6**, 7081, 7081 (2015).
[520] K. Wojciechowski *et al.*, Heterojunction modification for highly efficient organic-inorganic perovskite solar cells, *ACS Nano* **8**, 12701 (2014).
[521] O. Malinkiewicz, A. Yella, Y. H. Lee, G. Minguez Espallargas, M. Graetzel, M. K. Nazeeruddin, and H. J. Bolink, Perovskite solar cells employing organic charge-transport layers, *Nat. Photonics* **8**, 128 (2014).
[522] P. W. Liang, C. C. Chueh, S. T. Williams, and A. K. Y. Jen, Roles of Fullerene-Based Interlayers in Enhancing the Performance of Organometal Perovskite Thin-Film Solar Cells, *Adv. Energy Mater.* **5**, 1402321 (2015).
[523] C. Li *et al.*, Efficient perovskite/fullerene planar heterojunction solar cells with enhanced charge extraction and suppressed charge recombination, *Nanoscale* **7**, 9771 (2015).
[524] Z. A. Page, V. V. Duzhko, and T. Emrick, Conjugated Thiophene-Containing Polymer Zwitterions: Direct Synthesis and Thin Film Electronic Properties, *Macromolecules* **46**, 344 (2013).
[525] Z. A. Page, Y. Liu, V. V. Duzhko, T. P. Russell, and T. Emrick, Fulleropyrrolidine interlayers: Tailoring electrodes to raise organic solar cell efficiency, *Science* **346**, 441 (2014).
[526] Y. Liu, Z. Page, S. Ferdous, F. Liu, P. Kim, T. Emrick, and T. Russell, Dual Functional Zwitterionic Fullerene Interlayer for Efficient Inverted Polymer Solar Cells, *Adv. Energy Mater.* **5**, 1500405 (2015).
[527] B. Qi and J. Wang, Fill factor in organic solar cells, *Phys. Chem. Chem. Phys.* **15**, 8972 (2013).
[528] H. J. Snaith *et al.*, Anomalous Hysteresis in Perovskite Solar Cells, *J. Phys. Chem. Lett.* **5**, 1511 (2014).
[529] P. Qin *et al.*, Yttrium-substituted nanocrystalline TiO2 photoanodes for perovskite based heterojunction solar cells, *Nanoscale* **6**, 1508 (2014).
[530] V. W. Bergmann *et al.*, Real-space observation of unbalanced charge distribution inside a perovskite-sensitized solar cell, *Nat. Commun.* **5**, 5001, 5001 (2014).
[531] V. Palermo, M. Palma, and P. Samori, Electronic characterization of organic thin films by Kelvin probe force microscopy, *Adv. Mater.* **18**, 145 (2006).
[532] D. Liu, J. Yang, and T. L. Kelly, Compact Layer Free Perovskite Solar Cells with 13.5% Efficiency, *J. Am. Chem. Soc.* **136**, 17116 (2014).
[533] Y. Hou *et al.*, Inverted, Environmentally Stable Perovskite Solar Cell with a Novel Low-Cost and Water-Free PEDOT Hole-Extraction Layer, *Adv. Energy Mater.* **5**, 1500543 (2015).
[534] C. Tao *et al.*, 17.6% stabilized efficiency in low-temperature processed planar perovskite solar cells, *Energy Environ. Sci.* **8**, 2365 (2015).
[535] Q. Guo, C. Li, W. Y. Qiao, S. Ma, F. Z. Wang, B. Zhang, L. H. Hu, S. Y. Dai, and Z. A. Tan, The growth of a CH3NH3PbI3 thin film using simplified close space sublimation for efficient and large dimensional perovskite solar cells, *Energy Environ. Sci.* **9**, 1486 (2016).
[536] J. Min *et al.*, Interface Engineering of Perovskite Hybrid Solar Cells with Solution-Processed Perylene-Diimide Heterojunctions toward High Performance, *Chem. Mater.* **27**, 227 (2015).
[537] H. P. Zhou *et al.*, Interface engineering of highly efficient perovskite solar cells, *Science* **345**, 542 (2014).

[538] N. J. Jeon, J. H. Noh, W. S. Yang, Y. C. Kim, S. Ryu, J. Seo, and S. I. Seok, Compositional engineering of perovskite materials for high-performance solar cells, *Nature* **517**, 476 (2015).
[539] H. Nishimura, N. Ishida, A. Shimazaki, A. Wakamiya, A. Saeki, L. T. Scott, and Y. Murata, Hole-Transporting Materials with a Two-Dimensionally Expanded pi-System around an Azulene Core for Efficient Perovskite Solar Cells, *J. Am. Chem. Soc.* **137**, 15656 (2015).
[540] K. Rakstys *et al.*, Triazatruxene-Based Hole Transporting Materials for Highly Efficient Perovskite Solar Cells, *J. Am. Chem. Soc.* **137**, 16172 (2015).
[541] W. Z. Li, J. D. Fan, J. W. Li, Y. H. Mai, and L. D. Wang, Controllable Grain Morphology of Perovskite Absorber Film by Molecular Self-Assembly toward Efficient Solar Cell Exceeding 17%, *J. Am. Chem. Soc.* **137**, 10399 (2015).
[542] W. Zhang *et al.*, Ultrasmooth organic-inorganic perovskite thin-film formation and crystallization for efficient planar heterojunction solar cells, *Nat. Commun.* **6**, 6142 (2015).
[543] P. Docampo, J. M. Ball, M. Darwich, G. E. Eperon, and H. J. Snaith, Efficient organometal trihalide perovskite planar-heterojunction solar cells on flexible polymer substrates, *Nat. Commun.* **4**, 2761 (2013).
[544] J. Seo, S. Park, Y. C. Kim, N. J. Jeon, J. H. Noh, S. C. Yoon, and S. I. Seok, Benefits of very thin PCBM and LiF layers for solution-processed p-i-n perovskite solar cells, *Energy & Environmental Science* **7**, 2642 (2014).
[545] Y. Liu, L. A. Renna, M. Bag, Z. A. Page, P. Kim, J. Choi, T. Emrick, D. Venkataraman, and T. P. Russell, High Efficiency Tandem Thin-Perovskite/Polymer Solar Cells with a Graded Recombination Layer, *ACS Appl. Mater. Interfaces* **8**, 7070 (2016).
[546] P. Cheng and X. W. Zhan, Stability of organic solar cells: challenges and strategies, *Chem. Soc. Rev.* **45**, 2544 (2016).
[547] Z. Zhu *et al.*, High-Performance Hole-Extraction Layer of Sol–Gel-Processed NiO Nanocrystals for Inverted Planar Perovskite Solar Cells, *Angew. Chem.* **126**, 12779 (2014).
[548] K. C. Wang *et al.*, p-type Mesoscopic Nickel Oxide/Organometallic Perovskite Heterojunction Solar Cells, *Sci. Rep.* **4**, 4756 (2014).
[549] W. Y. Chen, L. L. Deng, S. M. Dai, X. Wang, C. B. Tian, X. X. Zhan, S. Y. Xie, R. B. Huang, and L. S. Zheng, Low-cost solution-processed copper iodide as an alternative to PEDOT:PSS hole transport layer for efficient and stable inverted planar heterojunction perovskite solar cells, *J. Mater. Chem. A* **3**, 19353 (2015).
[550] J. H. Kim, P. W. Liang, S. T. Williams, N. Cho, C. C. Chueh, M. S. Glaz, D. S. Ginger, and A. K. Y. Jen, High-Performance and Environmentally Stable Planar Heterojunction Perovskite Solar Cells Based on a Solution-Processed Copper-Doped Nickel Oxide Hole-Transporting Layer, *Adv. Mater.* **27**, 695 (2015).
[551] O. Malinkiewicz, C. Roldan-Carmona, A. Soriano, E. Bandiello, L. Camacho, M. K. Nazeeruddin, and H. J. Bolink, Metal-Oxide-Free Methylammonium Lead Iodide Perovskite-Based Solar Cells: the Influence of Organic Charge Transport Layers, *Adv. Energy Mater.* **4**, 1400345 (2014).
[552] Q. Q. Lin, D. M. Stoltzfus, A. Armin, P. L. Burn, and P. Meredith, An Hydrophilic Anode Interlayer for Solution Processed Organohalide Perovskite Solar Cells, *Adv. Mater. Int.* **3**, 1500420 (2016).
[553] C. Y. Huang, W. F. Fu, C. Z. Li, Z. Q. Zhang, W. M. Qiu, M. M. Shi, P. Heremans, A. K. Y. Jen, and H. Z. Chen, Dopant-Free Hole-Transporting Material with a C-3h Symmetrical Truxene Core for Highly Efficient Perovskite Solar Cells, *J. Am. Chem. Soc.* **138**, 2528 (2016).

[554] A. El Labban, H. Chen, M. Kirkus, J. Barbe, S. Del Gobbo, M. Neophytou, I. McCulloch, and J. Eid, Improved Efficiency in Inverted Perovskite Solar Cells Employing a Novel Diarylamino-Substituted Molecule as PEDOT:PSS Replacement, *Adv. Energy Mater.* **6**, 1502101 (2016).
[555] H. Choi, C. K. Mai, H. B. Kim, J. Jeong, S. Song, G. C. Bazan, J. Y. Kim, and A. J. Heeger, Conjugated polyelectrolyte hole transport layer for inverted-type perovskite solar cells, *Nat. Commun.* **6**, 7348 (2015).
[556] X. D. Li, X. H. Liu, X. Y. Wang, L. X. Zhao, T. G. Jiu, and J. F. Fang, Polyelectrolyte based hole-transporting materials for high performance solution processed planar perovskite solar cells, *J. Mater. Chem. A* **3**, 15024 (2015).
[557] Z. A. Page, Y. Liu, E. Puodziukynaite, T. P. Russell, and T. Emrick, Hydrophilic Conjugated Polymers Prepared by Aqueous Horner-Wadsworth-Emmons Coupling, *Macromolecules* **49**, 2526 (2016).
[558] D. Forgacs, M. Sessolo, and H. J. Bolink, Lead acetate precursor based p-i-n perovskite solar cells with enhanced reproducibility and low hysteresis, *J. Mater. Chem. A* **3**, 14121 (2015).
[559] Y. Liu, M. Bag, L. A. Renna, Z. A. Page, P. Kim, T. Emrick, D. Venkataraman, and T. P. Russell, Understanding Interface Engineering for High-Performance Fullerene/Perovskite Planar Heterojunction Solar Cells, *Adv. Energy Mater.* **6**, 1501606 (2016).
[560] J. S. Manser and P. V. Kamat, Band filling with free charge carriers in organonietal halide perovskites, *Nat. Photonics* **8**, 737 (2014).
[561] W. B. Yan, Y. L. Li, Y. Li, S. Y. Ye, Z. W. Liu, S. F. Wang, Z. Q. Bian, and C. H. Huang, High-performance hybrid perovskite solar cells with open circuit voltage dependence on hole-transporting materials, *Nano Energy* **16**, 428 (2015).
[562] Q. F. Xue *et al.*, Improving Film Formation and Photovoltage of Highly Efficient Inverted-Type Perovskite Solar Cells through the Incorporation of New Polymeric Hole Selective Layers, *Adv. Energy Mater.* **6**, 1502021 (2016).
[563] Q. Q. Lin, A. Armin, R. C. R. Nagiri, P. L. Burn, and P. Meredith, Electro-optics of perovskite solar cells, *Nat. Photonics* **9**, 106 (2015).
[564] J. P. C. Baena *et al.*, Highly efficient planar perovskite solar cells through band alignment engineering, *Energy Environ. Sci.* **8**, 2928 (2015).
[565] D. Yang, R. X. Yang, J. Zhang, Z. Yang, S. Z. Liu, and C. Li, High efficiency flexible perovskite solar cells using superior low temperature TiO2, *Energy Environ. Sci.* **8**, 3208 (2015).
[566] C. Roldan-Carmona, P. Gratia, I. Zimmermann, G. Grancini, P. Gao, M. Graetzel, and M. K. Nazeeruddin, High efficiency methylammonium lead triiodide perovskite solar cells: the relevance of non-stoichiometric precursors, *Energy Environ. Sci.* **8**, 3550 (2015).
[567] J. H. Heo, H. J. Han, M. Lee, M. Song, D. H. Kim, and S. H. Im, Stable semi-transparent CH3NH3PbI3 planar sandwich solar cells, *Energy Environ. Sci.* **8**, 2922 (2015).
[568] M. A. Green and T. Bein, PHOTOVOLTAICS Perovskite cells charge forward, *Nat. Mater.* **14**, 559 (2015).
[569] C. D. Bailie *et al.*, Semi-transparent perovskite solar cells for tandems with silicon and CIGS, *Energy Environ. Sci.* **8**, 956 (2015).
[570] J. P. Mailoa, C. D. Bailie, E. C. Johlin, E. T. Hoke, A. J. Akey, W. H. Nguyen, M. D. McGehee, and T. Buonassisi, A 2-terminal perovskite/silicon multijunction solar cell enabled by a silicon tunnel junction, *Appl. Phys. Lett.* **106**, 121105 (2015).

[571] H. Uzu, M. Ichikawa, M. Hino, K. Nakano, T. Meguro, J. L. Hernandez, H. S. Kim, N. G. Park, and K. Yamamoto, High efficiency solar cells combining a perovskite and a silicon heterojunction solar cells via an optical splitting system, *Appl. Phys. Lett.* **106**, 013506 (2015).
[572] C. C. Chen, S. H. Bae, W. H. Chang, Z. R. Hong, G. Li, Q. Chen, H. P. Zhou, and Y. Yang, Perovskite/polymer monolithic hybrid tandem solar cells utilizing a low-temperature, full solution process, *Mater. Horiz.* **2**, 203 (2015).
[573] Y. Yang, Q. Chen, Y. T. Hsieh, T. B. Song, N. De Marco, H. P. Zhou, and Y. Yang, Multilayer Transparent Top Electrode for Solution Processed Perovskite/Cu(In,Ga) (Se,S)(2) Four Terminal Tandem Solar Cells, *ACS Nano* **9**, 7714 (2015).
[574] S. Albrecht *et al.*, Monolithic perovskite/silicon-heterojunction tandem solar cells processed at low temperature, *Energy Environ. Sci.* **9**, 81 (2016).
[575] J. H. Heo and S. H. Im, CH3NH3PbBr3–CH3NH3PbI3 Perovskite–Perovskite Tandem Solar Cells with Exceeding 2.2 V Open Circuit Voltage, *Adv. Mater.* (2015).
[576] T. B. Song, Q. Chen, H. P. Zhou, C. Y. Jiang, H. H. Wang, Y. Yang, Y. S. Liu, J. B. You, and Y. Yang, Perovskite solar cells: film formation and properties, *J. Mater. Chem. A* **3**, 9032 (2015).
[577] M. J. Yang, Y. Y. Zhou, Y. N. Zeng, C. S. Jiang, N. P. Padture, and K. Zhu, Square-Centimeter Solution-Processed Planar CH3NH3PbI3 Perovskite Solar Cells with Efficiency Exceeding 15%, *Adv. Mater.* **27**, 6363 (2015).
[578] E. Della Gaspera, Y. Peng, Q. C. Hou, L. Spiccia, U. Bach, J. J. Jasieniak, and Y. B. Cheng, Ultra-thin high efficiency semitransparent perovskite solar cells, *Nano Energy* **13**, 249 (2015).
[579] C. Y. Chang, K. T. Lee, W. K. Huang, H. Y. Siao, and Y. C. Chang, High-Performance, Air-Stable, Low-Temperature Processed Semitransparent Perovskite Solar Cells Enabled by Atomic Layer Deposition, *Chem. Mater.* **27**, 5122 (2015).
[580] Y. Y. Zhou, M. J. Yang, W. W. Wu, A. L. Vasiliev, K. Zhu, and N. P. Padture, Room-temperature crystallization of hybrid-perovskite thin films via solvent-solvent extraction for high-performance solar cells, *J. Mater. Chem. A* **3**, 8178 (2015).
[581] L. Serrano-Lujan, N. Espinosa, T. T. Larsen-Olsen, J. Abad, A. Urbina, and F. C. Krebs, Tin- and Lead-Based Perovskite Solar Cells under Scrutiny: An Environmental Perspective, *Adv. Energy Mater.* **5**, 1501119 (2015).
[582] Z. C. He, B. Xiao, F. Liu, H. B. Wu, Y. L. Yang, S. Xiao, C. Wang, T. P. Russell, and Y. Cao, Single-junction polymer solar cells with high efficiency and photovoltage, *Nat. Photonics* **9**, 174 (2015).
[583] F. Lang, M. A. Gluba, S. Albrecht, J. Rappich, L. Korte, B. Rech, and N. H. Nickel, Perovskite Solar Cells with Large-Area CVD-Graphene for Tandem Solar Cells, *J. Phys. Chem. Lett.* **6**, 2745 (2015).
[584] Q. Lin, A. Armin, P. L. Burn, and P. Meredith, Organohalide Perovskites for Solar Energy Conversion, *Acc. Chem. Res.* **49**, 545 (2016).
[585] J. Seo, J. H. Noh, and S. I. Seok, Rational Strategies for Efficient Perovskite Solar Cells, *Acc. Chem. Res.* **49**, 562 (2016).
[586] J.-W. Lee, H.-S. Kim, and N.-G. Park, Lewis Acid–Base Adduct Approach for High Efficiency Perovskite Solar Cells, *Acc. Chem. Res.* **49**, 311 (2016).
[587] J. M. Ball, M. M. Lee, A. Hey, and H. J. Snaith, Low-temperature processed meso-superstructured to thin-film perovskite solar cells, *Energy Environ. Sci.* **6**, 1739 (2013).

[588] S. D. Stranks, G. E. Eperon, G. Grancini, C. Menelaou, M. J. P. Alcocer, T. Leijtens, L. M. Herz, A. Petrozza, and H. J. Snaith, Electron-Hole Diffusion Lengths Exceeding 1 Micrometer in an Organometal Trihalide Perovskite Absorber, *Science* **342**, 341 (2013).
[589] P. Zhao, J. Xu, C. Ma, W. Ren, L. Wang, L. Bian, and A. Chang, Spontaneous polarization behaviors in hybrid halide perovskite film, *Scr. Mater.* **102**, 51 (2015).
[590] R. Shao, M. P. Nikiforov, and D. A. Bonnell, Photo-induced Charge Dynamics on BaTIO 3 (001) Surface Characterized by Surface Probe Microscopy, *Departmental Papers (MSE)*, 108 (2006).
[591] E. Edri, S. Kirmayer, A. Henning, S. Mukhopadhyay, K. Gartsman, Y. Rosenwaks, G. Hodes, and D. Cahen, Why Lead Methylammonium Tri-Iodide Perovskite-Based Solar Cells Require a Mesoporous Electron Transporting Scaffold (but Not Necessarily a Hole Conductor), *Nano Lett.* **14**, 1000 (2014).
[592] Y. Zhou *et al.*, A universal method to produce low-work function electrodes for organic electronics, *Science* **336**, 327 (2012).
[593] X. Wen, J. Wu, M. Ye, D. Gao, and C. Lin, Interface engineering via an insulating polymer for highly efficient and environmentally stable perovskite solar cells, *Chem. Commun.* **52**, 11355 (2016).
[594] E. J. Juarez-Perez, R. S. Sanchez, L. Badia, G. Garcia-Belmonte, Y. S. Kang, I. Mora-Sero, and J. Bisquert, Photoinduced Giant Dielectric Constant in Lead Halide Perovskite Solar Cells, *J Phys Chem Lett* **5**, 2390 (2014).
[595] Q. Q. Lin, A. Armin, P. L. Burn, and P. Meredith, Organohalide Perovskites for Solar Energy Conversion, *Acc. Chem. Res.* **49**, 545 (2016).
[596] G. Xing, N. Mathews, S. Sun, S. S. Lim, Y. M. Lam, M. Grätzel, S. Mhaisalkar, and T. C. Sum, Long-Range Balanced Electron- and Hole-Transport Lengths in Organic-Inorganic $CH_3NH_3PbI_3$, *Science* **342**, 344 (2013).
[597] Y. Zhao and K. Zhu, Charge Transport and Recombination in Perovskite $(CH_3NH_3)PbI_3$ Sensitized TiO_2 Solar Cells, *J. Phys. Chem. Lett.* **4**, 2880 (2013).
[598] B. Suarez, V. Gonzalez-Pedro, T. S. Ripolles, R. S. Sanchez, L. Otero, and I. Mora-Sero, Recombination Study of Combined Halides (Cl, Br, I) Perovskite Solar Cells, *J. Phys. Chem. Lett.* **5**, 1628 (2014).
[599] W. Yang, Y. Yao, and C.-Q. Wu, Origin of the high open circuit voltage in planar heterojunction perovskite solar cells: Role of the reduced bimolecular recombination, *J. Appl. Phys.* **117**, 095502 (2015).
[600] H.-S. Kim, J.-W. Lee, N. Yantara, P. P. Boix, S. A. Kulkarni, S. Mhaisalkar, M. Grätzel, and N.-G. Park, High efficiency solid-state sensitized solar cell-based on submicrometer rutile TiO_2 nanorod and $CH_3NH_3PbI_3$ perovskite sensitizer, *Nano Lett.* **13**, 2412 (2013).
[601] F. Hou, Z. Su, F. Jin, X. Yan, L. Wang, H. Zhao, J. Zhu, B. Chu, and W. Li, Efficient and stable planar heterojunction perovskite solar cells with a MoO_3/PEDOT:PSS hole transporting layer, *Nanoscale*, 9427 (2015).
[602] Z. Zhu *et al.*, Efficiency enhancement of perovskite solar cells through fast electron extraction: The role of graphene quantum dots, *J. Am. Chem. Soc.* **136**, 3760 (2014).
[603] Z. Yang, J. Ren, Z. Zhang, X. Chen, G. Guan, L. Qiu, Y. Zhang, and H. Peng, Recent Advancement of Nanostructured Carbon for Energy Applications, *Chem. Rev.* **115**, 5159 (2015).
[604] X. Wang, Z. Li, W. Xu, S. A. Kulkarni, S. K. Batabyal, S. Zhang, A. Cao, and L. H. Wong, TiO_2 nanotube arrays based flexible perovskite solar cells with transparent carbon nanotube electrode, *Nano Energy* **11**, 728 (2015).

[605] M. Cai, V. T. Tiong, T. Hreid, J. Bell, and H. Wang, An efficient hole transport material composite based on poly (3-hexylthiophene) and bamboo-structured carbon nanotubes for high performance perovskite solar cells, *J. Mater. Chem. A* **3**, 2784 (2015).
[606] S. N. Habisreutinger, T. Leijtens, G. E. Eperon, S. D. Stranks, R. J. Nicholas, and H. J. Snaith, Enhanced Hole Extraction in Perovskite Solar Cells Through Carbon Nanotubes, *J. Phys. Chem. Lett.* **5**, 4207 (2014).
[607] Z. H. Wei, H. N. Chen, K. Y. Yan, X. L. Zheng, and S. H. Yang, Hysteresis-free multi-walled carbon nanotube-based perovskite solar cells with a high fill factor, *J. Mater. Chem. A* **3**, 24226 (2015).
[608] Z. Li *et al.*, Carbon nanotubes as an efficient hole collector for high voltage methylammonium lead bromide perovskite solar cells, *Nanoscale* **8**, 6352 (2016).
[609] P. Schulz, A. M. Dowgiallo, M. J. Yang, K. Zhu, J. L. Blackburn, and J. J. Berry, Charge Transfer Dynamics between Carbon Nanotubes and Hybrid Organic Metal Halide Perovskite Films, *J. Phys. Chem. Lett.* **7**, 418 (2016).
[610] S. P. Jeong, C. J. Boyle, and D. Venkataraman, Poly(methyl methacrylate) end-functionalized with hexabenzocoronene as an effective dispersant for multi-walled carbon nanotubes, *Rsc Advances* **6**, 6107 (2016).
[611] P. C. Ma, N. A. Siddiqui, G. Marom, and J. K. Kim, Dispersion and functionalization of carbon nanotubes for polymer-based nanocomposites: A review, *Compos. Part A Appl. Sci. Manuf.* **41**, 1345 (2010).
[612] S. K. Samanta, M. Fritsch, U. Scherf, W. Gomulya, S. Z. Bisri, and M. A. Loi, Conjugated Polymer-Assisted Dispersion of Single-Wall Carbon Nanotubes: The Power of Polymer Wrapping, *Acc. Chem. Res.* **47**, 2446 (2014).
[613] Y. J. Kim, T. S. Shin, H. Do Choi, J. H. Kwon, Y.-C. Chung, and H. G. Yoon, Electrical conductivity of chemically modified multiwalled carbon nanotube/epoxy composites, *Carbon* **43**, 23 (2005).
[614] Y. Ando, X. Zhao, H. Shimoyama, G. Sakai, and K. Kaneto, Physical properties of multiwalled carbon nanotubes, *Int. J. Inorg. Mater.* **1**, 77 (1999).
[615] N. Pellet, P. Gao, G. Gregori, T. Y. Yang, M. K. Nazeeruddin, J. Maier, and M. Grätzel, Mixed-Organic-Cation Perovskite Photovoltaics for Enhanced Solar-Light Harvesting, *Angew. Chem. Int. Ed. Engl.* **53**, 3151 (2014).
[616] V. Gonzalez-Pedro, E. J. Juarez-Perez, W.-S. Arsyad, E. M. Barea, F. Fabregat-Santiago, I. Mora-Sero, and J. Bisquert, General Working Principles of $CH_3NH_3PbX_3$ Perovskite Solar Cells, *Nano Lett.* **14**, 888 (2014).
[617] L. Bertoluzzi, P. P. Boix, I. Mora-Sero, and J. Bisquert, Theory of Impedance Spectroscopy of Ambipolar Solar Cells with Trap-Mediated Recombination, *J. Phys. Chem. C* **118**, 16574 (2014).
[618] H.-S. Kim, I. Mora-Sero, V. Gonzalez-Pedro, F. Fabregat-Santiago, E. J. Juarez-Perez, N.-G. Park, and J. Bisquert, Mechanism of carrier accumulation in perovskite thin-absorber solar cells, *Nat. Commun.* **4**, Article No. 2242 (2013).
[619] V. D. Mihailetchi, L. J. A. Koster, J. C. Hummelen, and P. W. M. Blom, Photocurrent Generation in Polymer-Fullerene Bulk Heterojunctions, *Phys. Rev. Lett.* **93**, 216601 (2004).
[620] P. P. Boix, G. Larramona, A. Jacob, B. Delatouche, I. Mora-Seró, and J. Bisquert, Hole transport and recombination in all-solid Sb_2S_3-sensitized TiO_2 solar cells using CuSCN as hole transporter, *J. Phys. Chem. C* **116**, 1579 (2011).

[621] T. Dürkop, S. A. Getty, E. Cobas, and M. S. Fuhrer, Extraordinary Mobility in Semiconducting Carbon Nanotubes, *Nano Lett.* **4**, 35 (2004).
[622] M. Bag, L. A. Renna, S. P. Jeong, X. Han, C. L. Cutting, D. Maroudas, and D. Venkataraman, Evidence for reduced charge recombination in carbon nanotube/perovskite-based active layers, *Chem. Phys. Lett.* **662**, 35 (2016).
[623] T. J. Savenije *et al.*, Thermally Activated Exciton Dissociation and Recombination Control the Carrier Dynamics in Organometal Halide Perovskite, *J. Phys. Chem. Lett.* **5**, 2189 (2014).
[624] H.-J. Jhuo, P.-N. Yeh, S.-H. Liao, Y.-L. Li, S. Sharma, and S.-A. Chen, Inverted perovskite solar cells with inserted cross-linked electron-blocking interlayers for performance enhancement, *J. Mater. Chem. A* **3**, 9291 (2015).
[625] J. Nelson, *The physics of solar cells* (World Scientific, 2003), Vol. 57.
[626] Y. Zhang, L. C. Tan, Q. X. Fu, L. Chen, T. Ji, X. T. Hu, and Y. W. Chen, Enhancing the grain size of organic halide perovskites by sulfonate-carbon nanotube incorporation in high performance perovskite solar cells, *Chem. Commun.* **52**, 5674 (2016).
[627] J. Peet, A. J. Heeger, and G. C. Bazan, "Plastic" Solar Cells: Self-Assembly of Bulk Heterojunction Nanomaterials by Spontaneous Phase Separation, *Acc. Chem. Res.* **42** (2009).
[628] A. Kojima, K. Teshima, Y. Shirai, and T. Miyasaka, Organometal Halide Perovskites as Visible-Light Sensitizers for Photovoltaic Cells, *J. Am. Chem. Soc.* **131**, 6050 (2009).
[629] A. Mei *et al.*, A hole-conductor–free, fully printable mesoscopic perovskite solar cell with high stability, *Science* **345**, 295 (2014).
[630] A. Walsh, Principles of Chemical Bonding and Band Gap Engineering in Hybrid Organic–Inorganic Halide Perovskites, *J. Phys. Chem. C* **119**, 5755 (2015).
[631] L. M. Pazos-Outón *et al.*, Photon recycling in lead iodide perovskite solar cells, *Science* **351**, 1430 (2016).
[632] R. S. Sanchez, V. Gonzalez-Pedro, J.-W. Lee, N.-G. Park, Y. S. Kang, I. Mora-Sero, and J. Bisquert, Slow Dynamic Processes in Lead Halide Perovskite Solar Cells. Characteristic Times and Hysteresis, *J. Phys. Chem. Lett.* **5**, 2357 (2014).
[633] B. C. O'Regan, P. R. F. Barnes, X. Li, C. Law, E. Palomares, and J. M. Marin-Beloqui, Optoelectronic Studies of Methylammonium Lead Iodide Perovskite Solar Cells with Mesoporous TiO2: Separation of Electronic and Chemical Charge Storage, Understanding Two Recombination Lifetimes, and the Evolution of Band Offsets during J–V Hysteresis, *J. Am. Chem. Soc.* **137**, 5087 (2015).
[634] S. van Reenen, M. Kemerink, and H. J. Snaith, Modeling Anomalous Hysteresis in Perovskite Solar Cells, *J. Phys. Chem. Lett.* **6**, 3808 (2015).
[635] J. A. Christians, J. S. Manser, and P. V. Kamat, Best Practices in Perovskite Solar Cell Efficiency Measurements. Avoiding the Error of Making Bad Cells Look Good, *J. Phys. Chem. Lett.* **6**, 852 (2015).
[636] Y. Yuan and J. Huang, Ion Migration in Organometal Trihalide Perovskite and Its Impact on Photovoltaic Efficiency and Stability, *Acc. Chem. Res.* **49**, 286 (2016).
[637] B. Chen, M. Yang, S. Priya, and K. Zhu, Origin of J–V Hysteresis in Perovskite Solar Cells, *J. Phys. Chem. Lett.* **7**, 905 (2016).
[638] G. Richardson, S. O'Kane, R. G. Niemann, T. Peltola, J. M. Foster, P. J. Cameron, and A. Walker, Can slow-moving ions explain hysteresis in the current-voltage curves of perovskite solar cells?, *Energy Environ. Sci.* (2016).

[639] Y. Guo, W. Sato, K. Shoyama, and E. Nakamura, Sulfamic Acid-Catalyzed Lead Perovskite Formation for Solar Cell Fabrication on Glass or Plastic Substrates, *J. Am. Chem. Soc.* **138**, 5410 (2016).
[640] C.-G. Wu, C.-H. Chiang, Z.-L. Tseng, M. K. Nazeeruddin, A. Hagfeldt, and M. Graetzel, High efficiency stable inverted perovskite solar cells without current hysteresis, *Energy & Environmental Science* **8**, 2725 (2015).
[641] J. P. Correa-Baena *et al.*, Unbroken Perovskite: Interplay of Morphology, Electro-optical Properties, and Ionic Movement, *Adv. Mater.* (2016).
[642] Y. Shao *et al.*, Grain boundary dominated ion migration in polycrystalline organic-inorganic halide perovskite films, *Energy Environ. Sci.* **9**, 1752 (2016).
[643] I. Levine *et al.*, Interface-Dependent Ion Migration/Accumulation Controls Hysteresis in MAPbI3Solar Cells, *J. Phys. Chem. C* (2016).
[644] Q. Lin, A. Armin, R. C. R. Nagiri, P. L. Burn, and P. Meredith, Electro-optics of perovskite solar cells, *Nat Photon* **9**, 106 (2015).
[645] H.-S. Kim and N.-G. Park, Parameters Affecting I–V Hysteresis of CH3NH3PbI3 Perovskite Solar Cells: Effects of Perovskite Crystal Size and Mesoporous TiO2 Layer, *J. Phys. Chem. Lett.* **5**, 2927 (2014).
[646] H.-S. Kim, I.-H. Jang, N. Ahn, M. Choi, A. Guerrero, J. Bisquert, and N.-G. Park, Control of I–V Hysteresis in CH3NH3PbI3 Perovskite Solar Cell, *J. Phys. Chem. Lett.* **6**, 4633 (2015).
[647] Y. Li *et al.*, Multifunctional Fullerene Derivative for Interface Engineering in Perovskite Solar Cells, *J. Am. Chem. Soc.* **137**, 15540 (2015).
[648] Y. Li *et al.*, High-efficiency robust perovskite solar cells on ultrathin flexible substrates, *Nat. Commun.* **7** (2016).
[649] K. Zuiderveld, in *Graphics gems IV* (Academic Press Professional, Inc., 1994), pp. 474.
[650] F. Meyer, Topographic Distance and Watershed Lines, *Signal Processing* **38**, 113 (1994).
[651] S. Eddins, Cell Segmentation, The MathWorks, Inc., 2006.
[652] D. Legland, K. Kiêu, and M.-F. Devaux, Computation of Minkowski measures on 2D and 3D binary images, *Image Anal. Stereol.* **26**, 83 (2007).
[653] Y. Liu, Z. A. Page, T. P. Russell, and T. Emrick, Finely Tuned Polymer Interlayers Enhance Solar Cell Efficiency, *Angew. Chem. Int. Ed. Engl.* **54**, 11485 (2015).
[654] J. A. Labastide, H. B. Thompson, S. R. Marques, N. S. Colella, A. L. Briseno, and M. D. Barnes, Directional charge separation in isolated organic semiconductor crystalline nanowires, *Nat. Commun.* **7** (2016).
[655] F. Paquin, G. Latini, M. Sakowicz, P.-L. Karsenti, L. Wang, D. Beljonne, N. Stingelin, and C. Silva, Charge Separation in Semicrystalline Polymeric Semiconductors by Photoexcitation: Is the Mechanism Intrinsic or Extrinsic?, *Phys. Rev. Lett.* **106**, 197401 (2011).
[656] A. P. Nazarov and D. Thierry, Scanning Kelvin probe study of metal/polymer interfaces, *Electrochim. Acta* **49**, 2955 (2004).
[657] J. Lü, E. Delamarche, L. Eng, R. Bennewitz, E. Meyer, and H. J. Güntherodt, Kelvin Probe Force Microscopy on Surfaces: Investigation of the Surface Potential of Self-Assembled Monolayers on Gold, *Langmuir* **15**, 8184 (1999).
[658] H. Yuan, H. Shimotani, A. Tsukazaki, A. Ohtomo, M. Kawasaki, and Y. Iwasa, Hydrogenation-Induced Surface Polarity Recognition and Proton Memory Behavior at Protic-Ionic-Liquid/Oxide Electric-Double-Layer Interfaces, *J. Am. Chem. Soc.* **132**, 6672 (2010).

[659] D. B. Strukov, G. S. Snider, D. R. Stewart, and R. S. Williams, The missing memristor found, *Nature* **453**, 80 (2008).
[660] J. Blanc and D. L. Staebler, Electrocoloration in SrTiO3: Vacancy drift and oxidation-reduction of transition metals, *Phys. Rev. B* **4**, 3548 (1971).
[661] Z. Xiao and J. Huang, Energy-Efficient Hybrid Perovskite Memristors and Synaptic Devices, *Adv. Electron. Mater.* **2**, 1600100 (2016).
[662] Conductive AFM (ORCA). *Asylum Research User Manual* (2010).